



Jesica Paola Rada Arias

Binucleating aroylhydrazonic ligands and their dicopper(II) complexes as new classes of potential anticancer agents: syntheses, chemical characterization and biological activity

Tese de Doutorado

Thesis presented to the Programa de Pós-graduação em Química of PUC-Rio in partial fulfillment of the requirements for the degree of Doutor em Química.

Advisor: Prof. Nicolás Adrián Rey

Co-Advisor: Prof. Ana Maria Percebom

Rio de Janeiro
August 2019



Jesica Paola Rada Arias

Binucleating aroylhydrazonic ligands and their dicopper(II) complexes as new classes of potential anticancer agents: syntheses, chemical characterization and biological activity

Thesis presented to the Programa de Pós-graduação em Química of PUC-Rio in partial fulfillment of the requirements for the degree of Doutor em Química. Approved by the undersigned Examination Committee.

Prof. Nicolás Adrián Rey

Advisor

Department of Chemistry - PUC-Rio

Prof. Ana Maria Percebom

Co-advisor

Department of Chemistry- PUC-Rio

Prof. Maribel Coromoto Navarro Acosta

UFJF

Prof. Maria Domingues Vargas

UFF

Prof. Marcos Dias Pereira

UFRJ

Prof. Jones Limberger

Department of Chemistry- PUC-Rio

Prof. Ricardo Queiroz Aucélio

Department of Chemistry- PUC-Rio

Rio de Janeiro, August 16th 2019

Jesica Paola Rada Arias

Doctorate candidate in Chemistry of the Pontifical Catholic University of Rio de Janeiro (PUC-Rio). She received her Master's degree in Chemistry from PUC-Rio (2015) and her Bachelor in Chemistry from University of Atlantic in (2008). She developed her Ph.D. internship at Sorbonne University (Campus UPMC, Chembio). She has experience in Organic, Inorganic and Analytical Chemistry.

Bibliographic data

Rada, Jesica Paola Rada

Binucleating aroylhydrazonic ligands and their dicopper(II) complexes as new classes of potential anticancer agents: syntheses, chemical characterization and biological activity / Jesica Paola Rada Arias; advisor: Nicolás Adrián Rey; co-advisor: Ana Maria Percebom – 2019.

316 f. : il. color. ; 30 cm

Tese (doutorado) – Pontifícia Universidade Católica do Rio de Janeiro, Departamento de Química.

Inclui bibliografia

1. Química – Teses. 2. Ligantes aroíl-hidrazônicos. 3. Complexos de cobre(II). 4. Citotoxicidade. 5. Agentes anticâncer. 6. Interação com proteínas e DNA. 7. Imagem celular. I. Rey, Nicolás Adrián. II. Percebom, Ana Maria. III. Pontifícia Universidade Católica do Rio de Janeiro. Departamento de Química. IV. Título.

Acknowledgments

The current doctoral project was developed in LABSO-Bio from PUC-Rio laboratories headed by Dr. Nicolás Adrián Rey, and in Chembio from Sorbonne Université thanks to CAPES fellowship: PDSE-88881.187965/2018-0. The doctoral scholarship was supported by CNPq.

This study was financed in part by the Coordenação de Aperfeiçoamento de Pessoal de Nível Superior - Brasil (CAPES) - Finance Code 001.

I appreciate the important supervision of the present thesis by advisor Prof. Nicolás A. Rey and my co-advisor Prof. Ana Maria Percebom, and all the opportunities given by the Department of Chemistry. I am grateful to the examining members for agreeing to evaluate my thesis, along with their suggestions and comments.

I thank Beatriz Bastos, for the support in my doctoral project during her Scientific Initiation at PUC-Rio, and for our friendship. I really thank Dr. Ricardo Q. Aucélio for the support and kindness during the last four years, and for basic analysis and the availability of LEEA laboratory for the fluorescence measurements. I thank Fátima Almeida for all the help, especially during the uncertain times when I came to Brazil.

I want to thank all the members of Chembio at Sorbonne Université in Paris, for giving me the opportunity to enrich my doctoral thesis in their installations, for the supervision, suggestions and interest put in my doctoral project. Thanks to Michèle Salmain, Vincent Corcé, Serge Thorimbert, Anne, Nathalie, Candice, Benoît, Franck, Pascal, Robin, Anissa, Jérémy and Geoffrey for your significant help and for the “Tea Time”.

I would like to thank the Brazilian students and friends: Jefferson, Rosangela, Joseany, Joseanie, Druval and Veronica; the Honduras committee: Evelina, Azucena and Oliver; my great Mexican friend Adi; and finally the Colombian committee: Stéphanie, Wendy, Marlin, Jarol, Luis Miguel and Carlos for the good times spent with all of you. *Los quiero muchísimo.*

I am also thankful to my nephews Alejandro and Jesús David and my nieces Sara and Emma (*les dedico esta tesis*), to my sister Mercedes and to my brother Eduardo for making me feel happy. To my mom, Olga Lucía, for the encouragement and the efforts she made for my academic education. To my father Eduardo and to Osvaldo. To my uncles and aunts, cousins and all members of my family.

Finally, I am grateful to my husband Antonio Pele for the help, the translation's reviews, for giving me courage to carry on and all the beautiful moments. *Merci!*

Last but not least, I acknowledge the Brazilian National Synchrotron Laboratory (LNLS-CNPEM) for SAXS beamtime (SAXS1 – 20160298) for SAXS analysis.

Abstract

Rada, Jesica Paola Arias; Rey, Nicolás Adrián (Advisor); Percebom, Ana Maria (Co-advisor). **Binucleating aroylhydrazonic ligands and their dicopper(II) complexes as new classes of potential anticancer agents: syntheses, chemical characterization and biological activity.** Rio de Janeiro, 2019. 316p. Tese de doutorado - Departamento de Química, Pontifícia Universidade Católica do Rio de Janeiro.

On the search of new chemotherapeutic agents differing from the classic cisplatin family drugs, aroylhydrazonic derivatives and their copper(II) complexes appear as promising compounds. This thesis reports on the design and syntheses of a novel combination of them through eight new aroylhydrazones and their fourteen perchlorate and/or acetate Cu₂-complexes **1–14**. The obtained bioinspired copper(II) complexes constitute structural models for the active sites of some type 3 copper enzymes. The compounds were fully characterized using various spectroscopic and analytical techniques. X-ray diffraction structures for four ligands and five complexes are described in detail. Compounds' stability was studied in cellular medium and their biological activity was examined. The results include a large study on the interaction of two thiophene (**H₃L1**) or furan (**H₃L2**) ligand derivatives and their respective μ -hydroxo dicopper complexes **1** and **2** (first set of compounds) respectively, with bovine serum albumin protein and calf thymus DNA using different spectroscopic techniques, which include the binding affinity to BSA and DNA using UV/Visible and/or fluorescence techniques. Additionally, scattering techniques revealed that the interaction between the compounds and BSA induces reversible aggregation of the biomolecules. As an important contribution of the present work, the plasmid DNA cleavage ability of the complexes **1** and **2** was studied by Dynamic Light Scattering. The changes of hydrodynamic radius values of pBR322 plasmid DNA are correlated to the nick induced by the complexes in the helices. Cytotoxic assays on some cancer cells revealed the high ability of **H₃L1** and **H₃L2**, and complexes **1** and **2** to induce cell death. On the other hand, the many biological properties, including anticancer activity, of the isoxazole molecule, motivated the inclusion of this moiety in two ligands **H₃L3** and **H₂L4**

and four complexes **3–6** (second set of compounds). Interaction of these isoxazole-aroilylhydrazonic ligand derivatives with DNA was directly studied by absorbance and fluorescence spectroscopy, as a result of the fluorescence properties displayed by the ligands. In the case of the isoxazole-aroilylhydrazonic complexes-DNA interaction, the ethidium bromide displacement assay revealed significant affinity by intercalation binding mode of the nucleic acid in the DNA sequence. Additionally, this work successfully demonstrated that ligands and complexes containing a phenol pendant arm instead of a pyridine one improve the *in vitro* cytotoxicity on human epithelial breast cancer cells, attaining nanomolar range. Metal chelation and transmetallation ability of binucleating ligands **H₃L₃** and **H₂L₄** and their copper complexes **3–6** with Fe(II), Fe(III) and Zn(II) from the biological medium was verified as an additional cell death induction anticancer strategy. Moreover, to study the interaction of the compounds with the biological system and to demonstrate their cell permeability, ligands (**H₃L₅–H₃L₇**) and complexes (**7–12**) were functionalized in their hydrazone moieties with potent fluorophores, such pyrene (**H₃L₅**) (set three of compounds), benzopyranothiophene (**H₃L₆**), or boron-dipyrromethene (**H₃L₇**) derivatives (set four of compounds). Fluorescence microscopy studies proved the presence of ligand **H₃L₇** inside cancer cells, proving its ability to pass through the cell membrane. Besides, co-localization analysis for organelles showed the affinity of this ligand for the mitochondria. Finally, motivated by the wide spectrum of biological properties of the isoniazid molecule and its use in chemotherapy, this thesis reports the syntheses, characterization and cytotoxicity studies on cancer cells of a new isonicotinoyl hydrazone ligand (**H₂L₈**) and its perchlorate or acetate copper(II) complexes **13** and **14** (set five of compounds), which are involved in a patent request.

Keywords

Aroylhydrazonic ligands; Copper(II) complexes; Cytotoxicity; Anticancer agents; Albumin protein; DNA; Cell imaging.

Resumo

Rada, Jesica Paola Arias; Rey, Nicolás Adrián (orientador); Percebom, Ana Maria (co-orientadora). **Ligantes binucleantes aroíl-hidrazônicos e seus complexos binucleares de cobre(II) como novas classes de potenciais agentes anticâncer: sínteses, caracterização química e atividade biológica.** Rio de Janeiro, 2019. 316p. Tese de Doutorado - Departamento de Química, Pontifícia Universidade Católica do Rio de Janeiro.

Na busca de novos quimioterápicos diferentes dos clássicos derivados de cisplatina, ligantes derivados aroíl-hidrazônicos e complexos de cobre(II) aparecem como compostos promissores. Esta tese relata o desenvolvimento e a síntese de uma nova combinação desses compostos a partir de oito ligantes bases de Schiff aroíl-hidrazônicos inéditos e seus Cu₂-complexos derivados de sais de perclorato ou acetato **1–14**. Os complexos de cobre(II) obtidos contêm em suas estruturas modelos estruturais de sítios ativos de algumas metaloenzimas. Os compostos foram amplamente caracterizados utilizando várias técnicas espectroscópicas e analíticas. As análises por difração de raios X de quatro ligantes e cinco complexos são descritas em detalhes nessa tese. A estabilidade dos compostos foi estudada em meio celular e sua atividade biológica foi analisada. Os resultados incluem um estudo da interação de dois ligantes derivados de tiofeno (**H₃L1**) ou furano (**H₃L2**) e seus respectivos complexos **1** e **2** (primeiro conjunto de compostos) com uma proteína e DNA do timo de vitelo (*calf thymus* DNA), com o objetivo de medir a afinidade de ligação à albumina sérica bovina e ao DNA usando as técnicas de absorção de UV/Visível e/ou fluorescência. Adicionalmente, foi visto através de técnicas de espalhamento de luz que a interação entre os compostos e a proteína é reversível. Uma importante contribuição do presente trabalho foi analisar a capacidade de clivagem do DNA plasmidial de dois complexos **1** e **2** usando a técnica de espalhamento de luz dinâmico. Neste trabalho são estudadas as alterações do raio hidrodinâmico do DNA plasmidial causada pelo corte nas hélices resultante da presença dos complexos. Ensaio de citotoxicidades em algumas células cancerígenas, revelaram a alta capacidade dos ligantes (**H₃L1** and **H₃L2**) e dos complexos (**1** e **2**) de induzir a morte celular. Ademais, as muitas propriedades

biológicas, incluindo a atividade anticancerígena do fragmento isoxazol, motivaram sua inclusão na estrutura dos ligantes **H₃L₃** and **H₂L₄** e complexos **3–6** (segundo conjunto de compostos). A combinação dessas estruturas pode vir a ser promissora na procura de novos medicamentos contra o câncer. A interação dos derivados dos ligantes isoxazol-aroíl-hidrazônicos com o DNA foi diretamente estudada por espectroscopia na absorvância e fluorescência, usando as propriedades luminescentes apresentadas pelos ligantes. No caso dos complexos, o ensaio de deslocamento de brometo de etídio revelou uma afinidade importante através da intercalação nos ácidos nucleicos da sequência do DNA. Adicionalmente, este trabalho conseguiu demonstrar que ligantes e complexos contendo um braço fenólico no lugar de um braço piridínico melhoram a citotoxicidade *in vitro* em células de câncer de mama epitelial humano, alcançando a faixa nanomolar. A capacidade de metalação e transmetalção dos ligantes binucleares **H₃L₃** e **H₂L₄** e seus complexos de cobre **3–6** com Fe(II), Fe(III) e Zn(II) provenientes do meio biológico foi verificada como uma estratégia adicional para induzir a morte de células cancerígenas. Além disso, para estudar a interação dos compostos com o sistema biológico e/ou para demonstrar a permeabilidade celular dos compostos, os ligantes (**H₃L₅–H₃L₇**) e complexos (**7–12**) foram funcionalizados com fluoróforos potentes como pireno (**H₃L₅**) (conjunto três de compostos), benzopirantiofeno (**H₃L₆**) ou borodipirrometeno (**H₃L₇**) (conjunto quatro de compostos) associados aos fragmentos hidrazônicos. Estudos de microscopia de fluorescência do ligando **H₃L₇** comprovaram sua presença dentro de células de câncer. Também, análises de co-localização para organelas mostraram a afinidade dos ligantes com a mitocôndria. Finalmente, motivada pelas propriedades biológicas da molécula isoniaziada e seu uso em tratamentos de quimioterapia, esta tese mostra de forma general a síntese, caracterização e citotoxicidade de um novo ligante isoniazídico (**H₂L₈**) e seus complexos de perclorato ou acetato de cobre(II) **13** e **14** (conjunto cinco de compostos) visando realizar um pedido de patente.

Palavras-chave

Ligantes derivados aroíl-hidrazônicos; Complexos de cobre(II); Citotoxicidade; Agentes Anticancerígenos; Proteínas de albumina; DNA; Anticancer agents; Imagem celular.

Table of contents

| | | |
|---------|---|----|
| 1 | Introduction | 37 |
| 1.1 | Research context | 37 |
| 1.2 | Thesis structure | 38 |
| 1.3 | Objectives of this work | 39 |
| 1.3.1 | General Objective | 39 |
| 1.3.2 | Specific objectives | 39 |
| 2 | Theoretical fundaments | 41 |
| 2.1 | Cancer: statistics and pathology | 41 |
| 2.2 | Cancer treatments | 44 |
| 2.3 | Chemotherapy drugs | 45 |
| 2.4 | Copper(II) complexes: promising antineoplastic agents? | 46 |
| 2.4.1 | Copper(II): the natural ion with interesting coordination chemistry | 46 |
| 2.4.1 | Cytotoxicity of copper(II) complexes | 47 |
| 2.6 | Copper(II) complexes containing biomimetic actives sites | 48 |
| 2.7 | Aroylhydrazones as ligands for copper(II) and their cytotoxicity | 48 |
| 3 | Experimental | 54 |
| 3.1 | Chemicals | 54 |
| 3.2 | Syntheses of precursors, ligands and complexes | 55 |
| 3.2.1 | Syntheses of precursors | 55 |
| 3.2.1.1 | Synthesis of HBPA | 55 |
| 3.2.1.2 | Synthesis of HBPAMFF | 55 |
| 3.2.1.3 | Synthesis of BMPAMFF | 57 |
| 3.2.1.4 | Synthesis of 4-MePh-BODIPY | 57 |
| 3.2.1.5 | Synthesis of FMeO-BODIPY-Hz | 58 |
| 3.2.2 | Synthesis of ligands | 60 |
| 3.2.2.1 | Synthesis of HBPAMF-thiophene-2-carbohydrazone (H ₃ L1) | 61 |
| 3.2.2.2 | Synthesis of HBPAMF-furan-2-carbohydrazone (H ₃ L2) | 61 |
| 3.2.2.3 | Synthesis of HBPAMF-5-phenylisoxazole-3-carbohydrazone ligand (H ₃ L3) | 61 |

| | |
|---|----|
| 3.2.2.4 Synthesis of BPMAMF-5-phenylisoxazole-3-carbohydrazone ligand (H ₂ L ₄) | 62 |
| 3.2.2.5 Synthesis of HBPAMF-4-(1-pyrenebutyric)carbohydrazone (H ₃ L ₅) | 62 |
| 3.2.2.6 Synthesis of the fluorescent ligand HBPAMF-4H-[1]-benzopyrano[4,3-b]thiophene-2-carbohydrazone (H ₃ L ₆) | 63 |
| 3.2.2.7 Synthesis of HBPAMF-BODIPY carbohydrazone ligand (H ₃ L ₇) | 63 |
| To prepare t | 63 |
| 3.2.2.8 Synthesis of the fluorescent ligand BPMAMF-4H-[1]-benzopyrano[4,3-b]thiophene-2-carbohydrazone (H ₂ L ₈) | 64 |
| 3.2.3 Synthesis of copper(II) complexes | 64 |
| 3.2.3.1 Synthesis of Complex 1 | 66 |
| 3.2.3.2 Synthesis of Complex 2 | 67 |
| 3.2.3.3 Synthesis of Complex 3 | 67 |
| 3.2.3.4 Synthesis of Complex 4 | 68 |
| 3.2.3.5 Synthesis of Complex 5 | 68 |
| 3.2.3.6 Synthesis of Complex 6 | 68 |
| 3.2.3.7 Synthesis of Complex 7 | 69 |
| 3.2.3.8 Synthesis of Complex 8 | 69 |
| 3.2.3.9 Synthesis of Complex 9 | 70 |
| 3.2.3.10 Synthesis of Complex 10 | 70 |
| 3.2.3.11 Synthesis of Complex 11 | 70 |
| 3.2.3.12 Synthesis of Complex 12 | 71 |
| 3.2.3.13 Synthesis of Complex 13 | 71 |
| 3.2.3.14 Synthesis of Complex 14 | 72 |
| 3.3 Measurements for chemical characterization | 74 |
| 3.3.1 Spectroscopic studies | 74 |
| 3.3.2 X-ray crystallography | 75 |
| 3.3.3 CHNS and copper content | 76 |
| 3.3.4 Thermogravimetric analysis and electrical conductivity | 77 |
| 3.4 Compound's stability | 77 |
| 3.4.1 Stability studies by UV/Visible spectroscopy | 77 |
| 3.4.2 Stability studies by ESI-MS | 77 |
| 3.5 Compounds' interaction with BSA, HSA and DNA | 78 |

| | |
|---|----|
| 3.5.1 BSA-binding studies of ligands H ₃ L1, H ₃ L2 and complexes 1 and 2 | 78 |
| 3.5.2 DNA binding studies of ligands H ₃ L1, H ₃ L2 and complexes 1 and 2 | 79 |
| 3.5.3 Scattering studies of BSA and plasmid DNA radii in the presence of the ligands H ₃ L1, H ₃ L2 and complexes 1 and 2 | 79 |
| 3.5.4 In vitro DNA interaction with ligands H ₃ L3, H ₂ L4 and complexes 3–6 | 81 |
| 3.5.4.1 DNA-compounds absorption titration studies | 81 |
| 3.5.4.2 Intercalation binding studies of ligands | 81 |
| 3.5.4.3 Ethidium bromide displacement from DNA by the complexes | 82 |
| 3.5.5 HSA-binding studies of ligand H ₃ L5 | 82 |
| 3.5.6 In vitro DNA interaction with ligand H ₃ L5 | 83 |
| 3.5.6.1 UV-vis studies of the DNA interaction with ligand H ₃ L5 | 83 |
| 3.5.6.2 Fluorescence studies of the DNA interaction with ligand H ₃ L5 | 84 |
| 3.6 In vitro anticancer assays | 84 |
| 3.6.1 Cytotoxicity assays for ligands H ₃ L1, H ₃ L2 and complexes 1 and 2 | 84 |
| Cell lines and culture conditions | 84 |
| Cell viability assay | 84 |
| 3.6.2 Cytotoxicity assays for ligands H ₃ L3–H ₃ L7 and complexes 3–12 | 85 |
| Cell lines and culture conditions | 85 |
| Cell viability assay | 85 |
| 3.6.3 Cytotoxicity assays for ligand H ₂ L8 and complexes 13 and 14 | 86 |
| Cell lines and culture conditions | 86 |
| Cell viability assay | 86 |
| 3.7 Cellular uptake and localization of H ₃ L7 by fluorescence microscopy | 87 |
| 3.8 Coordination and transmetallation with the essential Fe(II), Fe(III) and Zn(II) ions from cell medium | 88 |
| 4 Results and discussion I. Binucleating hydrazonic ligands and their μ -hydroxodicopper(II) complexes as promising structural motifs for enhanced antitumor activity | 89 |
| 4.1 Introduction | 89 |
| 4.2 Results and discussion | 90 |
| 4.2.1 Syntheses | 90 |

| | |
|--|-----|
| 4.2.2 Characterization of ligands and complexes | 92 |
| 4.2.2.1 Solution NMR of ligands | 92 |
| 4.2.2.2 ESI-MS analysis of ligands. | 97 |
| 4.2.2.3 Crystal structures of complexes 1 and 2 | 97 |
| 4.2.2.4 Vibrational properties of the compounds | 103 |
| Both | 103 |
| sh: shoulder. | 105 |
| 4.2.2.5 UV-Visible spectroscopy studies of the compounds | 106 |
| 4.2.3 Hydrolysis studies | 108 |
| 4.2.3.1 Stability of ligands | 108 |
| 4.2.3.2 Stability of complexes | 111 |
| 4.2.4 Evaluation of BSA binding through UV-Visible and fluorescence spectroscopies | 114 |
| 4.2.5 Influence of the compounds in BSA conformation by scattering techniques | 118 |
| 4.2.6 Determination of the binding constants towards ctDNA | 124 |
| 4.2.7 Influence of the compounds in pBR322 plasmid DNA conformation | 127 |
| 4.2.8 Cytotoxic activity | 131 |
| 4.3 Partial conclusions | 133 |
| 5 Results and discussion II. Isoxazole-arylhydrazones and their (perchlorate / acetate-derived) dinuclear copper(II) complexes as potential antiproliferative agents: syntheses and in vitro studies in epithelial human breast cancer cells | 136 |
| 5.1 Introduction | 136 |
| 5.2 Results and discussion | 137 |
| 5.2.1 Syntheses | 137 |
| 5.2.2 Characterization of ligands and complexes | 141 |
| 5.2.2.1 Solution NMR of ligands | 141 |
| 5.2.2.2 Crystal structures of the ligands and complexes 3 and 5 | 146 |
| 5.2.2.3 Vibrational properties of the compounds | 155 |
| 5.2.2.5 UV-Visible spectroscopy studies of the compounds | 159 |
| 5.2.3 Stability studies in DMSO and PBS | 161 |
| 5.2.4 Absorption and fluorescent ct-DNA interaction studies | 164 |
| 5.2.4.1 Absorption ct-DNA interaction studies | 164 |

| | |
|---|-----|
| 5.2.4.2 Fluorescence ct-DNA interaction studies | 167 |
| 5.2.5 In vitro cytotoxic activity | 171 |
| 5.2.5.1 Double-pyridine (BPMAMFF) or phenol-pyridine (HBPAMFF) fragment | 173 |
| 5.2.5.2 Perchlorate-complexes versus acetate-complexes | 174 |
| 5.2.5.3 Metal-free ligands versus copper(II) complexes | 174 |
| 5.2.6 Iron(II), Iron (III) and zinc(II) coordination studies | 175 |
| 5.2.7 Cytotoxicity versus iron/zinc coordination | 181 |
| 5.3 Partial conclusions | 182 |
| 6 Results and discussion III. A new luminescent pyrene-arylohydrazone Schiff base and its (perchlorate / acetate-derived) dicopper(II) complexes as potential antiproliferative agents: syntheses characterization and in vitro studies in epithelial human breast cancer cells | 183 |
| 6.1 Introduction | 183 |
| 6.2 Results and discussion | 184 |
| 6.2.1 Syntheses | 184 |
| 6.2.2 Characterization of the ligand and complexes | 187 |
| 6.2.2.1 Solution NMR of ligand H ₃ L5 | 187 |
| 6.2.2.2 Crystal structure of ligand H ₃ L5 | 190 |
| 6.2.2.3 Vibrational properties of the compounds | 195 |
| 6.2.2.4 Photophysical properties of the compounds | 197 |
| 6.2.3 Stability studies in DMSO and PBS | 202 |
| 6.2.4 Interaction of ligand H ₃ L5 with ctDNA | 202 |
| 6.2.4.1 ctDNA-H ₃ L5 interaction studies by UV-visible spectroscopy | 202 |
| 6.2.4.2 ctDNA-H ₃ L5 interaction studies by fluorescence spectroscopy | 203 |
| 6.2.5. Interaction of ligand H ₃ L5 with human serum albumin | 206 |
| 6.2.5.1 HSA-H ₃ L5 interaction studies by UV-visible spectroscopy | 206 |
| 6.2.4.2 HSA-H ₃ L5 interaction studies by fluorescence spectroscopy | 208 |
| 6.2.6 In vitro cytotoxic activity | 210 |
| 6.3 Partial conclusions | 212 |
| 7 Results and discussion IV. Two novel luminescent binucleating aroylhydrazonic ligands and their dicopper(II) complexes as potential anticancer agents: syntheses, chemical characterization, biological activity and cell imaging | 214 |

| | |
|---|------------|
| 7.1 Introduction | 214 |
| 7.2 Results | 215 |
| 7.2.1 Syntheses | 215 |
| 7.2.2 Characterization of ligands and complexes | 218 |
| 7.2.2.1 Solution NMR of ligands (122.5 | 218 221 |
| 7.2.2.2 Crystal structure of complex 9 | 222 |
| 7.2.2.3 Vibrational properties of the compounds The vibrational properties of ligand | 226 226 |
| 7.2.2.4 Photophysical properties of the compounds | 230 |
| 7.2.3 In vitro cytotoxic activity of the compounds | 236 |
| 7.2.4.1 Ligands H ₃ L6 versus H ₃ L7 and other HBPAMFF-Hz derivatives | 237 |
| 7.2.4.2 Ligands versus complexes activity | 238 |
| 7.2.4.2 Perchlorate-copper complexes versus acetate-copper complexes | 239 |
| 7.2.4 Cellular uptake and localization of H ₃ L7 by fluorescence microscopy | 241 |
| 7.3 Partial conclusions | 243 |
| 8 Results and discussion V. Novel binucleating isonicotinoyl hydrazonic ligand and its (perchlorate / acetate-derived) dicopper(II) complexes as potential anticancer agents: syntheses, chemical characterization, and cytotoxicity towards a breast cancer cell line | 245 |
| 8.1 Introduction | 245 |
| 8.2 Results and discussion | 246 |
| 8.2.1 Syntheses | 246 |
| 8.2.2 Characterization of the ligand and complexes | 247 |
| 8.2.2.1 Solution NMR of ligand H ₂ L8 | 247 |
| 8.2.2.2 Crystal structures of ligand H ₂ L8 | 251 |
| 8.2.2.3 UV-Visible and fluorescence spectroscopy studies of the compounds | 255 |
| 8.2.3 In vitro cytotoxic activity | 259 |
| 8.3 Partial conclusions | 261 |
| 9 General Conclusions | 263 |
| 10 Future work | 266 |

| | | |
|--------|--|-----|
| 11 | References | 268 |
| 12 | Attachment A: Communication of the work | 289 |
| 12.1 | Published paper | 289 |
| 12.2 | Communication and results dissemination | 290 |
| 12.2.1 | Oral presentation | 290 |
| 12.2.2 | Posters | 290 |
| 12.2.3 | Other academic events | 291 |
| 13 | Attachment B: Results | 292 |
| 13.1 | NMR spectra of the ligands and their precursors | 292 |
| 13.1.1 | NMR spectra of the precursors | 292 |
| 13.1.2 | NMR spectra of ligand H ₃ L1 | 293 |
| 13.1.3 | NMR spectra of ligand H ₃ L2 | 295 |
| 13.1.4 | NMR spectra of ligand H ₃ L3 | 296 |
| 13.1.5 | NMR spectra of ligand H ₃ L4 | 298 |
| 13.1.6 | NMR spectra of ligand H ₃ L5 | 299 |
| 13.1.7 | NMR spectra of ligand H ₃ L6 | 301 |
| 13.1.8 | NMR spectra of ligand H ₃ L7 | 302 |
| 13.1.9 | NMR spectra of ligand H ₃ L8 | 303 |
| 13.2 | FTIR and Raman spectra | 304 |
| 13.3 | Fluorescence image of cells by confocal microscopy | 309 |
| 13.4 | Fluorescence spectra of complexes 9–12 | 311 |
| 14 | Attachment C: Compounds terminology | 313 |

List of figures

- Figure 2.1. “Oncogenic mutations in the transcription factor p53 and in the small GTPase protein Ras (which individually have limited effects on promoting cancer) cooperate to transform normal cells into cancer cells [65]. In this example, p53 mutation affects the expression of group A genes and Ras mutation modifies the expression of group B genes. When both p53 and Ras are mutated in the same cell [67], they synergistically regulate a subset of genes (AB) known as cooperation response genes (CRGs), which turn out to be crucial mediators of tumour formation”. Adapted from LUO, J. and ELLEDGE, S. J. [63]. 43
- Figure 2.2. Chemical structure of the cisplatin, transplatin and carboplatin Pt-complexes. 45
- Figure 2.3. Structures of HBPAMFF and BPMAMFF molecules. 49
- Figure 2.4. Active sites of the mono or dioxygen binding coordination of (A) *Streptomyces* tyrosine [106]; (B) kidney bean PAP[107]; and catechol oxidase from sweet potato [108]. Adapted from (A) DECKER *et. al*; (B) STRATER *et. al*; and (C) SIEGBAHN. 50
- Figure 2.5. Chemical structures of aroylhydrazone ligands RDS-H₃L1 and RDS-H₃L2 synthesized from isoniazid (INH) and HDFMP or HBPAMFF moieties. 51
- Figure 2.6. Chemical structures of the Zn₂(II)-complexes RDS-1, RDS-2, RDS-3, and RDS-4 of RDS-H₃L1 or RDS-H₃L2. Adapted from DOS SANTOS R. [111]. 51
- Figure 2.7. Chemical structures of the Fe(II)Cu(II)-complex RDS-5, Fe(II)Zn(II)-complex RDS-6, and Cu₂(II)-complexes RDS-7, RDS-8, RDS-9, and RDS-10 of chelators RDS-H₃L1 or RDS-H₃L2. Adapted from DOS SANTOS R. [111]. 52
- Figure 3.1. Synthetic routes of precursors HBPAMFF and BPMAMFF. BPMA was obtained commercially. 56
- Figure 3.2. Synthetic routes of precursors 4-MePh-BODIPY and 4-HzPh-BODIPY. 58
- Figure 3.4. Structures of ligands H₃L1–H₂L8. 60
- Figure 3.5. Structures of complexes 1–8. 65
- Figure 3.6. Structures of complexes 9–14. 66
- Figure 3.3. Photographs taken during different steps of the synthesis of precursor, ligands and complexes: synthesis of 4-MePh-BODIPY after addition of (A) TFA and after addition of (B) BF₃-OEt₂; (C and D) 4-MePh-BODIPY purification by column chromatography, using SiO₂ as stationary phase and cyclohexane/ethyl acetate 8:1 as mobile

| | |
|---|-----|
| phase; (E) thin-layer chromatography of 4-MePh-BODIPY before purification, using cyclohexane/ethyl acetate 8:1 as mobile; (F) synthesis of FMeO-BODIPY-Hz after mixture of the precursors; (G) synthesis of FMeO-BODIPY-Hz by column chromatography using SiO ₂ as stationary phase and chloroform/MeOH/ammonium hydroxide 100:5:1 as mobile phase; (H) qualitative fluorescence of H ₃ L7 dissolved in MeOH and under an UV lamp; (I) qualitative fluorescence of complex 11 dissolved in chloroform and under an UV lamp; (J) qualitative fluorescence of complex 12 dissolved in chloroform and under an UV lamp; (K) appearance of the ligands after synthesis; (L) appearance of the complexes 1–10 and 13 and 14 after synthesis; (M) appearance of ligands H ₃ L7 after synthesis; (O) appearance of complex 11 after synthesis dissolved in DMSO; (P) optical photograph of H ₃ L1 crystals; (Q) optical photograph of H ₃ L2 crystals; (R) optical photograph of complex 1 crystals; (S); and optical photograph of complex 2 crystals. | 73 |
| Figure 4.1 Scheme of the synthesis of the binucleating ligands H ₃ L1 and H ₃ L2, and their respective μ -hydroxo dicopper(II) complexes 1 and 2. | 90 |
| Figure 4.2 Termogravimetric curve of complex 1. | 91 |
| Figure 4.3. Termogravimetric curve of complex 2. | 91 |
| Figure 4.4. ¹ H NMR spectra (400 MHz) of H ₃ L1 in DMSO- <i>d</i> ₆ at room temperature. | 92 |
| Figure 4.5. ¹ H NMR spectra (400 MHz) of H ₃ L2 in DMSO- <i>d</i> ₆ at room temperature. | 93 |
| Figure 4.6. ¹³ C NMR spectra (100 MHz) of H ₃ L1 in DMSO- <i>d</i> ₆ at room temperature. | 93 |
| Figure 4.7. ¹³ C NMR spectra (100 MHz) of H ₃ L2 in DMSO- <i>d</i> ₆ at room temperature. | 94 |
| Figure 4.8. Amide-related tautomerization process in H ₃ L1 (with the tautomers' percentages at equilibrium) and labelling system employed for the assignment of NMR data according to the XRD numbering scheme. | 95 |
| Figure 4.9. Left. Crystal structure of 1 (A) and 2 (B). The ellipsoids were drawn with 30% probability. Only one of the enantiomers is shown. Perchlorate counter-ions, disordered water molecules and most of the hydrogen atoms were omitted for the sake of clarity. Symmetry code: (i) $-x+1, -y+1, -z+1$. Right. The corresponding dimers, formed by a pair of enantiomers interacting through trifurcated hydroxo bridges (O2 and O2i donor atoms), with the copper(II) coordination spheres highlighted as coloured ellipsoids. | 98 |
| Figure 4.10. FTIR spectra of H ₃ L1 and complex 1 in KBr pellets in the 4000–500 cm ⁻¹ region. | 103 |
| Figure 4.11. FTIR spectra of H ₃ L1 and complex 1 in KBr pellets in the 1700–700 cm ⁻¹ region. | 104 |

- Figure 4.12. FTIR spectra of H₃L2 and complex 2 in KBr pellets in the 4000–500 cm⁻¹ region. 104
- Figure 4.13. FTIR spectra of H₃L2 and complex 2 in KBr pellets in the 1700–700 cm⁻¹ region. 105
- Figure 4.14. Absorption spectra of ligands (A) H₃L1 (4.6 × 10⁻⁵ M) and (B) H₃L2 (4.8 × 10⁻⁵ M), as well as their respective precursors: HBPAMFF (10.6 × 10⁻⁵ M), TCH (7.0 × 10⁻⁵ M) and FCH (4.0 × 10⁻⁵ M), in DMSO at r.t. And absorption spectra of complexes (C) 1 (left, 6.2 × 10⁻⁵ M) and (D) 2 (right, 7.0 × 10⁻⁵ M) recorded in DMSO at r.t. The spectra of H₃L1 (3.4 × 10⁻⁵ M) and H₃L2 (2.9 × 10⁻⁵ M) are included for the sake of comparison. *Insets*: Visible absorbance of 1 (5.0 × 10⁻³ M) and 2 (5.0 × 10⁻³ M) in the 500–900 nm region. 106
- Figure 4.15. Absorption spectra of H₃L1 (top, pH 6.15) and H₃L2 (bottom, pH 6.35) vs time in 10% DMSO at room temperature. [L] = 5 × 10⁻⁵ M. *Inset*: Spectra at 0 and 12 h for comparison. 109
- Figure 4.16. Absorption spectra over time (24 h) for the ligands H₃L1 (A) and H₃L2 (B), and complexes 1 (C) and 2 (D) in 10% DMSO-90% PBS (pH 7.4) at r.t. [L] = 1 × 10⁻⁵ M. 110
- Figure 4.17. Absorption spectra of 1 (top) and 2 (bottom), along 24 h, in 10% DMSO at r.t. [C] = 5 × 10⁻⁵ M. pH 6.0. *Inset*: C/C₀ versus time at different wavelengths. 111
- Figure 4.18. ESI-MS(+) spectra measured from fresh DMSO/MeOH solutions of H₃L1 (A) and H₃L2 (B). (C) complex 1 in fresh DMSO/H₂O solution. (D) 1 in DMSO/H₂O solution after 24 h at 23 ± 2 °C. (E) complex 2 in fresh DMSO/H₂O solution. (F) 2 in DMSO/H₂O solution after 24 h at 23 ± 2 °C. Capillary output voltage set at 50 V. All compounds were diluted in methanol (5:95) before injection. 113
- Figure 4.19. Isotopic pattern obtained experimentally (black curve) and simulated by the Isotope Distribution Calculator and Mass Spec Plotter tool (red vertical lines) for 1 and 2. 114
- Figure 4.20. Absorption spectra of BSA (1 μM) in a buffer solution (10 mM Tris-HCl and 10 mM NaCl, pH 7.40) in the absence and presence of complexes (A) and ligands (B) at a 5 μM. *Insets*: Detail of the 250–320 nm region. Fluorescence spectra, at 25 °C, of BSA (1 μM; λ_{ex} = 280 nm; λ_{em} = 353 nm) in the absence (red curve) and presence (black curves) of increasing concentrations (1-8 μM) of 1 (C) and 2 (D). *Insets*: The corresponding Stern-Volmer and Scatchard plots. 116
- Figure 4.21. Hydrodynamic diameter (nm) distribution, at 25 °C, of BSA samples (5 × 10⁻⁵ M) in the absence and presence of complexes 1 (A) and 2 (B) at BSA : complex molar ratios of 1 : 1, 1 : 7, 1 : 14, 1 : 21 and 1 : 28. (C) BSA in the absence and presence of Cu(ClO₄)₂·6 H₂O and free ligands H₃L1 and H₃L2 at a BSA : compound molar ratio equal to 1 : 28. Scattering angle: 90 °. Samples (2 mL, in 100 mM NaCl and 50 mM Tris buffer at pH 7.40) were filtered (0.25 μm) before performing the scattering measurements. 119

Figure 4.22. Auto-correlation functions of BSA samples (5×10^{-5} M) in the presence of 1 (A) and 2 (B) at different molar ratios and ligands and $\text{Cu}(\text{ClO}_4)_2 \cdot 6 \text{H}_2\text{O}$ at 28 molar ratio. Scattering angle: 90° . 25°C . 120

Figure 4.23. SAXS curves, at 25°C , of free BSA (5×10^{-5} M, in 100 mM NaCl and 50 mM Tris buffer at pH 7.40) in the absence and presence of complexes 1 (A) and 2 (B) at BSA : complex molar ratios of 1 : 1, 1 : 7, 1 : 14, 1 : 21 and 1 : 28. All samples were filtered ($0.45 \mu\text{m}$) before performing the scattering measurements. The curve fittings, using a Generalized Gaussian Coil model, for free BSA and BSA : complexes at 1 : 28 are included. 122

Figure 4.24. Gyrus radii of BSA protein with changes in its secondary structure and during the aggregation process. 123

Figure 4.25. SAXS curves of aqueous solutions containing pure BSA (5×10^{-5} M) and BSA in the presence of 28-fold excess 1, 2, $\text{H}_3\text{L1}$, $\text{H}_3\text{L2}$, and $\text{Cu}(\text{ClO}_4)_2 \cdot 6\text{H}_2\text{O}$. 25°C . 124

Figure 4.26. Absorption spectra and $1/(A_0 - A)$ versus $1/[\text{DNA}]$ plot (*insets*) of the copper(II) complexes 1 (A) and 2 (B) and the ligands $\text{H}_3\text{L1}$ (C) and $\text{H}_3\text{L2}$ (D) ($25 \mu\text{M}$, 3 mL, in 10% DMSO and 90% 50 mM Tris-HCl, pH 7.40) in the absence (red curve) and with increasing concentrations (black curves) of ctDNA ($5\text{--}50 \mu\text{M}$) at 25°C . Spectra were registered after an incubation time of 3 min from each ctDNA addition. 125

Figure 4.27. Hydrodynamic radius (nm) distribution of pBR322 plasmid DNA samples ($2.5 \mu\text{g mL}^{-1}$, 2 mL, in 10 mM Tris buffer, pH 7.40) in presence of (A) complex 1 ($10\text{--}50 \mu\text{M}$) and (B) complex 2 ($15\text{--}60 \mu\text{M}$). (C) pBR322 plasmid DNA in the presence of $\text{H}_3\text{L1}$, $\text{H}_3\text{L2}$ and the starting salt copper(II) perchlorate hexahydrate, all of them at a concentration of $50 \mu\text{M}$. Scattering angle: 90° . Incubation: 15 min at $25.0 \pm 0.1^\circ\text{C}$. 128

Figure 4.28. Auto-correlation functions of samples of DNA ($1.25 \mu\text{g}$ in 0.5 mL) in the presence of 1 and 2 at different molar ratios. Scattering angle: 90° at 25°C . 129

Figure 4.29. Estimation of the different plasmid pBR322 forms radii by extrapolation, based in the summary reported [179] by Latulippe and Zydney of R_g values from static light scattering analysis of supercoiled, open-circular, and linear isoforms of 5.76, 9.80, and 16.8 kbp plasmids in 10 mM Na_2EDTA , 200 mM NaCl solution. 129

Figure 5.1. Synthetic routes of ligands $\text{H}_3\text{L3}$ (top) and $\text{H}_2\text{L4}$ (bottom), and their copper(II) complexes from perchlorate 3 and 5 or acetate salts 4 and 6. 138

Figure 5.2. Termogravimetric curve of complex 3. 139

Figure 5.3. Termogravimetric curve of complex 4. 139

Figure 5.4. Termogravimetric curve of complex 5. 140

Figure 5.5. Termogravimetric curve of complex 6. 140

| | |
|---|-----|
| Figure 5.6. ^1H NMR spectrum (400 MHz) of $\text{H}_3\text{L3}$ in $\text{DMSO}-d_6$ at room temperature. | 142 |
| Figure 5.7. ^1H NMR spectrum (400 MHz) of $\text{H}_2\text{L4}$ in $\text{DMSO}-d_6$ at room temperature. | 142 |
| Figure 5.8. ^{13}C NMR spectrum (100 MHz) of $\text{H}_3\text{L3}$ in $\text{DMSO}-d_6$ at room temperature. | 143 |
| Figure 5.9. ^{13}C NMR spectrum (100 MHz) of $\text{H}_2\text{L4}$ in $\text{DMSO}-d_6$ at room temperature. | 143 |
| Figure 5.10. DEPT-135 spectrum (100 MHz) of $\text{H}_3\text{L3}$ in $\text{DMSO}-d_6$ at room temperature. | 144 |
| Figure 5.11. DEPT-135 spectrum (100 MHz) of $\text{H}_2\text{L4}$ in $\text{DMSO}-d_6$ at room temperature. | 144 |
| Figure 5.12. Crystal structure of ligands $\text{H}_3\text{L3}$ (A) and $\text{H}_2\text{L4}$ (B). Ellipsoids are drawn with 30% probability. Only hydrogen atoms involved in intramolecular bonds (orange dotted line) are shown for the sake of clarity. For $\text{H}_3\text{L3}$, only one of the enantiomers is shown. | 147 |
| Figure 5.13. Crystal structure of (A) complex 3 and (B) complex 6. Ellipsoids are drawn with 30% probability. Only hydrogen atoms involved in intramolecular hydrogen bonds (orange dotted line) are shown for the sake of clarity. Free water, DMSO or perchlorate counter-ion molecules were omitted for the sake of simplicity. For complex 3, one oxygen atom from the perchlorate ion is shown and only one of the enantiomers is shown. | 151 |
| Figure 5.14. FTIR spectrum of $\text{H}_3\text{L3}$ in KBr pellet and principal assignments. | 156 |
| Figure 5.15. FTIR spectrum of $\text{H}_2\text{L4}$ in KBr pellet and principal assignments. | 156 |
| Figure 5.16. FTIR spectrum of complex 3 in KBr pellet and principal assignments. | 157 |
| Figure 5.17. FTIR spectrum of complex 4 in KBr pellet and principal assignments. | 157 |
| Figure 5.18. FTIR spectrum of complex 5 in KBr pellet and principal assignments. | 158 |
| Figure 5.19. FTIR spectrum of complex 6 in KBr pellet and principal assignments. | 158 |
| Figure 5.20. Absorption spectra of ligand $\text{H}_3\text{L3}$, the corresponding dicopper complexes 3 and 4 and precursors HBPAMFF and PIH in $\text{H}_2\text{O}/\text{DMSO}$ 9:1. | 159 |
| Figure 5.21. Absorption spectra of ligand $\text{H}_2\text{L4}$, the corresponding dicopper complexes 5 and 6 and precursors BPMAMFF and PIH in $\text{H}_2\text{O}/\text{DMSO}$ 9:1 at 25 °C. | 159 |
| Figure 5.22. Visible spectra of complexes 3–6 in DMSO at 25 °C in the 500–900 nm region. | 161 |

Figure 5.23. Absorption spectra of ligands (A) H₃L3 and (B) H₂L4, and complexes (C) 3, (D) 4, (E) 5 and (F) 6, incubated for up to 72 h at room temperature. Concentration = 1×10^{-5} M in DMSO. *Inset*: C/C₀ versus time at wavelengths: 294 nm (A), 294 nm (B), 322 nm (C), 322 nm (D), 321 nm (E), and 321 nm (F). 162

Figure 5.24. Absorption spectra of ligands (A) H₃L3 and (B) H₂L4, and complexes (C) 3, (D) 4, (E) 5 and (F) 6 incubated for up to 72 h at 37°C. Concentration = 1×10^{-5} M in PBS/DMSO 99:1. *Inset*: C/C₀ versus time at wavelengths: 297 nm (A), 297 nm (B), 321 nm (C), 321 nm (D), 314 nm (E), and 314 nm (F). 163

Figure 5.25. Absorption spectra of ligands (A) H₃L3; (B) H₂L4 and complexes (C) 3; (D) 4; (E) 5; and (F) 6 at a 2.5×10^{-5} M alone or with increasing concentration of ct-DNA (arrow, 0 – 5×10^{-5} M) in PBS/DMSO 9:1 at 25°C. *Inset*: Plot of $1/A_0 - A$ versus $1/[ct-DNA]$ and its linear fit. 165

Figure 5.26. Fluorescence emission spectra in PBS/DMSO 99:1 at 25°C of ligands (A) H₃L3 and (B) H₂L4 (5 μM, $\lambda_{\text{exit}} = 350$ nm) alone or in the presence of ct-DNA (arrow, 0 – 120 μM). *Inset*: plot of $\log[(I_0 - I)/I]$ versus $\log[ct-DNA]$; and of a EB–DNA solution (EB = 5 μM and ct-DNA = 10×10^{-6} M, $\lambda_{\text{exit}} = 555$ nm) alone or in the presence (arrow, 0 – 50 μM) of complexes (C) 3; (D) 4; (E) 5; and (F) 6. *Inset*: plot of I/I_0 versus [complex] and its linear fit. 168

Figure 5.27. Stern-Volmer plots of I_0/I against the concentration of DNA for the interaction with ligands (A) H₃L3 and (B) H₃L4, and plots of $\log[(I_0 - I)/I]$ versus $\log [Q]$ for the interaction of DNA with complexes (C) 3, (D) 4, (E) 5 and (F) 6. 169

Figure 5.28 Dose-dependent effect expressed as the percentage of relative viability of MDA-MB-231 cells measured by the MTT assay for (A) H₃L3; (B) H₂L4; (C) 3; (D) 4; (E) 5; and (F) 6 after 72 h incubation at 37 °C. Data represent the mean of triplicate experiments. 172

Figure 5.29. Dose-dependent effect on MDA-MB-231 cells of ligands (A) and copper(II) complexes (B and C) after 72 h at 37 °C using the MTT assay. 173

Figure 5.30. Absorption spectra of ligands (A) H₃L3 and (B) H₂L4, and complexes (C) 3; (D) 4; (E) 5; and (F) 6 (10 μM) alone or in the presence of Fe(II), Fe(III) or Zn(II) in 2 : 1 metal ion : compounds mole ratio, in PBS/DMSO 99:1 incubated at 37°C for 1 h under nitrogen atmosphere. Metal-ion : iron(II) acetate, iron(III) chloride or zinc(II) chloride. 176

Figure 5.31. Absorption spectra of mixtures of ligands or complexes and Fe(II) at different Fe(II) : compounds mole ratios, measured after 1 h incubation at 37 °C under nitrogen atmosphere. 178

Figure 5.32. Absorption spectra of mixtures of ligands or complexes and Fe(III) at different Fe(III) : compounds mole ratios, measured after 1 h incubation at 37 °C under nitrogen atmosphere. 179

| | |
|--|-----|
| Figure 5.33. Absorption spectra of mixtures of ligands or complexes and Zn(II) at different Zn(II) : compounds mole ratios, measured after 1 h incubation at 37 °C under nitrogen atmosphere. | 180 |
| Figure 6.1. Synthetic routes of ligand H ₃ L5 and its copper(II) complexes from perchlorate 7 or acetate salts 8. | 185 |
| Figure 6.2. Termogravimetric curve of complex 7. | 186 |
| Figure 6.3. Termogravimetric curve of complex 8. | 186 |
| Figure 6.4. ¹ H NMR spectrum (400 MHz) of H ₃ L5 in DMSO- <i>d</i> ₆ at room temperature. | 187 |
| Figure 6.5. ¹³ C NMR spectrum (100 MHz) of H ₃ L5 in DMSO- <i>d</i> ₆ at room temperature. | 188 |
| Figure 6.6. DEPT-135 NMR spectrum (100 MHz) of H ₃ L5 in DMSO- <i>d</i> ₆ at room temperature. | 188 |
| Figure 6.7. Crystal structure of ligand H ₃ L5. The ellipsoids were drawn with 50% probability. Only one of the enantiomers is shown. Intramolecular and intermolecular hydrogen bonds are depicted as dotted line. | 190 |
| Figure 6.8. Molecular packing of ligand H ₃ L5. Hydrogen atoms have been omitted for the sake of clarification. Two possible positions of the pyrenebutyric moiety are shown. The isomers are showed with solid line bonds (90% of contribution) or with isotropic balls without solid line (10% contribution). | 194 |
| Figure 6.9. Crystal structure of ligand H ₃ L5. The ellipsoids were drawn with 50% probability highlighting the pyrenebutyric entity (inset). Two enantiomers are shown. | 194 |
| Figure 6.10. FTIR spectra of H ₃ L5 in KBr pellet and principal assignments. | 195 |
| Figure 6.11. FTIR spectra of complex 7 in KBr pellet and principal assignments. | 196 |
| Figure 6.12. FTIR spectra of complex 8 in KBr pellet and principal assignments. | 196 |
| Figure 6.13. Absorption spectrum of ligand H ₃ L5, as well as its respective precursors: HBPAMFF and PBH, and of complexes 7 and 8 recorded in H ₂ O/DMSO 9:1 at 298 K. | 197 |
| Figure 6.14. Absorption versus fluorescence emission spectra of ligand H ₃ L5 (λ _{excitation} = 352 nm) in 99:1 H ₂ O/DMSO and water respectively at 298 K. | 199 |
| Figure 6.15. Fluorescence emission spectra of ligand H ₃ L5 (λ _{excitation} = 352 nm; 10 μM), as well as its respective precursors: HBPAMFF (λ _{excitation} = 349 nm; 40 μM) and PBH (λ _{excitation} = 344 nm; 6 μM) in water at 298 K. | 200 |

Figure 6.16. Fluorescence spectra of pyrene at decreasing concentrations A($\times 10^{-2}$) – G($\times 10^{-4}$) in cyclohexane. Adapted from Briks and Christophorou, 1963 [204]. 200

Figure 6.17. Fluorescence emission spectra of ligand H₃L5 ($\lambda_{\text{excitation}} = 352 \text{ nm}$; $10 \mu\text{M}$) in water and organic solvents at 298 K. 201

Figure 6.18. Absorption spectra of ligand H₃L5 ($1 \mu\text{M}$, red curve) in a buffer solution (pH 7.40) at 25°C of in the absence and presence of ctDNA at increasing concentration (0.5 and $1 - 2 \mu\text{M}$, black curves). The absorbance of each addition of DNA was substrate from the spectra. 203

Figure 6.19. Fluorescence emission spectra in a buffer solution (pH 7.40) at 25°C of ligands H₃L5 ($1 \mu\text{M}$, $\lambda_{\text{exit}} = 352 \text{ nm}$) alone or in the presence of ctDNA (arrow, $0 - 2 \mu\text{M}$). Inset: plot of I/I_0 versus [ctDNA] and plot of $\log[(I_0 - I)/I]$ versus $\log[\text{ctDNA}]$ and their linear fit. 204

Figure 6.20. Absorption spectra of HSA ($9 \mu\text{M}$, red curve) protein in a buffer solution (pH 7.40) at 25 °C in the absence and presence of ligand H₃L5 at increasing concentration ($1 - 9 \mu\text{M}$, black curves). The absorbance of each addition of the ligand was substrated from the spectra. 207

Figure 6.21. Absorption spectra of ligand H₃L5 ($1 \mu\text{M}$, red curve) in a buffer solution (pH 7.40) and at 25 °C in the absence and presence of HSA protein at increasing concentration (0.5 and $1 - 10 \mu\text{M}$, black curves). The absorbance of each addition of HSA was substrate from the spectra. 208

Figure 6.22. Enhancement of the fluorescence emission of ligand H₃L5 ($1 \mu\text{M}$, red curve) in a buffer solution (pH 7.40) at 25 °C in the presence of HSA protein at increasing concentration (0.5 and $1 - 10 \mu\text{M}$, black curves). 209

Figure 6.23. Dose-dependent effect expressed as the percentage of relative viability of MDA-MB-231 cells measured by the MTT assay for (A) H₃L5; (B) complex 7 and (C) 8 after 72 h incubation at 37 °C. Data represent the mean of triplicate experiments. 210

Figure 6.24. Dose-dependent effect on MDA-MB-231 cells of ligand H₃L5 copper(II) complexes 7 and 8 after 72 h at 37 °C using the MTT assay. 212

Figure 7.1. Synthetic routes to ligands H₃L6 (top) and H₃L7 (bottom), and their copper(II) complexes from perchlorate 9 and 11 or acetate salts 10 and 12. 217

Figure 7.2. ¹H NMR spectrum (400 MHz) of H₃L6 in DMSO-*d*₆ at room temperature. 218

Figure 7.3. ¹³C NMR spectrum (100 MHz) of H₃L6 in DMSO-*d*₆ at room temperature. 219

- Figure 7.4. DEPT-135 spectrum (100 MHz) of H₃L6 in DMSO-*d*₆ at room temperature. 219
- Figure 7.5. ¹H NMR spectrum (400 MHz) of H₃L7 in DCM-*d*₂ at room temperature. 220
- Figure 7.6. Crystal structure of complex 9. The ellipsoids were drawn with 50% probability highlighting the copper's environments (inset). Hydrogen atoms and crystallization solvents were omitted for the sake of clarity. 222
- Figure 7.7. Molecular packing of complex 9. Hydrogen atoms have been omitted for clarify. 225
- Figure 7.8. FTIR spectra of H₃L6 in KBr pellet and principal assignments. 227
- Figure 7.9. FTIR spectra of H₃L7 in KBr pellet and principal assignments. 227
- Figure 7.10. FTIR spectra of complex 9 in KBr pellet and principal assignments. 228
- Figure 7.11. FTIR spectra of complex 10 in KBr pellet and principal assignments. 228
- Figure 7.12. FTIR spectra of complex 11 in KBr pellet and principal assignments. 229
- Figure 7.13. FTIR spectra of complex 12 in KBr pellet and principal assignments. 229
- Figure 7.14. Absorption spectra of ligand H₃L6, as well as of its precursors: HBPAMFF and BPTH, and its complexes 9 and 10 recorded in H₂O/DMSO 9:1 at 298 K. 231
- Figure 7.15. Absorption spectra of ligand H₃L7, as well as of its precursors HBPAMFF and its complexes 11 and 12 recorded in H₂O/DMSO 9:1 at 298 K. 232
- Figure 7.16. Absorption versus fluorescence emission spectra of ligand H₃L6 ($\lambda_{\text{excitation}} = 376 \text{ nm}$; 6 μM) in 99:1 H₂O/DMSO and water respectively at 298 K. 233
- Figure 7.17. Fluorescence emission spectra of (A) ligand H₃L6 ($\lambda_{\text{excitation}} = 376 \text{ nm}$; 6 μM), as well as its respective precursors: HBPAMFF ($\lambda_{\text{excitation}} = 349 \text{ nm}$; 40 μM) and BPTH ($\lambda_{\text{excitation}} = 351 \text{ nm}$; 5 μM) and (B) ligand H₃L6 and its complexes 9 ($\lambda_{\text{excitation}} = 407 \text{ nm}$; 7 μM) and 10 ($\lambda_{\text{excitation}} = 406 \text{ nm}$; 7 μM) in water at 298 K. (C). Fluorescence emission spectra of ligand H₃L6 ($\lambda_{\text{excitation}} = 407 \text{ nm}$; 7 μM) in water and organic solvents at 298 K. 234
- Figure 7.18. (A) Absorption versus fluorescence emission spectra of ligand H₃L7 ($\lambda_{\text{excitation}} = 485 \text{ nm}$; 50 nM) in 99:1 H₂O/DMSO and water respectively at 298 K; and (B) Fluorescence emission spectra of ligand H₃L7 ($\lambda_{\text{excitation}} = 475 \text{ nm}$; 50 nM) in water and organic solvents at 298 K. 235

Figure 7.19. Fluorescence emission spectra of (A) ligand H₃L7 ($\lambda_{\text{excitation}} = 475 \text{ nm}$; 50 nM), of its precursors HBPAMFF ($\lambda_{\text{excitation}} = 349 \text{ nm}$; 40 μM) and BPTH and its complexes 11 ($\lambda_{\text{excitation}} = 485 \text{ nm}$; 0.3 μM) and 12 ($\lambda_{\text{excitation}} = 485 \text{ nm}$; 1 μM), in water, at 298 K. 235

Figure 7.20. Dose-dependent effect expressed as the percentage of relative viability of MDA-MB-231 cells measured by the MTT assay for (A) H₃L6; (B) H₃L7; (C) 9; (D) 10; (E) 11; and (F) 12 after 72 h incubation at 37 °C. Data represent the mean of triplicate experiments. 236

Figure 7.21. Dose-dependent effect on MDA-MB-231 cells of ligands H₃L6 and copper(II) complexes 9 and 10 (left) and ligand H₃L6 and copper(II) complexes 11 and 12 (right) after 72 h, at 37 °C, using the MTT assay. 237

Figure 7.22. IC₅₀ values of MDA-MB-231 cells measured by the MTT assay for ligands and complexes containing the HBPAMFF-Hz framework, after 72 h incubation (or 36 h for furan and thiophene derivatives) at 37 °C. Data represent the mean of triplicate experiments. 240

Figure 7.23. Fluorescence images of the cellular uptake and intracellular localization of ligand H₃L7 in MDA-MB-231 cells after incubation for 45 min at 37 °C with: (A) DAPI (300 nM) and MTDR (200 nM); (B) DAPI and H₃L7 (1 μM) and (C) MTDR and H₃L7. DAPI (A) was excited at 405 nm and the emission was recorded at 410 – 450 nm. Ligand H₃L7 (B) was excited at 488 nm et the emission was recorded at 500 – 600 nm. MTDR (C) was excited at 552 nm and the emission was recorded at 600 – 700 nm. Scale bar: 20 μM . 242

Figure 8.1 Synthetic routes to ligand H₂L8 and its copper(II) complexes from perchlorate 13 and acetate 14 salts. 246

Figure 8.2. ¹H NMR spectrum (400 MHz) of H₂L8 in DMSO-*d*₆, at room temperature. 247

Figure 8.3. *E* and *Z* configurational isomers of H₂L8. 248

Figure 8.4. *E*-amide and *E*-imanol tautomeric isomers of H₃L1. 249

Figure 8.5. ¹³C NMR spectrum (100 MHz) of H₂L8 in DMSO-*d*₆, at room temperature. 250

Figure 8.6. DEPT-135 NMR spectrum (100 MHz) of H₂L8 in DMSO-*d*₆, at room temperature. 250

Figure 8.7. Crystal structure of ligand H₂L8. The ellipsoids were drawn with 50% probability. Only one of the enantiomers is shown. Intramolecular and intermolecular hydrogen bonds are depicted as dotted line. 252

Figure 8.8. Molecular packing of ligand H₂L8. Hydrogen atoms have been omitted for clarify. 254

| | |
|--|-----|
| Figure 8.9. Absorption spectra of ligand H ₂ L8, and of its precursors BPMAMFF and INH, and of complexes 13 and 14, recorded in H ₂ O/DMSO 9:1, at 298 K. | 256 |
| Figure 8.10. Concentration versus UV-visible absorption plots of ligand H ₂ L8 at different wavelengths in H ₂ O/DMSO 9:1 and at 298 K. | 257 |
| Figure 8.11. Concentration versus UV-visible absorption plots of complex 13 at different wavelengths in H ₂ O/DMSO 9:1 and at 298 K. | 257 |
| Figure 8.12. Concentration versus UV-visible absorption plots of complex 14 at different wavelengths in H ₂ O/DMSO 9:1 and at 298 K. | 258 |
| Figure 8.13. Fluorescence emission spectra of ligand H ₂ L8 ($\lambda_{\text{excitation}} = 345 \text{ nm}$; 10 μM), and of its respective precursors: BPMAMFF ($\lambda_{\text{excitation}} = 345 \text{ nm}$; 40 μM) and INH ($\lambda_{\text{excitation}} = 266 \text{ nm}$; 40 μM), in water, at 298 K. | 259 |
| Figure 8.14. Dose-dependent effect on MCF-7 cells of ligand H ₂ L8 and its copper(II) complexes 13 and 14 after 24 h, at 37 °C, using the MTT assay. | 260 |
| Figure 12.1. First page of the published paper corresponding to Chapter 4 [210]. | 289 |
| Figure 13.1. ¹ H NMR spectrum (400 MHz) of the precursor HBPAMFF in DCM- <i>d</i> ₂ at room temperature. | 292 |
| Figure 13.2. ¹ H NMR spectrum (400 MHz) of the precursor FMeO-BODIPY-Hz in chloroform- <i>d</i> at room temperature. | 293 |
| Figure 13.3. Correlation spectroscopy (¹ H- ¹ H COSY) NMR contour map (400 MHz) of H ₃ L1 in DMSO- <i>d</i> ₆ at room temperature, in the 6.5–9.0 ppm region. In the other regions, any H–H interaction from different carbons was observed. | 293 |
| Figure 13.4. Quantum coherence (¹ H- ¹³ C HSQC) NMR contour map of H ₃ L1 in DMSO- <i>d</i> ₆ at room temperature, in 9.0–6.6 ppm (left) and 4.0–1.5 ppm (right) ¹ H HSQC region. In the other regions, any C–H interaction was observed. | 294 |
| Figure 13.5. Bond correlation (¹ H- ¹³ C HMBC) NMR contour map of H ₃ L1 in DMSO- <i>d</i> ₆ at room temperature, in the 9.0–1.5 ppm ¹ H HMBC region. In the other regions, any interaction was observed. | 294 |
| Figure 13.6. Correlation spectroscopy (¹ H- ¹ H COSY) NMR contour map (400 MHz) of H ₃ L2 in DMSO- <i>d</i> ₆ at room temperature in the 6.5–9.0 ppm region. In the other regions, any H–H interaction from different carbons was observed. | 295 |
| Figure 13.7. Quantum coherence (¹ H- ¹³ C HSQC) NMR contour map of H ₃ L2 in DMSO- <i>d</i> ₆ at room temperature, in 9.0–6.6 ppm (left) and 4.0–1.5 ppm (right) ¹ H HSQC region. In the other regions, any C–H interaction was observed. | 295 |
| Figure 13.8. Bond correlation (¹ H- ¹³ C HMBC) NMR contour map of H ₃ L2 in DMSO- <i>d</i> ₆ at room temperature. | 296 |

Figure 13.9. Correlation spectroscopy (^1H - ^1H COSY) NMR contour map (400 MHz) of H₃L3 in DMSO-*d*₆ at room temperature in the 6.5–9.0 ppm region. In the other regions, any H–H interaction from different carbons was observed. 296

Figure 13.10. Quantum coherence (^1H - ^{13}C HSQC) NMR contour map of H₃L3 in DMSO-*d*₆ at room temperature, in the 9.0–6.6 ppm (left) and 4.0–1.5 ppm (right) ^1H HSQC region. In the other regions, any C–H interaction was observed. 297

Figure 13.11. Bond correlation (^1H - ^{13}C HMBC) NMR contour map of H₃L3 in DMSO-*d*₆ at room temperature, in the 9.0–1.5 ppm ^1H HMBC region. In the other regions, any interaction was observed. 297

Figure 13.12. Correlation spectroscopy (^1H - ^1H COSY) NMR contour map (400 MHz) of H₃L4 in DMSO-*d*₆ at room temperature in the 6.5–9.0 ppm region. In the other regions, any H–H interaction from different carbons was observed. 298

Figure 13.13. Quantum coherence (^1H - ^{13}C HSQC) NMR contour map of H₃L4 in DMSO-*d*₆ at room temperature, in the 9.0–6.6 ppm (left) and 4.0–1.5 ppm (right) ^1H HSQC region. In the other regions, any C–H interaction was observed. 298

Figure 13.14. Bond correlation (^1H - ^{13}C HMBC) NMR contour map of H₃L3 in DMSO-*d*₆ at room temperature, in the 9.0–1.5 ppm ^1H HMBC region. One additional interaction was observed at 12.4 ppm x 54.7 ppm (^1H - ^{13}C HMBC). 299

Figure 13.15. Correlation spectroscopy (^1H - ^1H COSY) NMR contour map (400 MHz) of H₃L5 in DMSO-*d*₆ at room temperature in the (left) 9.0–6.5 ppm region and in the (right) 6.5–1.5 ppm region. In the other regions, any H–H interaction from different carbons was observed. 299

Figure 13.16. Quantum coherence (^1H - ^{13}C HSQC) NMR contour map of H₃L5 in DMSO-*d*₆ at room temperature, in the 8.7–6.6 ppm (left) and 4.0–1.5 ppm (right) ^1H HSQC region. In the other regions, any C–H interaction was observed. 300

Figure 13.17. Bond correlation (^1H - ^{13}C HMBC) NMR contour map of H₃L5 in DMSO-*d*₆ at room temperature, in the 12.0–1.5 ppm ^1H HMBC region. 300

Figure 13.18. Correlation spectroscopy (^1H - ^1H COSY) NMR contour map (400 MHz) of H₃L6 in DMSO-*d*₆ at room temperature in the 6.5–9.0 ppm region. In the other regions, any H–H interaction from different carbons was observed. 301

Figure 13.19. Quantum coherence (^1H - ^{13}C HSQC) NMR contour map of H₃L6 in DMSO-*d*₆ at room temperature, in the 9.0–6.5 ppm (left) and 5.4–2.1 ppm (right) ^1H HSQC region. In the other regions, any C–H interaction was observed. 301

- Figure 13.20. Bond correlation (^1H - ^{13}C HMBC) NMR contour map of $\text{H}_3\text{L6}$ in $\text{DMSO}-d_6$ at room temperature, in the 9.0–1.5 ppm ^1H HMBC region. In the other regions, any interaction was observed. 302
- Figure 13.21. Correlation spectroscopy (^1H - ^1H COSY) NMR contour map (400 MHz) of $\text{H}_3\text{L7}$ in $\text{DCM}-d_2$ at room temperature in the 6.5–9.0 ppm region. In the other regions, any H–H interaction from different carbons was observed. 302
- Figure 13.22. Correlation spectroscopy (^1H - ^1H COSY) NMR contour map (400 MHz) of $\text{H}_3\text{L8}$ in $\text{DMSO}-d_6$ at room temperature in the 6.5–9.0 ppm region. In the other regions, any H–H interaction from different carbons was observed. 303
- Figure 13.23. FTIR spectra of HBPA in KBr pellets. 304
- Figure 13.24. FTIR spectra of HBPAMFF in KBr pellets. 304
- Figure 13.25. FTIR spectra of BPMAMFF in KBr pellets. 305
- Figure 13.26. FTIR and Raman spectra of $\text{H}_3\text{L1}$ in the region 1700–700 cm^{-1} . 305
- Figure 13.27. FTIR and Raman spectra of $\text{H}_3\text{L1}$ in the region 700–200 cm^{-1} . 306
- Figure 13.28. FTIR and Raman spectra of $\text{H}_3\text{L2}$ in the region 1700–700 cm^{-1} . 306
- Figure 13.29. FTIR and Raman spectra of $\text{H}_3\text{L2}$ in the region 700–200 cm^{-1} . 307
- Figure 13.30. FTIR and Raman spectra of complex 1 in the region 1700–700 cm^{-1} . 307
- Figure 13.31. FTIR and Raman spectra of complex 1 in the region 700–200 cm^{-1} . 308
- Figure 13.32. FTIR and Raman spectra of complex 2 in the region 1700–700 cm^{-1} . 308
- Figure 13.33. FTIR and Raman spectra of complex 2 in the region 700–200 cm^{-1} . 309
- Figure 13.34. Fluorescence images of the cellular uptake and intracellular localization of ligand $\text{H}_3\text{L7}$ in one MDA-MB-231 cell after incubation of 45 min at 37 °C with (A) DAPI (300 nM) and MTDR (200 nM), (B) DAPI and $\text{H}_3\text{L7}$ (1 μM), and (C) MTDR and $\text{H}_3\text{L7}$. DAPI (A) was excited at 405 nm (emission = 410–450 nm); ligand $\text{H}_3\text{L7}$ (B) at 488 nm (emission = 500–600 nm) and MTDR (C) at 552 nm (emission = 600–700 nm). Scale bar: 20 μM . 309
- Figure 13.35. Fluorescence images of the cellular uptake and intracellular localization of ligand $\text{H}_3\text{L7}$ in one MDA-MB-231 cell after incubation of 45 min at 37 °C with (A) DAPI (300 nM) and MTDR (200 nM), (B) DAPI and $\text{H}_3\text{L7}$ (1 μM), and (C) MTDR and $\text{H}_3\text{L7}$. DAPI (A) was excited at 405 nm (emission = 410–450 nm); ligand $\text{H}_3\text{L7}$ (B) at

488 nm (emission = 500–600 nm) and MTDR (C) at 552 nm (emission = 600–700 nm). Scale bar: 10 μ M. 310

Figure 13.36. Fluorescence images of the cellular uptake and intracellular localization of ligand H₃L7 in one MDA-MB-231 cell after incubation of 45 min at 37 °C with (A) DAPI (300 nM) and MTDR (200 nM), (B) DAPI and H₃L7 (1 μ M), and (C) MTDR and H₃L7. DAPI (A) was excited at 405 nm (emission = 410–450 nm); ligand H₃L7 (B) at 488 nm (emission = 500–600 nm) and MTDR (C) at 552 nm (emission = 600–700 nm). Scale bar: 20 μ M. 310

Figure 13.37. Fluorescence emission spectra of complexes 9 ($\lambda_{\text{excitation}} = 406$ nm; 7 μ M) and 10 ($\lambda_{\text{excitation}} = 407$ nm; 10 μ M) in water and DCM at 298 K. 311

Figure 13.38. Fluorescence emission spectra of complex 11 ($\lambda_{\text{excitation}} = 483$ nm; 1 μ M) in water and organic solvents at 298 K. 311

Figure 13.39. Fluorescence emission spectra of complex 12 ($\lambda_{\text{excitation}} = 483$ nm; 0.33 μ M) in water and organic solvents at 298 K. 312

List of tables

| | |
|--|-----|
| Table 4.1. ^1H (400 MHz) and ^{13}C (100 MHz) data for $\text{H}_3\text{L1}$ and $\text{H}_3\text{L2}$ in $\text{DMSO-}d_6$ at room temperature, along with the respective assignments. Chemical shifts (δ) are in ppm and coupling constants (J) are in Hz. | 96 |
| Table 4.2. Experimental details for complex 1. | 99 |
| Table 4.3. Experimental details for complex 2. | 100 |
| Table 4.4. Selected geometric parameters for complexes 1 and 2. | 101 |
| Table 4.5. H-bonding parameters for complex 1 (\AA , $^\circ$). | 102 |
| Table 4.6. H-bonding parameters for complex 2 (\AA , $^\circ$). | 102 |
| Table 4.7. Selected vibrational absorptions (cm^{-1}) for $\text{H}_3\text{L1}$ and $\text{H}_3\text{L2}$ and their complexes. | 105 |
| Table 4.8. UV-Vis absorption properties of $\text{H}_3\text{L1}$ and $\text{H}_3\text{L2}$, as well as those of their dicopper(II) complexes 1 and 2, in DMSO at r.t. Suggested assignments are also included. | 107 |
| Table 4.9. Quenching and binding parameters for the interaction of the complexes 1 and 2 with BSA, at $25\text{ }^\circ\text{C}$. | 117 |
| Table 4.10. Growth inhibition, expressed as $\text{IC}_{50} \pm \text{SD}$, of several cancer cell lines [HCT116 (colon, human); HT29 (colon, human); MDA-MB-231 (breast, human); and B16F10 (melanoma, mouse)] after incubation for 36 h in the presence of the synthesized compounds. The Selectivity Index (SI) was estimated based on the IC_{50} values obtained for the non-tumoral control Madin-Darby canine kidney (MDCK) cells, also included in the table. Values in bold correspond to those in the submicromolar range. | 132 |
| Table 5.1. ^1H (400 MHz) and ^{13}C (100 MHz) data for $\text{H}_3\text{L3}$ and $\text{H}_2\text{L4}$ in $\text{DMSO-}d_6$ at room temperature, along with the respective assignments. Chemical shifts (δ) are in ppm and coupling constants (J) are in Hz. | 145 |
| Table 5.2. Crystallographic data and structure refinement of ligands $\text{H}_3\text{L3}$ and $\text{H}_2\text{L4}$. | 148 |
| Table 5.3. Selected geometric parameters for ligands $\text{H}_3\text{L3}$ and $\text{H}_2\text{L4}$. | 149 |
| Table 5.4. H-bond length (d , \AA) for ligands $\text{H}_3\text{L3}$ and $\text{H}_2\text{L4}$. | 150 |
| Table 5.5. Crystallographic data and structure refinement of complexes 3 and 6. | 152 |
| Table 5.6. Selected geometric parameters for complexes 3 and 6. | 153 |
| Table 5.7. H-bond length (d , \AA) for complex 3. | 155 |

| | |
|--|-----|
| Table 5.8. H-bond length (d, Å) for complex 6. | 155 |
| Table 5.9. UV/Vis absorption properties of ligands H ₃ L3 and H ₃ L4 and dicopper(II) complexes 1–4 in H ₂ O/DMSO 9:1 in the range 230 – 500 nm, or in DMSO in the range 500 – 900 nm at 25 °C, and suggested assignments. | 160 |
| Table 5.10. Absorption features of the interaction of ligands H ₃ L3 and H ₂ L4 and their copper(II) complexes 3–6 with ct-DNA. | 166 |
| Table 5.11. Fluorescence features of the interaction of ligands H ₃ L3 and H ₂ L4 and their copper(II) complexes 3–6 with ct-DNA. | 170 |
| Table 5.12. IC ₅₀ values of the ligands H ₃ L3 and H ₂ L4 and their copper(II) complexes 3–6 on MDA-MB-231 cells. The precursor involved in the synthesis of each compound is also indicated. | 174 |
| Table 6.1. ¹³ C (100 MHz) data for H ₃ L5 in DMSO- <i>d</i> ₆ at room temperature, along with the respective assignments. Chemical shifts (δ) are in ppm. | 189 |
| Table 6.2. Crystallographic data and structure refinement of ligand H ₃ L5. | 191 |
| Table 6.3. Selected geometric parameters for ligand H ₃ L5. | 192 |
| Table 6.4. H-bond length (d, Å) and angles (°) for ligand H ₃ L5. | 193 |
| Table 6.5. Selected vibrational absorptions (cm ⁻¹) for H ₃ L5 and its complexes 7 and 8. | 197 |
| Table 6.6. UV/Vis absorption properties of ligands H ₃ L55 and dicopper(II) complexes 7 and 8 in H ₂ O/DMSO 9:1 in the range 230 – 500 nm at 25 °C, and suggested assignments. | 198 |
| Table 6.7. Fluorescence features of the interaction of ligands H ₃ L5 with ctDNA at pH 7.40 and at 25 °C. | 205 |
| Table 6.8. IC ₅₀ values of ligand H ₃ L5 and its copper(II) complexes 7 and 8 on MDA-MB-231 cancer cell line. Standard deviations of data are included. | 211 |
| Table 7.1. ¹ H (400 MHz) and ¹³ C (100 MHz) data for H ₃ L6 and ¹ H (400 MHz) for H ₃ L7 in DCM- <i>d</i> ₂ at room temperature, along with the respective assignments. Chemical shifts (δ) are in ppm and coupling constants (J) are in Hz. | 221 |
| Table 7.2. Crystallographic data and structure refinement of complex 9. | 223 |
| Table 7.3. H-bond length (d, Å) and angles (°) for complex 9. | 225 |
| Table 7.4. Selected geometric parameters for complex 9. | 226 |
| Table 7.5. Selected vibrational absorptions (cm ⁻¹) for H ₃ L6 and H ₃ L7 and their complexes 9 – 12. | 230 |
| Table 7.6. UV/Vis absorption properties of ligands H ₃ L6 and H ₃ L7 and dicopper(II) complexes 9–12 in H ₂ O/DMSO 9:1 in the range 230 – 500 nm at 25 °C, and suggested assignments. | 231 |

| | |
|--|-----|
| Table 7.7. IC ₅₀ values of ligands H ₃ L6 and H ₃ L7 and by their copper(II) complexes 9–12 on MDA-MB-231 cells and, IC ₅₀ values of the previous reported ligands and copper(II) complexes derived from HBPAMFF-Hz. | 239 |
| Table 8.1. ¹ H (400 MHz) and ¹³ C (100 MHz) data for H ₂ L8 in DMSO- <i>d</i> ₆ at room temperature, with the respective assignments. Chemical shifts (δ) are in ppm and coupling constants (<i>J</i>) are in Hz. | 251 |
| Table 8.2. Crystallographic data and structure refinement of ligand H ₂ L8. | 253 |
| Table 8.3. H-bond length (<i>d</i> , Å) and angles (°) for ligand H ₂ L8. | 254 |
| Table 8.4. Selected geometric parameters for ligand H ₂ L8. | 255 |
| Table 8.5. UV-Vis absorption properties of H ₂ L8, and of its dicopper(II) complexes 13 and 14 in H ₂ O/DMSO 9:1 at 298 K. Suggested assignments and standard deviation (mean ± S.D) are included. | 258 |
| Table 8.6. IC ₅₀ values of ligand H ₂ L8 and its copper(II) complexes 13 and 14 on MCF-7 cancer cell line. Standard deviations are included. | 261 |
| Table 13.1. Relation of the ligands terminology between the laboratory notebook, thesis manuscript and redacted papers. Chapter describing each compound is also included. | 313 |
| Table 13.2. Relation of the complexes terminology between the laboratory notebook, thesis manuscript and redacted papers. Chapter describing each compound is also included. | 314 |

List of abbreviations

| | |
|----------------|--|
| A549 | Human lung cancer cell line |
| BEL-7404 | Human hepatocellular carcinoma cell line |
| BODIPY | Boron-dipyrromethene |
| BPMAMFF | 2[-bis-(pyridylmethyl)aminomethyl]-4-methyl-6-formyl-phenol |
| BPTH | 4- <i>H</i> -[1]-benzopyrano[4,3- <i>b</i>]thiophene-2-carbohydrazide |
| BSA | Bovine serum albumin |
| Caco-2 | Human colon carcinoma cell line |
| CMFF | (2-chloromethyl-4-methyl-6-formyl)phenol |
| COs | Catechol oxidase |
| <i>ct</i> -DNA | <i>Calf thymus</i> DNA (or ctDNA) |
| DCM | Dichloromethane |
| DLS | Dynamic light scattering |
| DNA | Deoxyribonucleic acid |
| DMEM | Dulbecco Modified Eagle Medium |
| EB | Ethidium bromide |
| ESI+ | Electrospray ionization |
| ESI-MS | Electrospray ionization mass spectrometry |
| FCH | Furan-2-carbohydrazide |
| FMeO-BODIPY-Hz | fluor-methoxo-BODIPY-hydrazide |
| GLC4 | Small cell lung carcinoma |
| HeLa | Human epitheloid cervix carcinoma cell line |
| HepG2 | Human hepatocyte carcinoma cell line |
| HBPA | (2-hydroxybenzyl)(2-pyridylmethyl)amine |
| HBPAMFF | 3-[(2-hydroxybenzyl)(2-pyridylmethyl)amine]-2-hydroxy-5-methylbenzaldehyde |
| HBPAMFF-Hz | HBPAMFF-hydrazones |
| HRMS | High resolution mass spectrometry |

| | |
|------------------|--|
| HSA | Human serum albumin |
| Hz | Hydrazone |
| IC ₅₀ | Half maximal inhibitory concentration |
| INH | 4-Pyridinecarboxylic acid hydrazide (isoniazide) |
| K562 | Myelogenous leukemia |
| 4-MeBA | 4-methoxycarbonyl benzaldehyde |
| MCF-7 | Breast cancer cell line |
| MDA-MB-231 | Triple-negative human breast cancer cell line |
| MGC-803 | Human gastric cancer cell line |
| NMR | Nuclear magnetic resonance spectroscopy |
| ORTEP | Oak Ridge Thermal Ellipsoid Plot |
| PAPs | Purple acid phosphatase |
| PBH | 1-pyrenebutyric hydrazide |
| PBS | Phosphate buffered saline |
| PC3 | Human prostate cancer cell line |
| PIH | 5-phenylisoxazole-3-carbohydrazide |
| ROS | Reactive oxygen species |
| SAXS | Small-angle X-ray scattering |
| SI | Selectivity Index |
| SMMC-7721 | Human hepatocarcinoma cell line |
| TEA | Triethylamine |
| TCH | Thiophene-2-carbohydrazide |
| TEA | Triethylamine |
| TFA | Trifluoroacetic acid |
| TLC | Thin-layer chromatography |
| Tris | Tris(hydroxymethyl)aminomethane |
| U937 | Human leukemic monoblast cell line |
| WCR | World cancer report |
| WHO | World Health Organization |
| XRD | X-ray diffraction |

*...Todos se parecen a viejos conocidos,
hasta los perros y las mariposas ...
...Cómo quisiera estar allá,
en el allá de algunos antes,
el que nunca volví a encontrar,
más allá de recuerdos nostálgicos.*

*To Alejandro, Emma Sofía, Jesús David
and Sara Sofía*

Part I.

Introduction, objectives and theoretical fundamentals

1

Introduction

1.1

Research context

The limitations in the use and secondary effects of the anticancer drug cisplatin [1] have motivated the search for new chemotherapeutic agents differing from this drug treatment. In recent last years, aroylhydrazonic derivatives and copper(II) complexes appeared as promising compounds to achieve this goal. Copper ions present various advantages when compared to platinum, the metal present in cisplatin. First, copper(II) is an essential metal in human body with a large number of biological functions [2, 3] and presents interesting properties, such as multiple geometries and coordination numbers. Second, several copper(II) complexes synthesized recently confirmed their cytotoxic activity on cancer cells [4-22], which places them as a promising new-generation of chemotherapeutics. Indeed, some mixed-chelate copper complexes known as Casiopeínas® have entering in cancer clinical trials [23]. The reported studies on copper(II) complexes have proposed different mechanisms for cell death [17-21, 24-41]. Some dinuclear copper(II) complexes have demonstrated their ability to induce apoptosis in cancer cells [21, 40] and displayed remarkable *in vitro* cytotoxic activity, which was commonly better than cisplatin on different cancer cell lines [33, 37, 40]. Comparison of the cytotoxic activity of copper complexes with other metal-complexes (as Co, Zn or Ni) with the same ligand [42, 43] revealed the highest cell death potency of Cu-compounds. Besides, the addition of copper(II) ion to ligands commonly improves the antiproliferative activity in comparison to the metal-free chelator [33-40, 44]. Finally, both the metal-free and the coordinated hydrazone group have revealed biological activity as anticancer agents [45-57], which has motivated the inclusion of this moiety in the design of the compounds.

The main contribution of the present work relies both on the combination of independent entities [hydrazones and copper(II) complexes], each one bearing its

own anticancer properties, and on the exploration of the resulting cytotoxic ability of the new structures in cancer cells. In this sense, this thesis reports the syntheses and full characterization of eight new aroylhydrazone ligand derivatives and their dicopper complexes. The crystal structures of some ligands and complexes are described. Besides, *in vitro* biological properties of the compounds are studied.

Comparing chemical structures and *in cell* activity, it is hypothesized that subtle variations in the ligand frameworks (pyridine or phenol pending arms) can provide significant difference in the cytotoxic activities of the ligands and metal complexes. By the interesting cytotoxic activity of the metal-free ligands, it is also explored the ability of the binucleating aroylhydrazones to sequester metal ions from the biological medium as an additional mode of action.

1.2

Thesis structure

This thesis is structured in three main parts. Part I involves the current introduction and the chosen objectives (at the end of this section) to develop the present work (Chapter 1) and the theoretical fundamentals (Chapter 2), that describes the principal characteristics of cancer and the statistics of incidence in the world, Latin America and Brazil. Chemotherapy and other treatments are also discussed. A discussion about the state of art concerning the copper(II) complexes and recent approaches involving them as anticancer agents is included.

Part II is relative to (i) the experimental procedures, instrumentation and material used to achieve the proposed aims (Chapter 3); to (ii) the results concerning the syntheses, chemical and biological characterization of the compounds (Chapters 4–8); and lastly, to (iii) the general conclusions and future works of this thesis (Chapter 9). Each chapter corresponding to the results of this thesis (4–8) includes a short introduction on the subject. Important data and information to contextualize the different works are discussed as theoretical fundamentals.

Finally, Part III contains the expected future directions of the present work, references and attachments containing some additional information.

1.3

Objectives of this work

1.3.1

General Objective

To synthesize, characterize and explore the anticancer and biological properties of novel binucleating aroylhydrazonic ligands and their bioinspired dicopper(II) complexes.

1.3.2

Specific objectives

- ✓ To design and synthesize novel aroylhydrazonic ligands and their copper(II) complexes from the perchlorate and/or acetate salts.
- ✓ To characterize the compounds using spectroscopies, crystallographic and analytical methods, as infrared, electronic absorption, RMN, TGA, X-ray diffraction, among others.
- ✓ To examine the stability of the stock solutions (DMSO) of the compounds as well as in the medium used for the biological assays (PBS/DMSO).
- ✓ To study the interaction of ligands and complexes with serum albumin proteins responsible for the transport of drugs in blood of mammals using absorption and fluorescence spectroscopies.
- ✓ To analyze the changes in the hydrodynamic and gyration radius of BSA protein in the presence of the compounds by scattering studies.
- ✓ To evaluate the interaction of the compounds with *calf thymus* DNA by ultraviolet, visible and, when possible, fluorescence spectroscopies.
- ✓ To examine the plasmid DNA cleaving ability of the compounds, by monitoring changes in hydrodynamic radius of the biomolecule using dynamic light scattering.
- ✓ To determine the cytotoxicity of the compounds in cancer cells and non-tumoral cells using the MTT assay.
- ✓ To compare the cytotoxicity between (i) ligands and their complexes, (ii) perchlorate-complexes and acetate-complexes, and, finally, between (iii)

ligands containing, in the non-hydrazone moiety, a N_2O - set of donor atoms (i.e., **HBPAMFF**-derived) or a N_3 - one (**BPMAMFF**-derived), as well as between their metal complexes.

- ✓ To verify the ability of compounds to permeate the cell membrane using fluorescence microscopy and co-localize them into the cancer cells.

2

Theoretical fundamentals

The chapter describes the main topics related to the development of this thesis. Concepts and characteristics of cancer, chemotherapeutics and copper complexes are approached.

2.1

Cancer: statistics and pathology

According to the World Health Organization (WHO): “cancer is a generic term for a large group of diseases characterized by the growth of abnormal cells beyond their usual boundaries that can then invade adjoining parts of the body and/or spread to other organs”. WHO refers also the terms malignant tumours and neoplasms as other common terms used to call cancer [58].

The urgency to find effective treatments to combat this disease is motivated by the fact that cancer is the second leading cause of death globally and is estimated to account for 9.6 million death in 2018 [58], after heart diseases [59]. It is also important to highlight that cancer can affect almost any part of the body and has many anatomic and molecular subtypes that each require specific management strategies. WHO indicates the most common types of cancer in men to be lung, prostate, colorectal, stomach and liver cancer, while breast, colorectal, lung, cervix and thyroid cancer are the most common among women [58]. In Latin America and the Caribbean, the statistics of cancer has increased for prostate in men and cervix uteri in women, according to the last published report in 2012 [58].

The National Cancer Institute José Alencar Gomes da Silva from Brazil (INCA, in Portuguese: *Instituto Nacional do Câncer*) signals prostate cancer as the most common cancer in men in all regions of Brazil, a part of non-melanoma skin tumours. The number of new cases of prostate cancer are estimated in Brazil as 68.220 new cases for each year 2018-2019 biennium. These values correspond to an estimated risk of 66.12 new cases per 100,000 men.

For women, and without considering non-melanoma skin tumours, breast cancer is the most frequent cancer in Brazil. Thus, 59,700 new cases of this cancer are estimated for each year of the 2018-2019 biennium, with an estimated risk of 56.33 cases per 100,000 women. After prostate and breast cancer, uterine cervix cancer in women (16,370 cases) and trachea/bronchus/lung cancer in men (17,740 cases) are the next in the list of the most common types of cancer in Brazil [60].

Proto-oncogenes are normal genes responsible for the coding of proteins that help regulate cell growth and differentiation, signal transduction and the execution of mitotic signals, usually through their protein products [61]. Each proto-oncogene can become activated in a variety of tissue types, and once activated, the resulting oncogene is able to help transform the cells of these various tissues [62]. Multiple genetic alterations pave the way for the transformation of a normal cell into a cancer cell. At the core of this process are oncogenic (cancer-causing) mutations in critical genes, which lead to sustained proliferative drive and desensitization of the cell to cues that normally inhibit growth or promote cell death [63, 64]. Published works have shown that a single oncogene is insufficient to make normal cells cancerous, whereas cooperation between two distinct oncogenic mutations can do the job (Figure 2.1) [63, 65, 66].

The cooperation between two important oncogenic mutations in human cancers (Ras and of p53) was examined by Murray *et. al.*, [67] as suggested by the review of LUO, J. and ELLEDGE, S. J. [63]. Through growth-factor receptors that enhance cell proliferation, molecules are identified by GTPase proteins of the Ras family. On the other hand, “p53 is a gene transcription factor by stress such as DNA damage, oxygen shortage or the presence of oncogenes (such as mutant Ras) to halt cell proliferation and promote programmed cell death (apoptosis)”. LUO, J. and ELLEDGE, S. J. [62] refer also to the work of LAND and co-workers, which describe that malignant cells are made normal through the oncogenic mutations in either Ras or p53. However, jointly those mutations create the conditions of cancerous transformation that brings about tumour expansion [65]. Finally, GTPases refer to the broad category of guanosine triphosphate hydrolases [65].

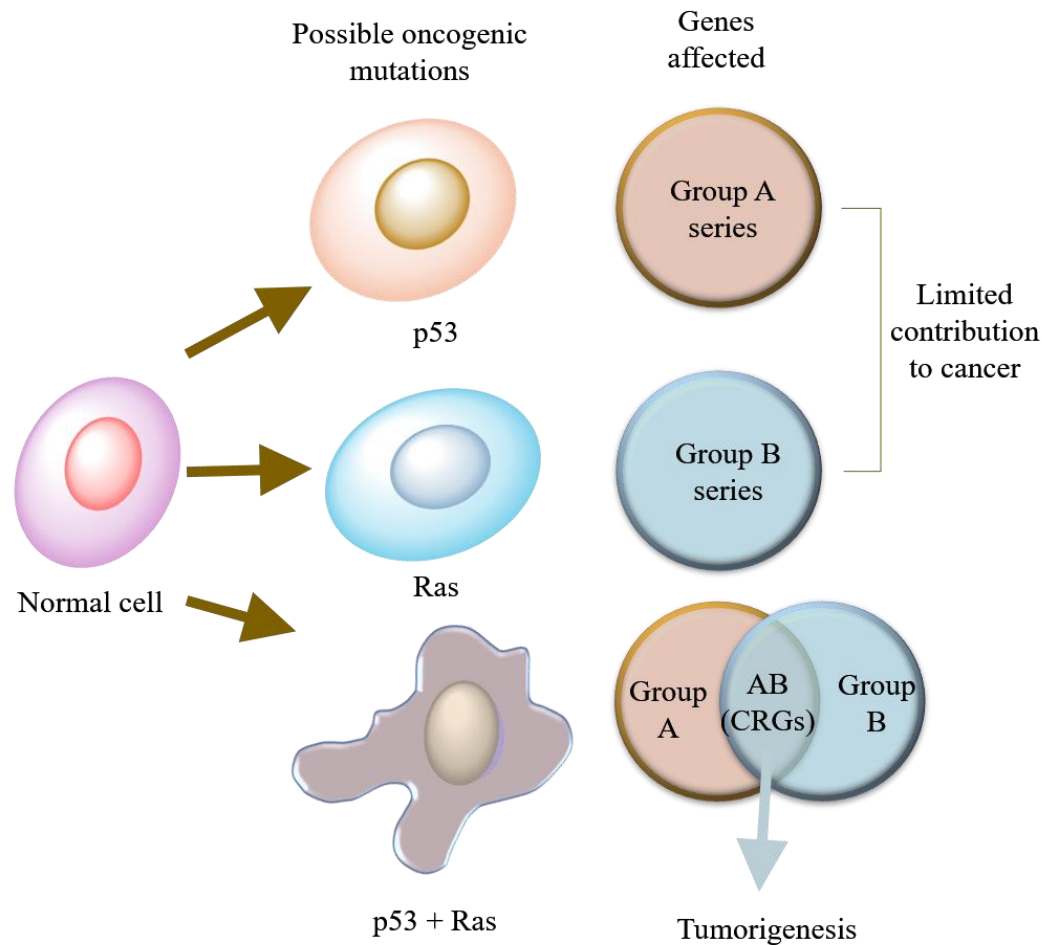


Figure 2.1. “Oncogenic mutations in the transcription factor p53 and in the small GTPase protein Ras (which individually have limited effects on promoting cancer) cooperate to transform normal cells into cancer cells [65]. In this example, p53 mutation affects the expression of group A genes and Ras mutation modifies the expression of group B genes. When both p53 and Ras are mutated in the same cell [67], they synergistically regulate a subset of genes (AB) known as cooperation response genes (CRGs), which turn out to be crucial mediators of tumour formation”. Adapted from LUO, J. and ELLEDGE, S. J. [63].

The increase of the expression level or activity of a proto-oncogene in the mutation process can lead to the formation of oncogenes. Chial [68] noticed that the oncogene activation presents steps that lead to a hyperactive gene product, increased transcription and gene amplification [68]. Once cell multiplication is developed, new blood vessels are created to carry nutrients to the cells, and forming malignant tumours. This process is called angiogenesis. These new malignant cells may also have the ability to detach and migrate from the tumour, initially invading the surrounding tissues, and may reach the interior of a blood vessel or lymphatic

vessel and through them, spread to organs distant from the site where the tumour started, forming the metastases [60, 69].

2.2

Cancer treatments

According to the National Cancer Institute from Spain, there are currently many types of cancer treatments, of which the main ones are surgery, radiotherapy and chemotherapy. Alternative therapies include phototherapy, immunotherapy (that help the immune system to treat cancer), targeted therapy (it acts directly on changes that promote the growth, division and spread of cancer cells), hormone treatment and stem cell transplantation. The Institute indicates that most cancer patients receive more than one type of treatment [70].

Despite the different options to treat cancer that appeared in the last years, all of these treatments have significant restrictions, according to the World Health Organization. For example, surgery and sometimes radiotherapy are used with satisfying results when the tumour presents a small size and is localized. Besides, chemotherapy can be effective for a small number of cancers, such as hematological malignancies (leukemia and lymphomas) [58]. On the other hand, immunotherapy has been largely studied and developed in the last years to treat cancer. The valuable contributions in medicine have awarded the Nobel Prize in Medicine in 2018 to cancer immunotherapy researchers James P. Allison, PhD, of The University of Texas MD Anderson Cancer Center, and Dr. Tasuku Honjo of Kyoto University in Japan [71]. Nevertheless, immunotherapy still presents adverse effects and limitations in its use and success results in patients [72].

Finally, WHO signals that cancer treatments can cause side effects when they affect healthy tissues and organs. Some of the most common side effects are: anaemia, hair loss, delirium, diarrhea, pain, edema, constipation, lack of appetite, fatigue, infection, nausea and vomiting. Problems of neuropathy, memory and concentration problems, mouth and neck, sleep, sexual and fertility, and urinary problems are also reported.

2.3

Chemotherapy drugs

Cancer chemotherapy consists of treating cancer with the use of strong-acting drugs aiming to reduce the number of neoplastic cells and preserving the normal ones. However, most chemotherapeutic agents act in a non-specific manner, injuring both normal and malignant cells, particularly fast growing cells, such as gastrointestinal, capillary and immune cells [61].

The antineoplastic drugs present quite different chemical characteristics and pharmacological mechanisms. However, DNA appears in chemotherapy as a major target of antitumour drugs to kill malignant cells, using organic compounds, such as taxol and vinblastine, as well as metal complexes, such as cisplatin and carboplatin [73]. The pharmaceutical use of inorganic compounds, notably those containing metals, was quite limited until the early 1960s when the antitumour properties of *cis*-diaminodichloroplatinum(II), known as cisplatin, were discovered [73]. The synthesis of cisplatin was first described by Michele Peyrone in 1845 and its structure was only elucidated half a century later by Werner [74]. Only in 1965, the antitumour properties of cisplatin were accidentally discovered by the American physicist Barnett Rosenberg and his colleagues [75]. Subsequently, Rosenberg and co-workers reported that only the *cis*-form was responsible for the antitumour activity observed, excluding the *trans*-isomer (Figure 2.2) [76]. Clinical trials began in the 1970s, and as early as 1978 cisplatin had its use approved by the North American Food and Drug Administration [74].

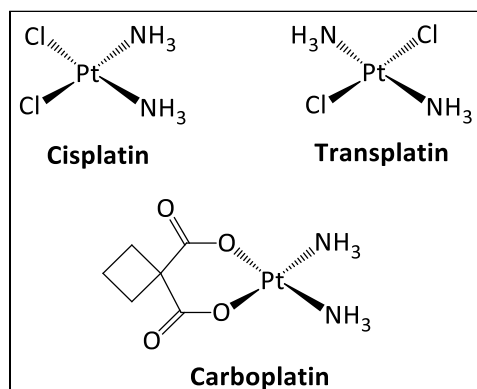


Figure 2.2. Chemical structure of the cisplatin, transplatin and carboplatin Pt-complexes.

Although there are many side effects reported for cisplatin as a chemotherapeutic agent, it continues to be one of the most widely used treatments in cancer patients, normally combined with other drugs [77, 78]. In addition to the side effects, the use of the drug to treat cancer is limited by both toxicological considerations (such as nephrotoxicity and neurotoxicity, as well as damage to the gastrointestinal tract mucosa) and cellular resistance to the compound [79]. Several factors can be attributed to this acquired resistance to cisplatin; among them, the deactivation of the drug by proteins and peptides containing sulphur in the plasma, the occurrence of damaged DNA repair and the decrease of the accumulation in the cells [74, 79]. Carboplatin (Figure 2.2), another platinum anticancer drug used in the clinic, has displayed a more favourable toxicity profile for some tumours than cisplatin [80]. As cisplatin, this drug presents side effects, as hematotoxicity [81].

Hence, the search for new potential anticancer compounds with less undesired side effects is still a challenge nowadays.

2.4

Copper(II) complexes: promising antineoplastic agents?

2.4.1

Copper(II): the natural ion with interesting coordination chemistry

Since the fortuitous discovery of the antitumour activity of cisplatin, the search for new metal-based anticancer agents has increased dramatically. Even though, very few new inorganic antineoplastic drugs have entered the clinic in the last decades, mainly due to toxicity issues. A published review discussed recent examples of different types of cell death induced by anticancer drugs based on metal complexes. Among these drugs, there are complexes of platinum, ruthenium, gallium, titanium, iron, copper, palladium, osmium, iridium and gold. Especially in the case of copper, the authors emphasize its relevance as a crucial element for all living organisms, and important for the function of several metalloenzymes [82].

Copper is an essential metal in human body with several biological functions [2, 3], and exhibits singularly interesting properties, multiple coordination numbers and geometric structures. Taking into account the natural ubiquitous occurrence of copper, a reduction of side effects is expected in comparison with the widely used

platinum anticancer compounds cisplatin, carboplatin and oxaliplatin [83]. Also, due to the fundamental differences between the chemistry of copper complexes and those of platinum, one can also expect diverse mechanisms of action. These features make copper complexes remarkably attractive in the discovery of new active compounds against tumours, as alternatives to cisplatin. In fact, the potential of copper complexes as a novel class of therapeutics for an extensive range of diseases, including cancer, has been previously discussed [84-86]. Actually, some Casiopeínas® copper complexes are entering in cancer clinical trials [23].

2.4.1

Cytotoxicity of copper(II) complexes

Santini and co/workers have published a review specifically describing copper complexes as anticancer agents that have emerged between the years 2008-2012 [4]. The authors present an analysis of the antineoplastic activities of the copper (I), copper (II) and copper (III) complexes when combined with different organic binders, and also highlight the increase in the number of publications in this field since 2000 [4].

After 2012, a large number of copper(II) complexes synthesized has been shown to present cytotoxic activity on cancer cells [4-22], highlighting these complexes as a promising new-generation of anticancer therapeutics. In the field of anticancer applications, some mechanisms proposed for cell death caused by mono- and di-copper complexes, involve the production of reactive oxygen species (ROS) [24, 25], inducing mitochondrial toxicity [26-28] and DNA interaction and damage [17-21, 24, 29-41]. Besides, some dinuclear copper complexes appeared to induce apoptosis in cancer cells [21, 40]. Dinuclear copper(II) complexes have displayed remarkable *in vitro* cytotoxic activity, which was commonly better than cisplatin on human hepatocarcinoma cell line SMMC-7721 [37], human gastric cancer MGC-803 cell line [40], human hepatocellular carcinoma BEL-7404 cell line [40], and on human lung cancer A549 cancer cell line [33]. Additionally, excellent Half Maximal Inhibitory Concentration (IC₅₀) values in the micromolar range and greater on human hepatocyte carcinoma HepG2 cancer cells [33-37], in the nanomolar range, on human epitheloid cervix carcinoma HeLa cell line [38], human colon carcinoma Caco-2 cell line [38], human leukemic monoblast U937 cell line

[39] and on breast cancer MCF-7 cell line [44] have been reported. Concerning MDA-MB-231 cells, scientific works reported IC_{50} values for dinuclear copper(II) complexes higher than 100 μ M [87], in the micromolar [88-91], and more recently in the nanomolar range [43].

Comparison of the cytotoxic activity of copper complexes with those of other zinc-derivatives of the same ligand [43], revealed the highest cell death potency of Cu-complexes. Also, studies of a synthesized series of cobalt, nickel and copper complexes using the same organic ligands showed that the copper(II) derivatives possess a better DNA cleavage activity than the corresponding cobalt and nickel compounds [42]. Besides, the addition of copper(II) ion to ligands, commonly improves the antiproliferative activity compared with the metal-free chelator [33-40, 44].

2.6

Copper(II) complexes containing biomimetic active sites

During the last decade, the use of dicopper(II) compounds has constituted an interesting tendency in this area, since bimetallic copper cores are abundant in nature. A typical example is that of catechol oxidases (COs), a group of ubiquitous type-3 dicopper enzymes. The crystal structure of sweet potato catechol oxidase has been already described and possesses, in its resting Cu(II)Cu(II) state, two cupric ions bridged by an exogenous hydroxo ligand (Figure 2.3) [92]. This result has triggered the scientific interest in the synthesis of biomimetic models for the active site of COs [93, 94]. The phosphatase-like and nuclease activity of dinuclear copper(II) complexes with similar active sites of these proteins was also demonstrated [95, 96]. The catalytic mechanism of hydrolysis probably involves terminal coordination of the phosphate diester to one of the cupric ions and subsequent intramolecular nucleophilic attack by the bridging hydroxide [97, 98]. The reported results suggest that this class of compounds could also perform properly as potential antineoplastic agents. Indeed, this fact was confirmed towards the GLC4 (small cell lung carcinoma) and K562 (myelogenous leukemia) cell line [95]. In addition, very recently, Cao *et al.* proved that the changes in the chelating arms on ligands allows for the regulation of the reactivity of their dinuclear copper(II) complexes towards DNA [99].

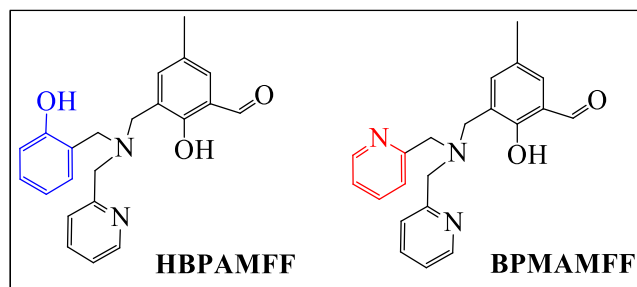


Figure 2.3. Structures of **HBPAMFF** and **BPMAMFF** molecules.

Some dinuclear copper(II) complexes mimicking the active sites of type 3 copper proteins were synthesized and explored as potential antineoplastic agents [100, 101]. Under this perspective, 3-[(2-hydroxybenzyl)(2-pyridylmethyl)amine]-2-hydroxy-5-methylbenzaldehyde - **HBPAMFF**[102] (with a set of N₂O-O donor atoms), as well as 2[-bis-(pyridylmethyl)aminomethyl]-4-methyl-6-formyl-phenol - **BPMAMFF** [103, 104] (with N₃-O donor atoms) (Figure 2.3) are molecules proposed as synthetic fragments to mimic the coordination sites of metalloenzymes, for example, purple acid phosphatases (PAPs) or COs (Figure 2.4). In the dinuclear complexes, the copper(II) centers are bridged by the deprotonated phenolic oxygen coming from this precursor. For the syntheses of biomimetic dicopper(II) complexes, the inclusion of the additional μ -O⁻ bridging phenolic group in the binucleating ligand, which is not necessarily present in the active site of the enzyme (as in PAPs; Figure 2.4-B) is a common feature.

Additional to the inclusion of μ -O⁻ donor groups bridged to copper(II) centres [17-22], in the search to mimic the active sites of Cu(II)Cu(II)-proteins, some complexes containing other bridged ligand donors were reported and the anticancer activity were explored. Thus, N-bridged dicopper based on adenine [38], pyrazine [39] and guanazole [41] were already reported. The syntheses of Cu₂(μ -oxamido) derivatives [33-37], Cu₂(μ -chloro) [32, 105], Cu₂(μ -sulfonato) complexes [40].

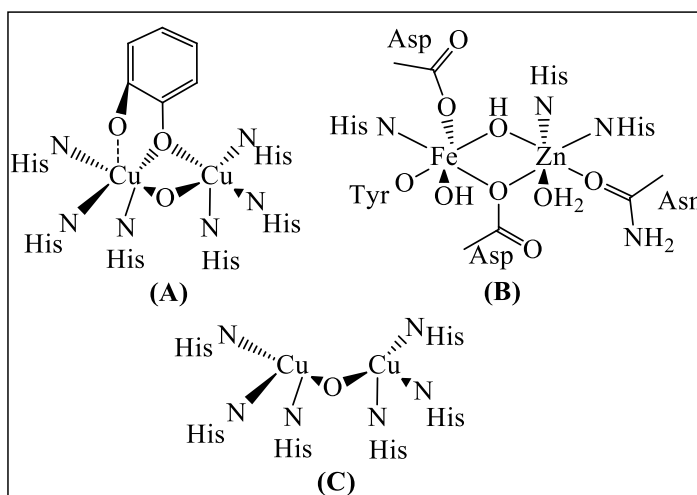


Figure 2.4. Active sites of the mono or dioxygen binding coordination of (A) *Streptomyces* tyrosine [106]; (B) kidney bean PAP[107]; and catechol oxidase from sweet potato [108]. Adapted from (A) DECKER *et. al*; (B) STRATER *et. al*; and (C) SIEGBAHN.

2.7

Aroylhydrazones as ligands for copper(II) and their cytotoxicity

In such a highly active field of research, a large variety of ligands has been used to synthesize copper complexes with potential antiproliferative action. Santini and co-workers [4] published a comprehensive review on coordination compounds of this metal reported between 2008 and 2012 as having antitumour activity. More recently, cytotoxic copper complexes comprising a diversity of ligands have been described, amongst which hydrazides and *N,N*-heterocycles [5], derivatives of coumarin [6], aroylhydrazones [7], thiosemicarbazones [8], β -diketones and *N*-heterocycles [9], phenanthroline [10], tripodal pyrazolyl amines [11], nalidixic acid [12], benzimidazoles [13, 14], fluoroquinolones [15], and a 1,2,4-triazole-derived Schiff base [16]. In some cases, their ability to induce apoptotic cell death was demonstrated [5, 12, 14, 15].

Particularly, aroylhydrazones constitute a diverse family of bidentate N,O-donors with a vast spectrum of biological activities [109]. In fact, in recent years many metal-free hydrazone derivatives and hydrazone metal complexes have been tested as anticancer agents [45-57]. In the work related to her master's degree in the Chemistry Department of the *Pontifical Universidade Católica do Rio de Janeiro* (PUC-Rio), Rafaela dos Santos reported the syntheses and characterization of two aroylhydrazone ligands (Figure 2.5) and their dicopper(II) complexes [110].

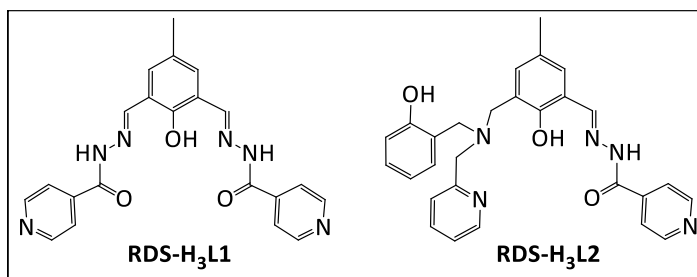


Figure 2.5. Chemical structures of aroylhydrazone ligands **RDS-H₃L1** and **RDS-H₃L2** synthesized from isoniazid (**INH**) and **HDFMP** or **HBPAMFF** moieties.

In her doctoral thesis, Rafaela dos Santos revealed the antiproliferative activity of **RDS-H₃L1** and **RDS-H₃L2** ligands on human lung cancer A549, and human prostate cancer PC3 cell lines. Antiproliferative activities were also tested for the synthesized Zn₂(II)- and Cu₂(II)-complexes of the **RDS-H₃L1** ligand, and Zn₂(II)-, Fe(III)Cu(II)-, Fe(III)Zn(II)- and Cu₂(II)-complexes of the nonsymmetrical ligand **RDS-H₃L2** (Figures 2.6 and 2.7) [111].

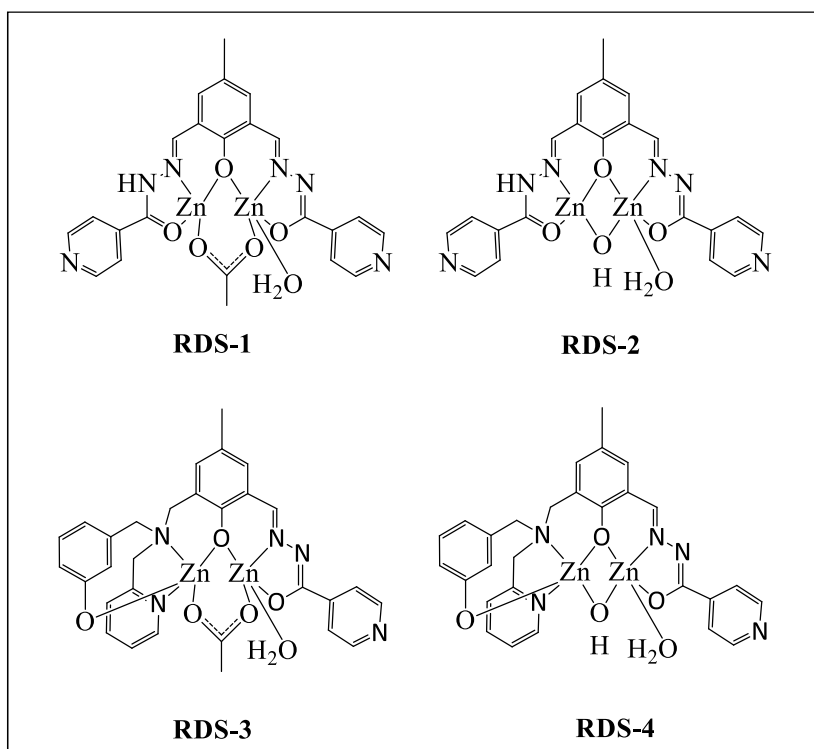


Figure 2.6. Chemical structures of the Zn₂(II)-complexes **RDS-1**, **RDS-2**, **RDS-3**, and **RDS-4** of **RDS-H₃L1** or **RDS-H₃L2**. Adapted from DOS SANTOS R. [111].

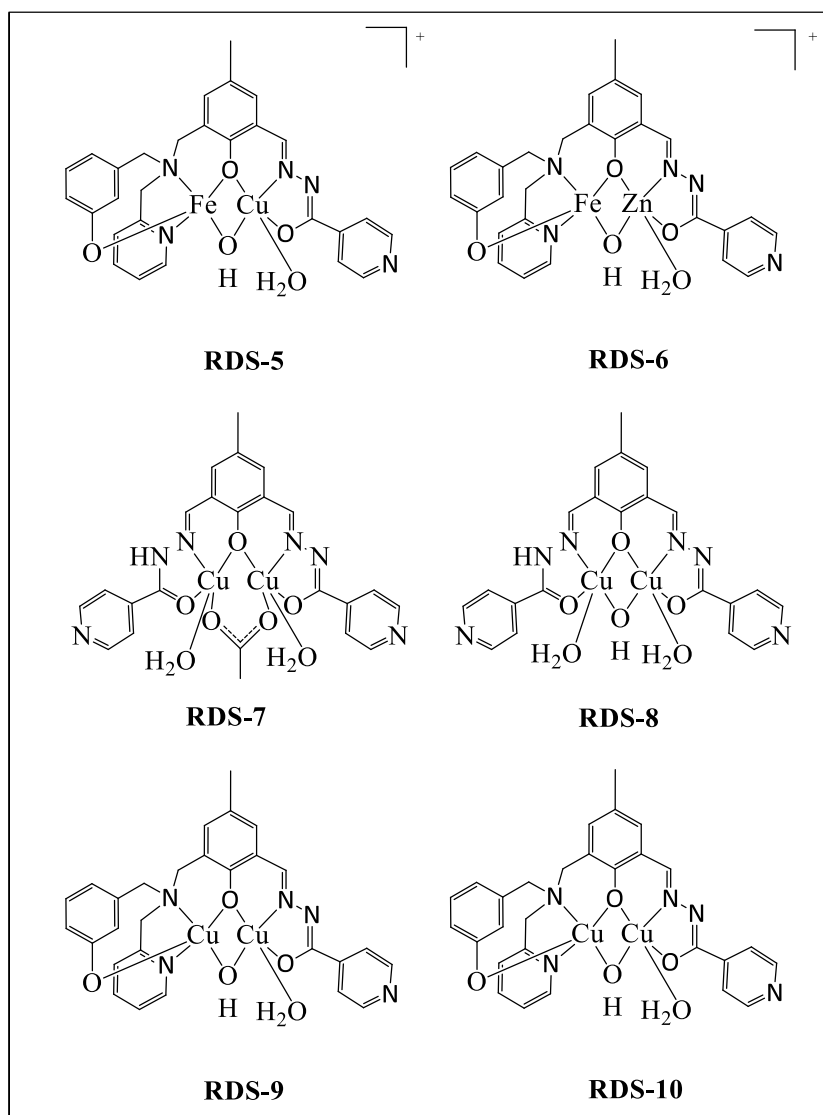


Figure 2.7. Chemical structures of the Fe(II)Cu(II)-complex **RDS-5**, Fe(II)Zn(II)-complex **RDS-6**, and Cu₂(II)-complexes **RDS-7**, **RDS-8**, **RDS-9**, and **RDS-10** of chelators **RDS-H₃L1** or **RDS-H₃L2**. Adapted from DOS SANTOS R. [111].

The results of cell death showed that the compounds derived from ligand **RDS-H₃L2** are more cytotoxic than the compound derived from **RDS-H₃L1**. A second important contribution of Dos Santos was the identification of the highest cytotoxic activity among all dinuclear copper(II) complexes in both cancer cell lines tested. The IC₅₀ values for compounds **RDS-9** and **RDS-10** were reported as <10 μM.

Part II.

Experimental procedures, results and conclusion

3

Experimental

The current chapter describes the experimental procedures, chemical, instrumentation and materials used to achieve the proposed aims. The synthetic protocols employed to obtain the precursors, ligands and complexes are also reported.

3.1

Chemicals

Acetone (DMK), acetonitrile (MeCN), diethyl ether (Et₂O), dimethyl sulfoxide (DMSO), dichloromethane (DCM), ethanol (EtOH), methanol (MeOH), isopropyl alcohol (iPrOH), triethylamine (Et₃N), sodium tetrahydroborate, hydrochloric acid, chloroform, anhydrous sodium sulfate, potassium hydroxide, copper(II) perchlorate hexahydrate, sodium bicarbonate, hydrazine hydrate, boron trifluoride diethyl etherate, human serum albumin (HSA) and *calf thymus* DNA (*ct*-DNA) were obtained from Sigma-Aldrich; sodium chloride were purchased from Sigma-Aldrich or VWR PROLABO; tris(hydroxymethyl)aminomethane (tris) was acquired from BIO-RAD or EUROMEDEX; 4-methoxycarbonyl benzaldehyde, tetrachloro-1,4-benzoquinone (chloranil) and 2,4-dimethylpyrrole were from TCI Chemicals; furan-2-carbohydrazide and thiophene-2-carbohydrazide were purchased from Acros Organics and Sigma-Aldrich; bovine serum albumin (BSA) was from Fluka. Plasmid DNA pBR322 was from Thermo Fisher. Reagents for the synthesis of BODIPY precursor were purchased from Acros Organics and/or Sigma-Aldrich. All these chemicals were used without any type of treatment or further purification.

3.2

Syntheses of precursors, ligands and complexes

3.2.1

Syntheses of precursors

3.2.1.1

Synthesis of HBPA

The synthesis of the pendant arm (2-hydroxybenzyl)(2-pyridylmethyl)amine (**HBPA**) from 2-(aminomethyl)pyridine and 2-hydroxybenzaldehyde was previously reported (Figure 3.1) [112, 113]. The reaction conditions of reaction were slightly modified or optimized in the present study: 2-(aminomethyl)pyridine (7.9 g, 73 mmol) and 2-hydroxybenzaldehyde (7.7 mL, 73 mmol) were stirred in 50 mL MeOH for one hour, with the subsequent gentle, portionwise addition of solid NaBH₄ (2.8 g, 73 mmol) at 0 °C. The mixture was stirred overnight and, then, pH was adjusted to 5–6 with a 4 mol L⁻¹ HCl aqueous solution.

The solvent was removed under reduced pressure on rotary evaporator at 45 °C and the product, redissolved in 60 mL of chloroform and then washed with 5 × 40 mL portions of a saturated sodium bicarbonate solution and once with water, waiting 15 minutes between the separations.

The product was extracted with chloroform (3 × 30 mL) and the organic phase dried over anhydrous sodium sulfate. Chloroform was evaporated and the product was allowed to stand in Et₂O in the freezer for three days. A colourless crystalline solid was separated. M.p. = 63 °C, yield = 9.0 g (42 mmol, 58%). The spectroscopic features were in agreement with the literature (Figure 13.23).

3.2.1.2

Synthesis of HBPAMFF

The precursor 3-[(2-hydroxybenzyl)(2-pyridylmethyl)amine]-2-hydroxy-5-methylbenzaldehyde (**HBPAMFF**) was synthesized as described previously [102] from **HBPA** and (2-chloromethyl-4-methyl-6-formyl)phenol (**CMFF**) (Figure 3.1)

[104], according to the following modified conditions: **HBPA** (2.3 g, 10.4 mmol) and TEA (1.5 mL, 10.4 mmol) were both dissolved together in 40 mL DCM and then slowly added at 0 °C to 40 mL of a **CMFF** (2.0 g, 10.4 mmol) solution in DCM. The mixture was stirred for 3 h at room temperature and then washed and extracted, as described above for **HBPA**.

The product was allowed to stand in iPrOH at –18 °C (freezer conditions) for 12 h, and a white crystalline solid was separated. M.p. = 103-104 °C, yield = 2.9 g (8 mmol, 77%). The spectroscopic features were in agreement with those published in the literature (Figure 13.24).

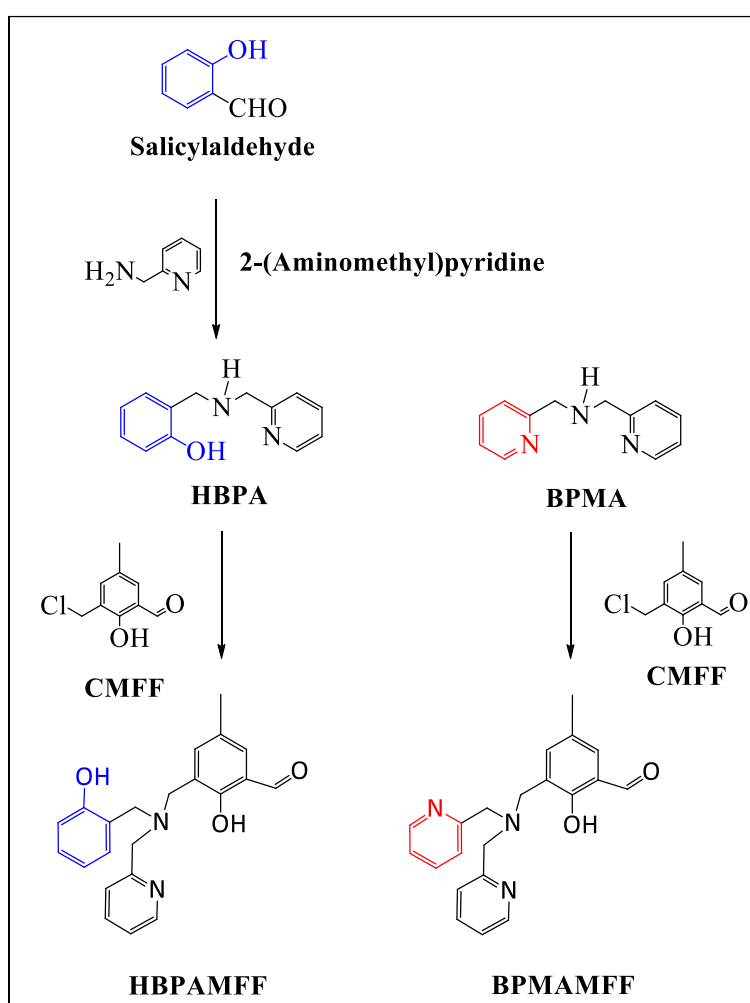


Figure 3.1. Synthetic routes of precursors **HBPAMFF** and **BPMAMFF**. **BPMA** was obtained commercially.

3.2.1.3

Synthesis of BMPAMFF

The precursor 2-[bis(pyridylmethyl)aminomethyl]-4-methyl-6-formylphenol (BPMAMFF) (1.0 g, 4.9 mmol) was obtained from CMFF (0.9 g, 4.9 mmol) and bis(2-pyridylmethyl)amine according to the described procedures (Figure 3.1) [104, 114]. M.p. = 127-129 °C, yield = 1.4 g (4 mmol, 83%). The spectroscopic features were in agreement with the literature (Figure 13.25).

3.2.1.4

Synthesis of 4-MePh-BODIPY

The fluorescent precursor 5,5-difluoro-10-(4-methoxycarbonylphenyl)-1,3,7,9-tetramethyl-BODIPY (**4-MePh-BODIPY**) (**BODIPY** = boron-dipyrromethene) was synthesized from 4-methoxycarbonyl benzaldehyde (**4-MeBA**) and 2,4-dimethylpyrrole as previously reported (Figure 3.2) [115], and following the modified conditions to optimize the synthesis and separation: the light yellow reaction solution containing 4-methoxycarbonyl benzaldehyde (328 mg, 2 mmol) and 2,4-dimethylpyrrole (380 mg, 4 mmol) was stirred in dry DCM under argon atmosphere and room temperature for 20 min.

Then, one drop of trifluoroacetic acid (TFA) was added to the reaction solution, which immediately became dark wine colour (Figure 3.3-A), and then, the solution was stirred overnight at room temperature and argon atmosphere. After that, solid tetrachloro-1,4-benzoquinone (chloranil) (492 mg, 2 mmol) was added and the reaction was stirred further 1 h. Then, 6 mL of TEA was added and the solution was stirred for 30 min.

After, 6 mL of boron trifluoride diethyl etherate ($\text{BF}_3\text{-OEt}_2$) was slowly added to the reaction solution, which was stirred further 2 h. The fluorescence of the solution was verified under a UV lamp (Figure 3.3-B). The reaction solution was washed three times with 70 mL with distilled water. If a black solid precipitated, the solution was filtered under reduced pressure through a layer of cotton. The organic phase was dried with solid anhydrous MgSO_4 and filtered, and the solvent was evaporated.

The compound was purified by column chromatography using SiO₂ (200 g) as stationary phase (Figure 3.3-C). The solid obtained (6 g) was dissolved in DCM, and then the solvent was evaporated in a rotavapor in the presence of SiO₂ (20 g). When necessary, the product was purified a second time, employing the same conditions (Figure 3.3-D). Mobile phase was cyclohexane/ethyl acetate 8:1 (Figure 3.3-E). The yield (105 mg, 0.28 mmol, 14%) was in accord with the literature.

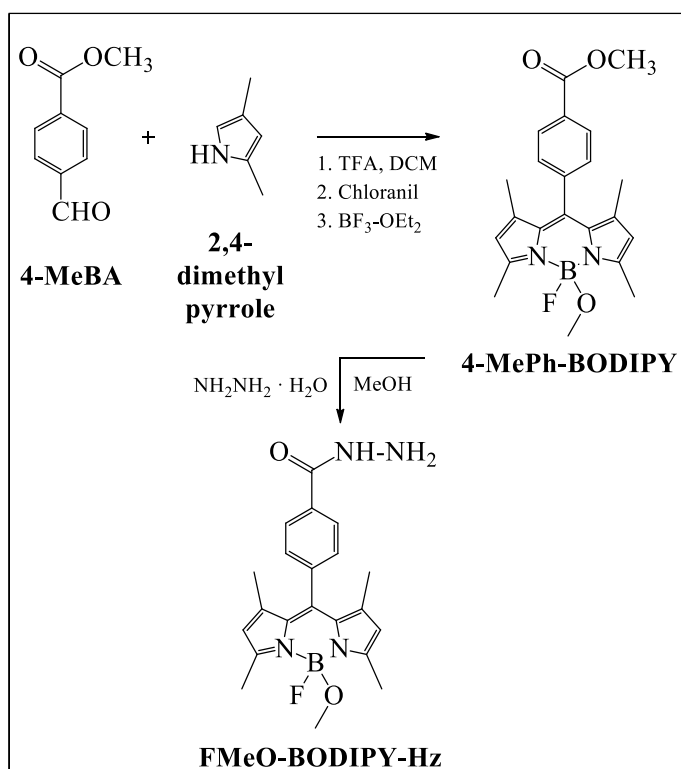


Figure 3.2. Synthetic routes of precursors **4-MePh-BODIPY** and **4-HzPh-BODIPY**.

3.2.1.5

Synthesis of FMeO-BODIPY-Hz

5-fluoro-5-methoxy-10-(4-methoxycarbonylphenyl)-1,3,7,9-tetramethyl-BODIPY (**FMeO-BODIPY-Hz**) was synthesized from **4-MePh-BODIPY** (140 mg, 0.37 mmol) and 6 mL of hydrazine hydrate NH₂NH₂·H₂O, under argon atmosphere, following the procedures previously described (Figures 3.2 and 3.3-F) [116]. The reaction was monitored by thin-layer chromatography (TLC) using as the mobile phase cyclohexane/ethyl acetate 8:1. When the reagent **4-MePh-BODIPY** was completely consumed (after 24 h), MeOH was removed in a

rotavapor. The product was dissolved in 70 mL DCM and then, washed with 70 mL of water (3 x). The aqueous phase was washed once with 20 mL DCM. Water was removed with solid anhydrous MgSO_4 and the solvent was evaporated.

The compound was purified by column chromatography using SiO_2 (50 g) as stationary phase (Figure 3.3-G). The solid obtained (100 mg) was dissolved in DCM, and then the solvent was evaporated in a rotavapor in the presence of SiO_2 (5 g). Mobile phase was chloroform/MeOH/ammonium hydroxide 100:5:1. When necessary, the product was purified using a second chromatographic column in the same conditions. Yield = 79.1 mg (0.20 mmol, 54%). NMR spectroscopic features show the formation of the 5-fluoro-5-methoxy-10-(4-methoxycarbonylphenyl)-1,3,7,9-tetramethy-BODIPY (Figure 13.2).

3.2.2

Synthesis of the ligands

The structures of the ligands are shown in Figure 3.4.

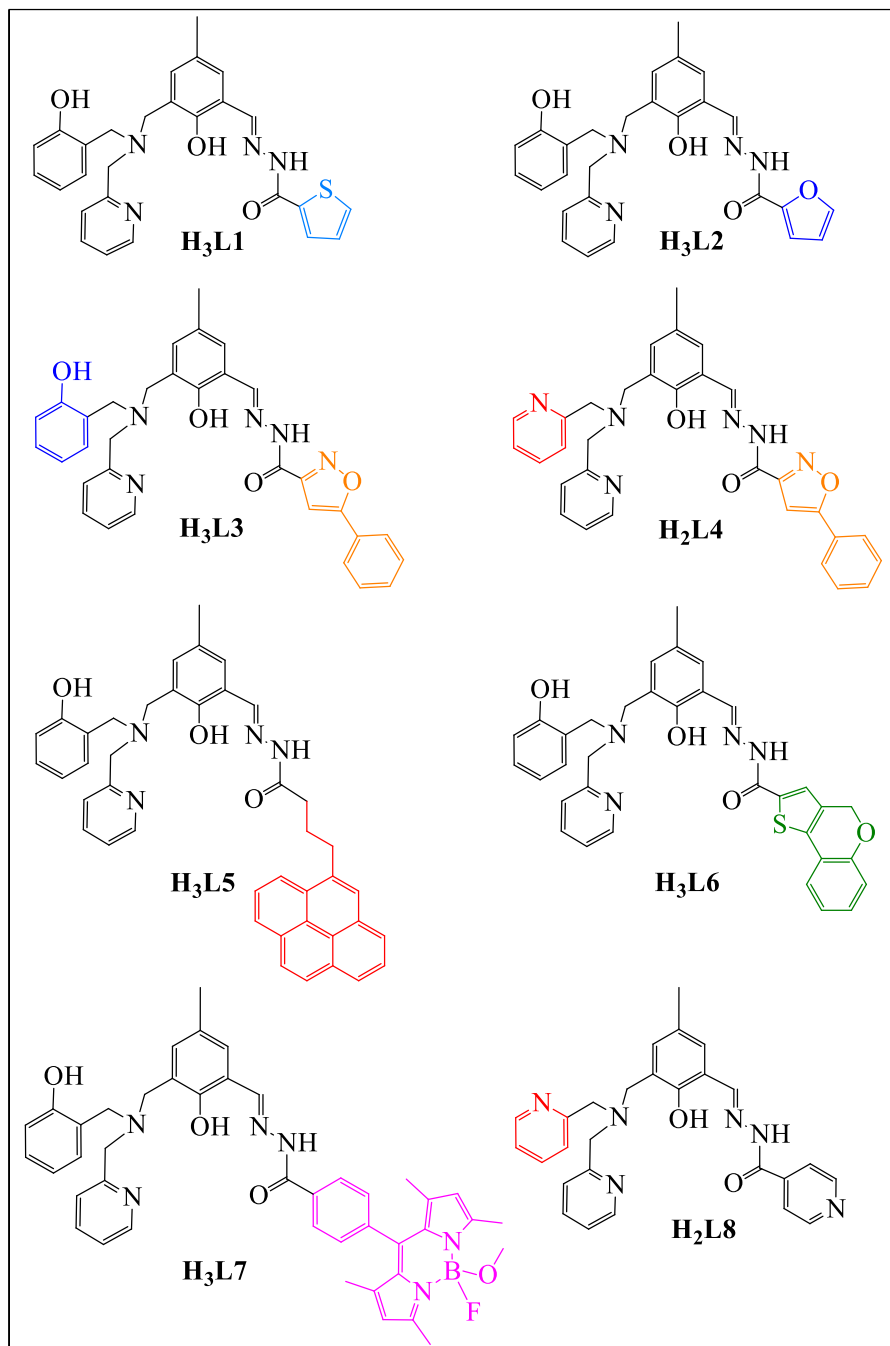


Figure 3.4. Structures of ligands H₃L1–H₂L8.

3.2.2.1

Synthesis of HBPAMF-thiophene-2-carbohydrazone (**H₃L1**)

This ligand was prepared by dropwise adding a methanolic solution (10 mL) of thiophene-2-carbohydrazone (**TCH**, 586.3 mg, 4 mmol) to 30 mL of a slightly heated solution containing the precursor **HBPAMFF** (1.45 g, 4 mmol) in MeOH/Et₂O 1:1. The mixture was left under reflux for 2 h and, after 30 minutes of cooling, the product was filtered off and washed with ice-cold Et₂O. Figure 3.3-K shows the appearance of all ligands after synthesis. M.p. = 187 °C, yield = 1.8 g (3.7 mmol, 92%). Recrystallization in MeOH afforded light yellow crystals with hexagonal geometry. Optical photographs of **H₃L1** crystals can be found in Figure 3.3-P. Single-crystal size was too small for an X-ray diffraction (XRD) analysis. Elemental analysis (%) – calculated for C₂₇H₂₆O₃N₄S (486.63 g mol⁻¹): C 66.6, H 5.4, N 11.5, S 6.6; found: C 66.1, H 5.5, N 11.8, S 6.7.

3.2.2.2

Synthesis of HBPAMF-furan-2-carbohydrazone (**H₃L2**)

This ligand was prepared from furan-2-carbohydrazone (**FCH**, 514.7 mg, 4 mmol) in 5 mL MeOH and **HBPAMFF** (1.45 g, 4 mmol) following the same procedure followed to synthesize **H₃L1**. M.p. = 185 °C, yield = 1.6 g (3.4 mmol, 85%). Light yellow crystals with hexagonal geometry were obtained by recrystallization in MeOH (Figure 3.3-Q). Single-crystals were analyzed by XRD, but the peaks presented low intensity. Elemental analysis (%) – calculated for C₂₇H₂₆O₄N₄ (470.57 g mol⁻¹): C 68.9, H 5.6, N 11.9; found: C 68.4, H 5.6, N 12.3.

3.2.2.3

Synthesis of HBPAMF-5-phenylisoxazole-3-carbohydrazone ligand (**H₃L3**)

Compound **H₃L3** was synthesized from **HBPAMFF** (2 mmol) and 5-phenylisoxazole-3-carbohydrazone (**PIH**) (2 mmol), separately dissolved in MeOH/DCM 1:1 (v/v) (10 mL). **PIH** was slowly added to the **HBPAMFF** solution. To evaporate DCM in the solution, the reaction flask was heated in an open

atmosphere for some minutes. Then, the mixture was refluxed over 3 h, and, after cooling to room temperature, the solid was separated by filtration and washed with cold acetonitrile. The white solid was dried under reduced pressure and recrystallized in acetonitrile to afford colourless crystals. M.p. = 174 °C, yield = 1.1 g (1.9 mmol, 96%). Elemental analysis calcd. (%) $C_{32}H_{29}N_5O_4$ (547.22 g mol⁻¹): C 70.2, H 5.3, N 12.8; found: C 69.9, H 5.4, N 13.2.

3.2.2.4

Synthesis of BPMAMF-5-phenylisoxazole-3-carbohydrazone ligand (H₂L4)

PIH (1.5 mmol) dissolved in MeOH/DCM 1:1 (v/v) (10 mL) was added dropwise to a solution of **BPMAMFF** (1.5 mmol) in MeOH (10 mL). The mixture reaction followed the same process followed to synthesize **H₃L3**. Single crystals were obtained by dissolving the white solid in acetonitrile. M.p. = 159 – 162 °C, yield = 665.2 mg (1.3 mmol, 87%). Elemental analysis calcd. (%) for $C_{31}H_{28}N_6O_3$ (532.22 g mol⁻¹): C 69.9, H 5.3, N 15.8; found: C 70.5, H 5.4, N 16.5.

3.2.2.5

Synthesis of HBPAMF-4-(1-pyrenebutyric)carbohydrazone (H₃L5)

This fluorescent ligand was synthesized as follows. Initially, the **HBPAMFF** (0.65 mmol) and 1-pyrenebutyric hydrazide (**PBH**) (0.65 mmol) were dissolved separately in 10 mL MeOH/DCM 1:1, and then, the **PBH** was slowly added to the **HBPAMFF** solution. DCM was evaporated from the solvent mixture by heating the reaction flask in open atmosphere for some minutes. The resulting solution was stirred and heated for 4.5 h. After 15 min of cooling, the solvent was removed with a Pasteur pipette; the light yellow solid obtained was washed with ice-cold MeOH and the solvent, removed with a pipette (three times). The solid was dried at room temperature. M.p. = 190 °C, yield = 420 mg (0.65 mmol, 99%). The solid was recrystallized in MeOH, affording light yellow crystals with hexagonal geometry. Elemental analysis calcd. (%) for $C_{42}H_{38}N_4O_3$ (646.78 g mol⁻¹): C 78.0, H 5.9, N 8.7; found: C 77.6, H 6.0, N 8.9.

3.2.2.6

Synthesis of the fluorescent ligand **HBPAMF-4H-[1]-benzopyrano[4,3-*b*]thiophene-2-carbohydrazone (H₃L6)**

This fluorescent ligand was synthesized from **HBPAMFF** (1.6 mmol) and **4H-[1]-benzopyrano[4,3-*b*]thiophene-2-carbohydrazide (BPTH)** (1.6 mmol) both dissolved separately in 40 mL DMSO/MeOH 3:1. **BPTH** was slowly added to the **HBPAMFF** solution. DCM was evaporated from the solvent mixture by heating the reaction flask in open atmosphere for some minutes. The resulting solution was additionally stirred and heated for 3 h. After 15 min, the precipitate was filtered, washed with ice-cold MeOH and dried under reduced pressure at 80 °C overnight to remove the solvents. M.p. = 215 °C, yield = 945 mg (1.6 mmol, 99%). The solid was recrystallized in DMK/MeOH 1:1 and small size light yellow crystals were obtained. Elemental analysis calcd. (%) for C₃₄H₃₀N₄O₄S (590.77 g mol⁻¹): C 69.1, H 5.1, N 9.5, S 5.43; found: C 68.4, H 5.2, N 10.3, S 6.4.

3.2.2.7

Synthesis of **HBPAMF-BODIPY carbohydrazone ligand (H₃L7)**

To prepare this fluorescent ligand **HBPAMFF** (0.08 mmol) was dissolved in 2 mL MeOH and the solution heated for some minutes, and then leaved to cool at room temperature. The fluorophore fluoro-methoxy-**BODIPY-hydrazide (FMeO-BODIPY-Hz)** (0.08 mmol) was dissolved separately in 4 mL MeOH and dropwise added to the **HBPAMFF** solution. Reaction mixture was heated for 2 h and then, stirred overnight at room temperature. Monitoring the reaction solution by TLC (mobile phase: DCM/MeOH/NH₄OH 10:0.5:0.1) showed that **FMeO-BODIPY-Hz** was consumed. The mixture was then transferred to a beaker and the solvent, removed with a Pasteur pipette. The cinnabar red solid was washed by dropping ice-cold MeOH and removing the solvent with a Pasteur pipette (three times). The product was dried at room temperature. Crystals were obtained by recrystallizing the product in MeCN. Single-crystal size was too small for X-ray diffraction (XRD) analysis. Figure 3.3-M shows the appearance of this ligand after synthesis. The product, dissolved in MeOH, is fluorescent under an UV lamp (Figure 3.3-H). M.p. = 220 °C, yield = 37 mg (0.05 mmol, 63%). Elemental analysis

calcd. (%) for $C_{43}H_{44}N_6O_4$ ($738.66 \text{ g mol}^{-1}$): C 69.9, H 6.0, N 11.4; found: C 68.3, H 6.1, N 12.5.

3.2.2.8

Synthesis of the fluorescent ligand **BPMAMF-4H-[1]-benzopyrano[4,3-b]thiophene-2-carbohydrazone (H₂L₈)**

This ligand was prepared using the precursor **BPMAMFF** (2 mmol) and 4-pyridinecarboxylic acid hydrazide (**INH**, or isoniazide) (2 mmol). **BPMAMFF** was dissolved in 10 mL DCM/MeOH (v/v) 1:1 and ultrasonic bath. Then, **INH** previously dissolved in 5 mL DCM/MeOH 1:1 was slowly added to the **BPMAMFF** solution. The reaction mixture was stirred and heated for 3 h. To the orange oil obtained, 30 mL of DCM/MeOH 1:1 were added. After two weeks, yellow hexagonal crystals were separated by filtration and washed with ice-cold MeOH and then the solvent was removed using a Pasteur pipette. M.p. = 215 °C, yield = 746 mg (1.6 mmol, 99%). Elemental analysis calcd. (%) for $C_{27}H_{26}N_6O_2$ ($466.53 \text{ g mol}^{-1}$): C 69.5, H 5.6, N 18.0; found: C 69.2, H 6.1, N 18.7.

3.2.3

Synthesis of the copper(II) complexes

Caution! Perchlorate salts of metal complexes containing organic ligands are potentially explosive and should be handled with care. Only small amounts should be prepared.

Complexes **1** and **2** were prepared from the chelators **H₃L₃** and **H₂L₄** respectively, and copper(II) perchlorate hexahydrate.

Complexes **3** and **4** were prepared from copper(II) perchlorate hexahydrate and **H₃L₃** and **H₂L₄**, respectively, while complexes **5** and **6** were obtained from copper(II) acetate monohydrate and **H₃L₃** and **H₂L₄**, respectively.

Complexes **7** and **8** were prepared from the ligand **H₃L₅** and copper(II) perchlorate hexahydrate and copper(II) acetate monohydrate, respectively.

Complexes **9** and **10** were prepared from ligand **H₃L₆** and copper(II) perchlorate hexahydrate and copper(II) acetate monohydrate, respectively, while

complexes **11** and **12** were prepared from ligand **H₃L7** and copper(II) perchlorate hexahydrate and copper(II) acetate monohydrate, respectively.

Finally, complexes **13** and **14** were prepared from ligand **H₂L8** and copper(II) perchlorate hexahydrate and copper(II) acetate monohydrate, respectively.

The structures of the complexes are shown in Figure 3.5 and Figure 3.6.

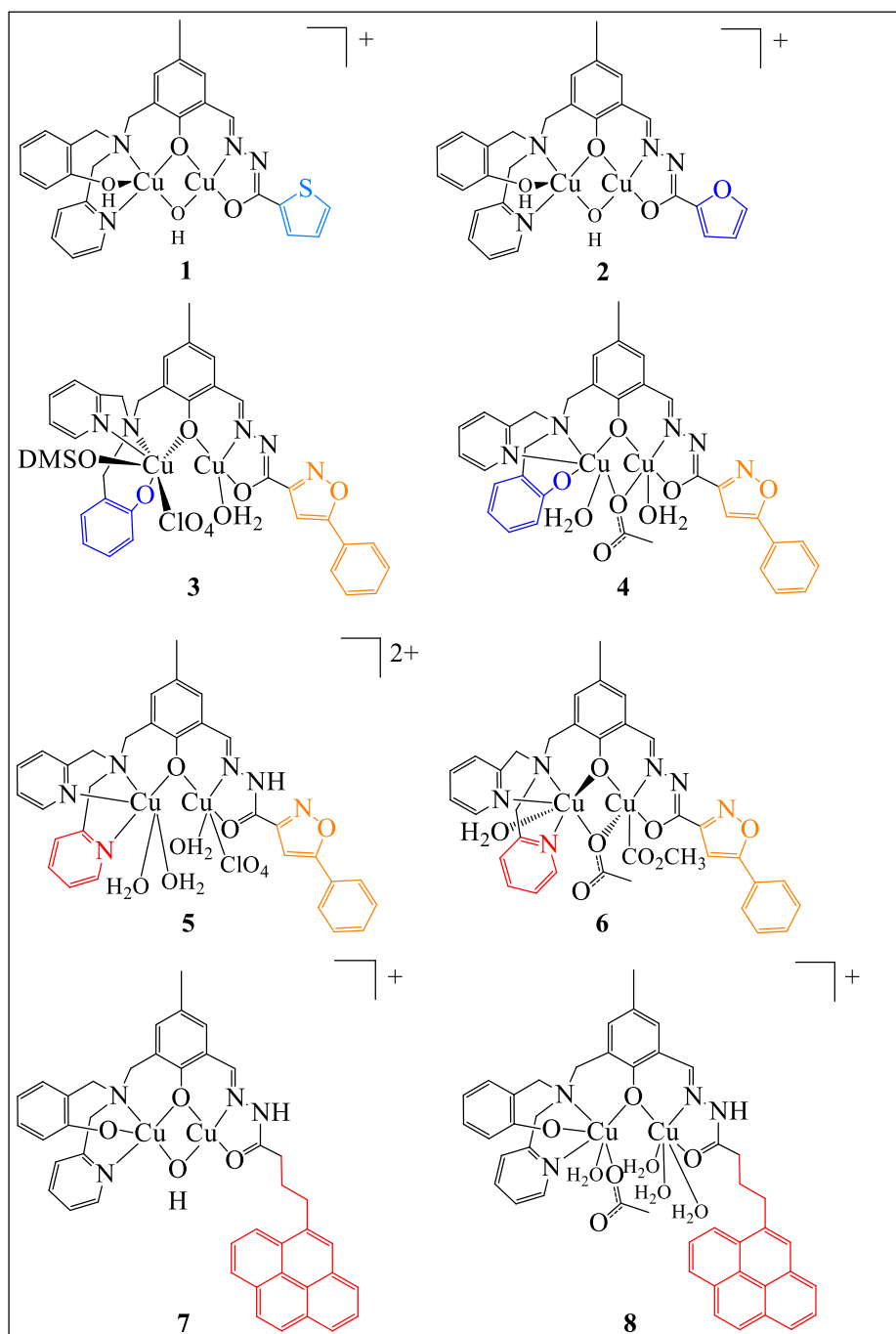


Figure 3.5. Structures of complexes **1–8**.

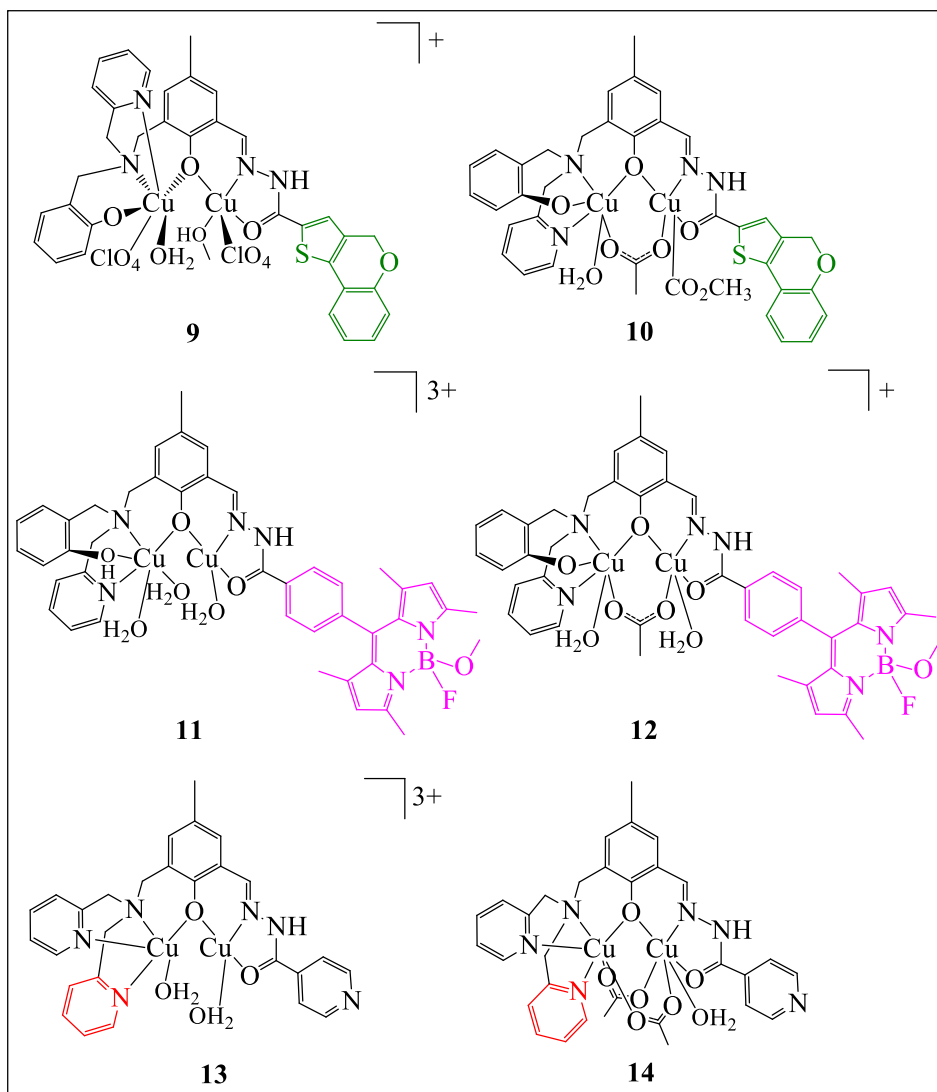


Figure 3.6. Structures of complexes **9–14**.

3.2.3.1

Synthesis of Complex **1**

$\text{Cu}(\text{ClO}_4)_2 \cdot 6\text{H}_2\text{O}$ (378.1 mg, 1.0 mmol) was dissolved in 3 mL MeOH and dropwise added to a solution of the **H₃L1** ligand (243.32 mg, 0.5 mmol) in 35 mL of a MeOH/MeCN 6:1 mixture. The reactants were heated for 40 minutes and, then, 1 mL of a methanolic KOH solution (1 M, 1 mmol) was added. Heating and stirring were maintained for another 20 minutes. Figure 3.3-L shows the appearance of complexes **1–10** and **13** and **14** after synthesis. After 12 h, the green solid was filtered off and washed with ice-cold MeOH. The dry solid was recrystallized in EtOH, affording dark green crystals (Figure 3.3-R) suitable for XRD analysis.

Yield = 220 mg (0.29 mmol, 58%). Elemental analysis (%) – calcd. for $[\text{Cu}_2(\mu\text{-OH})(\text{C}_{27}\text{H}_{24}\text{N}_4\text{O}_3\text{S})]\text{ClO}_4\cdot 2\text{H}_2\text{O}$ ($764.21 \text{ g mol}^{-1}$): C 42.4, H 3.8, N 7.3, S 4.2; found: C 42.9, H 3.9, N 7.5, S 4.0. ICP-OES calcd.: Cu 16.6; found: 15.8.

3.2.3.2

Synthesis of Complex 2

This complex was prepared according to the same procedure followed to synthesize **1** from **H₃L₂** (235.3 mg, 0.5 mmol) and $\text{Cu}(\text{ClO}_4)_2\cdot 6\text{H}_2\text{O}$ (378.1 mg, 1.0 mmol). Complex **2** was recrystallized in DCM/DMK/EtOH 1:1:1, obtaining dark green crystals (Figure 3.3-S) suitable for XRD analysis.

Yield = 266 mg (0.36 mmol, 72%). Elemental analysis (%) – calcd. for $[\text{Cu}_2(\mu\text{-OH})(\text{C}_{27}\text{H}_{24}\text{N}_4\text{O}_4)]\text{ClO}_4\cdot \text{H}_2\text{O}$ ($730.12 \text{ g mol}^{-1}$): C 44.4, H 3.7, N 7.7; found: C 44.0, H 3.7, N 7.4. ICP-OES calcd.: Cu 17.4; found: 17.3.

3.2.3.3

Synthesis of Complex 3

H₃L₃ (0.5 mmol) was dissolved in MeOH/DCM 1:1 (10 mL). Then, $\text{Cu}(\text{ClO}_4)_2\cdot 6\text{H}_2\text{O}$ (1 mmol) in MeOH (3 mL) was added dropwise to the yellow ligand solution. The dark green reaction mixture was heated and stirred for 40 min. After that, KOH (1 M, 1.5 mmol, 1.5 mL in MeOH) was added. Stirring was maintained further 20 minutes. After 12 h at room temperature, the product was filtered and washed with ice-cold MeOH. Then, MeOH was removed under reduced pressure. The dark green solid was recrystallized by slow evaporation in DMSO, forming single crystals.

Yield = 468.5 mg (0.49 mmol, 99%). Elemental analysis (%) – calcd. for $[\text{Cu}_2(\text{C}_{32}\text{H}_{26}\text{N}_5\text{O}_4)(\text{ClO}_4)(\text{DMSO})(\text{H}_2\text{O})]\cdot \text{DMSO}$ ($945.38 \text{ g mol}^{-1}$): C 45.7, H 4.3, N 7.4; found: C 44.7, H 4.0, N 7.0. ICP-OES calcd.: Cu 13.4; found: 13.1.

3.2.3.4

Synthesis of Complex 4

Complex **4** was prepared by heating for 40 min the mixture obtained by dropwise addition of copper(II) acetate monohydrate (0.5 mmol in 10 mL MeOH) to **H₃L₃** (0.25 mmol) in MeOH/DCM 1:1 (10 mL). After one day, the dark green solid was filtered at room temperature and washed with ice-cold MeOH. Then, the product was dried under reduced pressure.

Yield = 200.1 mg (0.25 mmol, 99%). Elemental analysis (%) – calcd. for $[\text{Cu}_2(\mu\text{-CO}_2\text{CH}_3)(\text{C}_{32}\text{H}_{23}\text{N}_4\text{O}_4)(\text{H}_2\text{O})_2]\cdot 2\text{H}_2\text{O}$ (802.78 g mol⁻¹): C 50.8, H 4.6, N 8.7; found: C 50.5, H 4.4, N 8.6. ICP-OES calcd.: Cu 15.8; found: 16.0.

3.2.3.5

Synthesis of Complex 5

The same procedure was followed as for complex **1**, from copper(II) perchlorate hexahydrate (0.8 mmol) and **H₂L₄** (0.4 mmol) in MeOH (10 mL). After 40 min, KOH (0.8 mmol) was added. Stirring was maintained further 20 minutes. After one day, the dark green solid was filtered at room temperature and washed with ice-cold MeOH. Then, the product was dried under reduced pressure.

Yield = 400.2 mg (0.38 mmol, 95%). Elemental analysis (%) – calcd. for $[\text{Cu}_2(\text{C}_{31}\text{H}_{27}\text{N}_6\text{O}_3)(\text{ClO}_4)_2(\text{H}_2\text{O})]\text{ClO}_4\cdot 4\text{H}_2\text{O}$ (1047.1 g mol⁻¹): C 35.6, H 3.6, N 8.0; found: C 34.8, H 3.5, N 7.7. ICP-OES calcd.: Cu 12.4; found: 13.1.

3.2.3.6

Synthesis of Complex 6

H₂L₄ was dissolved in MeOH (10 mL) and copper(II) acetate monohydrate (0.8 mmol in 10 mL MeOH) was slowly added to the yellow solution. The next steps were identical to those followed to synthesize complex **1**. The dark green solid was recrystallized by slow evaporation in DMF and single crystals were obtained.

Yield = 331.5 mg (0.39 mmol, 98%). Elemental analysis (%) – calcd. for $[\text{Cu}_2(\mu\text{-CO}_2\text{CH}_3)(\text{C}_{31}\text{H}_{26}\text{N}_6\text{O}_3)(\text{CO}_2\text{CH}_3)(\text{H}_2\text{O})] \cdot 2\text{H}_2\text{O}$ (829.79 g mol⁻¹): C 50.7, H 4.6, N 10.1; found: C 50.7, H 4.6, N 10.4. ICP-OES calcd.: Cu 15.3; found: 15.3.

3.2.3.7

Synthesis of Complex 7

Copper(II) perchlorate hexahydrate (0.66 mmol) dissolved in MeOH (5 mL) and slowly added to a yellow solution containing ligand **H₃L5** (0.33 mmol) previously dissolved in MeOH/DCM 1:1 (10 mL) for 40 min. After that KOH/MeOH (0.66 mmol) was added and the stirring was maintained further 20 minutes. After 12 h were obtained small single hexagonal crystals and dark green colour. It was observed that these crystals lost solvent, turning difficult its characterization using XRD technique.

Yield = 225.4 mg (0.25 mmol, 76%). Elemental analysis (%) – calcd. for $[\text{Cu}_2(\mu\text{-OH})(\text{C}_{42}\text{H}_{36}\text{N}_4\text{O}_3)(\text{H}_2\text{O})]\text{ClO}_4$ (906.33 g mol⁻¹): C 55.7, H 4.4, N 6.2; found: C 54.4, H 4.3, N 6.2. ICP-OES calcd.: Cu 14.6; found: 14.6.

3.2.3.8

Synthesis of Complex 8

This complex was prepared from ligand **H₃L5** (0.33 mmol in 10 mL MeOH/DCM 1:1) and copper(II) acetate monohydrate (0.66 mmol in 10 mL MeOH) for 40 min. After three days, the dark green solid was filtered at room temperature and washed with ice-cold MeOH. Then, the product was dried under reduced pressure.

Yield = 250.5 mg (0.39 mmol, 98%). Elemental analysis calcd. (%) for $[\text{Cu}_2(\mu\text{-CO}_2\text{CH}_3)(\text{C}_{42}\text{H}_{36}\text{N}_4\text{O}_3)(\text{CO}_2\text{CH}_3)(\text{H}_2\text{O})_3] \cdot 6\text{H}_2\text{O}$ (1052.1 g mol⁻¹): C 52.5, H 5.7, N 5.3; found: C 52.0, H 5.6, N 5.2. ICP-OES calcd.: Cu 12.2; found: 12.5.

3.2.3.9

Synthesis of Complex 9

H₃L6 (0.3 mmol) was dissolved in 60 mL THF/MeOH 2:1, under heating for some minutes. When the solution attained room temperature, the copper(II) perchlorate hexahydrate (0.6 mmol) previously dissolved in 5 mL MeOH was added dropwise to the yellow ligand solution. Then, the procedures described to synthesize complex **3** was followed. After two days the solvent was removed with a Pasteur pipette. The product was dried at room temperature. The dark green crystals were suitable for XRD analysis.

Yield = 210.9 mg (0.21 mmol, 70%). Elemental analysis (%) – calcd. for $[\text{Cu}_2(\text{C}_{34}\text{H}_{28}\text{N}_4\text{O}_4)(\text{H}_2\text{O})(\text{CH}_3\text{OH})]_2\text{ClO}_4 \cdot \text{H}_2\text{O} \cdot \text{CH}_3\text{OH}$ (1014.76 g mol⁻¹): C 42.6, H 4.0, N 5.5; found: C 42.7, H 3.9, N 5.3. ICP-OES calcd.: Cu 14.0; found: 14.2.

3.2.3.10

Synthesis of Complex 10

H₃L6 (0.3 mmol) was dissolved in 60 mL THF/MeOH 2:1, under heating for some minutes. When the solution attained room temperature, copper(II) acetate monohydrate (0.66 mmol in 10 mL MeOH) was added dropwise to the yellow ligand solution. The dark green oil obtained was diluted in 30 mL MeCN. When the solutions attained room temperature, the solid was filtered, washed with ice-cold MeOH and dried under reduced pressure.

Yield = 198.9 mg (0.22 mmol, 75%). Elemental analysis (%) – calcd. for $[\text{Cu}_2(\mu\text{-CO}_2\text{CH}_3)(\text{CO}_2\text{CH}_3)(\text{C}_{34}\text{H}_{28}\text{N}_4\text{O}_4)(\text{H}_2\text{O})]_2\text{H}_2\text{O}$ (887.90 g mol⁻¹): C 51.4, H 4.5, N 6.3, S 3.5; found: C 50.7, H 4.4, N 6.9, S 4.2. ICP-OES calcd.: Cu 15.8; found: 16.0.

3.2.3.11

Synthesis of Complex 11

This luminescent complex was synthesized from ligand **H₃L7** (0.024 mmol in 2.5 mL MeOH) and copper(II) perchlorate hexahydrate (0.048 mmol in 2.5 mL MeOH), following the procedures described to obtain complex **3**. The solvent was

removed with a Pasteur pipette; the red solid was washed with ice-cold MeOH and the solvent, removed with a pipette (three times). The solid was dried at room temperature. In chloroform and under a UV lamp, the product was fluorescent (Figure 3.3-I). Figure 3.3-O shows the appearance of complex **11** dissolved in DMSO.

Yield = 23.5 mg (0.018 mmol, 73%). Elemental analysis (%) – calcd. for $[\text{Cu}_2(\text{C}_{43}\text{H}_{43}\text{N}_6\text{O}_4\text{BF})(\text{H}_2\text{O})_3]3\text{ClO}_4 \cdot 7\text{H}_2\text{O}$ (1343.25 g mol⁻¹): C 38.5, H 4.7, N 6.2; found: C 37.5, H 4.4, N 6.1. ICP-OES calcd.: Cu 11.5; found: 11.8.

3.2.3.12

Synthesis of Complex 12

The luminescent complex **12** was synthesized by dissolving ligand **H3L7** (0.024 mmol) in 2.5 mL MeOH and adding copper(II) acetate monohydrate (0.048 mmol in 10 mL MeOH). The reaction solution was heated and stirred for 40 min. Then, the solvent was removed with a Pasteur pipette; the red solid was washed with ice-cold MeOH and the solvent, removed with a pipette (three times). The solid was dried at room temperature. In chloroform and under a UV lamp, the product was fluorescent (Figure 3.3-J).

Yield = 13.4 mg (0.012 mmol, 50%). Elemental analysis (%) – calcd. for $[\text{Cu}_2(\mu\text{-CO}_2\text{CH}_3)(\text{C}_{43}\text{H}_{42}\text{N}_6\text{O}_4\text{BF})(\text{CO}_2\text{CH}_3)] \cdot 7\text{H}_2\text{O}$ (1107.93 g mol⁻¹): C 50.7, H 4.6, N 10.1; found: C 50.7, H 4.6, N 10.4. ICP-OES calcd.: Cu 15.3; found: 15.3.

3.2.3.13

Synthesis of Complex 13

H2L8 (0.5 mmol) was dissolved in 10 mL MeOH and then, copper(II) perchlorate hexahydrate (1 mmol) previously dissolved in 5 mL MeOH was slowly added. The methodology was in accordance to the procedure followed to synthesize complex **5**.

Yield = 250 mg (0.25 mmol, 50%). Elemental analysis (%) – calcd. for $[\text{Cu}_2(\text{OH})_2(\text{C}_{27}\text{H}_{25}\text{O}_2\text{N}_6)]3\text{ClO}_4 \cdot 5\text{H}_2\text{O}$: (1016.07 g mol⁻¹): C 31.9, H 3.8, N 8.3; found: C 28.4, H 3.5, N 8.7.

3.2.3.14

Synthesis of Complex 14

Complex **14** was obtained by dissolving ligand **H₂L8** (0.26 mmol) in 5 mL MeOH and then dropping slowly to the ligands solution copper(II) acetate monohydrate (0.53 mmol) previously dissolved in 10 mL MeOH. The reaction solution was heated and stirred for 40 min. The methodology was in accordance to the procedure followed to synthesize complex **4**.

Yield = 218 mg (0.25 mmol, 96%). Elemental analysis (%) – calcd. for $[\text{Cu}_2(\mu\text{-CO}_2\text{CH}_3)_2(\text{OH}_2)(\text{C}_{27}\text{H}_{24}\text{O}_2\text{N}_6)] \cdot 8\text{H}_2\text{O}$ (871.84 g mol⁻¹): C 42.7, H 5.6, N 9.6; found: C 42.6, H 5.7, N 10.9. ICP-OES calcd.: Cu 14.6; found: 15.0.

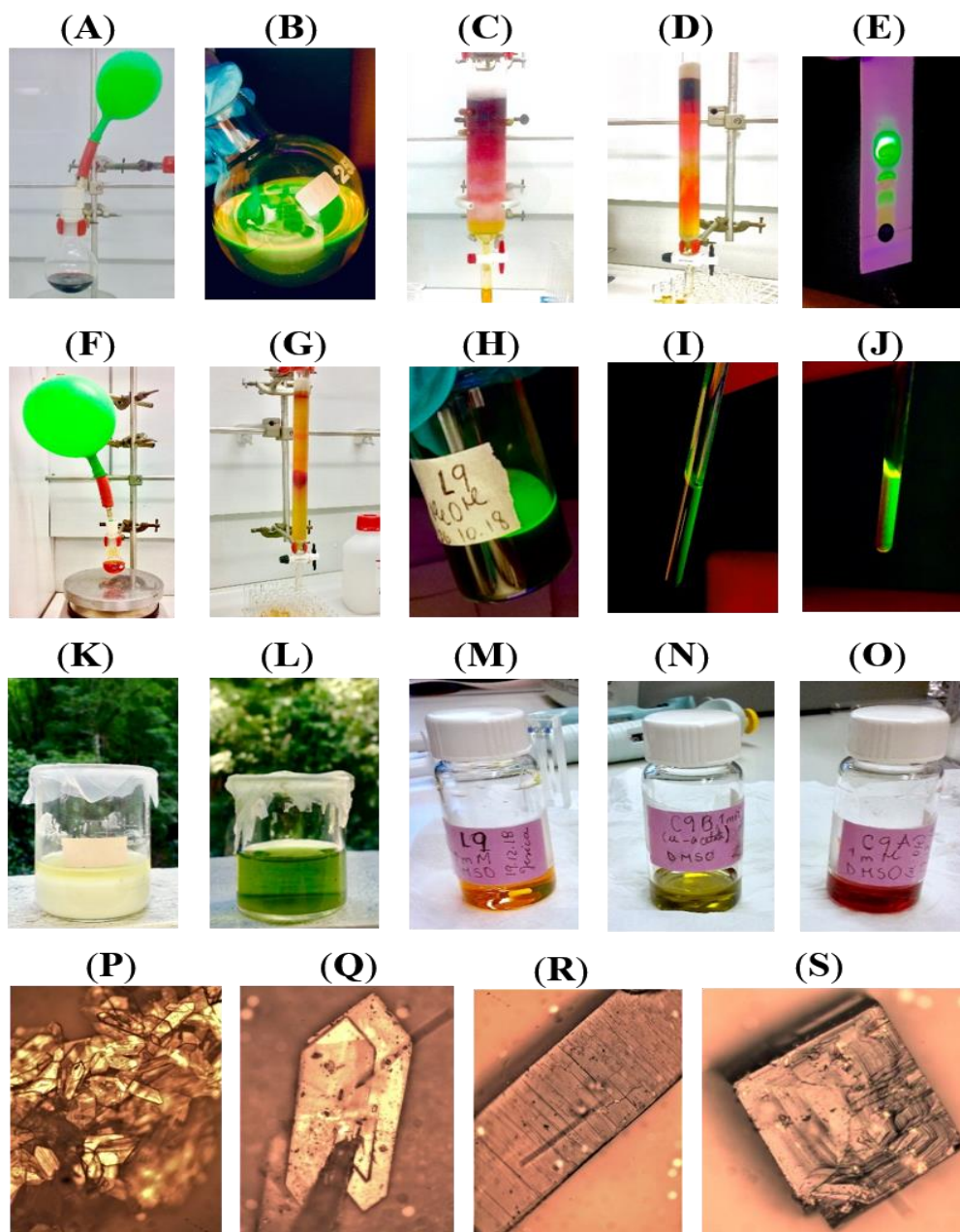


Figure 3.3. Photographs taken during different steps of the synthesis of precursor, ligands and complexes: synthesis of **4-MePh-BODIPY** after addition of (A) TFA and after addition of (B) $\text{BF}_3\cdot\text{OEt}_2$; (C and D) **4-MePh-BODIPY** purification by column chromatography, using SiO_2 as stationary phase and cyclohexane/ethyl acetate 8:1 as mobile phase; (E) thin-layer chromatography of **4-MePh-BODIPY** before purification, using cyclohexane/ethyl acetate 8:1 as mobile; (F) synthesis of **FMeO-BODIPY-Hz** after mixture of the precursors; (G) synthesis of **FMeO-BODIPY-Hz** by column chromatography using SiO_2 as stationary phase and chloroform/MeOH/ammonium hydroxide 100:5:1 as mobile phase; (H) qualitative fluorescence of **H₃L7** dissolved in MeOH and under an UV lamp; (I) qualitative fluorescence of complex **11** dissolved in chloroform and under an UV lamp; (J) qualitative fluorescence of complex **12** dissolved in chloroform and under an UV lamp; (K) appearance of the ligands after synthesis; (L) appearance of the complexes **1–10** and **13** and **14** after synthesis; (M) appearance of ligands **H₃L7** after synthesis; (N) appearance of complex **11** after synthesis dissolved in DMSO; (O) appearance of complex **11** after synthesis dissolved in DMSO; (P) optical photograph of **H₃L1** crystals; (Q) optical photograph of **H₃L2** crystals; (R) optical photograph of complex **1** crystals; (S); and optical photograph of complex **2** crystals.

3.3

Measurements for chemical characterization

3.3.1

Spectroscopic studies

Absorption spectra over the wavelength range 900–250 nm were recorded in a Lambda 35 (Perkin-Elmer) or a Cary 100 (Agilent) or Cary 50 (Varian) spectrophotometers with a temperature controlled equipment. Softwares were provided by the manufacturers. The fluorescent properties of the compounds in different solvents were analysed in a Jasco PF-6200 spectrofluorimeter or, alternatively, in a Perkin Elmer spectrofluorimeter LS 55. Softwares were provided by the manufacturers.

The ligands were characterized by 1D and 2D nuclear magnetic resonance spectroscopy (NMR). The spectra were recorded on a Bruker Avance III HD-400, Bruker Avance III nanobay 400 or Bruker Avance III nanobay 300 spectrometers and calibrated in reference to the residual peaks for DMSO-*d*₆ 2.50 (¹H) and 39.52 (¹³C) ppm and for CD₂Cl₂ 5.33 (¹H) and 54.24 (¹³C) ppm. Coupling constants (*J*) are given in Hz and chemical shifts are reported in ppm. Spectra were processed by using the TopSpin 3.6.1 software.

Mid-infrared (MIR) spectra were acquired on a Perkin-Elmer Spectrum 400 FTIR spectrophotometer, at room temperature, in KBr pellets, with a resolution of 4 cm⁻¹ in the 4000–450 cm⁻¹ range. Each measurement corresponds to a total of 16 scans. The spectra were processed by using the Perkin-Elmer Spectrum 10.03.09 software. Raman spectra were collected at room temperature using a micro-Raman spectroscopy confocal Horiba Xplora ONE™ Jobin Yvon with a spectral resolution of 10 cm⁻¹ in the 3500–700 cm⁻¹ range. The Raman microscope was equipped with a Charged Coupled Device (CCD) detector, and with an integrated camera and a Kohler illumination for transmission and reflection illumination. The laser beam was focused onto the samples through a 50x microscope objective. Different lasers were used as the excitation source: 532 nm (for ligands) and 785 nm (for the complexes). The samples were placed on quartz sample slides. In order to achieve a sufficient signal-to-noise ratio, the Raman spectra were collected in a dark room with exposure time of 2 s and 20 accumulations. An objective lens with a 10x

magnification was used to acquire the optical photographs of the compounds. The spectra were processed by using the LabSpec 6 software.

3.3.2

X-ray crystallography

The crystallographic measurements for complexes **1** and **2** were carried out in collaboration with Dr. Renata Diniz, from the Chemistry Department of the *Universidade Federal de Juiz de Fora*, Brazil.

Single-crystal data of complexes **1** and **2** were collected using a Rigaku Agilent SuperNova diffractometer with MoK α ($\lambda = 0.71073$ Å) radiation at room temperature (293–294 K). The data collection, cell refinements and data reduction were performed using the CrysAlisPro software [117]. The structures were solved and refined using SHELXS and SHELXL packages [118]. The method described by A. C. Larson [119] was used to refine an empirical isotropic extinction parameter, x , applying a multiscan absorption correction [120]. The structures of the compounds were drawn with the Mercury program [121]. All atoms were refined with anisotropic parameters, except hydrogen atoms, which were located from Fourier difference maps, set in calculated positions and refined as riding atoms. For both compounds, disordered solvent molecules were observed in the crystal lattice. Due to this fact, the SQUEEZE [122] methodology was applied to obtain a better description of the complexes. In this method, the electronic density of the solvent is removed from crystal data, which allows for a description of the compound based on an improved model.

The crystallographic measurements for ligands **H₃L₃**, **H₂L₄**, **H₃L₅**, **H₂L₈**, as well as for complexes **3**, **6** and **9** were carried out by Engs. Jérémy Forté and Geoffrey Gontard, from the CHEMBIO group of the *Sorbonne Université*, France.

For ligands **H₂L₄**, **H₃L₅**, **H₂L₈** and complex **3**, a single crystal of each compound was selected, mounted onto a cryoloop and transferred into a cold nitrogen gas stream. Intensity data were collected with a Bruker Kappa APEX-II CCD diffractometer using a micro-focused Cu K α radiation ($\lambda = 1.54178$ Å). For ligand **H₃L₃** and complexes **6** and **9**, a single crystal was selected, mounted onto a cryoloop and transferred into a cold nitrogen gas stream. Intensity data were

collected with a Bruker Kappa APEX-II CCD diffractometer using a graphite-monochromated Mo $K\alpha$ radiation ($\lambda = 0.71073 \text{ \AA}$).

Data collections of these set of ligands and complexes were performed at 200 K, with the Bruker APEXIII suite. Unit-cell parameters determinations, integrations and data reductions were carried out with SAINT program. SADABS was used for scaling and absorption corrections. The structures were solved with SHELXT [123] and refined by full-matrix least-squares methods with SHELXL [118] using Olex2 software package [124] or WinGX suite [125] respectively. All non-hydrogen atoms were refined anisotropically. Symmetry codes and data deviation were obtained by using the PLATON software. Distance and angles were calculated with DIAMOND or MERCURY softwares.

These structures were deposited at the Cambridge Crystallographic Data Centre with numbers CCDC 1851259 (complex **1**), 1851260 (complex **2**), 1912562 (**H₂L4**), 1899672 (complex **3**), 1912561 (**H₃L3**) and 1899668 (complex **6**). Supplementary crystallographic data free of charge from this thesis can be obtained via www.ccdc.cam.ac.uk.

3.3.3

CHNS and copper content

Elemental analysis was performed to determine the CHNS content in ligands and complexes on a ThermoElectron analyser equipment, model Flash EA 1112. All the measurements were carried out in triplicate with 1% as the maximum standard deviation. Elemental analysis measurements were provided as collaboration with Dr. Ricardo Aucélio from LEEA research group of PUC-Rio.

Copper content in the complexes was estimated using an inductively coupled plasma optical emission ICP-OES spectrometer Perkin-Elmer Optima 7300 DV. Samples were treated with nitric acid and diluted in water. Measurements were performed with the dye laser pulsed in the 324.7 nm line for copper.

3.3.4

Thermogravimetric analysis and electrical conductivity

Thermogravimetric curves were acquired in a Thermogravimetric Analyzer Perkin Elmer, Pyris 1 TGA. TGA scans were performed from 25 to 900 °C at 10 °C min⁻¹ under flowing dry air atmosphere. Curve optimization and calculations were processed in the Pyris v 8.0.0.0172 software.

The conductivity measurements were performed at room temperature in an electrical conductivity 650MA Analyser. In order to obtain a final concentration of 1×10^{-3} mol L⁻¹, the copper(II) complexes were dissolved in MeCN.

3.4

Compound's stability

3.4.1

Stability studies by absorption spectroscopy

The stability of the synthesized ligands and complexes was monitored by UV/Vis in H₂O/DMSO 9:1 and/or in PBS/DMSO 9:1 medium, at pH 7.40. DMSO was used to assure for the complete dissolution of the compounds. The hydrazone-related bands were used as reference.

3.4.2

Stability studies by ESI-MS

Results of ESI-MS came from a collaboration with Dr. Mauricio Lanznaster, from *Laboratório Multiusuário de espectrometria de massas (LAMEM)* of the *Universidade Federal Fluminense, Brazil*.

In addition, the stability for ligands **H₃L1**, **H₃L2** and complexes **1** and **2** was investigated by electrospray ionization mass spectrometry (ESI-MS). The analyses were carried out in a Perkin-Elmer SQ-300 mass spectrometer. Stock solutions containing the samples were prepared by dissolving 1.0 mg of the compounds in 100 µL of DMSO (MS grade), and diluting the initial solutions by the addition of 900 µL of deionized water. Both **H₃L1** and **H₃L2** ligands precipitated after the

dilution step. Thus, 900 μL of methanol (MS grade) were used in the preparation of the ligands stock solutions instead of water. Aliquots of 50 μL of the stock solutions of all samples were diluted in 950 μL of methanol and analysed by direct infusion. Analyses of the stock solutions of the complexes were also performed after 24 h of aging. Standard configuration parameters for the positive mode were used, with the capillary output voltage (CAPEX) set at 50 V. Isotopic patterns were simulated using the Isotope Distribution Calculator and Mass Spec Plotter tool [126].

3.5

Interaction of the compounds with BSA, HSA and DNA

3.5.1

BSA-binding studies of ligands H₃L1, H₃L2 and complexes 1 and 2

The interaction between BSA and the synthesized compounds was confirmed by absorption spectroscopy, while binding constants were determined only for the complexes using fluorescence spectroscopy.

For the latter measurements, a Perkin Elmer spectrofluorimeter LS 55 with an optical light filter corresponding to 50% of light attenuation was used. The excitation wavelength was fixed at 280 nm and emission was recorded in the range from 290 to 500 nm. The excitation and emission slits were 6 nm. All measurements were performed at 25 °C. Samples were prepared with a fixed concentration of BSA (1 μM) and varying the concentration of complexes from 0 to 8 μM . For that, BSA solution was prepared in a buffer (10 mM Tris-HCl containing 10 mM NaCl, pH 7.40) and stored at 4 °C. Concentration of BSA was determined using the molar absorptivity of 43,824 $\text{M}^{-1} \text{cm}^{-1}$ at 280 nm. Stock solutions of complexes (1 mM) were prepared in DMSO. Mixtures of BSA and complex **1** or **2** solutions in the appropriate proportions were analysed after 3 minutes of incubation at 25 °C. This timepoint was chosen on the basis of previous preliminary tests performed on the system, which indicated that the equilibrium condition was fully reached after such a reaction time. For absorption measurements, samples were prepared with a BSA : compound molar ratio of 1 : 5 and blanks with the same concentrations of the compounds were subtracted.

3.5.2

DNA binding studies of ligands H₃L1, H₃L2 and complexes 1 and 2

In order to study the interaction of the synthesized compounds with DNA, the corresponding compound-DNA binding constant (K_b) was determined by absorption spectroscopy. For that, an Agilent spectrophotometer Cary 100, in the range 600–250 nm, was used. Samples were placed in a quartz cuvette with 1 cm pathlength. Absorbance was measured for samples with fixed concentration of the synthesized compounds (25 μ M, 3 mL) and increasing concentrations (0-50 μ M) of DNA. Absorbance corresponding to free DNA was subtracted by adding an equal amount of DNA to the samples and to the reference solution. Stock solution was prepared by dissolving sodium salt ctDNA (2 mg mL⁻¹) in a buffer solution (50 mM Tris-HCl containing 50 mM NaCl, pH 7.40) and keeping the solution cold overnight. DNA concentration per nucleotide was determined by diluting 20 times an aliquot of the stock solution and using the molar absorptivity value of 6600 M⁻¹ cm⁻¹ at 260 nm [7, 127]. ctDNA stock solution was stored at -20 °C until use. All samples were analysed in a proportion of 10% DMSO and 90% Tris-HCl (50 mM, 50 mM NaCl, pH 7.40), at 25 °C. The 260/280 nm absorbance ratio of ctDNA diluted (20 x) stock solution was 1.8-1.9, indicating DNA was sufficiently free of protein. Analyses of ctDNA solution in pure buffer and ctDNA solution in mixtures containing 10% DMSO and 90% buffer presented identical spectra.

3.5.3

Scattering studies of BSA and plasmid DNA radii in the presence of the ligands H₃L1, H₃L2 and complexes 1 and 2

For Dynamic Light Scattering (DLS) experiments, around 1 mL of each filtered sample was transferred to dispensable cells, which were incubated for 5 min (BSA samples) or 15 min (DNA samples) at 25.0 \pm 0.1 °C inside the instrument, to achieve thermal stabilization. The measurements were carried out using a compact Nano-particle Analyzer SZ-100 Horiba Scientific. The instrument is equipped with a semiconductor laser excitation solid laser (532 nm, 10 mW) light source and photomultiplier tubes (PMT) detector. The scattering angle (θ) was set at 90° and each sample was measured 20 times for 120 seconds, at 25.0 \pm 0.1 °C.

The SZ-100 Horiba for Windows software was used to record and fit the correlation functions, gaining the size distributions through the CONTIN algorithm. The average of mean hydrodynamic diameter was calculated discarding the measurements with the correlation function showing some kind of flaw. For Small-Angle X-ray Scattering (SAXS) measurements, BSA samples were analyzed in the same conditions previously described for DLS technique. Temperature was set at 25.0 ± 0.5 °C and controlled using a water-bath. The sample holder was a mica window cell and the data frames were collected during 120 seconds (exposure intervals).

All SAXS measurements were performed on the beamline at the Brazilian Synchrotron Light Laboratory (LNLS, Campinas, Brazil). The beam wavelength was 1.548 Å. SAXS data were acquired using the X-ray two-dimensional detector CCD-MAR165 (MarResearch, USA) and the sample-to-detector distance was 902 mm, covering a momentum transfer range of $5 < q < 0.1 \text{ nm}^{-1}$.

The experimental curves are showed as X-ray scattered intensity, $I(q)$, versus the scattering vector. SAXS experimental data were fitted to calculate the gyration radius, R_g , of the particles using the Generalized Gaussian Coil model [128, 129] provided by Sasfit program [130].

A stock solution of Bovine Serum Albumin (essentially fatty acid free), with concentration of 5×10^{-5} M was prepared in 100 mM NaCl and 50 mM Tris buffer, whose pH was tuned with HCl solution (Tris-HCl) at physiological 7.40. The protein concentration in the stock solutions was determined by absorbance at 280 nm (ϵ : $0.667 \text{ mL mg}^{-1} \text{ cm}^{-1}$). Copper(II) complexes stock solutions were prepared in DMSO. Different aliquots were added to 2800 μL of the BSA stock solution in order to obtain solutions with molar ratios of: 1.5, 7, 14, 21 and 28. Moreover, a volume of DMSO was added to obtain Complexes-BSA solutions with 10% DMSO. All the solutions were clarified by ultrafiltration through a PTFE syringe filter with a 0.45 μm pore size and 0.25 mm diameter (LCR). For comparison, measurements were also performed with BSA blank in 10% DMSO (in the absence of the products) and blank of the complexes (in the absence of the BSA) in 2800 μL of the Tris-HCl/NaCl buffer. Ligands-BSA and complex counterion-BSA measurements were carried out in a unique molar ratio: 28. To test the stability of

the copper(II) complexes-BSA over time, DLS measurements were repeated during 24 h at every 3 h.

DNA at a $25 \mu\text{g mL}^{-1}$ stock solutions were prepared in 10 mM Tris-HCl at physiological pH (7.40). Ligands and complexes solutions were prepared as previously described. Compounds-DNA mixtures were prepared in 10% DMSO solution, with $2.5 \mu\text{g mL}^{-1}$ DNA final concentration. The concentration of ligands and complexes was varied. In addition, blanks of DNA and the compounds with the same final concentration were prepared. The solutions were analyzed by DLS.

3.5.4

***In vitro* DNA interaction with ligands H₃L3, H₂L4 and complexes 3–6**

3.5.4.1

DNA-compounds absorption titration studies

The absorbance of the compound ($25 \mu\text{M}$, 3 mL, quartz cuvette, 1 cm pathlength) in 9 : 1 Tris-HCl (50 mM, pH 7.40) : DMSO, were measured in an Agilent spectrophotometer Cary 100 (250 – 600 nm) at 25 °C. The concentration of DNA (0 – 50 μM) was gradually increased in the titration solutions and subtracted to the reference solution. Solid ct-DNA was dissolved (2 mg mL^{-1} , 50 mM Tris-HCl and 50 mM NaCl, pH 7.40) and kept cold overnight. DNA concentration per nucleotide (dil. 20 x) was calculated ($\epsilon = 6600 \text{ M}^{-1} \text{ cm}^{-1}$ at 260 nm) and the absorbance ratio at 260/280 nm (1.8 – 1.9) indicated that the solution was sufficiently free of protein. Ct-DNA stock solution was stored at $-20 \text{ }^\circ\text{C}$ until use. Stock solutions of the compounds (1 mM) were prepared in DMSO.

3.5.4.2

Intercalation binding studies of ligands

The emission spectra of ligand solutions ($5 \mu\text{M}$, 3 mL) in 99 : 1 buffer (50 mM Tris-HCl, 5 Mm NaCl, pH 7.40) : DMSO, with excitation wavelength at 350 nm were recorded in a Perkin Elmer spectrofluorimeter LS 55 with 6 nm of entrance and exit slits at 25 °C. The influence of ct-DNA (0 – 120 μM) on the ligand spectra

was evaluated by monitoring the emission band in the range 450 – 650 nm. Free ct-DNA solution did not show any fluorescence emission in the tested range. The spectra of buffer : DMSO blank was correct to the fluorescence measurement.

3.5.4.3

Ethidium bromide displacement from DNA by the complexes

Copper complexes showed no fluorescence emission in the tested conditions. The intercalation of the complexes with ct-DNA was indirectly examined as the quenching emission caused by the displacement of EB complexed in the DNA. DNA-EB complex solution was prepared at saturated binding sites [131], it is, one molecule of EB (5 μM) per two pairs of DNA bases (10 μM) (4 : 1 DNA nucleotides : EB mole ratio). The influence in the possible intercalation effect was studied by exciting at 555 nm the titration solutions with increasing concentration of complexes (0 – 50 μM) and monitoring the emission in the range of 575 to 775 nm. Buffer (pH 7.40), DNA and compound solutions, measured conditions and n and K_b determination followed the methodology previously reported [127]. The quenching mechanism was estimated using the suppression equation (like the Stern-Volmer equation) $I_0/I = 1 + K_s[Q] = 1 + K_q\tau_0[Q]$ [132] with 23 ns fluorescence intrinsic lifetime, τ_0 of the EB-DNA system [133].

3.5.5

HSA-binding studies of ligand H₃L5

To examine the interaction of ligand **H₃L5** with HSA protein (lyophilized powder, fatty acid free and globulin free) by fluorescence spectroscopy, the concentration of this ligand was maintained at 1 μM in 9:1Tris-HCl/DMSO (1.5 mL, quartz cuvette, 1 cm pathlength) and the concentration of the HSA was gradually increased in each addition sample titration 0 – 10 μM . The HSA stock solution at 15.5 μM was prepared in 50 mM Tris-HCl and 100 mM NaCl, at pH 7.40 buffer solution and stocked at 4 °C until use. Concentration of HSA was determined using the molar absorptivity of 34445 $\text{M}^{-1} \text{cm}^{-1}$ (ϵ) at 280 nm. Stock solution of **H₃L5** was prepared in DMSO. Fluorescence measurements (1.5 mL,

quartz cuvette, 1 cm pathlength) were recorded in a Jasco PF-6200 spectrofluorimeter in the 363 to 650 nm range, at 25 °C. The excitation and emission slits were 5 nm. Samples containing different proportions of HSA and the ligand were incubated for 15 min and then, analysed by exciting at 342 nm.

To examine the interaction of ligand **H₃L5** with HSA protein by absorption spectroscopy, the spectra of the ligand were also obtained before and after addition of HSA protein. Blanks containing the same concentration of the protein in each sample were subtracted from the spectra.

3.5.6

***In vitro* DNA interaction with ligand H₃L5**

Stock solution of ctDNA at 2 mg mL⁻¹ (kept cold overnight) was prepared in 50 mM Tris-HCl and 50 mM NaCl buffer at pH 7.40. Ct-DNA stock solution was stored at -20 °C until use. After dilution of 20 times, the concentration of DNA per nucleotide was determined by UV-Visible absorption at 260 nm using $\epsilon = 6600 \text{ M}^{-1} \text{ cm}^{-1}$ at 260 nm [7, 127]. By verifying the absorbance ratio at 260/280 nm (1.8 – 1.9), it was established that the DNA solution was sufficiently free of protein. Stock solution of ligand **H₃L5** was prepared in DMSO. Blanks containing the same concentration of DNA in each sample were subtracted from the spectra.

3.5.6.1

Absorption studies of the DNA interaction with ligand H₃L5

The interaction mode between the ctDNA and ligand **H₃L5** was examined using absorption spectroscopy. For that, the concentration of the ligand was fixed at 1 μM and that of the ctDNA, varied from 0 – 2 μM in the samples (9:1Tris-HCl/DMSO). The absorbance of the different **H₃L5** : ctDNA ratios (3 mL, quartz cuvette, 1 cm pathlength) in Tris-HCl (50 mM, pH 7.40) were recorded in a Cary 50 (Varian) spectrophotometer with a temperature controlled equipment in the 240 – 600 nm range at 25 °C.

3.5.6.2

Fluorescence studies of the DNA interaction with ligand H₃L5

The binding constant (K_b) and interaction mode of the ligand (1 μ M) with ctDNA (0 – 2 μ M) was determined by recording the emission spectra of the ctDNA-ligand samples in a Jasco PF-6200 spectrofluorimeter with a temperature controlled equipment in the 350 – 650 nm range at 25 °C. Samples (3 mL, quartz cuvette, 1 cm pathlength) were excited at 352 nm with 5 nm of entrance and exit slits at 25 °C. The emission spectra of the ctDNA blanks any fluorescence emission in the tested range. The spectra of 9:1 Tris-HCl/DMSO blank was subtracted to the spectra.

3.6

In vitro anticancer assays

3.6.1

Cytotoxicity assays for ligands H₃L1, H₃L2 and complexes 1 and 2

Results of the cytotoxicity assays for ligands **H₃L1**, **H₃L2** and complexes **1** and **2** were provided by the student Luciano Anselmino and Dr. Claudio O. Fernández and Dr. Mauricio Menacho-Márquez from The Max Planck Laboratory for Structural Biology, Chemistry and Molecular Biophysics of Rosario (MPLbioR, UNR-MPIbpC) and the *Instituto de Investigaciones para el Descubrimiento de Fármacos de Rosario* (IIDEFAR, UNR-CONICET) of the *Universidad Nacional de Rosario*, Argentina.

Cell lines and culture conditions: In the present study is used a panel of cell lines to evaluate the antitumoral potential of the described compounds. This panel includes two human colorectal cancer cell lines (HCT116 and HT29), a human triple negative breast cancer cell line (MDA-MB-231) and a melanoma cell line derived from mice (B16F10). As a non-tumoral control is used Madin-Darby canine kidney cells. All cells were incubated at 37 °C with 5% CO₂ and cultured in Dulbecco Modified Eagle Medium (DMEM) media supplemented with 10% fetal calf serum (FCS), penicillin (10 μ g mL⁻¹), and streptomycin (100 μ g mL⁻¹).

Cell viability assay: For *in vitro* studies of cell proliferation inhibition by the different compounds on cells, 5 × 10³ cells/well were plated on 96-well culture

plates. After attachment, different concentrations of drugs were added and cells were allowed to grow for 36 hours. The number of living cells was estimated by the tetrazolium salt reduction method (MTT, Sigma Aldrich) as described before [134, 135]. Proliferation was expressed as the percentage of control untreated samples. Concentrations of drugs decreasing cell proliferation by 50% (IC_{50}) were estimated from the absorption curves as a function of the concentration of the analysed compound by means of the GraphPad Prism 7 program. The final concentration of DMSO in the culture media was never higher than 1% and was carefully checked that the solvent has no effect on cell growth at such a low level.

3.6.2

Cytotoxicity assays for ligands H₃L3–H₃L7 and complexes 3–12

Cytotoxicity assays for ligands **H₃L3–H₃L7** and complexes **3–12** were performed by the Dr. Vincent Corcé from the research group CHEMBIO of the *Sorbonne Université*, France.

Cell lines and culture conditions: MDA-MB-231 cells were cultivated in Dulbecco's Modified Eagle Medium (DMEM) supplemented with 10% fetal bovine serum and 1% antibiotic mixture. Cells were grown in atmosphere containing 5% CO₂ at 37 °C.

Cell viability assay: Stock solutions of compounds at 1 mM were prepared in DMSO and sterilized through 0.20 µm PTFE-20/25 filter. To evaluate the biological activity of the ligands and complexes cell viability was estimated using the colorimetric 3-(4,5-dimethylthiazol-2-yl)-2,5-diphenyltetrazolium bromide (MTT)-based assay [135]. Cells were seeded at 2×10^3 cells/well (100 µL) in 96-well plate. After 24 h, cell medium was aspirated and cells were treated with various concentrations of the ligands and complexes (0.01 – 10 µM). Compounds were diluted to desired concentration in cell medium containing 1% DMSO. In the untreated control wells, DMSO was added to 1% final concentration. Wells were incubated for another 72 h at 37 °C under 5% CO₂.

To determine the growth inhibitory effect, MTT (0.5 mg mL⁻¹ in culture medium, 20 µL/well) was added, and plates were incubated for 3 h at 37 °C. Supernatants were discarded and DMSO (200 µL) was added to each well. Then, the plated were mixed gently for some minutes in a variable-speed rocker.

Absorbance at $\lambda = 560$ nm was measured with a microplate reader (Fluostar Optima, BMG Labtech). All the values were corrected from background absorbance. The ratio of the absorbance of treated to untreated cells gives the percentage of surviving cells. The percentage of cell viability (%) relative to the untreated control cells versus the concentration (μM) of compound was plotted and fitted to a sigmoidal logistic function. Finally, the concentration decreasing cell proliferation by 50 % (IC_{50}) was calculated by interpolating from the resulting equation of the curves. The reported IC_{50} values present as a mean of triplicate experiments (mean \pm S.D).

3.6.3

Cytotoxicity assays for ligand **H₂L8** and complexes **13** and **14**

Cytotoxicity assays for ligands **H₂L8** and complexes **13** and **14** were performed by the PhD student Farzaneh Ghasemi, as collaboration with the research group directed by Prof. Marcos Dias Pereira in the Biochemistry Department of the *Universidade Federal do Rio de Janeiro* (UFRJ).

Cell lines and culture conditions: The human breast cancer cell line MCF-7 was obtained from the Cell Bank of Hospital Universitário Clementino Fraga Filho, UFRJ, Brazil, and was maintained in DMEM (Dulbecco's modified Eagle's medium; Invitrogen, São Paulo, SP, Brazil) supplemented with 10% (v/v) FBS (fetal bovine serum; Invitrogen) and L-glutamine.

Cell viability assay: MTT [3-(4,5-dimethylthiazol-2-yl)-2,5-diphenyltetrazolium bromide] assay [135] was used for evaluation of cytotoxic effects of **13**, **14** and their ligand **H₂L8** on MCF-7. Cells (1×10^4 cells/well) seeded in a 96 well plates were incubated in DMEM with FBS for 24 h at 37 °C in a 5% CO_2 humidified atmosphere. After 24h, the cells were incubated with the MTT reagent (0.5 mg mL^{-1} in DMEM without FBS) for 3 h at 37 °C in a 5% CO_2 humidified atmosphere. Thereafter, the formazan crystals were dissolved in DMSO (100 μL), and the plate was subjected to absorption measurement at 570 nm using a Microplate reader PowerWave HT. The reduction of MTT to formazan was measured spectrophotometrically that directly related to cell viability.

3.7

Cellular uptake and localization of H₃L7 by fluorescence microscopy

Fluorescence microscopy in cells were performed in collaboration with Dr. Claude Marie Bachelet from the *Institut du Cerveau et de la Moelle Epinière* as well as with the doctors Michèle Salmain and Vincent Corcé from the research group CHEMBIO of *Sorbonne Université*.

The emissive properties of ligand **H₃L7** were used to examine the cellular uptake and localization of the compound in MDA-MB-231 cancer cells using fluorescence confocal microscopy. For that, MDA-MB-231 cells were purchased from ATCC and were seeded in 24-well plate at a density of 1×10^5 cells/well (500 μ L). Cells were cultivated in DMEM supplemented with 10% fetal bovine serum, Glutamax I and 1% kanamycin. Cells were grown for 24 h under humidified atmosphere containing 5% CO₂ at 37 °C. After this time, cell medium was discarded from the wells, and then exposed to ligand **H₃L7** (1 μ M, previously sterilized its stock solution at 1 mM in DMSO through 0.20 μ m PTFE-20/25 filter). The mixture was diluted with cellular medium and incubated further 3 h under the same atmosphere conditions.

In order to visualize **H₃L7** into cells, a co-localization analysis for organelles was performed by incubating MDA-MB-231 cells with a nucleus-staining dye 4',6-diamidino-2-phenylindole (DAPI, 300 nM) and a mitochondria-staining dye MitoTracker Deep Red (MTDR, 200 nM) for 45 min. Cells were independently excited to monitor the compounds at 488 nm (ligand **H₃L7**, 500–600 nm emission region), at 405 nm (DAPI, 410–450 nm emission region) and at 552 nm (MTDR, 600–700 nm emission region). Finally, cells were examined using a fluorescence inverted microscope Olympus 1X71 equipped with a CCD camera and a confocal Leica SP8. A magnification of 40 \times with Asept Uni'gel US immersion were used to take the confocal images with Softworx 6.5.2 software.

3.8

Coordination and transmetallation with the essential Fe(II), Fe(III) and Zn(II) ions from cell medium

In order to explore the coordination and transmetallation of the synthesized compounds with the essential Fe(II), Fe(III) and Zn(II) ions, titration of ligands **H₃L3**, **H₂L4** and copper(II) complexes **3–6** solutions with iron(II) acetate, iron(III) chloride and zinc(II) chloride was monitored by absorption spectroscopy. The concentration of the compounds was 1×10^{-5} M, and the concentration of the salts was increased from 0.5 to 2.5 fold. Solutions were prepared in PBS/DMSO 99:1 and incubated at 37 °C in a shaker under nitrogen atmosphere for 1 h. As indicated above, the UV/Vis absorption of the compound solutions decreases with time in the tested conditions (PBS/DMSO mixture and 37 °C). To take into account the progressive degradation of the ligands and complexes, samples containing the same Fe (or Zn) : compound mole ratios were prepared separately and measured immediately after incubation. Blanks corresponding to the concentration of metal salts in the samples were subtracted from the spectra.

Results and discussion I. Binucleating hydrazonic ligands and their μ -hydroxodicopper(II) complexes as promising structural motifs for enhanced antitumor activity

Paper published as: “*Binucleating Hydrazonic Ligands and Their μ -Hydroxodicopper(II) Complexes as Promising Structural Motifs for Enhanced Antitumor Activity*” Rada JPA, Bastos BSM, Anselmino L, Franco CHJ, Diniz R, Fernández CO, Menacho-Márquez M, Percebom AM, Rey NA, Inorg. Chem. 2019, 58, 8800–8819, DOI: 10.1021/acs.inorgchem.9b01195 (See Figure 12.1).

It is important to remark that all information taken from Chapter 4 of this thesis, must be cited as: RADA, J. P.; BASTOS, B. S. M.; ANSELMINO, L.; FRANCO, C. H. J.; LANZMASTER, M.; DINIZ, R.; FERNÁNDEZ, C. O.; MENACHO-MÁRQUEZ, M.; PERCEBOM, A. M., and REY, N. A. Binucleating Hydrazonic Ligands and Their μ -Hydroxodicopper(II) Complexes as Promising Structural Motifs for Enhanced Antitumor Activity. Inorganic Chemistry, v. 58, n. 13, p. 8800-8819, 2019/07/01, 2019.

4.1

Introduction

The concepts developed in this chapter are based in the hypothesis that, modifying previously known compartmental ligands, such as **HBPAMFF** [102, 136], through the addition of an aroylhydrazone moiety represents a simple way to attain a new set of versatile unsymmetrical binucleating ligands. These ligands allow for the synthesis of interesting novel dicopper(II) compounds displaying different geometries and even distinct coordination numbers at each cupric center. In fact, in a current publication by the research group of Catherine Belle [137], two unsymmetrical ligands derived from bis(2-pyridylmethyl)aminomethyl-2-hydroxy-5-methyl benzaldehyde and 4-methyl or 4,4-dimethyl-3-thiosemicarbazide, as well as their dinuclear and tetranuclear phenoxo-bridged copper(II) complexes, were described and extensively studied by structural, spectroscopic, electrochemical and ESI-MS methods. In this stimulating scenario, and motivated by the search of novel structural motifs for the development of potential antiproliferative agents, the present work describes the first two hydroxo-bridged dicopper(II) complexes

containing unsymmetrical hydrazonic binucleating ligands, as well as evaluates them as candidates for prospective antitumor drugs.

4.2

Results and discussion

4.2.1

Syntheses

Both ligands, as well as their respective dicopper(II) complexes, were obtained in good yields and in a crystalline form. Because of the tetrahedral amine nitrogen displaying three different substituents, all the ligands and complexes were isolated as a pair of optical isomers. Figure 4.1 shows the scheme of the synthesis of the binucleating ligands **H3L1** and **H3L2**, and their respective μ -hydroxo dicopper(II) complexes **1** and **2**.

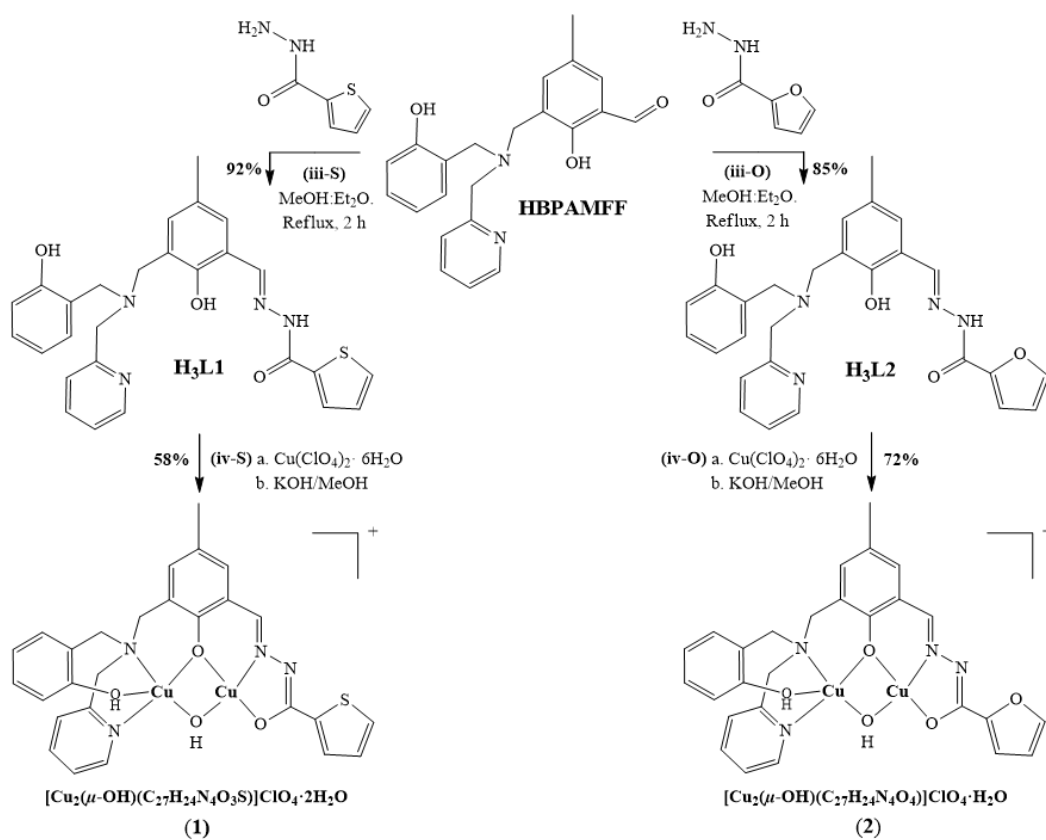


Figure 4.1 Scheme of the synthesis of the binucleating ligands **H3L1** and **H3L2**, and their respective μ -hydroxo dicopper(II) complexes **1** and **2**.

In the TGA analysis for complex **1**, the weight loss was approximately 5.3% (calcd 4.7%) between 25 and 278 °C, corresponding to the removal of two hydration water molecules (Figure 4.2). Molar conductivity in acetonitrile for complex **1** was $180 \text{ ohm}^{-1} \text{ cm}^2 \text{ mol}^{-1}$ (1:1 electrolyte system) [138], consistent with the presence of one single perchlorate as counter-ion. In the case of **2**, the weight loss between 25 and 221 °C in the TGA analysis was in accordance to the elimination of only one hydration water molecule (Figure 4.3). Molar conductivity in acetonitrile was $144 \text{ ohm}^{-1} \text{ cm}^2 \text{ mol}^{-1}$ (1:1 electrolyte system) [138], consistent with the presence of one single perchlorate as counter-ion.

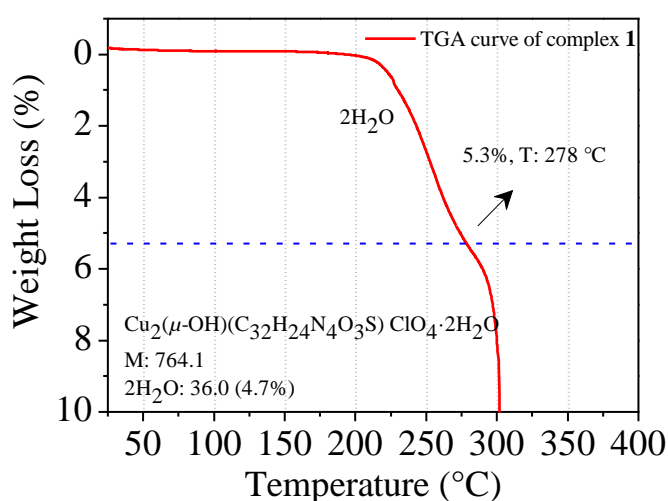


Figure 4.2 Termogravimetric curve of complex **1**.

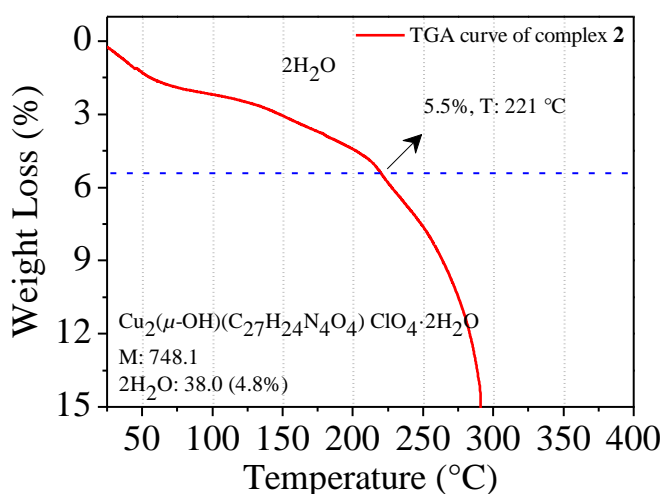


Figure 4.3. Termogravimetric curve of complex **2**.

4.2.2

Characterization of ligands and complexes

4.2.2.1

Solution NMR of ligands

Ligands were fully characterized using multinuclear NMR. The experimental data set includes, along with 1D ^1H and ^{13}C spectra (Figures 4.4–4.7), COSY, HSQC and HBMC contour maps (Figures 13.3–13.8).

It is well-known that aroylhydrazone derivatives can present geometric isomerism with respect to the azomethine group as well as amide-related tautomerization processes [139–141]. In both ligands, the (*E*) isomer is virtually the only one existing. However, duplicated sets of signals in the ^1H and ^{13}C NMR spectra of **H₃L1** indicate the presence, in DMSO-*d*₆ solution, of both iminol and amido tautomers (Figure 4.8).

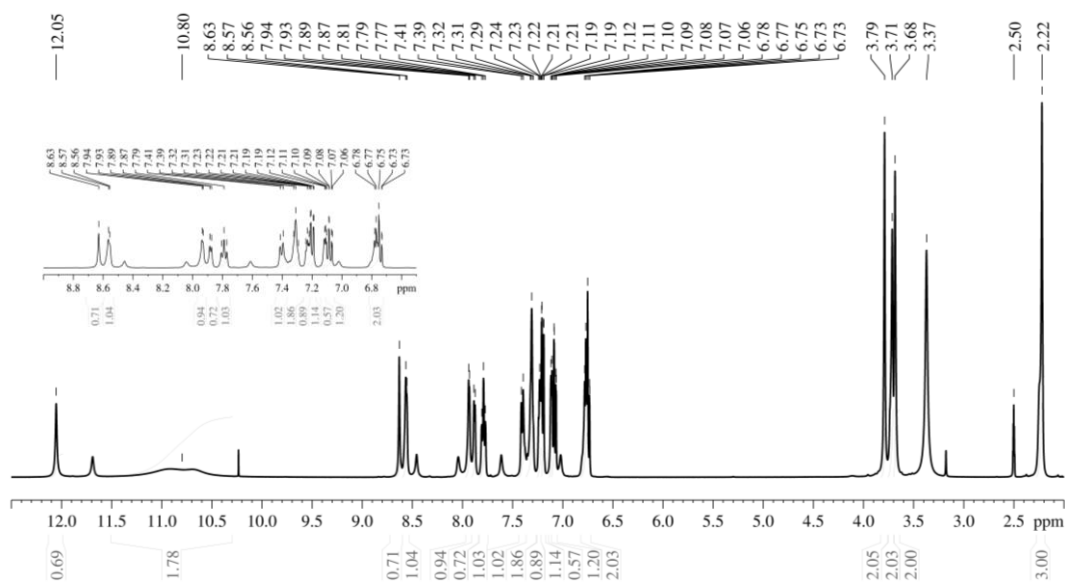


Figure 4.4. ^1H NMR spectra (400 MHz) of **H₃L1** in DMSO-*d*₆ at room temperature.

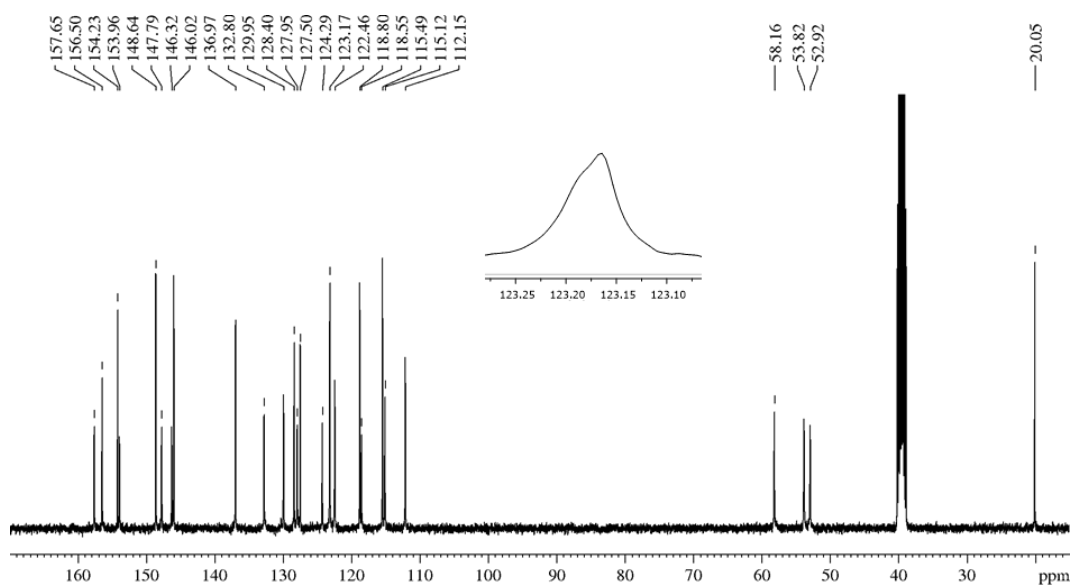


Figure 4.7. ^{13}C NMR spectra (100 MHz) of **H₃L2** in $\text{DMSO}-d_6$ at room temperature.

As in the ^{13}C spectrum of this ligand the carbonyl signal at 161.04 ppm is not part of the main set, it suggests that the iminol form constitutes the predominating species. This is expected since the tautomer is stabilized by intramolecular hydrogen bonding between O1—H and N2.

In contrast, **H₃L2** does not show any duplicated signal and, thus, exists in just one tautomeric form in the tested conditions. The absence of the carbonyl resonance above 160 ppm represents supporting evidence that, for both ligands, the same species prevail at equilibrium. Since iminol $[-(\text{HO})\text{C}=\text{N}-\text{N}=\text{C}-]$ seems to be much more stable in solution, the present NMR analysis focusses only on this tautomer.

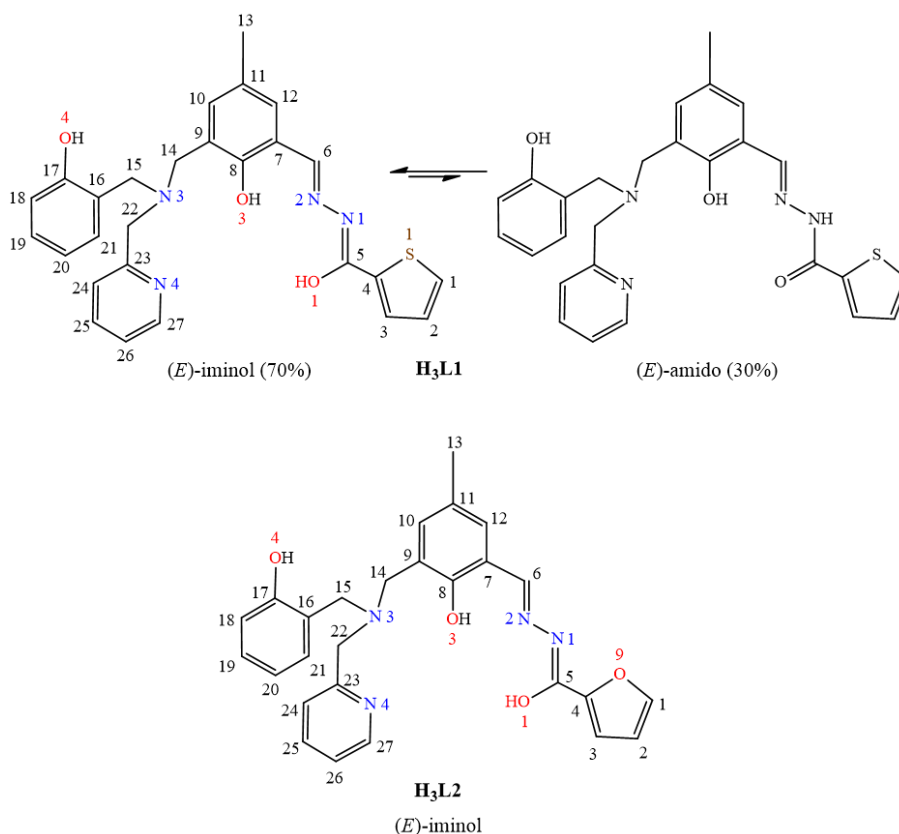


Figure 4.8. Amide-related tautomerization process in **H₃L1** (with the tautomers' percentages at equilibrium) and labelling system employed for the assignment of NMR data according to the XRD numbering scheme.

The chemical shifts previously published by our research group for the precursor **HBPAMFF** were employed as a starting point for the assignment of the non-hydrazone moiety of the ligands [136]. 2D COSY maps helped us to confirm the identity of aromatic hydrogen nuclei, since some signals appear overlapped and, in the case of **H₃L1**, duplicated due to the iminol / amide tautomerism. As expected, the ¹H and ¹³C NMR spectra of **H₃L2** are very similar to those of **H₃L1** except for the absence of tautomeric equilibrium in the former under the conditions of the present study.

A complete assignment of the hydrogen and carbon nuclei for the new ligands **H₃L1** and **H₃L2** is reported (Table 4.1).

Table 4.1. ^1H (400 MHz) and ^{13}C (100 MHz) data for **H₃L1** and **H₃L2** in DMSO-*d*₆ at room temperature, along with the respective assignments. Chemical shifts (δ) are in ppm and coupling constants (J) are in Hz.

| C/H | H ₃ L1 | | | H ₃ L2 | |
|------|---------------------|---|---------------------|---|--|
| | δ_{C} | δ_{H} | δ_{C} | δ_{H} | |
| 1 | 129.10 | 7.94 (d, 1H, $^3J_{\text{HH}} = 4.5$) | 146.02 | 7.96 (d, 1H, $^3J_{\text{HH}} = 1.4$) | |
| 2 | 128.21 | 7.23 (t, 1H, $^3J_{\text{HH}} = 4.5$) | 112.15 | 6.70 (dd, 1H, $^3J_{\text{HH}} = 3.4$, $^3J_{\text{HH}} = 1.4$) | |
| 3 | 132.04 | 7.88 (d, 1H, $^3J_{\text{HH}} = 4.5$) | 122.46 | 7.33-7.30 (m, 2H)* | |
| 4 | 137.83 | – | 146.32 | – | |
| 5 | 157.48 | – | 153.96 | – | |
| 6 | 147.17 | 8.63 (s, 1H) | 147.79 | 8.64 (s, 1H) | |
| 7 | 118.67 | – | 118.55 | – | |
| 8 | 154.27 | – | 154.23 | – | |
| 9 | 124.21 | – | 124.29 | – | |
| 10 | 132.80 | 7.12 (s, 1H) | 132.80 | 7.12 (s, 1H) | |
| 11 | 127.51 | – | 127.50 | – | |
| 12 | 127.70 | 7.32-7.30 (m, 2H)* | 127.95 | 7.27 (s, 1H) | |
| 13 | 20.07 | 2.22 (s, 3H) | 20.05 | 2.21 (s, 3H) | |
| 14 | 53.14 | 3.71 (s, 2H) | 52.92 | 3.70 (s, 2H) | |
| 15 | 53.74 | 3.68 (s, 2H) | 53.82 | 3.69 (s, 2H) | |
| 16 | 123.16 | – | 123.17** | – | |
| 17 | 156.48 | – | 156.50 | – | |
| 18 | 115.48 | 6.77 (d, 1H, $^3J_{\text{HH}} = 8.0$) | 115.49 | 6.77 (d, 1H, $^3J_{\text{HH}} = 7.4$) | |
| 19 | 128.41 | 7.09 (td, 1H, $^3J_{\text{HH}} = 7.7$, $^4J_{\text{HH}} = 1.5$) | 128.40 | 7.09 (td, 1H, $^3J_{\text{HH}} = 7.4$, $^4J_{\text{HH}} = 1.0$) | |
| 20 | 118.82 | 6.75 (t, 1H, $^3J_{\text{HH}} = 7.4$) | 118.80 | 6.75 (t, 1H, $^3J_{\text{HH}} = 7.4$) | |
| 21 | 129.97 | 7.20 (dd, 1H, $^3J_{\text{HH}} = 7.4$, $^4J_{\text{HH}} = 1.0$) | 129.95 | 7.20 (dd, 1H, $^3J_{\text{HH}} = 7.4$, $^4J_{\text{HH}} = 1.0$) | |
| 22 | 58.10 | 3.79 (s, 2H) | 58.16 | 3.78 (s, 2H) | |
| 23 | 157.60 | – | 157.65 | – | |
| 24 | 123.20 | 7.41 (d, 1H, $^3J_{\text{HH}} = 7.4$) | 123.17** | 7.40 (d, 1H, $^3J_{\text{HH}} = 7.8$) | |
| 25 | 137.00 | 7.80 (t, 1H, $^3J_{\text{HH}} = 7.4$) | 136.97 | 7.78 (td, 1H, $^3J_{\text{HH}} = 7.8$, $^4J_{\text{HH}} = 1.6$) | |
| 26 | 122.48 | 7.32-7.30 (m, 2H)* | 115.12 | 7.33-7.30 (m, 2H)* | |
| 27 | 148.61 | 8.56 (d, 1H, $^3J_{\text{HH}} = 3.9$) | 148.64 | 8.56 (d, 1H, $^3J_{\text{HH}} = 4.1$) | |
| O1–H | – | 12.05 (s, 1H) | – | 12.06 (s, 1H) | |

*Overlapped signals. **Unresolved asymmetric signal (see Inset of Figure 4.7). Signal multiplicity - s: singlet, d: doublet, t: triplet, dd: doublet of doublets, td: triplet of doublets.

4.2.2.2

ESI-MS analysis of ligands.

Two prominent peaks were observed at (m/z^+) 509 and 995 for **H₃L1**, and at (m/z^+) 493 and 963 for **H₃L2**. These peaks were assigned, respectively, to sodium-associated monomeric and dimeric species [**H₃L** + Na]⁺ and [(**H₃L**)₂ + Na]⁺.

4.2.2.3

Crystal structures of complexes 1 and 2

Figure 4.9 shows the structures of the cationic complexes present in $[\text{Cu}_2(\mu\text{-OH})(\text{C}_{27}\text{H}_{24}\text{N}_4\text{O}_3\text{S})]\text{ClO}_4 \cdot 2\text{H}_2\text{O}$ (1) and $[\text{Cu}_2(\mu\text{-OH})(\text{C}_{27}\text{H}_{24}\text{N}_4\text{O}_4)]\text{ClO}_4 \cdot \text{H}_2\text{O}$ (2). Detailed crystal data, collection and refinement parameters can be found in Tables 4.2 and 4.3. Selected bond distances and angles are listed in Table 4.4.

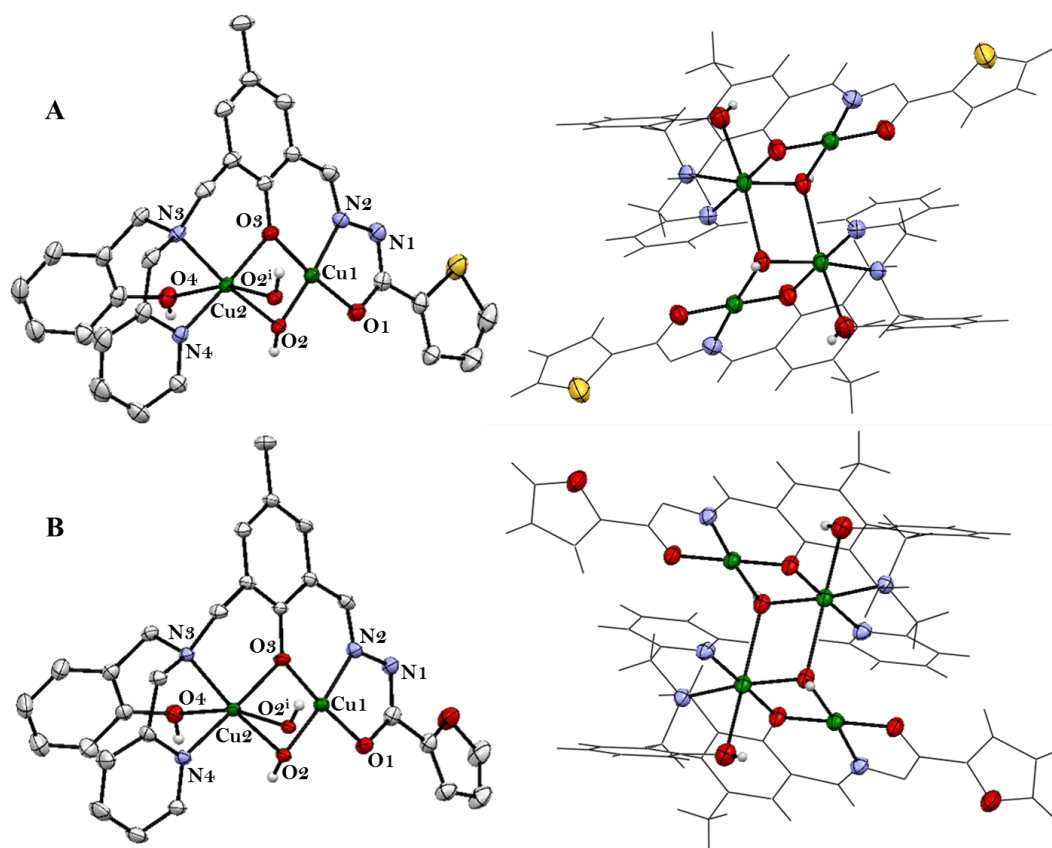


Figure 4.9. Left. Crystal structure of 1 (A) and 2 (B). The ellipsoids were drawn with 30% probability. Only one of the enantiomers is shown. Perchlorate counter-ions, disordered water molecules and most of the hydrogen atoms were omitted for the sake of clarity. Symmetry code: (i) $-x+1, -y+1, -z+1$. Right. The corresponding dimers, formed by a pair of enantiomers interacting through trifurcated hydroxo bridges (O2 and O2ⁱ donor atoms), with the copper(II) coordination spheres highlighted as coloured ellipsoids.

Table 4.2. Experimental details for complex **1**.

| | |
|---|------------------------------------|
| Crystal | Complex 1 |
| Chemical formula | $C_{27}H_{25}ClCu_2N_4O_8S$ |
| M_r (g mol ⁻¹) | 728.10 |
| Crystal system, space group | Monoclinic, $P21/c$ |
| Temperature (K) | 293 |
| a, b, c (Å) | 10.8166(1), 21.0642(2), 14.6498(2) |
| β (°) | 106.415(1) |
| V (Å ³) | 3201.80(6) |
| Z | 4 |
| Radiation type | Mo $K\alpha$ |
| μ (mm ⁻¹) | 1.528 |
| Crystal size (mm) | 0.41 × 0.36 × 0.23 |
| Data collection | |
| Diffractometer | SuperNova, Dual, Atlas S2 |
| No. of measured, independent and observed | 68355, 8419, 7522 |
| R_{int} | 0.011 |
| Refinement | |
| $R[F^2 > 2\sigma(F^2)], wR(F^2), S$ | 0.034, 0.103, 1.06 |
| No. of parameters | 417 |
| No. of restraints | 0 |
| $\Delta\rho_{max}, \Delta\rho_{min}$ (e Å ⁻³) | 1.55, -0.70 |

Table 4.3. Experimental details for complex **2**.

| | |
|--|---|
| Crystal | Complex 2 |
| Chemical formula | C ₂₇ H ₂₅ ClCu ₂ N ₄ O ₉ |
| <i>Mr</i> (g mol ⁻¹) | 712.04 |
| Crystal system, space group | Monoclinic, <i>P21/c</i> |
| Temperature (K) | 294 |
| <i>a</i> , <i>b</i> , <i>c</i> (Å) | 10.5312(5), 14.8760(7), 18.8006(9) |
| β (°) | 91.967(5) |
| <i>V</i> (Å ³) | 2943.6(2) |
| <i>Z</i> | 4 |
| Radiation type | Mo <i>K</i> α |
| μ (mm ⁻¹) | 1.595 |
| Crystal size (mm) | 0.17 x 0.25 x 0.65 |
| Data collection | |
| Diffractometer | SuperNova, Dual, Atlas S2 |
| No. of measured, independent and observed | 81145, 7904, 5908 |
| <i>R</i> _{int} | 0.0845 |
| Refinement | |
| <i>R</i> [<i>F</i> ² > 2σ(<i>F</i> ²)], <i>wR</i> (<i>F</i> ²), <i>S</i> | 0.0522, 0.1185, 1.031 |
| No. of parameters | 391 |
| No. of restraints | 0 |
| Δρ _{max} , Δρ _{min} (e Å ⁻³) | 0.707, -0.595 |

The crystal structures indicate that both complexes generate dimeric arrangements containing two partially deprotonated (**HL1**²⁻ or **HL2**²⁻) ligands and four divalent copper centers. In fact, compounds **1** and **2** are quite similar, exhibiting two crystallographically independent metal sites (Cu1 and Cu2) with inter-metallic distances of 2.944 and 2.923 Å, respectively.

Cu1, which is coordinated by the hydrazonic moiety of the ligand, comprising the donor atoms N2 and O1 (corresponding to the iminolate form), shows a square planar geometry with a slightly distorted plane [average distances among atoms and the best plane are 0.012(4) and 0.03(1) Å, correspondingly, for complexes **1** and **2**. Endogenous (O3) phenoxo and exogenous (O2) hydroxo bridges complete the coordination sphere. On the other hand, Cu2 exhibits an N₂O₄-type octahedral environment distorted by a pronounced Jahn-Teller effect.

Table 4.4. Selected geometric parameters for complexes **1** and **2**.

| Bond distances (Å) | | |
|------------------------|-----------|------------|
| | 1 | 2 |
| Cu1—O1 | 1.910(1) | 1.895(2) |
| Cu1—O2 | 1.933(1) | 1.924(2) |
| Cu1—O3 | 1.914(1) | 1.908(2) |
| Cu1—N2 | 1.911(2) | 1.905(2) |
| Cu2—O2 | 1.952(1) | 1.949(2) |
| Cu2—O3 | 1.960(1) | 1.956(2) |
| Cu2—O4 | 2.574(2) | 2.570(2) |
| Cu2—N3 | 2.005(2) | 2.003(2) |
| Cu2—N4 | 1.984(2) | 1.976(2) |
| Cu2—O2 ⁱ | 2.599(2) | 2.590(2) |
| Bond angles (°) | | |
| | 1 | 2 |
| Cu1—O2—Cu2 | 98.49(6) | 97.99(9) |
| Cu1—O3—Cu2 | 98.90(6) | 98.32(9) |
| O1—Cu1—O2 | 103.49(6) | 102.05(9) |
| O1—Cu1—O3 | 175.23(6) | 175.67(10) |
| O1—Cu1—N2 | 82.46(7) | 83.06(10) |
| O2—Cu1—O3 | 80.89(5) | 81.54(8) |
| O2—Cu1—N2 | 174.02(6) | 174.72(10) |
| O3—Cu1—N2 | 93.14(7) | 93.42(10) |
| O2—Cu2—O3 | 79.25(6) | 79.69(8) |
| O2—Cu2—N3 | 171.01(6) | 171.60(9) |
| O2—Cu2—N4 | 103.26(6) | 102.72(9) |
| O2—Cu2—O2 ⁱ | 85.79(6) | 82.11(9) |
| O3—Cu2—O4 | 97.38(8) | 97.48(9) |
| O3—Cu2—N3 | 92.15(6) | 92.20(9) |
| O3—Cu2—N4 | 177.48(6) | 177.43(9) |
| O4—Cu2—N3 | 86.59(7) | 86.42(9) |
| O4—Cu2—N4 | 81.36(7) | 83.39(9) |
| N3—Cu2—N4 | 85.37(7) | 85.43(10) |

Symmetry code: (i) $-x + 1, -y + 1, -z + 1$.

| Crystal | Complex 1 |
|-----------------------------|---|
| Chemical formula | C ₂₇ H ₂₅ ClCu ₂ N ₄ O ₈ S |
| Mr (g mol ⁻¹) | 728.10 |
| Crystal system, space group | Monoclinic, P21/c |

The equatorial plane contains the tertiary amine N3 and the pyridine N2 nitrogen atoms, in addition to the O3 phenoxo and O2 hydroxo bridges. Apical positions are occupied by the protonated phenol oxygen O4 and by the bridging hydroxo O2ⁱ atom of another dinuclear unit, constituting a nice example of a trifurcated bridge, with the structural function of maintaining the dimer's integrity. When the compounds are in solution, those interactions are probably disrupted, and Cu2 should assume a square pyramidal geometry. Furan and thiophene rings are not involved in coordination.

Two perchlorate counter-ions, located in voids, were also observed in the crystal lattice for each complex dimer. Dimers present moderate O...O hydrogen bonds between both the terminal endogenous (O4) and the bridging exogenous (O2) hydroxide and the perchlorate counter-ions. The crystal packing is also stabilized by weak CH...O interactions involving perchlorate and methylene groups. Moreover, for complex **1**, CH...S interactions between the ligands could be identified too. A complete list of the hydrogen-bond geometries present in complexes **1** and **2** can be found in supplemental Tables 4.5 and 4.6, respectively.

Table 4.5. H-bonding parameters for complex **1** (Å, °).

| D—H...A | D—H | H...A | D...A | D—H...A |
|------------------------------|------|-------|------------|---------|
| O2—H2A...O6 ⁱⁱ | 0.82 | 2.170 | 3.038 (15) | 177.0 |
| O4—H4...O8 ⁱⁱ | 0.82 | 1.940 | 2.740 (9) | 166.0 |
| C23—H23A...O1 ⁱ | 0.97 | 2.460 | 3.206 (3) | 134.0 |
| C23—H23B...O5 ⁱⁱⁱ | 0.97 | 2.330 | 3.252 (5) | 158.0 |

Symmetry codes: (i) 1 - x, - y, 2 - z; (ii) x, y, 1 + z; (iii) 1 - x, - 1/2 + y, 1 + 1/2 - z.

Table 4.6. H-bonding parameters for complex **2** (Å, °).

| D—H...A | D—H | H...A | D...A | D—H...A |
|----------------------------|------|-------|-----------|---------|
| O2—H2A...O5 | 0.82 | 2.120 | 2.940 (4) | 173.0 |
| O4—H4...O6 | 0.82 | 1.940 | 2.758 (4) | 176.0 |
| C22—H22A...O1 ⁱ | 0.97 | 2.360 | 3.097 (4) | 132.0 |

Symmetry code: (i) - x + 1, - y + 1, - z + 1.

4.2.2.4

Vibrational properties of the compounds

Both **H₃L1** and **H₃L2** and their corresponding dicopper(II) complexes **1** and **2** were studied under the perspective of vibrational (IR and Raman) spectroscopy. Raman versus FTIR spectra are available in Attachment B chapter, in Figures 13.26–13.33. Figures 13.23 and 13.24 show respectively the infrared spectra of the **HBPA** and **HBPAMFF** precursors.

When comparing the vibrational bands of the free ligands to those of their metal compounds (Figures 4.10–4.13), complexation is evidenced. Probably, the most patent amongst them are related to the deprotonation of the hydrazonic group upon coordination. For example, in the infrared spectrum of **H₃L1**, the NH stretching mode is observed at 3151 cm⁻¹, and the band at 1555 cm⁻¹ is assigned to the amide N–H bending vibration. In the **TCH** precursor, this mode appears at 1542 cm⁻¹ [142]. The complete absence of these bands in the FTIR spectrum of **1**, as well as the pronounced shift of the ν C=O band to lower wavenumbers, indicate that the ligand loses the amide hydrogen and is coordinated in its iminolate form, which is in agreement with the acidic nature of this group and the use of stoichiometric sodium hydroxide during the last step of the complexes' syntheses.

As expected, specific bands for the perchlorate counter-ions are also present in the vibrational spectra of complexes **1** and **2**.

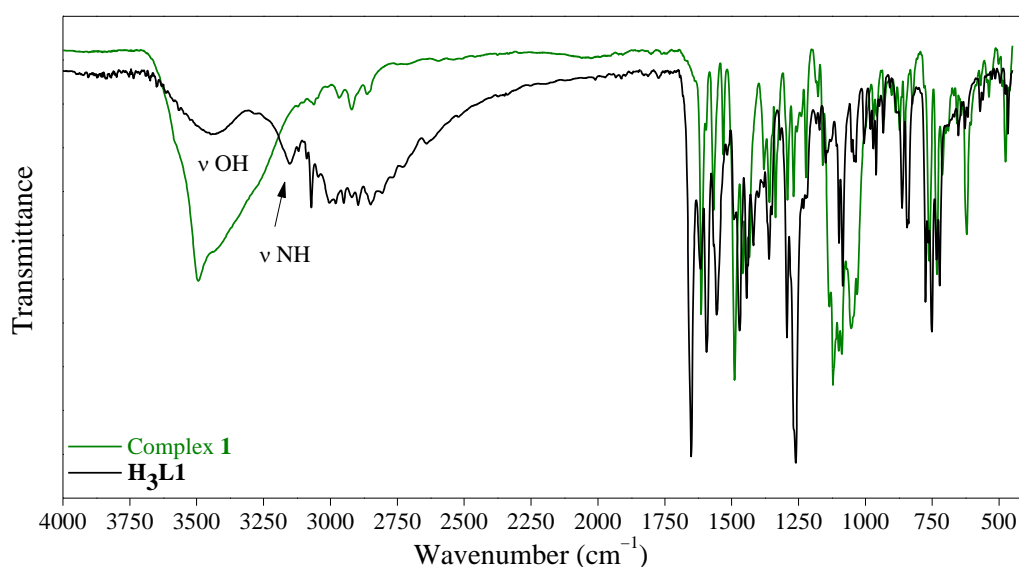


Figure 4.10. FTIR spectra of **H₃L1** and complex **1** in KBr pellets in the 4000–500 cm⁻¹ region.

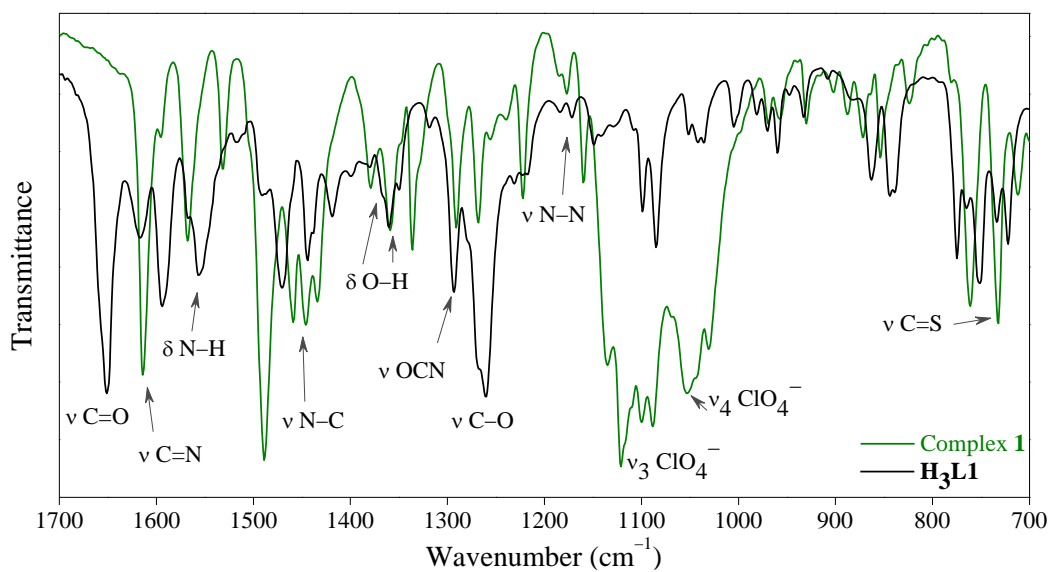


Figure 4.11. FTIR spectra of **H₃L1** and complex **1** in KBr pellets in the 1700–700 cm^{-1} region.

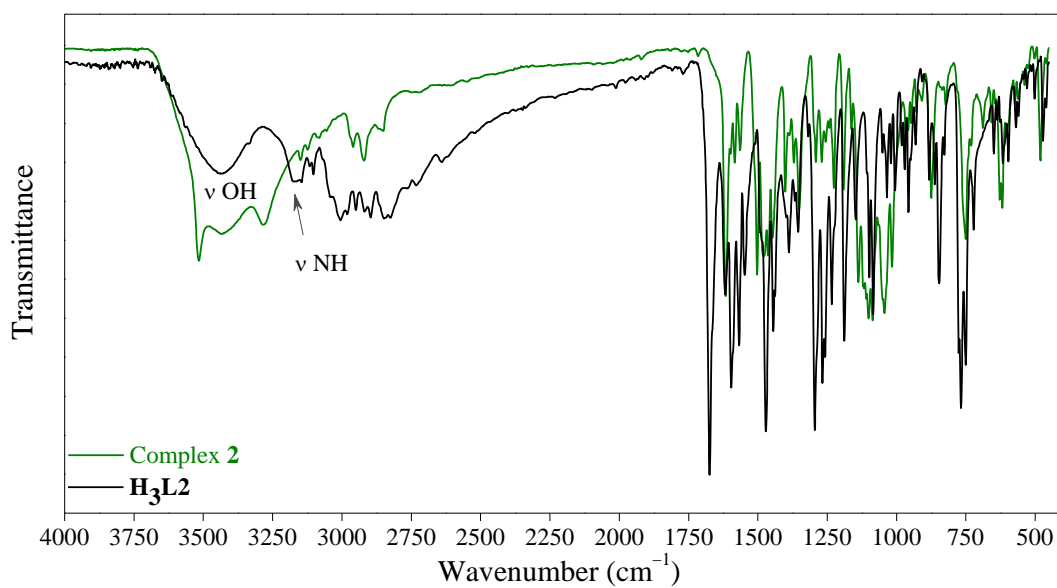


Figure 4.12. FTIR spectra of **H₃L2** and complex **2** in KBr pellets in the 4000–500 cm^{-1} region.

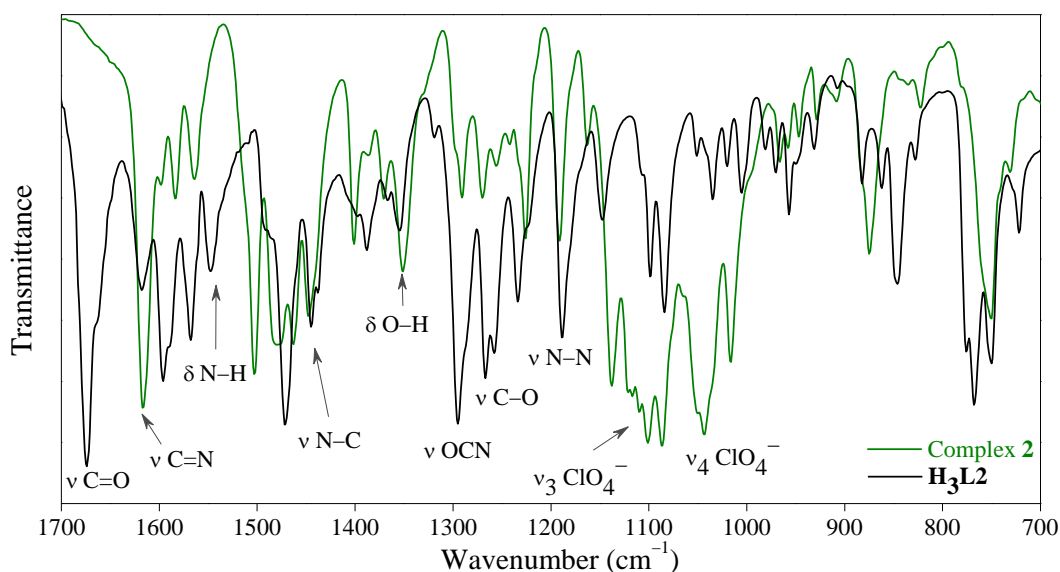


Figure 4.13. FTIR spectra of **H₃L2** and complex **2** in KBr pellets in the 1700–700 cm⁻¹ region.

The main vibrational frequencies of **H₃L1**, **H₃L2** and their coordination compounds, along with the proposed assignments, are summarized in Table 4.7.

Table 4.7. Selected vibrational absorptions (cm⁻¹) for **H₃L1** and **H₃L2** and their complexes.

| H₃L1 | | H₃L2 | | 1 | | 2 | | Assignment |
|------------------------|----------------|------------------------|-------|----------|-------|----------------|-------|--|
| IR | Raman | IR | Raman | IR | Raman | IR | Raman | |
| 3446 | – | 3440 | – | 3490 | – | 3432 | – | ν OH |
| 3151 | – | 3149 | – | – | – | – | – | ν NH |
| 1651 | 1645 | 1674 | 1668 | 1488 | 1485 | 1502 | 1501 | ν C=O/ν C–O* |
| 1618 | 1614 | 1616 | 1608 | 1614 | 1615 | 1616 | 1607 | C=N |
| 1555 | 1556 | 1545 | 1546 | – | – | – | – | δ N–H |
| 1366 (sh) | 1365 (s.b.) | 1358 (sh) | 1365 | – | – | – | – | δ O–H |
| 1360 | 1358 | 1355 | 1352 | 1359 | – | 1351 | – | δ O–H |
| 1172 | 1171 | 1169 (sh) | 1171 | 1177 | 1175 | 1179 (s.b.) | 1177 | ν N–N |
| – | – | – | – | 1120 | – | 1118 | – | ν ₃ ClO ₄ ⁻ |
| – | – | – | – | 1052 | 1053 | 1045 | 1043 | ν ₄ ClO ₄ ⁻ |

sh: shoulder. *C=O for ligands and C–O for complexes.

4.2.2.5

Absorption spectroscopy studies of the compounds

Both **H₃L1** and **H₃L2** display five foremost absorptions in the 250–500 nm spectral range, as shown in Figure 4.14 (top), in which the spectra of the precursor **HBPAMFF** and the respective hydrazides are also shown for the sake of comparison. Three of those absorption bands are also present in the precursors and are probably related to thiophene / furan and **HBPAMFF** transitions.

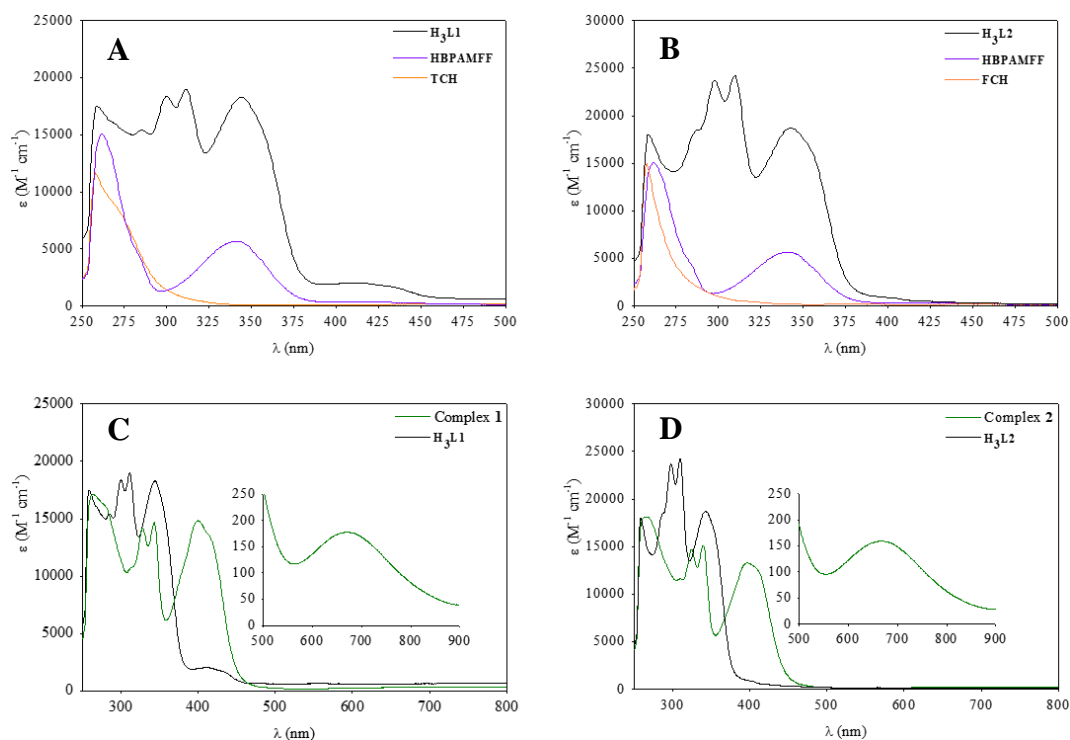


Figure 4.14. Absorption spectra of ligands (A) **H₃L1** (4.6×10^{-5} M) and (B) **H₃L2** (4.8×10^{-5} M), as well as their respective precursors: **HBPAMFF** (10.6×10^{-5} M), **TCH** (7.0×10^{-5} M) and **FCH** (4.0×10^{-5} M), in DMSO at r.t. And absorption spectra of complexes (C) **1** (left, 6.2×10^{-5} M) and (D) **2** (right, 7.0×10^{-5} M) recorded in DMSO at r.t. The spectra of **H₃L1** (3.4×10^{-5} M) and **H₃L2** (2.9×10^{-5} M) are included for the sake of comparison. *Insets*: Visible absorbance of **1** (5.0×10^{-3} M) and **2** (5.0×10^{-3} M) in the 500–900 nm region.

The most intense absorption band occurs at 312 (**H₃L1**) and 310 (**H₃L2**) nm, followed by strong absorption centered at 300 (**H₃L1**) and 298 (**H₃L2**) nm, corresponding to the aroylhydrazone transitions, since they are completely absent in the spectra of precursors. The upper half of Table 4.8 displays the absorption

bands of both ligands along with their respective molar absorptivity coefficients and suggested assignments.

The absorption profiles of the complexes are very similar to those of the respective ligands. Nevertheless, the bands related to the hydrazone group and to the **HBPAMFF**-derived central phenol system are bathochromically shifted in the spectra of **1** and **2** (Figure 4.14, bottom). The presence of the iminolate tautomeric form in the complexes, as well as the deprotonation of the central (bridging) phenol group upon coordination, increase the electron delocalization all over this moiety of the ligand. In both complexes, a broad low-intensity (Table 4.8, lower half) absorption is also observed from 550 to 800 nm. These bands, centred at 667 nm for both **1** and **2**, are attributed to *d-d* transitions between the electronic states of the copper centers. The presence of charge transfer bands can certainly not be ruled out, although their observation may be impaired due to overlapping with the intra-ligand absorptions.

Table 4.8. UV-Vis absorption properties of **H₃L1** and **H₃L2**, as well as those of their dicopper(II) complexes **1** and **2**, in DMSO at r.t. Suggested assignments are also included.

| H₃L1 | | H₃L2 | | Assignment |
|------------------------|--|------------------------|--|--|
| λ (nm) | ϵ (M ⁻¹ cm ⁻¹) | λ (nm) | ϵ (M ⁻¹ cm ⁻¹) | |
| 344 | 18500 | 343 | 18700 | HBPAMFF rings |
| 312 | 18900 | 310 | 24000 | CO-NH-N=N |
| 300 | 18300 | 298 | 23500 | CO-NH-N=N |
| 286 | 15100 | 287 | 18000 | Furan / thiophene and HBPAMFF rings |
| 259 | 15000 | 258 | 14100 | |
| 1 | | 2 | | Assignment |
| λ (nm) | ϵ (M ⁻¹ cm ⁻¹) | λ (nm) | ϵ (M ⁻¹ cm ⁻¹) | |
| 667 | 180 | 667 | 150 | <i>d-d</i> transitions |
| 400 | 14730 | 397 | 13200 | HBPAMFF rings |
| 343 | 14500 | 340 | 15000 | CO-NH-N=N |
| 329 | 14100 | 325 | 14500 | CO-NH-N=N |
| 313 | 10900 | 310 | 11300 | HBPAMFF rings |
| 281(sh) | 16800 | 287 | 14300 | Furan / thiophene and HBPAMFF rings |
| 264 | 18000 | 265 | 17800 | |

4.2.3

Hydrolysis studies

Substances containing the hydrazone group are known to be prone to dissociate into the respective carbonyl compound and hydrazide in water. However, an aqueous medium is necessary for most biological tests and, even more significant, water constitutes the universal physiological solvent. For this reason, the stability of ligands and complexes was monitored by absorption spectroscopy, over 24 h, in water solutions containing 10% DMSO to assure for the complete dissolution of the compounds. The hydrazone-related bands at 312/299 nm (**H₃L1**), 308/299 nm (**H₃L2**), 343/330 nm (**1**), and 333/320 nm (**2**) were used as reference. Notice that, in this medium, ligands and complexes absorbance are slightly shifted.

4.2.3.1

Stability of ligands

Over the first 12 h of assay, the absorbance of the ligands solutions decrease by around 90% (Figure 4.15). With time, the bands associated to the hydrazone group remain in the same position. However, the wavelenghts from the **HBPAMFF**-related absorptions are slightly blue-shifted for both ligands, approaching that of the free **HBPAMFF** precursor. This absorption band of **HBPAMFF**, at about 340 nm, has a molar absorptivity that is around one third of those related to the associated bands in **H₃L1** and **H₃L2**. Therefore, our results suggest that, in aqueous solution, ligands are hydrolysed in a relative fast way. The ligands were also assayed in pure (100%) DMSO and in 10% DMSO-90% PBS buffer (pH 7.4).

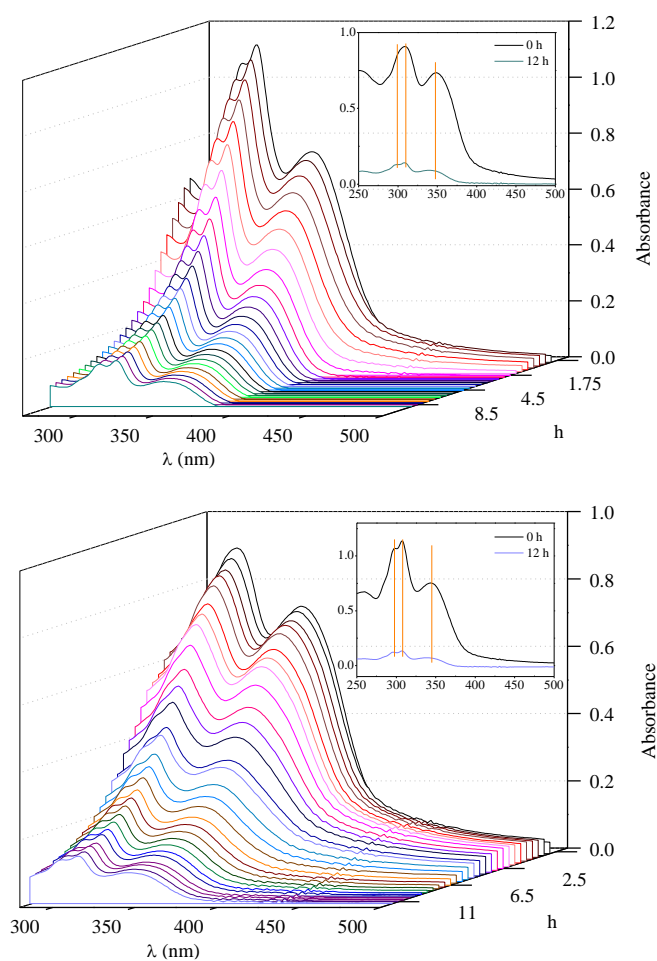


Figure 4.15. Absorption spectra of **H₃L1** (top, pH 6.15) and **H₃L2** (bottom, pH 6.35) vs time in 10% DMSO at room temperature. $[L] = 5 \times 10^{-5}$ M. *Inset*: Spectra at 0 and 12 h for comparison.

In the organic medium, both **H₃L1** and **H₃L2** demonstrate a remarkable stability, keeping more than 90% of the initial absorption values along the 24 h monitoring at room temperature. Although not as stable as in pure DMSO, the ligands are more resistant to hydrolysis in the “buffered” medium than in 10% DMSO-90% water. The initial absorption value decrease for **H₃L1** was only 31% over 24 h, while that for **H₃L2** was 63% under the same experimental conditions, which is in accord with the acid nature of the hydrazone hydrolysis, as can be observed in Figures 4.16-A and B.

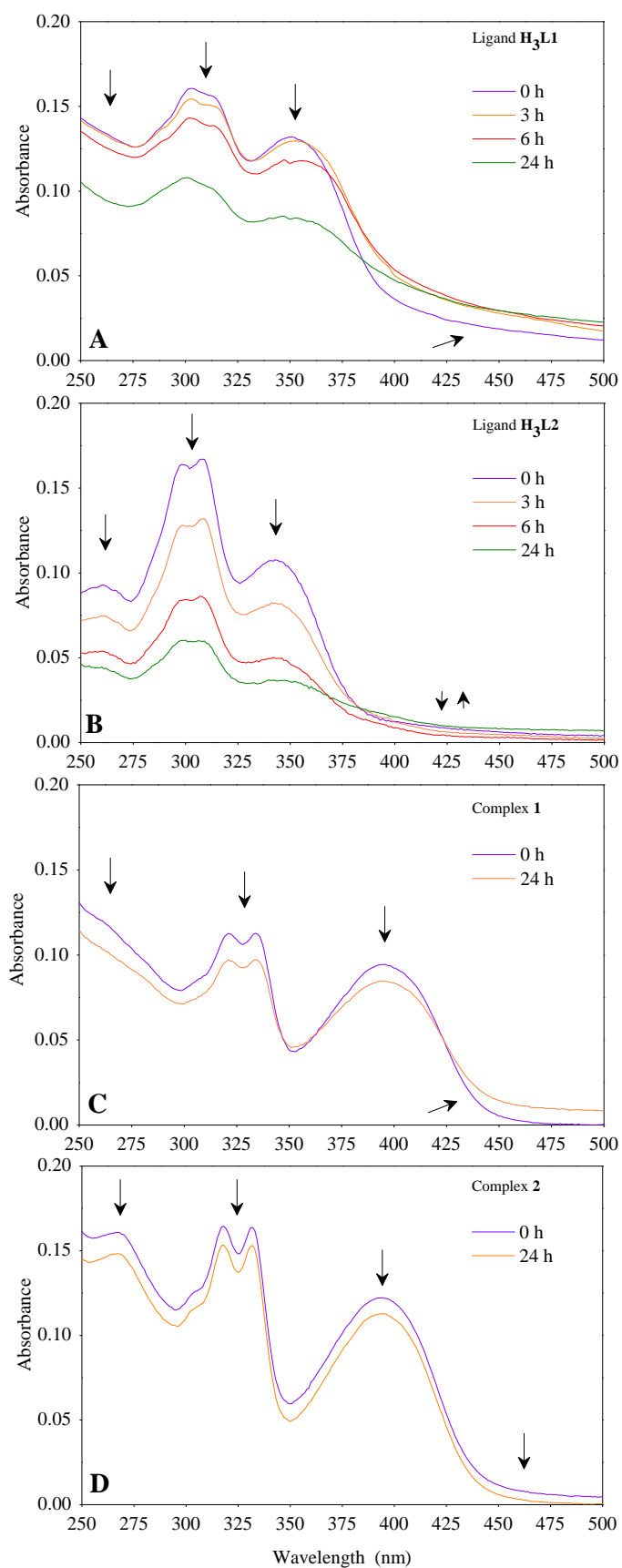


Figure 4.16. Absorption spectra over time (24 h) for the ligands **H₃L1** (A) and **H₃L2** (B), and complexes **1** (C) and **2** (D) in 10% DMSO-90% PBS (pH 7.4) at r.t. [] = 1×10^{-5} M.

Over 24 h, both complexes' solutions in 10% DMSO contain 85% (**1**) and 91% (**2**) of their initial absorption (Figure 4.17) and, in this sense, are quite resistant to dissociation. Since the hydrolysis of hydrazones begins with protonation of the azomethine nitrogen, coordination through this donor-atom should prevent that reaction. When dissolved in a 10% DMSO-90% PBS buffer (pH 7.4) medium, the stabilities of complexes **1** and **2** remain relatively unchanged (Figures 4.16-C and D).

4.2.3.2

Stability of complexes

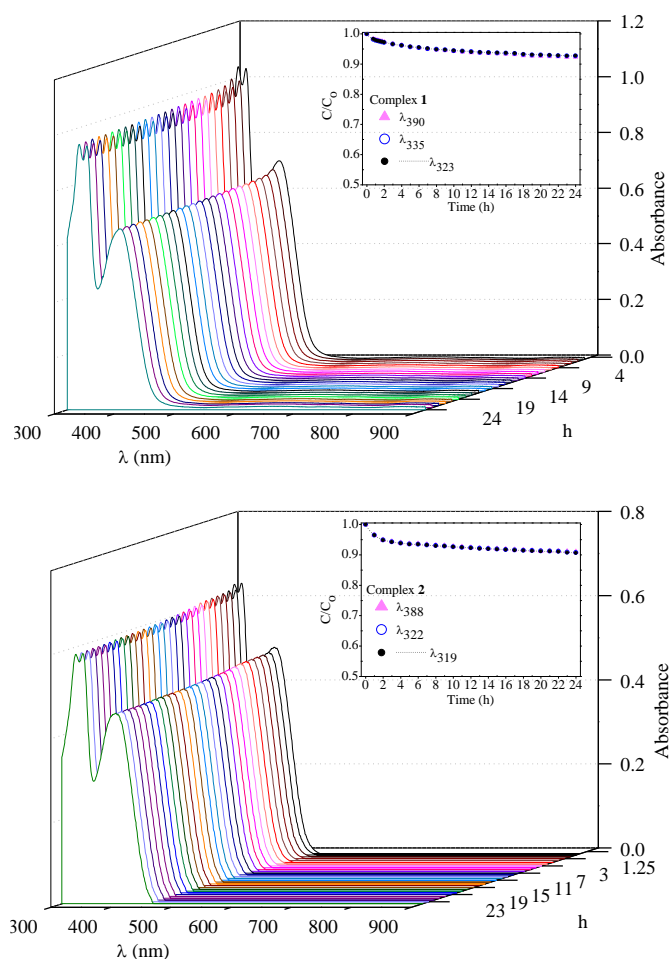


Figure 4.17. Absorption spectra of **1** (top) and **2** (bottom), along 24 h, in 10% DMSO at r.t. $[C] = 5 \times 10^{-5}$ M. pH 6.0. *Inset:* C/C_0 versus time at different wavelengths.

The structural integrity of the complexes in aqueous solution, up to 24 h at room temperature (23 ± 2 °C), was confirmed by ESI-MS analyses (Figure 4.18). DMSO/water (1:9) stock solutions aliquots were analysed immediately and after 24 h, by direct infusion, after previous dilution in methanol (5:95). The mass spectra of both complexes are similar, with three main peaks at (m/z^+) 611, 625 and 671 for **1** and 627, 641 and 687 for **2**, which were assigned, respectively, to the species $[\text{Cu}_2(\text{HL})(\text{OH})]^+$, $[\text{Cu}_2(\text{HL})(\text{CH}_3\text{O})]^+$ and $[\text{Cu}_2(\text{L})(\text{DMSO})]^+$, the latter without any exogenous bridging group between the copper(II) ions. In the specific case of complex **1**, additional peaks at (m/z^+) 663 and 741 were also observed in the spectrum after 24 h of aging, and attributed to the species $[\text{Cu}_2(\text{HL})(\text{OH})(\text{OH}_2)_2]^+$ and $[\text{Cu}_2(\text{HL})(\text{OH})(\text{OH}_2)_2(\text{DMSO})]^+$. All the discussed assignments were supported by comparisons between experimental and simulated isotopic patterns (Figure 4.19). No evidence for dissociation or hydrolysis of the coordinated ligands was found. In this sense, and considering that the species $[\text{Cu}_2(\text{HL})(\text{CH}_3\text{O})]^+$ constitutes an “artifact” due to the presence of methanol used in the dilutions for ESI-MS measurements, can be conclude that, under the experimental conditions employed in the biological assays described below, the main metal-containing species present should be the dinuclear cations themselves characterized by XRD, $[\text{Cu}_2(\text{HL})(\text{OH})]^+$, and the DMSO-substituted derivative $[\text{Cu}_2(\text{L})(\text{DMSO})]^+$, in which the μ -hydroxo bridge is replaced by a terminal solvent molecule.

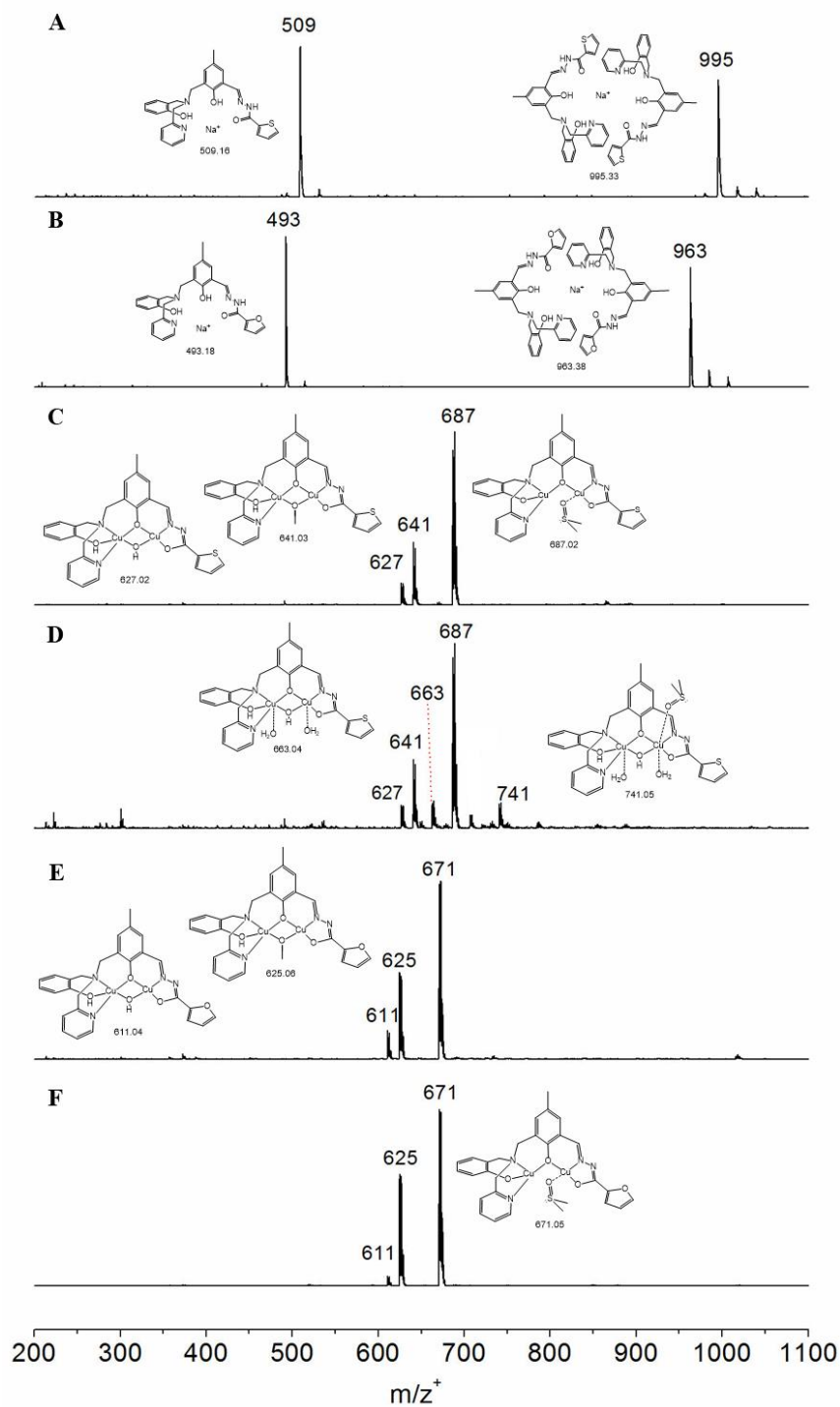


Figure 4.18. ESI-MS(+) spectra measured from fresh DMSO/MeOH solutions of **H₃L1** (A) and **H₃L2** (B). (C) complex **1** in fresh DMSO/H₂O solution. (D) **1** in DMSO/H₂O solution after 24 h at 23 ± 2 °C. (E) complex **2** in fresh DMSO/H₂O solution. (F) **2** in DMSO/H₂O solution after 24 h at 23 ± 2 °C. Capillary output voltage set at 50 V. All compounds were diluted in methanol (5:95) before injection.

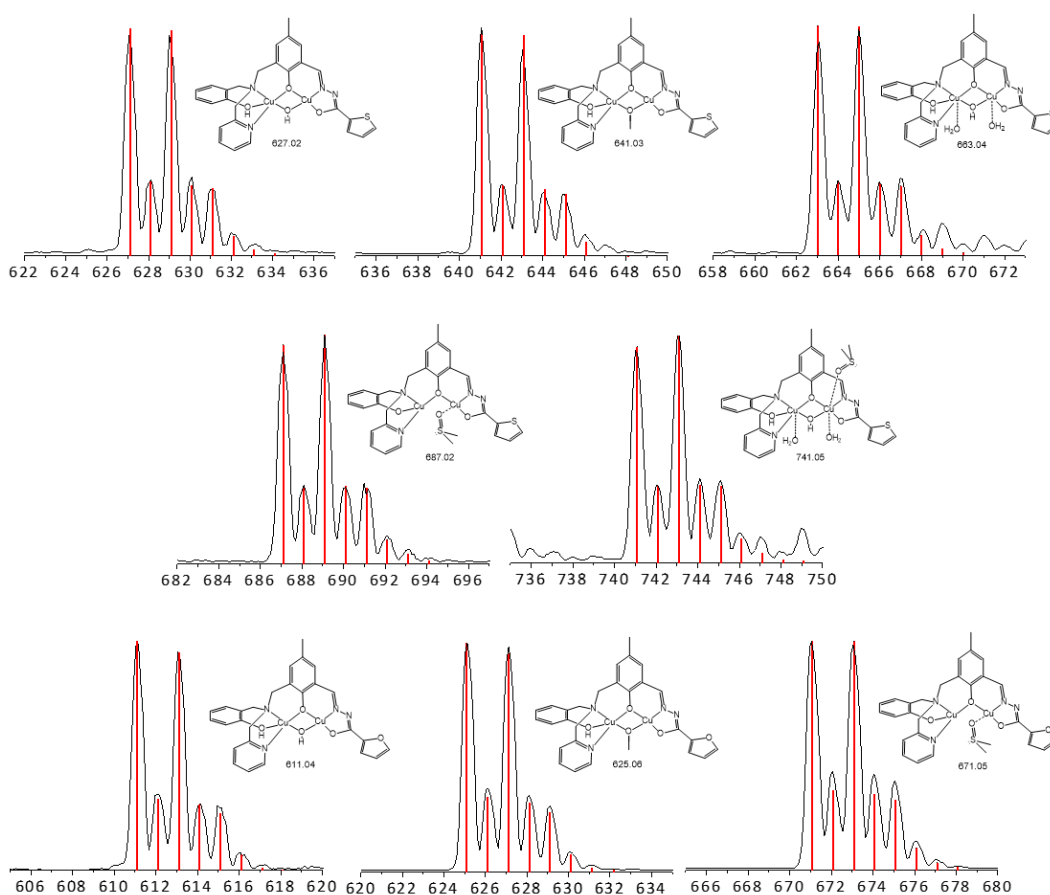


Figure 4.19. Isotopic pattern obtained experimentally (black curve) and simulated by the Isotope Distribution Calculator and Mass Spec Plotter tool (red vertical lines) for **1** and **2**.

4.2.4

Evaluation of BSA binding through absorption and fluorescence spectroscopies

Due to the importance of serum albumin in the transportation of drugs in vertebrates, this class of proteins have been extensively studied, as well as their interaction with potential pharmacological agents, including organic ligands and coordination complexes. The bovine variant BSA presents chemical properties similar to those of human serum albumin [143], HSA, with only a few differences [144]. Thus, BSA has been largely used as a model in order to study the interactions with many compounds, including copper complexes [16, 145-148]. These complexes are well-known for their BSA binding propensity, showing strong affinity for the protein [149-152]. In recent studies, authors evaluated the interactions of both HSA and BSA with copper(II) complexes. The values found

for the binding constants, as well as for the number of binding sites, are in agreement [153-156], although exceptions, as the work of Manna [157], were identified.

Absorption spectroscopy is a common and useful technique to study structural changes of albumin proteins [13, 158]. In the presence of the complexes **1** and **2**, the absorption band at 205 nm, related to the peptide bonds of the protein [159], is red-shifted and an intense absorption decrease is observed (Figure 4.20-A). This hypochromic effect is probably due to the induced perturbation of BSA α -helices by the complexes, while the shift towards longer wavelengths is produced by changes in the polarity of their surroundings [160]. BSA presents similar spectral changes in the presence of free ligands (Figure 4.20-B). The band at 280 nm, on the other hand, is associated with the aromatic amino acids in the protein [159]. Although upon addition of the copper(II) complexes its intensity seems to remain unchanged (Figure 4.20-B, Inset), this absorbance increases slightly in the presence of the ligands, indicating that interaction of **H₃L1** and **H₃L2** with BSA modifies the microenvironments of the residues of its aromatic amino acids [160].

On the other hand, fluorescence spectroscopy has been widely used as an efficient technique for the analysis of BSA conformational changes and binding with different compounds [13]. Figures 4.20-C and D present the effect of copper(II) complexes in the fluorescence emission of BSA. Following the addition of **1** or **2** to a BSA solution, the protein fluorescence intensity at 353 nm gradually decreases when the concentration of the complexes increases, suggesting that the quenching mechanism could be primarily of the static type, i.e., through the generation of a protein-complex adduct in the ground state (before excitation).

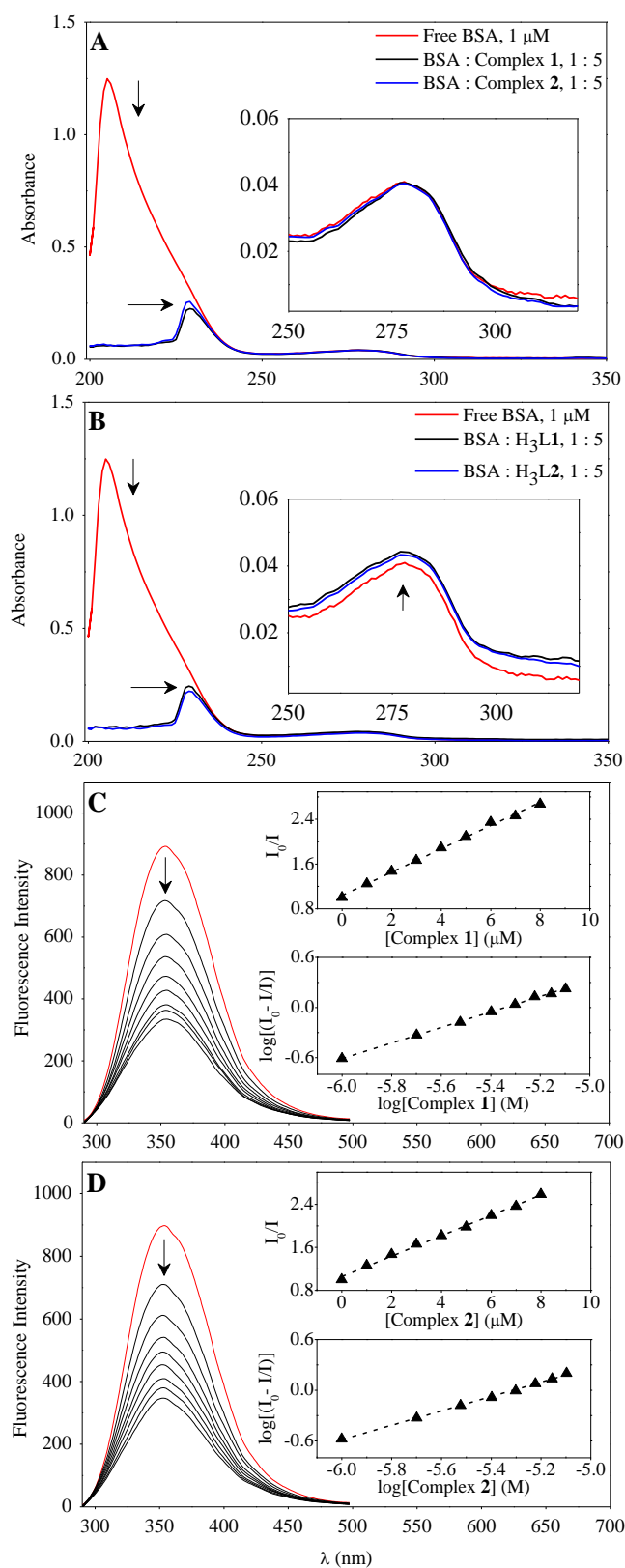


Figure 4.20. Absorption spectra of BSA (1 μM) in a buffer solution (10 mM Tris-HCl and 10 mM NaCl, pH 7.40) in the absence and presence of complexes (A) and ligands (B) at a 5 μM . *Insets:* Detail of the 250–320 nm region. Fluorescence spectra, at 25 $^\circ\text{C}$, of BSA (1 μM ; $\lambda_{\text{ex}} = 280 \text{ nm}$; $\lambda_{\text{em}} = 353 \text{ nm}$) in the absence (red curve) and presence (black curves) of increasing concentrations (1–8 μM) of **1** (C) and **2** (D). *Insets:* The corresponding Stern-Volmer and Scatchard plots.

Due to the significant absorbance of the complex-BSA solutions at the emission wavelength, the fluorescence measurement was treated to correct the “inner filter” effect (Equation 4.1) [161]. This equation is limited to solutions with absorbance lower than 0.3.

$$F_{corr} = F_{obs} \cdot \text{antilog} [(A_{ex} + A_{em})/2] \quad (\text{Eq 4.1})$$

Where F_{corr} and F_{obs} are, respectively, the corrected and measured fluorescence intensities. A_{ex} corresponds to the absorption value at the excitation wavelength used to acquire the fluorescence spectra and A_{em} , to the absorption value at the emission wavelength in a 1.0 cm pathlength cuvette. The suppression-equation (Equation 4.2, also know as Stern-Volmer equation) [132] was used to infer in a more accurate way the main quenching mechanism and to determine the respective constants:

$$I_0/I = 1 + K_S [Q] = 1 + K_q \tau_0 [Q] \quad (\text{Eq 4.2})$$

Where I_0 and I are, correspondingly, the steady-state fluorescence intensities in the absence and presence of the quencher. $[Q]$ is the quencher concentration, K_q is the biomolecular quenching rate constant, and τ_0 is the average intrinsic lifetime of protein in the absence of quencher, equal to 10^{-8} s [162]. The suppression-constant (also known as Stern-Volmer equation) for the adduct formation, K_S , can be determined directly from the slope of the straight line obtained when I_0/I versus $[Q]$ is plotted. K_S and K_q constants for complexes **1** and **2** can be found in Table 4.9.

Table 4.9. Quenching and binding parameters for the interaction of the complexes **1** and **2** with BSA, at 25 °C.

| Compound | K_S ($\times 10^5 \text{ M}^{-1}$) | K_q ($\times 10^{13} \text{ M}^{-1} \text{ s}^{-1}$) | K_b ($\times 10^4 \text{ M}^{-1}$) | n |
|----------|--|--|--|------|
| 1 | 2.1 ± 0.04 | 2.08 | 9.23 | 0.93 |
| 2 | 1.9 ± 0.04 | 1.90 | 3.29 | 0.85 |

The maximum value of the K_q parameter for a mechanism to be considered of a pure dynamic quenching type is $2.0 \times 10^{10} \text{ M}^{-1} \text{ s}^{-1}$. Complexes **1** and **2** presented K_q values about 3 order of magnitude higher than that expected for a

diffusion-controlled fluorescence quenching [160], indicating that the systems under study are dominated by a static quenching mechanism, caused by the interaction between BSA and the complexes.

To determine the binding constants, K_b , and the number of complexes bound to each BSA unit, n , the Scatchard equation was employed (Equation 4.3) [163].

$$\log [(I_0 - I)/I] = \log K_b + n \log [Q] \quad (\text{Eq 4.3})$$

In the linear fit plot of Equation 4.3, the intercept (inset of Figure 4.20) corresponds to $\log K_b$ and the slope, to n .

The calculated protein binding constants (Table 4.9) are $9.23 \times 10^4 \text{ M}^{-1}$ and $3.29 \times 10^4 \text{ M}^{-1}$ for complexes **1** and **2**, respectively. Therefore, the affinity of **1** for BSA is 2.8 times higher than that of **2**. The K_b values found are perfectly comparable to those obtained for the interaction of BSA with previously reported copper(II) complexes [145]. The calculated n parameter indicates a single binding site in BSA for the complexes.

4.2.5

Influence of the compounds in BSA conformation by scattering techniques

Scattering techniques have recently been used as an alternative tool to other spectroscopic methods for characterizing the structures formed due to the interaction between different compounds and BSA [99, 164-168]. Figure 4.21 presents the size distributions of BSA before and after the addition of different concentrations of **1** and **2**. The corresponding auto-correlation functions are presented in the Figure 4.22. Native BSA has only one population with hydrodynamic diameter of $8.6 \pm 0.1 \text{ nm}$. Both ligands and complexes are too small to be detected by DLS and do not exhibit significant scattering intensity.

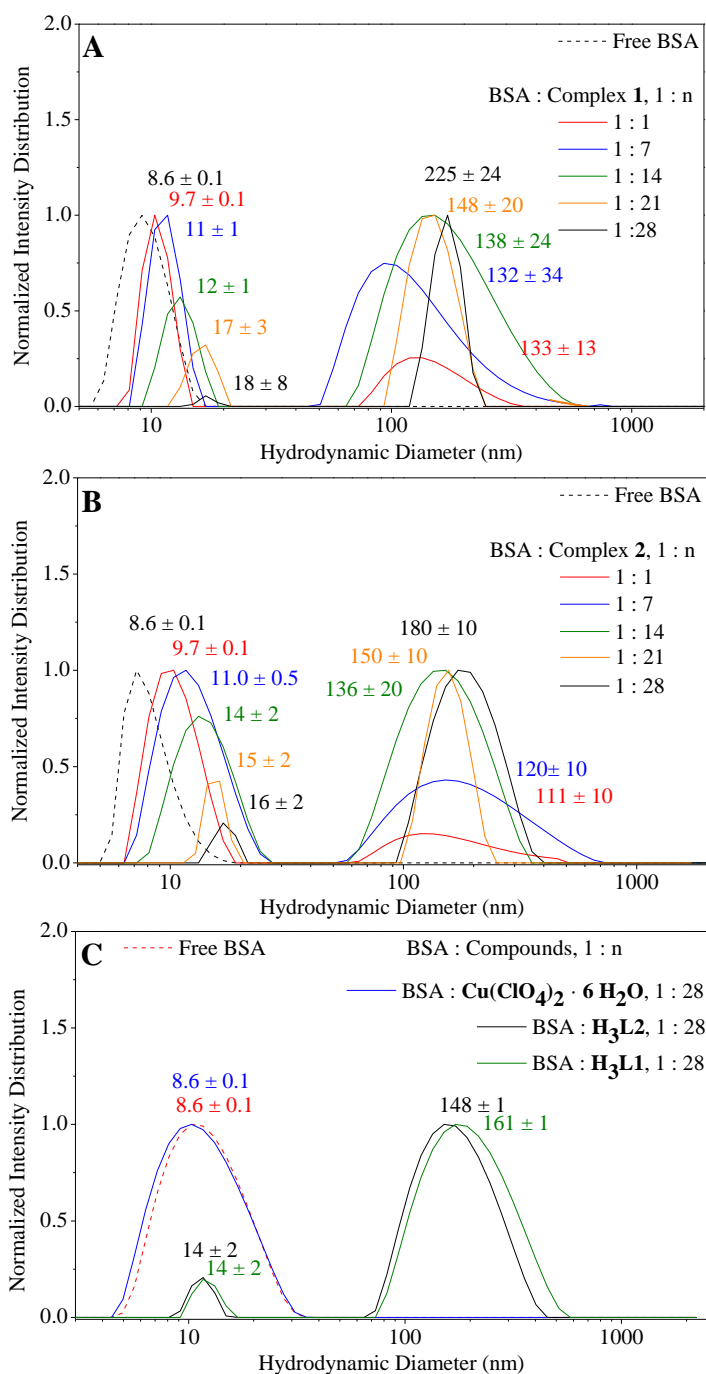


Figure 4.21. Hydrodynamic diameter (nm) distribution, at 25 °C, of BSA samples (5×10^{-5} M) in the absence and presence of complexes **1** (A) and **2** (B) at BSA : complex molar ratios of 1 : 1, 1 : 7, 1 : 14, 1 : 21 and 1 : 28. (C) BSA in the absence and presence of $\text{Cu}(\text{ClO}_4)_2 \cdot 6 \text{H}_2\text{O}$ and free ligands H_3L_1 and H_3L_2 at a BSA : compound molar ratio equal to 1 : 28. Scattering angle: 90 °. Samples (2 mL, in 100 mM NaCl and 50 mM Tris buffer at pH 7.40) were filtered (0.25 μm) before performing the scattering measurements.

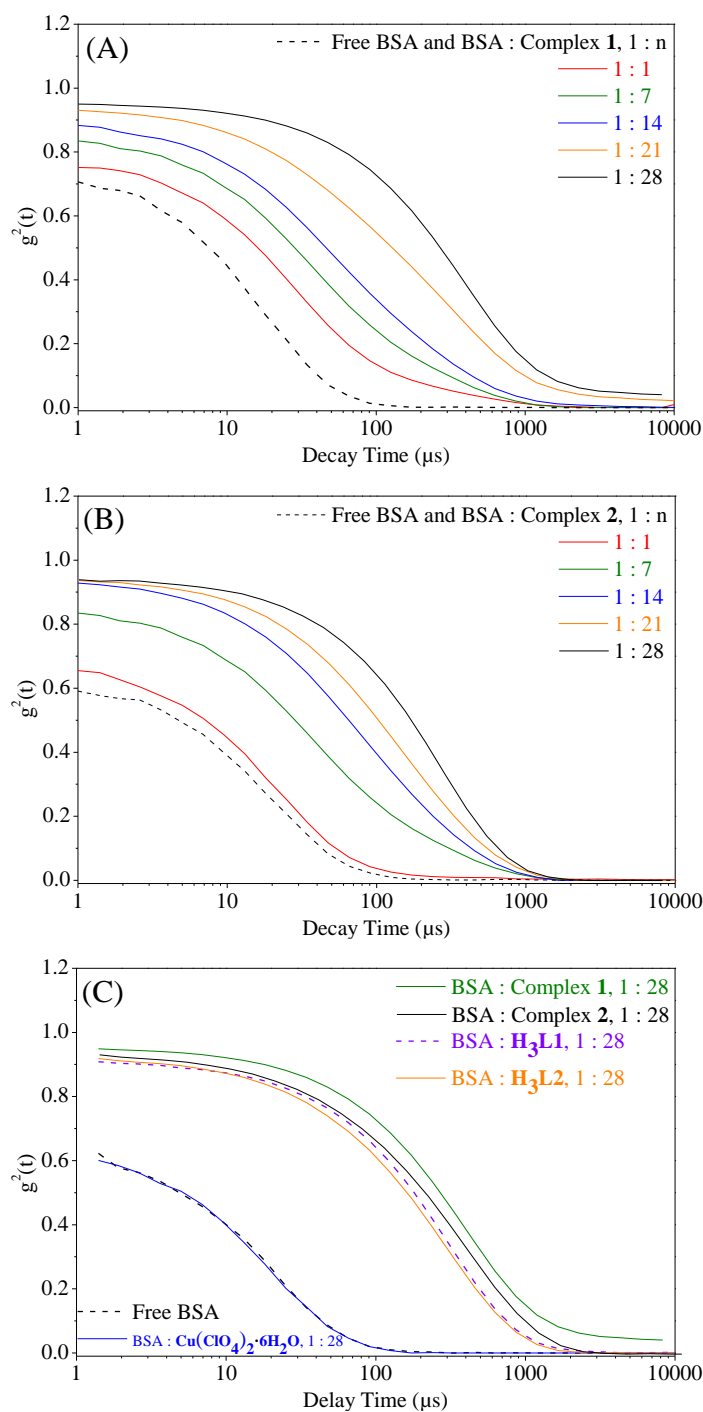


Figure 4.22. Auto-correlation functions of BSA samples (5×10^{-5} M) in the presence of **1** (A) and **2** (B) at different molar ratios and ligands and $\text{Cu}(\text{ClO}_4)_2 \cdot 6 \text{H}_2\text{O}$ at 28 molar ratio. Scattering angle: 90° . 25°C .

Upon addition of **1**, the diameter gradually increases up to 18 nm and a new population of larger particles (from 133 to 225 nm) is observed, which are probably related to the formation of aggregates. Non-filtered compound-BSA samples, i.e., preserving the whole spectrum of particles' sizes, were also analyzed and indicate

that the addition of **1** to BSA solutions leads to the formation of another population of aggregates larger than 1 μm (which are not adequate to be precisely characterized by DLS, since they present a high scattering intensity making the samples more turbid). Similar trends were observed for **2** and ligands **H₃L1** and **H₃L2**, as also shown in Figure 4.21-B and Figure 4.22. However, ligands caused a minor change in the hydrodynamic size of BSA when compared with their respective complexes under the same conditions (BSA : compound molar ratio of 1 : 28). The obtained results indicate that interaction of the ligands and specially the complexes with BSA cause its aggregation. Although the increment in size of the first population is not significant to evidence the occurrence of conformational changes in the secondary structure of BSA, the obtained values agree with the results from the literature. By DLS measurements, Adel and co-workers [169] reported a hydrodynamic radius for BSA of 3.8 ± 0.2 nm, whereas Yu and collaborators [168] obtained a 7.13 nm hydrodynamic diameter for this protein. In the same direction, Zocchi reported a value of 8 nm for the native BSA hydrodynamic diameter, using micro-mechanical measurements [170]. Also in accordance with our data, Li and colleagues [167] observed that the addition of an organic compound (pterodonic acid) leads to an increase of the hydrodynamic diameter of BSA from 7.3 to 22.8 nm and to the arising of a second population of larger particles.

Along time, the frequency of the first BSA population (non-aggregated) increases, while the frequency of the population corresponding to aggregated BSA decreases. This observation indicates that aggregation is reversible and could be related to a trend of release of the copper complexes with time and the return of the protein to its native form. A comparison between the frequencies of BSA populations in the presence of **1** and **2** after an incubation period of 24 h shows that the protein disaggregates faster for complex **2** than for complex **1**. This behaviour could be expected based on the value for the binding constant obtained by fluorescence spectroscopy, which is lower for complex **2** than for complex **1**.

To better evaluate the conformational changes of BSA, SAXS can complement DLS because X-rays have a shorter wavelength than the visible light and are more adequate to evaluate smaller dimensions. Figure 4.23 presents the experimental curves of scattering intensity, I , as a function of the scattering vector, q , obtained for samples containing BSA and different concentrations of **1** and **2**.

Samples containing only the complexes do not present significant scattering intensity.

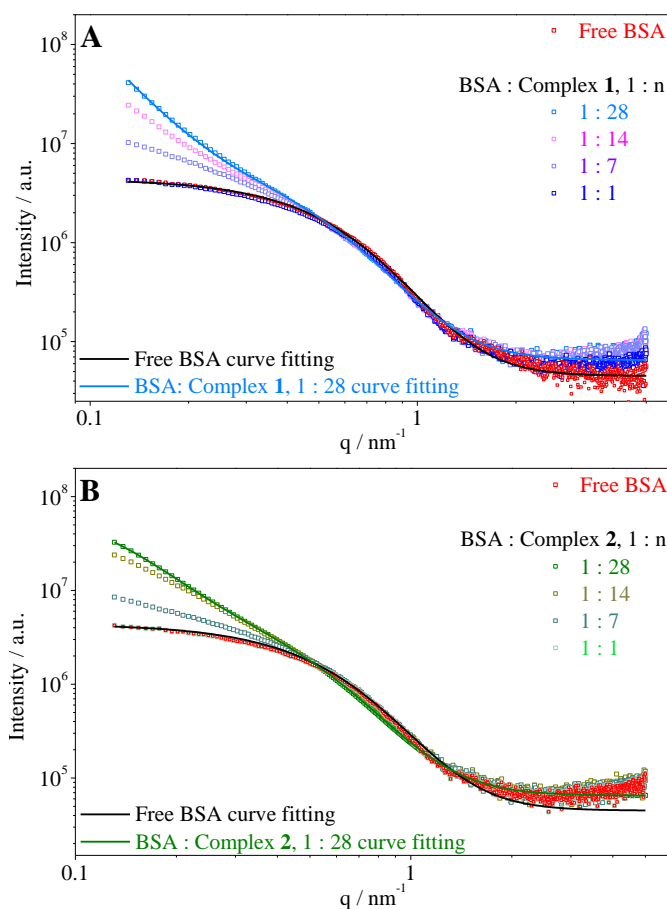


Figure 4.23. SAXS curves, at 25 °C, of free BSA (5×10^{-5} M, in 100 mM NaCl and 50 mM Tris buffer at pH 7.40) in the absence and presence of complexes **1** (A) and **2** (B) at BSA : complex molar ratios of 1 : 1, 1 : 7, 1 : 14, 1 : 21 and 1 : 28. All samples were filtered (0.45 μm) before performing the scattering measurements. The curve fittings, using a Generalized Gaussian Coil model, for free BSA and BSA : complexes at 1 : 28 are included.

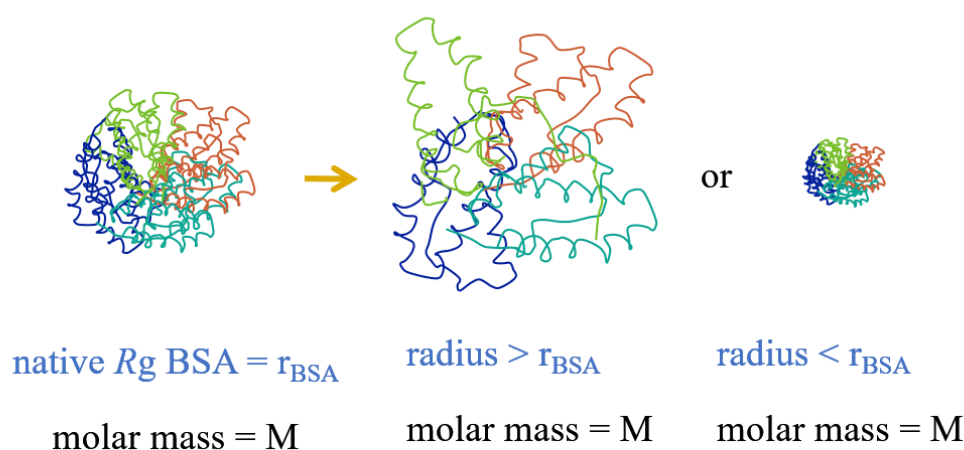
The fitted curve corresponding to the solution of free BSA provided a gyration radius, R_g , of 3.5 nm. Upon addition of complexes, the intensity is increased in the low q -region but is not affected in the high q -region. This indicates that the form factor of BSA is not significantly affected by the presence of the complexes, although there is an aggregation generating larger particles. The samples with higher concentration of complexes were also fitted considering the existence of two populations.

The best fitting resulted in R_g values of 3.8 and 68 nm, for **1**, and 3.9 and 52 nm for **2**, respectively. However, the size of the second population is too large for

the available q -region, and one can only affirm that there are aggregates with $R_g \geq 68$ nm (**1**-BSA system) and ≥ 52 nm (**2**-BSA system). The dimensions of the protein after addition of the complexes are only slightly bigger (3.8 and 3.9 nm for **1** and **2**, respectively) than those of free BSA. Once more, the results indicate that there is no significant change in size, which could evidence conformational changes on the secondary structure (Figure 4.24). Yet, the interaction between the complexes and BSA also induces a process of aggregation, confirming the results obtained by DLS.

For the sake of comparison, the copper salt $\text{Cu}(\text{ClO}_4)_2 \cdot 6\text{H}_2\text{O}$ itself does not induce protein aggregation (Figure 4.25).

(A) Changes in the secondary structure of BSA versus R_g



(B) Aggregation process of BSA with no changes of R_g

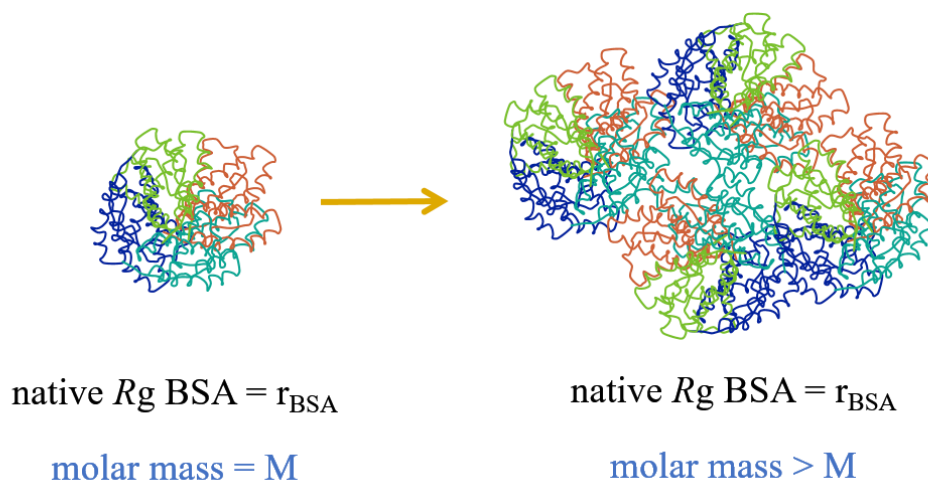


Figure 4.24. Gyration radii of BSA protein with changes in its secondary structure and during the aggregation process.

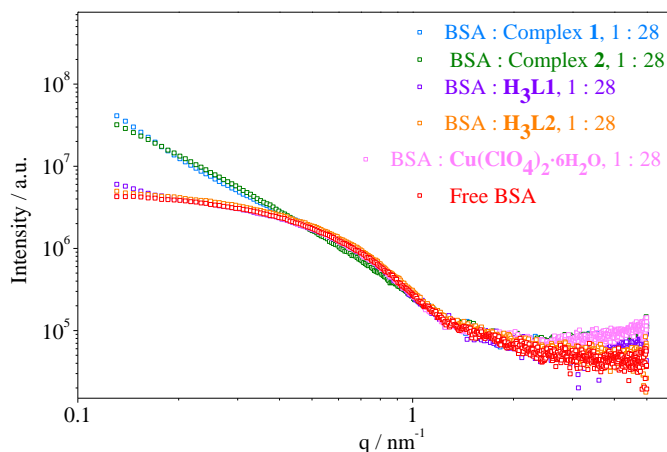


Figure 4.25. SAXS curves of aqueous solutions containing pure BSA (5×10^{-5} M) and BSA in the presence of 28-fold excess **1**, **2**, **H₃L1**, **H₃L2**, and **Cu(ClO₄)₂·6H₂O**. 25 °C.

4.2.6

Determination of the binding constants towards ctDNA

To evaluate the properties of the new compounds as potential anticancer drugs, the study of their interaction with DNA constitutes a significant step in order to better understand the possible mechanism of action involved [127]. Copper(II) complexes have demonstrated a great ability to bind to and cleave DNA [29, 42, 153]. In the present study, absorption spectroscopy was used to investigate the interactions of the synthesized compounds with ctDNA through titration experiments. Upon addition of increasing amounts ctDNA to solutions containing **1** and **2**, a clear hypochromic effect is observed in the complexes absorption bands, which suggests an interaction with the biopolymer (Figure 4.26-A and B). Hypochromism is commonly associated with intercalative binding [165]. The free ligands **H₃L1** and **H₃L2** present a similar behaviour in the presence of ctDNA (Figure 4.26-C and D).

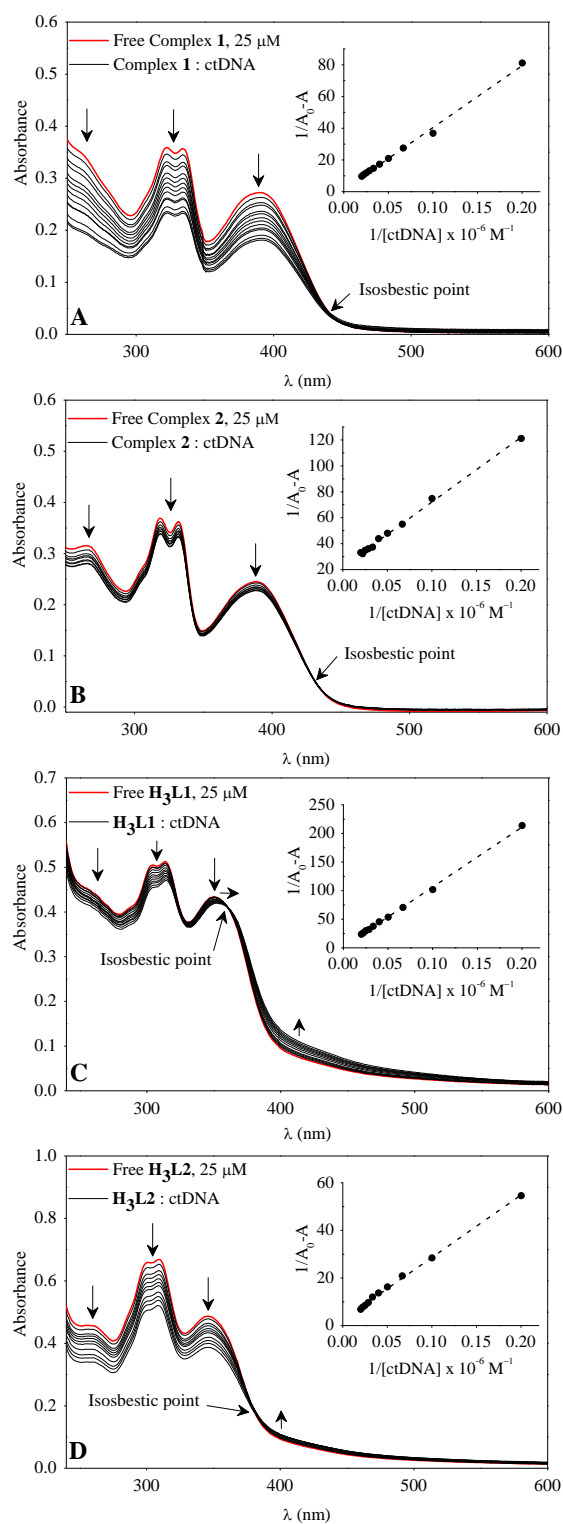


Figure 4.26. Absorption spectra and $1/(A_0 - A)$ versus $1/[\text{DNA}]$ plot (*Insets*) of the copper(II) complexes **1** (A) and **2** (B) and the ligands $\text{H}_3\text{L1}$ (C) and $\text{H}_3\text{L2}$ (D) (25 μM , 3 mL, in 10% DMSO and 90% 50 mM Tris-HCl, pH 7.40) in the absence (red curve) and with increasing concentrations (black curves) of ctDNA (5–50 μM) at 25 $^\circ\text{C}$. Spectra were registered after an incubation time of 3 min from each ctDNA addition.

The binding constants were determined by monitoring the absorption bands centred at 322 and 317 nm for complexes **1** and **2**, respectively, as well as those at 314 and 309 nm for the ligands **H₃L1** and **H₃L2**, correspondingly. Treatment of the experimental data was performed by using a modified form of the Benesi-Hildebrand equation (Equation 4.4) [171, 172]:

$$\frac{1}{A_0 - A} = \frac{1}{(\varepsilon_b - \varepsilon_f)} \cdot \frac{1}{[\text{compound}]_0} + \frac{1}{K_b(\varepsilon_b - \varepsilon_f)} \cdot \frac{1}{[\text{compound}]_0} \cdot \frac{1}{[\text{DNA}]} \quad (\text{Eq 4.4})$$

Where A_0 and A are the absorption values for the compounds in the absence and presence of DNA, respectively; ε_b and ε_f correspond to the molar absorptivities of the fully-bound to DNA and of the free compound, correspondingly; $[\text{compound}]_0$ is the initial concentration of the compound; $[\text{DNA}]$ is the concentration of added DNA and K_b is the binding constant. A plot of $1/(A_0 - A)$ versus $1/[\text{DNA}]$ gives the intercept equal to $1/(\varepsilon_b - \varepsilon_f) \times 1/[\text{compound}]_0$ and slope equivalent to $1/K_b(\varepsilon_b - \varepsilon_f) \times 1/[\text{compound}]_0$. Thus, K_b is determined by the ratio of intercept to slope (Figure 4.26-A, B, C and D, insets). The calculated binding constants for complexes **1** and **2** are $(3.50 \pm 0.08) \times 10^3 \text{ M}^{-1}$ and $(4.38 \pm 0.08) \times 10^4 \text{ M}^{-1}$, respectively. These values are comparable with those obtained for other reported copper(II) complexes[165]. However, they are lower than the values usually found for representative DNA intercalators, such as ethidium bromide (which is around 10^5 - 10^6 M^{-1}) [173]. This outcome could indicate that intercalation between the base pairs is not the main mode of interaction of the synthesized dicopper(II) complexes with DNA. On the other hand, a binding constant of $(1.64 \pm 0.08) \times 10^3 \text{ M}^{-1}$ was calculated for **H₃L1**, and one of $(7.91 \pm 0.08) \times 10^3 \text{ M}^{-1}$ for **H₃L2**.

According to the binding results, complex **2** presents higher affinity than complex **1** towards ctDNA, a trend also observed with **H₃L2** in comparison to **H₃L1**. The free ligands showed a minor intercalator ability than their respective dinuclear complexes, which is in agreement with results previously reported for other aroylhydrazones and their copper(II) complexes [7]. The lower intercalative affinity of **1** could be related to its higher reactivity towards DMSO, as shown by ESI-MS(+) measurements, since the DMSO-substituted species should present an impaired planarity regarding the intercalative moiety constituted by the central

phenol ring and the aroylhydrazone-derived pendant arm. As mentioned above, experimental data indicate that coordination to copper(II) increases the binding affinity for DNA.

4.2.7

Influence of the compounds in pBR322 plasmid DNA conformation

In many previous reports, both mononuclear and dinuclear copper(II) complexes have shown cleavage activity on plasmid DNA [4, 174-177]. The effects of cleavage agents over plasmids, leading to their transition from supercoiled (Form I) to circular (Form II) and to linear (Form III) conformations of DNA, have been largely studied by gel and capillary electrophoresis. Recently, however, scattering techniques had their importance increased in this context [178].

In this work, DLS measurements were also used to evaluate the influence of the synthesized compounds in pBR322 plasmid DNA conformation. To carry out these studies, it was not possible to use SAXS because the samples do not present significant X-ray scattering in this range of concentrations. Solutions of pure native plasmid DNA were not detected by DLS either, probably due to the absence of sufficient contrast.

Figure 4.27 presents the size distributions of DNA macromolecules in aqueous solutions with different concentrations of complexes **1** (A) and **2** (B). Figure 4.28 presents the corresponding auto-correlation functions. When the complexes are added to the pBR322 DNA solutions, a population is observed with mean hydrodynamic radius of 58 ± 4 nm and 73 ± 6 nm, for **1** (10 μ M) and **2** (15 μ M), respectively. This population was attributed to the plasmid Form I. In previous static light scattering studies, the gyration radius (R_g) of different plasmid DNAs have been measured [179]. From these results, the expected radius of pBR322 plasmids, used in the present work, can be estimated by extrapolation (Figure 4.29) as 89 nm for Form I, 124 nm for Form II and 171 nm for Form III.

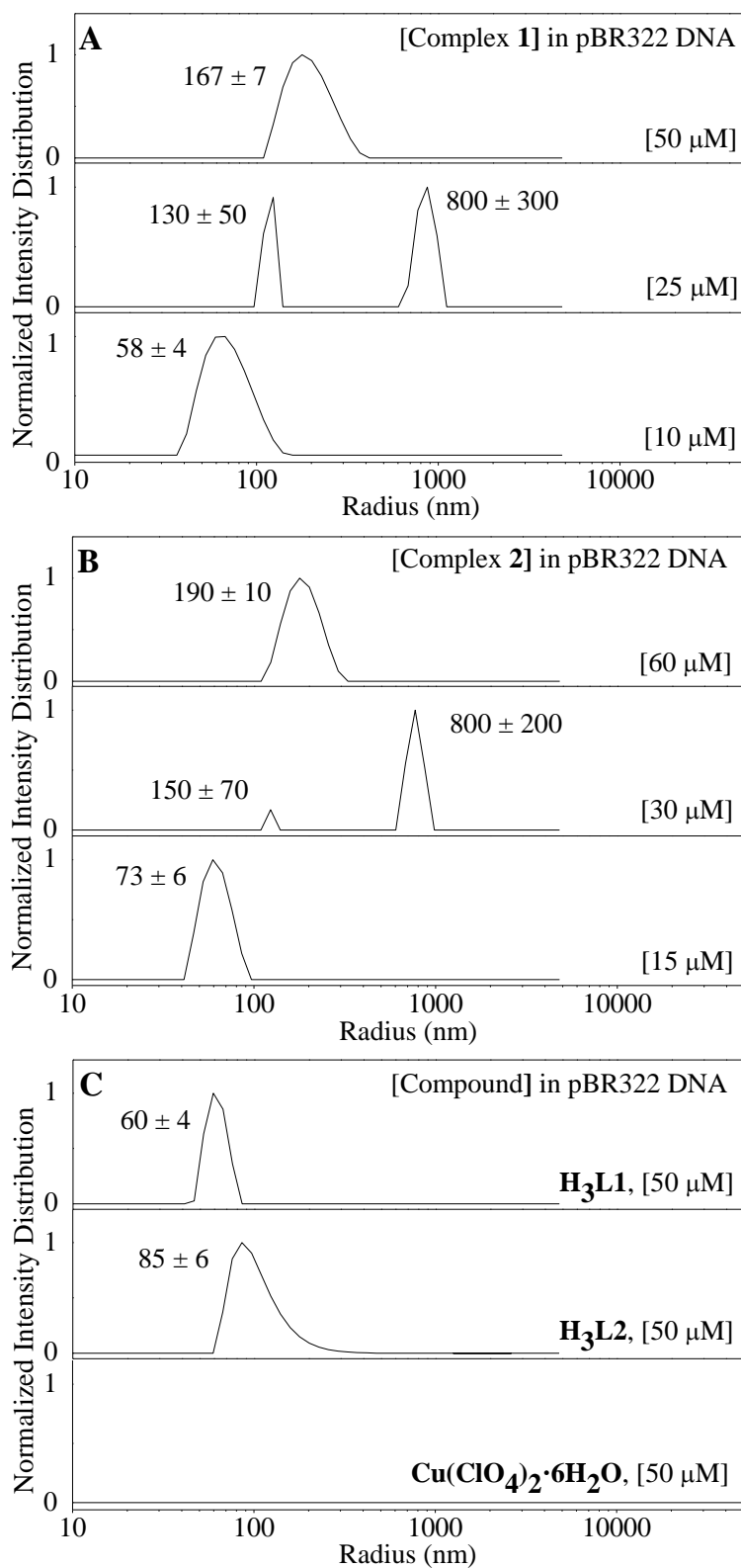


Figure 4.27. Hydrodynamic radius (nm) distribution of pBR322 plasmid DNA samples ($2.5 \mu\text{g mL}^{-1}$, 2 mL, in 10 mM Tris buffer, pH 7.40) in presence of (A) complex 1 (10–50 μM) and (B) complex 2 (15–60 μM). (C) pBR322 plasmid DNA in the presence of $\text{H}_3\text{L1}$, $\text{H}_3\text{L2}$ and the starting salt copper(II) perchlorate hexahydrate, all of them at a concentration of 50 μM . Scattering angle: 90° . Incubation: 15 min at $25.0 \pm 0.1^\circ\text{C}$.

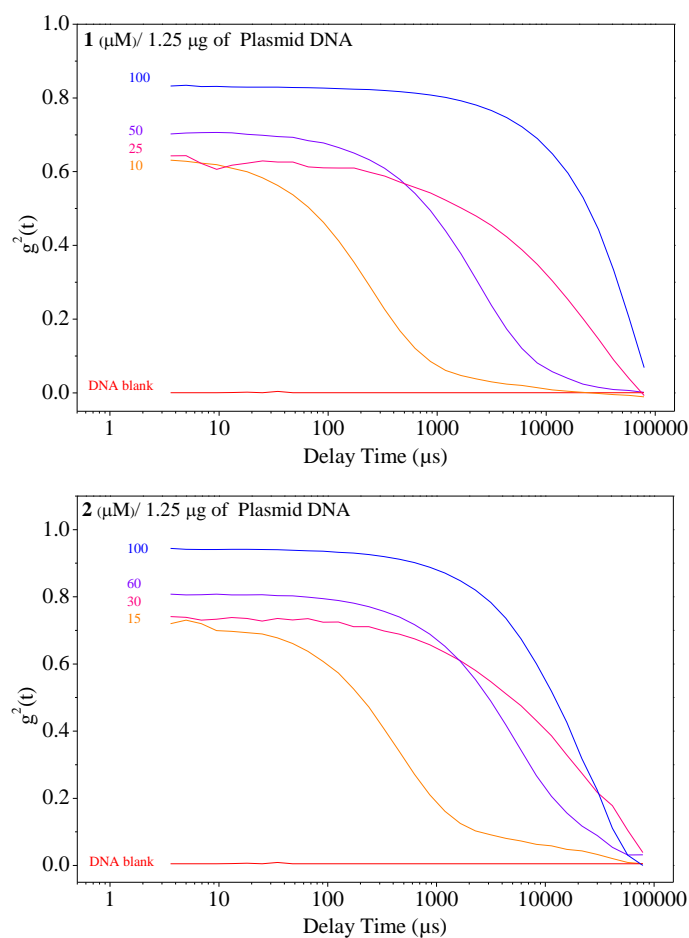


Figure 4.28. Auto-correlation functions of samples of DNA (1.25 μg in 0.5 mL) in the presence of **1** and **2** at different molar ratios. Scattering angle: 90° at 25°C .

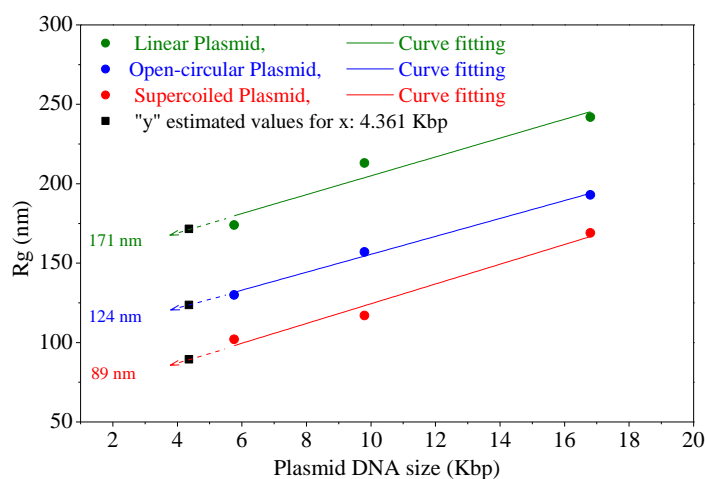


Figure 4.29. Estimation of the different plasmid pBR322 forms radii by extrapolation, based in the summary reported [179] by Latulippe and Zydney of R_g values from static light scattering analysis of supercoiled, open-circular, and linear isoforms of 5.76, 9.80, and 16.8 kbp plasmids in 10 mM Na_2EDTA , 200 mM NaCl solution.

Analysing the observed radii values, it is possible to infer that, at low concentrations of the tested complexes (up to 10 μM for **1** and 15 μM for **2**), the interaction is not strong enough to alter dramatically the conformational structure of pBR322 plasmids. Nevertheless, and taking into account that the free plasmid had not been detected due to the low contrast of its solution, it is deduced that the complexes interact with plasmids causing a significant increase in their contrast, which allowed to obtain the auto-correlation functions. The observed differences between the hydrodynamic radius of plasmid Form I in the presence of the complexes and the free plasmid gyration radius estimated by extrapolation is possibly due to an electrostatic interaction between the positively charged dicopper(II) complexes and the negatively charged phosphate groups of pBR322, which can be responsible for DNA compaction [180] in the solutions containing **1** and **2**. Further addition of **1** (25 μM) or **2** (30 μM) caused a significant increase on the plasmid hydrodynamic radius to 130 ± 50 and 150 ± 70 nm, respectively. The obtained values are similar to the estimated for the circular plasmid Form II (~ 125 nm). However, the generation of a second population of larger scattering particles (800 ± 300 and 800 ± 200 nm) is observed as well. These particles could be related to the formation of plasmid aggregates, making difficult to guarantee the biopolymer form at this point. When plasmid pBR322 is in presence of higher concentrations of complexes **1** (50 μM) or **2** (60 μM), only one population is observed in each case, with hydrodynamic radius of 167 ± 7 and 190 ± 10 nm, respectively. A single population indicates that plasmid DNA disaggregates, and the size observed might indicate the occurrence of cleavage to Form III, whose R_g was estimated as ~ 170 nm. On the other hand, the free ligands **H₃L1** and **H₃L2** have not shown this property (Figure 4.27-C). It is noteworthy that the starting copper salt **Cu(ClO₄)₂·6H₂O** was previously reported as being non-active towards the cleavage of plasmid pBR322 DNA [181].

DLS measurements were repeated during 1 day, in order to test the particles' stability in the **1**-DNA and **2**-DNA samples containing, respectively, the complexes at final concentrations of 50 and 60 μM . After 24 h, no significant changes were observed in the hydrodynamic radii of 167 (**1**-DNA) and 190 nm (**2**-DNA), which indicates that the process is, overall, irreversible. The difference between the reversibility of the interactions with BSA and those with DNA is mainly related to the nuclease activity exhibited by the complexes. Although the interactions of **1** and

2 with DNA certainly possess electrostatic and intercalative components, covalent binding involving an oxygen donor-atom from the biopolymer's phosphate diester backbone to one coordinatively unsaturated copper center in the complexes should also be important. This constitutes the first step in the general catalytic mechanism of hydrolysis proposed for artificial bioinspired phosphatases / nucleases displaying bimetallic cores at their active sites. The metal centers in such a class of catalysts usually work cooperatively and, in this sense, dissimilarities in terms of their coordination spheres could increase the complementarity needed in order to potentialize cooperativity between the metal centers.

A smaller amount of complex **1**, when compared to complex **2**, is needed to cause an increase in the hydrodynamic radii of pBR322 plasmid DNA, which is, in fact, the opposite trend observed for their intercalation ability. In general, DLS results indicate that complexes interact more strongly with DNA than their free ligands, as expected based on the binding constants determined by absorption spectroscopy. Additionally, the complexes presented the capacity to cleave DNA, which constitutes an assumed mode of action for potential anticancer agents.

4.2.8

Cytotoxic activity

In order to determine the putative antineoplastic activity of the synthesized compounds, it was evaluated their effect and that of their ligands on cell proliferation, using a panel of different cancer cell lines. By performing tetrazolium salt reduction assays, was observed that all the analyzed compounds effectively decreased cancer cell proliferation, *in vitro*, in a dose-dependent manner (data not shown). Indeed, IC₅₀ values obtained for all the tested cell lines fit into the micromolar range, with even some submicromolar values (Table 4.10). Interestingly, compounds **1** and **2** seemed to be more effective than their respective ligands, affecting cell proliferation at lower doses. Nevertheless, these complexes showed a decreased selectivity against cancer cells after analyzing their effect on non-tumoral cells MDCK.

Table 4.10. Growth inhibition, expressed as $IC_{50} \pm SD$, of several cancer cell lines [HCT116 (colon, human); HT29 (colon, human); MDA-MB-231 (breast, human); and B16F10 (melanoma, mouse)] after incubation for 36 h in the presence of the synthesized compounds. The Selectivity Index (SI) was estimated based on the IC_{50} values obtained for the non-tumoral control Madin-Darby canine kidney (MDCK) cells, also included in the table. Values in bold correspond to those in the submicromolar range.

| Cell line | H ₃ L1 | | 1 | | H ₃ L2 | | 2 | |
|-------------------|---------------------------------|-----|---------------------------------|-----|---------------------------------|------|----------------------|-----|
| | IC_{50} (μ M) | SI | IC_{50} (μ M) | SI | IC_{50} (μ M) | SI | IC_{50} (μ M) | SI |
| HCT116 | 3.0 \pm 0.5 | 2.9 | 0.6 \pm 0.6 | 1.2 | 5.2 \pm 0.1 | 2.8 | 1.4 \pm 0.5 | 1.7 |
| HT29 | 2.1 \pm 0.4 | 4.1 | 0.8 \pm 0.5 | 0.8 | 4.2 \pm 0.4 | 3.5 | 1.9 \pm 0.5 | 1.3 |
| MDA-MB-231 | 1.0 \pm 0.2 | 8.5 | 0.9 \pm 0.3 | 0.7 | 0.7 \pm 0.3 | 22.6 | 1.2 \pm 0.3 | 2.0 |
| B16F10 | 0.9 \pm 0.4 | 9.8 | 0.3 \pm 0.5 | 2.0 | 0.6 \pm 0.7 | 24.9 | 1.2 \pm 0.5 | 2.0 |
| MDCK (control) | 8.6 \pm 0.3 | – | 0.7 \pm 0.4 | – | 14.7 \pm 0.31 | – | 2.5 \pm 0.4 | – |

The highest antiproliferative effects among the compounds tested are undoubtedly seen for **1**, which is also the most reactive complex regarding plasmid DNA cleavage (as shown by the DLS studies). However, complex **1** is not the one with the highest intercalation affinity, as **2** presents a binding constant towards ctDNA 10 times greater than the one determined for **1**.

Interactions of complexes **1** and **2** with double-stranded DNA seem to involve electrostatic (since complexes are both cationic), intercalative and coordinative components. Therefore, in such a multifaceted panorama, to point out the most significant factor for an improved antiproliferative activity is not straightforward. On the other hand, our results suggest that DNA-damaging capacity is directly related to cytotoxicity, while a higher binding affinity towards ctDNA seems to be associated to an enhanced Selectivity Index.

Concerning the ligands, hydrolysis constitutes an aspect to be taken into account, particularly in the case of **H₃L2**. Nevertheless, they also present an interesting antiproliferative profile, with IC_{50} values in the low micromolar range. A possible mechanism for the cytotoxicity exhibited by the ligands could be related to the formation of metal complexes in the culture medium or inside the cells. The compounds thus generated could either be cytotoxic *per se* or, alternatively, their formation could deplete the available amount of some physiologically relevant metal ions, such as iron(III). However, additional work would be necessary in order

to confirm this hypothesis. What is certain is that the free ligands are much less toxic to the MDCK control cells than the dicopper(II) complexes **1** and **2**.

So, from a medicinal chemistry point of view, ligands **H₃L1** and, especially, **H₃L2** seem to be more promising than their respective metal compounds due to their higher Selectivity Index, particularly in the case of the human breast cell line MDA-MB-231 and of the mouse melanoma cell line B16F10. However, their apparent susceptibility to hydrolysis should impair this performance, although their reversible binding to serum albumin could partially protect them from this undesirable side-reaction.

On the other hand, the dicopper(II) complexes are much more stable and are also able to bind serum albumin in a reversible manner. Despite their higher intrinsic activity, as mentioned above, they are less selective towards cancer cells (i.e., more toxic for the MDCK control cells). Yet, binding to serum albumin could reduce their toxicity in living systems. A better panorama regarding the real significance of these complexes as anticancer agents can only be obtained after *in vivo* tests, which are already underway and will be the subject of future reports.

4.3

Partial conclusions

Two novel C_1 symmetric binucleating ligands comprising hydrazonic moieties and their μ -hydroxo dicopper(II) complexes, **1** and **2**, were synthesized and fully characterized.

X-ray diffraction analyses indicate that both coordination compounds are very similar in structural terms and generate dimeric arrangements containing two partially deprotonated ligands and four divalent copper centers.

Although absorption measurements indicate that the free ligands are quite susceptible to hydrolysis in a 90% water-containing medium, complexation to copper(II) ions seems to prevent this reaction. The dinuclear metal compounds reported in this work are, indeed, very stable in aqueous solution, both concerning ligand hydrolysis and complex dissociation.

ESI-MS(+) analyses confirmed that the main metal-containing species present in a 10% DMSO/H₂O solution should be the dinuclear cations characterized by XRD, $[\text{Cu}_2(\text{HL})(\text{OH})]^+$, as well as the DMSO-substituted derivative

$[\text{Cu}_2(\text{L})(\text{DMSO})]^+$, in which the μ -hydroxo bridge is replaced by a terminal solvent molecule.

Both complexes and ligands show high affinity for BSA, the observed static quenching of the protein fluorescence being due to interaction with the compounds. Additionally, scattering techniques (DLS and SAXS) suggest that the complexes and their free ligands interact with BSA in a reversible manner. Since BSA is an important protein involved in the transportation of drugs in the biological system, possessing similar properties to those of HSA, the observed results indicate that the new compounds could be targeted through blood transport.

Biological activity of the compounds also includes interaction with ctDNA, with the complexes showing a higher affinity than their respective ligands. Moreover, plasmid pBR322 DNA cleavage results from DLS indicate that the complexes interact electrostatically with plasmid DNA at low concentrations. At the higher concentrations of 50 μM (**1**) or 60 μM (**2**), in contrast, data seem to point out to the occurrence of DNA cleavage to Form III (linear). Along time, the value of the hydrodynamic radius for plasmid DNA Form III remained stable and, therefore, the process is not reversible.

Concerning the ability of causing damage to plasmid pBR322 DNA, complex **1** is more active than **2**. Both ligands and their dicopper(II) complexes display potent antiproliferative activity in the cancer cell lines evaluated, occasionally even in the submicromolar range. Once the effect of the metal complexes on tumour cells proliferation was analyzed, it was clear that addition of copper(II) to the ligands **H₃L1** and **H₃L2** increased their activity.

Our data on cellular models correlate quite well with the DNA interaction experiments, as IC_{50} values are smallest for **1**, which showed the highest activity on DNA by DLS studies. Thus, although the presence of the furan ring seems to be important for an improved DNA intercalation ability (which can involve the formation of anchoring hydrogen bonds between **2** and the biopolymer), the thiophene ring can somehow increase the reactivity of **1** towards DNA.

Probably, both complexes would be acting at the DNA level, by promoting replicative stress or (most likely) cleavage, leading to checkpoint responses and onset of apoptosis. However, further studies should be addressed to confirm this hypothesis.

Finally, the present work shows that aroylhydrazone-derived binucleating ligands and their dinuclear μ -hydroxo dicopper(II) complexes may represent a promising structural starting point for the development of highly active potential antitumor agents.

5

Results and discussion II. Isoxazole-arylohydrazones and their (perchlorate / acetate-derived) dinuclear copper(II) complexes as potential antiproliferative agents: syntheses and *in vitro* studies in epithelial human breast cancer cells

The present chapter was redacted in order to be published as an article in a scientific journal. Hence, it is important to verify the existence of the final published paper before citing the data here described.

5.1

Introduction

As was previously related in this thesis, the copper(II) complexes have been presented anticancer activity. In this Chapter, the inclusion of the hydrazone group have been motivated, since in recent years many metal-free and coordinate hydrazone derivatives have been tested as anticancer agents [45-57]. Additionally, the 5-phenylisoxazole group was chosen to complete the structure of the ligands in this chapter. Isoxazole compounds are known to present a large variety of biological activities [182]. Consequently, this molecular fragment has become popular for the design of potent drugs, including, for example, anticancer drugs [183]. Indeed, some isoxazole-containing drugs have been approved for the treatment of various diseases, such as, anti-inflammatory antibacterial, antiviral, antifungal, anti-tuberculosis and anti-microbial, among others. [184].

The novel contribution of this chapter relies both in the combination of three independent entities [i.e., isoxazole, hydrazones and copper(II) complexes], each one bearing its own anticancer properties, and in the exploration of the resulting cytotoxic activity of the new structures on cancer cells. This chapter reports the syntheses and full characterization of two new isoxazole-arylohydrazones and their (perchlorate / acetate-derived) dinuclear copper(II) complexes.

On the basis of this work was to examine if a subtle variation in the ligand framework (pyridine or phenol pending arm) provides a significant difference in their cytotoxic activity. Moreover, was hypothesized that the incorporation of bioactive sites in the complexes' structure will improve their interaction with DNA. In this context, a study involving the *in vitro* interaction of these compounds with calf-thymus DNA by absorption and fluorescence spectroscopies is described in detail. Drawing on the interesting cytotoxic activity of the metal-free ligands, is also explored the ability of this set of aroylhydrazones and their complexes to coordinate metal ions from the biological medium, as an additional anticancer strategy.

5.2

Results and discussion

5.2.1

Syntheses

To synthesize the two binucleating Schiff base ligands derived from **HBPAMFF** (ligand, **H₃L₃**) or **BPMAMFF** (ligand, **H₂L₄**) and 5-phenylisoxazole-3-carbohydrazone (**PIH**), equimolar amounts of both precursors were refluxed in methanol for three hours. Colourless crystals of the ligands were obtained by recrystallization in acetonitrile. The isolated ligands were mixed with copper(II) perchlorate hexahydrate salt (1 : 2 equivalent respectively) in the presence of potassium hydroxide and refluxed for one hour. The synthesized binuclear copper(II) complexes were formulated as $[\text{Cu}_2(\text{L}3^{-3})(\text{ClO}_4)(\text{DMSO})(\text{H}_2\text{O})]\text{DMSO}$ (**3**) and $[\text{Cu}_2(\text{L}4^{-1})(\text{ClO}_4)_2(\text{H}_2\text{O})]\text{ClO}_4 \cdot 4\text{H}_2\text{O}$ (**5**). Additionally, ligands were mixed with copper(II) acetate monohydrate (1 : 2 equivalents respectively) and refluxed for 40 min. In this case, these binuclear copper(II) complexes were formulated as $[\text{Cu}_2(\mu\text{-COOCH}_3)(\text{L}3^{-3})(\text{H}_2\text{O})_2] \cdot 2\text{H}_2\text{O}$ (**4**) and $[\text{Cu}_2(\mu\text{-COOCH}_3)(\text{L}4^{-2})(\text{COOCH}_3)(\text{H}_2\text{O})] \cdot 2\text{H}_2\text{O}$ (**6**) (Figure 5.1).

Complexes **3** and **6** were recrystallized in DMSO and DMF respectively, and single dark green crystals were obtained. The compounds were isolated in good yields (87% – 99%) and were characterized by elemental analysis, spectroscopic techniques and single-crystal X-ray diffraction (XRD) analyses (for ligands and

complexes **3** and **6**). Additionally, the percentage of copper(II) and water in the complexes was determined by inductively coupled plasma optical emission spectrometry (ICP-OES) and thermogravimetric analysis (TGA), respectively. The electrolytic nature of the complexes was estimated by conductivity measurements.

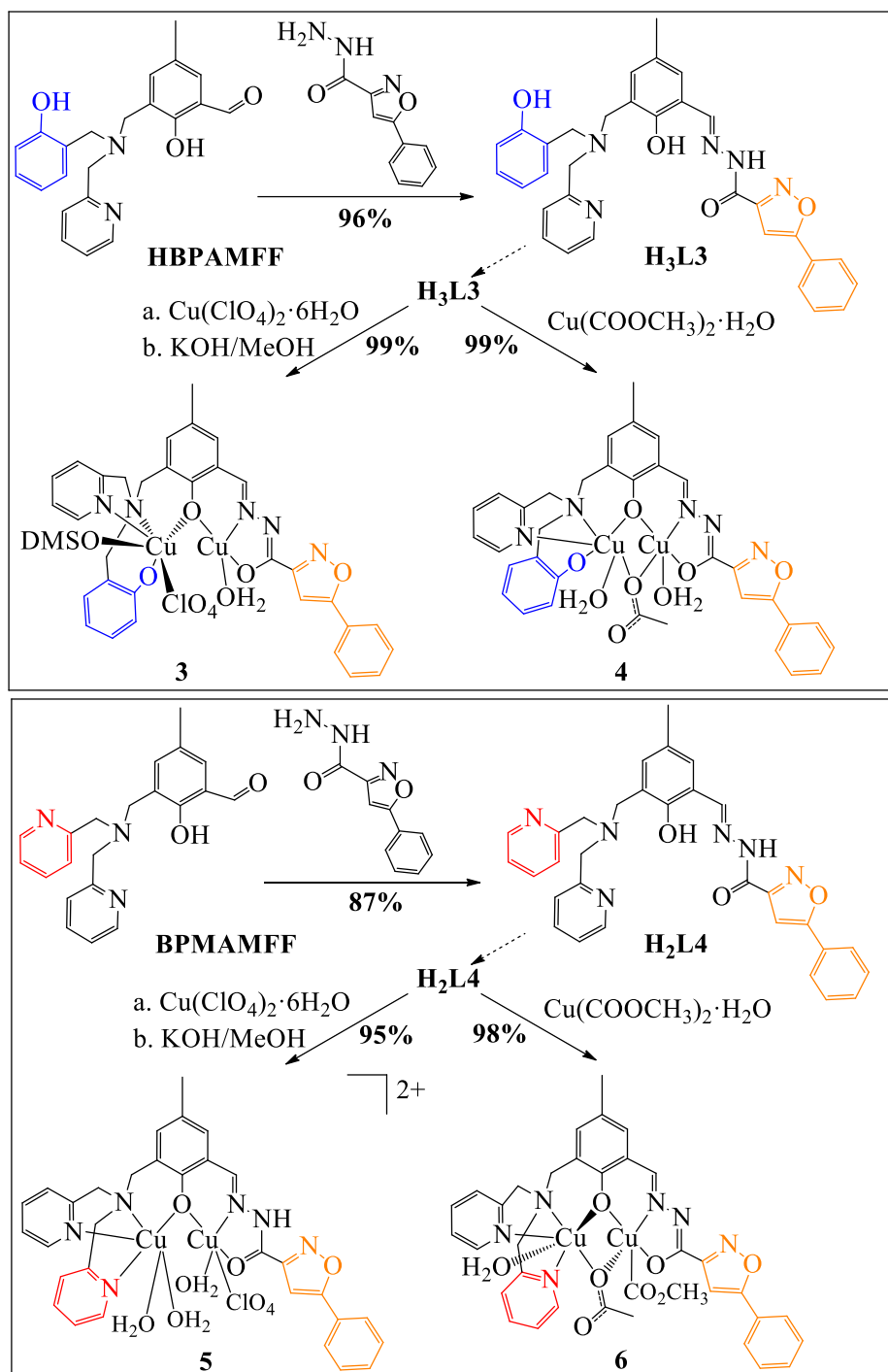


Figure 5.1. Synthetic routes of ligands **H₃L3** (top) and **H₂L4** (bottom), and their copper(II) complexes from perchlorate **3** and **5** or acetate salts **4** and **6**.

In the TGA analysis for complex **3**, the weight loss was approximately 3.7% (calcd 3.3%) between 25 and 137 °C, corresponding to the removal of one hydration water molecule and one coordinate water molecule. The weight loss corresponding to the removal of one uncoordinated molecule of DMSO was observed (Figure 5.2).

Molar conductivity measured in acetonitrile indicates complex **3** as a non-electrolyte [138].

In the TGA analysis for complex **4**, the weight loss was approximately 4.2% (calcd 3.9%) between 25 and 72 °C, corresponding to the removal of two hydration water molecules. The weight loss corresponding to the removal of three coordinate water molecules and one coordinate acetate also was observed (Figure 5.3).

Molar conductivity measured in acetonitrile indicates complex **4** as a non-electrolyte [138].

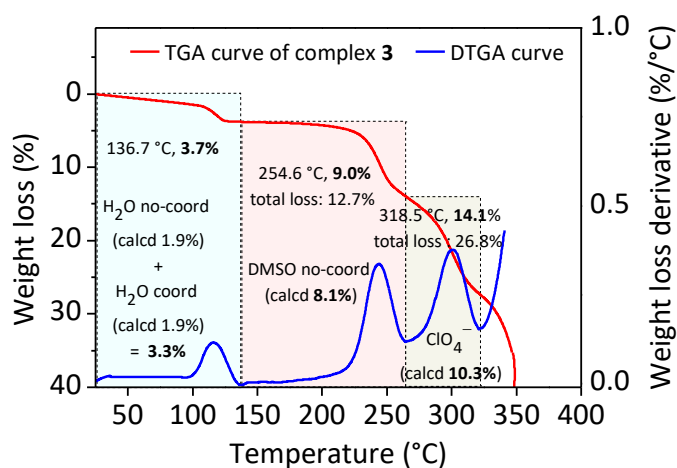


Figure 5.2. Termogravimetric curve of complex **3**.

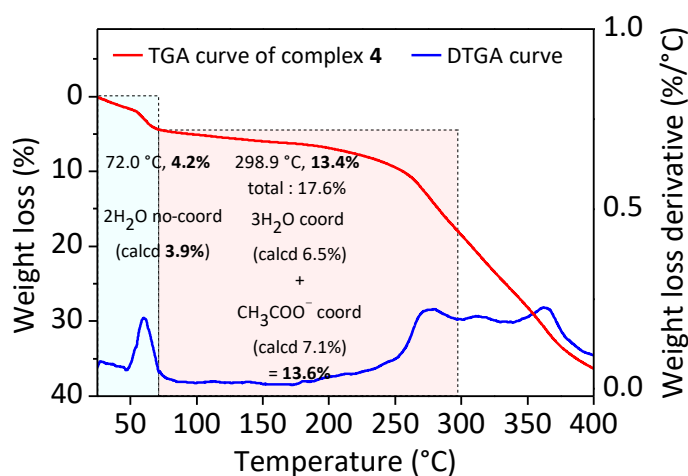


Figure 5.3. Termogravimetric curve of complex **4**.

In the TGA analysis for complex **5**, the weight loss was approximately 5.0% (calcd 5.1%) between 25 and 108 °C, corresponding to the removal of three hydration water molecules. The weight loss corresponding to the removal of three coordinate water molecules and three perchlorates molecules also was observed (Figure 5.4).

Molar conductivity in acetonitrile ($334 \text{ ohm}^{-1} \text{ cm}^2 \text{ mol}^{-1}$) of complex **5** correlates with 1 : 2 electrolyte system [138].

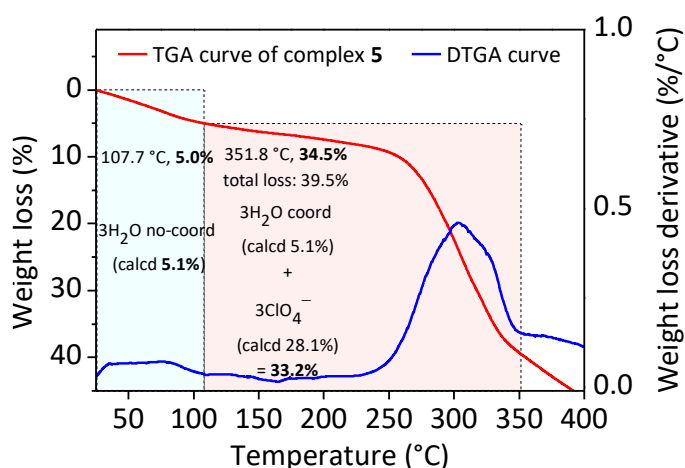


Figure 5.4. Thermogravimetric curve of complex **5**.

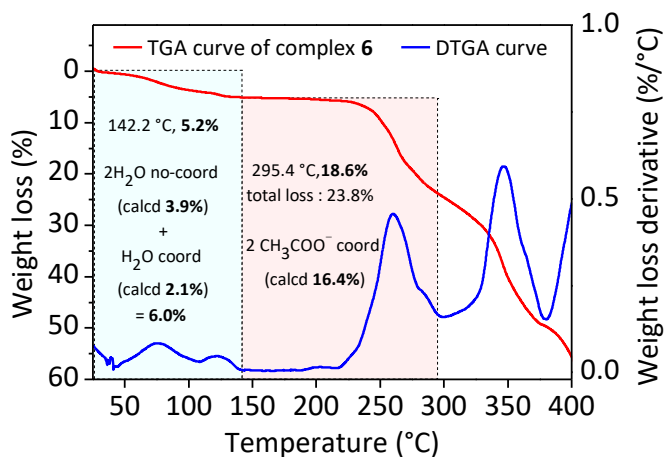


Figure 5.5. Thermogravimetric curve of complex **6**.

In the TGA analysis for complex **6**, the weight loss was approximately 5.2% (calcd 6.0%) between 25 and 142 °C, corresponding to the removal of two hydration

water molecules and one coordinate water molecule. The weight loss corresponding to the removal of two coordinate acetate molecules also was observed (Figure 5.5).

Molar conductivity measured in acetonitrile indicates complex **6** as a non-electrolyte [138].

5.2.2

Characterization of the ligands and complexes

5.2.2.1

Solution NMR of ligands

Both ligands were fully characterized by NMR spectroscopy. The experimental data set includes 1D ^1H and ^{13}C spectra (Figures 5.6–5.11), COSY, HSQC and HBMC contour maps (Figures 13.9–13.14).

In the ^1H NMR spectrum of **H₃L₃** (Figure 5.6), the hydrogens corresponding to the CH_2 and CH_3 groups appear at the lowest frequencies. Phenol central ring shifts to low field, followed respectively by the phenol and the pyridine pendant arms. Finally, the hydrogens of the isoxazole group appear at higher frequencies. No tautomeric equilibrium was perceived in the case of **H₃L₃** in the tested conditions.

The ^1H NMR spectrum of **H₂L₄** (Figure 5.7) is similar to the spectrum of **H₃L₃**. Nevertheless, for **H₂L₄** in solution, the spectrum shows duplications of the resonance signals (integration < 1%). It was described that aroylhydrazone derivatives can present geometric isomers (*E* / *Z*) and constitutional isomers due to tautomerization processes (iminol / amide forms) [139-141]. The observed duplication of signals for **H₂L₄** is assigned to the *E*-iminol and *E*-amide forms.

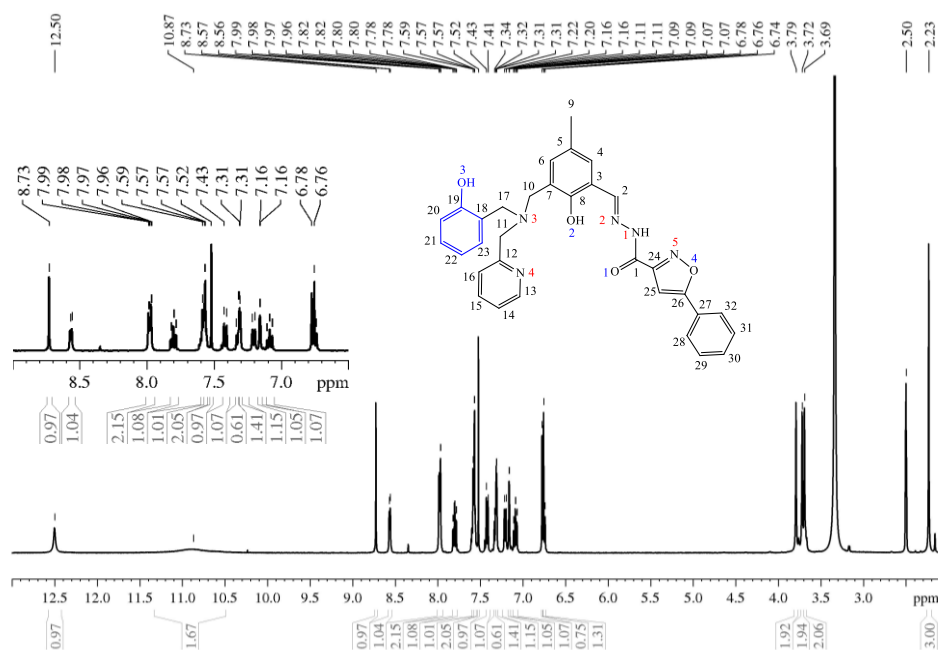


Figure 5.6. ^1H NMR spectrum (400 MHz) of H_3L_3 in $\text{DMSO}-d_6$ at room temperature.

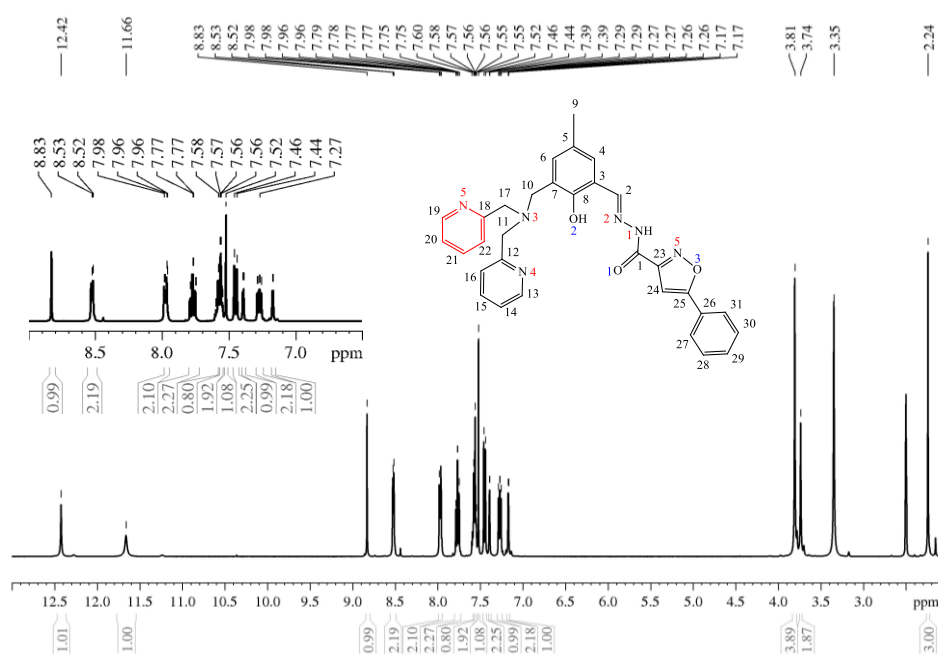


Figure 5.7. ^1H NMR spectrum (400 MHz) of H_2L_4 in $\text{DMSO}-d_6$ at room temperature.

In order to confirm the principal isomer present in solution, Distortionless Enhanced Polarization Transfer (DEPT-135) spectrum (Figure 5.10 and 5.11) was recorded and compared to the ^{13}C NMR spectrum (Figure 5.8 and 5.9).

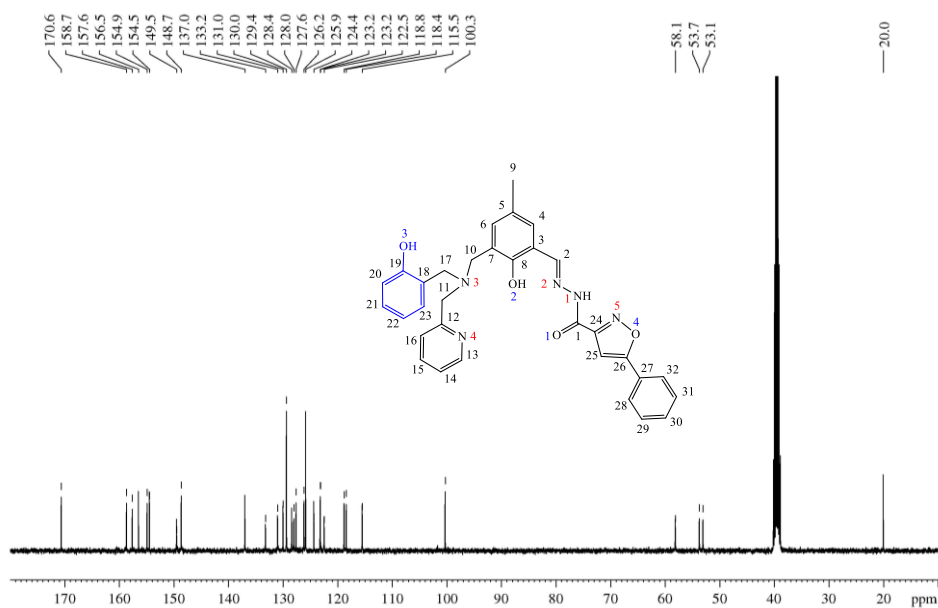


Figure 5.8 ^{13}C NMR spectrum (100 MHz) of **H₃L3** in $\text{DMSO}-d_6$ at room temperature.

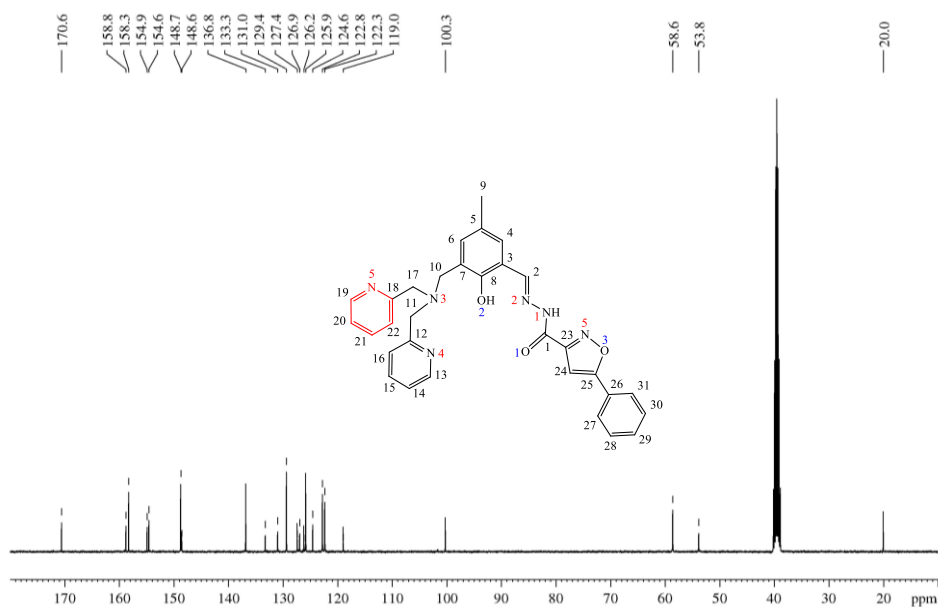


Figure 5.9. ^{13}C NMR spectrum (100 MHz) of **H₂L4** in $\text{DMSO}-d_6$ at room temperature.

Besides, the corresponding CO (aroylhydrazone group) peak at 158.8 ppm in the ^{13}C NMR spectrum is virtually absent in the DEPT-135 spectrum (Figure 5.11, inset), revealing that this carbon is mainly quaternary.

Additionally, in the ^{13}C NMR or DEPT-135 spectra, no extra carbon was observed. Consequently, the principal form of **H₂L4** ligand was attributed to the *E*-amide isomer form $[(\text{O}=\text{C})-\text{NH}-\text{N}=\text{C}-]$. Also, integration of the peaks in the ^1H

NMR spectrum indicates that the *E*-iminol form $[-(\text{HO})\text{C}=\text{N}-\text{N}=\text{C}-]$ represents less than 1% of the isomer in **H₂L4** solution. Accordingly, only the (*E*-amide) form will be discussed in this work.

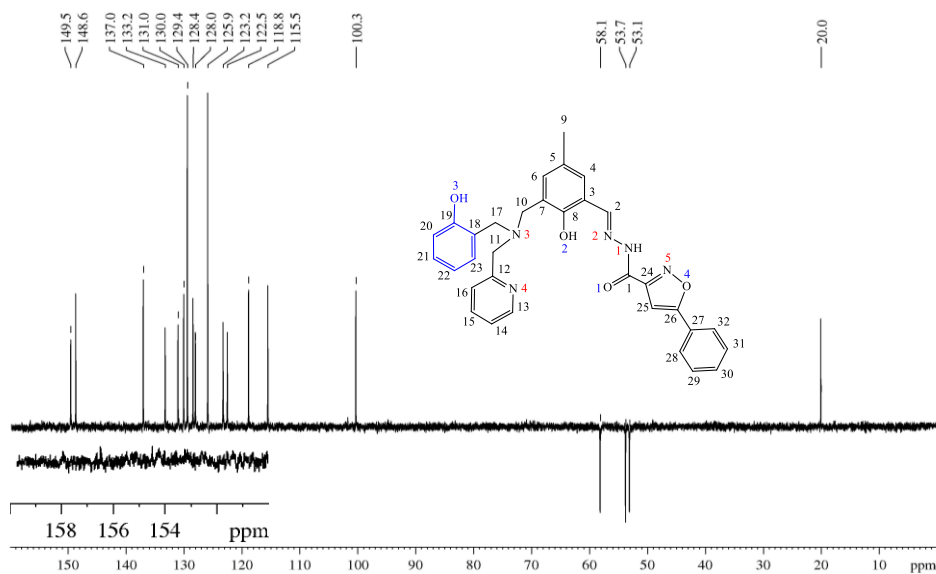


Figure 5.10. DEPT-135 spectrum (100 MHz) of **H₃L3** in DMSO-*d*₆ at room temperature.

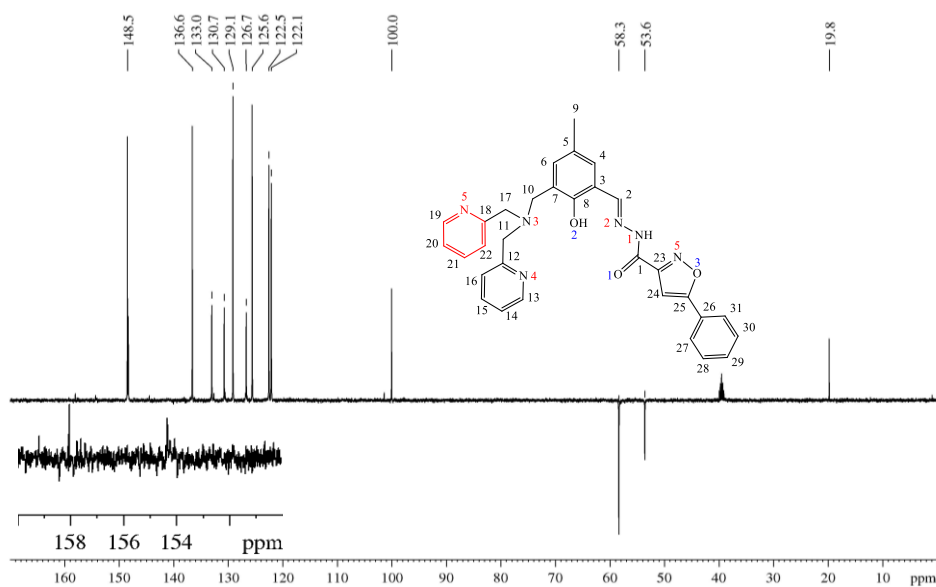


Figure 5.11. DEPT-135 spectrum (100 MHz) of **H₂L4** in DMSO-*d*₆ at room temperature.

Complete ¹H and ¹³C NMR assignments for the ligands are given in Table 5.1.

Table 5.1. ^1H (400 MHz) and ^{13}C (100 MHz) data for **H₃L3** and **H₂L4** in DMSO-*d*₆ at room temperature, along with the respective assignments. Chemical shifts (δ) are in ppm and coupling constants (J) are in Hz.

| C/H | H ₃ L3, δ_{C} | H ₃ L3, δ_{H} | H ₃ L4, δ_{C} | H ₂ L4, δ_{H} |
|------|---|---|---|--|
| 1 | 158.7 | – | 158.8 | – |
| 2 | 149.5 | 8.73 (s, 1H) | 148.6 | 8.83 (s, 1H) |
| 3 | 118.4 | – | 119.0 | – |
| 4 | 122.5 | 7.34 (s, 1H) | 126.9 | 7.39 (s, 1H) |
| 5 | 127.6 | – | 127.4 | – |
| 6 | 132.2 | 7.16 (s, 1H) | 133.3 | 7.17 (s, 1H) |
| 7 | 124.4 | – | 124.6 | – |
| 8 | 154.5 | – | 154.6 | – |
| 9 | 20.0 | 2.23 (s, 3H) | 20.0 | 2.24 (s, 3H) |
| 10 | 53.1 | 3.72 (s, 2H) | 53.8 | 3.74 (s, 2H) |
| 11 | 58.1 | 3.79 (s, 2H) | 58.6* | 3.81 (s, 4H)* |
| 12 | 157.6 | – | 158.3 | – |
| 13 | 148.7 | 8.56 (d, 1H, $^3J_{\text{HH}} = 4.2$) | 148.7 | 8.52 (d, 2H, $^3J_{\text{HH}} = 4.1$)* |
| 14 | 128.0 | 7.31 (t, 1H, $^3J_{\text{HH}} = 2.6$) | 122.3* | 7.27 (td, 2H, $^3J_{\text{HH}} = 6.6$, $^4J_{\text{HH}} = 0.8$)* |
| 15 | 137.0 | 7.80 (td, 1H, $^3J_{\text{HH}} = 7.7$, $^4J_{\text{HH}} = 1.7$) | 136.8 | 7.77 (td, 2H, $^3J_{\text{HH}} = 7.7$, $^4J_{\text{HH}} = 1.7$)* |
| 16 | 123.2 | 7.42 (d, 1H, $^3J_{\text{HH}} = 7.8$) | 122.8* | 7.45 (d, 2H, $^3J_{\text{HH}} = 7.8$)* |
| 17 | 53.7 | 3.69 (s, 2H) | 58.6* | 3.81 (s, 4H)* |
| 18 | 123.2 | – | 158.3 | – |
| 19 | 156.5 | – | 148.7* | 8.52 (d, 2H, $^3J_{\text{HH}} = 4.1$)* |
| 20 | 115.5 | 6.78 (s, 1H) | 122.3* | 7.27 (td, 2H, $^3J_{\text{HH}} = 6.6$, $^4J_{\text{HH}} = 0.8$)* |
| 21 | 128.4 | 7.09 (td, 1H, $^3J_{\text{HH}} = 7.8$, $^4J_{\text{HH}} = 1.6$) | 136.8 | 7.77 (td, 2H, $^3J_{\text{HH}} = 7.7$, $^4J_{\text{HH}} = 1.7$)* |
| 22 | 118.8 | 6.75 (d, 1H, $^3J_{\text{HH}} = 7.6$) | 122.8* | 7.45 (d, 2H, $^3J_{\text{HH}} = 7.8$)* |
| 23 | 130.0 | 7.21 (dd, 1H, $^3J_{\text{HH}} = 7.6$, $^4J_{\text{HH}} = 1.1$) | 154.9 | – |
| 24 | 154.9 | – | 100.3 | 7.52 (s, 1H) |
| 25 | 100.3 | 7.52 (s, 1H) | 170.6 | – |
| 26 | 170.6 | – | 126.2 | – |
| 27 | 126.2 | – | 125.9* | 7.98 – 7.96 (m, 2H)* |
| 28 | 125.9* | 7.99 – 7.96 (m, 2H)* | 129.4* | 7.56 – 7.57 (m, 2H)* |
| 29 | 131.0* | 7.57 (m, 2H)* | 131.0* | 7.58 (s, 1H) |
| 30 | 129.4 | 7.59 (s, 1H) | 129.4* | 7.56 – 7.57 (m, 2H)* |
| 31 | 131.0* | 7.57 (m, 2H)* | 125.9* | 7.98 – 7.96 (m, 2H)* |
| 32 | 125.9* | 7.99 – 7.96 (m, 2H)* | – | – |
| O2–H | – | 10.87 (s, br, 2H)* | – | 12.42 (s, 1H) |
| O3–H | – | 10.87 (s, br, 2H)* | – | – |
| N1–H | – | 12.50 (s, 1H) | N1–H | 11.66 (s, 1H) |

*Overlapped signals. *symmetric signal Signal multiplicity - s: singlet, d: doublet, t: triplet, dd: doublet of doublets, td: triplet of doublets.

5.2.2.2

Crystal structures of the ligands and complexes 3 and 5

The information corresponding to the crystallographic results was provided by Eng. Jérémy Forté, from the CHEMBIO group of the *Sorbonne Université*, France. Some modifications or additions were made to the original text.

The ORTEP view of the molecular structures of isoxazole-hydrazonic ligands derived from the aldehyde precursors **HBPMAMFF** and **BPMAMFF** are shown in Figure 5.12. Additionally, the crystallographic data and structural refinement parameters can be found in Table 5.2. Both ligands crystallized in the monoclinic system, space group $P 2_1/c$. The crystal structure of **H₃L₃** was a racemate due to the chiral nature of the molecule due to the presence of the N3 center. Nonetheless, the space group was centrosymmetric, and two enantiomers are observed in the crystal.

Phenylisoxazole, carbon hydrazide and mesitol groups are in a same plane. Only a weak torsion is observed between phenylisoxazole and carbon hydrazide groups, corresponding to dihedral angles NCCN of $15.492(174)^\circ$ for **H₃L₃** and $16.088(230)^\circ$ for **H₂L₄**. Additionally, in both ligands, the heteroatoms N1 and O2 are protonated. For **H₃L₃**, O3 from the **HBPA** phenol arm was also protonated. Selected geometric parameters for **H₃L₃** and **H₂L₄** are shown in Table 5.3.

For ligand **H₂L₄**, only one intramolecular H-bond was observed, while for **H₃L₃**, one extra intramolecular hydrogen bond was identified from the phenol group of the **HBPA** moiety (Figure 5.12 and Table 5.4). Thus, in both cases, the hydrogen atom connected to atom O2 of the mesitol group directly towards atom N2 of hydrazide group to create a six-membered ring. The ligand supplementary intramolecular H-bond in **H₃L₃**, corresponds to O3–H hydrogen and tertiary amine (N3), also creating a 6-atom ring (Figure 5.12 and Table 5.4).

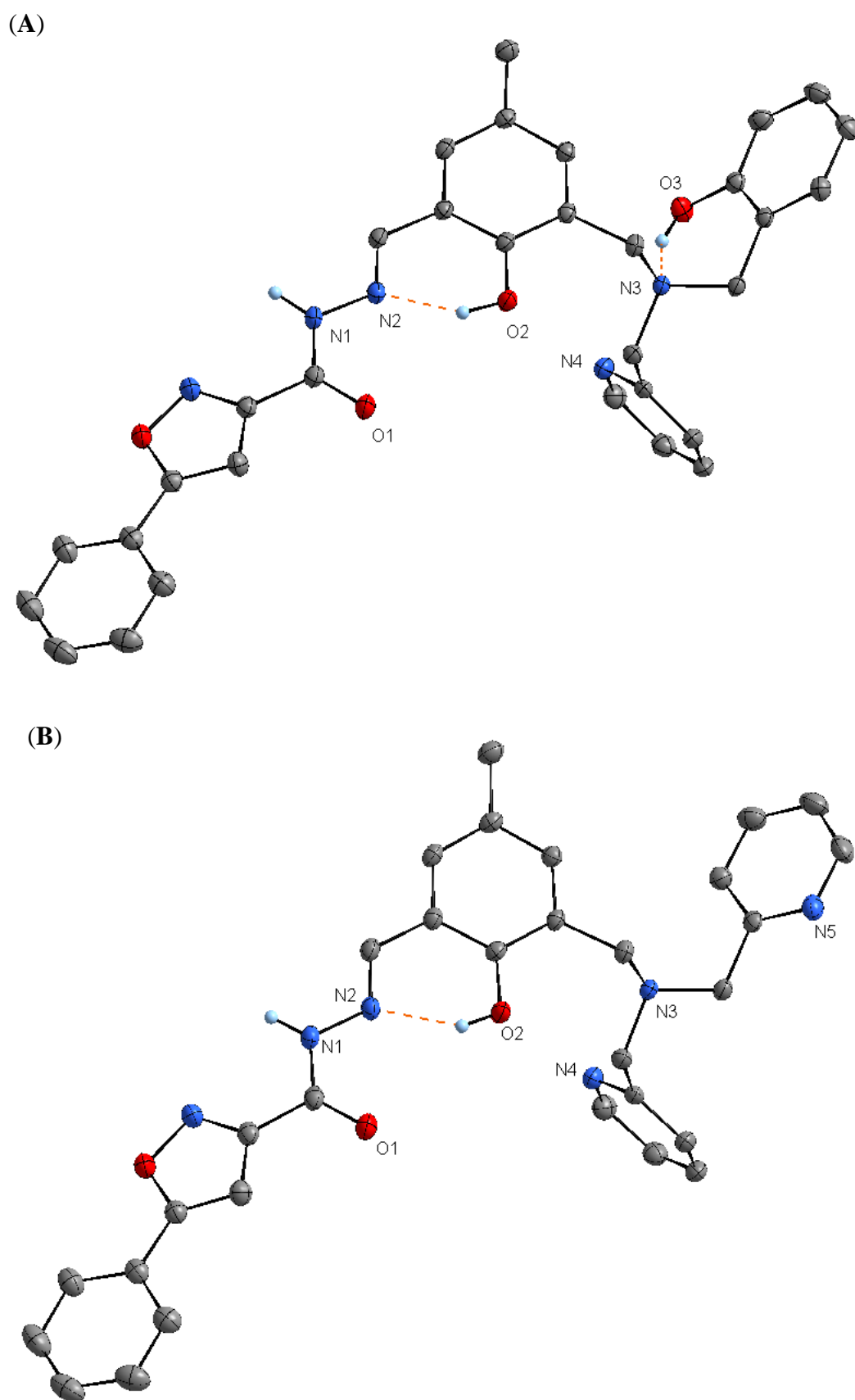


Figure 5.12. Crystal structure of ligands **H₃L3** (A) and **H₂L4** (B). Ellipsoids are drawn with 30% probability. Only hydrogen atoms involved in intramolecular bonds (orange dotted line) are shown for the sake of clarity. For **H₃L3**, only one of the enantiomers is shown.

Table 5.2. Crystallographic data and structure refinement of ligands **H₃L3** and **H₂L4**.

| | H₃L3 | H₂L4 |
|--|---|---|
| CCDC number | 1912562 | 1912561 |
| Empirical formula | C ₃₂ H ₂₉ N ₅ O ₄ | C ₃₁ H ₂₈ N ₆ O ₃ |
| Formula weight (g/mol) | 547.60 | 532.59 |
| Temperature (K) | 200 | 200 |
| Crystal system | Monoclinic | Monoclinic |
| Space group | P2 ₁ /c | P2 ₁ /c |
| a (Å) | 24.7630(4) | 25.116(3) |
| b (Å) | 10.2652(2) | 10.2971(10) |
| c (Å) | 10.9150(2) | 10.4295(11) |
| α (°) | 90 | 90 |
| β (°) | 101.4770(10) | 99.590(7) |
| γ (°) | 90 | 90 |
| Volume (Å ³) | 2719.08(9) | 2659.6(5) |
| Z | 4 | 4 |
| ρ _{calc} (g/cm ³) | 1.338 | 1.330 |
| Absorption coefficient μ (mm ⁻¹) | 0.732 (CuKα) | 0.089 (MoKα) |
| F(000) | 1152 | 1120 |
| Crystal size (mm ²) | 0.48 x 0.12 x 0.11 | 0.20 x 0.15 x 0.05 |
| Wavelength λ (Å) | 1.54178 | 0.71073 |
| 2θ range (°) | 7.286 – 133.282 | 3.29 – 56.75 |
| Miller indexes ranges | -29 ≤ h ≤ 29, -12 ≤ k ≤ 12, -11 ≤ l ≤ 12 | -33 ≤ h ≤ 24, -13 ≤ k ≤ 13, -11 ≤ l ≤ 13 |
| Measured reflections | 27305 | 22268 |
| Unique reflections | 4808 | 6610 |
| R _{int} / R _{sigma} | 0.0265 / 0.0159 | 0.0446 / 0.0458 |
| Reflections [I ≥ 2σ(I)] | 4334 | 3997 |
| Restraints | 0 | 0 |
| Parameters | 381 | 363 |
| Goodness-of-fit F ² | 1.031 | 1.001 |
| Final R indexes ^{b,c} | R1 = 0.0330 | R1 = 0.0932, |
| [all data] | wR2 = 0.0797 | wR2 = 0.1084 |
| Final R indexes ^{a,b} | R1 = 0.0295 | R1 = 0.0448 |
| [I ≥ 2σ(I)] | wR2 = 0.0767 | wR2 = 0.0914 |
| Largest diff. peak/hole (e/Å ³) | 0.19/-0.15 | 0.22/-0.16 |

^a R1 = $\sum ||F_o| - |F_c|| / \sum |F_o|$. ^b wR2 = $[\sum (w(F_o^2 - F_c^2)) / \sum (w(F_o^2)^2)]^{1/2}$

Table 5.3. Selected geometric parameters for ligands **H₃L3** and **H₂L4**.

| Bond distances (Å) | | | |
|---------------------------|------------------------|------------|------------------------|
| | H₃L3 | | H₂L4 |
| O3-C19 | 1.3638(13) | O1-C1 | 1.2215(19) |
| O2-C8 | 1.3588(13) | O2-C8 | 1.3597(18) |
| O4-N5 | 1.4090(13) | O3-C25 | 1.355(2) |
| O4-C26 | 1.3555(15) | O3-N6 | 1.4089(17) |
| N3-C17 | 1.4807(13) | N1-C1 | 1.347(2) |
| N3-C10 | 1.4843(13) | N1-N2 | 1.3754(17) |
| N3-C11 | 1.4745(13) | N2-C2 | 1.282(2) |
| O1-C1 | 1.2210(14) | N3-C17 | 1.4664(18) |
| N1-N2 | 1.3783(13) | N3-C11 | 1.4716(18) |
| N1-C1 | 1.3501(15) | N3-C10 | 1.4799(18) |
| N4-C12 | 1.3445(14) | N4-C13 | 1.339(2) |
| N4-C13 | 1.3394(16) | N4-C12 | 1.3430(19) |
| N2-C2 | 1.2825(15) | N5-C18 | 1.338(2) |
| N5-C24 | 1.3081(15) | – | – |
| Bond angles (°) | | | |
| | H₃L3 | | H₂L4 |
| C26-O4-N5 | 109.00(8) | C25-O3-N6 | 108.92(12) |
| C17-N3-C10 | 110.99(8) | C1-N1-N2 | 116.25(13) |
| C11-N3-C17 | 111.98(8) | C2-N2-N1 | 118.92(13) |
| C11-N3-C10 | 110.65(8) | C17-N3-C11 | 111.15(11) |
| C1-N1-N2 | 116.11(9) | C17-N3-C10 | 109.40(11) |
| C13-N4-C12 | 117.43(10) | C11-N3-C10 | 110.35(11) |
| C2-N2-N1 | 118.60(10) | C13-N4-C12 | 117.35(14) |
| C24-N5-O4 | 104.80(9) | C18-N5-C19 | 116.86(16) |
| N4-C12-C16 | 122.02(10) | C23-N6-O3 | 104.88(13) |
| N4-C12-C11 | 116.40(9) | O1-C1-N1 | 124.88(15) |
| O2-C8-C7 | 118.28(9) | O1-C1-C23 | 118.67(15) |
| O2-C8-C3 | 121.89(9) | N1-C1-C23 | 116.40(14) |
| O3-C19-C18 | 120.63(10) | N2-C2-C3 | 119.72(14) |
| O3-C19-C20 | 118.74(10) | O2-C8-C3 | 121.86(13) |
| N3-C10-C7 | 111.84(8) | N3-C10-C7 | 112.86(12) |
| N2-C2-C3 | 119.69(10) | N3-C11-C12 | 112.29(11) |
| N5-C24-C1 | 123.24(11) | N4-C12-C16 | 121.88(14) |
| N5-C24-C25 | 112.31(10) | N4-C12-C11 | 115.91(13) |
| O4-C26-C27 | 118.00(10) | N3-C10-C7 | 112.86(12) |
| C25-C26-O4 | 108.99(10) | N4-C13-C14 | 124.04(16) |
| N3-C11-C12 | 111.34(8) | N3-C17-C18 | 112.70(12) |
| O1-C1-N1 | 124.78(10) | N5-C18-C22 | 122.40(15) |
| O1-C1-C24 | 118.41(10) | N5-C18-C17 | 116.00(14) |
| N1-C1-C24 | 116.75(10) | N5-C19-C20 | 123.90(18) |
| – | – | N6-C23-C24 | 112.14(14) |
| – | – | N6-C23-C1 | 122.33(15) |

Table 5.4. H-bond length (d, Å) for ligands **H₃L3** and **H₂L4**.

| D-H...A | H₃L3 | | H₂L4 | |
|-------------------------|------------------------|------------|------------------------|------------|
| | d(H...A) | d(D...A) | d(H...A) | d(D...A) |
| O2-H2...N2 | 1.76 | 2.5925(12) | 1.84 | 2.5777(17) |
| O3-H3...N3 | 1.78 | 2.6430(12) | – | – |
| N1-H1...N4 ⁱ | 2.11 | 3.0132(14) | 2.13 | 2.9777(19) |

*Symmetry codes: (i) x, 0.5-y, 0.5+z (**H₃L3**) and x, 0.5-y, -0.5+z (**H₂L2**)*

In both structures, one intermolecular H-bond was present between the hydrogen N1–H (hydrazide group) and the N4 atom (pyridine groups) of a nearby molecule of the ligands. It was observed that intermolecular hydrogen bond lengths are shorter than the intramolecular ones. Nevertheless, these H-bonds contribute to the stability of crystals by creating a network of neighboring molecules.

Finally, crystal structures of the ligands were stabilized by van der Waals-type weak interactions (CH...N, CH...O and CH...C). The symmetry codes were x, 1.5-y, 0.5+z and x, 1.5-y, 0.5+z for **H₃L3** and **H₂L4** respectively.

The Oak Ridge Thermal Ellipsoid Plot (ORTEP) view of the molecular structures of isoxazole-complexes **3** and **6** derived, from ligands **H₃L3** and **H₂L4** respectively are shown in Figure 5.13. Additionally, the crystallographic data and structural refinement parameters can be found in Table 5.5. Selected geometric parameters for complexes **3** and **6** are shown in Table 5.6. Complex **3** crystallized in the triclinic system, space group P-1, while complex **6**, in the monoclinic system, space group P2₁/c. For complex **3** just one of the enantiomers is shown.

In the asymmetric unit of complex **3**, one DMSO molecule was coordinated to the Cu1 atom. Besides, one additional DMSO appeared as uncoordinated solvent. In the structure, the copper Cu1 described a slightly distorted square plane geometry with the atoms O1 and N2 (hydrazone group), O2 (phenoxo group) and O5 (water molecule). In the Cu1 environment there is a DMSO solvent molecule near to the apical position. This proximity can surely help to stabilize the crystal, but the determined distance 2.954 (Å) was too long to consider Cu1 in a square pyramidal geometry.

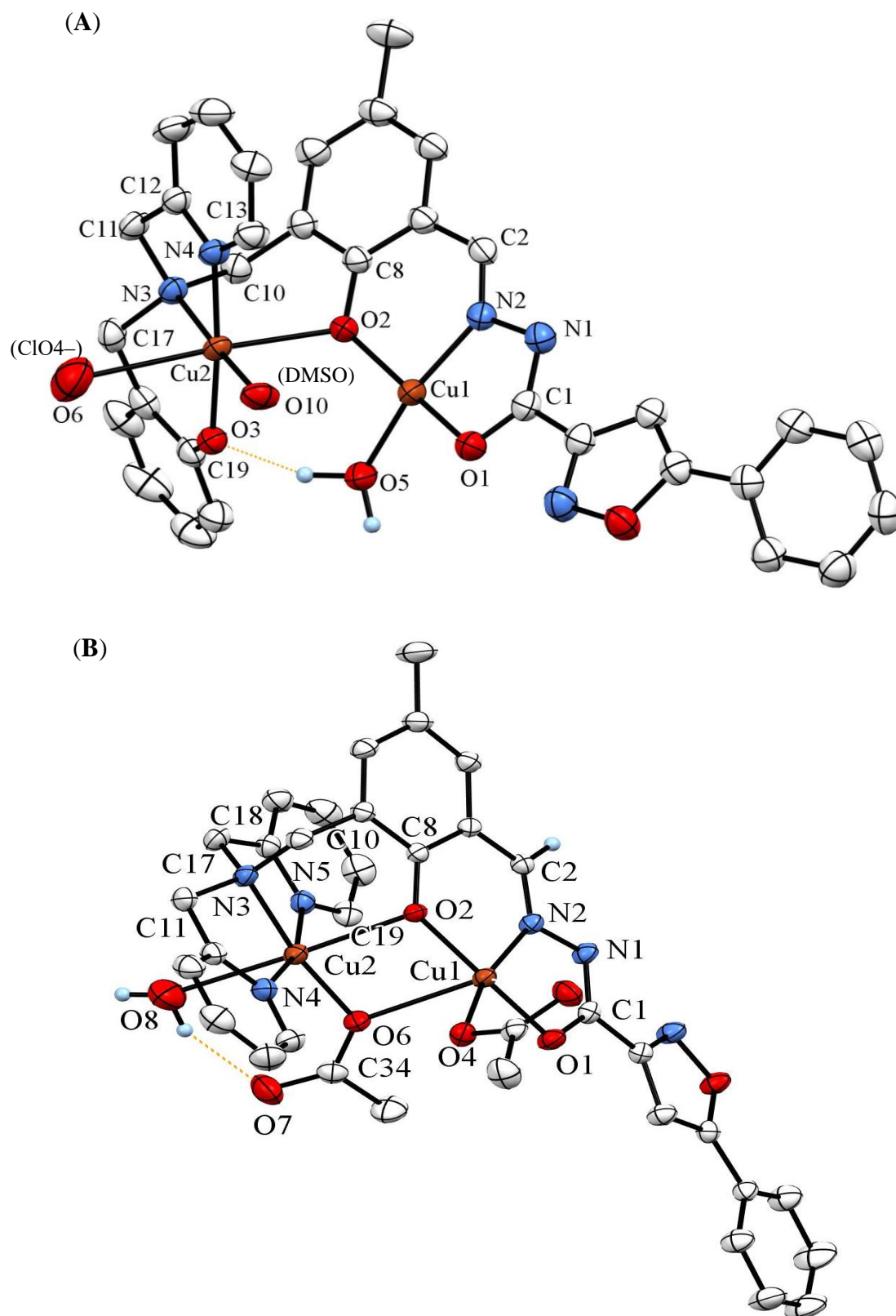


Figure 5.13. Crystal structure of (A) complex **3** and (B) complex **6**. Ellipsoids are drawn with 30% probability. Only hydrogen atoms involved in intramolecular hydrogen bonds (orange dotted line) are shown for the sake of clarity. Free water, DMSO or perchlorate counter-ion molecules were omitted for the sake of simplicity. For complex **3**, one oxygen atom from the perchlorate ion is shown and only one of the enantiomers is shown.

Table 5.5. Crystallographic data and structure refinement of complexes **3** and **6**.

| | 3 | 6 |
|--|---|--|
| CCDC number | 1899672 | 1899668 |
| Empirical formula ^a | C ₃₆ H ₄₀ N ₅ O ₁₁ S ₂ ClCu ₂ | C ₃₅ H ₃₈ N ₆ O ₁₀ Cu ₂ |
| Formula weight (g/mol) | 945.38 | 829.79 |
| Temperature (K) | 200 | 200 |
| Crystal system | Triclinic | Monoclinic |
| Space group | P-1 | P2 ₁ /c |
| a (Å) | 10.8984(2) | 10.3269(5) |
| b (Å) | 12.5370(3) | 19.6052(8) |
| c (Å) | 15.9749(3) | 18.2854(9) |
| α (°) | 71.6540(10) | 90 |
| β (°) | 88.4770(10) | 102.470(2) |
| γ (°) | 75.8410(10) | 90 |
| Volume (Å ³) | 2005.81(7) | 3614.7(3) |
| Z | 2 | 4 |
| ρ _{calc} (g/cm ³) | 1.565 | 1.525 |
| Absorption coefficient μ (mm ⁻¹) | 3.449 (CuKα) | 1.243 (MoKα) |
| F(000) | 972 | 1712 |
| Crystal size (mm ²) | 0.25 x 0.20 x 0.10 | 0.32 x 0.13 x 0.09 |
| Wavelength λ (Å) | 1.54178 | 0.71073 |
| 2θ range (°) | 8.38 – 133.292 | 3.086 – 61.204 |
| Miller indexes ranges | -12 ≤ h ≤ 12, -14 ≤ k ≤ 14, -18 ≤ l ≤ 19 | -14 ≤ h ≤ 11, -21 ≤ k ≤ 28, -26 ≤ l ≤ 26 |
| Measured reflections | 21310 | 72519 |
| Unique reflections | 7054 | 11094 |
| R _{int} / R _{sigma} | 0.0183 / 0.0186 | 0.0634 / 0.0506 |
| Reflections [I ≥ 2σ(I)] | 6542 | 7361 |
| Restraints | 0 | 0 |
| Parameters | 518 | 490 |
| Goodness-of-fit F ² | 1.038 | 1.001 |
| Final R indexes ^{b,c} | R1 = 0.0425, | R1 = 0.0796, |
| [all data] | wR2 = 0.1164 | wR2 = 0.0978 |
| Final R indexes ^{b,c} | R1 = 0.0402, | R1 = 0.0401, |
| [I ≥ 2σ(I)] | wR2 = 0.1138 | wR2 = 0.0831 |
| Largest diff. peak/hole (e/Å ³) | 1.12/-0.71 | 0.43/-0.49 |

^aIncluding solvent molecules. ^b $R1 = \sum ||F_o| - |F_c|| / \sum |F_o|$. ^c $wR2 = [\sum(w(F_o^2 - F_c^2)) / \sum(w(F_o^2)^2)]^{1/2}$

Table 5.6. Selected geometric parameters for complexes **3** and **6**.

| Bond distances (Å) | | | | |
|---------------------------|------------|--|------------|------------|
| 3 | | | 6 | |
| Cu1-O1 | 1.9243(23) | | Cu1-O1 | 1.9681(16) |
| Cu1-N2 | 1.9164(21) | | Cu1-N2 | 1.9343(18) |
| Cu1-O2 | 1.8996(20) | | Cu1-O2 | 1.9606(14) |
| Cu1-O5 | 1.9294(22) | | Cu1-O4 | 1.9417(14) |
| Cu2-O2 | 2.3051(16) | | Cu2-O2 | 2.3801(15) |
| Cu2-N4 | 2.0017(21) | | Cu2-N5 | 2.0085(17) |
| Cu2-N3 | 2.0160(25) | | Cu2-N3 | 2.0355(19) |
| Cu2-O3 | 1.9179(18) | | Cu2-N4 | 2.0139(18) |
| Cu2-O10 | 1.9942(24) | | Cu2-O6 | 1.9376(16) |
| Cu1-O10 | 2.9541(19) | | Cu1-O6 | 2.5794(17) |
| Cu2-O6 | 2.7037(22) | | Cu2-O8 | 2.5557(24) |
| Cu1-Cu2 | 3.4002(4) | | Cu1-Cu2 | 3.4024(5) |
| N1 ⁱ -Cu1 | 3.1172(22) | | – | – |
| Bond angles (°) | | | | |
| 3 | | | 6 | |
| Cu1-O2-Cu2 | 107.54(8) | | Cu1-O2-Cu2 | 103.75(6) |
| O1-Cu1-N2 | 81.96(9) | | O1-Cu1-N2 | 80.89(7) |
| O1-Cu1-O2 | 167.23(9) | | O1-Cu1-O2 | 170.42(6) |
| O1-Cu1-O5 | 95.57(9) | | O1-Cu1-O4 | 91.97(6) |
| O2-Cu1-N2 | 93.95(9) | | O2-Cu1-N2 | 92.06(7) |
| O2-Cu1-O5 | 90.91(9) | | O2-Cu1-O4 | 96.28(6) |
| N2-Cu1-O5 | 167.7(1) | | N2-Cu1-O4 | 165.69(7) |
| N3-Cu2-O3 | 95.54(8) | | N3-Cu2-N4 | 82.05(8) |
| N3-Cu2-N4 | 83.67(9) | | N3-Cu2-N5 | 83.10(7) |
| N3-Cu2-O10 | 174.08(9) | | N3-Cu2-O6 | 171.35(7) |
| O3-Cu2-N4 | 175.73(9) | | N4-Cu2-N5 | 163.65(8) |
| O3-Cu2-O10 | 90.28(8) | | N4-Cu2-O6 | 102.54(7) |
| N4-Cu2-O10 | 90.45(9) | | N5-Cu2-O6 | 93.08(7) |
| Cu1-O10-Cu2 | 84.44(7) | | Cu1-O6-Cu2 | 96.71(6) |
| O10-Cu1-O2 | 74.53(7) | | O6-Cu1-O2 | 77.11(5) |
| O10-Cu1-N2 | 114.47(8) | | O6-Cu1-N2 | 112.53(7) |
| O10-Cu1-O1 | 96.07(8) | | O6-Cu1-O1 | 99.51(6) |
| O10-Cu1-O5 | 77.75(8) | | O6-Cu1-O4 | 80.76(6) |
| O2-Cu2-N3 | 90.64(8) | | O2-Cu2-N3 | 89.88(6) |
| O2-Cu2-O3 | 91.42(7) | | O2-Cu2-N4 | 99.72(6) |
| O2-Cu2-N4 | 92.78(8) | | O2-Cu2-N5 | 87.04(6) |
| O2-Cu2-O10 | 90.32(8) | | O2-Cu2-O6 | 82.15(6) |
| O2-Cu2-O6 | 176.20(8) | | O2-Cu2-O8 | 177.42(6) |
| O6-Cu2-N3 | 92.56(9) | | O8-Cu2-N3 | 89.10(7) |
| O6-Cu2-O3 | 86.24(8) | | O8-Cu2-N4 | 82.49(7) |
| O6-Cu2-N4 | 89.60(9) | | O8-Cu2-N5 | 90.48(7) |
| O6-Cu2-O10 | 86.71(9) | | O8-Cu2-O6 | 98.72(7) |
| N1 ⁱ -Cu1-O5 | 87.87(8) | | – | – |
| N1 ⁱ -Cu1-O1 | 90.62(8) | | – | – |
| N1 ⁱ -Cu1-N2 | 80.11(8) | | – | – |
| N1 ⁱ -Cu1-O2 | 100.63(7) | | – | – |
| N1 ⁱ -Cu1-O10 | 164.64(6) | | – | – |

Symmetry code: (i) 1-x, -y, 1-z

For copper Cu2, the coordination polyhedron around this atom is a heavily axially distorted octahedron. In the equatorial plane, Cu2 is coordinated by N3, O3 and N4 (pyridine) atoms from the meridional **HBPA** moiety, as well as to the O10 (DMSO solvent). In addition, the apical position is occupied by the O2 atom of the bridged phenoxo group. The oxygen O6 atom from a perchlorate ion is observed at 2.704 Å from Cu2, completing the distorted elongated octahedral environment.

Concerning the hydrogen bonds in **3**, one water molecule created two O5–H \cdots O bonds, contributing to crystal stability of the complex. Thus, O5–H5A bonds O3 atom (**HBPA** moiety) forming a hexagonal ring and O5–H5A bonds O11 (free DMSO, not showed) (Table 5.7). No intermolecular H-bonds were observed. Finally, the crystal structure of complex **3** was stabilized by intermolecular van der Waals weak interactions, Cu1 \cdots N1ⁱ (from another nearby molecule, 1-x, -y, 1-z symmetry code), forming a pseudo dimer in the crystal.

On the other hand, in the structure of complex **6**, the Cu1 atom is in a slightly distorted square pyramidal environment, coordinated in basal plane to O1 and N2 of the hydrazone group, to O2 of a phenoxo group and to O4 of an acetate ligand. Finally, O6 of another acetate ligand occupied the apical position. It was noticed that Cu1 in complex **6** presents a similar (ONOO) coordination environment, regarding the base plane to that of Cu1 in complex **3**. On the other hand, the Cu2 of complex **6** conformed a distorted octahedral environment, coordinated in the equatorial plane to the following atoms: the tertiary amine N3 (**BPMA** moiety), N4 and N5 (pyridine groups), and finally, O6 (acetate anion). Additionally, the O2 atom (bridged phenoxo group) is in the apical position, and the O8 atom (water molecule) appears near to the second apical position, completing the distorted elongated octahedral environment of Cu2.

In complex **6** three water molecules were highlighted in the asymmetric unit, which contribute to crystal stability by forming a hydrogen bonds network with the hydrazone group (N1 and O1) and the acetate ligands (O4 and O7) (Table 5.8).

The crystal structure was also stabilized by CH \cdots N6ⁱ and CH \cdots O3ⁱⁱ van der Waals interaction between the hydrogens of nearby molecules of the isoxazole group, with x, 1.5-y, -0.5+z and 1-x, -0.5+y, 0.5-z symmetry codes respectively.

Table 5.7. H-bond length (d, Å) for complex **3**.

| D-H...A | d(H...A) | d(D...A) |
|--------------|----------|----------|
| O5-H5A...O3 | 1.70 | 2.625(3) |
| O5-H5B...O11 | 1.65 | 2.613(4) |

Table 5.8. H-bond length (d, Å) for complex **6**.

| D-H...A | d(H...A) | d(D...A) |
|------------------------------|----------|-----------|
| O8-H8A...O9 ⁱ | 1.89 | 2.712(3) |
| O8-H8B...O7 | 1.95 | 2.733(3) |
| O9-H9D...O1 | 2.06 | 2.855(3) |
| O9-H9E...O10A | 1.98 | 2.720(4) |
| O9-H9E...O10B ⁱⁱ | 2.13 | 2.94(3) |
| O10A-H10C...N1 ⁱⁱ | 2.18 | 3.019(3) |
| O10A-H10D...O4 | 2.13 | 2.957(3) |
| O10B-H10F...N1 | 2.12 | 2.839(33) |

Symmetry codes: (i) $-1+x, y, z$ and (ii) $x, 1.5-y, 0.5+z$

Comparing **3** with **6**, some similarities were noticed: (i) both complexes presented two crystallographically independent metal sites occupied by copper atoms (Cu1 and Cu2) in asymmetric unit; (ii) the Cu1-Cu2 distances were constants in the two complexes; (iii) the isoxazole group was not involved in the copper coordination; and finally, (iv) both complexes presented one bridging phenoxo group. A second bridging interaction was also observed for complex **6**. Concerning the stabilities of the crystals, complex **6** was stabilized especially by hydrogen bonds, while **3**, by van der Waals interactions.

5.2.2.3

Vibrational properties of the compounds

The IR spectra in the solid state and KBr pellet of ligands **H₃L₃** (Figure 5.14) and **H₂L₄** (Figure 5.15) exhibit characteristic bands for phenol, amine and carbonyl groups near 3433 – 3444 cm⁻¹, 3140 cm⁻¹ and 1675 cm⁻¹ respectively. Some bands were assigned as follows for **H₃L₃**: 3440 w, br (ν OH), 3144 w, br (ν NH), 1673 s (ν C=O), 1615 m (ν C=N), 1593 s (δ NH), 1443 s, (ν N–C), 1350 m (δ OH), 1268 s (ν OCN), 1237 s (ν C–O), 1168 m (ν N–N), and **H₂L₄**: 3433 w, br (ν

OH), 3136 w, br (ν NH), 1676 s (ν C=O), 1617 m (ν C=N), 1592 s (δ NH), 1445 s, (ν N–C), 1352 m (δ OH), 1266 s (ν OCN), 1239 s (ν C–O), 1166 m (ν N–N).

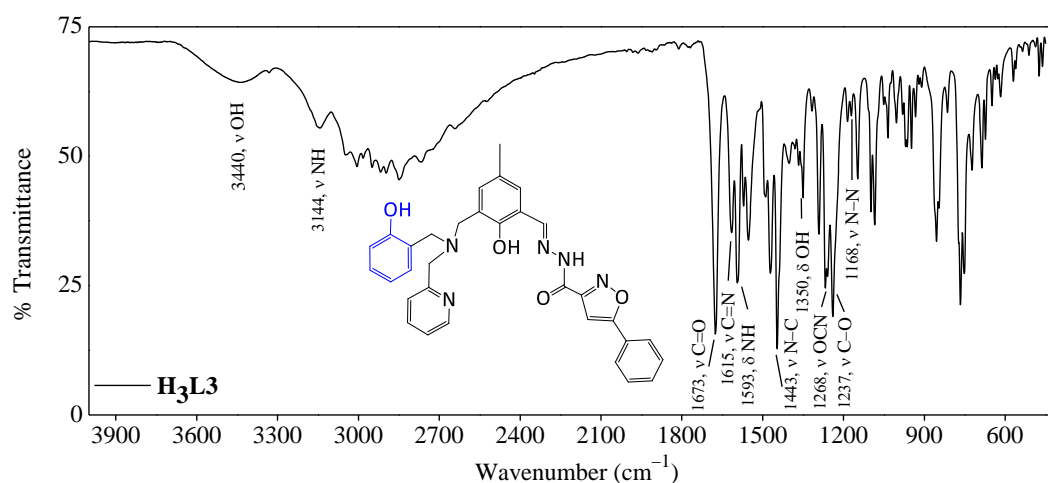


Figure 5.14. FTIR spectrum of **H₃L3** in KBr pellet and principal assignments.

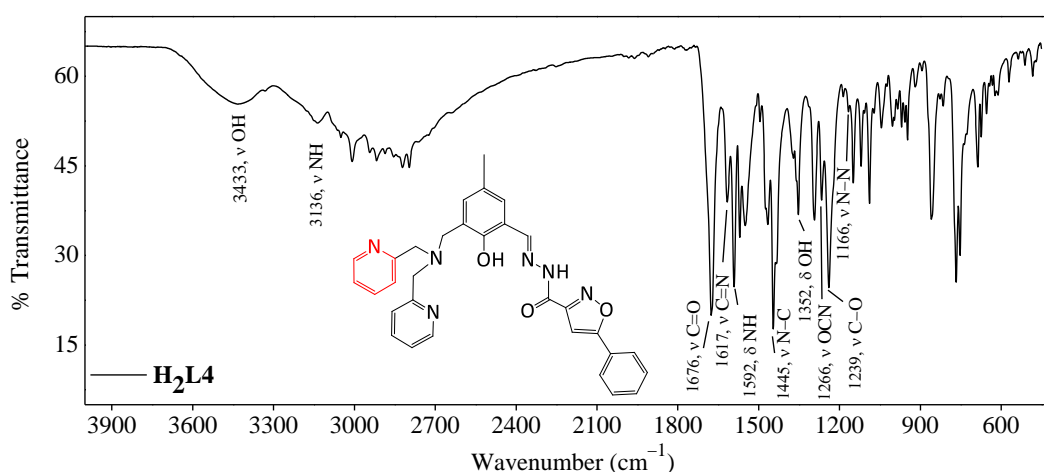


Figure 5.15. FTIR spectrum of **H₂L4** in KBr pellet and principal assignments.

The IR spectra of complexes **3–6** (Figure 5.16–5.19) show strong broad bands characteristic for OH from water near 3430 cm^{-1} . The corresponding bands for the amine (ν NH) and the carbonyl (ν C=O) groups present in the spectra of **H₃L3** and **H₂L4** disappear in the spectra of complexes **3**, **4** and **6**, suggesting coordination of the aroylhydrazone group in the iminolate form. Furthermore, the stretching C–O bands in the spectra of the ligands near $\sim 1235\text{ cm}^{-1}$ shifted to $\sim 1285\text{ cm}^{-1}$ in the spectra of the complexes ($\sim 50\text{ cm}^{-1}$).

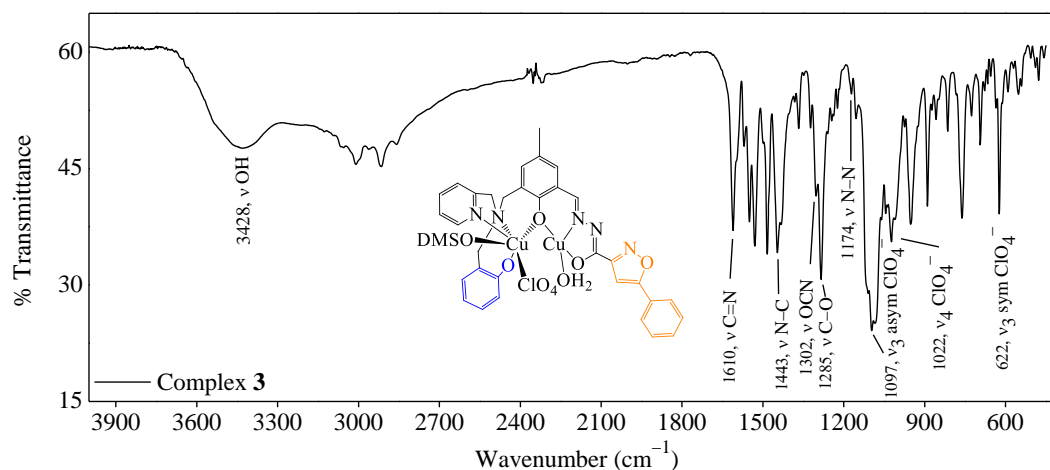


Figure 5.16. FTIR spectrum of complex **3** in KBr pellet and principal assignments.

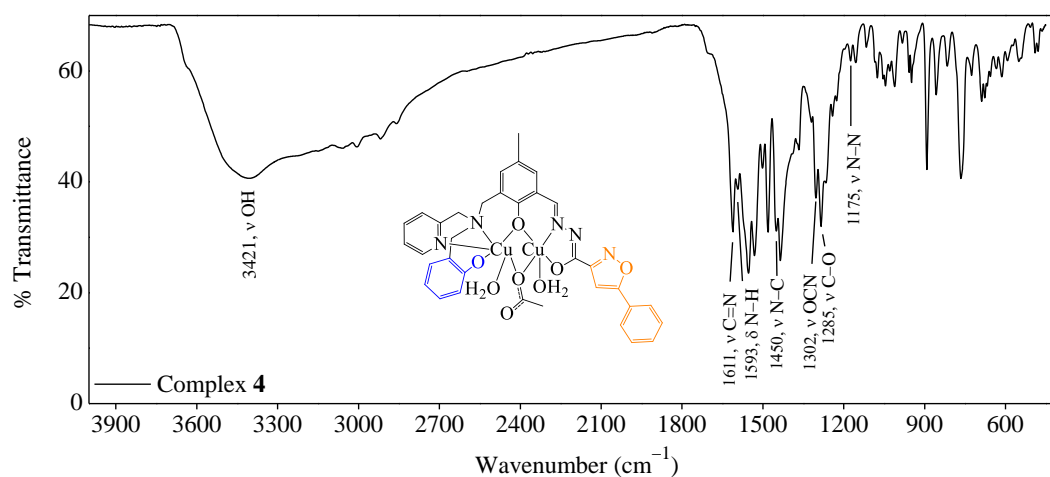


Figure 5.17. FTIR spectrum of complex **4** in KBr pellet and principal assignments.

Taking into account the elemental analysis and molar conductivity of complex **4**, the hydrogen hydrazone group (NH) seemed to be conserved in the complex. The characteristic Schiff base azomethine group bands in the IR spectra of the complexes and ligands [185] are located near 1610 cm^{-1} .

Additionally, the IR spectra of complexes **3** and **5** present strong bands characteristic of coordinated ClO_4^- group, corresponding to antisymmetric ν_3 and symmetric ν_3 , and ν_4 modes [186]. The latter bands are located at 1097 cm^{-1} , 1022 cm^{-1} and 622 cm^{-1} , respectively, in the spectrum of complex **3**, and at 1108 cm^{-1} , 1031 cm^{-1} and 625 cm^{-1} in that of complex **5**. The presence of the perchlorate bands confirms the coordination of the perchlorate ion ($\text{Cu}-\text{ClO}_4$).

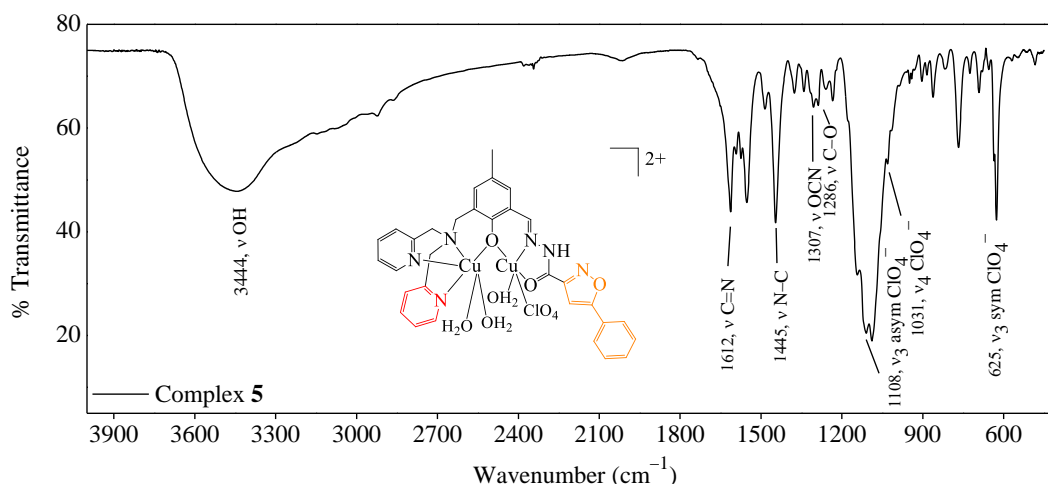


Figure 5.18. FTIR spectrum of complex **5** in KBr pellet and principal assignments.

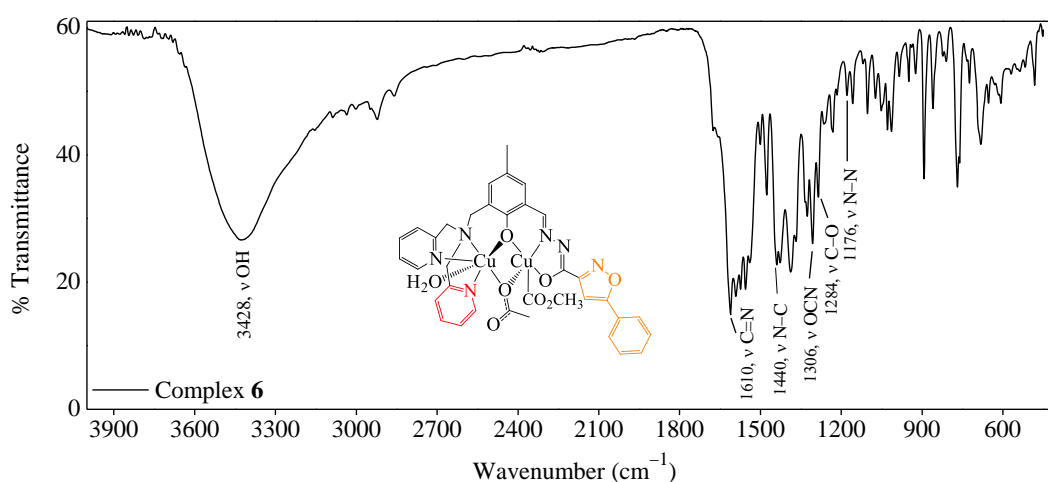


Figure 5.19. FTIR spectrum of complex **6** in KBr pellet and principal assignments.

Principal bands were assigned as follows for the complexes:

Complex 3: 3428 m, br (ν OH), 1610 m (ν C=N), 1443 m, (ν N-C), 1302 m, sh (ν OCN), 1285 s (ν C-O), 1174 w (ν N-N), 1097 s (ν_3 asym ClO_4^-), 1022 m (ν_4 ClO_4^-), 622 m (ν_3 sym ClO_4^-).

Complex 4: FTIR (KBr, cm^{-1}): 3421 m, br (ν OH), 1611 m (ν C=N), 1593 w (δ NH), 1450 m, sh (ν N-C), 1302 w, (ν OCN), 1285 m (ν C-O), 1175 w (ν N-N).

Complex 5: 3444 m, br (ν OH), 1612 m (ν C=N), 1593 w (δ NH), 1445 m, (ν N-C), 1261 w, sh (ν OCN), 1286 s (ν C-O), 1108 s (ν_3 asym ClO_4^-), 1031 m, sh (ν_4 ClO_4^-), 625 m (ν_3 sym ClO_4^-).

Complex 6: FTIR (KBr, cm^{-1}): 3428 m, br (ν OH), 1610 m (ν C=N), 1440 m, sh (ν N-C), 1306 m, (ν OCN), 1284 m (ν C-O), 1176 w (ν N-N).

5.2.2.5

Absorption spectroscopic studies of the compounds

The electronic spectra of the complexes and ligands (at a 5 – 50 μM) in $\text{H}_2\text{O}/\text{DMSO}$ 9:1 (ν/ν) show five absorption bands in the 230–500 nm region (Figures 5.20 and 5.21). In the spectrum of ligand **H₃L3**, absorption bands associated with **HBPAMFF** moiety are located at 343 nm (broad) and 262 nm (shoulder).

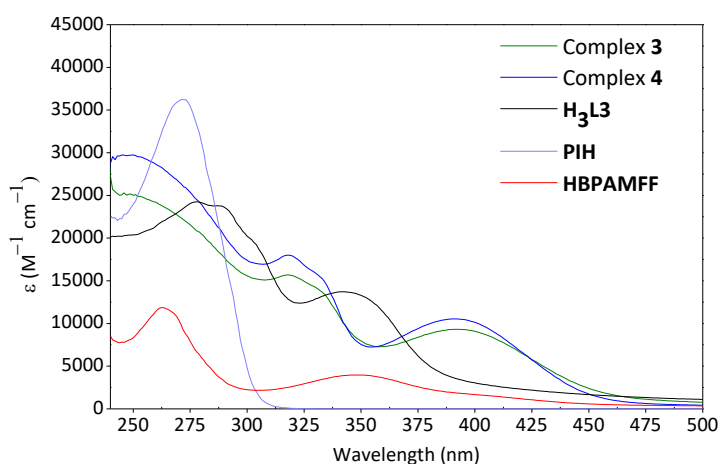


Figure 5.20. Absorption spectra of ligand **H₃L3**, the corresponding dicopper complexes **3** and **4** and precursors **HBPAMFF** and **PIH** in $\text{H}_2\text{O}/\text{DMSO}$ 9:1.

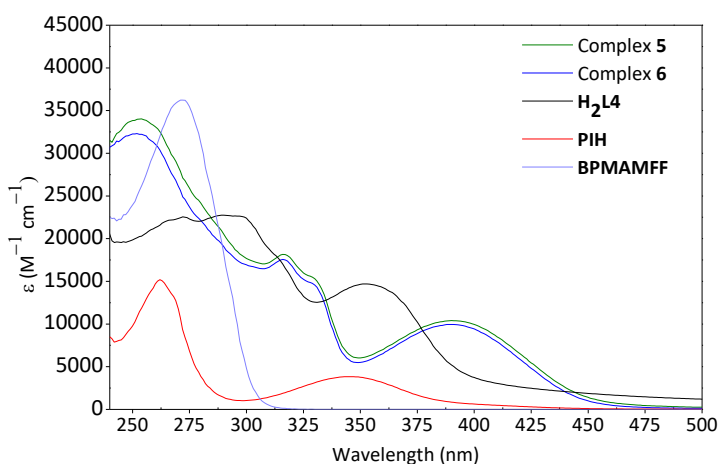


Figure 5.21. Absorption spectra of ligand **H₂L4**, the corresponding dicopper complexes **5** and **6** and precursors **BPMAMFF** and **PIH** in $\text{H}_2\text{O}/\text{DMSO}$ 9:1 at 25 °C.

The band assigned to the **PIH** hydrazide pendant arm is observed at 278 nm. Finally, two bands completely absent in the precursors, appeared in the **H₃L₃** absorption spectrum (Figure 5.20).

Consequently, the latter bands were assigned to the aroylhydrazone electronic transitions [CO–NH–N=N] and are located at 301 and 290 nm. In the absorption spectrum of complex **3**, the **HBPAMFF** moiety absorption redshifted from 343 nm to 392 nm. This change was attributed to the deprotonation and coordination of the phenol and pyridine groups in the **HBPAMFF** moiety with copper ions. The absorption band in the spectrum of complex **3** corresponding to **PIH** (at 278 nm in **H₃L₃**) and **HBPAMFF** (at 262 nm in **H₃L₃**) moieties appeared as shoulders in the 280–247 nm region. Finally, the aroylhydrazone electronic transitions in complex **3** redshifted to 334 and 318 nm, suggesting coordination with copper ions.

Table 5.9. UV/Vis absorption properties of ligands **H₃L₃** and **H₃L₄** and dicopper(II) complexes **1–4** in H₂O/DMSO 9:1 in the range 230 – 500 nm, or in DMSO in the range 500 – 900 nm at 25 °C, and suggested assignments.

| Ligands | | | | | | | | Assignment |
|-----------------------------------|--------------|-----------------------------------|--------------|----------------|--------------|----------------|--------------|-----------------------------------|
| H₃L₃ | | H₂L₄ | | | | | | |
| λ (nm) | ϵ^* | λ (nm) | ϵ^* | | | | | |
| 343 | 14000 | 353 | 15800 | | | | | HBPAMFF rings |
| 301 | 20300 | 314 | 18800 | | | | | CO–NH–N=N |
| 290 | 23700 | 299 | 23300 | | | | | CO–NH–N=N |
| 278(sh) | 24200 | 273(sh) | 23000 | | | | | PIH rings |
| 262 | 21800 | 260 | 21600 | | | | | HBPAMFF rings |
| Complexes | | | | | | | | Assignment |
| 3 | | 4 | | 5 | | 6 | | |
| λ (nm) | ϵ^* | λ (nm) | ϵ^* | λ (nm) | ϵ^* | λ (nm) | ϵ^* | |
| 676 | 95 | 679 | 97 | 675 | 110 | 672 | 102 | <i>d–d</i> transition |
| 392 | 9500 | 390 | 12000 | 392 | 10700 | 390 | 10300 | HBPAMFF rings |
| 334 | 13700 | 330 | 15000 | 334 | 14000 | 330 | 15000 | CO–NH–N=N |
| 318 | 16400 | 317 | 18000 | 318 | 18600 | 317 | 18000 | CO–NH–N=N |
| 280(sh) | 21800 | 280(sh) | 22500 | 280(sh) | 25000 | 280(sh) | 22800 | PIH / HBPAMFF rings |
| 247 | 26800 | 253 | 30000 | 247 | 34500 | 253 | 33200 | |

* M⁻¹ cm⁻¹

The electronic absorption spectrum of **H₂L4** presents similar bands comparing to **H₃L3** (Figure 5.21). Complex **5** prepared with **H₂L4** and copper(II) perchlorate salt has a similar spectrum to complex **3** (Figures 5.20 and 5.21). Nevertheless, all four copper(II) complexes showed an almost identical absorption profile in the $\lambda = 230\text{--}500$ nm region. All molar extinction coefficients of complexes and ligands in H₂O/DMSO 9:1, are given in Table 5.9.

Additionally, in DMSO (at 1 – 5 mM), the electronic spectra of copper complexes present a broad and weak absorption band centered at 676 nm ($\epsilon = 95 \text{ M}^{-1} \text{ cm}^{-1}$) for **3**, at 679 nm ($\epsilon = 97 \text{ M}^{-1} \text{ cm}^{-1}$) for **4**, at 675 nm ($\epsilon = 110 \text{ M}^{-1} \text{ cm}^{-1}$) for **5**, and at 672 nm ($\epsilon = 102 \text{ M}^{-1} \text{ cm}^{-1}$) for **6** (Figure 5.22). These bands are attributed to *d–d* transitions between the electronic states of the copper centres [187, 188]. The *d–d* transition bands of the complexes were examined in DMSO due to the low solubility of the compounds at the tested concentration in H₂O/DMSO 9:1 medium.

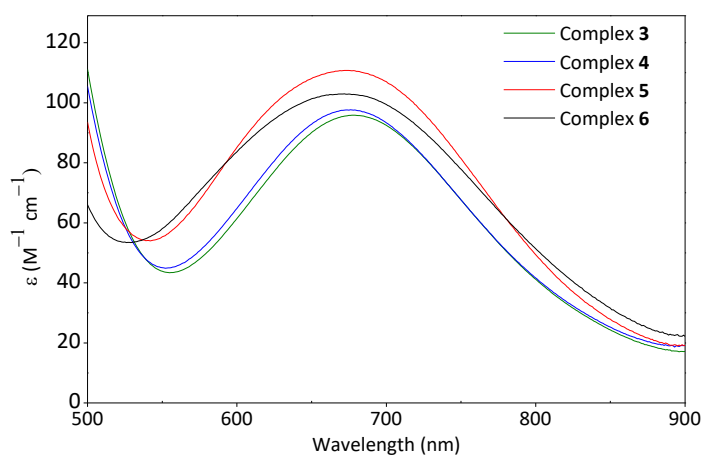


Figure 5.22. Visible spectra of complexes **3–6** in DMSO at 25 °C in the 500–900 nm region.

5.2.3

Stability studies in DMSO and PBS

Prior to exploring their potential application as anticancer drugs, the stability of complexes **3–6** in relevant temperature and cellular medium was explored (37 °C, pH 7.4). Absorption experiments were performed to test the stability of the compounds in pure DMSO and PBS/DMSO 99:1 (v/v) mixture. Absorption spectra of the compounds at a 1×10^{-5} M in DMSO revealed

insignificant variations during incubation times of 24 h at room temperature (Figure 5.23). After 24 h, perchlorate complexes **3** and **5** presented the highest stabilities in DMSO, with residual concentration corresponding to 95% of the initial concentration, C_0 , while the residual concentration of ligands was equal to 93% of C_0 on average.

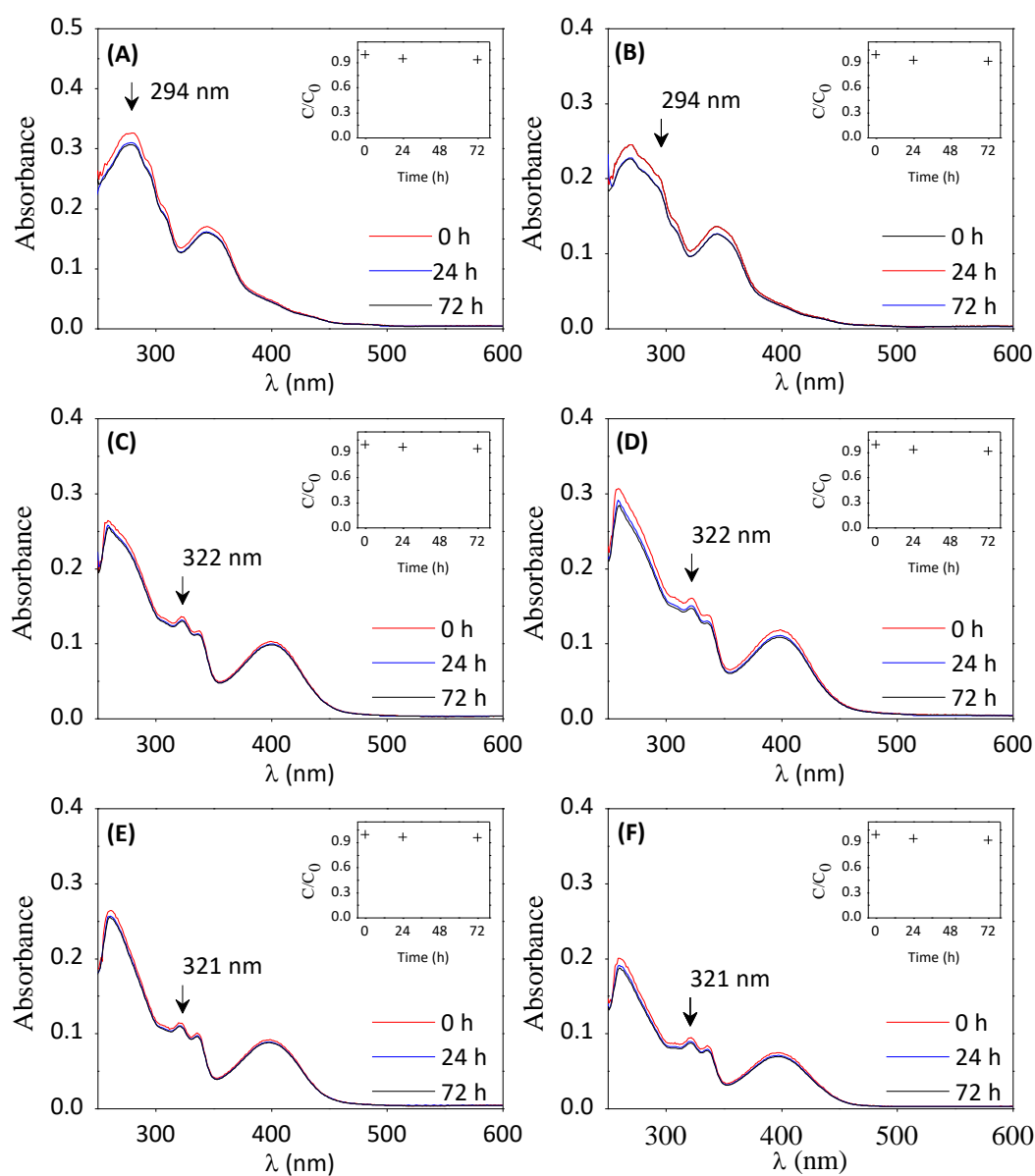


Figure 5.23. Absorption spectra of ligands (A) **H₃L₃** and (B) **H₂L₄**, and complexes (C) **3**, (D) **4**, (E) **5** and (F) **6**, incubated for up to 72 h at room temperature. Concentration = 1×10^{-5} M in DMSO. Inset: C/C_0 versus time at wavelengths: 294 nm (A), 294 nm (B), 322 nm (C), 322 nm (D), 321 nm (E), and 321 nm (F).

The compounds were also incubated in PBS/DMSO 99:1 at 37°C for 72 h, and significant changes were observed in their absorption spectra (Figure 5.24). During the first hours (1 – 6 h and 24 h), the spectra of complexes and ligands presented similar behaviour in the tested conditions (Figure 5.24). After 24 h, the average concentration of the compounds in the solution was 55% of C_0 . After 72 h, the complexes were reasonably more stable than the ligands, the calculated average concentrations was 36% of C_0 for the complexes and 12% and 5% C_0 for ligands **H₃L3** and **H₂L4** respectively.

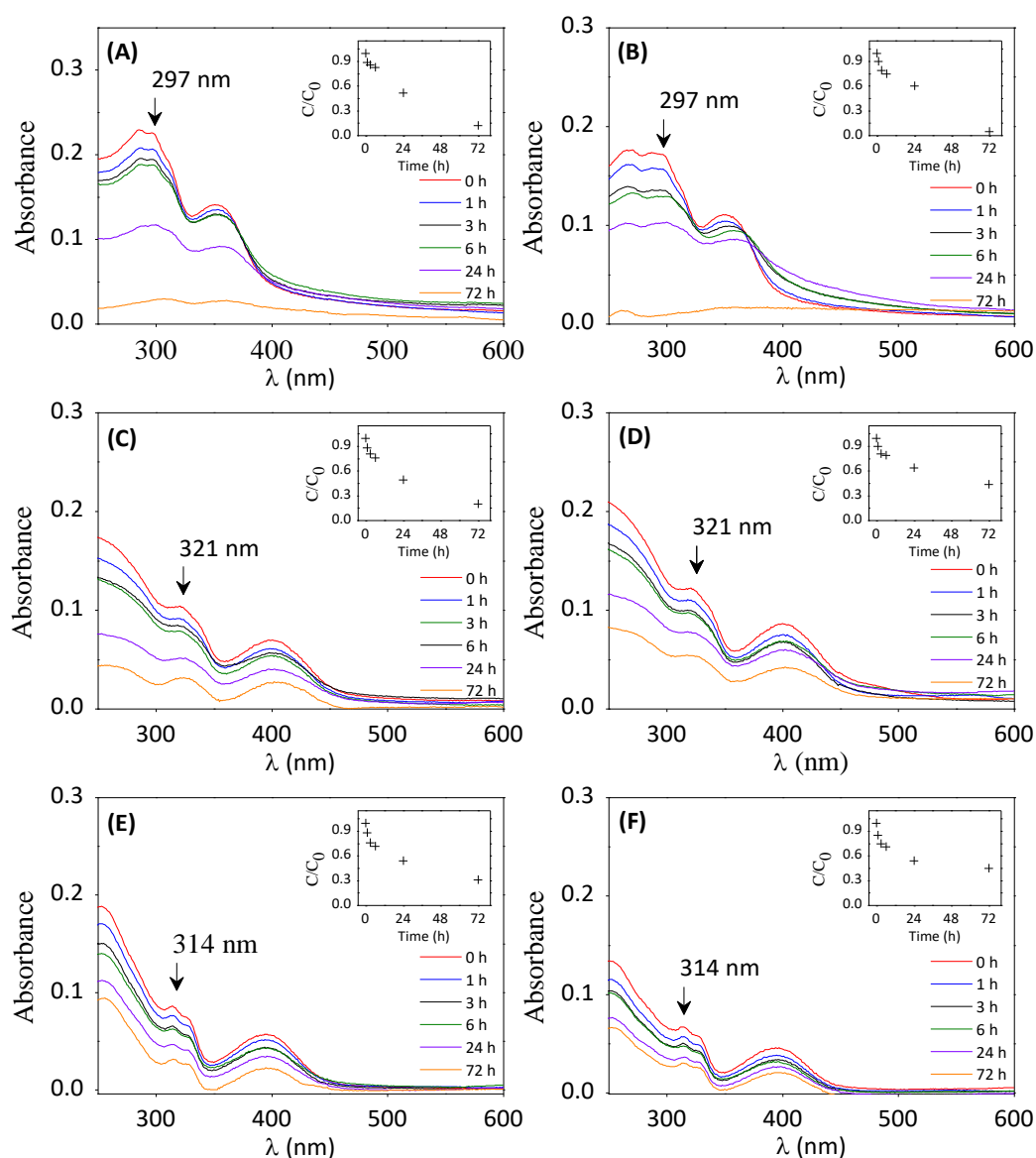


Figure 5.24. Absorption spectra of ligands (A) **H₃L3** and (B) **H₂L4**, and complexes (C) **3**, (D) **4**, (E) **5** and (F) **6** incubated for up to 72 h at 37°C. Concentration = 1×10^{-5} M in PBS/DMSO 99:1. *Inset*: C/C_0 versus time at wavelengths: 297 nm (A), 297 nm (B), 321 nm (C), 321 nm (D), 314 nm (E), and 314 nm (F).

Hydrazone derivatives can be hydrolysed in water solution to carbonyl and hydrazide precursors [189]. When hydrazones are involved in metal complexation, the hydrolysis process is prevented due to the involvement of the azomethine nitrogen in coordination. Hydrolytic reactions can explain why ligands are less stable than complexes in aqueous medium. Nevertheless, it is important to notice that free hydrazone precursor **PIH** presented an absorption band at $\lambda = 271$ nm with higher molar extinction coefficient than the absorption bands in the ligand and complex spectra and with time, any absorption bands from ligands or complexes presented a hypochromic effect, saving conclusion concerning the hydrolysis of the compounds and formation of free **PIH**. The observed result suggests that precipitation is the dominant process responsible for the hypochromism observed of the absorption spectrum of the compound. On the other hand, in the solid state, both ligands and complexes are stable for months.

5.2.4

Absorption and fluorescent ct-DNA interaction studies

Since DNA replication plays an important role in cancer cell proliferations, the DNA interaction of a large number of ligands and copper complexes was explored as a proposed cell death mechanism [17-20, 32-40]. The present work includes the evaluation of the *in-vitro* DNA interaction of synthesized free ligands and their dicopper(II) complexes. For that, absorption and fluorescence spectroscopies was used to elucidate binding affinity and interaction mode of the compounds with ct-DNA.

5.2.4.1

Absorption ct-DNA interaction studies

Figure 5.25 shows the significant spectral changes upon addition of ct-DNA to the ligand and complex solutions. It is observed that upon DNA addition, the absorption bands show a hypochromic effect (Table 5.10) more marked for the hydrazones bands (near to 296 nm in ligands and 315 nm in complexes), but also for the **HABPAMFF** or **BPMAMFF** bands.

In general, the hypochromism was more remarkable for **HBPAMFF** derivatives **H₃L3**, complex **3** and **4**, up to 43%. The decrease of the absorbance of the compounds caused by ct-DNA was accompanied by a slightly redshift displacement of the bands. The red shift was more pronounced in the case of the absorption bands associated to the **HBPAMFF** or **BPMAMFF** moieties, near to 350 nm for ligands and near to 390 nm for complexes (Table 5.10). The hypochromism and redshift in the absorption spectra are associated to the intercalation of the compounds to DNA base pairs in the stacking mode. In contrary, the hyperchromism in the absorbance indicates minor groove binding [190].

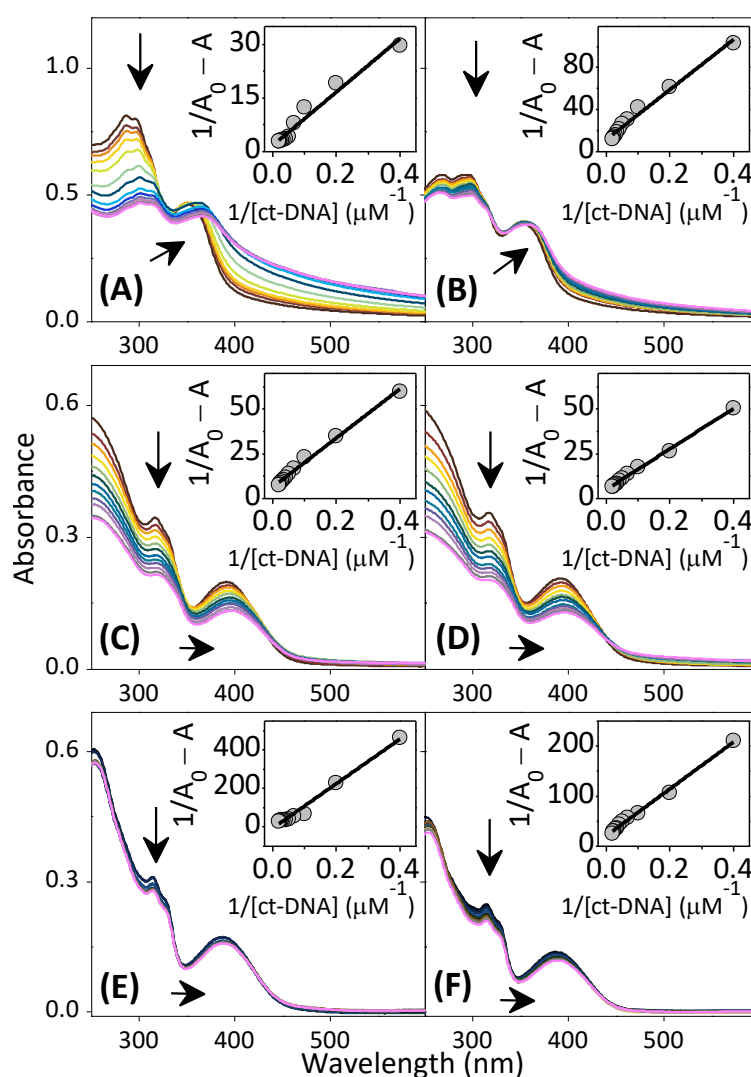


Figure 5.25. Absorption spectra of ligands (A) **H₃L3**; (B) **H₂L4** and complexes (C) **3**; (D) **4**; (E) **5**; and (F) **6** at a 2.5×10^{-5} M alone or with increasing concentration of ct-DNA (arrow, $0 - 5 \times 10^{-5}$ M) in PBS/DMSO 9:1 at 25°C. Inset: Plot of $1/A_0 - A$ versus $1/[ct-DNA]$ and its linear fit.

Benesi-Hildebrand equation (Equation 5.1) [191] with the modified approach of Equation 5.2.

$$[\text{DNA}]/(\varepsilon_a - \varepsilon_f) = [\text{DNA}]/(\varepsilon_b - \varepsilon_f) + 1/K_b(\varepsilon_b - \varepsilon_f) \quad (\text{Eq 5.1})$$

where, ε_a = absorbance value observed divided by the concentration of the compound ($A_{\text{obs}}/[\text{compound}]$), ε_f = extinction coefficient of the free compound; ε_b = extinction coefficient of compound when fully bound to DNA; $[\text{DNA}]$ = concentration of added DNA; and K_b = binding constant.

Modified Benesi-Hildebrand equation (Equation 5.2) [171, 172] was used to estimate the compound-DNA binding constants:

$$1/(A_0 - A) = [1/(\varepsilon_b - \varepsilon_f) \cdot 1/[\text{compound}]_0] + [1/K_b(\varepsilon_b - \varepsilon_f) \cdot 1/[\text{compound}]_0 \cdot 1/[\text{DNA}]] \quad (\text{Eq 5.2})$$

The calculated K_b values (Table 5.10) reveal a similar interaction of the ligand **H₃L₃** ($4.82 \times 10^4 \text{ M}^{-1}$) and complexes **3** ($4.68 \times 10^4 \text{ M}^{-1}$) and **4** ($4.75 \times 10^4 \text{ M}^{-1}$), which contain in their structure a phenol group than the ligand **H₂L₄** and complexes **5** and **6** with a pyridine group arm.

Table 5.10. Absorption features of the interaction of ligands **H₃L₃** and **H₂L₄** and their copper(II) complexes **3–6** with ct-DNA.

| Compound | Band [A/A ₀ (%), $\Delta\lambda$ (nm)] ^[a] | K_b ($\times 10^4 \text{ M}^{-1}$) ^[b] |
|-----------------------------------|--|---|
| H₃L₃ | 296 [43, 4]; 351 [12, 13] | (4.8 ± 0.1) |
| H₂L₄ | 296 [14, 2]; 353 [2, 5] | (4.5 ± 0.1) |
| 3 | 316 [38, 2]; 391 [34, 5] | (4.7 ± 0.1) |
| 4 | 316 [43, 2]; 391 [38, 5] | (4.8 ± 0.1) |
| 5 | 314 [10, 2]; 388 [8, 5] | (2.1 ± 0.1) |
| 6 | 314 [16, 2]; 388 [15, 5] | (4.4 ± 0.1) |

[a] Hypochromism and λ red shift. [b] (mean ± S.D).

The obtained binding constants are larger (of the order of $\sim 10^1 \text{ M}^{-1}$ or $\sim 10^2 \text{ M}^{-1}$) than those reported for other hydrazone ligands [127, 192] and comparable

with those reported for other copper(II) complexes [153, 190, 193]. In brief, the hypochromism and redshift of the ligands and complexes solutions upon DNA titration suggests that these compounds interact with DNA via intercalation. This result was expected due to the planar nature of the molecules of the isoxazole-arylohydrazone moiety of the ligands and their copper(II) complexes. In general, the hypochromism was less pronounced for the **BPMAMFF** derivatives (ligand **H₂L4** and complexes **5** and **6**), and the calculated K_b values for the ligands and complexes were smaller than the binding constant for the conventional DNA intercalator ethidium bromide, EB, using absorbance titration (of the order of $\sim 10^5 \text{ M}^{-1}$) [194]. Therefore, fluorescence spectroscopy was used to better clarify the possible interaction mode of the synthesized compounds with DNA.

5.2.4.2

Fluorescence ct-DNA interaction studies

Both ligands presented a fluorescence emission band ($\lambda_{\text{exit}} = 350 \text{ nm}$), at 530 nm in the spectrum of **H₃L3** and at 503 nm, in the spectrum of **H₂L4** in the tested conditions. In order to study their affinity and interaction mode with DNA, their fluorescence band was monitored during titration with ct-DNA. In the emission spectra of the ligands, fluorescence emission is observed to decrease without wavelength shift when the concentration of ct-DNA increases in the solutions (Figure 5.26, A and B). The quenching emission $\Delta I/I_0$ of the bands caused by the DNA was up to 19% (Table 5.11 and Figure 5.27, A and B).

The “inner filter effect” was corrected to the fluorescence measurement. For that Equation 5.3 [161] was used, which is limited to solutions with absorption lower than 0.3 and measured in a 1.0 cm pathlength cuvette.

$$F_{\text{corr}} = F_{\text{obs}} \cdot \text{antilog} [(A_{\text{ex}} + A_{\text{em}})/2] \quad (\text{Eq 5.3})$$

where, F_{corr} = corrected and measured fluorescence intensity; F_{obs} = measured fluorescence intensity; A_{ex} = UV/Vis absorption value at the excitation wavelength used in the fluorescence measurements; and A_{em} = the absorbance in the emission wavelength.

Scatchard equation (Equation 5.4) [163] was used to calculate the ct-DNA-compound number of active sites (n) the binding constants (K_{b2}).

$$\log[(I_0 - I)/I] = \log K_{b2} + n \log[Q] \quad (\text{Eq 5.4})$$

where, K_b = ct-DNA binding constant and corresponds to the intercept in the equation, and n = the number of binding site and correspond to the slopes.

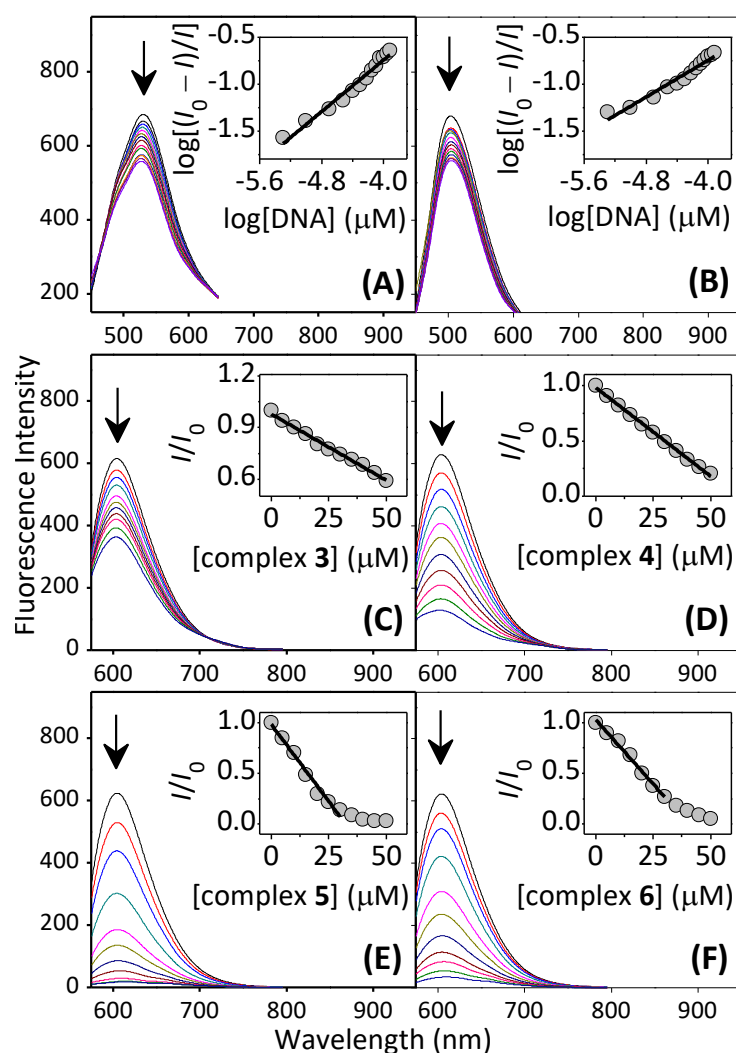


Figure 5.26. Fluorescence emission spectra in PBS/DMSO 99:1 at 25°C of ligands (A) **H₃L₃** and (B) **H₂L₄** (5 μM, $\lambda_{\text{exit}} = 350$ nm) alone or in the presence of ct-DNA (arrow, 0 – 120 μM). Inset: plot of $\log[(I_0 - I)/I]$ versus $\log[\text{ct-DNA}]$; and of a EB–DNA solution (EB = 5 μM and ct-DNA = 10×10^{-6} M, $\lambda_{\text{exit}} = 555$ nm) alone or in the presence (arrow, 0 – 50 μM) of complexes (C) **3**; (D) **4**; (E) **5**; and (F) **6**. Inset: plot of I/I_0 versus [complex] and its linear fit.

K_{b2} of ligand **H₃L₃** was higher than **H₂L₄**, and dramatically lower than that observed for the classic DNA intercalator, ethidium bromide EB ($\sim 10^7 \text{ M}^{-1}$). The calculated number of active sites, suggests that one ligand molecule interacts with one nucleic acid from the DNA.

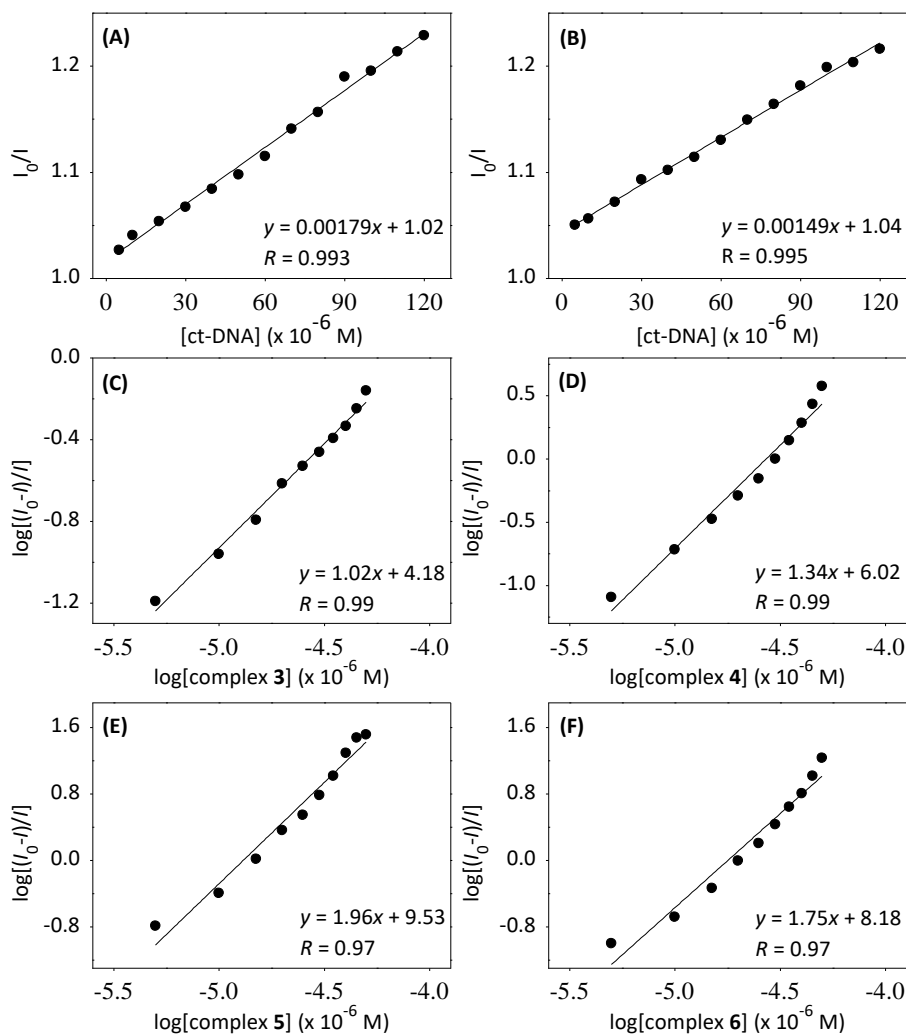


Figure 5.27. Stern-Volmer plots of I_0/I against the concentration of DNA for the interaction with ligands (A) **H₃L₃** and (B) **H₃L₄**, and plots of $\log[(I_0 - I)/I]$ versus $\log [Q]$ for the interaction of DNA with complexes (C) **3**, (D) **4**, (E) **5** and (F) **6**.

On the contrary, copper(II) complexes do not display fluorescence emission in the analysed spectral range. Therefore, their interaction with DNA was indirectly examined through EB displacement assays. Hence, the fluorescence emission ($\lambda_{\text{exit}} = 555 \text{ nm}$) of a EB–DNA complex solution was monitored in the absence and presence of the synthesized complexes.

Figure 5.26 (C–F) shows the changes in the quenching emission band ($\lambda_{\text{emis}} = 604 \text{ nm}$) upon each incremental addition of the copper complexes to the EB–DNA system. The evident hypochromism (without shift) was more intense in the case of complexes **5** and **6**, up to on average 96% (Table 5.11). Free EB, DNA and the dicopper(II) complex solutions are independently not fluorescent in the range and conditions tested. Consequently, the decreasing of the initial emission intensity of EB–DNA solution (the fluorescent system) is related to the replacement of EB from the ct-DNA caused by the complexes intercalation between the base pairs of the DNA sequence.

Table 5.11. Fluorescence features of the interaction of ligands **H₃L3** and **H₂L4** and their copper(II) complexes **3–6** with ct-DNA.

| Compound | I/I_0 (%) ^[c] | K_s (M^{-1}) ^[b] | K_{app} or K_{b2} (M^{-1}) ^[b, d] | n |
|------------------------|----------------------------|--|---|-----|
| H₃L3 | 19 | – | $(1.0 \pm 0.2) \times 10^2$ | 0.6 |
| H₂L4 | 18 | – | $(1.7 \pm 0.1) \times 10^1$ | 0.5 |
| 3 | 41 | $(2.7 \pm 0.1) \times 10^4$ | $(7.9 \pm 0.1) \times 10^5$ | 1.0 |
| 4 | 79 | $(9.9 \pm 0.1) \times 10^4$ | $(1.7 \pm 0.1) \times 10^6$ | 1.3 |
| 5 | 97 | $(7.5 \pm 0.1) \times 10^5$ | $(3.2 \pm 0.1) \times 10^6$ | 2.0 |
| 6 | 95 | $(3.2 \pm 0.1) \times 10^5$ | $(2.7 \pm 0.1) \times 10^6$ | 1.8 |

[b] (mean \pm S.D). [c] Fluorescence quenching. [d] K_{app} (for complex), K_{b2} (for ligand).

The binding constants of the complexes with DNA (K_{app}) were calculated indirectly from the binding constant of EB ($K_{\text{EB}} = 1.0 \times 10^7 \text{ M}^{-1}$), using the equation $K_{\text{EB}} \times [\text{EB}] = K_{\text{app}} \times [\text{complex}]$. In the equation [EB] refers to the concentration of EB (5 μM) and [complex] represents the concentration of the complexes when the initial fluorescence emission intensity of EB–DNA system is reduced by 50% [190]. In brief, K_{app} values when the complexes displaced 50% of EB were in the 10^6 M^{-1} , in the decreasing sequence: complexes **5** > **6** > **4** > **3** (Table 5.11). The found values are comparable with other dinuclear copper(II) complexes which mimic bioactive sites [88]. Additionally, using the suppression-equation (also known as Stern-Volmer equation) (Equation 5.5) [132] the ct-DNA quenching rate constants (K_q) were calculated using 23 ns [133] as average intrinsic lifetime (τ_0) of ct-DNA in the absence of quencher EB and the suppression-constant for ct-DNA-complexes formation (K_s).

$$I_0/I = 1 + K_s[Q] = 1 + K_q\tau_0[Q] \quad (\text{Eq 5.5})$$

K_q values were $2.67 \times 10^{12} \text{ M}^{-1} \text{ s}^{-1}$, $9.92 \times 10^{12} \text{ M}^{-1} \text{ s}^{-1}$, $7.49 \times 10^{13} \text{ M}^{-1} \text{ s}^{-1}$, $3.19 \times 10^{13} \text{ M}^{-1} \text{ s}^{-1}$ for complexes **3**, **4**, **5** and **6** respectively. It must be noted that, the calculated quenching rate constants are in the order of 10^2 or 10^3 higher than the maximum K_q of a pure dynamic quenching mechanism for diffusion-controlled ($2.0 \times 10^{10} \text{ M}^{-1} \text{ s}^{-1}$) [160]. Then, the found K_q indicate that in the displacement of EB from DNA by the complexes a static quenching mechanism is mainly involved. The calculated suppression-constants for the titration of EB–DNA system with the complexes are shown in Table 5.11. A comparisons of the binding constants (Table 5.11) of the ligands (K_{b2}) and complexes (K_{app}) with ct-DNA obtained through EB displacement assay, reveals a higher ability of the copper complexes (up to five orders of magnitude) to interact with the adjacent nucleic acid from DNA than the metal-free ligands. This result can be associated to the inclusion of the Cu(II)-Cu(II) system and atoms donor coordination similar to the active site of metalloenzymes as tyrosine, PAPs and COs, in the design of the complexes. For example, previous copper(II) complexes with the active site of COs exhibited phosphate diester hydrolysis activity [96], probably involving terminal coordination [97, 98]. The ability of the complexes containing COs-design to interact with phosphate groups suggests a better affinity of the compounds with the phosphate groups in the DNA sequence, explaining the larger binding constants found for complexes than ligands.

The number of active sites (Equation 5.4 [163]; Figure 5.27, C–F) was higher for complexes ($n = 1$ or 2) than for ligands ($n = 0.5$). Finally, taking into account the results obtained from both absorption and fluorescence spectroscopic techniques, it is possible to conclude that the intercalation mode is evidently more pronounced in the complexes-DNA interaction, while the interaction of ligands with the DNA base pair is dominated by non-intercalative interactions.

5.2.5

***In vitro* cytotoxic activity**

The investigation of the cytotoxic effect of the designed ligands and their respective copper(II) complexes (two for each ligand) was one of the main goals of the current work. In this respect, three comparisons have been made:

First, was intended to compare structurally similar ligands, only differing by one of their aromatic rings, with a phenol for **H₃L3** and a pyridine for **H₂L4**. Second, was also intended to compare dicopper(II) complexes differing by their first coordination sphere obtained by treating the ligands with copper(II) perchlorate hexahydrate (complexes **3** and **5**) or copper(II) acetate monohydrate (complexes **4** and **6**). Third, was intended to compare the cytotoxicity of the copper(II) complexes with their respective metal-free carbohydrazone ligands.

Cytotoxicity studies were carried out on the cultured human epithelial breast cancer cell line, MDA-MB-231. Cells were exposed to medium containing different concentrations of each ligand or copper(II) complex continuously for 72 h. Cytotoxicity was evaluated as the ability of the compounds to inhibit cell growth using the MTT assay [135]. The concentration dependence on cell viability can be observed in Figure 5.28 and 5.29. Figures demonstrate that, in general, when the concentration of the compounds increases, the percentage of cell viability progressively decreases (a concentration-dependent effect).

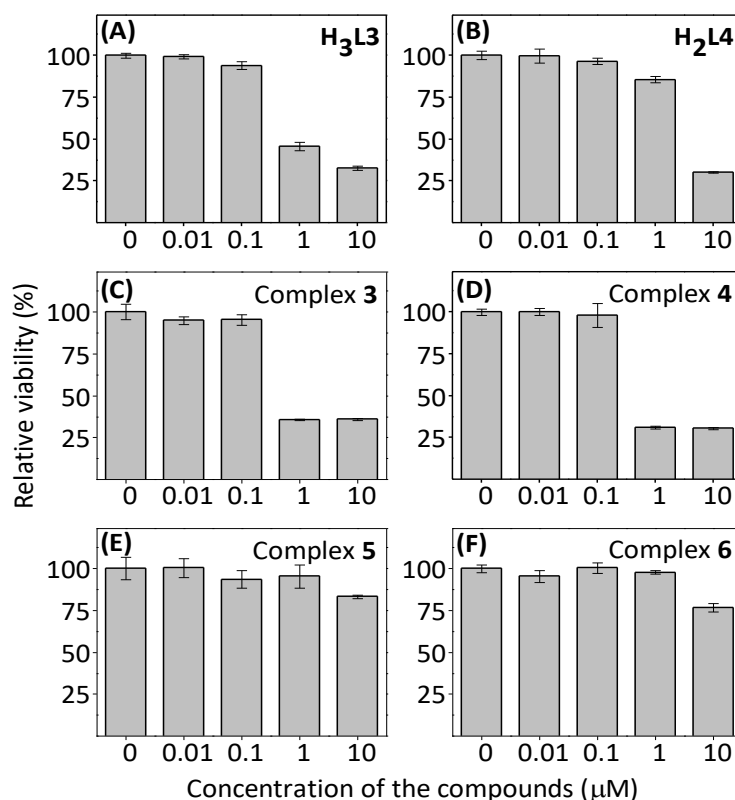


Figure 5.28 Dose-dependent effect expressed as the percentage of relative viability of MDA-MB-231 cells measured by the MTT assay for (A) **H₃L3**; (B) **H₂L4**; (C) **3**; (D) **4**; (E) **5**; and (F) **6** after 72 h incubation at 37 °C. Data represent the mean of triplicate experiments.

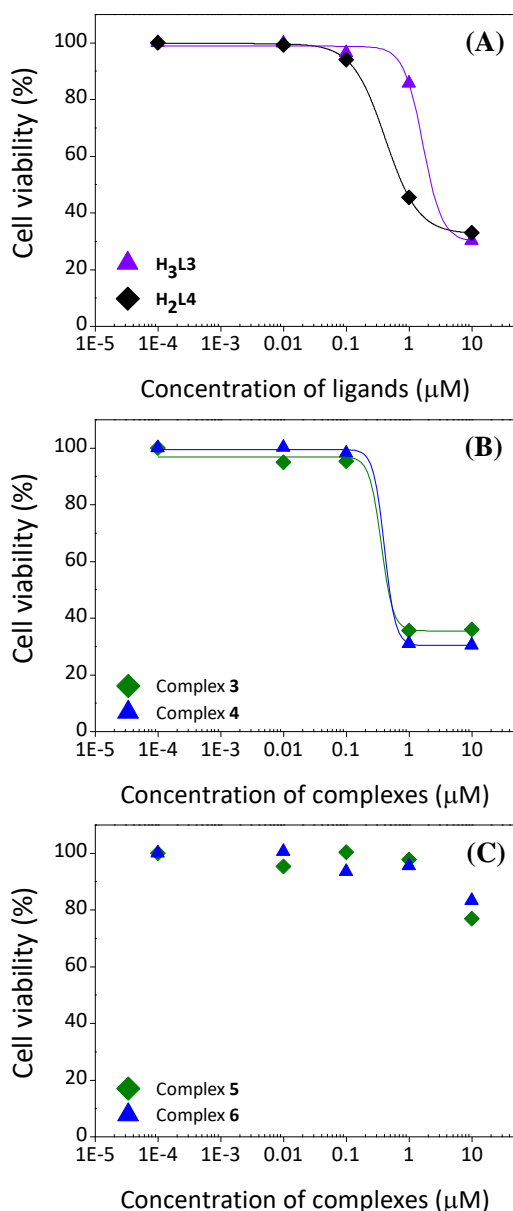


Figure 5.29. Dose-dependent effect on MDA-MB-231 cells of ligands (A) and copper(II) complexes (B and C) after 72 h at 37 °C using the MTT assay.

5.2.5.1

Double-pyridine (BPMAMFF) or phenol-pyridine (HBPAMFF) fragment

As depicted in Table 5.12, compounds based on the phenol-pyridine precursor **HBPAMFF** exhibited considerably higher cytotoxicity on MDA-MB-231 cells. The IC_{50} of compounds **H₃L₃**, **3** and **4** were in the submicromolar range, while **BPMAMFF**-derived compounds displayed a micromolar potency towards the tested cell line. This clearly implies that **H₃L₃** substantially affected

proliferation more efficiently than **H₂L4**, and complexes **3** and **4** more efficiently than **5** and **6**.

Table 5.12. IC₅₀ values of the ligands **H₃L3** and **H₂L4** and their copper(II) complexes **3–6** on MDA-MB-231 cells. The precursor involved in the synthesis of each compound is also indicated.

| Compound | IC ₅₀ [μM] ^[a] | precursor | Ion from copper salt |
|------------------------|--------------------------------------|-----------|----------------------------------|
| H₃L3 | 0.29 ± 0.03 | HBPAMFF | – |
| H₂L4 | 4.30 ± 0.50 | BPMAMFF | – |
| 3 | 0.45 ± 0.03 | HBPAMFF | ClO ₄ ⁻ |
| 4 | 0.49 ± 0.01 | HBPAMFF | CH ₃ COO ⁻ |
| 5 | > 10 | BPMAMFF | ClO ₄ ⁻ |
| 6 | > 10 | BPMAMFF | CH ₃ COO ⁻ |

^[a] Determined after 72 h incubation in triplicate (mean ± S.D)

5.2.5.2

Perchlorate-complexes versus acetate-complexes

In general, perchlorate or acetate copper complex derivatives presented similar cytotoxic potency on MDA-MB-231 cells. The IC₅₀ standard deviations suggests that the calculated values for perchlorate or acetate complexes **3** and **4** (from **H₃L3**) can be considered identical. For perchlorate or acetate complexes **5** and **6** (from **H₂L4**), the reported IC₅₀ were both determined as >10 μM.

5.2.5.3

Metal-free ligands versus copper(II) complexes

In contrast to what has been previously observed [15, 16, 195], IC₅₀ values of the ligands were lower than those of their respective complexes, and ligand **H₃L3** is notably the most potent compound within the set. Metal-free hydrazone derivatives have previously showed good IC₅₀ values on MDA-MB-231 cells [196]. Nevertheless, this work highlights that the potent cytotoxic effect of ligand **H₃L3** is due not only to its **PIH** hydrazone moiety, but to its combination with the phenol and pyridine entities present as pendant arms in the hard-side of this ligand.

5.2.6

Iron(II), Iron (III) and zinc(II) coordination studies

The work published by Geersing *et. al* reports that in physiological conditions, N5 donor ligands can chelate intracellular metal ions, such as Fe(II), Fe(III) and Zn(II), and additionally, copper complexes can exchange their copper(II) ions with these metal ions [197]. Intracellular chelation as a strategy to induce cancer cell death was particularly studied during the last years [198]. Thus, the discovery of new compounds with such a transchelation ability becomes an alternative strategy to develop potent anticancer drugs.

Taking into consideration, firstly, the ability of similar reported Schiff base ligands to coordinate iron(II), iron(III) and zinc(II) ions [102, 112], and secondly, the higher cytotoxic activity of ligand **H₃L3**, and finally, the reduced cytotoxicity of complexes in comparison to ligands, was evaluated the ability of ligands **H₃L3** and **H₂L4** to chelate Fe(II), Fe(III) and Zn(II) ions under physiological conditions by absorption spectroscopy, as iron and/or zinc chelation could be responsible for their antiproliferative properties. Figure 5.30 shows the hypochromism observed in the absorption spectrum of mixtures of the ligands (1 equiv.) and Fe(II), Fe(III), Zn(II) or Cu(II) ions (2 equiv. in each case).

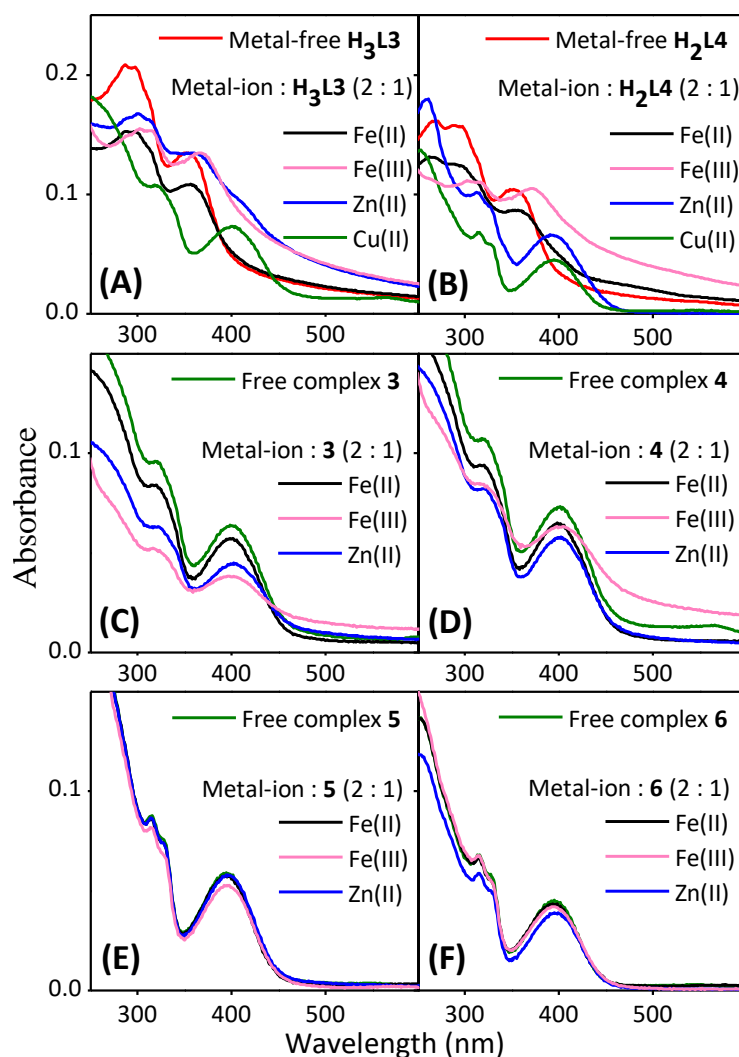


Figure 5.30. Absorption spectra of ligands (A) **H₃L3** and (B) **H₂L4**, and complexes (C) **3**; (D) **4**; (E) **5**; and (F) **6** (10 μ M) alone or in the presence of Fe(II), Fe(III) or Zn(II) in 2 : 1 metal ion : compounds mole ratio, in PBS/DMSO 99:1 incubated at 37°C for 1 h under nitrogen atmosphere. Metal-ion : iron(II) acetate, iron(III) chloride or zinc(II) chloride.

The mixture of **H₂L4** and Zn(II) gives an extra band near to 400 nm that may be assigned to the dizinc complex by analogy with the dicopper complex. Additionally, curves are redshifted. This effect is particularly marked for **H₂L4**, which presents a red shift 14 and 40 nm of their **PIH** hydrazones and **BPMAMFF** bands respectively. The better affinity of Zn(II) (Lewis borderline acid) to N₃-donor site (Lewis borderline base) than to N₂PhOH-donor site (Lewis hard base) can constitute a putative explanation for the higher decrease and red shift of the absorbance in the spectrum of **H₂L4** than **H₃L3**.

It is noteworthy that the addition of Fe(II) (Lewis borderline acid) to the solutions of ligands does not induce any red shift of the bands corresponding to the

hydrazone moieties. Nevertheless, the band at 354 nm in the spectra is redshifted suggesting the complexation with iron occurs mainly at the **HBPAMFF (H₃L₃)** or **BPMAMFF (H₂L₄)** pendant arm, instead of the **PIH** hydrazone group. In the spectra of the ligands, the absorbance around 400 – 600 nm corresponding to the Fe(II)-complexes formation is observed. This absorbance was more notable in the spectrum of **H₂L₄** than in the spectrum of **H₃L₃**.

Finally, the addition of iron(III) produces important changes in the spectrum of the ligands. The decrease of the absorption bands is accompanied with a blue shift of their **PIH** hydrazone (around 5 nm) and **HBPAMFF (H₃L₃)** or **BPMAMFF (H₂L₄)** bands (around 25 nm). Upon complexations, an additional absorbance comparable in magnitude with the absorbances of the **PIH** and **HBPAMFF (H₃L₃)** or **BPMAMFF (H₂L₄)** fragments was observed in the spectra of the ligands at 400 – 600 nm. This absorbance was assigned to Fe(III)-ligands complexation, taking into account that Fe^{III}₂-complexes of similar ligands presented absorption bands in the 400 – 800 nm wavelength [112].

A second series of experiments was made to assess whether the copper ions in complexes **3–6** could be replaced by iron or zinc. Figure 5.30 shows that addition of Fe(II) or Zn(II) to solutions of complexes **3** or **4** induces a decrease of the absorbance without significant wavelength shift. The addition of Fe(III) produces a relevant decrease of the absorbance with a red shift 2 nm of their **HBPAMFF** (complex **3**) or **BPMAMFF** (complex **4**) bands. The higher absorbance decrease upon addition of Fe(III) to the solutions of complex **3** and complex **4** (60% and 33% respectively) than upon addition of Fe(II) (13% and 19% respectively) can be related to the affinity of the phenolate oxygen towards the iron(III) ions. A minor effect is noticed in the spectrum of the copper complexes **5** and **6** upon addition of iron(II), iron(III) and zinc(II) ions. Specifically, the absorption spectrum of complex **5** exhibited few changes in the tested metal-ions media. Additional metal-ion : compounds mole ratio experiments are shown in Supporting Information (Figures 5.31–5.33).

These results suggest that the transmetalation process could occur under physiological conditions between the copper(II) present in **3** and **4**, which are by the way the most active complexes, and intracellular iron(II) or zinc(II) ions.

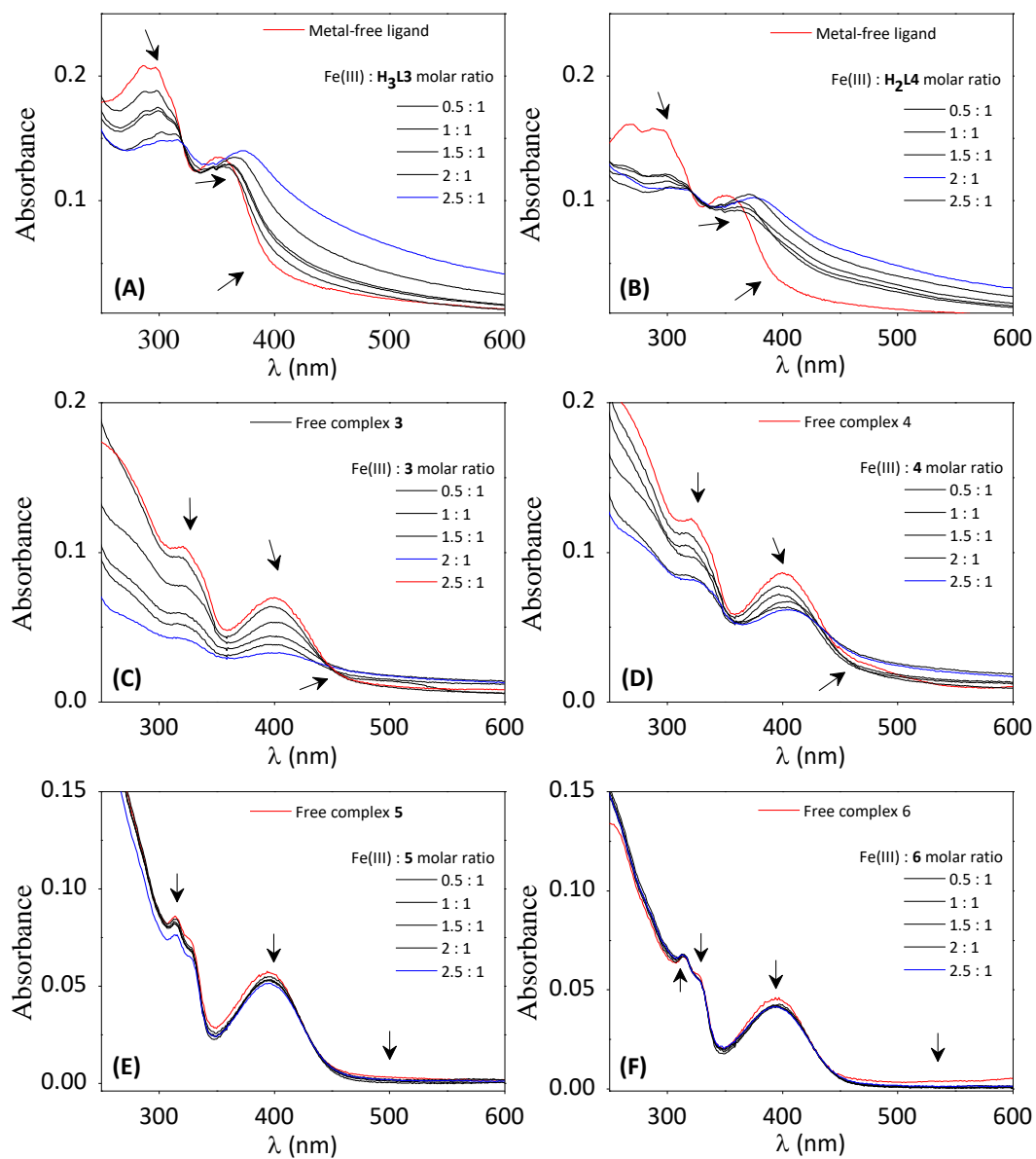


Figure 5.31. Absorption spectra of mixtures of ligands or complexes and Fe(II) at different Fe(II) : compounds mole ratios, measured after 1 h incubation at 37 °C under nitrogen atmosphere.

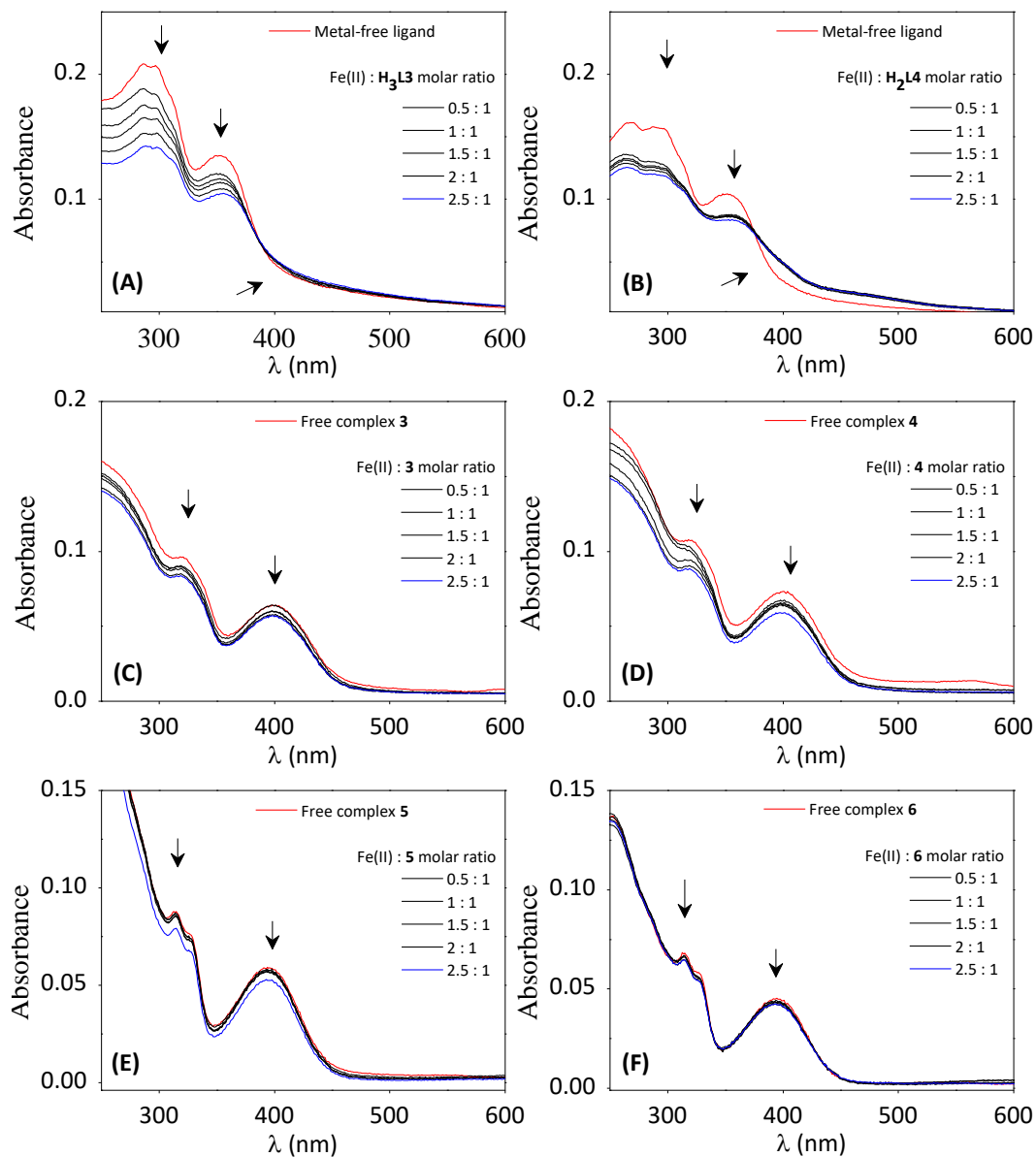


Figure 5.32. Absorption spectra of mixtures of ligands or complexes and Fe(III) at different Fe(III) : compounds mole ratios, measured after 1 h incubation at 37 °C under nitrogen atmosphere.

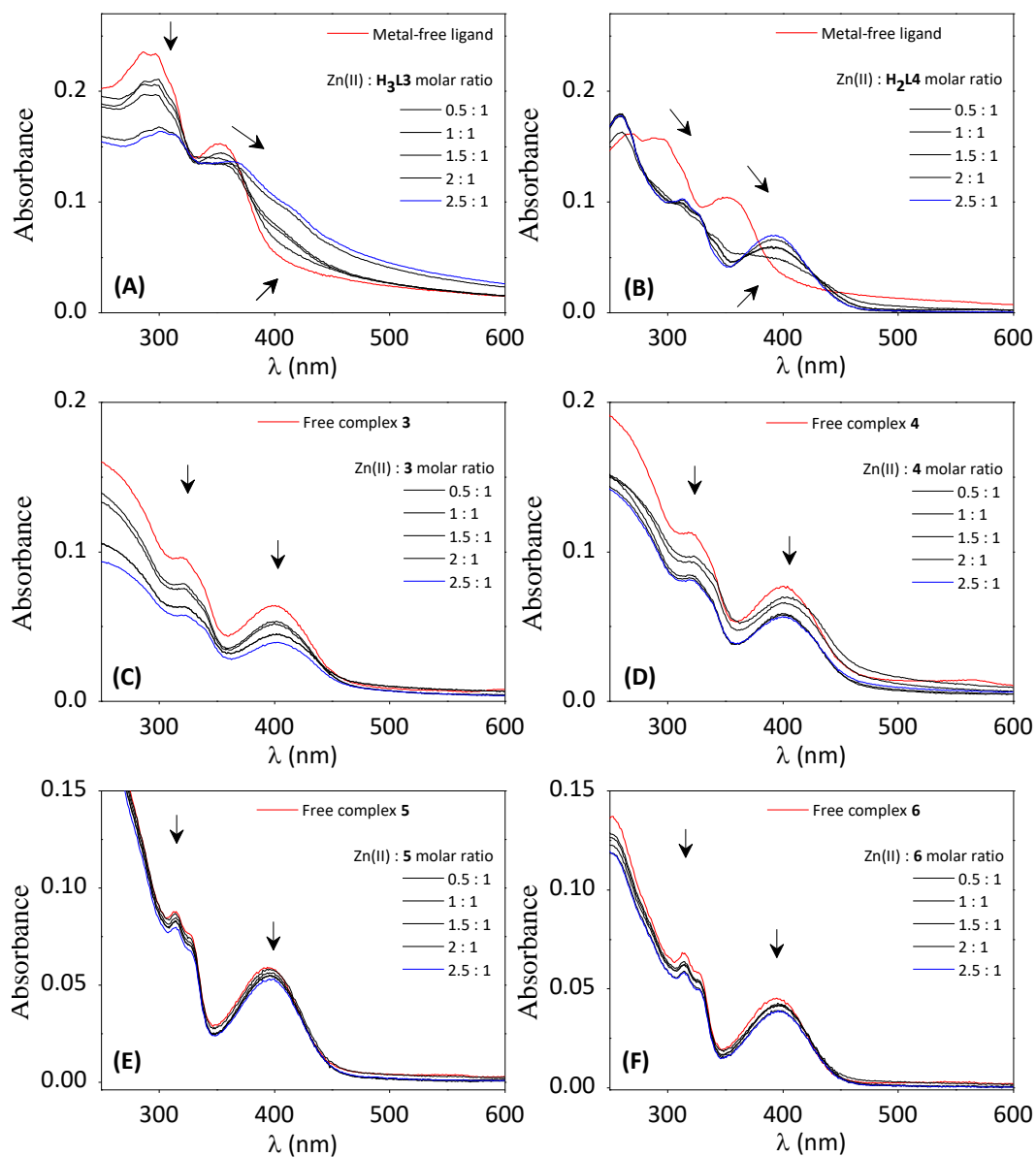


Figure 5.33. Absorption spectra of mixtures of ligands or complexes and Zn(II) at different Zn(II) : compounds mole ratios, measured after 1 h incubation at 37 °C under nitrogen atmosphere.

Potentiometric measurements are currently underway to confirm the results obtained by absorption spectroscopy concerning the metalation and the putative transmetalation between the synthesized compounds and essential metal ions.

5.2.7

Cytotoxicity versus iron/zinc coordination

The relationship between the antiproliferative activity of the compounds and their ability to coordinate essential ions is a crucial point to evaluate. In general, some relationships can be observed between the ability of compounds (followed by UV/Vis absorption experiments) to sequester Fe(II), Fe(III) and Zn(II) ions from the physiological medium and the measured IC₅₀ values.

For instance, in both experiments, no relevant differences are observed between perchlorate-copper complexes and acetate-copper complexes. It means that complexes **3** and **4** (perchlorate or acetate complexes of **H₃L₃**) show similar cytotoxicity on cancer cells and transmetalation ability. In the same direction, complexes **5** and **6** (from **H₂L₄**) also share similar properties.

Comparing ligands and their copper complexes, a similar conclusion can be found. The remarkably better anticancer activity of the ligands correlates with their higher potential to coordinate biological metals, such as iron, zinc and copper, in comparison with the corresponding complexes. Besides, the lower IC₅₀ values for the ligands than for complexes suggest that the found cytotoxicity is probably due to a set of complexes formed in the cellular medium upon addition of the metal-free ligands, rather than only because of the Cu(II)-complexes.

Finally, despite the fact that ligand **H₃L₃** (from **HBPAMFF** moiety) and its respective copper complexes **3** and **4** exhibited more important cytotoxic activity and affinity to Fe(III) than ligand **H₂L₄** (from **BPMAMFF** moiety), **H₂L₄** seems to chelate more efficiently iron(II) and zinc(II) ions than the compounds derived from the **HBPAMFF** precursor.

Highlighting these results, it is proposed first, that the notable cytotoxic activity of the compounds is due mainly to the design of the molecules, and second, that the chelation of essential intracellular metals necessary, for example, for the regulation of cell cycle [198], improves the anticancer activity, especially in the case of molecules with vacant sites to coordinate metal-ions, such as metal-free ligands, and complexes containing a phenol pendant arm.

5.3

Partial conclusions

Two novel isoxazole-arylhyazone Schiff base ligands and their dicopper(II) complexes from perchlorate and acetate salts were synthesized and fully characterized by spectroscopic and analytical techniques. The absorption bands in the spectra of ligands and complexes were successfully assigned to the isoxazole-arylhyazone, and **HBPAMFF** or **BPMAMFF** moieties.

Ligands and complexes stability was monitored by UV/Vis absorption. In DMSO, the six compounds showed high stability, while copper complexes were more stable than ligands at relevant temperature (37° C) and pH, similar to the cellular medium, probably due to the better solubility of the complexes in aqueous medium. Complexes and ligands interact with DNA through intercalative and non-intercalative modes, respectively. Metal-free ligands displayed fluorescent properties, while complexes were not fluorescent. The competitive EB displacement assay revealed a strong affinity of the DNA for Cu₂-complexes in the 10⁶ M⁻¹ range.

Compounds' cytotoxicity was examined on human epithelial breast cancer cells by the MTT assay [135]. The results evidenced that the ligand and its Cu₂-complexes containing a phenol pendant arm in their structure (**HBPAMFF**-derived) showed important higher cytotoxicity ability than those derived from the **BPMAMFF** precursor.

In addition, the new ligands exhibited the ability to coordinate to Fe(II), Fe(III), Cu(II) and Zn(II) ions from the cellular medium, while copper(II) complexes seem able to interchange their Cu(II) ions with Fe(III) ions from the medium. Our results suggest that the design of the molecules are the principal reason for the excellent cytotoxic activity, and the ability to sequester essential intracellular metals is responsible for the improvement observed in the cell death induction.

6

Results and discussion III. A new luminescent pyrene-arylohydrazone Schiff base and its (perchlorate / acetate-derived) dicopper(II) complexes as potential antiproliferative agents: syntheses characterization and *in vitro* studies in epithelial human breast cancer cells

The present chapter was redacted in order to be published as an article in a scientific journal. Hence, it is important to verify the existence of the final published paper before citing the data here described herein.

6.1

Introduction

The large number of studies published in the last years related to the anticancer properties of copper(II) complexes, as their antiproliferative activity on cancer cells and their high interaction with DNA, place these compounds as a promising class of anticancer agents [4-22]. In addition to antitumoral properties displayed by copper(II) complexes, arylohydrazones constitute a diverse family of bidentate N,O-donors with a vast spectrum of biological activities [109]. In fact, in recent years, many metal-free and coordinate hydrazone derivatives have been tested as anticancer agents [45-57].

It is well-known that the pyrene group can intercalate the double-stranded DNA [199]. Besides, cell proliferation assay and the DNA interaction of copper complexes appending in their structures a pyrene group was recently reported [200]. Thus, it is hypothesized that the incorporation of the pyrene group to a hydrazone binucleating ligand could improve the interaction of compounds with DNA.

This chapter describes the syntheses and characterization of a pyrene-derived hydrazone ligand and its dicopper(II) complexes. The design of the compounds includes framework-moieties individually with their own anticancer

properties such as the hydrazone group, copper(II) complexes and the intercalative pyrene group.

The binding interaction of ligand **H₃L5** towards ct-DNA was examined based on the fluorescent properties of the compound and on absorption spectroscopy. Besides, the *in vitro* cytotoxic activity on the MDA-MB-231 human breast cancer cell line of the binucleating metal-free ligand, as well as of its dicopper(II) complexes was explored. MDA-MB-231 cells present resistance to chemotherapy and are common by involved in metastasis and reappearance processes [201]. Breast cancer constitutes, unfortunately, the second most common type of tumour in the world [58].

6.2

Results and discussion

6.2.1

Syntheses

The fluorescent binucleating Schiff base ligand **H₃L5** was obtained from equimolar amounts of precursors 3-[(2-hydroxybenzyl)(2-pyridylmethyl)amine]-2-hydroxy-5-methylbenzaldehyde (**HBPAMFF**) and 1-pyrenebutyric acid hydrazide (**PBH**) refluxed in 10 mL MeOH/DCM 1:1 for 4.5 h. After recrystallization in MeOH, colourless crystals of **H₃L5** were obtained.

Copper(II) complexes **7** and **8** were prepared from the isolated ligand mixed with copper(II) perchlorate hexahydrate salt (1 : 2 equivalent, respectively) in the presence of potassium hydroxide (**7**) or copper(II) acetate monohydrate (**8**), correspondingly. The complexes were formulated as $[\text{Cu}_2(\mu\text{-OH})(\text{HL5})(\text{H}_2\text{O})]\text{ClO}_4$ (**7**) and $[\text{Cu}_2(\mu\text{-CO}_2\text{CH}_3)(\text{HL5})(\text{CO}_2\text{CH}_3)(\text{H}_2\text{O})_4]\cdot 5\text{H}_2\text{O}$ (**8**) (Figure 6.1).

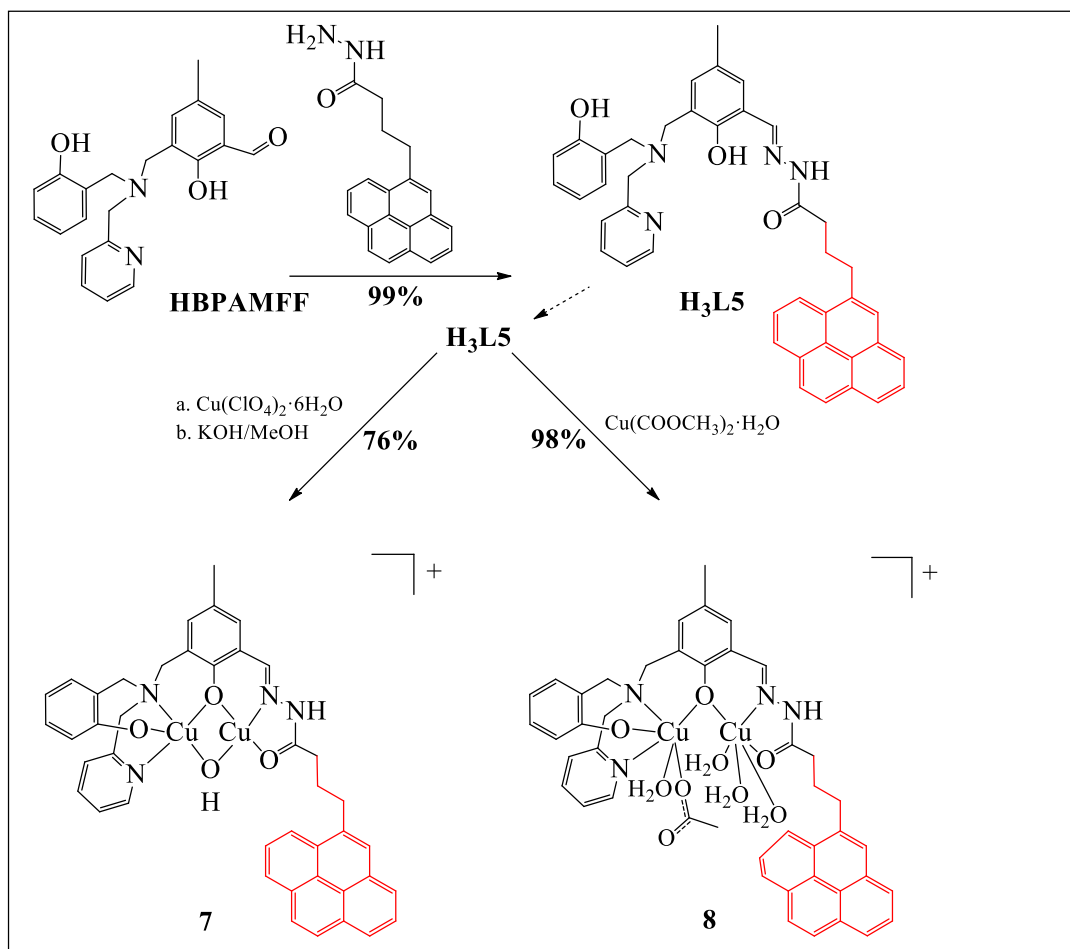


Figure 6.1. Synthetic routes of ligand **H₃L5** and its copper(II) complexes from perchlorate **7** or acetate salts **8**.

The ligand (99%, quantitative) and the complexes **7** (76%) and **8** (98%) were isolated in good yields and were characterized by elemental analysis, spectroscopic techniques and single-crystal X-ray diffraction analyses (XRD) (for **H₃L5**).

The electrolytic nature of the complexes was analysed by conductivity measurements. Moreover, the percentage of water in the complexes was determined by thermogravimetric analysis (TGA).

The weight loss obtained by TGA analysis for complex **7** of approximately 12.0% (calcd 13.0%) between 25 and 319.8 °C was assigned to the removal of one coordinate water molecule and one uncoordinated perchlorate molecules per molecule of complex **7** (Figure 6.2).

Molar conductivity measured in acetonitrile ($127 \text{ ohm}^{-1} \text{ cm}^2 \text{ mol}^{-1}$) of complex **7** indicates a 1 : 1 electrolyte system [138].

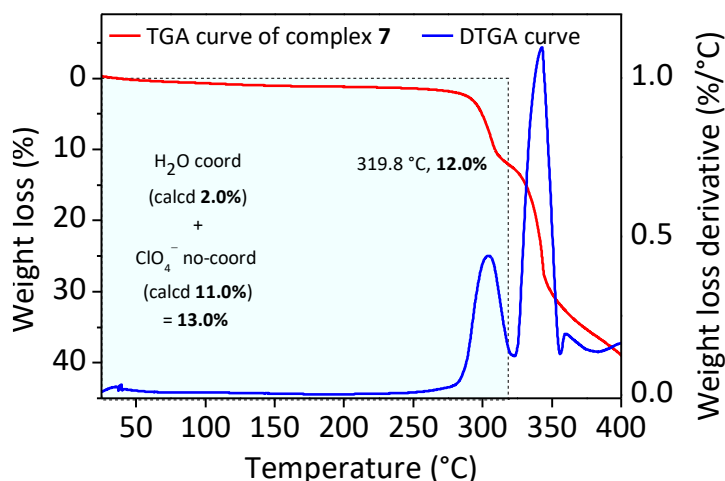


Figure 6.2. Termogravimetric curve of complex **7**.

The weight loss in the TGA analysis for complex **8**, approximately 10.0% (calcd 10.3%) between 25 and 128.3 °C, was assigned to the removal of six hydration water molecules. The weight loss corresponding to the removal of three coordinated water molecules, and two coordinate acetates was also observed (Figure 6.3).

Molar conductivity measured in acetonitrile indicates complex **8** as a non-electrolyte ($13 \text{ ohm}^{-1} \text{ cm}^2 \text{ mol}^{-1}$) [138].

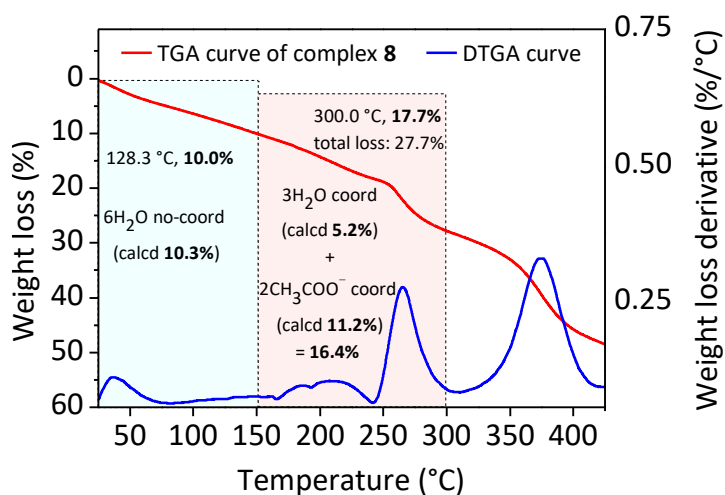


Figure 6.3. Termogravimetric curve of complex **8**.

6.2.2

Characterization of the ligand and complexes

6.2.2.1

Solution NMR of ligand **H₃L5**

The ^1H NMR spectrum was recorded for **H₃L5** in deuterated DMSO. The experimental data set includes 1D ^1H and ^{13}C spectra (Figures 6.4–6.6), and COSY, HSQC and HBMBC contour maps (Figures 13.15–13.17). Regarding the ligand formation, a signal related to the imine proton assigned to the $\text{N}=\text{C}-\text{H}$ hydrazone system appeared at 8.57 ppm.

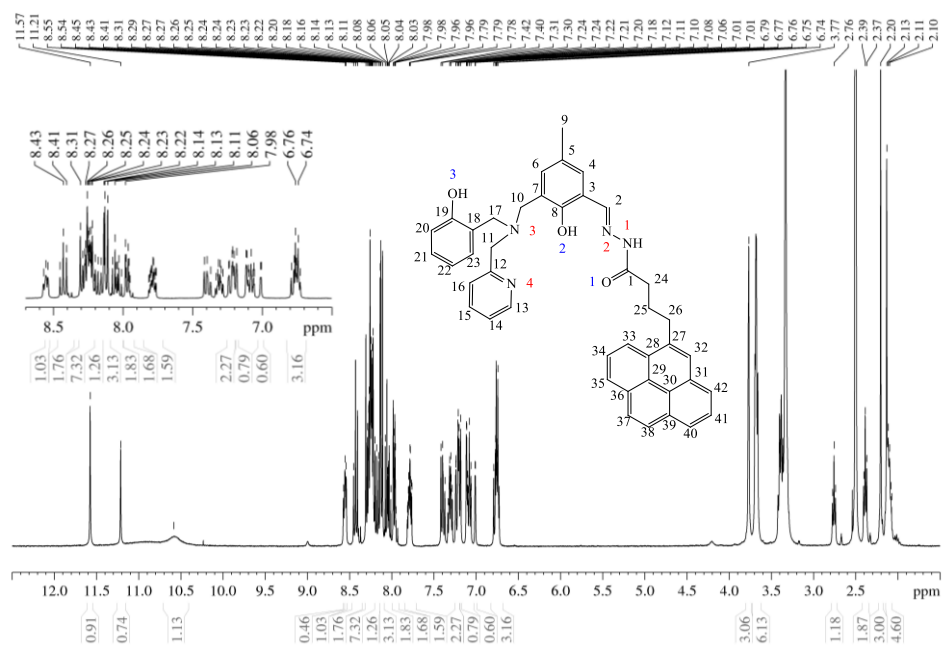


Figure 6.4. ^1H NMR spectrum (400 MHz) of **H₃L5** in $\text{DMSO}-d_6$ at room temperature.

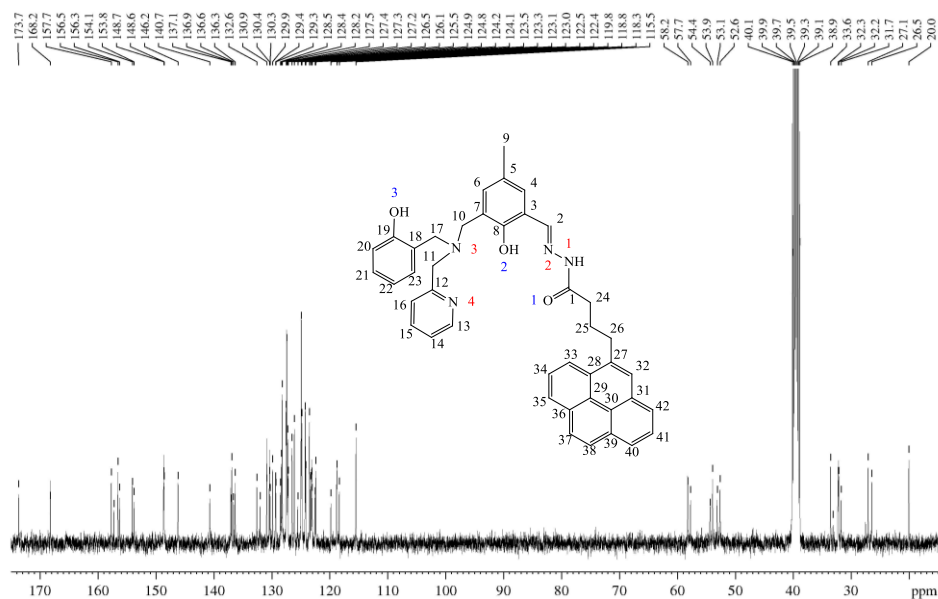


Figure 6.5. ^{13}C NMR spectrum (100 MHz) of **H₃L5** in $\text{DMSO}-d_6$ at room temperature.

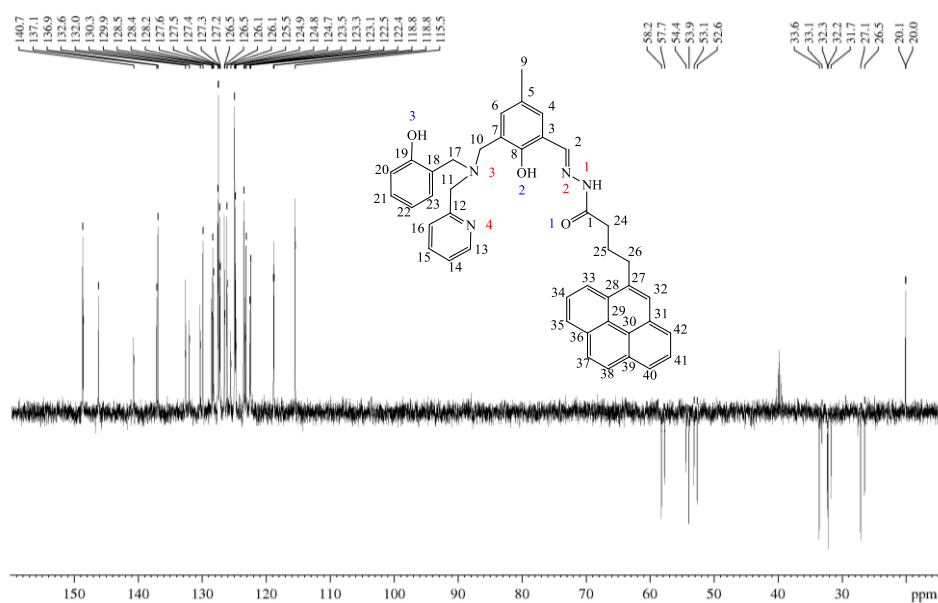


Figure 6.6. DEPT-135 NMR spectrum (100 MHz) of **H₃L5** in $\text{DMSO}-d_6$ at room temperature.

For ligand **H₃L5**, the hydrogens corresponding to signals at the lower frequencies in the 2.07–3.77 ppm region were assigned to the alkyl groups CH_2 and CH_3 . A set of singlet, doublet, triplet and multiplet signals in the 6.73–8.55 ppm region was assigned to the aromatic protons of both **HBPAMFF** and pyrene moieties. In the aromatic region, it was observed that the signals corresponding to the phenol central ring shift to lower field when compared with the pyridine pendant

arm. The protons of –OH groups exhibited a singlet at 11.21 ppm and 10.58 ppm, whereas the broad signal at 11.57 ppm was assigned to the azometine –HC=N group.

The ^{13}C NMR assignments for ligand **H₃L5** are given in Table 6.1. On the other hand, due to the complexity and strong signals overlapping in the ^1H NMR spectrum, the signals corresponding to the 38 hydrogens present in **H₃L5** were not completely assigned to each hydrogen. Nevertheless, the structure of ligand **H₃L5** was analyzed by X-Ray diffraction analysis, which showed the presence of isomers in the solid state.

Table 6.1. ^{13}C (100 MHz) data for **H₃L5** in DMSO-*d*₆ at room temperature, along with the respective assignments. Chemical shifts (δ) are in ppm.

| C | H ₃ L5, δ_{C} | C | H ₃ L5, δ_{C} |
|----|--|----|--|
| 1 | 173.7*/168.2 | 24 | 33.1*/33.6 |
| 2 | 148.6*/148.7 | 25 | 26.5*/27.1 |
| 3 | 118.4 | 26 | 31.7*/32.2/32.3 |
| 4 | 122.5*/122.4 | 27 | 136.6*/136.3 |
| 5 | 127.4 (127.37) | 28 | 129.4/129.3** |
| 6 | 132.0*/132.6 | 29 | 131.0* |
| 7 | 124.3*/124.2 | 30 | 129.4 |
| 8 | 153.8*/154.1 | 31 | 129.4/129.3** |
| 9 | 20.0/20.1* | 32 | 123.5*/123.3 |
| 10 | 52.6/53.1* | 33 | 119.8/119.4* |
| 11 | 57.7*/58.2 | 34 | 124.9* |
| 12 | 157.3*/157.7 | 35 | 126.5* |
| 13 | 146.2 | 36 | 130.9/130.4** |
| 14 | 128.2 | 37 | 126.1/126.0* |
| 15 | 137.1*/136.9 | 38 | 126.1/126.0* |
| 16 | 123.1 | 39 | 130.9/130.4** |
| 17 | 53.9/54.37* | 40 | 126.5* |
| 18 | 123.0*/123.2 | 41 | 124.9* |
| 19 | 156.3*/156.5 | 42 | 124.8*/124.7 |
| 20 | 115.5 | | |
| 21 | 128.5*/128.4 | | |
| 22 | 118.8*/118.7 | | |
| 23 | 130.3*/129.9 | | |

*Overlapped signals. **Signal from isomers.

6.2.2.2

Crystal structure of ligand **H₃L5**

The ORTEP view of the molecular structure of this novel 1-pyrenebutyric-hydrazonic ligand is shown in Figure 6.7. Additionally, the crystallographic data and structural refinement parameters can be found in Table 6.2. Ligand **H₃L5** crystallized in the monoclinic system, space group $P2_1/c$.

According to the results, the formed C2–N2 bond from the hydrazonic group has a length of 1.278(2) Å, which is in agreement with a C=N system (1.28 Å) [165]. Similarly, the C1–O1 bond with a distance of 1.223(2) Å, is slightly shorter than the standard C=O bond distance (1.24 Å) [127].

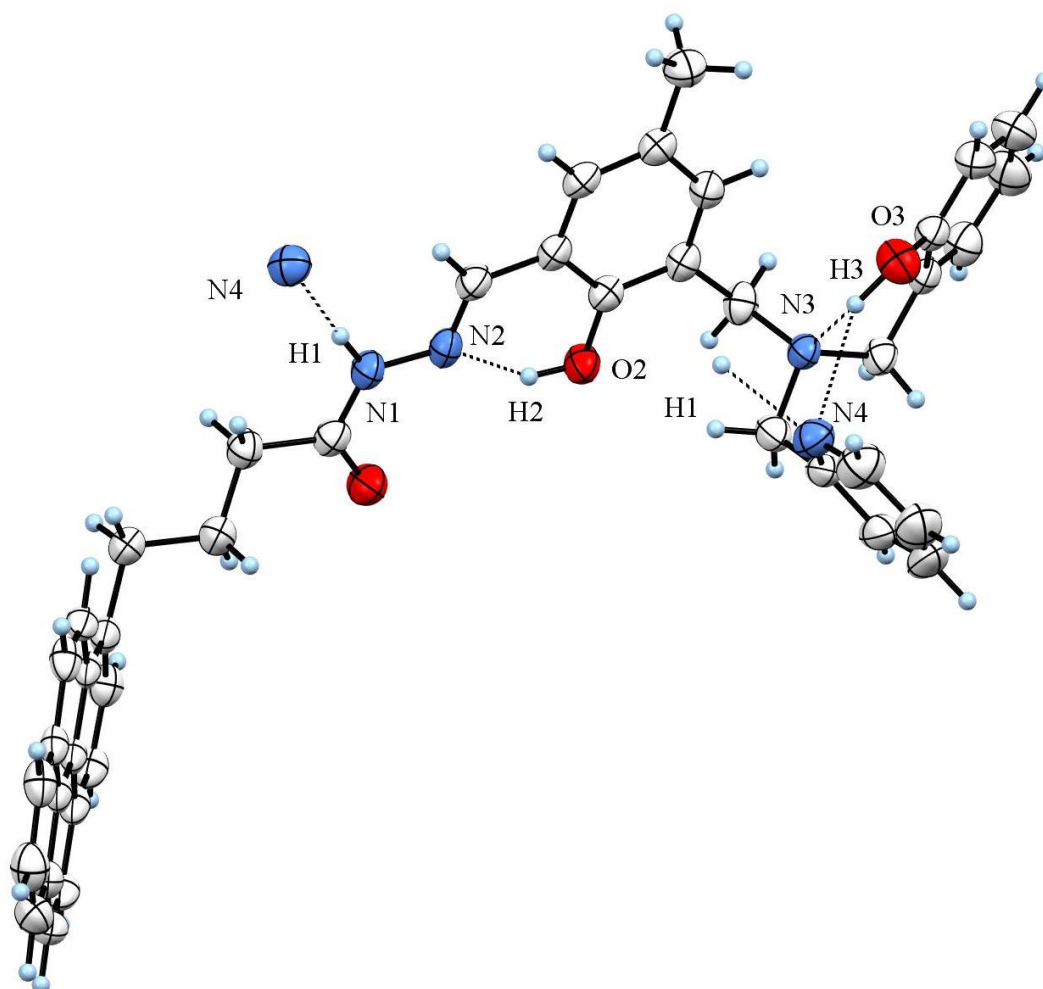


Figure 6.7. Crystal structure of ligand **H₃L5**. The ellipsoids were drawn with 50% probability. Only one of the enantiomers is shown. Intramolecular and intermolecular hydrogen bonds are depicted as dotted line.

Table 6.2. Crystallographic data and structure refinement of ligand **H₃L5**.

| H₃L5 | |
|--|---|
| Empirical formula | C ₄₂ H ₃₈ N ₄ O ₃ |
| Formula weight (g/mol) | 646.76 |
| Temperature (K) | 200(1) K |
| Crystal description | colourless |
| Crystal system | Monoclinic |
| Space group | P2 ₁ /c |
| a (Å) | 28.6086(5) |
| b (Å) | 10.4611(2) |
| c (Å) | 11.2839(2) |
| α (°) | 90 |
| β (°) | 97.1580(10) |
| γ (°) | 90 |
| Volume (Å ³) | 3350.70(11) |
| Z | 4 |
| ρ _{calc} (g/cm ³) | 1.282 |
| Absorption coefficient μ (mm ⁻¹) | 0.645 |
| Crystal size (mm ³) | 0.198 × 0.181 × 0.016 |
| Wavelength λ (Å) | 1.54178 |
| Radiation type | Cu Kα |
| 2θ range (°) | 3.112 to 133.278 |
| Miller indexes ranges | -33 ≤ h ≤ 34, -12 ≤ k ≤ 12, -13 ≤ l ≤ 11 |
| Measured reflections | 27387 |
| Unique reflections | 5924 |
| Goodness-of-fit F ² | 1.019 |
| Final R indexes | R1 = 0.0575 |
| [all data] | wR2 = 0.1066 |
| Final R indexes | R1 = 0.0399 |
| [I ≥ 2σ(I)] | wR2 = 0.0973 |
| Refinement | |
| Data | 5924 |
| No. of parameters | 519 |
| No. of restraints | 18 |
| Largest diff. peak/hole (e/Å ³) | 0.25,-0.12 |

In the solid state, this ligand presents two protonated heteroatoms: O2 and N1. Both intramolecular and intermolecular hydrogens bonds are observed in ligand **H₃L5** (Figure 6.7) as was found for **H₃L3** (Chapter 5). Three intramolecular H-bonds were observed in the structure of ligand **H₃L5**. One of them corresponds to the H-bond formed between the O2–H from the phenol central ring and the N2 from hydrazone arm, constituting a hexagonal ring. Selected geometric parameters regarding **H₃L5** are shown in Table 6.3.

Table 6.3. Selected geometric parameters for ligand **H₃L5**.

| Bond distances (Å) | | Bond angles (°) | |
|--------------------|----------|-----------------|------------|
| O1-C1 | 1.223(2) | C1-N1-N2 | 120.55(14) |
| O2-C8 | 1.362(2) | C2-N2-N1 | 116.63(14) |
| O3-C19 | 1.365(2) | C11-N3-C10 | 111.18(13) |
| N1-N2 | 1.375(2) | C11-N3-C17 | 111.70(12) |
| N1-C1 | 1.353(2) | C17-N3-C10 | 111.45(13) |
| N2-C2 | 1.278(2) | C13-N4-C12 | 118.28(17) |
| N3-C10 | 1.479(2) | O1-C1-N1 | 123.55(16) |
| N3-C11 | 1.474(2) | O1-C1-C24 | 123.24(16) |
| N3-C17 | 1.477(2) | N1-C1-C24 | 113.21(14) |
| N4-C12 | 1.342(2) | N2-C2-C3 | 121.47(15) |
| N4-C13 | 1.339(3) | O2-C8-C3 | 121.18(14) |
| – | – | O2-C8-C7 | 119.11(14) |
| – | – | N3-C10-C7 | 111.86(13) |
| – | – | N3-C11-C12 | 110.82(13) |
| – | – | N4-C12-C11 | 116.00(15) |
| – | – | N4-C12-C16 | 121.63(18) |
| – | – | N4-C13-C14 | 123.4(2) |
| – | – | N3-C17-C18 | 110.94(13) |
| – | – | O3-C19-C18 | 121.00(15) |
| – | – | O3-C19-C20 | 118.17(16) |

The two other H-bonds in the molecules are both involved with the O3–H group from the phenol pendant arm. The acceptor nitrogen atoms are from the amine (N3) and the pyridine (N4) groups. It is important to highlight that the H-bond in the O3—H3···N3 system with 1.798 Å value is clearly a strong hydrogen bond (2.2 – 2.5 Å) [202], whereas the O3—H3···N4 hydrogen bond with 2.693 Å

value, seems to correspond to a moderate (2.5 – 3.2 Å, mostly electrostatic) [202] hydrogen bond. Nonetheless, the presence of this latter hydrogen bond (O3—H3···N4) results in the formation of a pentagonal ring, which can supply stability to the ligand (Figure 6.8). The formed N3···H3···N4 angle is 124.0°.

An intermolecular hydrogen bond connects the N1–H atoms of the hydrazone group with the nitrogen of the pyridine pendant arm (N4) of another **H₃L5** molecule as acceptor group (Figure 6.8). It is worth noting that, as expected, intermolecular hydrogen bond lengths are larger than the intramolecular ones (Table 6.4).

Table 6.4. H-bond length (d, Å) and angles (°) for ligand **H₃L5**.

| D—H···A | d(D—H) | d(H···A) | d(D···A) | D—H···A (°) |
|-------------------------|---------|----------|----------|-------------|
| O2—H2A···N2 | 0.93(2) | 1.80(2) | 2.619(2) | 145(2) |
| O3—H3···N3 | 1.04(2) | 1.71(2) | 2.661(2) | 149(2) |
| N1—H1···N4 ⁱ | 0.90(2) | 2.12(2) | 3.014(2) | 170(2) |

Symmetry codes: (i) x, 1/2-y, 1/2+z.

The unit cell is represented by the interaction of four individual molecules of ligand **H₃L5** forming the extensive network (Figure 6.9). The figure exhibits the presence of two isomers in the structure of ligand **H₃L5**, corresponding to two possible positions of the pyrenebutyric moiety in the crystal (Figure 6.9). One of the isomers contributed to 90% and is presented in the figure with solid line bonds, while the second isomer represented the remaining 10% and is shown using isotropic balls without solid line bonds. Besides, ligand **H₃L5** contains in its structure an asymmetric N group (**HBPA** moiety). Nevertheless, this ligand crystallized in the space group P2₁/c, which presents an inversion centre. Consequently, two enantiomers are found in the unit cell (Figure 6.8). Only one of these enantiomers is discussed in this work.

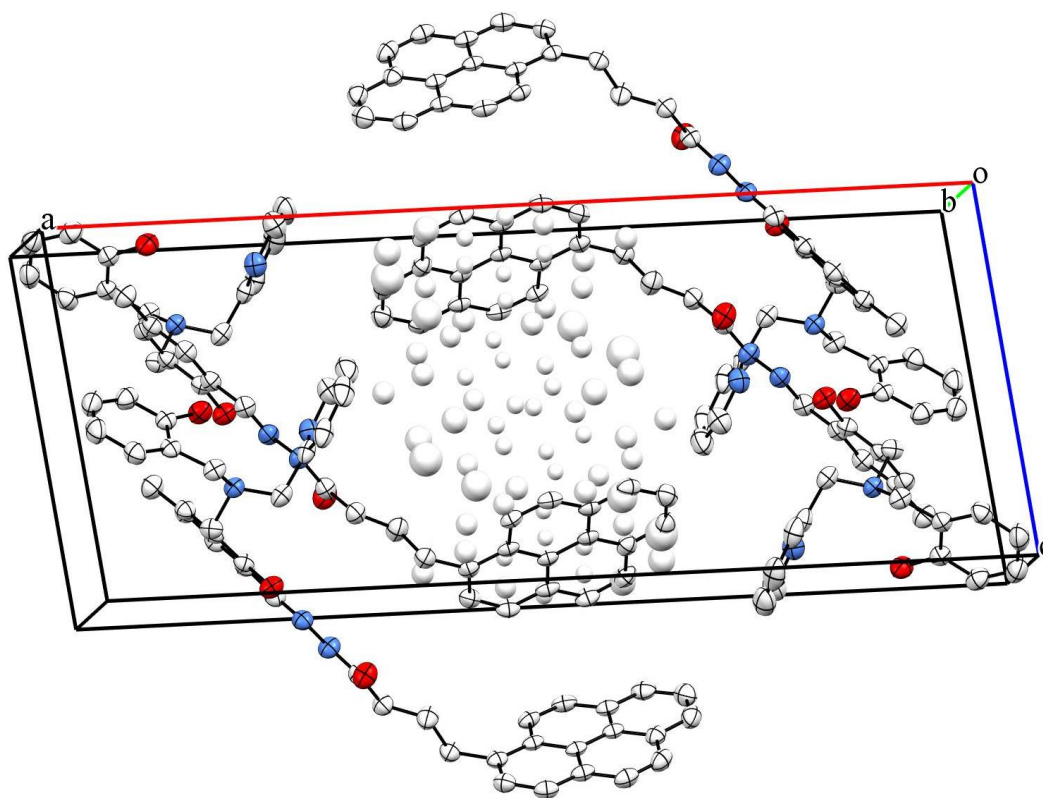


Figure 6.8. Molecular packing of ligand **H₃L5**. Hydrogen atoms have been omitted for the sake of clarification. Two possible positions of the pyrenebutyric moiety are shown. The isomers are shown with solid line bonds (90% of contribution) or with isotropic balls without solid line (10% contribution).

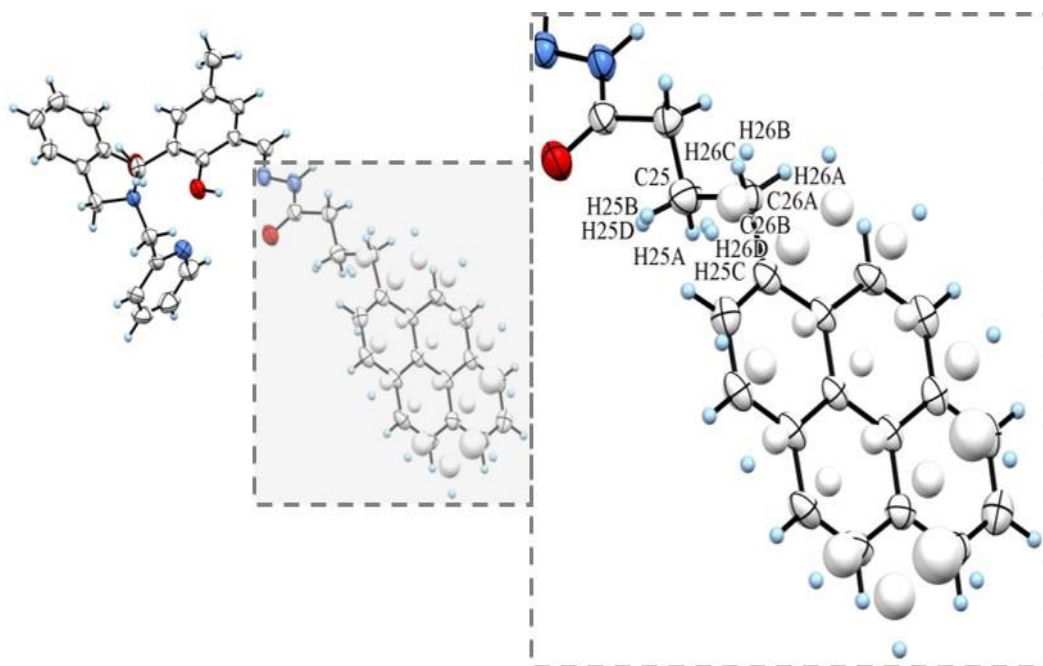


Figure 6.9. Crystal structure of ligand **H₃L5**. The ellipsoids were drawn with 50% probability highlighting the pyrenebutyric entity (inset). Two enantiomers are shown.

6.2.2.3

Vibrational properties of the compounds

Infrared spectroscopy was used to study the vibrational properties of the synthesized pyrene-ligand **H₃L5** (Figure 6.10), as well as, of its copper(II) complexes **7** and **8** synthesized from copper(II) perchlorate hexahydrate (Figure 6.11) or copper(II) acetate monohydrate (Figure 6.12), respectively.

The spectra of ligand **H₃L5** in KBr exhibits some vibrational bands corresponding to the heteroatoms present in the molecule in the solid state (Figure 6.10). Thus, the stretching and bending modes of OH and NH were identified (Table 6.5.). Vibrational bands related to the C–N bond were also found (Table 6.5.). The stretching corresponding to C=O vibration appeared in the spectrum at 1687 cm⁻¹. It is important to notice that the absence of this vibration band (C=O) in the spectra of the complexes is a sign of the complexation process (Figure 6.11 and 6.12).

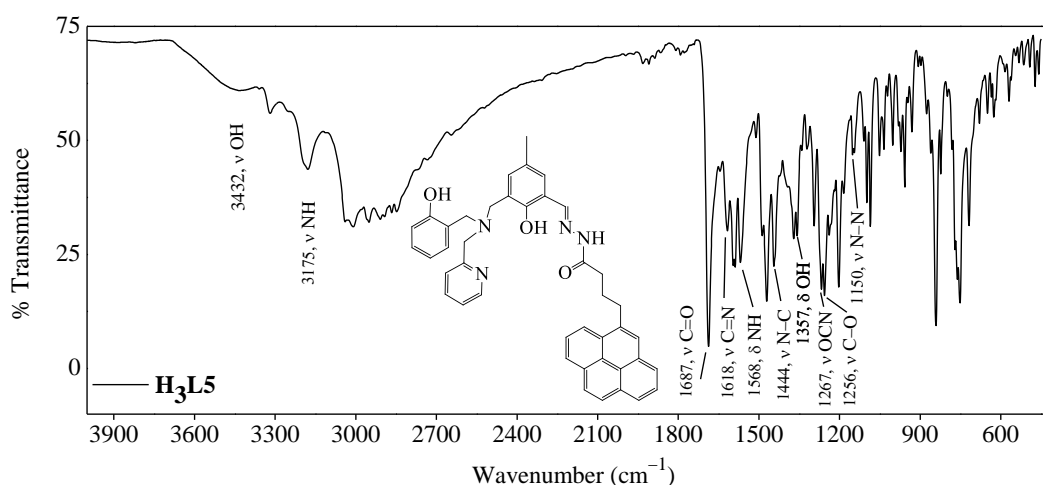


Figure 6.10. FTIR spectra of **H₃L5** in KBr pellet and principal assignments.

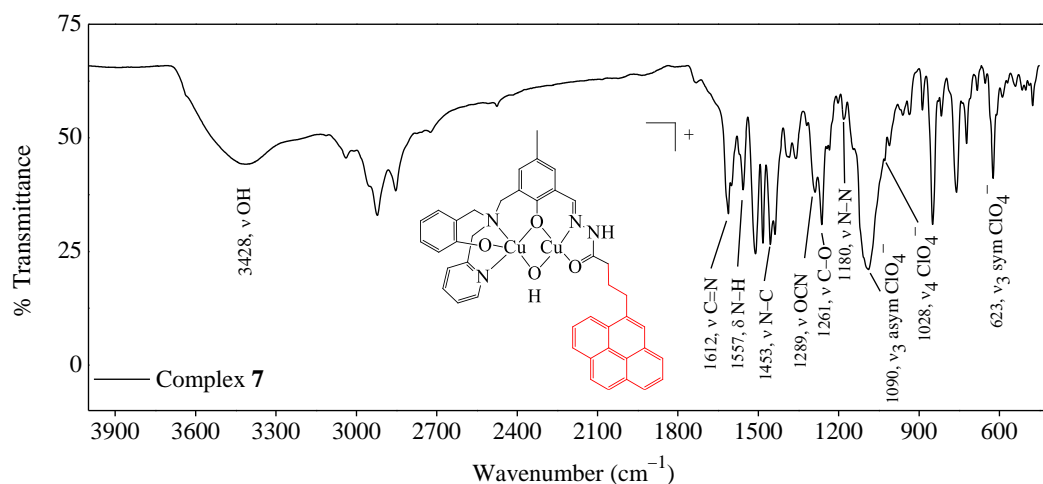


Figure 6.11. FTIR spectra of complex **7** in KBr pellet and principal assignments.

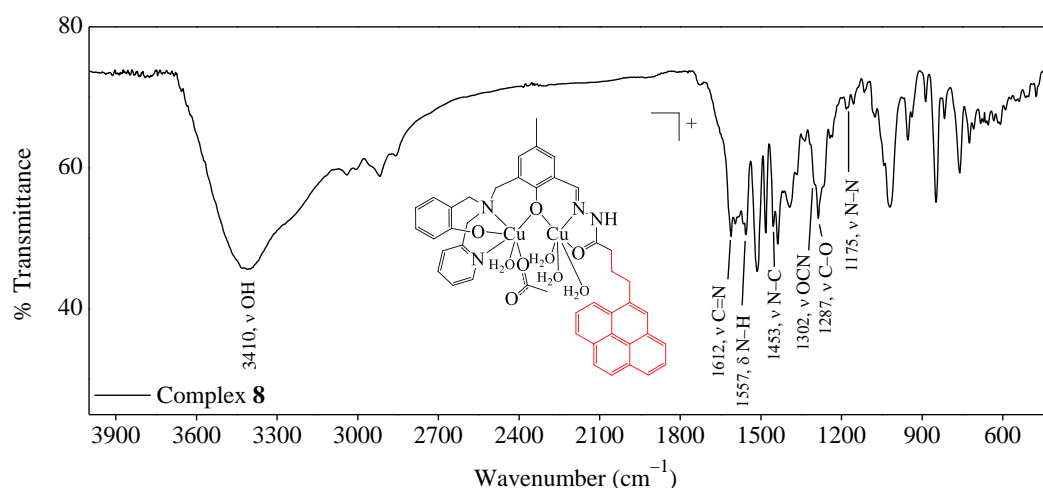


Figure 6.12. FTIR spectra of complex **8** in KBr pellet and principal assignments.

Additionally, complexation causes a displacement of the phenol C–O stretching band, which appears in the spectra of the ligand **H₃L5** at 1256 cm⁻¹ and shifts in the complexes **7** and **8** spectra to 1262 and 1287 cm⁻¹, respectively.

A main point associated to the hydrazone group can be highlighted. In ligand **H₃L5** the N–H bending mode appears at 1568 cm⁻¹, and upon coordination, this band continues to be observed in the spectra of the complexes, which means that the ligand is coordinated in its amido form.

Perchlorate counter-ion bands were observed in the vibrational spectra of complex **7**, as can be seen in Figure 6.11 and Table 6.5.

The main vibrational frequencies of **H₃L5** and its coordination compounds, along with the proposed assignments, are summarized in Table 6.5.

Table 6.5. Selected vibrational absorptions (cm⁻¹) for **H₃L5** and its complexes **7** and **8**.

| H₃L5 | Complex 7 | Complex 8 | Assignment |
|------------------------|------------------|------------------|--|
| 3432 | 3428 | 3410 | ν OH |
| 3175 | – | – | ν NH |
| 1687 | – | – | ν C=O |
| 1618 | 1612 | 1612 | C=N |
| 1568 | 1557 | 1557 | δ N–H |
| 1444 | 1453 | 1453 | ν N–C |
| 1357 | – | – | δ O–H |
| 1150 | 1180 | 1175 (sh) | ν N–N |
| – | 1090 | – | ν ₃ ClO ₄ ⁻ |
| – | 1028 | – | ν ₄ ClO ₄ ⁻ |

6.2.2.4

Photophysical properties of the compounds

The spectral features of ligand **H₃L5** displays seven principal absorption bands in the UV region, as can be seen in Figure 6.13. The figure also includes the absorption spectra of its precursors **HBPAMFF** and **PBH**.

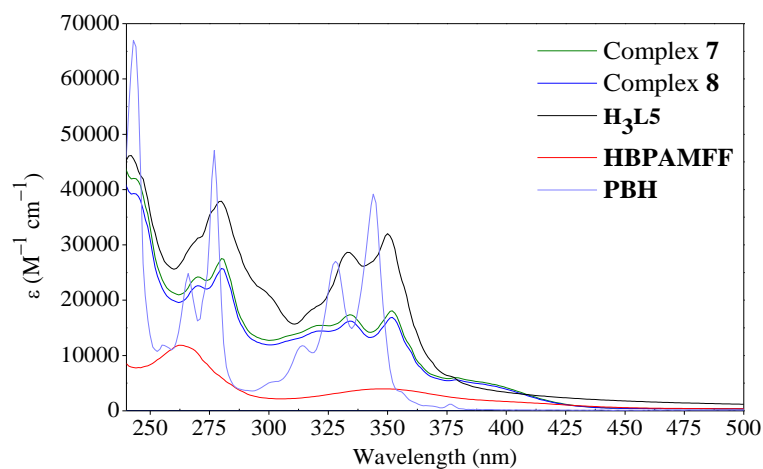


Figure 6.13. Absorption spectrum of ligand **H₃L5**, as well as its respective precursors: **HBPAMFF** and **PBH**, and of complexes **7** and **8** recorded in H₂O/DMSO 9:1 at 298 K.

For comparison, it was possible to correlate the absorptions bands in the ligand spectrum with the aromatic ring presence in this ligand and also in its precursors. Most of the bands in the absorption spectrum of **H₃L5** correspond to both **HBPAMFF** and **PBH** moieties, since these precursors show visible absorptions at similar wavelengths. In this sense, five bands (Table 6.6) were assigned to the π - π^* transitions of the central ring, two pendant-arms and pyrenebutyric moieties. Consequently, the remaining absorption band clearly corresponds to the hydrazonic transitions. This band is absent in the spectra of the precursors and appears as a shoulder. It corresponds then to transitions of the CO-NH-N=N system.

In general, the absorption spectra of complexes **7** and **8** are very similar to that of its precursor ligand **H₃L5** (Figure 6.13). Nevertheless, some differences are evident upon complexation. Thus, one extra band corresponding to the π - π^* transition in the **HBPAMFF** moiety is observed. This latter band is overlapped with the **PBH** absorption in the spectrum of the metal-free ligand. After coordination this band is redshifted and appears as an independent band at ~390 nm in the spectra of the copper(II) complexes (Figure 6.13). This result is in agreement with the coordination of copper(II) ions with the **HBPAMFF** moiety and not with the pyrenebutyric framework and corresponds to the coordination via the pyridine group and deprotonation of the phenol groups.

Table 6.6. UV/Vis absorption properties of ligands **H₃L55** and dicopper(II) complexes **7** and **8** in H₂O/DMSO 9:1 in the range 230 – 500 nm at 25 °C, and suggested assignments.

| H₃L5 | | Complex 7 | | Complex 8 | | Assignment |
|------------------------|---|------------------|---|------------------|---|---------------------|
| λ (nm) | ϵ (M ⁻¹ cm ⁻¹)* | λ (nm) | ϵ (M ⁻¹ cm ⁻¹)* | λ (nm) | ϵ (M ⁻¹ cm ⁻¹)* | |
| | | 390 | 5300 ± 100 | 389 | 4500 ± 100 | HBPAMFF ring |
| 352 | 38000 ± 800 | 352 | 19000 ± 900 | 352 | 17000 ± 800 | PBH / HBPAMFF rings |
| 335 | 34000 ± 800 | 333 | 18000 ± 400 | 333 | 16600 ± 200 | PBH / HBPAMFF rings |
| 321 | 22300 ± 400 | 320 | 15500 ± 500 | 320 | 14400 ± 500 | PBH / HBPAMFF rings |
| 300 | 27000 ± 600 | 307 | 13500 ± 300 | 307 | 12500 ± 300 | CO-NH-N=N |
| 282 | 43000 ± 1300 | 280 | 29000 ± 1000 | 280 | 26000 ± 800 | PBH / HBPAMFF rings |
| 271 | 35000 ± 1000 | 270 | 25300 ± 800 | 269 | 22600 ± 700 | PBH / HBPAMFF rings |
| 246 | 48000 ± 1800 | 243 | 42000 ± 900 | 243 | 39000 ± 900 | PBH ring |

Besides, another redshift of the bands is observed in the spectrum of the complexes when compared to ligand **H₃L5**. As previously discussed, the hydrazonic system appears in the ligand's spectrum at 300 nm. Coordination causes the displacement of this band to 307 nm in the spectra of the complexes.

Ligand **H₃L5** was designed with a pyrene substituent to explore its fluorescence properties. In biological studies, fluorescence is an important tool, which allows different ways to evaluate the interaction of the compound with the biological system. The detection of the molecules inside the cells by fluorescence microscopy is one of these examples [203]. In order to examine the fluorescence qualitative properties of ligand **H₃L5** in aqueous medium, the emission spectrum of this ligand was obtained by exciting at 352 nm a solution containing **H₃L5**. Figure 6.14 shows a typical mirror image related to the absorption and emission spectra of ligand **H₃L5**. The fluorescence spectrum exhibited four fluorescence bands at 474 nm, 416 nm (shoulder), 396 nm and 378 nm. The observed band at 378 nm corresponds to 26 nm Stokes shift ($\lambda_{\text{excitation}} = 352 \text{ nm}$).

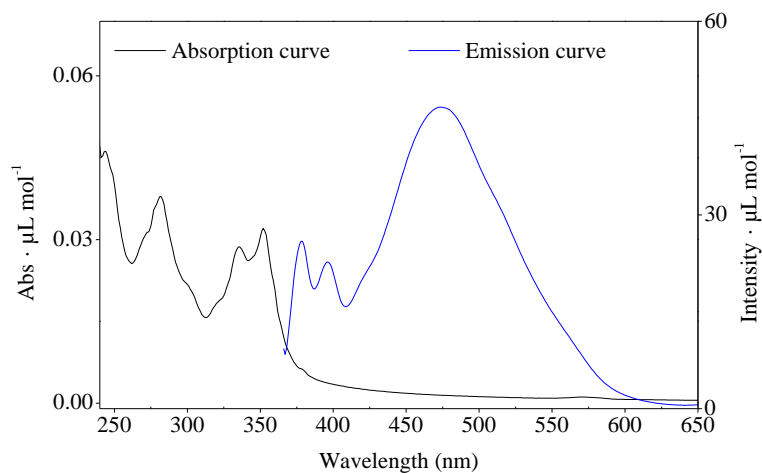


Figure 6.14. Absorption versus fluorescence emission spectra of ligand **H₃L5** ($\lambda_{\text{excitation}} = 352 \text{ nm}$) in 99:1 H₂O/DMSO and water respectively at 298 K.

The emission spectra of the precursors **HBPAMFF** ($\lambda_{\text{excitation}} = 349 \text{ nm}$) and **PBH** ($\lambda_{\text{excitation}} = 344 \text{ nm}$) in aqueous medium were also obtained by exciting their solutions (Figure 6.15).

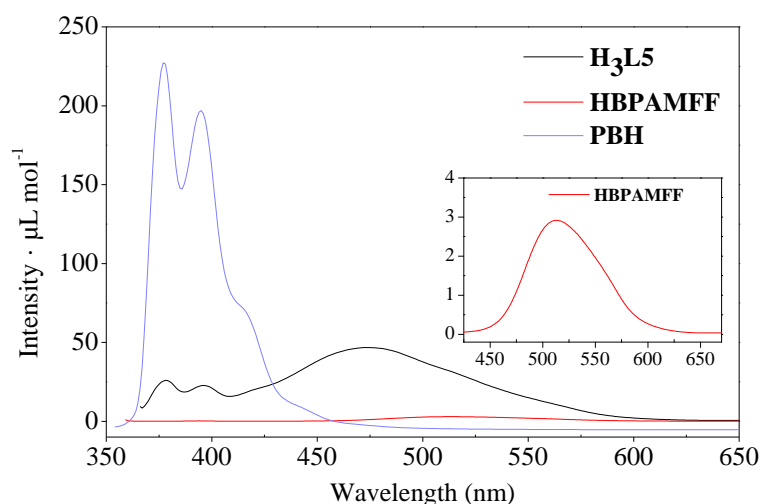


Figure 6.15. Fluorescence emission spectra of ligand **H₃L5** ($\lambda_{\text{excitation}} = 352 \text{ nm}$; $10 \mu\text{M}$), as well as its respective precursors: **HBPAMFF** ($\lambda_{\text{excitation}} = 349 \text{ nm}$; $40 \mu\text{M}$) and **PBH** ($\lambda_{\text{excitation}} = 344 \text{ nm}$; $6 \mu\text{M}$) in water at 298 K.

Some remarks can be appreciated by comparing the emission spectra profiles of the precursors **HBPAMFF** (at 512 nm) and **PBH** (415 nm, 395 nm and 377 nm) to that of ligand **H₃L5**. For example, the bands at 396 nm and 378 nm can be associated to the **PBH** ring while the emission band at 474 nm seems have a contribution of both, **HBPAMFF** and **PBH** moieties. Besides, it is well-known that the pyrene group can form excimers at higher wavelength than the monomers [204] (Figure 6.16). Thus, the emission band at 396 nm can also indicate the presence of excimers in the solutions of ligand **H₃L5**.

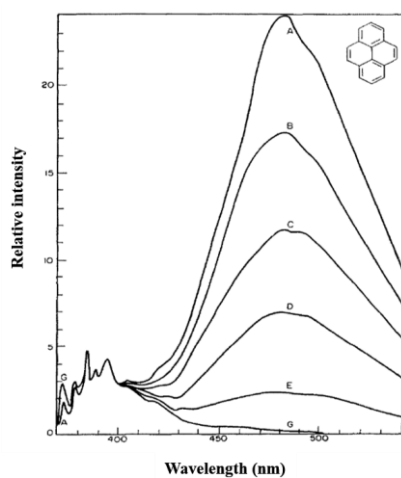


Figure 6.16. Fluorescence spectra of pyrene at decreasing concentrations A ($\times 10^{-2}$) – G ($\times 10^{-4}$) in cyclohexane. Adapted from Briks and Christophorou, 1963 [204].

Comparing the emission intensity of ligand **H₃L5** with that of its precursors (in u.a · $\mu\text{L mol}^{-1}$), it was evident that the addition of **PBH** group to **HBPAMFF** moiety leads to a partial quenching of the emission. Additionally, the emission bands of **PBH** appear 1 nm redshifted in emission spectrum of **H₃L5**.

In order to study the influence of the solvent in the fluorescence emission of the solution containing ligand **H₃L5**, measurements were carried out after dissolving this ligand in acetone, water, DCM, MeOH and MeCN (Figure 6.17).

Figure 6.17 shows that Band I (see in the figure) displayed a higher intensity in polar protic solvents, such as water or MeOH, than in polar aprotic solvents, such as acetone or MeCN or DCM. Additionally, a redshift is observed in Band I in protic solvents. Thus, this effect suggests that hydrogen bonds are formed between the heteroatoms in the ligand molecule and the protic solvents, such as water or MeOH [205].

The higher intensity in DCM than the other tested solvent of Bands II, III and IV in the fluorescence emission spectrum of **H₃L5** was associated to the better solubility of the pyrene group in DCM medium than, for example, in MeOH or acetone solvents [206].

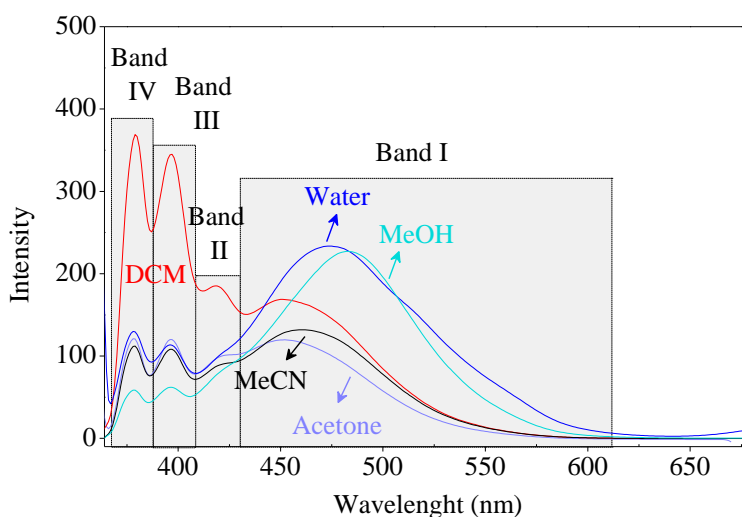


Figure 6.17. Fluorescence emission spectra of ligand **H₃L5** ($\lambda_{\text{excitation}} = 352 \text{ nm}$; $10 \mu\text{M}$) in water and organic solvents at 298 K.

The luminescent spectrum of ligand **H₃L5** was continuously measured for 30 min. The stability of the emission spectrum demonstrated to be appropriated for

biological test, as for example, the interaction with the DNA and albumin proteins through fluorescence spectroscopy.

The emission spectra of complexes **7** and **8** derived from ligand **H₃L5** were also investigated in different solvents: acetone, DCM, MeCN, MeOH and water. Neither of these complexes were non-emissive in these solvents and emitting at 390 nm or 352 nm.

6.2.3

Stability studies in DMSO and PBS

The stability of the compounds was evaluated in DMSO and also in PBS, as a relevant biological medium (37 °C, pH 7.4), by absorption spectroscopy during 24 h. This study was carried out in order to explore their potential application in cytotoxicity assays on cancer cells. Thus, the experiments tested the stability of the compounds in pure DMSO and PBS/DMSO 99:1 (v/v) mixture. DMSO was the solvent used to prepare the stock solutions of the compounds for the biological tests.

In DMSO, the absorption spectra of compounds at a 1×10^{-5} M showed an insignificant changes after of 24 h at room temperature. Thus, ligand **H₃L5** presented 98% of the initial concentration (C_0), while complexes **7** and **8**, 96% and 94% respectively of the C_0 . On the other hand, in PBS/DMSO 99:1 and after 24 h, ligand **H₃L5** presented 89% of C_0 , while the complexes **7** and **8**, 92% and 91% respectively of the C_0 .

6.2.4

Interaction of ligand **H₃L5** with ctDNA

6.2.4.1

ctDNA-**H₃L5** interaction studies by absorption spectroscopy

The interaction with DNA is a common anticancer property explored for new antitumoral compounds, since the cisplatin molecule is one of the most active chemotherapeutics, involves the interaction and damage of DNA from the nucleus of the cancer cells [207, 208], and inhibiting the cell's proliferation. Accordingly,

the interaction between the synthesized ligand **H₃L5** and *calif thymus* DNA (ctDNA) was explored using both absorption and fluorescence spectroscopies.

The absorption bands corresponding to **HBPAMFF**, hydrazone and pyrenebutyric moieties of ligand **H₃L5** decreased when the concentration of ctDNA was gradually increased Figure 6.18. Besides, a redshift of 2 nm was observed (Figure 6.18). The hypochromism was ~34% when molar ratio of was **H₃L5** : ctDNA 1 : 2. It is known that the intercalation process in the UV-Visible absorption studies involving DNA give hyperchromism and/or redshifts [190], while minor groove binding leads to a hyperchromism in the absorbance.

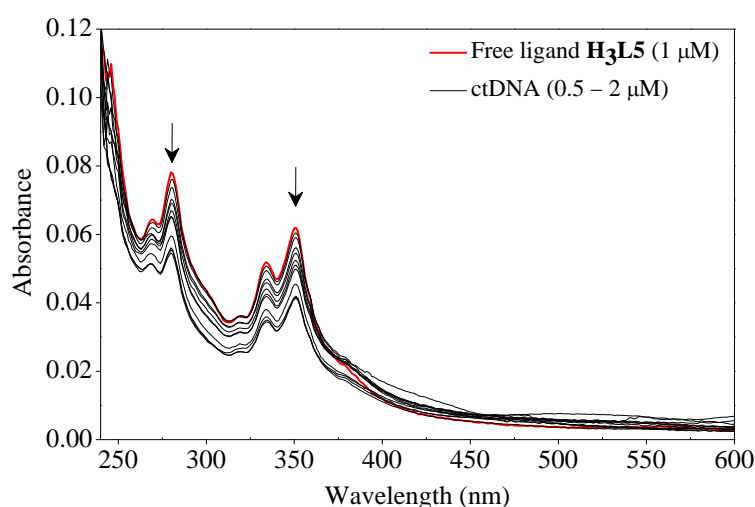


Figure 6.18. Absorption spectra of ligand **H₃L5** (1 μ M, red curve) in a buffer solution (pH 7.40) at 25°C of in the absence and presence of ctDNA at increasing concentration (0.5 and 1 – 2 μ M, black curves). The absorbance of each addition of DNA was substrate from the spectra.

6.2.4.2

ctDNA-H₃L5 interaction studies by fluorescence spectroscopy

To complement the results obtained by absorption spectroscopic technique, fluorescence emission measurements were carried with the **H₃L5**-ctDNA samples. This technique allows to determine the binding constant of the compound-DNA interaction, and also to define the number of actives sites of the biomolecule when exposed to compounds (Figure 6.19).

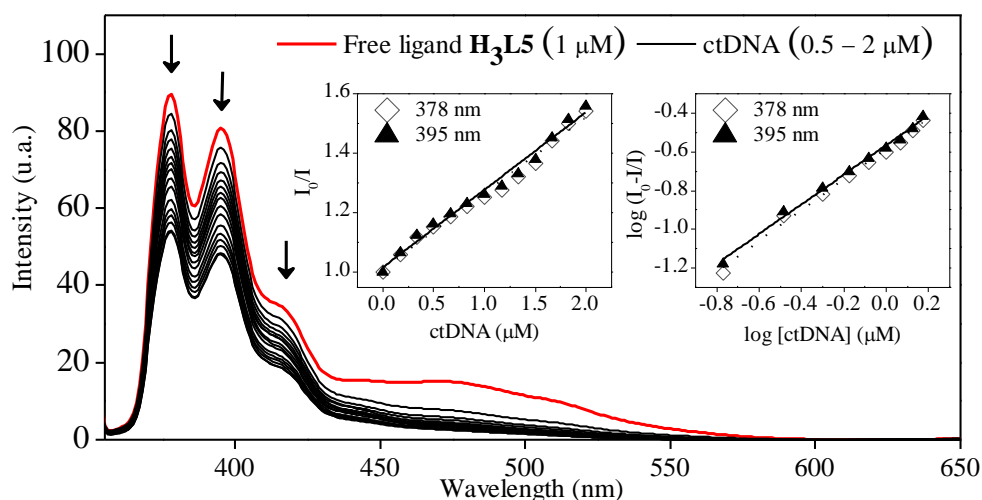


Figure 6.19. Fluorescence emission spectra in a buffer solution (pH 7.40) at 25°C of ligands **H₃L5** (1 μM, $\lambda_{\text{exit}} = 352$ nm) alone or in the presence of ctDNA (arrow, 0 – 2 μM). Inset: plot of I_0/I versus [ctDNA] and plot of $\log[(I_0 - I)/I]$ versus $\log[\text{ctDNA}]$ and their linear fit.

The ctDNA-**H₃L5** solutions displayed an important absorption in the absorption spectra in the tested region for fluorescence studies (Figure 6.18). This absorption was lesser than 0.3, which made possible the correction of the “inner filter” effect using Equation 6.1 [161] to the fluorescence measurements.

$$F_{\text{corr}} = F_{\text{obs}} \cdot \text{antilog} [(A_{\text{ex}} + A_{\text{em}})/2] \quad (\text{Eq 6.1})$$

After confirm the linearity of the data ($R = 0.99$) using the Stern-Volmer plot (I_0/I versus the concentration of the quencher, ctDNA), as can be observed in Figure 6.19 (inset at left), the binding parameters were determine using and Scatchard equation (Equation 6.2) [163]:

$$\log [(I_0 - I)/I] = \log K_b + n \log [Q] \quad (\text{Eq 6.2})$$

Plotting Equation 6.2 (inset at right), it was possible to determine the $\log K_b$ and n which correspond respectively to the intercept and to the slope of the linear curve.

The binding constant between ctDNA and ligand **H₃L5** was $2.8 \times 10^5 \text{ M}^{-1}$ (Table 6.7), while the number of active sites was 0.84, suggesting the existence of an 1 : 1 **H₃L5** : pair of base of ctDNA complex. These results are higher (of the

order of $\sim 10^2 \text{ M}^{-1}$ or $\sim 10^3 \text{ M}^{-1}$) than previous reported for hydrazone ligands [127, 192] and comparable with $4.52 \times 10^5 \text{ M}^{-1} K_b$ and 2.5 n values reported by Ghosh and co-workers, for a pyrene base and ctDNA interaction, which was associated to intercalative binding modes. Nevertheless, the found K_b was lower than the classic intercalator compound ethidium bromide (EB) with K_b value = $1 \times 10^7 \text{ M}^{-1}$ [133].

Comparing the determined K_b in this work with that reported in Chapter 5 for an isoxazole-arylhyazone ligand derivative from **HBPAMFF** moiety, it was observed that the pyrene-arylhyazone ligand (this work) presents a dramatically higher interaction with ctDNA (in the order of $\sim \times 10^3$) than the previous reported isoxazole derivative (**H3L3**), when analyzed in similar conditions. This result proves that the inclusion of a planar system in the structure of the ligands, such as a pyrene group, can improve their interaction with DNA, which is an important property in the search for new anticancer drugs.

In general, the UV-visible absorption analysis indicated the interaction of ligand **H3L5** with ctDNA by intercalation binding mode, as suggested by the hypochromism and redshift observed in the absorption spectra of the ligand upon DNA titration. This result agrees with the planar nature of the pyrene group, which is well-known to intercalate in the double-stranded DNA [199]. Results were verified by fluorescence spectroscopy and the **H3L5**-ctDNA binding parameters were determined. Binding constant for **H3L5**-ctDNA was significantly larger than for other hydrazone ligands, but lesser than for the intercalator EB.

Table 6.7. Fluorescence features of the interaction of ligands **H3L5** with ctDNA at pH 7.40 and at 25 °C.

| Wavelength | $K_b \text{ (M}^{-1}\text{)}^a$ | n | R |
|------------|---------------------------------|------|------|
| 379 | $(2.7 \pm 0.1) \times 10^5$ | 0.85 | 0.99 |
| 398 | $(2.8 \pm 0.1) \times 10^5$ | 0.82 | 0.99 |
| Mean | 2.8×10^5 | 0.84 | |

^a (mean \pm S.D).

6.2.5.

Interaction of ligand H₃L5 with human serum albumin

6.2.5.1

HSA-H₃L5 interaction studies by absorption spectroscopy

With respect to the anticancer agent transport in the body, the interaction with albumin proteins, such as human serum albumin (HSA), is an important property, since this ability of the compounds implies that they can be carried by proteins [209], accelerating their delivery. Displaying the possible transport of new compounds in the human blood by albumin proteins, their interaction is frequently addressed using the UV-Visible absorption technique, which gives information related to the structural changes of these proteins [13, 158].

The absorption band corresponding to the peptide bonds of HSA at 220 nm [159], showed an absorption decrease in presence of ligand **H₃L5**. Besides, a redshift of 13 nm was observed (Figure 6.20). The decrease of the absorbance can be assigned to the perturbation of the α -helices of the protein caused by the presence of the ligand [160]. Additionally, the redshift can be explained by changes in the polarity of the protein's surroundings [160].

In contrast, the band at 280 nm increased progressively without any shift with the concentration of the ligand was increased (Figure 6.20). In albumin proteins, this latter band represents the aromatic amino acids in the protein [159]. Results suggest that the presence of the ligand leads to changes in the HSA molecules and in their microenvironment.

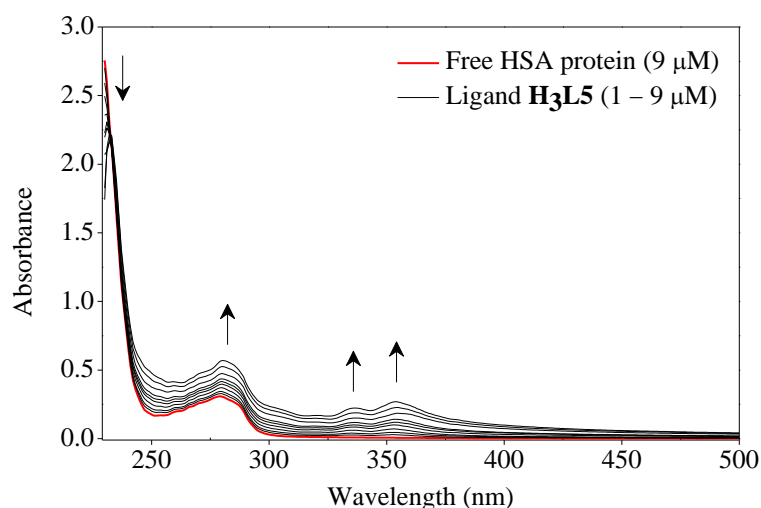


Figure 6.20. Absorption spectra of HSA (9 μM , red curve) protein in a buffer solution (pH 7.40) at 25 $^{\circ}\text{C}$ in the absence and presence of ligand **H₃L5** at increasing concentration (1 – 9 μM , black curves). The absorbance of each addition of the ligand was substrated from the spectra.

Besides, two additional bands were observed in the spectra of HSA in the presence of ligand **H₃L5**. The absorbance of these bands increased when the concentration of the ligand increased, which can be associated to a new HSA-ligand **H₃L5** system (Figure 6.20). Similar behaviour was found when the interaction of similar ligands (**H₃L1** and **H₃L2**) with the BSA protein was tested [210]. The reported study demonstrated that the presence of binucleating Schiff base ligands containing in their structure both **HBPAMFF** and hydrazones moieties cause aggregation of the albumin protein BSA (Chapter 4, item 4.2.4).

The absorption spectrum of the tested ligand was also verified upon increasing the concentration of HSA protein. Addition of the protein to the solution containing ligand **H₃L5** led to an increase in the absorbance of the bands at 332 nm and 350 nm (Figure 6.21). These results confirm those observed upon titration of the HSA with the ligand, and suggest the formation of a new HSA-ligand **H₃L5** system. Finally, as was observed in Figure 6.20, free HSA did not show any absorption in the 325 – 500 nm wavelength.

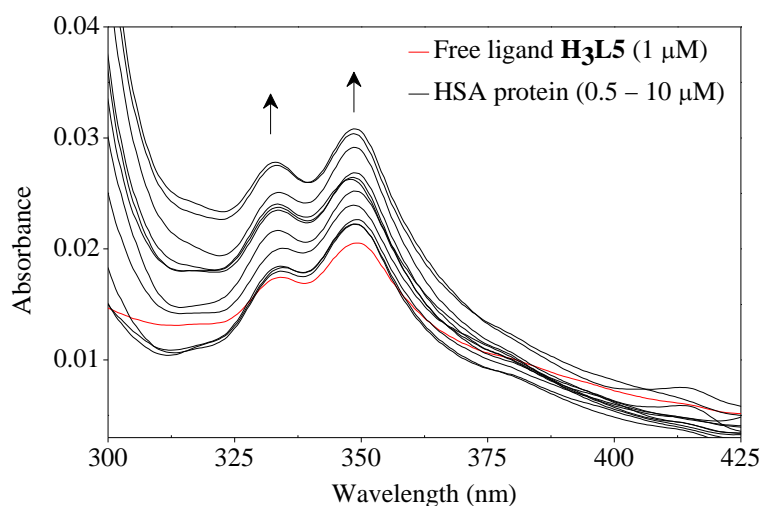


Figure 6.21. Absorption spectra of ligand **H₃L5** (1 μ M, red curve) in a buffer solution (pH 7.40) and at 25 $^{\circ}$ C in the absence and presence of HSA protein at increasing concentration (0.5 and 1 – 10 μ M, black curves). The absorbance of each addition of HSA was substrate from the spectra.

6.2.4.2

HSA-H₃L5 interaction studies by fluorescence spectroscopy

Fluorescence spectroscopy has been used with success to study the interaction of albumin with organic ligands and copper complexes [13, 149-152, 165], as it allows to observe conformational changes in proteins and to determine binding parameters.

Therefore, in order to reach the biological characterization of the compounds in this work, the effect of HSA protein in the fluorescence properties of ligand **H₃L5** was explored. Figure 6.22 shows that in the presence of HSA the fluorescence emission of ligand **H₃L5** increased linearly ($R = 0.99$) as can be observed in the Stern-Volmer plot (Figure 6.22, inset), using I/I_0 to obtain positives values. It was observed that the fluorescence intensity of **H₃L5** increased upon each addition of HSA. At 398 and 379 nm the intensity of the fluorescence increased to $\sim 60\%$ when the concentration of HSA was twice the concentration of ligand **H₃L5**. This result suggests that ligand **H₃L5** can interact with the HSA protein.

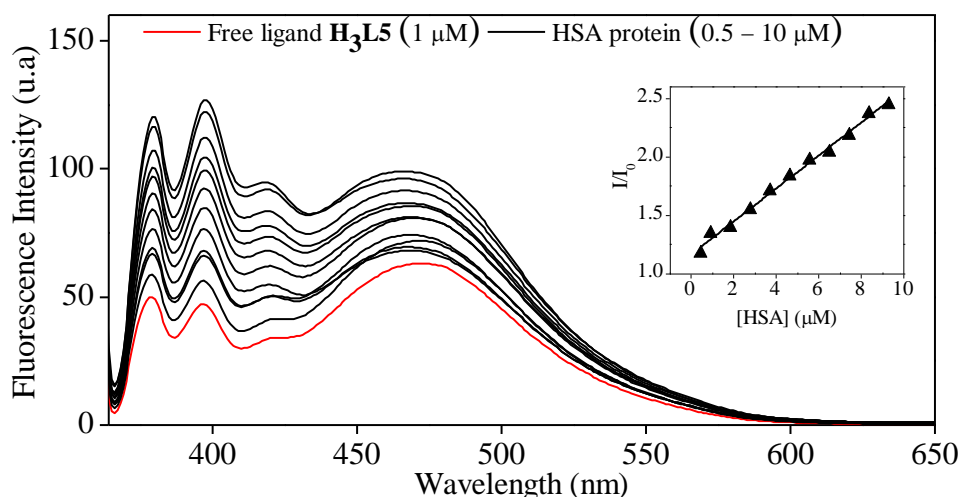


Figure 6.22. Enhancement of the fluorescence emission of ligand **H₃L5** (1 μ M, red curve) in a buffer solution (pH 7.40) at 25 $^{\circ}$ C in the presence of HSA protein at increasing concentration (0.5 and 1 – 10 μ M, black curves).

A similar fluorescence enhancement effect was observed between the avidin protein and an organic ligand derived from pyrene [211]. In this latter study, the authors reported the increase in the fluorescence intensity of the pyrene-ligand at 460 nm in the presence of the protein [211]. MATSUSHITA and MORIGUCHI largely studied the interaction of pyrene-1-butyric acid and serum animal albumins [212]. In this latter work, it was found that various albumin proteins enhanced the fluorescence intensity of the pyrene-1-butyric. For these systems the binding constants were determined using the equilibrium dialysis method [212].

Finally, it was demonstrated that aroylhydrazonic derivatives of **HBPAMFF** precursor formed aggregates with bovine serum albumin protein [210], and additionally, the aggregation process enhances the intensity in HSA [213]. Thus, increase of the fluorescence emission in the **H₃L5** spectrum in the presence of HSA could be related to the aggregation process.

In brief, absorption and fluorescence results suggest that ligand **H₃L5** can interact with albumin HSA protein, which is responsible for the transport of drug in human body. The enhancement in the fluorescence intensity of the pyrene derivative caused by the presence of albumin protein was previously observed in some works. Aroylhydrazonic ligands with **HBPAMFF** framework could be involved in aggregation process with albumin proteins. Thus, various processes could be responsible for the increase of absorbance and fluorescence of ligand **H₃L5**

in the presence of HSA. Consequently, additional analysis are necessary to examine the nature of the **H₃L5**-HSA interaction.

6.2.6

In vitro cytotoxic activity

One of the goals of this thesis was to test the ability of the synthesized compounds to kill cancer cells. Thus, the *in vitro* antiproliferative activity of ligand **H₃L5** and its dicopper(II) complexes against the human breast cancer cell line MDA-MB-231 was assessed through the MTT assay [135].

The presence of the compounds on the tested cancer cells after an exposure period of 72 h at different concentrations caused a decrease in the relative cellular viability (Figures 6.23 and 6.24).

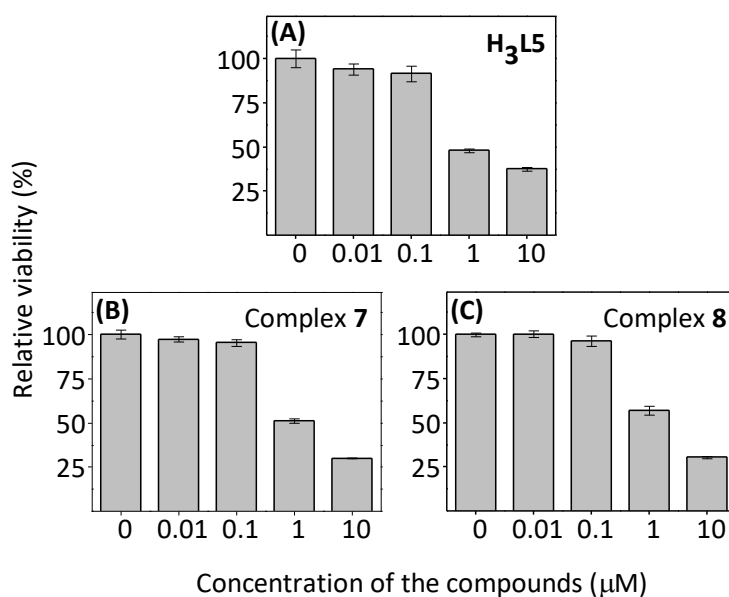


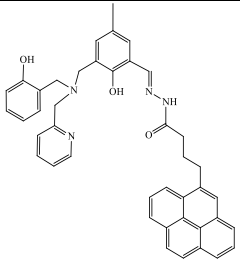
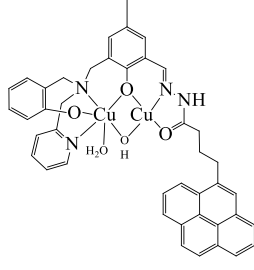
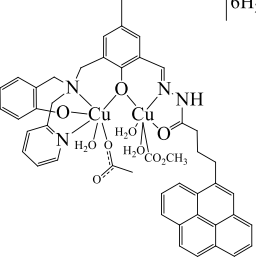
Figure 6.23. Dose-dependent effect expressed as the percentage of relative viability of MDA-MB-231 cells measured by the MTT assay for (A) **H₃L5**; (B) complex **7** and (C) **8** after 72 h incubation at 37 °C. Data represent the mean of triplicate experiments.

The presence of the compounds on the tested cancer cells after an exposure period of 72 h at different concentrations of the compounds caused a decrease of their relative viability (Figures 6.23 and 6.24).

In contrast to the commonly observed in cytotoxic assays [15, 16, 195], results showed that the metal-free ligand **H₃L5** displayed higher antiproliferative

activity when compared with its copper(II) complexes **7** and **8** at more than a 50% level (Table 6.8). The possible reason for the ligand to be more potent than the complexes can be explained by its higher ability to sequester metal ions from the cellular medium, as discussed in Chapter 5 (item: 5.2.5 – 5.2.7). Additionally, the growth inhibition activity followed the order: ligand **H3L5** > complex **8** > complex **7**.

Table 6.8. IC₅₀ values of ligand **H3L5** and its copper(II) complexes **7** and **8** on MDA-MB-231 cancer cell line. Standard deviations of data are included.

| Compound | IC ₅₀ (μM) | Standard deviation | Compound' structure |
|------------------|-----------------------|--------------------|---|
| H3L5 | 0.35 | 0.02 |  |
| Complex 7 | 1.05 | 0.07 |  ClO ₄ |
| Complex 8 | 1.35 | 0.01 |  6H ₂ O |

Regarding the copper(II) complexes, it is important to highlight that the perchlorate-complex **7** needed a lesser concentration to kill cancer cells than the acetate-complex **8**. The cytotoxic profile of the compounds and the fitted curve to determine the IC₅₀ values are shown in Figure 6.24.

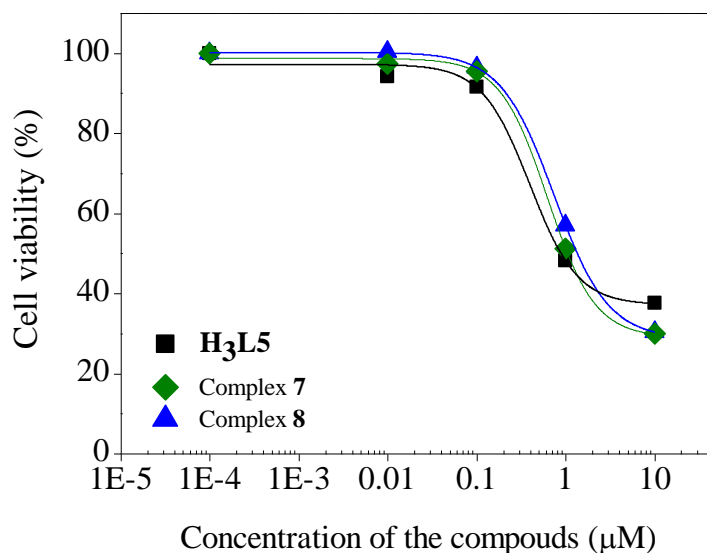


Figure 6.24. Dose-dependent effect on MDA-MB-231 cells of ligand **H₃L₅** copper(II) complexes **7** and **8** after 72 h at 37 °C using the MTT assay.

6.3

Partial conclusions

A novel 1-pyrenebutyric acid hydrazone-derived Schiff base ligand **H₃L₅** and its dicopper(II) complexes **7** and **8** were synthesized and fully characterized by spectroscopic and analytical techniques.

X-ray diffraction analyses of the synthesized ligand indicate the presence of isomers in the solid state. In solution, NMR analyses shows also the occurrence of isomers.

Absorption bands of the compounds were assigned to its precursor moieties and the formed hydrazone bond. Effects upon coordination in the absorption bands were identified.

Fluorescence emission spectra of the compounds were examined in aqueous medium and organic solvents. Ligand **H₃L₅** displayed fluorescence properties, while its copper(II) complexes **7** and **8** were not fluorescent in the tested conditions.

After 24 h, ligand **H₃L₅** and its copper(II) complexes were stable in DMSO and in the relevant cellular medium PBS (37 °C, pH 7.4), as indicated by UV-Vis absorption measurements. Thus, their stability was appropriate to perform biological tests.

The absorption and fluorescence properties of **H₃L5**, functionalized with a pyrene fluorophore, were used to examine its interactions with ctDNA and HSA protein. The results showed an **H₃L5**-ctDNA intercalative binding mode. This work suggests the improvement of the ligand-DNA interaction by the functionalization of the compound with the potent intercalative pyrene group.

The found interaction between the albumin protein and **H₃L5** implies that HSA could target this ligand in the human body, accelerating the efficacy of this potent anticancer drug. With respect to the enhancement of the fluorescence intensity of ligand **H₃L5** produced by HSA, additional analysis should be performed in order to better understand the nature of the **H₃L5**-HSA interaction.

The cytotoxicity of the compounds on human epithelial breast cancer cells was assessed by the well-known MTT assay, since breast cancer is the second most common form of cancer in the world. The results evidenced that all of the synthesized compounds are active against cancer cells, which is an important result based on the resistance displayed by the MDA-MB-231 cell line to chemotherapeutic treatments. Additionally, the binucleating ligand **H₃L5** presented the best antiproliferative activity among the set of compounds, and perchlorate-copper(II) complex was more active than the acetate-copper(II) one.

In conclusion, this work reported the synthesis and characterization of a new aroylhydrazone-derived binucleating ligand and its μ -hydroxo dicopper(II) complexes. All of these compounds displayed promising structural properties to be potential antitumour agents. Finally, the found relation between the structure of the compounds and their biological activity and cytotoxicity can direct the design of new compounds with even better potent anticancer profiles.

Results and discussion IV. Two novel luminescent binucleating aroylhydrazonic ligands and their dicopper(II) complexes as potential anticancer agents: syntheses, chemical characterization, biological activity and cell imaging

The present chapter was redacted in order to be published as an article in a scientific journal. Hence, it is important to verify the existence of the final published paper before citing the data here described.

7.1

Introduction

In contrast to cisplatin, the most used metal in cancer chemotherapy [78], copper is an essential ion in human body with several biological functions [2, 3]. When bound to a large variety of organic ligands, the resulting copper(II) complexes have proved their ability to interact with DNA and to cut the double-strand formed by the nucleic acids in the DNA molecule [17-21, 24, 29-41], hindering cancer cell proliferation. Regarding cancer cell death, reported dinuclear copper(II) complexes demonstrate the induction of apoptotic cell death [21, 40].

Furthermore, both ligands and complexes containing in their structures both 3-[(2-hydroxybenzyl)(2-pyridylmethyl)amine]-2-hydroxy-5-methylbenzaldehyde (**HBPAMFF**) [102] and hydrazone systems (**HBPAMFF-Hz**) [210] (also discussed in Chapter 5 and 6) demonstrate their capacity to interact with albumin proteins, responsible for the transport of the drug in the blood [143], probably involving aggregation process [210]. Additionally, these compounds established their high antiproliferation activity on a set of cancer cell lines, such as human colon, human breast and mouse melanoma.

Considering the anticancer properties displayed by the **HBPAMFF-Hz** molecules, this work aims to functionalize the hydrazone group with potent

fluorophores in order to evaluate the ability of the new compounds to enter into the cells. Hence, compounds comprising the boron-dipyrromethene (**BODIPY**) molecule [214] in their structure have been explored as anticancer agents in recent years [203, 215-217]. Besides, cellular uptake of the **BODIPY** derivatives were successfully analysed through cell imaging technique using the fluorescence properties of these compounds [203, 215, 216]. On the other hand, 4-*H*-[1]-benzopyrano[4,3-*b*]thiophene-2-carbohydrazide (**BPTH**) is a potent fluorophore that has been used, for example, to identify glycoproteins through fluorescent detection method [218].

The novel contributions of present study are the design, syntheses and characterization of new **HMPAMFF-Hz** derived ligands and copper(II) complexes that include in their structure potent fluorophore moieties, in order to evaluate them as candidates for prospective antitumour drugs, including their ability to pass the barrier of the membrane cell. Finally, selection of MDA-MB-231 cancer cells to test the antitumour activity of the designed compounds were motivated by the fact that breast cancers present the second highest both incidence and mortality rates in the world and Latin America and the Caribbean [58].

7.2

Results

7.2.1

Syntheses

Two fluorescent binucleating Schiff base ligands, **H₃L6** and **H₃L7**, were obtained from the precursor **HBPAMFF** and the fluorophores 4-*H*-[1]-benzopyrano[4,3-*b*]thiophene-2-carbohydrazide (**BPTH**) (ligand **H₃L6**) or fluor-methoxy-**BODIPY-hydrazide** (**FMeO-BODIPY-Hz**) (ligand **H₃L7**). The compounds were refluxed in equimolar amounts in MeOH or 1:1 MeCN/MeOH. Ligand **H₃L6** crystalized as small colourless hexagonal crystals.

Furthermore, copper(II) complexes **9–12** were prepared from the synthesized ligands and copper(II) perchlorate hexahydrate salt (1 : 2 equivalent, respectively) in the presence of potassium hydroxide (**9** and **11**) or copper(II) acetate monohydrate (**10** and **12**), respectively. Complexes from ligand **H₃L6** were

formulated as $[\text{Cu}_2(\text{HL6})(\text{ClO}_4)_2(\text{H}_2\text{O})(\text{CH}_3\text{OH})]\text{H}_2\text{O}\cdot\text{CH}_3\text{OH}$ (**9**) and $[\text{Cu}_2(\mu\text{-CH}_3\text{COO})_2(\text{HL6})(\text{H}_2\text{O})]2\text{H}_2\text{O}$ (**10**) (Figure 7.1). Complexes from ligand **H3L7** were formulated as $[\text{Cu}_2(\text{HL6})(\text{H}_2\text{O})_3]3\text{ClO}_4\cdot 7\text{H}_2\text{O}$ (**11**) and $[\text{Cu}_2(\mu\text{-CH}_3\text{COO})(\text{HL6})(\text{H}_2\text{O})_2]\text{COOCH}_3\cdot 5\text{H}_2\text{O}$ (**12**) (Figure 7.1).

The ligands **H3L6** (99%, quantitative) and **H3L7** (63%) and their respective copper(II) complexes **9** (70%) and **10** (75%), and **11** (73%) and **12** (50%) were obtained in good yields and characterized by elemental analysis, spectroscopic techniques and single-crystal X-ray diffraction (XRD) analysis (for complex **9**).

The electrolytic nature of the complexes was analyzed by conductivity measurements. Molar conductivity measured in acetonitrile of complexes **9** ($34 \text{ ohm}^{-1} \text{ cm}^2 \text{ mol}^{-1}$), and **10** ($7 \text{ ohm}^{-1} \text{ cm}^2 \text{ mol}^{-1}$) indicated that these are non-electrolyte systems, whereas complexes **11** ($362 \text{ ohm}^{-1} \text{ cm}^2 \text{ mol}^{-1}$) and **12** ($134 \text{ ohm}^{-1} \text{ cm}^2 \text{ mol}^{-1}$) are, respectively 1 : 3 and 1 :1 electrolyte systems [138].

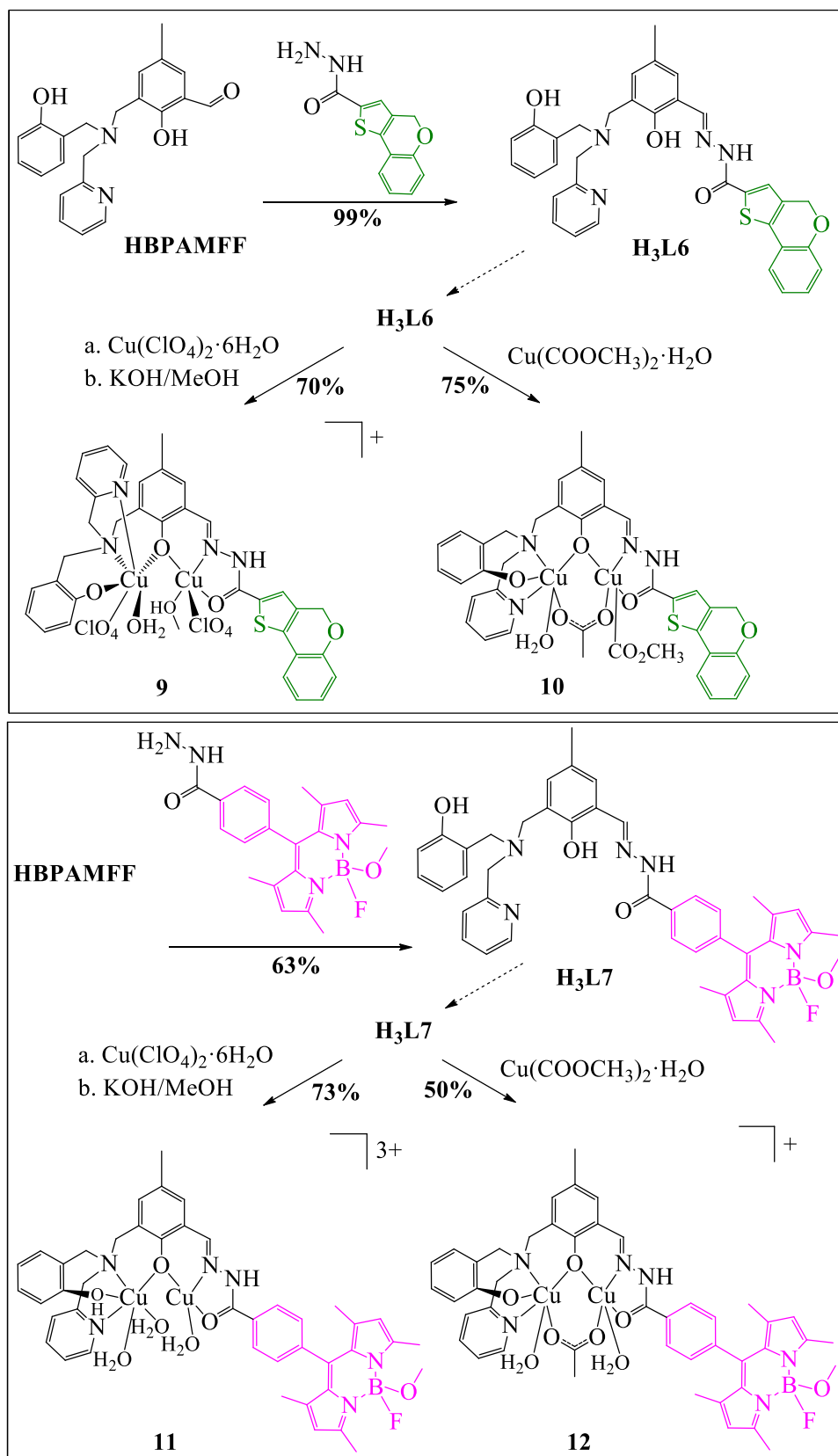


Figure 7.1. Synthetic routes to ligands **H₃L6** (top) and **H₃L7** (bottom), and their copper(II) complexes from perchlorate **9** and **11** or acetate salts **10** and **12**.

7.2.2

Characterization of ligands and complexes

7.2.2.1

Solution NMR of ligands

The ^1H NMR spectrum of **H₃L6** recorded in deuterated DMSO (Figure 7.2) confirmed its synthesis. Thus, the imine proton assigned to the $\text{N}=\text{C}-\text{H}$ hydrazone system appeared at 8.56 ppm in the ^1H NMR spectrum, while the peak corresponding to the aldehyde system of the precursor **HBPAMFF** is absent in the spectrum (Figure 13.1). The signals associated to the alkyl groups in **H₃L6** appeared at lowest frequencies, followed by the aromatic hydrogens and finally by the heteroatoms hydrogens $-\text{OH}$ (from phenols) and $-\text{NH}$ (from hydrazone). The signal at 8.56 ppm was assigned to the $\text{N}=\text{C}-\text{H}$ hydrazone framework.

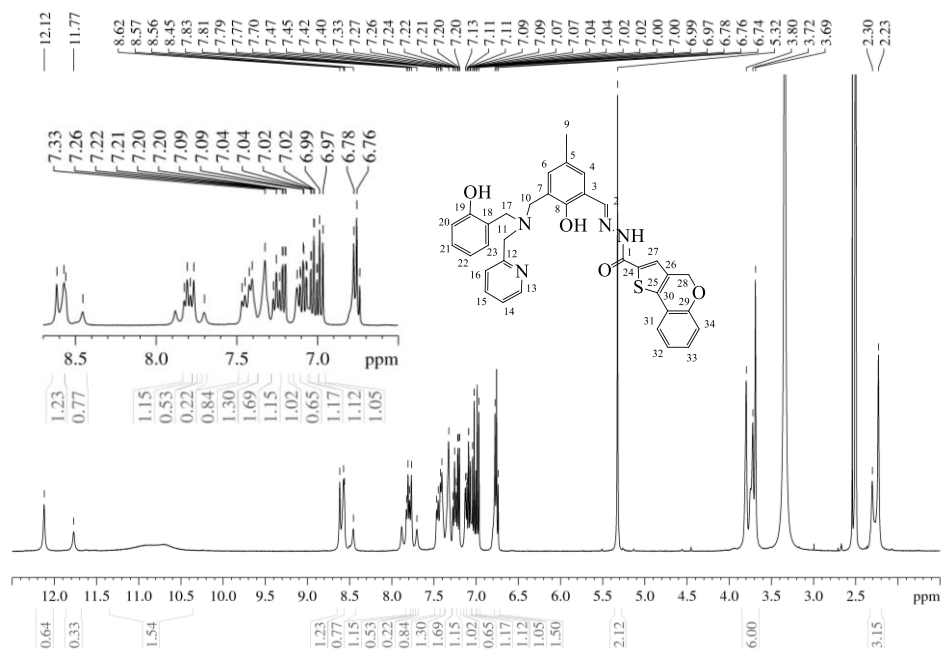


Figure 7.2. ^1H NMR spectrum (400 MHz) of **H₃L6** in $\text{DMSO}-d_6$ at room temperature.

As previously discussed (Chapter 4 – 6), hydrazone derivatives allow the formation of both geometric (*E* / *Z*) and tautomeric isomers in solution (iminol / amide forms) [139-141]. The ^1H NMR spectrum for **H₃L6** showed duplication of the signals. This effect was clearer for the $-\text{NH}$ peak (from the hydrazone) and the

OH peak, at 12.12 ppm (~70%) and 11.77 ppm (~30%), associated respectively to the *E*-amide (–NH) and *E*-iminol isomers (–OH). In the ^{13}C NMR for ligand **H₃L6** (Figure 7.3) the signal for C=O of the *E*-amide isomer appeared at 157.6 ppm, while the peak corresponding to the C=C–OH isomer form was located at 160.8 ppm. These latter signal was absent in the DEPT-135 spectrum for ligand **H₃L6** (Figure 7.4).

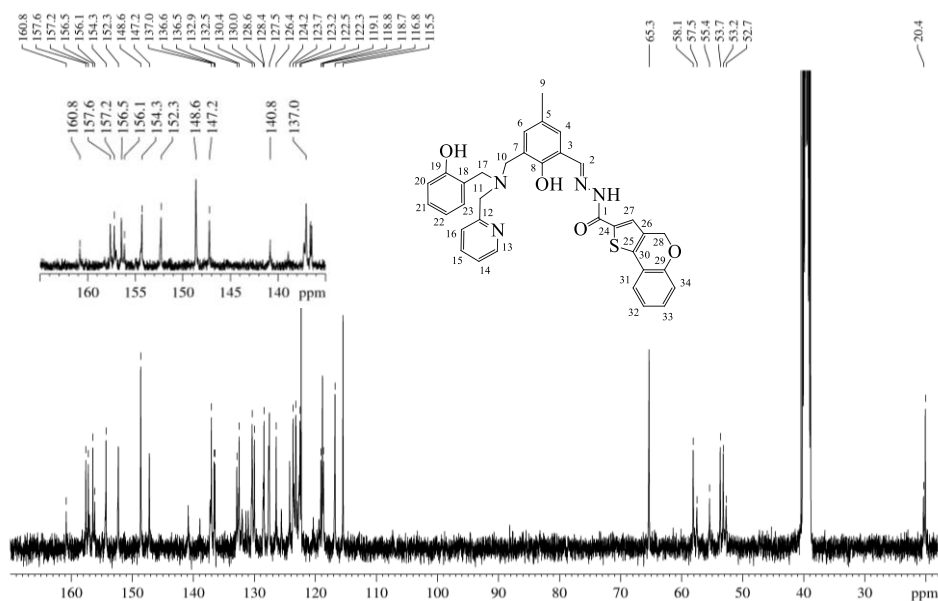


Figure 7.3. ^{13}C NMR spectrum (100 MHz) of **H₃L6** in $\text{DMSO}-d_6$ at room temperature.

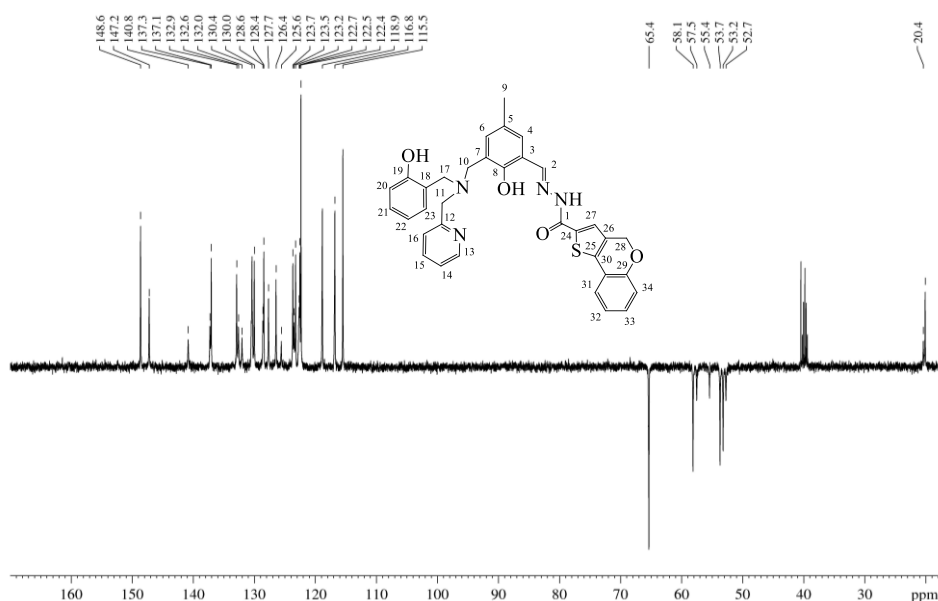


Figure 7.4. DEPT-135 spectrum (100 MHz) of **H₃L6** in $\text{DMSO}-d_6$ at room temperature.

All NMR assignments for the hydrogens and carbons of ligand **H₃L6** are available in Table 6.1. Signals corresponding to both isomers were differentiated.

On the other hand, the ¹H NMR spectrum for **H₃L7** recorded in deuterated DCM (Figure 7.5) was very similar to the spectrum for **H₃L7** concerning the **HBPAMFF-Hz** substituent. The signals associated to **FMeO-BODIPY-Hz** moiety were assigned by comparing of the spectrum of this latter (Figure 13.2) with the spectrum of **H₃L7**. No significant signals of isomers were detected in the ¹H NMR spectrum. All the hydrogen signal assignments of the NMR for **H₃L7** can be found in Table 7.1. Finally, some symmetrical signals from the **FMeO-BODIPY-Hz** were observed in the ¹H NMR spectrum of **H₃L7**, as specified in the table.

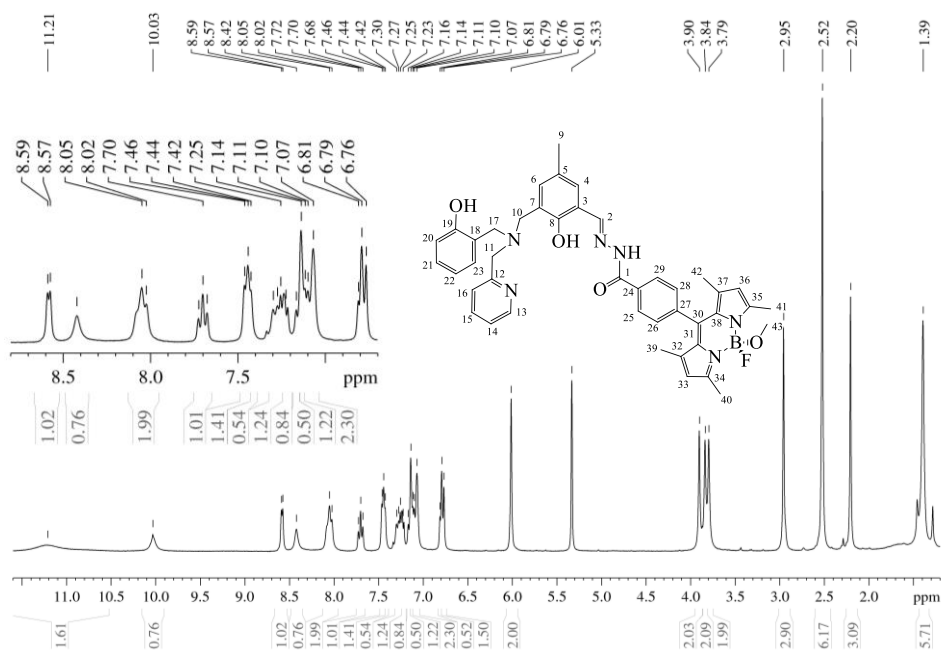


Figure 7.5. ¹H NMR spectrum (400 MHz) of **H₃L7** in DCM-d_2 at room temperature.

Table 7.1. ^1H (400 MHz) and ^{13}C (100 MHz) data for **H₃L6** and ^1H (400 MHz) for **H₃L7** in $\text{DCM}-d_2$ at room temperature, along with the respective assignments. Chemical shifts (δ) are in ppm and coupling constants (J) are in Hz.

| C/H | H₃L6 , δ_{C} | H₃L6 , δ_{H} | H₃L7 , δ_{H} |
|------|--|---|--|
| 1 | 157.6 | – | – |
| 2 | 147.2 | 8.56 (s, 1H) | 8.42 (s, 1H) |
| 3 | 118.7 | – | – |
| 4 | (122.5*/122.3)* | 7.35 (m, 2H)* | 7.42 (s, 1H) |
| 5 | 127.5 | – | – |
| 6 | 132.9*/132.5 | 7.13 (s, 1H) | 7.16 (s, 1H) |
| 7 | 124.2 | – | – |
| 8 | 154.3 | – | – |
| 9 | 20.4*/20.1 | 2.30*/2.23 (s, 3H) | 2.20 (s, 3H) |
| 10 | 53.2/52.7* | 3.74 (s, 2H) | 3.84 (s, 2H) |
| 11 | 58.1/57.5* | 3.81 (s, 2H) | 3.90 (s, 2H) |
| 12 | 157.6/157.2* | – | – |
| 13 | 148.6 | 8.59 (d, 1H, $^3J_{\text{HH}} = 4.0$) | 8.59 (d, 1H, $^3J_{\text{HH}} = 4.3$) |
| 14 | 127.7*/127.5 | 7.35 (m, 2H)* | 7.27 (t, 1H, $^3J_{\text{HH}} = 7.5$) |
| 15 | 137.3*/137.0 | 7.81 (t 1H, $^3J_{\text{HH}} = 7.7$) | 7.70 (d, 1H, $^3J_{\text{HH}} = 7.5$) |
| 16 | 123.2 | 7.41 (d, 1H, $^3J_{\text{HH}} = 7.4$) | 7.45 (d, 1H, $^3J_{\text{HH}} = 7.5$) |
| 17 | 53.7/55.4* | 3.69 (s, 2H) | 3.79 (s, 2H) |
| 18 | 123.1 | – | – |
| 19 | 156.5/156.2* | – | – |
| 20 | 115.5 | 6.77 (s, 1H) | 6.81 (s, 1H) |
| 21 | 128.6*/128.4 | 7.09 (td, 1H, $^3J_{\text{HH}} = 7.8$, $^4J_{\text{HH}} = 1.6$) | 7.09 (t, 1H, $^3J_{\text{HH}} = 7.6$) |
| 22 | 118.8 | 6.74 (d, 1H, $^3J_{\text{HH}} = 7.4$) | 6.77 (d, 1H, $^3J_{\text{HH}} = 7.6$) |
| 23 | 130.3*/130.0 | 7.21 (dd, 1H, $^3J_{\text{HH}} = 7.5$, $^4J_{\text{HH}} = 1.3$) | 7.23 (dd, 1H, $^3J_{\text{HH}} = 7.6$) |
| 24 | 136.6/136.5* | – | – |
| 25 | 100.3 | – | 8.05 (s, 1H)* |
| 26 | 170.6 | – | 7.14 (s, 2H)* |
| 27 | 126.4 | 7.77/7.70* (s, 1H) | – |
| 28 | 65.3 | 5.32 (s, 2H) | 7.14 (s, 2H)* |
| 29 | 152.3 | – | 8.05 (s, 1H)* |
| 30 | 129.4 | – | – |
| 31 | 123.7 | 7.46 (d, 1H, $^3J_{\text{HH}} = 7.4$) | – |
| 32 | (122.5*/122.3)* | 7.02 (td, 1H, $^3J_{\text{HH}} = 7.6$, $^4J_{\text{HH}} = 1.0$) | – |
| 33 | 130.5*/130.4 | 7.25 (t, 1H, $^3J_{\text{HH}} = 7.4$) | 6.01 (s, 2H)* |
| 34 | 116.8 | 6.98 (d, 1H, $^3J_{\text{HH}} = 8.1$) | – |
| 35 | – | – | – |
| 36 | – | – | 6.01 (s, 2H)* |
| 37 | – | – | – |
| 38 | – | – | – |
| 39 | – | – | 1.39 (s, 1H)* or 2.52 (s, 6H)* |
| 40 | – | – | 1.39 (s, 1H)* or 2.52 (s, 6H)* |
| 41 | – | – | 1.39 (s, 1H)* or 2.52 (s, 6H)* |
| 42 | – | – | 1.39 (s, 1H)* or 2.52 (s, 6H)* |
| 43 | – | – | 2.95 (s, 3H) |
| O2–H | – | 10.80 (s, br, 2H)* | 10.03 (s, 1H) |
| O3–H | – | 10.80 (s, br, 2H)* | 11.21 (s, br, 2H)* |
| N1–H | – | 12.12/11.77* [†] (s, 1H) | 11.21 (s, br, 2H)* |

*Overlapped signals. *isomer signal with less intensity. Signal multiplicity - s: singlet, d: doublet, t: triplet, dd: doublet of doublets, td: triplet of doublets. [†]Iminol form (C–OH).

7.2.2.2

Crystal structure of complex **9**

The analysis of complex **9** by a single crystal X-ray diffraction study showed that this compound crystallized in the triclinic system in space group P-1. Figure 7.6 shows the Oak Ridge Thermal Ellipsoid Plot (ORTEP) view of the neutral complex structure with chemical formula $[\text{Cu}_2(\text{HL6})(\text{ClO}_4)_2(\text{H}_2\text{O})(\text{CH}_3\text{OH})]\text{H}_2\text{O}\cdot\text{CH}_3\text{OH}$ (**9**). Two coordinated perchlorate ions and one methanol molecule were identified in the complex crystals. Table 7.2 lists significant crystallographic data and refinement parameters.

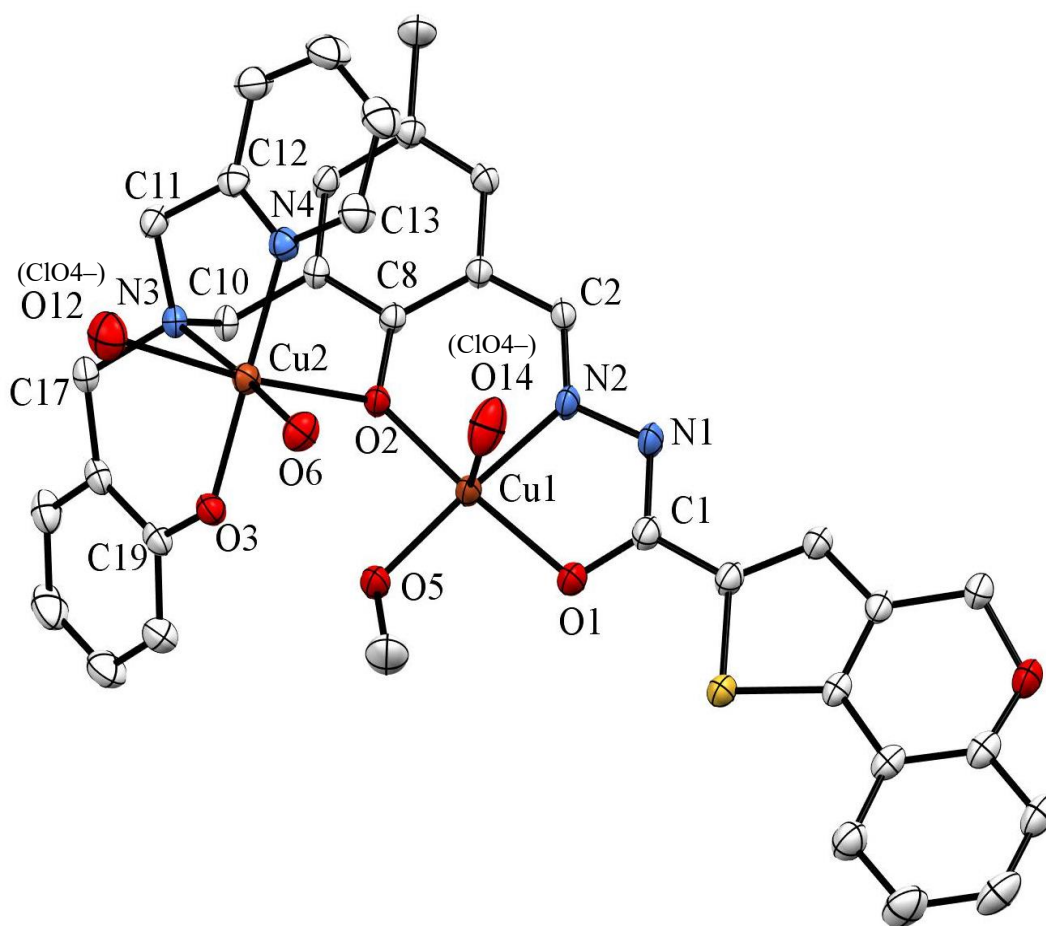


Figure 7.6. Crystal structure of complex **9**. The ellipsoids were drawn with 50% probability highlighting the copper's environments (inset). Hydrogen atoms and crystallization solvents were omitted for the sake of clarity.

Table 7.2. Crystallographic data and structure refinement of complex **9**.

| 9 | |
|--|--|
| Empirical formula | C ₃₆ H ₄₀ Cl ₂ Cu ₂ N ₄ O ₁₆ S |
| Formula weight (g/mol) | 1014.76 |
| Temperature (K) | 200(1) K |
| Crystal description | green |
| Crystal system | Triclinic |
| Space group | P-1 |
| a (Å) | 10.3691(5) |
| b (Å) | 11.1316(6) |
| c (Å) | 19.5583(10) |
| α (°) | 79.8180(10) |
| β (°) | 78.6480(10) |
| γ (°) | 66.1730(10) |
| Volume (Å ³) | 2012.76(18) |
| Z | 2 |
| ρ _{calc} (g/cm ³) | 1.674 |
| Absorption coefficient μ (mm ⁻¹) | 1.320 |
| Crystal size (mm ³) | 0.32 × 0.158 × 0.132 |
| Wavelength λ (Å) | 0.71073 |
| Radiation type | Mo Kα |
| 2θ range (°) | 4.024 to 61.142 |
| Miller indexes ranges | -14 ≤ h ≤ 14, -15 ≤ k ≤ 15, -27 ≤ l ≤ 27 |
| Measured reflections | 40008 |
| Unique reflections | 12322 |
| Goodness-of-fit F ² | 1.032 |
| Final R indexes | R1 = 0.0522 |
| [all data] | wR2 = 0.1007 |
| Final R indexes | R1 = 0.0370 |
| [I ≥ 2σ(I)] | wR2 = 0.0940 |
| Refinement | |
| Data | 12322 |
| No. of parameters | 594 |
| No. of restraints | 38 |
| Largest diff. peak/hole (e/Å ³) | 0.76,-0.66 |

In the solid state, the structure of complex **9** indicates that the precursor ligand has the form **HL6**²⁻. It is observed that upon complexation, the hydrogen N–H from the hydrazone moiety is conserved. The complex exhibits two independent copper sites with 3.757 Å inter-metallic distance.

For the complex **9**, the copper ion Cu1 was coordinated by both N2 and O1 atoms from the hydrazone framework. Besides, Cu1 coordinates three additional –O donor atoms from (i) the central ring, (ii) one perchlorate ion and (iii) one methanol molecule. The resulting square pyramidal geometry (Figure 7.7) presents a slightly distorted plane with copper-donor atoms distances varying between 1.888 – 1.974 Å in the pyramidal base. The oxygen from the perchlorate in the apical position was located at 2.602 Å distance from Cu1. All angles of the pyramidal environment varying between 81.65 – 94.45°.

On the other hand, Cu2 was coordinated by two oxygen and two nitrogens from **HBPAMFF** moiety. Two additional oxygens from both perchlorate and water molecules completed the octahedral geometry of complex **9**. Measurements of the distances and angles of the atoms revealed a pronounced Jahn-Teller effect causing an elongated octahedral form (Figure 7.7). Hence, the Cu1–donor atoms (N₂O₄) distance bonds of the axial plane varied between 1.943 – 2.007 Å, whereas those of the equatorial plane were 2.648 Å (Cu1–perchlorate) and 2.479 Å (Cu1–phenol central ring). All angles of the environment of the distorted elongated octahedral vary between 83.31 – 99.82°.

It was noted that in the ORTEP of complex **9**, the phenol from the central ring (O2) was in an endogenous bridged position, while the rings of the precursors **BPTH** and **FH-BODIPY** were not complexed to the metal copper. The structure presented one methanol solvate and one uncoordinated water molecule.

Two intramolecular H-bonds were observed in the complex structure. The crystal packing formed by two molecules of **9** (Figure 7.7) was also stabilized by strong and weak intermolecular H-bonds from both complex **9** molecules and solvate molecules. A complete list of the hydrogen-bond geometries present in complexes **9** is described in Table 7.3. Selected geometric parameters for complex **9** are shown in Table 7.4.

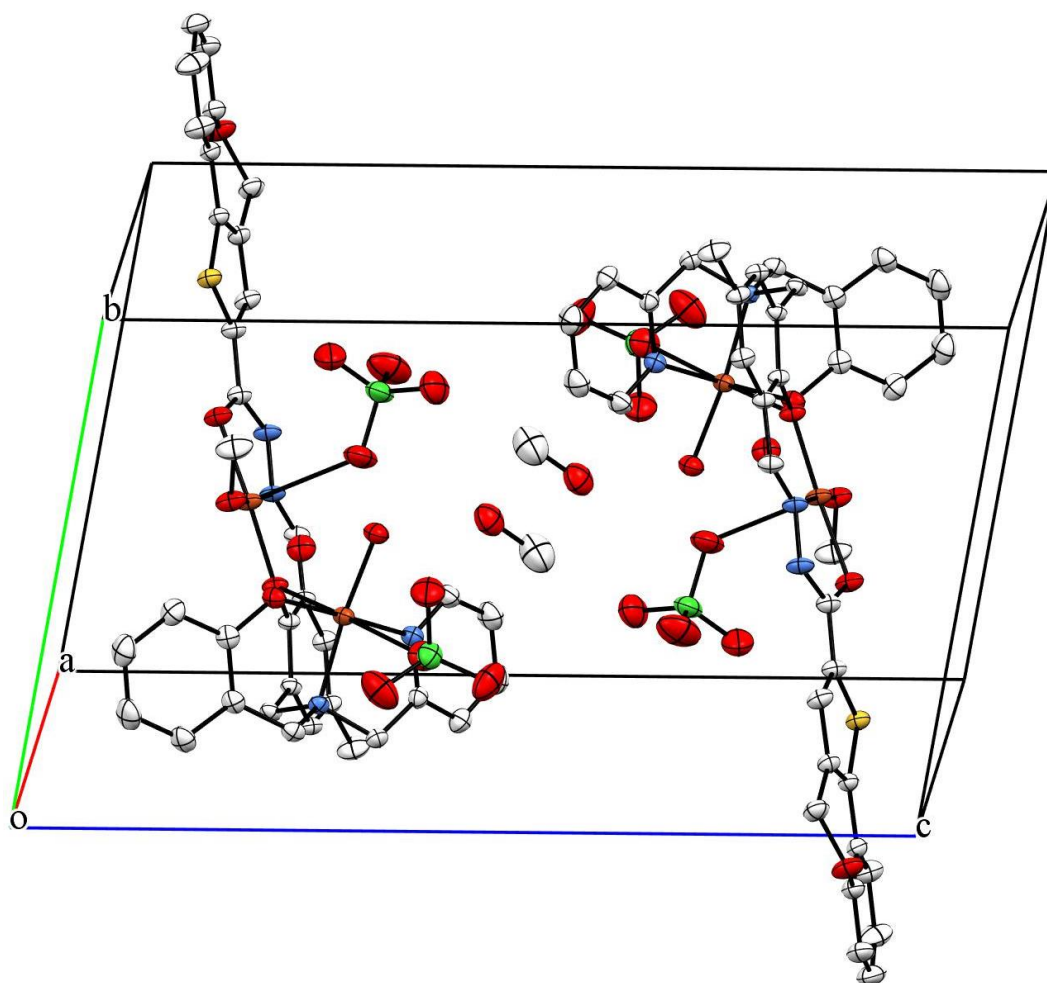


Figure 7.7. Molecular packing of complex **9**. Hydrogen atoms have been omitted for clarify.

Table 7.3. H-bond length (d, Å) and angles (°) for complex **9**.

| D—H...A | d(D—H) | d(H...A) | d(D...A) | D—H...A (°) |
|----------------------------|---------|----------|----------|-------------|
| N1—H1...O8* | 0.78(3) | 1.94(3) | 2.714(3) | 174(3) |
| O5—H5...O3 | 0.74(3) | 1.87(3) | 2.605(2) | 177(2) |
| O6—H6B...O14 | 0.83 | 1.92 | 2.731(3) | 167 |
| O6—H6A...O7* | 0.82 | 1.81 | 2.628(3) | 173 |
| O7*—H7...O10 ⁱ | 0.88(5) | 2.31(4) | 3.000(3) | 135(4) |
| O7*—H7...O9 | 0.88(5) | 2.40(4) | 3.044(3) | 131(3) |
| O8*—H8A...O3 ⁱⁱ | 0.85 | 1.89 | 2.734(2) | 171 |
| O8*—H8b...O9 ⁱⁱ | 0.85 | 2.08 | 2.877(3) | 156 |

Symmetry codes: (i) $2-x, 1-y, 1-z$, (ii) $-1+x, y, z$. *solvate molecule.

Table 7.4. Selected geometric parameters for complex **9**.

| Bond distances (Å) | | Bond angles (°) | |
|--------------------|----------|-----------------|------------|
| O1-C1 | 1.223(2) | C1-N1-N2 | 120.55(14) |
| O2-C8 | 1.362(2) | C2-N2-N1 | 116.63(14) |
| O3-C19 | 1.365(2) | C11-N3-C10 | 111.18(13) |
| N1-N2 | 1.375(2) | C11-N3-C17 | 111.70(12) |
| N1-C1 | 1.353(2) | C17-N3-C10 | 111.45(13) |
| N2-C2 | 1.278(2) | C13-N4-C12 | 118.28(17) |
| N3-C10 | 1.479(2) | O1-C1-N1 | 123.55(16) |
| N3-C11 | 1.474(2) | O1-C1-C24 | 123.24(16) |
| N3-C17 | 1.477(2) | N1-C1-C24 | 113.21(14) |
| N4-C12 | 1.342(2) | N2-C2-C3 | 121.47(15) |
| N4-C13 | 1.339(3) | O2-C8-C3 | 121.18(14) |
| – | – | O2-C8-C7 | 119.11(14) |
| – | – | N3-C10-C7 | 111.86(13) |
| – | – | N3-C11-C12 | 110.82(13) |
| – | – | N4-C12-C11 | 116.00(15) |
| – | – | N4-C12-C16 | 121.63(18) |
| – | – | N4-C13-C14 | 123.4(2) |
| – | – | N3-C17-C18 | 110.94(13) |
| – | – | O3-C19-C18 | 121.00(15) |
| – | – | O3-C19-C20 | 118.17(16) |

7.2.2.3

Vibrational properties of the compounds

The vibrational properties of ligand **H₃L6** derivative from benzopyranothiophene, as well as for ligand **H₃L7** were studied using vibrational spectroscopy. The vibrational properties of their dinuclear copper(II) complexes **9** and **11**, **10** and **12** prepared with perchlorate or acetate salts respectively, were also studied in this work. Principal evidences concerning the formation of important bonds after syntheses of the compounds, and the comparison of the infrared spectra between ligands and their complexes are discussed. Figures 7.8–7.13 show the vibrational bands of the free ligands and those of their metal compounds.

In the spectra of ligands **H₃L6** and **H₃L7** in KBr, some vibrational bands corresponding to the heteroatoms present in the molecules in the solid state are observed (Figure 7.8 and 7.9). Hence, the stretching and bending modes of OH and

NH were identified in both spectra in the 3430 cm^{-1} – 3190 cm^{-1} region (Table 7.5.). The spectra of the complexes **9–12** show the strong broad bands near to 3420 cm^{-1} – 34200 cm^{-1} , which were associated with OH from water.

The stretching corresponding to the C=O vibration appeared in the spectra at 1661 cm^{-1} in the spectrum of ligand **H₃L6** and at 1661 cm^{-1} in the spectrum of ligand **H₃L7**.

Complexation caused a displacement of the C–O stretching band, which appears in the spectrum of the ligand **H₃L6** at 1268 cm^{-1} and in that of ligand **H₃L7** at 1264 cm^{-1} (Figure 7.8–7.13). These bands were shifted in the spectra of the complexes at lower wavenumber. These results suggest the coordination of the C=O hydrazone moiety of the ligands with the copper(II) in the iminolate form.

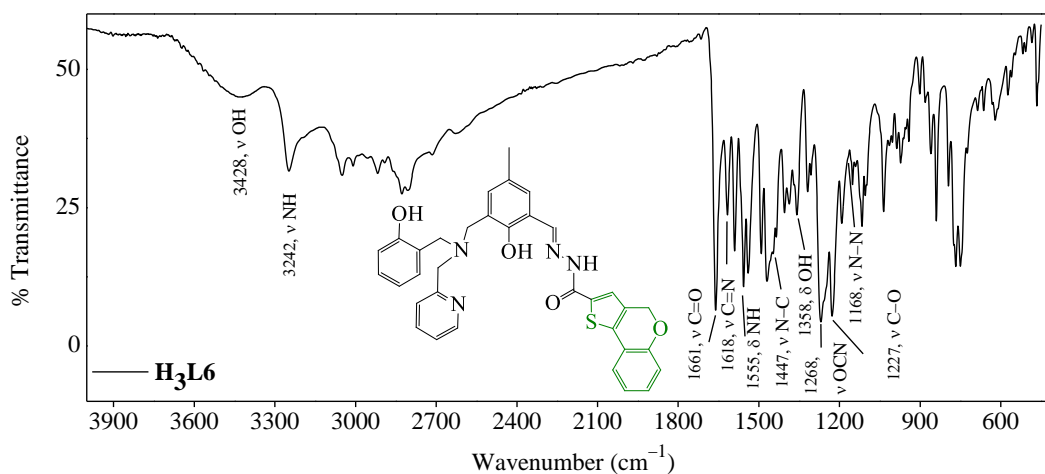


Figure 7.8. FTIR spectra of **H₃L6** in KBr pellet and principal assignments.

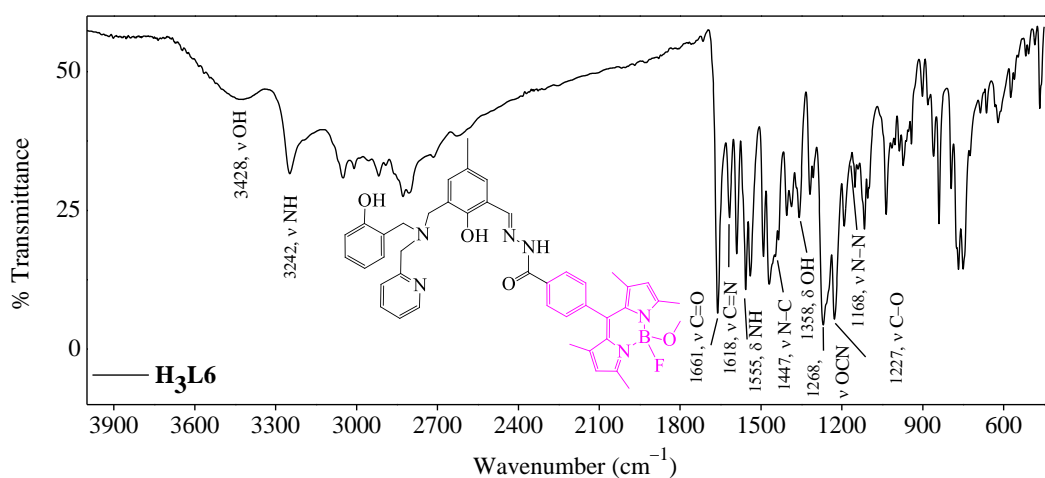


Figure 7.9. FTIR spectra of **H₃L7** in KBr pellet and principal assignments.

The characteristic bands in the IR spectra of complexes and ligands for Schiff base azomethine group [185] are located near to 1615 cm^{-1} . Vibrational bands related to the C–N bond were also found (Table 7.5.) in the spectra of the ligands. Besides, the NH stretching mode N–H bending vibration associated to the amide group appeared near to 3200 cm^{-1} and to 1544 cm^{-1} respectively. In the infrared spectra of the complexes, N–H bending vibration was observed near to 1550 cm^{-1} . Results indicate that upon complexation, the hydrogen from the hydrazoneic group is conserved.

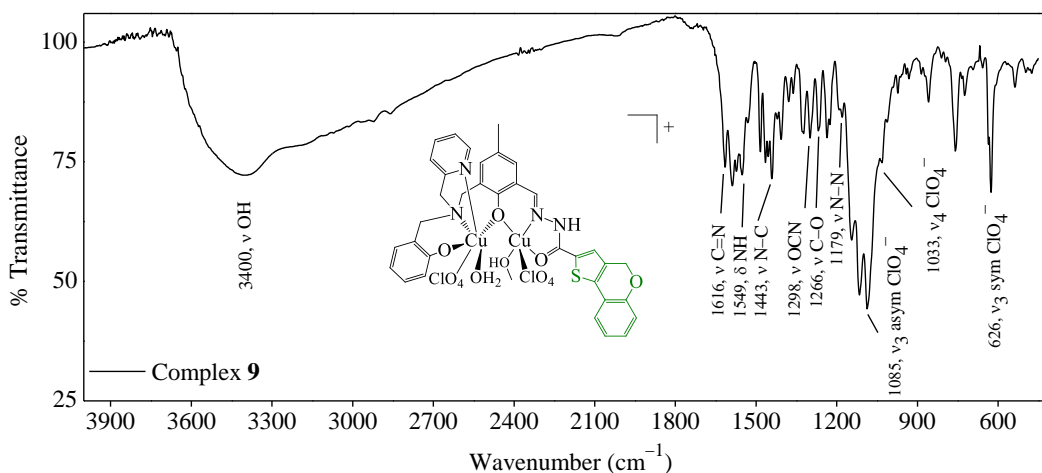


Figure 7.10. FTIR spectra of complex **9** in KBr pellet and principal assignments.

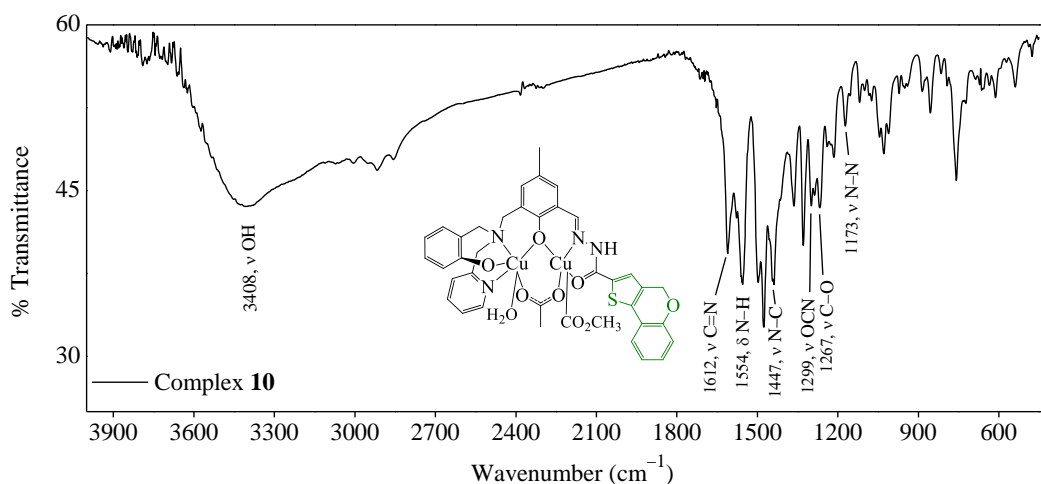


Figure 7.11. FTIR spectra of complex **10** in KBr pellet and principal assignments.

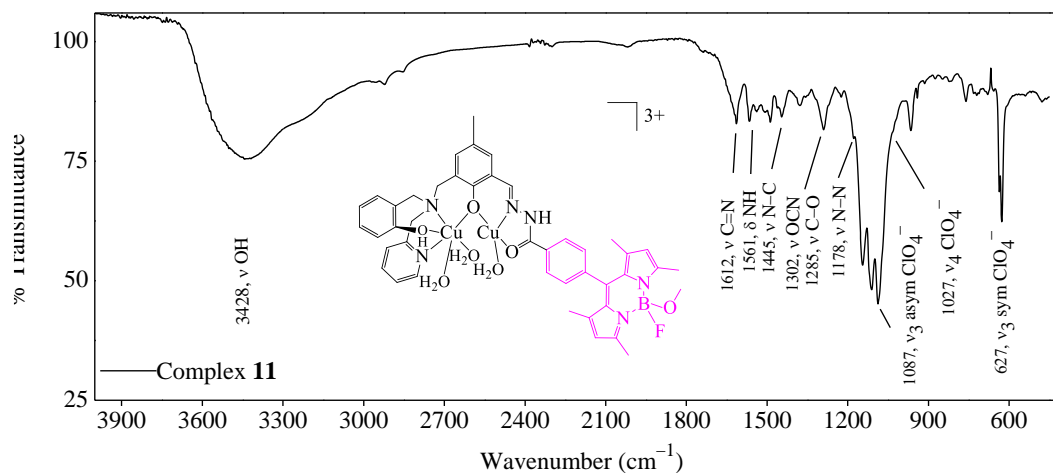


Figure 7.12. FTIR spectra of complex **11** in KBr pellet and principal assignments.

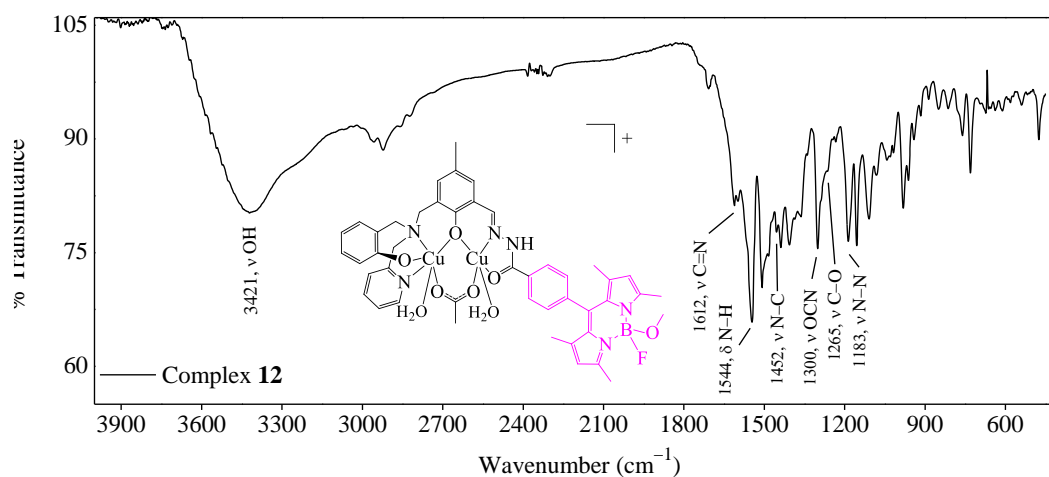


Figure 7.13. FTIR spectra of complex **12** in KBr pellet and principal assignments.

Additionally, the spectra of the complexes displayed strong characteristic vibration bands associated to antisymmetric ν_3 and symmetric ν_3 , and ν_4 modes as contre-ion and coordinate forms [186]. Most relevant assignments are proposed in Table 7.5.

Table 7.5. Selected vibrational absorptions (cm⁻¹) for **H₃L6** and **H₃L7** and their complexes **9** – **12**.

| H₃L7 | H₃L8 | 9 | 10 | 11 | 12 | Assignment |
|------------------------|------------------------|----------|-----------|-----------|-----------|--|
| 3428 | 3423 | 3400 | 3408 | 3428 | 3421 | ν OH |
| 3242 | 3194 | – | – | – | – | ν NH |
| 1661 | 1671 | – | – | – | – | ν C=O |
| 1618 | 1616 | 1616 | 1612 | 1612 | 1612 | C=N |
| 1555 | 1542 | 1549 | 1554 | 1561 | 1544 | δ N–H |
| 1168 | 1176 | 1179 | 1173 | 1178 | 1183 | ν N–N |
| – | – | 1085 | – | 1087 | – | ν ₃ ClO ₄ ⁻ |
| – | – | 1033 | – | 1027 | – | ν ₄ ClO ₄ ⁻ |

7.2.2.4

Photophysical properties of the compounds

The absorption spectral window of ligands **H₃L6** and **H₃L7**, and of their precursors **HBPAMFF** and **BPTH** (for **H₃L6**) are shown in Figures 7.14 and 7.15. The spectra of the synthesized complexes **9–12** are also included in the figures.

For ligand **H₃L6**, the absorption spectrum displays four principal absorptions in the 250–450 nm region. The most intense absorption band at 376 nm was assigned by comparison of the spectra, to both **HBPAMFF** and **BPTH** precursor moieties. Hence, this latter band corresponds to the π–π* from aromatic ring. It is also observed that the band at 376 nm was redshifted with respect to the bands present in the spectra of the precursors of ligand **H₃L6**. Additional three bands at 314 nm, 285 nm and 263 nm were also present in the spectra of both precursors. Finally, the absorbance corresponding to the hydrazonic transitions for ligands containing **HBPAMFF-Hz** moieties were reported as two bands in the 300 – 350 nm range [210] (and Chapter 4 and 5). Consequently, the absorption band at 314 nm probably represents also the transitions from the hydrazonic system.

Table 7.6 shows the absorption bands from ligands **H₃L6** and **H₃L7** and their complexes, as well as, the molar absorptivity coefficients calculated from the plot of the concentration versus UV-visible absorbance.

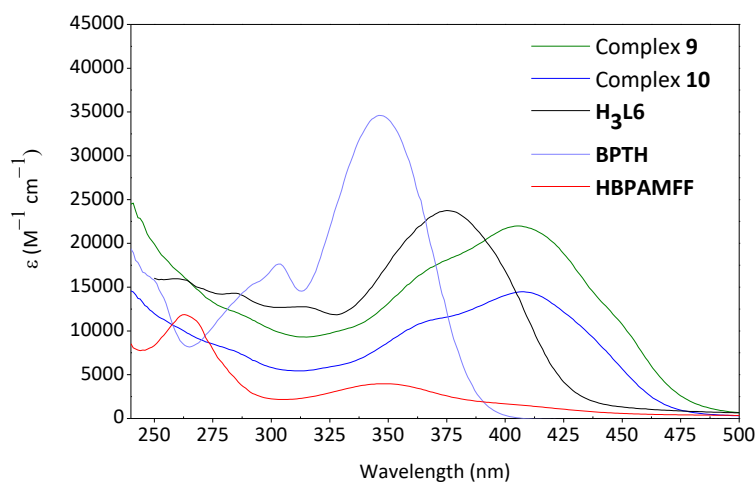


Figure 7.14. Absorption spectra of ligand **H₃L6**, as well as of its precursors: **HBPAMFF** and **BPTH**, and its complexes **9** and **10** recorded in H₂O/DMSO 9:1 at 298 K.

Table 7.6. UV/Vis absorption properties of ligands **H₃L6** and **H₃L7** and dicopper(II) complexes **9–12** in H₂O/DMSO 9:1 in the range 230 – 500 nm at 25 °C, and suggested assignments.

| Ligands | | | | | | | | Assignment |
|------------------------|--------------|------------------------|--------------|---------------------------------------|--------------|----------------|--------------|--------------------------------------|
| H₃L6 | | H₃L7 | | | | | | |
| λ (nm) | ϵ^* | λ (nm) | ϵ^* | | | | | |
| – | – | 511 | 31900 | BODIPY rings | | | | |
| – | – | 483(sh) | 18900 | BODIPY rings | | | | |
| 376 | 23800 | 350 | 15600 | BPTH* and HBPAMFF rings | | | | |
| 314 | 12700 | 311 | 18200 | CO–NH–N=N and BPTH* | | | | |
| – | – | 300 | 18000 | CO–NH–N=N | | | | |
| 285 | 14300 | 286 | 17000 | HBPAMFF rings | | | | |
| 263 | 16000 | – | – | HBPAMFF rings | | | | |
| Complexes | | | | | | | | Assignment |
| 9 | | 10 | | 11 | | 12 | | |
| λ (nm) | ϵ^* | λ (nm) | ϵ^* | λ (nm) | ϵ^* | λ (nm) | ϵ^* | |
| – | – | – | – | 505 | 18500 | 502 | 26000 | BODIPY rings |
| – | – | – | – | 480(sh) | 11500 | 480(sh) | 13000 | BODIPY rings |
| 406 | 22000 | 408 | 14600 | 397 | 9000 | 390 | 10300 | HBPAMFF rings |
| 365 | 16700 | 366 | 11000 | – | – | – | – | BPTH rings |
| – | – | – | – | 344 | 8700 | 341 | 11500 | CO–NH–N=N |
| 329 | 10000 | 328 | 6100 | 328 | 8700 | 327 | 13000 | CO–NH–N=N and BPTH* |
| – | – | – | – | 311 | 8300 | 311 | 11800 | CO–NH–N=N |
| 289 | 11200 | 285 | 7600 | – | – | – | – | BPTH and HBPAMFF rings |
| 264 | 15500 | 260 | 10400 | 277 | 10200 | 267 | 14700 | HBPAMFF rings |

* M⁻¹ cm⁻¹. * for ligand or complexes derived from **BPTH**.

On the other hand, the absorption spectrum of ligand **H₃L7** displayed six main bands (Figure 7.15). The bands at 511 nm (with most intense absorption) and 483 nm (shoulder) clearly correspond to the typical **BODIPY** spectra [219]. Consequently, these bands were assigned to the transitions of the **FMeO-BODIPY-Hz** moiety in ligand **H₃L7**. **BODIPY** molecule, does not show any absorption in the 250 – 400 nm range [219]. Hence, the bands at 350 nm and 286 nm were assigned to **HBPAMFF** transitions. Finally, the remaining absorption bands at 311 nm and 300 nm clearly correspond to hydrazone transitions, since these bands are absent in the spectra of the precursors.

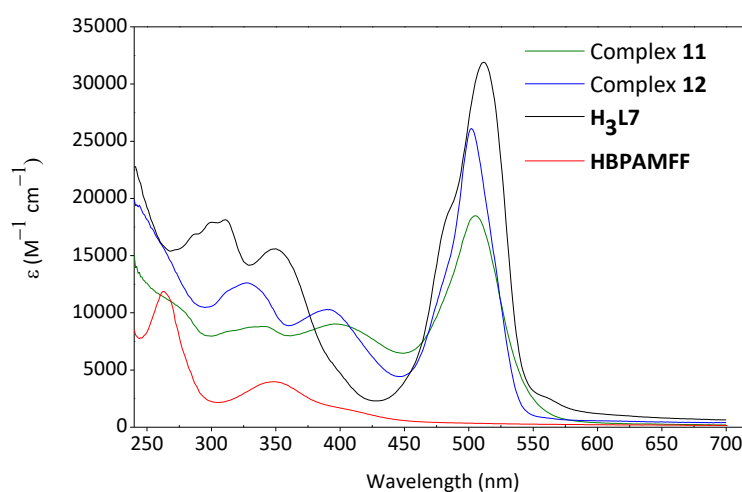


Figure 7.15. Absorption spectra of ligand **H₃L7**, as well as of its precursors **HBPAMFF** and its complexes **11** and **12** recorded in H₂O/DMSO 9:1 at 298 K.

Overall, the synthesized copper complexes from ligands **H₃L6** and **H₃L7** showed very close absorption spectra to their precursors (Figures 7.14 and 7.15). Thus, for complexes **9** and **10**, the complexation process caused a redshift for all the spectrum and one extra band (shoulder) was observed in the 425–475 nm region. By comparing the spectra, this band (initially overlapped with the **BPTH** absorption) was associated to the coordinate **HBPAMFF** rings (Figure 7.14).

Finally, for complexes **11** and **12**, upon coordination the bands corresponding to the electronic transitions of the **HBPAMFF** rings and the hydrazone systems were redshifted (Figure 7.15), while the absorption bands associated to the **BODIPY** transitions were blueshifted.

Each of the two designed ligands in this work includes a non-coordinating fluorophore system. Therefore, the fluorescence properties of the ligands and their copper(II) complexes were qualitatively examined in aqueous medium and organic solvents.

BPTH-compounds were excited at their maximum absorption wavelength. Thus, when excited at 376 nm, the emission spectrum of **H₃L6** showed a band located at 536 nm, which corresponds to 40 nm Stokes shift (Figure 7.16). The comparison of this emission band of **H₃L6** with that of its precursor **BPTH** indicates the redshift in the emission spectrum with a lower intensity caused by the formation of the hydrazone framework (Figure 7.17).

Increasing the polarity of the solvent, as acetone, MeOH and MeCN, the emission intensity successively decreased. Nevertheless, ligand **H₃L6** exhibited its maximum emission in DCM as is observed in Figure 7.17 (C). In contrast, when dissolved in water, the emission intensity of this ligand was higher than in organic solvents.

Complexation of the ligand caused a quenching in the fluorescence. Thus, the emission spectra of complexes **9** and **10** displayed a low intensity as is shown in Figure 7.17 (B). It was observed also that the fluorescence band was blueshifted. Additional emission spectra of these complexes in DCM can be found in Attachment B (item 13.3).

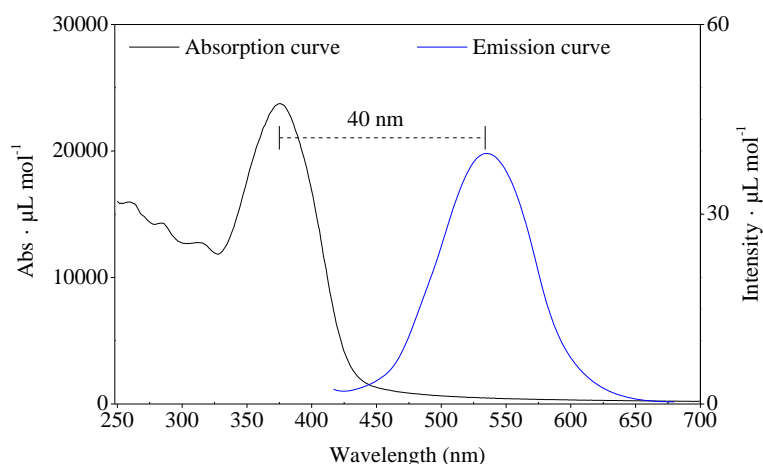


Figure 7.16. Absorption versus fluorescence emission spectra of ligand **H₃L6** ($\lambda_{\text{excitation}} = 376$ nm; 6 μM) in 99:1 H₂O/DMSO and water respectively at 298 K.

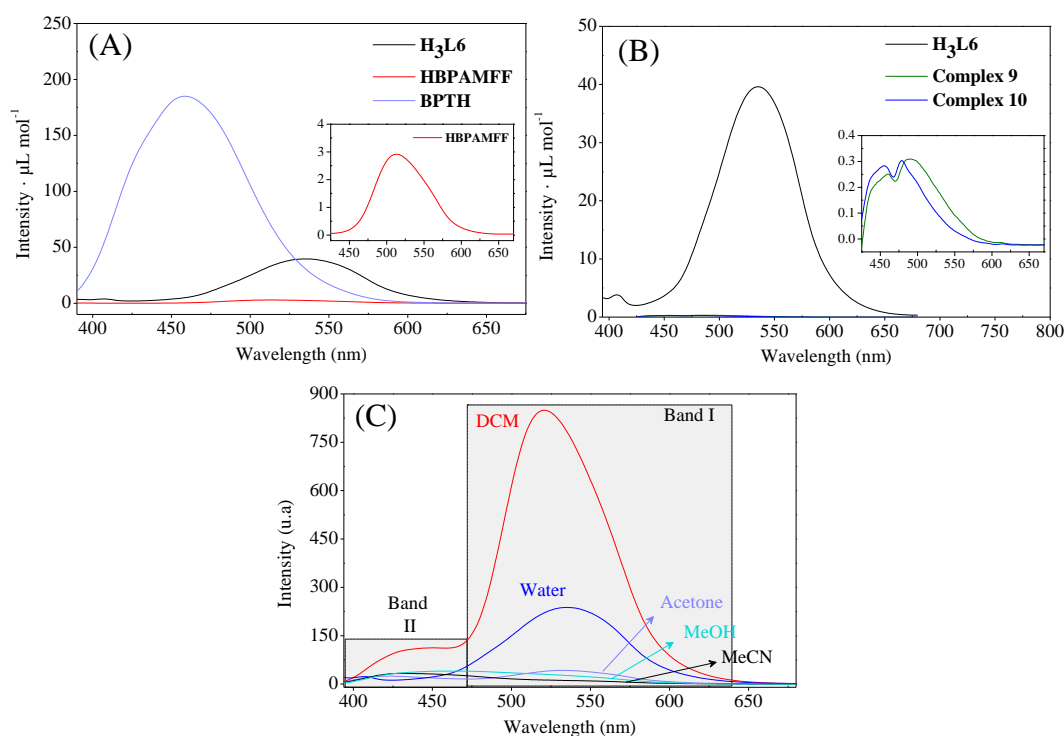


Figure 7.17. Fluorescence emission spectra of (A) ligand **H₃L6** ($\lambda_{\text{excitation}} = 376$ nm; 6 μM), as well as its respective precursors: **HBPAMFF** ($\lambda_{\text{excitation}} = 349$ nm; 40 μM) and **BPTH** ($\lambda_{\text{excitation}} = 351$ nm; 5 μM) and (B) ligand **H₃L6** and its complexes **9** ($\lambda_{\text{excitation}} = 407$ nm; 7 μM) and **10** ($\lambda_{\text{excitation}} = 406$ nm; 7 μM) in water at 298 K. (C). Fluorescence emission spectra of ligand **H₃L6** ($\lambda_{\text{excitation}} = 407$ nm; 7 μM) in water and organic solvents at 298 K.

Ligand **H₃L7** and its copper complexes (with a **BODIPY** entity) were excited at the shoulder absorption band near to 485 nm, due to the short Stokes shift presented by these compounds at 511 nm wavelength. Ligand **H₃L7** displayed a band located at 509 nm (Figure 7.18-A). Emission spectrum of ligand **H₃L7** corresponds to a characteristic emission spectrum of its **BODIPY** fragment [220].

As expected, the ligand displayed the highest fluorescence intensity in organic solvents (Figure 7.18-B). **BODIPY** derivatives commonly present a strong emission in organic solvents, while in aqueous solutions the emission can decrease dramatically the fluorescence of the compounds. This effect is related to the formation of dimers or higher aggregate non-emissive in water [221, 222].

Both **BODIPY**-complexes displayed fluorescence properties. Nevertheless, the complex prepared with the acetate copper salt, **12** showed a significant higher emission intensity than that prepared with the perchlorate, **11** (Figure 7.19). Upon complexation, the fluorescence bands were not shifted. Additional emission spectra

of complexes **11** and **12** in organic solvents can be found in Attachment B (item 13.3).

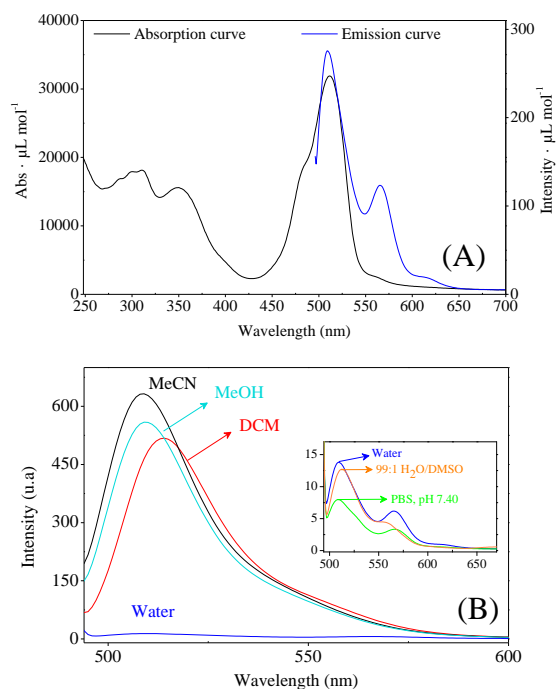


Figure 7.18. (A) Absorption versus fluorescence emission spectra of ligand **H₃L7** ($\lambda_{\text{excitation}} = 485$ nm; 50 nM) in 99:1 H₂O/DMSO and water respectively at 298 K; and (B) Fluorescence emission spectra of ligand **H₃L7** ($\lambda_{\text{excitation}} = 475$ nm; 50 nM) in water and organic solvents at 298 K.

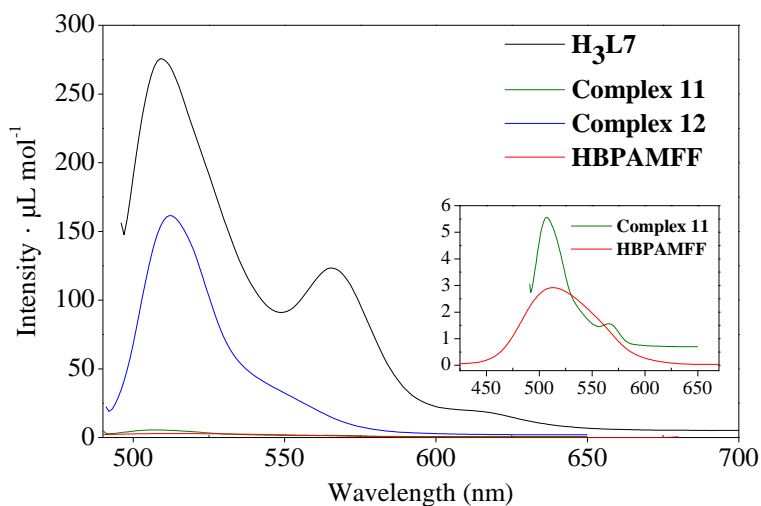


Figure 7.19. Fluorescence emission spectra of (A) ligand **H₃L7** ($\lambda_{\text{excitation}} = 475$ nm; 50 nM), of its precursors **HBPAMFF** ($\lambda_{\text{excitation}} = 349$ nm; 40 μM) and **BPTH** and its complexes **11** ($\lambda_{\text{excitation}} = 485$ nm; 0.3 μM) and **12** ($\lambda_{\text{excitation}} = 485$ nm; 1 μM), in water, at 298 K.

7.2.3

In vitro cytotoxic activity of the compounds

To measure the influence of the synthesized compounds on cancer cell growth, the *in vitro* antiproliferative activity of the ligands **H₃L6** and **H₃L7**, and complexes **9–12** was evaluated in MDA-MB-231 human breast cancer cell line by the MTT assay [135]. Cells were treated with different concentrations of the compounds for 72 h at 37 °C.

For all cases, the exposure of the compounds to the tested cancer cells for a period of 72 h at different concentrations caused a decrease of their relative viability (Figure 7.20). The cytotoxic profiles of the compounds and the fitted curves to determine the IC₅₀ values are shown in Figure 7.21.

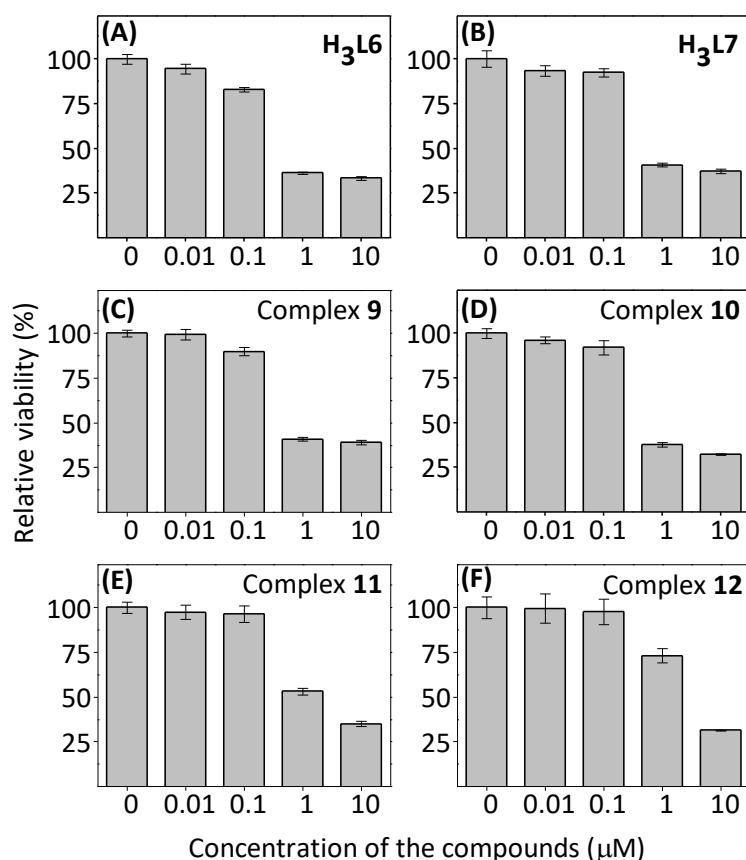


Figure 7.20. Dose-dependent effect expressed as the percentage of relative viability of MDA-MB-231 cells measured by the MTT assay for (A) **H₃L6**; (B) **H₃L7**; (C) **9**; (D) **10**; (E) **11**; and (F) **12** after 72 h incubation at 37 °C. Data represent the mean of triplicate experiments.

The four novel copper(II) complexes exhibited IC_{50} values (Table 7.7) in the micromolar and/or submicromolar range when tested on MDA-MB-231 cells. These results are interesting for three principal reasons. First, the MDA-MB-231 cancer cell line is known to present not only resistance to the cancer chemotherapy and metastasis, but also recurrence appearance [201]. Second, breast cancers report the second highest both incidence and mortality rates in the world [58]. Finally, in some cases, MDA-MB-231 cells revealed the highest resistance when exposed to copper complexes as cytotoxic agents in a set of metal-complexes, as was reported by Boulsourani and co-workers [87].

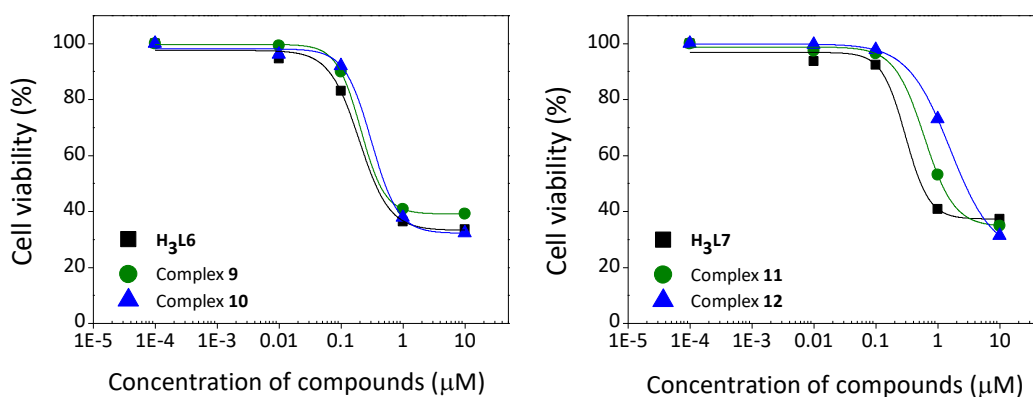


Figure 7.21. Dose-dependent effect on MDA-MB-231 cells of ligands **H₃L6** and copper(II) complexes **9** and **10** (left) and ligand **H₃L6** and copper(II) complexes **11** and **12** (right) after 72 h, at 37 °C, using the MTT assay.

One of the main goals of this work was to relate the structure of the new compounds with their ability to inhibit cell growth. Thus, three comparisons are discussed: the antiproliferative activity of (i) ligand **H₃L6** versus ligand **H₃L7**, (ii) the ligands versus their copper complexes and (iii) perchlorate versus acetate copper(II) complexes. An analysis of the cytotoxic results on MDA-MB-231 cancer cell line for ligands and complexes in this research and other **HBPAMFF-Hz** derivatives (Chapter 4–6) is included.

7.2.4.1

Ligands **H₃L6** versus **H₃L7** and other **HBPAMFF-Hz** derivatives

Cell viability results showed that both synthesized ligands displayed high potential to inhibit cancer cell growth, with IC_{50} values in the submicromolar range.

Nevertheless, it was noticed that ligand **H3L6** with the **BPTH** substituent group was approximately three times more cytotoxic on the tested cells than ligand **H3L7** containing the substituent **FMeO-BODIPY** (Table 7.7). This result indicated that not only the **HBPAMFF** moiety is responsible for the activity of the ligands, but both, **HBPAMFF** and the non-coordinating group associated to the hydrazone framework.

Comparing the IC_{50} of **H3L6** with other ligands with the **HBPAMFF-Hz** moiety (Table 7.7), it is quite remarkable that **H3L6** presented the highest antiproliferative activity ($IC_{50} = 90 \pm 10$ nM) among all the **HBPAMFF-Hz** derived compounds reported in the present work. However, it is important to highlight that all these ligands are potent antiproliferative agents, a property which can be clearly associated to their **HBPAMFF-Hz** systems.

7.2.4.2

Ligands versus complexes activity

Contrary to what has been frequently reported [15, 16, 195], the results of this work indicated the higher cytotoxic activity of both ligands **H3L6** and **H3L7** than their respective complexes prepared from perchlorate or acetate copper salts. For MDA-MB-231 cells, copper complexes also commonly displayed a better antiproliferative activity than their precursor ligands [223, 224].

The capacity of the binucleating **HBPAMFF-Hz** ligands to sequester copper(II) and other essential metal ions, such as Fe(III), Fe(II) and Mn(II), as a new anticancer strategy, was discussed in a previous work (Chapter 5). By exposing cancer cells to **HBPAMFF-Hz** ligands, complexation process could occur using the metal ions available inside the cells. Thus, the amount of essential metals for cells growth could decrease in the culture medium, and the formed complexes have themselves the structural ability to induce cell death. Gaur and co-workers published a comprehensive review on intracellular chelation by iron and copper ions, and the advantage of this new anticancer drug approach [198]. Capturing copper(II) ions from the cellular medium gives to the compounds an additional property as anticancer agents. Hence, an excess of copper(II) has been related to cancer progression and tumour angiogenesis, since they can stimulate the proliferation of cells and migration [225, 226]. Analysis to confirm these hypothesis

remains to be more explored. For instance, the better activities on MDA-MB-231 cells of the metal-free ligands containing **HBPAMFF-Hz** moieties than their complexes were established (Table 7.7 and Figure 7.22).

7.2.4.2

Perchlorate-copper complexes versus acetate-copper complexes

Efforts to determine differences in the antiproliferative activity of copper(II) complexes prepared from the same ligand and from perchlorate copper(II) hexahydrate or acetate copper(II) monohydrate were reported (Chapter 5). Nevertheless, in this latter study (Chapter 5) the reported IC₅₀ values for the perchlorate or acetate complexes was considered identical when standard deviations of the results were considered.

Table 7.7. IC₅₀ values of ligands **H₃L6** and **H₃L7** and by their copper(II) complexes **9–12** on MDA-MB-231 cells and, IC₅₀ values of the previous reported ligands and copper(II) complexes derived from **HBPAMFF-Hz**.

| Compound | IC ₅₀ [μM] | H _z -substituent | Ion from copper salt | Reference |
|------------------------|----------------------------|-----------------------------|----------------------------------|--------------|
| Ligands | | | | |
| H₃L6 | 0.09 ± 0.01 ^[a] | BPTH | – | This Chapter |
| H₃L7 | 0.28 ± 0.02 ^[a] | FMeO-BODIPY | – | This Chapter |
| H₃L1 | 1.02 ± 0.24 ^[b] | Thiophene | – | [210] |
| H₃L2 | 0.65 ± 0.26 ^[b] | Furan | – | [210] |
| H₃L3 | 0.29 ± 0.03 ^[a] | PIH | – | Chapter 5 |
| H₃L4 | 0.35 ± 0.02 ^[b] | Pyrene | – | Chapter 6 |
| Complexes | | | | |
| 9 | 0.41 ± 0.01 ^[a] | BPTH | ClO ₄ [–] | This Chapter |
| 10 | 0.51 ± 0.08 ^[a] | BPTH | CH ₃ COO [–] | This Chapter |
| 11 | 1.15 ± 0.08 ^[a] | FMeO-BODIPY | ClO ₄ [–] | This Chapter |
| 12 | 2.71 ± 0.06 ^[a] | FMeO-BODIPY | CH ₃ COO [–] | This Chapter |
| 1 | 0.90 ± 0.28 ^[b] | Thiophene | ClO ₄ [–] | [210] |
| 2 | 1.21 ± 0.28 ^[b] | Furan | ClO ₄ [–] | [210] |
| 3 | 0.45 ± 0.03 ^[a] | PIH | ClO ₄ [–] | Chapter 5 |
| 4 | 0.49 ± 0.01 ^[a] | PIH | CH ₃ COO [–] | Chapter 5 |
| 7 | 1.05 ± 0.07 ^[a] | Pyrene | ClO ₄ [–] | Chapter 6 |
| 8 | 1.35 ± 0.01 ^[a] | Pyrene | CH ₃ COO [–] | Chapter 6 |

Incubation in triplicate (mean ± S.D) determined after ^[a]72 h or ^[b]32 h

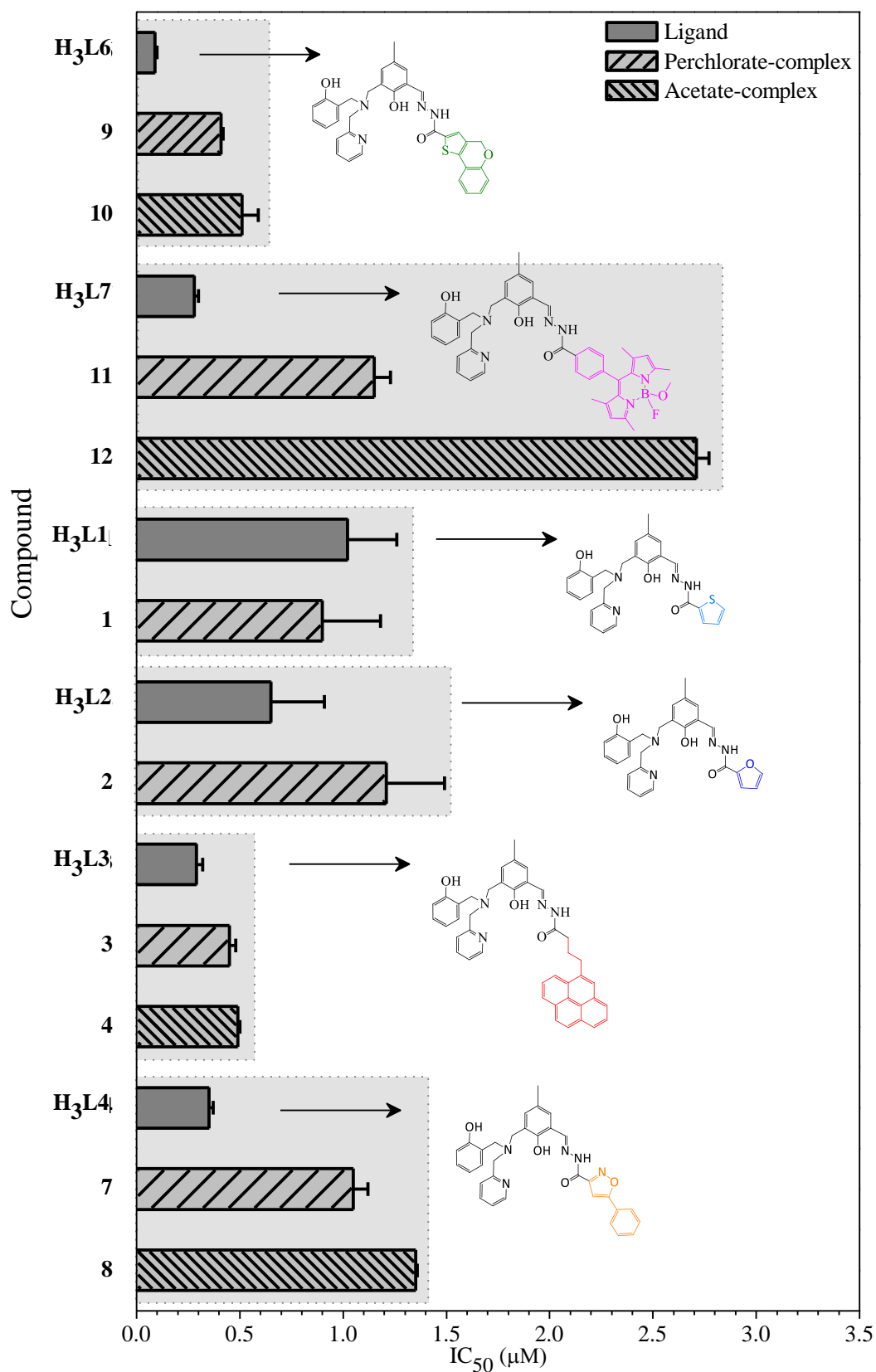


Figure 7.22. IC₅₀ values of MDA-MB-231 cells measured by the MTT assay for ligands and complexes containing the **HBPAMFF-Hz** framework, after 72 h incubation (or 36 h for furan and thiophene derivatives) at 37 °C. Data represent the mean of triplicate experiments.

Considering the results of the cytotoxic assays for complexes **9–12** obtained in this work with the previously reported (Table 7.7), a significant higher antiproliferative property for the perchlorate-complexes was observed. This difference was more pronounced for complex **11** (perchlorate complex) and **12** (acetate complex). Thus, complex **11** was more than 50% active than complex **12** in the tested cells.

In brief, all the ligands and complexes containing **HBPAMFF-Hz** framework displayed interesting anticancer activity on MDA-MB-231 cells. Ligands presented lower IC₅₀ values than their copper(II) complexes, probably due to the ability of this type of compounds to coordinate to essential metal ions. Additionally, copper complexes prepared with perchlorate copper(II) salts were more potent than acetate-copper complexes to inhibit cell growth. The better cell viability results followed the order: ligand **H₃L6** > ligand **H₃L7** > complex **9** > complex **10** > complex **11** > complex **12**. Finally, significant differences in the cytotoxicity of the compounds were found when the non-coordinating group was varied.

7.2.4

Cellular uptake and localization of **H₃L7** by fluorescence microscopy

The penetration of the compounds in cancer cells to induce cell death is limited by the cell membrane. Thus, in this work, the luminescence properties of **H₃L7** were used as a tool to examine the permeability and cellular localization of this ligand in the cells through fluorescence confocal microscopy. **H₃L7** was chosen for this study taking into account its higher emission intensity compared to **H₃L6**. Analysis was performed after exposing MDA-MB-231 cells to the ligand for 3 h at 37 °C. Additionally, cells were treated with nucleus and mitochondria dyes for 45 min in order to co-locate the ligand into the cancer cells.

Figure 7.23 shows that at low concentration (1 μM) and after incubation, ligand **H₃L7** was observed mainly in the cells in a perinuclear localization, proving that cellular uptake has occurred. Besides, Figure 7.23 shows significant mitochondrial localization of the compounds in MDA-MB-231 cells, suggesting that cells death is produced by mitochondrial damage.

Mitochondrion-targeted is an interesting property of an anticancer candidate, considering that mitochondria play important functions in cells, related to the metabolism, energy conversion and apoptotic cells death [227-229]. Besides, it is known that mitochondria are involved in the development of cancer cells [22, 230]. Consequently, the results suggest that ligand **H₃L7** could represent an attractive alternative to the cisplatin drug, since cisplatin involves an action mechanism principally by the generation of DNA lesion and damage closely, which is related to the cancer chemotherapy resistant [231]. The mitochondria localization ability of **BODIPY** molecule and also of the BODIPY-copper(II) complexes was previously reported [232].

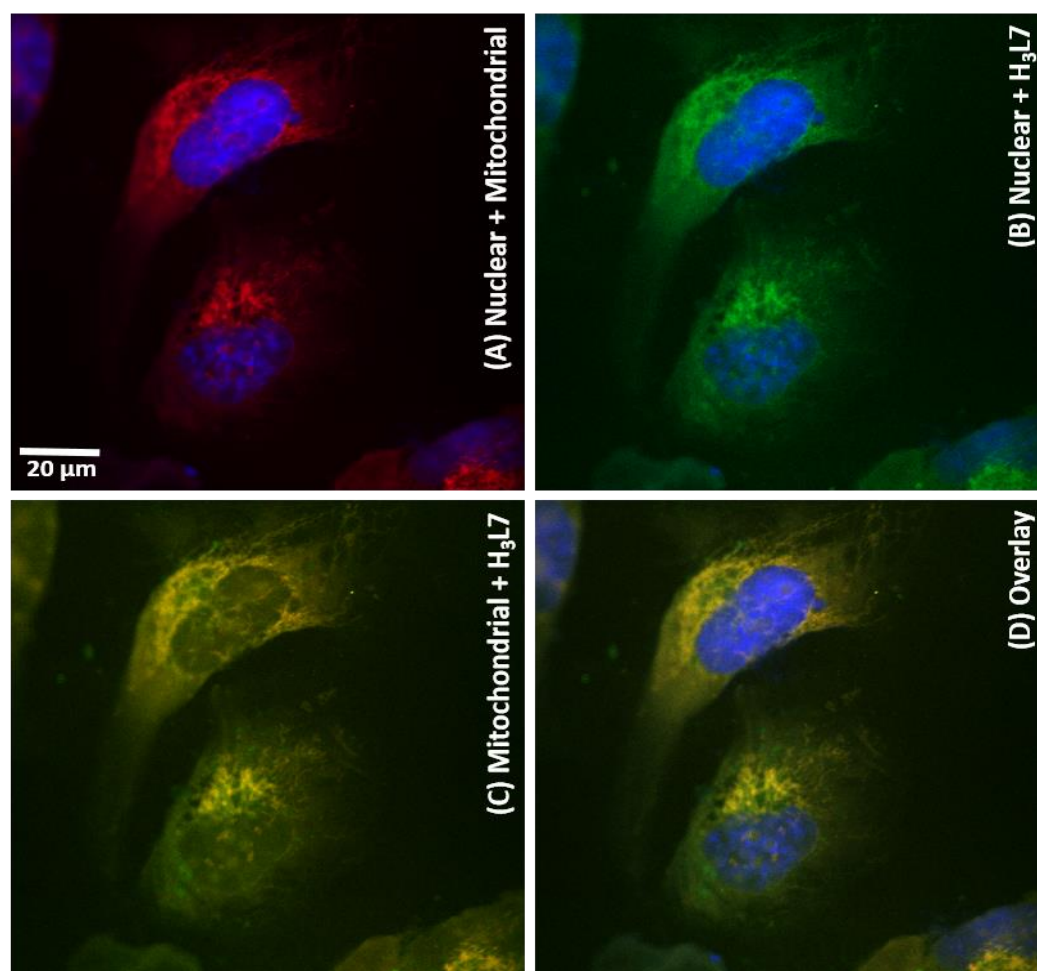


Figure 7.23. Fluorescence images of the cellular uptake and intracellular localization of ligand **H₃L7** in MDA-MB-231 cells after incubation for 45 min at 37 °C with: (A) DAPI (300 nM) and MTDR (200 nM); (B) DAPI and **H₃L7** (1 μM) and (C) MTDR and **H₃L7**. DAPI (A) was excited at 405 nm and the emission was recorded at 410 – 450 nm. Ligand **H₃L7** (B) was excited at 488 nm and the emission was recorded at 500 – 600 nm. MTDR (C) was excited at 552 nm and the emission was recorded at 600 – 700 nm. Scale bar: 20 μM.

Without dyes or the ligand **H₃L7** in cellular medium, cells did not show any emission in the tested conditions. Additional fluorescence images of MDA-MB-231 cells treated with DAPI, MTDR and ligand **H₃L7** are shown in Attachment B, Figures 13.34 – 13.36. These latter figures showed scale bar of 10 μ M and 20 μ M.

7.3

Partial conclusions

Two novel binucleating ligands derived from the **HBPAMFF** and hydrazone systems, as well as their perchlorate-dicopper(II) complexes **9** and **10**, and acetate-dicopper(II) complexes **11** and **12** were synthesized and characterized using spectroscopic and analytical techniques.

The molecular structure of complex **9** was established by an X-ray diffraction analysis. In the solid state, complex **9** was formed by the partially deprotonated ligand **H₃L6** and two copper centres with octahedral or square pyramidal environments.

Electronic profiles of the compounds were discussed and associated to the precursor bands of ligands and complexes. Additionally, the fluorescence properties of the synthesized compounds were explored and exploited in the biological testes.

The cytotoxicity of the compounds was studied by the MTT assay on MDA-MB-231 cancer cells, known to be a resistance cell line to the chemotherapy and the second most common cancer in the world. The results were discussed by associating the activity to the structure of the compound. The binucleating ligands displayed the highest cytotoxic activity, followed by the complex containing coordinated perchlorate ion, and finally by the copper(II) complexes with acetate in their structures. The results were compared to those obtained for the other **HBPAMFF-Hz** compounds reported herein.

The emission properties of ligand **H₃L7** due to the presence of the **FMeO-BODIPY-Hz** entity, was used for cellular imaging. The results showed the ability of this ligand to permeate the cell membrane of MDA-MB-231 cancer cells in a short time and its significant mitochondria accumulation. Therefore, this compound may be an important alternative to the nucleous-targeted cisplatin drug with known chemoresistance effect.

Interestingly, this work reaffirms that all the **HBPAMFF**-hydrazonic ligands and their copper(II) complexes synthesized up to now present very high antiproliferative activities in cancer cells. The cytotoxic properties are probably originated from mitochondrial damage.

Finally, all of these primary results suggest that the synthesized **HBPAMFF**-hydrazonic ligands and their dicopper(II) complexes present remarkable anticancer properties and are suitable for future studies as potential antitumour agents.

Results and discussion V. Novel binucleating isonicotinoyl hydrazonic ligand and its (perchlorate / acetate-derived) dicopper(II) complexes as potential anticancer agents: syntheses, chemical characterization, and cytotoxicity towards a breast cancer cell line

The present thesis chapter contains information that is included in a patent application. For all data referring the results described herein, it is important to verify the appropriated form to cite.

8.1

Introduction

Aroylhydrazones constitute a diverse family of bidentate N,O-donors with a vast spectrum of biological activities [109]. In recent years, many metal-free and coordinated hydrazone derivatives have been tested as anticancer agents [45-57]. Particularly, isoniazide is a molecule used for tuberculosis and cancer chemotherapy [233, 234]. Dos Santos R. reported the syntheses and characterization of novel aroylhydrazone ligands and their copper(II) complexes derived from 4-pyridinecarboxylic acid hydrazide (**INH** or isoniazide) and/or the 3-[(2-hydroxybenzyl)(2-pyridylmethyl)amine]-2-hydroxy-5-methylbenzaldehyde (**HBPAMFF**) moiety (Figure 2.6) [110]. She also reported the antiproliferative activity of an isoniazide derivative **RDS-H₃L₂** on human lung cancer A549, and human prostate cancer PC3 cell lines. The antiproliferative activity was tested for the Cu₂(II)-complexes prepared from ligand **RDS-H₃L₂** (Figures 2.6 and 2.7) [111]. The goal of the present study is to verify if a ligand framework similar to that of **RDS-H₃L₂** provides significant cytotoxic activity on the breast cancer cell line MCF-7.

8.2

Results and discussion

8.2.1

Syntheses

To synthesize the Schiff base ligand **H₂L8** derived from 2[*bis*-(pyridylmethyl)aminomethyl]-4-methyl-6-formyl-phenol **BPMAMFF** and isoniazide, equimolar amounts of both precursors were refluxed in methanol for three hours. Colourless crystals of **H₂L8** were obtained by recrystallization in DCM/MeOH 1:1. Copper(II) perchlorate hexahydrate salt (1 : 2 equivalent respectively) was added to this ligand in the presence of potassium hydroxide to obtain the copper(II) complex formulated as [Cu₂(OH₂)₂(L2)(ClO₄)]₃ClO₄·5H₂O (**13**). Additionally, **H₂L8** was mixed with copper(II) acetate monohydrate (1 : 2 equivalents respectively) to obtain the binuclear copper(II) complex formulated as [Cu₂(μ-CH₃COO)₂(OH₂)(L2)]·8 H₂O (**14**) (Figure 8.1).

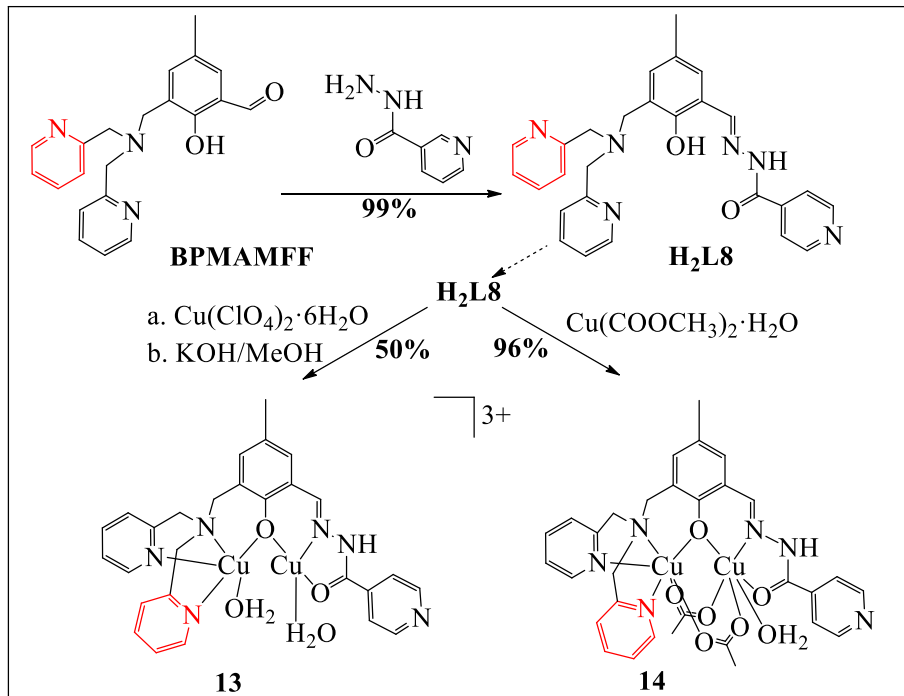


Figure 8.1 Synthetic routes to ligand **H₂L8** and its copper(II) complexes from perchlorate **13** and acetate **14** salts.

The ligand (99%, quantitative) and the complexes **13** (50%) and **14** (96%) were isolated in good yields and were characterized by elemental analysis, spectroscopic techniques and single-crystal X-ray diffraction (XRD) analysis (for the ligand). Additionally, the percentage of copper(II) in the complexes was determined by inductively coupled plasma optical emission spectrometry (ICP-OES) The electrolytic nature of the complexes was estimated by conductivity measurements.

Molar conductivity in acetonitrile ($468 \text{ ohm}^{-1} \text{ cm}^2 \text{ mol}^{-1}$) of complexes **13** and **14** indicated a 1 : 3 electrolyte, and a non-electrolyte systems, respectively [138].

8.2.2 Characterization of the ligand and complexes

8.2.2.1 Solution NMR of ligand **H₂L8**

The ^1H NMR spectrum of **H₂L8** in solution shows twenty-one resonances for the twenty-six hydrogens existing in this ligand (Figure 8.2).

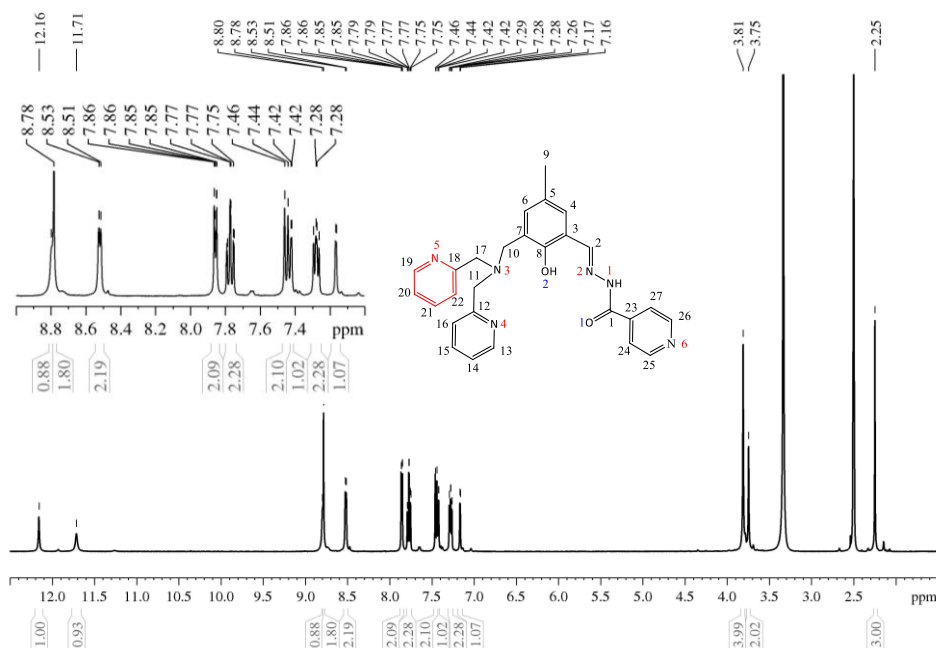


Figure 8.2. ^1H NMR spectrum (400 MHz) of **H₂L8** in $\text{DMSO}-d_6$ at room temperature.

In the ^1H NMR spectrum of this ligand, the hydrogens corresponding to the CH_2 and CH_3 groups appear at the highest field, while phenol central ring appeared at the lowest field, followed respectively by the symmetric pyridine pendant arms.

The resonance signals were duplicated, due to the presence of isomers in the solution (6% and 94%). The structure of the hydrazone molecules allow the formation of both geometric (*E* / *Z*) and tautomeric isomers in solution (iminol / amide forms) [139-141]. Regarding the geometric forms, it is evident that the *Z* isomer presents higher energy than *E* isomer due to the proximity of the isoniazidic ring to the other aromatic groups in the ligand (Figure 8.3).

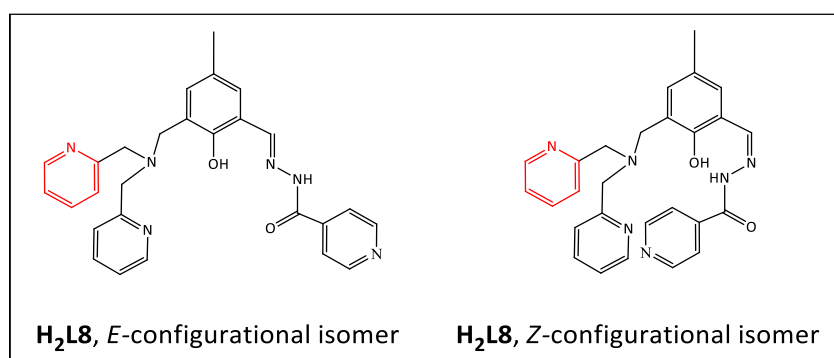


Figure 8.3. *E* and *Z* configurational isomers of **H₂L8**.

With respect to the tautomeric forms, in aroylhydrazone molecules it is possible to observe the *E*-iminol [$-(\text{HO})\text{C}=\text{N}-\text{N}=\text{C}-$] and *E*-amide forms [$(\text{O}=\text{C})-\text{NH}-\text{N}=\text{C}-$] (Figure 8.4).

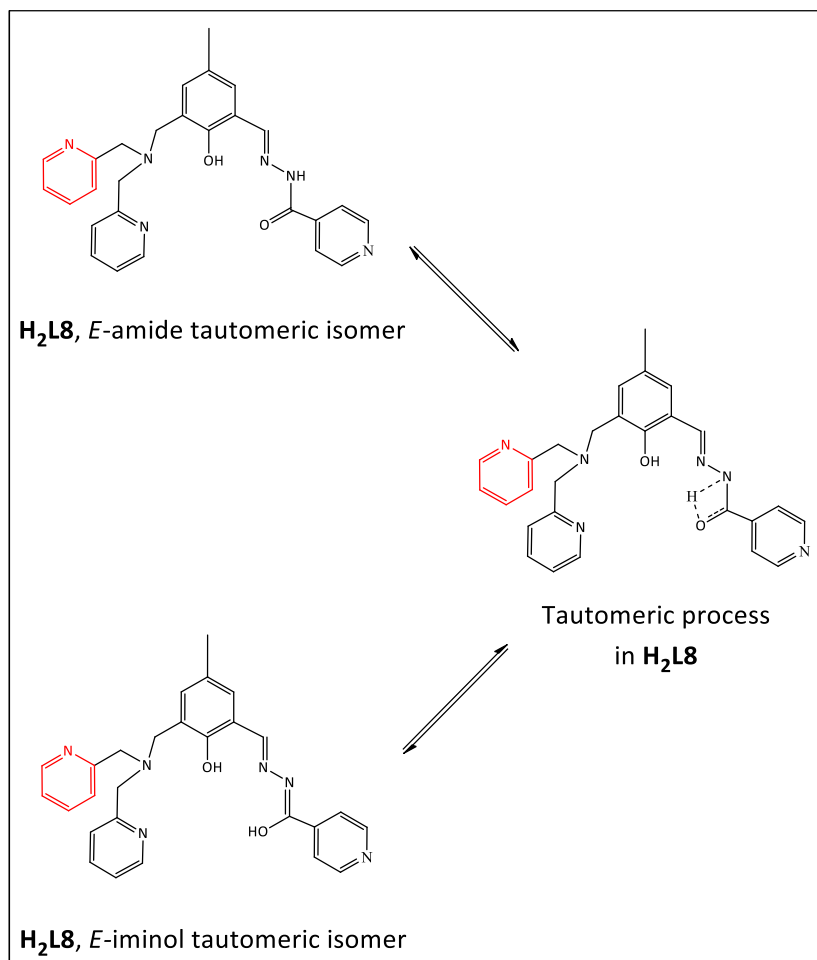


Figure 8.4. *E*-amide and *E*-iminol tautomeric isomers of **H₃L1**.

In order to verify the principal isomer of **H₂L8** in solution, analysis of the ¹³C NMR and DEPT-135 spectroscopy were carried out.

In the ¹³C NMR spectrum (Figure 8.5), a signal at 161.2 ppm appears, which is assigned to the CO of the aroylhydrazone corresponding to a quaternary carbon, suggesting that the principal form of the ligand is in *E*-amide conformation. This signal is absent in the DEPT-135 spectrum (Figure 8.6). In ¹³C NMR spectra (Figure 8.3), all signals were assigned to the 27 carbon present in this ligand and no extra carbon was observed (C–OH). Thus, the principal isomer in the **H₂L8** ligand solution was assigned to the *E*-amide form, and the low duplication of the signals correspond to the *E*-iminol form.

The integration of the duplicated signals in ¹H NMR spectrum indicates that *E*-iminol form represents less approximately 6% of the isomer in **H₂L8** solution.

Accordingly, only the (*E*-amide) form is discussed in this work. A complete ^1H and ^{13}C NMR assignment for the ligands is given in Table 8.1.

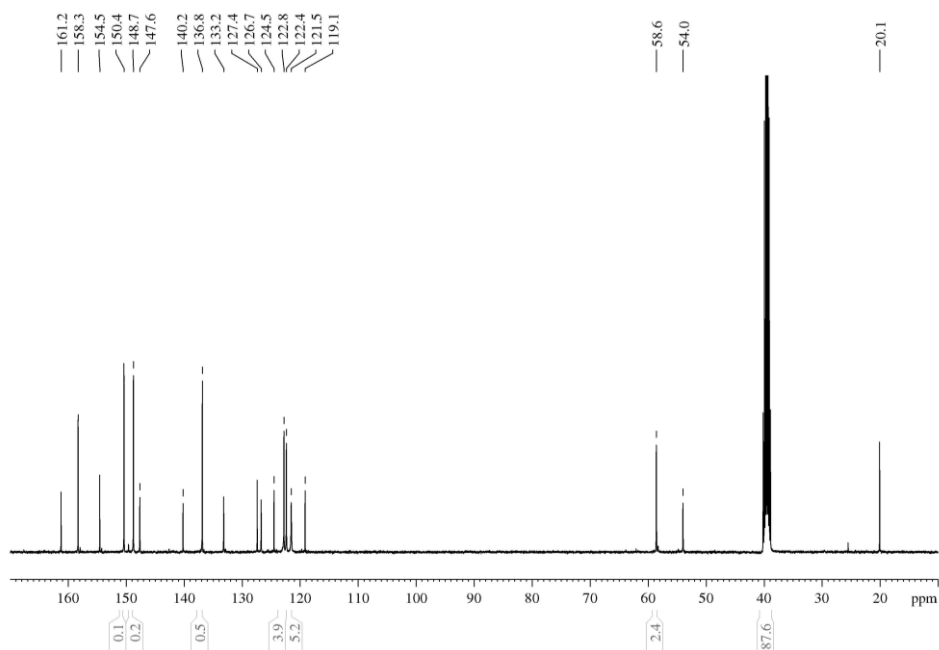


Figure 8.5. ^{13}C NMR spectrum (100 MHz) of **H₂L8** in $\text{DMSO-}d_6$, at room temperature.

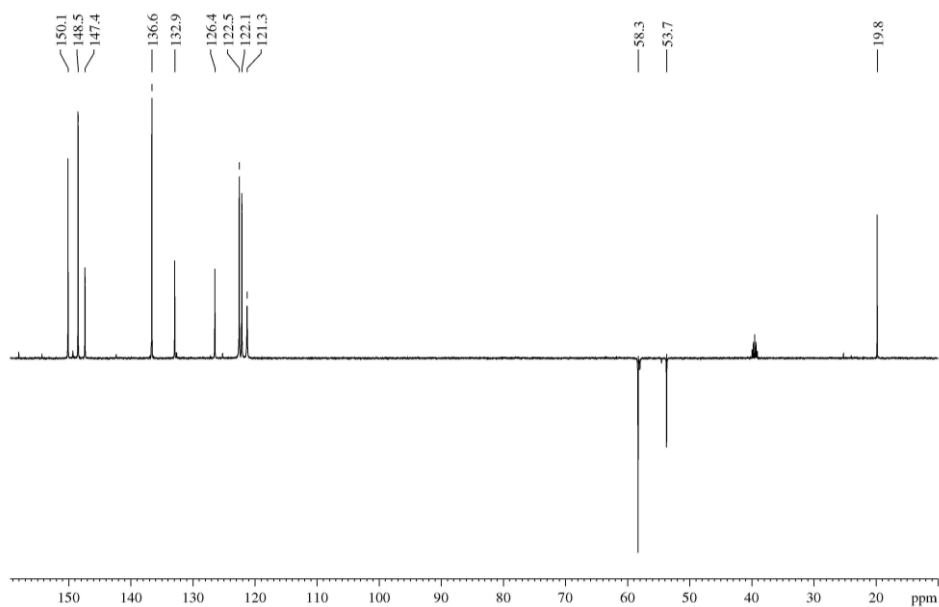


Figure 8.6. DEPT-135 NMR spectrum (100 MHz) of **H₂L8** in $\text{DMSO-}d_6$, at room temperature.

Table 8.1. ^1H (400 MHz) and ^{13}C (100 MHz) data for **H₂L8** in DMSO-*d*₆ at room temperature, with the respective assignments. Chemical shifts (δ) are in ppm and coupling constants (*J*) are in Hz.

| C/H | H ₂ L8, δ_{C} | H ₂ L8, δ_{H} |
|------|--|--|
| 1 | 161.2 | – |
| 2 | 147.6 | 8.80 (s, 1H) |
| 3 | 119.1 | – |
| 4 | 126.7 | 7.42 (s, 1H) |
| 5 | 127.4 | – |
| 6 | 133.2 | 7.17 (s, 1H) |
| 7 | 124.5 | – |
| 8 | 154.5 | – |
| 9 | 20.1 | 2.23 (s, 3H) |
| 10 | 54.0 | 3.75 (s, 2H) |
| 11 | 58.6* | 3.81 (s, 4H)* |
| 12 | 158.3* | – |
| 13 | 148.7* | 8.52 (d, 2H, $^3J_{\text{HH}} = 4.2$)* |
| 14 | 122.4* | 7.27 (td, 2H, $^3J_{\text{HH}} = 5.0$, $^4J_{\text{HH}} = 0.7$)* |
| 15 | 136.8* | 7.77 (td, 2H, $^3J_{\text{HH}} = 7.7$, $^4J_{\text{HH}} = 1.7$)* |
| 16 | 122.8* | 7.45 (d, 2H, $^3J_{\text{HH}} = 7.8$)* |
| 17 | 58.6* | 3.81 (s, 4H)* |
| 18 | 158.3* | – |
| 19 | 148.7* | 8.52 (d, 2H, $^3J_{\text{HH}} = 4.2$)* |
| 20 | 122.4* | 7.27 (td, 2H, $^3J_{\text{HH}} = 5.0$, $^4J_{\text{HH}} = 0.7$)* |
| 21 | 136.8* | 7.77 (td, 2H, $^3J_{\text{HH}} = 7.7$, $^4J_{\text{HH}} = 1.7$)* |
| 22 | 122.8* | 7.45 (d, 2H, $^3J_{\text{HH}} = 7.8$)* |
| 23 | 140.2 | – |
| 24 | 121.5* | 7.85 (d, 2H, $^3J_{\text{HH}} = 4.5$)* |
| 25 | 150.4 | 8.78 (s, 2H)* |
| 26 | 150.4 | 8.78 (s, 2H)* |
| 27 | 121.5* | 7.85 (d, 2H, $^3J_{\text{HH}} = 4.5$)* |
| O2–H | – | 11.71 (s, 1H) |
| N1–H | N1–H | 12.16 (s, 1H) |

*Overlapped signals. *symmetric signal. Signal multiplicity - s: singlet, d: doublet, t: triplet, dd: doublet of doublets, td: triplet of doublets.

8.2.2.2

Crystal structure of ligand H₂L8

Single crystal X-ray diffraction analysis showed that ligand **H₂L8** crystallized in the orthorhombic space group Pbc_a. The Oak Ridge Thermal Ellipsoid Plot (ORTEP) view is given in Figure 8.7, while Table 8.2 lists significant

crystallographic data and refinement parameters. In the solid state, this ligand presents two protonated heteroatoms O2 and N1.

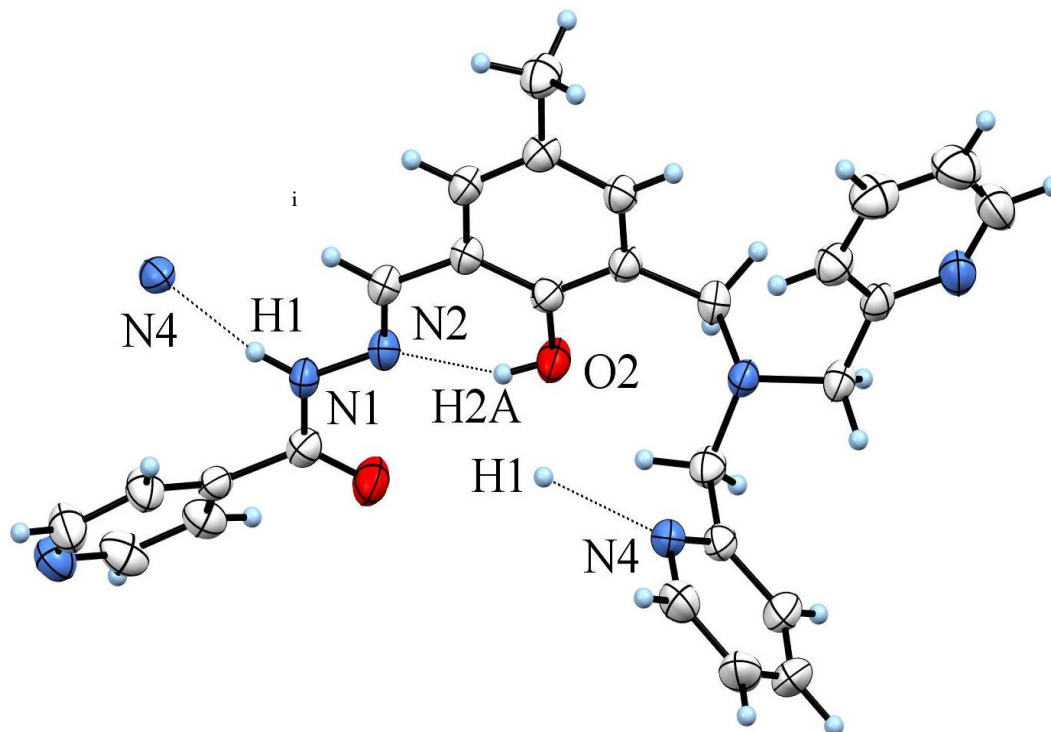


Figure 8.7. Crystal structure of ligand **H₂L8**. The ellipsoids were drawn with 50% probability. Only one of the enantiomers is shown. Intramolecular and intermolecular hydrogen bonds are depicted as dotted line.

Both intramolecular and intermolecular hydrogens bonds are observed in the structure of ligand **H₂L8** (Figure 8.7), as found in **H₂L4** (Chapter 5). The intramolecular H-bond is formed between the O2–H from the phenol central ring and the N2 from the hydrazone arm, resulting in a hexagonal ring. The intermolecular hydrogen bond connects the N1–H atom of the hydrazone group to the pyridine nitrogen pendant arm (N4) of another **H₂L8** molecule, which acts as an acceptor group (Figure 8.7). Intermolecular hydrogen bond distances are larger than the intramolecular ones (Table 8.3). Nevertheless, hydrogen bonds contribute to the stability of the molecules network.

Table 8.2. Crystallographic data and structure refinement of ligand **H₂L8**.

| H₂L8 | |
|--|---|
| Empirical formula | C ₂₇ H ₂₆ N ₆ O ₂ |
| Formula weight (g/mol) | 466.54 |
| Temperature (K) | 200(1) K |
| Crystal description | yellow needle |
| Crystal system | Orthorhombic |
| Space group | Pbca |
| a (Å) | 10.3497(2) |
| b (Å) | 10.5482(3) |
| c (Å) | 43.8090(11) |
| α (°) | 90 |
| β (°) | 90 |
| γ (°) | 90 |
| Volume (Å ³) | 4782.7(2) |
| Z | 8 |
| ρ _{calc} (g/cm ³) | 1.296 |
| Absorption coefficient μ (mm ⁻¹) | 0.684 |
| Crystal size (mm ³) | 0.5 × 0.05 × 0.05 |
| Wavelength λ (Å) | 1.54178 |
| Radiation type | Cu Kα |
| 2θ range (°) | 5.882 to 66.564 |
| Miller indexes ranges | -12 ≤ h ≤ 12, -10 ≤ k ≤ 12, -50 ≤ l ≤ 52 |
| Measured reflections | 22748 |
| Unique reflections | 4192 |
| Goodness-of-fit F ² | 1.028 |
| Final R indexes | R1 = 6.06 % |
| [all data] | wR2 = 10.15% |
| Final R indexes | R1 = 3.88 % |
| [I ≥ 2σ(I)] | wR2 = 9.07% |
| Refinement | |
| Data | 4192 |
| No. of parameters | 318 |
| No. of restraints | 0 |
| Largest diff. peak/hole (e/Å ³) | 0.151,-0.189 |

Table 8.3. H-bond length (d, Å) and angles (°) for ligand **H₂L8**.

| D—H...A | d(D—H) | d(H...A) | d(D...A) | D—H...A (°) |
|-------------------------|--------|----------|----------|-------------|
| O2—H2A...N2 | 0.84 | 1.185 | 2.591(2) | 146 |
| N1—H1...N4 ⁱ | 0.88 | 2.097 | 2.960(2) | 166 |

Symmetry codes: (i) 3/2-x, 1/2+y, z.

Additional van der Waals-type weak interactions appear in the ligand structure in order to stabilize the molecule. Thus C9—H9C...N5ⁱ and C2—H2B...N4ⁱ interactions are noticed in its crystal structure.

The molecular packing of **H₂L8** is determined by the interaction of eight molecules forming the extensive network (Figure 8.8). Selected geometric parameters for ligand **H₂L8** are shown in Table 8.4.

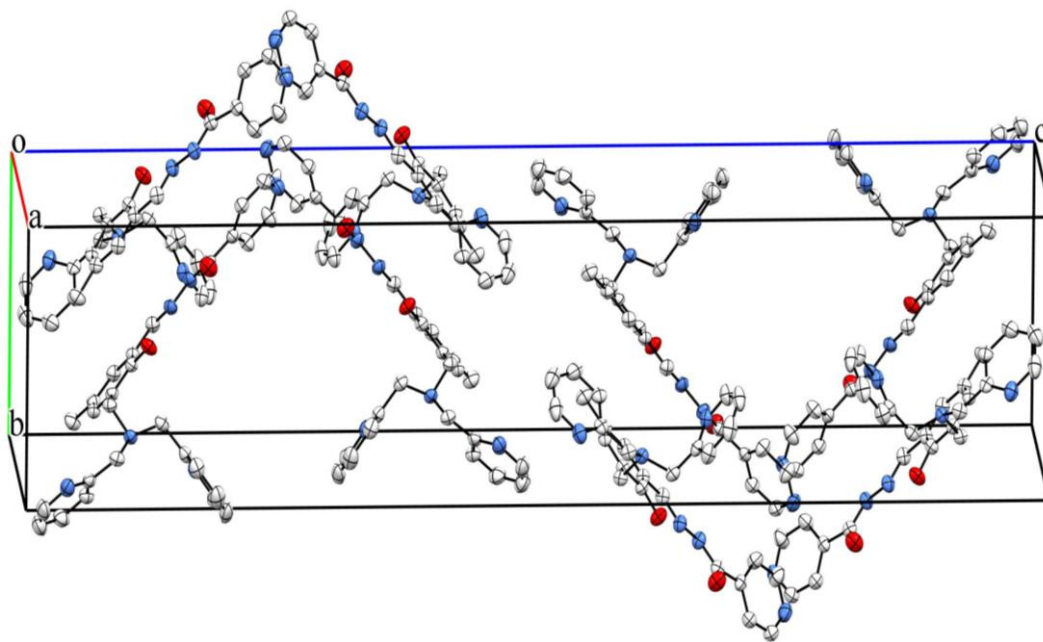


Figure 8.8. Molecular packing of ligand **H₂L8**. Hydrogen atoms have been omitted for clarify.

Table 8.4. Selected geometric parameters for ligand **H₂L8**.

| Bond distances (Å) | | Bond angles (°) | |
|--------------------|------------|-----------------|------------|
| O1-C1 | 1.220(2) | C1-N1-N2 | 117.48(13) |
| O2-C8 | 1.356(2) | C2-N2-N1 | 117.79(13) |
| N1-C1 | 1.357(2) | C17-N3-C11 | 111.14(12) |
| N1-N2 | 1.3779(19) | C17-N3-C10 | 110.08(13) |
| N2-C2 | 1.286(2) | C11-N3-C10 | 110.29(13) |
| N3-C17 | 1.465(2) | C13-N4-C12 | 118.30(15) |
| N3-C11 | 1.467(2) | C18-N5-C19 | 116.98(18) |
| N3-C10 | 1.483(2) | C26-N6-C25 | 115.96(17) |
| N4-C13 | 1.336(3) | O1-C1-N1 | 123.59(16) |
| N4-C12 | 1.343(2) | O1-C1-C23 | 120.91(16) |
| N5-C18 | 1.342(2) | N1-C1-C23 | 115.49(14) |
| N5-C19 | 1.345(3) | N2-C2-C3 | 119.94(14) |
| N6-C26 | 1.328(3) | N3-C10-C7 | 112.62(13) |
| N6-C25 | 1.332(3) | N3-C11-C12 | 111.92(15) |
| – | – | N4-C12-C16 | 121.38(18) |
| – | – | N4-C12-C11 | 116.13(14) |
| – | – | N4-C13-C14 | 123.1(2) |
| – | – | N3-C17-C18 | 112.58(13) |
| – | – | N5-C18-C22 | 122.08(17) |
| – | – | N5-C18-C17 | 115.95(15) |
| – | – | N5-C19-C20 | 123.90(19) |
| – | – | N6-C25-C24 | 124.17(19) |
| – | – | N6-C26-C27 | 124.52(19) |

8.2.2.3

Absorption and fluorescence spectroscopic studies of the compounds

The absorption spectrum of ligand **H₂L8** in H₂O/DMSO 9:1 displays four principal absorptions in the UV region, as shown in Figure 8.9. In the figure the absorption spectra of its precursors **BPMAMFF** and **INH** was also included. By comparison, it was possible to assign one absorption at 345 nm corresponding to the $\pi-\pi^*$ transition of the **BPMAMFF** (central ring and two arms of the molecules).

Two bands at 268 nm and 263 nm are also present in the spectra of both **BPMAMFF** and **INH** precursors. Thus, these absorptions were assigned to the central ring, two pendant-arms and isoniazidic moieties. Consequently, the remaining absorption band clearly corresponds to hydrazoneic transitions, since this band is absent in the spectra of the precursors. This hydrazoneic band corresponds to the most intense absorption in the spectra.

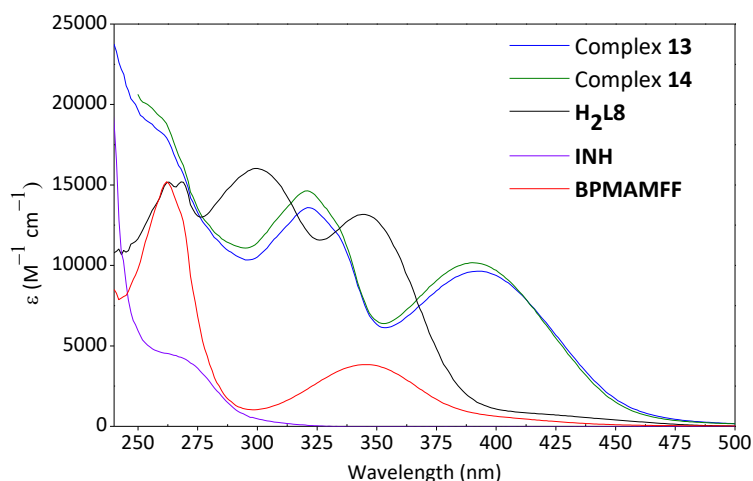


Figure 8.9. Absorption spectra of ligand **H₂L8**, and of its precursors **BPMAMFF** and **INH**, and of complexes **13** and **14**, recorded in H₂O/DMSO 9:1, at 298 K.

In general, the absorption spectra of complexes **13** and **14** are very similar to that of their precursor ligand **H₂L8** (Figure 8.9). The difference is related to a redshift process of all the bands due to coordination of the copper(II) ions to the arms and central ring of the ligands and the deprotonation of the phenol group and tautomeric form of the hydrazone group (azo).

The molar absorptivity coefficients of ligand **H₂L8** were analysed in H₂O/DMSO 9:1 (Figures 8.10) and determined as can be found in Table 8.5.

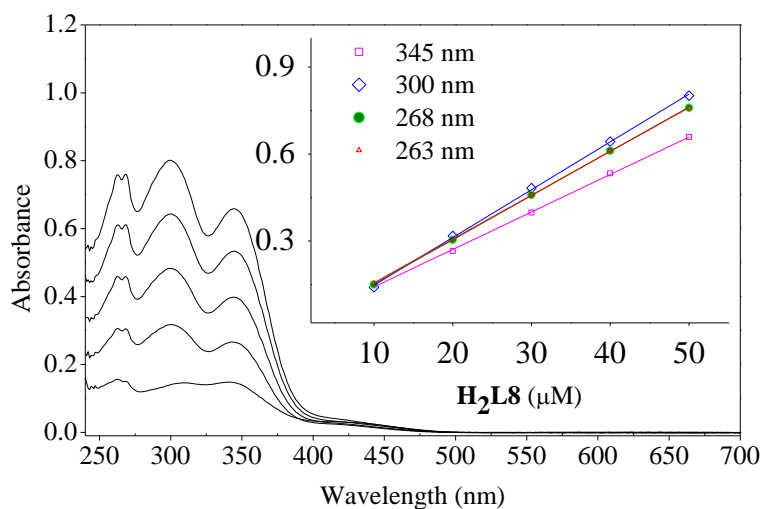


Figure 8.10. Concentration versus UV-visible absorption plots of ligand **H₂L8** at different wavelengths in $\text{H}_2\text{O}/\text{DMSO}$ 9:1 and at 298 K.

The molar absorptivity coefficients of the complexes were analysed in $\text{H}_2\text{O}/\text{DMSO}$ 9:1 (Figures 8.11 and 8.12) and determined as can be found in Table 8.5.

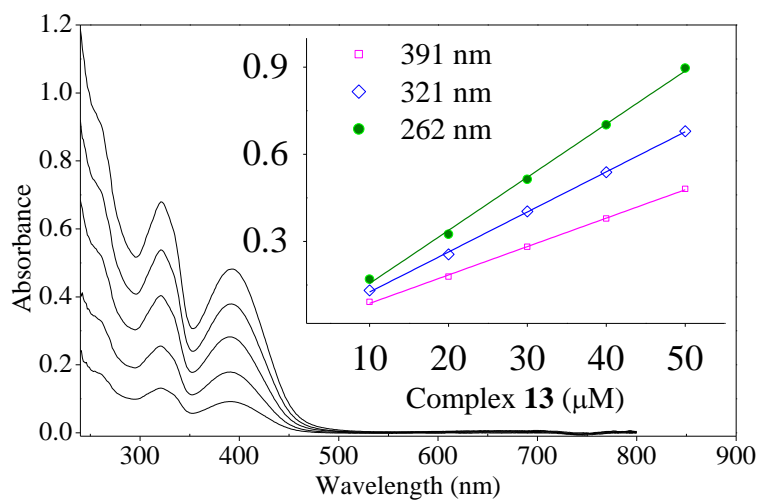


Figure 8.11. Concentration versus UV-visible absorption plots of complex **13** at different wavelengths in $\text{H}_2\text{O}/\text{DMSO}$ 9:1 and at 298 K.

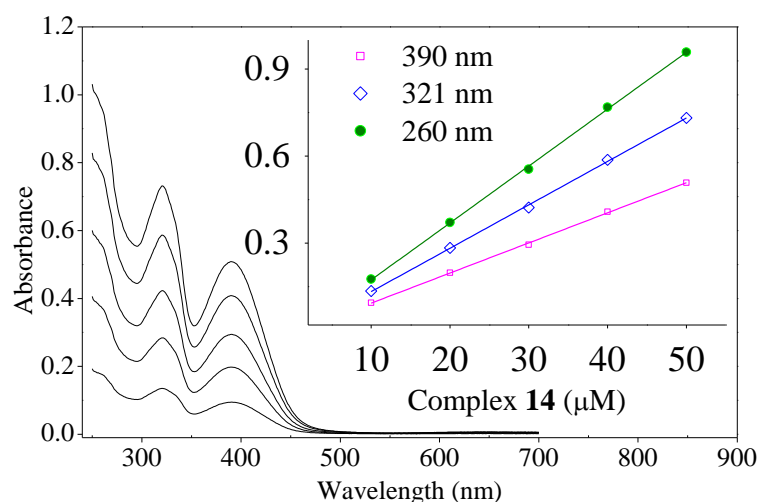


Figure 8.12. Concentration versus UV-visible absorption plots of complex **14** at different wavelengths in H₂O/DMSO 9:1 and at 298 K.

Table 8.5 shows the absorption bands for ligand **H₂L8**, and their molar absorptivity coefficients calculated from the plot of the concentration versus UV-visible absorbance (Figure 8.10).

Table 8.5. UV-Vis absorption properties of **H₂L8**, and of its dicopper(II) complexes **13** and **14** in H₂O/DMSO 9:1 at 298 K. Suggested assignments and standard deviation (mean ± S.D) are included.

| H₂L8 | | Complex 13 | | Complex 14 | | Assignment |
|------------------------|---|-------------------|---|-------------------|---|---------------------|
| λ (nm) | ϵ (M ⁻¹ cm ⁻¹)* | λ (nm) | ϵ (M ⁻¹ cm ⁻¹)* | λ (nm) | ϵ (M ⁻¹ cm ⁻¹)* | |
| 345 | 12900 ± 200 | 391 | 9800 ± 200 | 390 | 10400 ± 200 | BPMAMFF ring |
| 300 | 16500 ± 200 | 321 | 13800 ± 200 | 321 | 15000 ± 200 | CO–NH–N=N |
| 268 | 15250 ± 70 | 262 | 18300 ± 400 | 260 | 19600 ± 200 | INH / BPMAMFF rings |
| 262 | 15100 ± 50 | | | | | |

* (mean ± S.D)

The biological properties of a compound in the cellular medium, fluorescence is an important property. It allows, for example, the detection of the molecules in the cells by fluorescence microscopy [203]. In order to examine the fluorescence properties of ligand **H₂L8** and its copper(II) complexes **13** and **14** in aqueous medium, their emission spectra were obtained by exciting at 345 nm solutions containing the ligands and its precursor ($\lambda_{\text{excitation}}$ **BPMAMFF** = 345 nm; $\lambda_{\text{excitation}}$ **INH** = 266 nm), as well as the copper(II) complexes ($\lambda_{\text{excitation}}$ = 390 nm) (Figure 8.13).

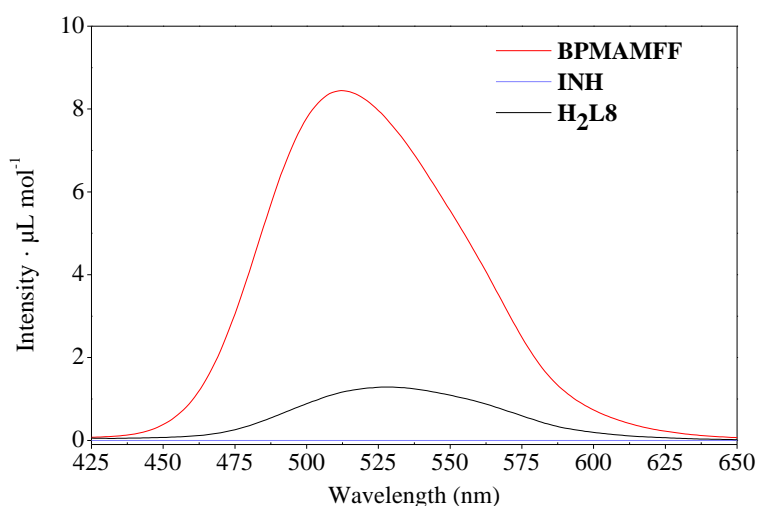


Figure 8.13. Fluorescence emission spectra of ligand **H₂L8** ($\lambda_{\text{excitation}} = 345 \text{ nm}$; $10 \mu\text{M}$), and of its respective precursors: **BPMAMFF** ($\lambda_{\text{excitation}} = 345 \text{ nm}$; $40 \mu\text{M}$) and **INH** ($\lambda_{\text{excitation}} = 266 \text{ nm}$; $40 \mu\text{M}$), in water, at 298 K.

By comparing intensity values (in u.a. $\cdot \mu\text{L mol}^{-1}$) of emission bands of precursor **BPMAMFF** (at 512 nm) with ligand **H₂L8**, it is evident that the addition of the isoniazidic-hydarzone group to **BPMAMFF** moiety give a partial quenching of the emission. Nevertheless, the emission spectra of **H₂L8** exhibits one band centred at 528 nm ($\lambda_{\text{excitation}} = 345 \text{ nm}$), which corresponds to 183 nm Stokes shift. Other interesting biological tests are suggested to be carried out taking advantage of the luminescent properties of the isoniazidic-ligand **H₂L8**. For example, its interaction with DNA and albumin proteins through fluorescence spectroscopy might provide results interesting for obtain information about the DNA binding constant or the ability to the compound to across the membrane of the cells.

Precursor **INH** and both copper(II) complexes **13** and **14** do not present any emission band in the fluorescence spectra in the tested conditions.

8.2.3

In vitro cytotoxic activity

In order to test the anticancer properties, the MTT assay [135] was used to study the *in vitro* antiproliferative activity of the isoniazidic-ligand **H₂L8** and its

copper(II) complexes against the human breast cancer cell line MCF-7. The effect of different concentrations of the compounds on the viability of the tested cancer cells was analysed after an exposure period of 24 h (Figure 8.14). Cisplatin was used as reference. The results indicate that both copper(II) complexes **13** and **14** has a higher antiproliferative activity than the metal-free ligand, as can be seen in the cytotoxic profiles in Figure 8.14. These results are in agreement with previously reported work, in which copper(II) complexes are notably more potent compound than their respective ligands [15, 16, 195].

In addition, complex **14** has the highest inhibition activity in the micromolar concentration range, whereas ligand **H₂L8** has the lowest one (Table 8.6) (**14** > **13** > **H₂L8**). It means that the complex prepared from **H₂L8** and copper(II) acetate monohydrate, which presents two acetate group coordinate to the metal ion, requires lower concentration to kill cancer cell than the complexes without bridged μ -O groups.

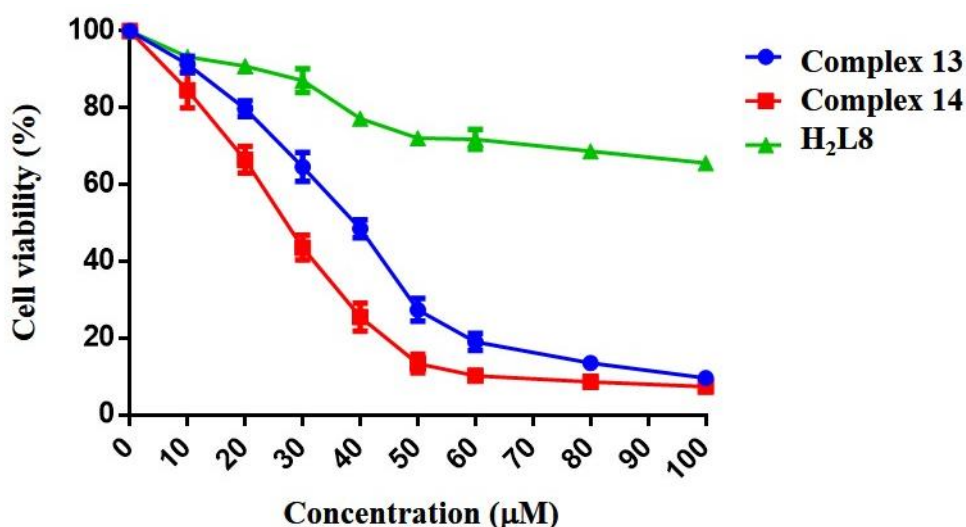
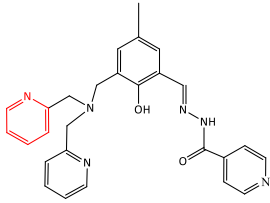
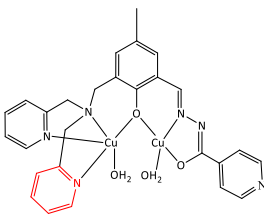
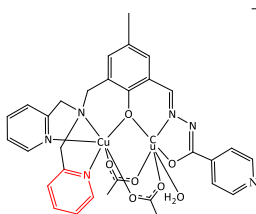
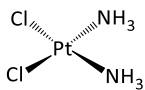


Figure 8.14. Dose-dependent effect on MCF-7 cells of ligand **H₂L8** and its copper(II) complexes **13** and **14** after 24 h, at 37 °C, using the MTT assay.

Table 8.6. IC₅₀ values of ligand **H₂L8** and its copper(II) complexes **13** and **14** on MCF-7 cancer cell line. Standard deviations are included.

| Compound | IC ₅₀ (μM) | Standard deviation | Compound' structure |
|------------------------|-----------------------|--------------------|--|
| H₂L8 | >100 | – |  |
| Complex 13 | 36.49 | 0.10 |  3ClO ₄ ·5H ₂ O |
| Complex 14 | 25.59 | 0.11 |  8H ₂ O |
| Cisplatin | 13.86 | 0.12 |  |

The cytotoxic activity of classic platinum complex, cisplatin, is significantly higher in comparison with copper complexes, against human breast cancer cells under the same tested, as was indicate by the IC₅₀ values.

Additional biological tests of ligand **H₂L8** and its copper(II) complexes **13** and **14** will be performed by the PhD student Farzaneh Ghasemi, as collaboration with the research group directed by PhD. Marcos Dias Pereira in the *Universidade Federal do Rio de Janeiro* (UFRJ).

8.3

Partial conclusions

One isoniazidic-BPMAMFF Schiff Base ligand and its copper(II) complexes from perchlorate and acetate salts have been synthesized in good yields (50% - 99%). The compounds were characterized by NMR and absorption

spectroscopy and analytical techniques. The ligand was analysed by an X-ray diffraction study.

The absorption bands in the spectra of the synthesized ligand and complexes were analysed and assigned to their precursor and their new hydrazonic moieties. The metal-free ligand displayed fluorescent properties, while complexes were not fluorescent.

The crystal structure of ligand **H₂L8** revealed two protonated heteroatoms and both intramolecular and intermolecular hydrogen bonds. Some van der Waals interactions were observed.

The cytotoxicity of the compound was examined on a human breast cancer cell line by the MTT assay. The results evidenced that Cu₂-complexes showed a important higher cytotoxic ability than the metal-free ligand.

General Conclusions

Eight novel aroylhydrazone ligands and their acetate and/or perchlorate-derived dicopper(II) complexes (14 in total) were synthesized and fully characterized, through analytical and spectroscopic techniques. The single crystal structures of four ligands and five complexes were determined by X-ray diffraction analyses. The absorption bands in the spectra of the ligands and complexes were successfully assigned to the aroylhydrazones and **HBPAMFF** or **BPMAMFF** moieties.

DMSO solutions of free ligands and complexes exhibited high stability, while the copper complexes were more stable than their respective ligands in relevant temperature and cellular medium (37 °C, pH 7.4).

Absorption and fluorescence spectroscopic studies showed that complexes **3–6** and ligands **H3L3** and **H2L4** interact with DNA through the intercalative and non-intercalative modes, respectively. Competitive EB displacement assay revealed strong affinity of the DNA for Cu₂-complexes (**3–6**) in the 10⁶ M⁻¹ range.

The plasmid DNA cleavage ability of complexes **1** and **2** was successfully demonstrated by Dynamic Light Scattering studies. It was possible to identify the changes in the hydrodynamic radius value of the pBR322 plasmid DNA relative to the nick in the helices by the complexes. Consequently, DNA damage in the nucleus of the cells can be proposed as a putative cell death mechanism.

The interaction of ligands **H3L1** and **H2L2** and their μ -hydroxo complexes **1** and **2** with BSA, as well as the interaction of ligand **H3L5** with HSA, demonstrated an important affinity of the compounds for those proteins. Additionally, scattering techniques (DLS and SAXS) suggest that the complexes and their free ligands interact with BSA in a reversible manner. Since albumins are important proteins involved in the transportation of drugs in the biological system, the observed results indicate that the new compounds could be targeted through blood transport.

Cytotoxic assays on different cancer cells revealed a high ability of ligands and complexes to induce cell death.

In contrast to what is commonly observed, in some cases ligands were more cytotoxic than their respective complexes. In order to explain those results, the metal-chelation and transmetalation ability of the binucleating ligands and their copper complexes towards Fe(II), Fe(III) and Zn(II) present in the biological medium were verified, as an additional anticancer strategy. Ligands **H₃L₃** and **H₂L₄** were able to coordinate to Fe(II), Fe(III), Zn(II) and Cu(II) from cellular medium, while copper(II) complexes seem to interchange their Cu(II) with Fe(III) ions. Our results suggest firstly that the design of the molecules is the main reason for the excellent cytotoxic activity observed, and secondly that their ability to capture essential intracellular metals can greatly improve the cell death induction.

The cytotoxicity of the ligands **H₃L₃** and **H₂L₄** and complexes **3–6** on human epithelial breast cancer cells by the MTT assay highlighted that ligand **H₃L₃** and its dicopper(II) complexes **3** and **4**, containing a phenol pendant arm, showed (attaining nanomolar range) a much higher cytotoxicity than ligand **H₂L₄** and complexes **5** and **6**, containing a pyridine pendant arm.

The ability of the compounds to permeate the cell membrane and to induce cell death is a crucial property of a compound in the search for new anticancer drugs. In this work, fluorescence microscopy was used to demonstrate the presence of the fluorescent ligand **H₃L₇** within the cells and its affinity to the mitochondria organelle.

Finally, the present work shows that aroylhydrazone-derived ligands and their dicopper(II) complexes may represent a promising structural starting point for the development of highly active potential antitumor agents.

Part III.

Future work, references and attachments

Future work

The results of the present research show promising ligands and complexes in the search for new anticancer drugs. Nevertheless, some additional questions need to be explored in future works. Some suggestions can be addressed:

- ✓ To test the cytotoxic activity of the ligands and complexes in Chapter 5–8 on additional cancer cell lines different to the MDA-MB-231 cell lines, and also on non-tumoral cells, as SI is an important parameter.
- ✓ To determine the cytotoxic activity of the compounds in Chapter 5–8 during 24 h.
- ✓ To verify the *in vitro* ability of the compounds to induce apoptosis, using for example, Annexin V-FTIC/PI double staining assay or fluorescence microscopy monitoring.
- ✓ To use molecular docking studies to predict the binding sites of the compounds on albumin protein or on DNA.
- ✓ To examine the *in vivo* anticancer properties of the compounds using tumor xenograft studies.
- ✓ To carry out synchronous $\Delta 15$ and $\Delta 60$ fluorescent measurements to obtain information about the spectral properties of tyrosine and tryptophan residues in the protein in order to specify the interaction of the biomolecule with the synthesized compounds.
- ✓ To compare the obtained results on the cleavage of plasmid DNA by the complexes using dynamic light scattering with other classic techniques, such as viscosity measurements or agarose gel electrophoresis.
- ✓ To explore in more detail, the luminescent properties of the compounds at different pH and temperatures, as well as, to determine their fluorescence quantum yields. Additionally, to determine the existence of excimers in ligands **H₃L5** (derivatives pyrene molecule) solutions by testing the fluorescence emission profiles at different concentrations.

- ✓ To prepare Fe(II), Fe(III) and Zn(II) complexes with the reported ligands in this work, in order to test and compare their cytotoxic activity on tumoral cells with the synthesized Cu₂-complexes described herein, and associate the results with the metalation and transmetalation processes in the biological medium.
- ✓ To explore the stability of ligand **H₃L5** and its complexes after 72 h, and also the stability of ligands **H₃L6–H₂L8** and their complexes for 24 and 72 h.

Besides the cytotoxicity of the compounds on cancer cells, ligands and complexes have been shown to display many biological properties in previous works. It is an important suggestion to explore the additional biological properties of the synthesized compounds, such as antifungal, antihistaminic and/or antimicrobial.

References

- [1] STEWART, W. E. and WILD, P. C. World Cancer Report 2014. 2014, 150 cours Albert Thomas, 69372 Lyon Cedex 08, France: International Agency for Research on Cancer. p. 632.
- [2] OTTENWAELDER, X. and HERRES-PAWLIS, S. Bio-inorganic chemistry of copper. **Inorganica Chimica Acta**, v. 481, n., p. 1-3, 2018/09/01/, 2018.
- [3] MUKHERJEE, R. N. The bioinorganic chemistry of copper. **Indian Journal of Chemistry - Section A**, v. 42, n. 9, p. 2175-2184, 2003.
- [4] SANTINI, C.; PELLEI, M.; GANDIN, V.; PORCHIA, M.; TISATO, F., and MARZANO, C. Advances in Copper Complexes as Anticancer Agents. **Chemical Reviews**, v. 114, n. 1, p. 815-862, 2014/01/08, 2014.
- [5] PAIXÃO, D. A.; MARZANO, I. M.; JAIMES, E. H. L.; PIVATTO, M.; CAMPOS, D. L.; PAVAN, F. R.; DEFLON, V. M.; MAIA, P. I. D. S.; DA COSTA FERREIRA, A. M.; UEHARA, I. A.; SILVA, M. J. B.; BOTELHO, F. V.; PEREIRA-MAIA, E. C.; GUILARDI, S., and GUERRA, W. Novel copper(II) complexes with hydrazides and heterocyclic bases: Synthesis, structure and biological studies. **Journal of Inorganic Biochemistry**, v. 172, n., p. 138-146, 2017/07/01/, 2017.
- [6] PIVETTA, T.; VALLETTA, E.; FERINO, G.; ISAIA, F.; PANI, A.; VASCELLARI, S.; CASTELLANO, C.; DEMARTIN, F.; CABIDDU, M. G., and CADONI, E. Novel coumarins and related copper complexes with biological activity: DNA binding, molecular docking and in vitro antiproliferative activity. **Journal of Inorganic Biochemistry**, v. 177, n., p. 101-109, 2017/12/01/, 2017.
- [7] RAMACHANDRAN, E.; GANDIN, V.; BERTANI, R.; SGARBOSSA, P.; NATARAJAN, K.; BHUVANESH, N. S. P.; VENZO, A.; ZOLEO, A.; GLISENTI, A.; DOLMELLA, A.; ALBINATI, A., and MARZANO, C. Synthesis, characterization and cytotoxic activity of novel copper(II) complexes with aroylhydrazone derivatives of 2-Oxo-1,2-dihydrobenzo[h]quinoline-3-carbaldehyde. **Journal of Inorganic Biochemistry**, v. 182, n., p. 18-28, 2018/05/01/, 2018.
- [8] VENKATACHALAM, T. K.; BERNHARDT, P. V.; NOBLE, C. J.; FLETCHER, N.; PIERENS, G. K.; THURECHT, K. J., and REUTENS, D. C. Synthesis, characterization and biological activities of semicarbazones and their copper complexes. **Journal of Inorganic Biochemistry**, v. 162, n., p. 295-308, 2016/09/01/, 2016.
- [9] ALMEIDA, J. D. C.; PAIXÃO, D. A.; MARZANO, I. M.; ELLENA, J.; PIVATTO, M.; LOPES, N. P.; FERREIRA, A. M. D. C.; PEREIRA-MAIA, E. C.; GUILARDI, S., and GUERRA, W. Copper(II) complexes with β -diketones and N-donor heterocyclic ligands: Crystal structure, spectral

- properties, and cytotoxic activity. **Polyhedron**, v. 89, n., p. 1-8, 2015/03/29/, 2015.
- [10] IGLESIAS, S.; ALVAREZ, N.; TORRE, M. H.; KREMER, E.; ELLENA, J.; RIBEIRO, R. R.; BARROSO, R. P.; COSTA-FILHO, A. J.; KRAMER, M. G., and FACCHIN, G. Synthesis, structural characterization and cytotoxic activity of ternary copper(II)-dipeptide-phenanthroline complexes. A step towards the development of new copper compounds for the treatment of cancer. **Journal of Inorganic Biochemistry**, v. 139, n., p. 117-123, 2014/10/01/, 2014.
- [11] MASSOUD, S. S.; LOUKA, F. R.; DUCHARME, G. T.; FISCHER, R. C.; MAUTNER, F. A.; VANČO, J.; HERCHEL, R.; DVOŘÁK, Z., and TRÁVNÍČEK, Z. Copper(II) complexes based on tripodal pyrazolyl amines: Synthesis, structure, magnetic properties and anticancer activity. **Journal of Inorganic Biochemistry**, v. 180, n., p. 39-46, 2018/03/01/, 2018.
- [12] LOGANATHAN, R.; GANESHPANDIAN, M.; BHUVANESH, N. S. P.; PALANIANDAVAR, M.; MURUGANANTHAM, A.; GHOSH, S. K.; RIYASDEEN, A., and AKBARSHA, M. A. DNA and protein binding, double-strand DNA cleavage and cytotoxicity of mixed ligand copper(II) complexes of the antibacterial drug nalidixic acid. **Journal of Inorganic Biochemistry**, v. 174, n., p. 1-13, 2017/09/01/, 2017.
- [13] HU, J.; LIAO, C.; GUO, Y.; YANG, F.; SANG, W., and ZHAO, J. A. Copper(II) complexes inducing apoptosis in cancer cells, and demonstrating DNA and HSA interactions. **Polyhedron**, v. 132, n., p. 28-38, 2017/08/16/, 2017.
- [14] HU, J.; GUO, Y.; ZHAO, J. A., and ZHANG, J. In vitro antitumor activity of novel benzimidazole-based Cu(II) complexes. **Bioorganic & Medicinal Chemistry**, v. 25, n. 20, p. 5733-5742, 2017/10/15/, 2017.
- [15] BYKOWSKA, A.; KOMARNICKA, U. K.; JEŻOWSKA-BOJCZUK, M., and KYZIOŁ, A. CuI and CuII complexes with phosphine derivatives of fluoroquinolone antibiotics – A comparative study on the cytotoxic mode of action. **Journal of Inorganic Biochemistry**, v. 181, n., p. 1-10, 2018/04/01/, 2018.
- [16] TYAGI, P.; TYAGI, M.; AGRAWAL, S.; CHANDRA, S.; OJHA, H., and PATHAK, M. Synthesis, characterization of 1,2,4-triazole Schiff base derived 3d-metal complexes: Induces cytotoxicity in HepG2, MCF-7 cell line, BSA binding fluorescence and DFT study. **Spectrochimica Acta Part A**, v. 171, n., p. 246-257, 2017/01/15/, 2017.
- [17] SAMA, F.; RAIZADA, M.; ASHAFQAQ, M.; AHAMAD, M. N.; MANTASHA, I.; IMAN, K.; SHAHID, M.; RAHISUDDIN; ARIF, R.; SHAH, N. A., and SALEH, H. A. M. Synthesis, structure and DNA binding properties of a homodinuclear Cu(II) complex: An experimental and theoretical approach. **Journal of Molecular Structure**, v. 1176, n., p. 283-289, 2019/01/15/, 2019.
- [18] IQBAL, M.; ALI, S.; TAHIR, M. N.; MUHAMMAD, N.; SHAH, N. A.; SOHAIL, M., and PANDARINATHAN, V. Synthesis, crystal structure and electrochemical and DNA binding studies of oxygen bridged-copper(II) carboxylate. **Journal of Molecular Structure**, v. 1093, n., p. 135-143, 2015/08/05/, 2015.

- [19] JAYAMANI, A.; SENGOTTUVELAN, N.; KANG, S. K., and KIM, Y.-I. Mono- and binuclear copper(II) complexes of the bipyridine ligand: Structural, electrochemical and biological studies. **Polyhedron**, v. 98, n., p. 203-216, 2015/09/25/, 2015.
- [20] SURESHBABU, P.; MOHAMMAD JUNAID, Q.; UPADHYAY, C.; VICTORIA, W.; PITCHAVEL, V.; NATARAJAN, S., and SABIAH, S. Di and Tetranuclear Cu(II) Complexes with Simple 2-Aminoethylpyridine: Magnetic Properties, Phosphodiester Hydrolysis, DNA Binding/Cleavage, Cytotoxicity and Catecholase Activity. **Polyhedron**, v., n., p., 2019/02/20/, 2019.
- [21] MONTAGNER, D.; GANDIN, V.; MARZANO, C., and ERXLEBEN, A. DNA damage and induction of apoptosis in pancreatic cancer cells by a new dinuclear bis(triazacyclonane) copper complex. **Journal of Inorganic Biochemistry**, v. 145, n., p. 101-107, 2015/04/01/, 2015.
- [22] PRZYJOJSKI, J. A.; MYERS, N. N.; ARMAN, H. D.; PROSVIRIN, A.; DUNBAR, K. R.; NATARAJAN, M.; KRISHNAN, M.; MOHAN, S., and WALMSLEY, J. A. Dinuclear and heptanuclear complexes of copper(II) with 7-azaindole ligand: Synthesis, characterization, magnetic properties, and biological activity. **Journal of Inorganic Biochemistry**, v. 127, n., p. 175-181, 2013/10/01/, 2013.
- [23] BECCO, L.; GARCÍA-RAMOS, J. C.; AZUARA, L. R.; GAMBINO, D., and GARAT, B. Analysis of the DNA Interaction of Copper Compounds Belonging to the Casiopeínas® Antitumoral Series. **Biological Trace Element Research**, v. 161, n. 2, p. 210-215, 2014/11/01, 2014.
- [24] SILVA, P. P.; GUERRA, W.; DOS SANTOS, G. C.; FERNANDES, N. G.; SILVEIRA, J. N.; DA COSTA FERREIRA, A. M.; BORTOLOTTI, T.; TERENCEZI, H.; BORTOLUZZI, A. J.; NEVES, A., and PEREIRA-MAIA, E. C. Correlation between DNA interactions and cytotoxic activity of four new ternary compounds of copper(II) with N-donor heterocyclic ligands. **Journal of Inorganic Biochemistry**, v. 132, n., p. 67-76, 2014/03/01/, 2014.
- [25] PILON, A.; LORENZO, J.; RODRIGUEZ-CALADO, S.; ADÃO, P.; MARTINS, A. M.; VALENTE, A., and ALVES, L. G. New Cyclams and Their Copper(II) and Iron(III) Complexes: Synthesis and Potential Application as Anticancer Agents. **ChemMedChem**, v. 14, n. 7, p. 770-778, 2019.
- [26] GARCÍA-RAMOS, J. C.; GUTIÉRREZ, A. G.; VÁZQUEZ-AGUIRRE, A.; TOLEDANO-MAGAÑA, Y.; ALONSO-SÁENZ, A. L.; GÓMEZ-VIDALES, V.; FLORES-ALAMO, M.; MEJÍA, C., and RUIZ-AZUARA, L. The mitochondrial apoptotic pathway is induced by Cu(II) antineoplastic compounds (Casiopeínas®) in SK-N-SH neuroblastoma cells after short exposure times. **BioMetals**, v. 30, n. 1, p. 43-58, February 01, 2017.
- [27] ZHOU, W.; WANG, X.; HU, M.; ZHU, C., and GUO, Z. A mitochondrion-targeting copper complex exhibits potent cytotoxicity against cisplatin-resistant tumor cells through multiple mechanisms of action. **Chemical Science**, v. 5, n. 7, p. 2761-2770, 2014.
- [28] LONG, C.; SLATOR, C.; MCKEE, V.; MOLPHY, Z.; KELLETT, A., and BROWN, T. Di-copper metallodrugs promote NCI-60 chemotherapy via singlet oxygen and superoxide production with tandem TA/TA and AT/AT

- oligonucleotide discrimination. **Nucleic Acids Research**, v. 46, n. 6, p. 2733-2750, 2018.
- [29] ZANVETTOR, N. T.; NAKAHATA, D. H.; DE PAIVA, R. E. F.; RIBEIRO, M. A.; CUIN, A.; CORBI, P. P., and FORMIGA, A. L. B. Copper(II), palladium(II) and platinum(II) complexes with 2,2-thiophen-yl-imidazole: Synthesis, spectroscopic characterization, X-ray crystallographic studies and interactions with calf-thymus DNA. **Inorganica Chimica Acta**, v. 443, n., p. 304-315, 2016/03/24/, 2016.
- [30] VIQUEIRA, J.; DURÁN, M. L.; GARCÍA-VÁZQUEZ, J. A.; CASTRO, J.; PLATAS-IGLESIAS, C.; ESTEBAN-GÓMEZ, D.; ALZUET-PIÑA, G.; MOLDES, A., and NASCIMENTO, O. R. Modulating the DNA cleavage ability of copper(ii) Schiff bases through ternary complex formation. **New Journal of Chemistry**, v. 42, n. 18, p. 15170-15183, 2018.
- [31] ŁODYGA-CHRUSCIŃSKA, E.; PILO, M.; ZUCCA, A.; GARRIBBA, E.; KLEWICKA, E.; ROWIŃSKA-ŻYREK, M.; SYMONOWICZ, M.; CHRUSCIŃSKI, L., and CHESHCHEVIK, V. T. Physicochemical, antioxidant, DNA cleaving properties and antimicrobial activity of fisetin-copper chelates. **Journal of Inorganic Biochemistry**, v. 180, n., p. 101-118, 2018/03/01/, 2018.
- [32] TISHCHENKO, K.; BELOGLAZKINA, E.; PROSKURNIN, M.; MALINNIKOV, V.; GUK, D.; MURATOVA, M.; KRASNOVSKAYA, O.; UDINA, A.; SKVORTSOV, D.; SHAFIKOV, R. R.; IVANENKOV, Y.; ALADINSKIY, V.; SOROKIN, I.; GROMOV, O.; MAJOUGA, A., and ZYK, N. New copper(II) thiohydantoin complexes: Synthesis, characterization, and assessment of their interaction with bovine serum albumin and DNA. **Journal of Inorganic Biochemistry**, v. 175, n., p. 190-197, 2017/10/01/, 2017.
- [33] ZHENG, K.; YAN, M.-X.; LI, Y.-T.; WU, Z.-Y., and YAN, C.-W. Synthesis and structure of new dicopper(II) complexes bridged by N-(2-hydroxy-5-methylphenyl)-N'-[3-(dimethylamino)propyl]oxamide with in vitro anticancer activity: A comparative study of reactivities towards DNA/protein by molecular docking and experimental assays. **European Journal of Medicinal Chemistry**, v. 109, n., p. 47-58, 2016/02/15/, 2016.
- [34] XU, X.-W.; LI, X.-J.; ZHU, L.; LI, Y.-T.; WU, Z.-Y., and YAN, C.-W. Synthesis and structure of dicopper(II) complexes bridged by N-(5-chloro-2-hydroxyphenyl)-N'-[3-(methylamino)propyl]oxamide: Evaluation of DNA/protein binding, DNA cleavage, and in vitro anticancer activity. **Journal of Photochemistry and Photobiology B**, v. 147, n., p. 9-23, 2015/06/01/, 2015.
- [35] ZHAO, F.-J.; ZHAO, H.-Q.; LIU, F.; LI, Y.-T.; WU, Z.-Y., and YAN, C.-W. Synthesis and crystal structure of new dicopper(II) complexes with N,N'-bis-(dipropylenetriamine)oxamide as bridging ligand: Effects of the counterions on DNA/protein-binding property and in vitro antitumor activity. **Journal of Photochemistry and Photobiology B**, v. 143, n., p. 148-162, 2015/02/01/, 2015.
- [36] ZHENG, K.; ZHU, L.; LI, Y.-T.; WU, Z.-Y., and YAN, C.-W. Synthesis and crystal structure of new dicopper(II) complexes having asymmetric N,N'-bis(substituted)oxamides with DNA/protein binding ability: In vitro anticancer activity and molecular docking studies. **Journal of**

- Photochemistry and Photobiology B**, v. 149, n., p. 129-142, 2015/08/01/, 2015.
- [37] ZHU, L.; ZHENG, K.; LI, Y.-T.; WU, Z.-Y., and YAN, C.-W. Synthesis and structure elucidation of new μ -oxamido-bridged dicopper(II) complex with in vitro anticancer activity: A combined study from experiment verification and docking calculation on DNA/protein-binding property. **Journal of Photochemistry and Photobiology B**, v. 155, n., p. 86-97, 2016/02/01/, 2016.
- [38] FERREIRA, B. J. M. L.; BRANDÃO, P.; MEIRELES, M.; MARTEL, F.; CORREIA-BRANCO, A.; FERNANDES, D. M.; SANTOS, T. M., and FÉLIX, V. Synthesis, structural characterization, cytotoxic properties and DNA binding of a dinuclear copper(II) complex. **Journal of Inorganic Biochemistry**, v. 161, n., p. 9-17, 2016/08/01/, 2016.
- [39] BERA, P.; BRANDÃO, P.; MONDAL, G.; SANTRA, A.; JANA, A.; MOKHAMATAM, R. B.; MANNA, S. K.; MANDAL, T. K., and BERA, P. An unusual iminoacylation of 2-amino pyridyl thiazole: Synthesis, X-ray crystallography and DFT study of copper(II) amidine complexes and their cytotoxicity, DNA binding and cleavage study. **Polyhedron**, v. 159, n., p. 436-445, 2019/02/01/, 2019.
- [40] LI, M.; KONG, L. L.; GOU, Y.; YANG, F., and LIANG, H. DNA binding, cytotoxicity and apoptosis induction activity of a mixed-ligand copper(II) complex with taurine Schiff base and imidazole. **Spectrochimica Acta Part A: Molecular and Biomolecular Spectroscopy**, v. 128, n., p. 686-693, 2014/07/15/, 2014.
- [41] HERNÁNDEZ-GIL, J.; FERRER, S.; CASTIÑEIRAS, A.; LIU-GONZÁLEZ, M.; LLORET, F.; RIBES, Á.; ČOGA, L.; BERNECKER, A., and MAREQUE-RIVAS, J. C. Two Novel Ternary Dicopper(II) μ -Guanazole Complexes with Aromatic Amines Strongly Activated by Quantum Dots for DNA Cleavage. **Inorganic Chemistry**, v. 53, n. 1, p. 578-593, 2014/01/06, 2014.
- [42] PATIL, S. A.; PRABHAKARA, C. T.; HALASANGI, B. M.; TORAGALMATH, S. S., and BADAMI, P. S. DNA cleavage, antibacterial, antifungal and anthelmintic studies of Co(II), Ni(II) and Cu(II) complexes of coumarin Schiff bases: Synthesis and spectral approach. **Spectrochimica Acta Part A**, v. 137, n., p. 641-651, 2015/02/25/, 2015.
- [43] RAFI, U. M.; MAHENDIRAN, D.; HALEEL, A. K.; NANKAR, R. P.; DOBLE, M., and RAHIMAN, A. K. New pyridazine-based binuclear nickel(ii), copper(ii) and zinc(ii) complexes as prospective anticancer agents. **New Journal of Chemistry**, v. 40, n. 3, p. 2451-2465, 2016.
- [44] BELOGLAZKINA, E. K.; KRASNOVSKAYA, O. O.; GUK, D. A.; TAFEENKO, V. A.; MOISEEVA, A. A.; ZYK, N. V., and MAJOUGA, A. G. Synthesis, characterization, and cytotoxicity of binuclear copper(II) complexes with tetradentate nitrogen-containing ligands bis-5-(2-pyridylmethylidene)-3,5-dihydro-4H-imidazol-4-ones. **Polyhedron**, v. 148, n., p. 129-137, 2018/07/01/, 2018.
- [45] FEKRI, R.; SALEHI, M.; ASADI, A., and KUBICKI, M. Synthesis, characterization, anticancer and antibacterial evaluation of Schiff base ligands derived from hydrazone and their transition metal complexes. **Inorganica Chimica Acta**, v. 484, n., p. 245-254, 2019/01/01/, 2019.

- [46] MO, Q.; DENG, J.; LIU, Y.; HUANG, G.; LI, Z.; YU, P.; GOU, Y., and YANG, F. Mixed-ligand Cu(II) hydrazone complexes designed to enhance anticancer activity. **European Journal of Medicinal Chemistry**, v. 156, n., p. 368-380, 2018/08/05/, 2018.
- [47] TAHA, M.; ALI SHAH, S. A.; AFIFI, M.; ZULKEFLEE, M.; SULTAN, S.; WADOOD, A.; RAHIM, F., and ISMAIL, N. H. Morpholine hydrazone scaffold: Synthesis, anticancer activity and docking studies. **Chinese Chemical Letters**, v. 28, n. 3, p. 607-611, 2017/03/01/, 2017.
- [48] MANDEWALE, M. C.; PATIL, U. C.; SHEDGE, S. V.; DAPPADWAD, U. R., and YAMGAR, R. S. A review on quinoline hydrazone derivatives as a new class of potent antitubercular and anticancer agents. **Beni-Suef University Journal of Basic and Applied Sciences**, v. 6, n. 4, p. 354-361, 2017/12/01/, 2017.
- [49] LINDGREN, E. B.; DE BRITO, M. A.; VASCONCELOS, T. R. A.; DE MORAES, M. O.; MONTENEGRO, R. C.; YONEDA, J. D., and LEAL, K. Z. Synthesis and anticancer activity of (E)-2-benzothiazole hydrazones. **European Journal of Medicinal Chemistry**, v. 86, n., p. 12-16, 2014/10/30/, 2014.
- [50] WANG, Y.; YAN, H.; MA, C., and LU, D. Synthesis and anticancer activities of novel 8-azapurine carbocyclic nucleoside hydrazones. **Bioorganic & Medicinal Chemistry Letters**, v. 25, n. 20, p. 4461-4463, 2015/10/15/, 2015.
- [51] KAPLÁNEK, R.; JAKUBEK, M.; RAK, J.; KEJÍK, Z.; HAVLÍK, M.; DOLENSKÝ, B.; FRYDRYCH, I.; HAJDÚCH, M.; KOLÁŘ, M.; BOGDANOVÁ, K.; KRÁLOVÁ, J.; DŽUBÁK, P., and KRÁL, V. Caffeine-hydrazones as anticancer agents with pronounced selectivity toward T-lymphoblastic leukaemia cells. **Bioorganic Chemistry**, v. 60, n., p. 19-29, 2015/06/01/, 2015.
- [52] RAHMAN, F.-U.; BHATTI, M. Z.; ALI, A.; DUONG, H.-Q.; ZHANG, Y.; YANG, B.; KOPPIREDDI, S.; LIN, Y.; WANG, H.; LI, Z.-T., and ZHANG, D.-W. Homo- and heteroleptic Pt(II) complexes of ONN donor hydrazone and 4-picoline: A synthetic, structural and detailed mechanistic anticancer investigation. **European Journal of Medicinal Chemistry**, v. 143, n., p. 1039-1052, 2018/01/01/, 2018.
- [53] DENG, J.; GOU, Y.; CHEN, W.; FU, X., and DENG, H. The Cu/ligand stoichiometry effect on the coordination behavior of aroyl hydrazone with copper(II): Structure, anticancer activity and anticancer mechanism. **Bioorganic & Medicinal Chemistry**, v. 24, n. 10, p. 2190-2198, 2016/05/15/, 2016.
- [54] ALTINTOP, M. D.; ÖZDEMİR, A.; TURAN-ZITOUNI, G.; ILGİN, S.; ATLI, Ö.; İŞCAN, G., and KAPLANCIKLİ, Z. A. Synthesis and biological evaluation of some hydrazone derivatives as new anticandidal and anticancer agents. **European Journal of Medicinal Chemistry**, v. 58, n., p. 299-307, 2012/12/01/, 2012.
- [55] NAGENDER, P.; NARESH KUMAR, R.; MALLA REDDY, G.; KRISHNA SWAROOP, D.; POORNACHANDRA, Y.; GANESH KUMAR, C., and NARSAIAH, B. Synthesis of novel hydrazone and azole functionalized pyrazolo[3,4-b]pyridine derivatives as promising anticancer agents. **Bioorganic & Medicinal Chemistry Letters**, v. 26, n. 18, p. 4427-4432, 2016/09/15/, 2016.

- [56] NASR, T.; BONDOCK, S., and YOUNS, M. Anticancer activity of new coumarin substituted hydrazide–hydrazone derivatives. **European Journal of Medicinal Chemistry**, v. 76, n., p. 539-548, 2014/04/09/, 2014.
- [57] RICHARDSON, D. R. and MILNES, K. The potential of iron chelators of the pyridoxal isonicotinoyl hydrazone class as effective antiproliferative agents II: the mechanism of action of ligands derived from salicylaldehyde benzoyl hydrazone and 2-hydroxy-1-naphthylaldehyde benzoyl hydrazone. **Blood**, v. 89, n. 8, p. 3025-38, Apr 15, 1997.
- [58] INTERNATIONAL AGENCY FOR RESEARCH ON CANCER. World Cancer Report 2014, B.W.S.a.C.P. Wild, Editor. 2014, World Health Organization: Lyon, France. p. 630.
- [59] SIEGEL, R. L.; MILLER, K. D., and JEMAL, A. Cancer statistics, 2019. **CA: A Cancer Journal for Clinicians**, v. 69, n. 1, p. 7-34, 2019.
- [60] INSTITUTO NACIONAL DE CÂNCER JOSÉ ALENCAR GOMES DA SILVA. Estimativa 2018: incidências de câncer no Brasil **COORDENAÇÃO DE ENSINO** ed. 2017, Rio de Janeiro, Brasil: Ministério da Saúde INCA. 128.
- [61] ALMEIDA, V. L. D.; LEITÃO, A.; REINA, L. D. C. B.; MONTANARI, C. A.; DONNICI, C. L., and LOPES, M. T. P. Câncer e agentes antineoplásicos ciclo-celular específicos e ciclo-celular não específicos que interagem com o DNA: uma introdução. **Química Nova**, v. 28, n., p. 118-129, 2005.
- [62] WEINBERG, R. A. Oncogenes and the molecular biology of cancer. **The Journal of cell biology**, v. 97, n. 6, p. 1661-1662, 1983.
- [63] LUO, J. and ELLEDGE, S. J. Deconstructing oncogenesis. **Nature**, v. 453, n., p. 995, 06/18/online, 2008.
- [64] HANAHAN, D. and WEINBERG, R. A. The Hallmarks of Cancer. **Cell**, v. 100, n. 1, p. 57-70, 2000/01/07/, 2000.
- [65] LAND, H.; PARADA, L. F., and WEINBERG, R. A. Tumorigenic conversion of primary embryo fibroblasts requires at least two cooperating oncogenes. **Nature**, v. 304, n. 5927, p. 596-602, 1983/08/01, 1983.
- [66] RULEY, H. E. Adenovirus early region 1A enables viral and cellular transforming genes to transform primary cells in culture. **Nature**, v. 304, n. 5927, p. 602-606, 1983/08/01, 1983.
- [67] MCMURRAY, H. R.; SAMPSON, E. R.; COMPITELLO, G.; KINSEY, C.; NEWMAN, L.; SMITH, B.; CHEN, S.-R.; KLEBANOV, L.; SALZMAN, P.; YAKOVLEV, A., and LAND, H. Synergistic response to oncogenic mutations defines gene class critical to cancer phenotype. **Nature**, v. 453, n., p. 1112, 05/25/online, 2008.
- [68] CHIAL, H. Proto-oncogenes to oncogenes to cancer. **Nature Education**, v. 1, n. 1, p. 1-33, 2008.
- [69] BURNEY, I. Cancer Chemotherapy and Biotherapy: Principles and Practice. **Sultan Qaboos University Medical Journal**, v. 11, n. 3, p. 424-425, 2011.
- [70] NACIONAL CANCER INSTITUTE. Types of cancer treatment. <https://www.cancer.gov/about-cancer/treatment/types>. . 2019 29/05/2019].
- [71] STACY, S. Cancer Immunotherapy Researchers. <https://www.cancer.org/latest-news/nobel-prize-awarded-to-cancer-immunotherapy-researchers.html>. 2018 01/06/2019].

- [72] MARTINS, F.; SOFIYA, L.; SYKIOTIS, G. P.; LAMINE, F.; MAILLARD, M.; FRAGA, M.; SHABAFROUZ, K.; RIBI, C.; CAIROLI, A.; GUEX-CROSIER, Y.; KUNTZER, T.; MICHELIN, O.; PETERS, S.; COUKOS, G.; SPERTINI, F.; THOMPSON, J. A., and OBEID, M. Adverse effects of immune-checkpoint inhibitors: epidemiology, management and surveillance. **Nature Reviews Clinical Oncology**, v., n., p., 2019/05/15, 2019.
- [73] FONTES, A. P. S.; ALMEIDA, S. G. D., and NADER, L. D. A. Compostos de platina em quimioterapia do câncer. **Química Nova**, v. 20, n., p. 398-406, 1997.
- [74] ALDERDEN, R. A.; HALL, M. D., and HAMBLEY, T. W. The Discovery and Development of Cisplatin. **Journal of Chemical Education**, v. 83, n. 5, p. 728, 2006/05/01, 2006.
- [75] BARNETT ROSENBERG, L. V. C., EUGENE B. GRIMLEY AND ANDREW J. THOMSON. The Inhibition of Growth or Cell Division in Escherichia coli by Different Ionic Species of Platinum(IV) Complexes. **The Journal of Biological Chemistry**, v. 242, n., p. 1347-1352, March 25, 1967, 1967.
- [76] ROSENBERG, B.; RENSHAW, E.; VANCAMP, L.; HARTWICK, J., and DROBNIK, J. Platinum-induced filamentous growth in Escherichia coli. **J Bacteriol**, v. 93, n. 2, p. 716-21, Feb, 1967.
- [77] REISNER, E.; ARION, V. B.; KEPPLER, B. K., and POMBEIRO, A. J. L. Electron-transfer activated metal-based anticancer drugs. **Inorganica Chimica Acta**, v. 361, n. 6, p. 1569-1583, 5/5/, 2008.
- [78] PETERS, G. Cancer drug resistance: a new perspective. v. 1. 2018. 1-5.
- [79] KELLAND, L. R.; SHARP, S. Y.; O'NEILL, C. F.; RAYNAUD, F. I.; BEALE, P. J., and JUDSON, I. R. Mini-review: discovery and development of platinum complexes designed to circumvent cisplatin resistance. **Journal of Inorganic Biochemistry**, v. 77, n. 1-2, p. 111-115, 10/1/, 1999.
- [80] HO, G. Y.; WOODWARD, N., and COWARD, J. I. G. Cisplatin versus carboplatin: comparative review of therapeutic management in solid malignancies. **Critical Reviews in Oncology/Hematology**, v. 102, n., p. 37-46, 2016/06/01/, 2016.
- [81] CHENG, Y.-J.; WU, R.; CHENG, M.-L.; DU, J.; HU, X.-W.; YU, L.; ZHAO, X.-K.; YAO, Y.-M.; LONG, Q.-Z.; ZHU, L.-L.; ZHU, J.-J.; HUANG, N.-W.; LIU, H.-J.; HU, Y.-X., and WAN, F. Carboplatin-induced hematotoxicity among patients with non-small cell lung cancer: Analysis on clinical adverse events and drug-gene interactions. **Oncotarget**, v. 8, n. 19, p. 32228-32236, 2016.
- [82] TAN, C. P.; LU, Y. Y.; JI, L. N., and MAO, Z. W. Metallomics insights into the programmed cell death induced by metal-based anticancer compounds. **Metallomics**, v. 6, n. 5, p. 978-95, May, 2014.
- [83] NDAGI, U.; MHLONGO, N., and SOLIMAN, M. E. Metal complexes in cancer therapy - an update from drug design perspective. **Drug Des Devel Ther**, v. 11, n., p. 599-616, 2017.
- [84] WEHBE, M.; LEUNG, A. W. Y.; ABRAMS, M. J.; ORVIG, C., and BALLY, M. B. A Perspective - can copper complexes be developed as a novel class of therapeutics? **Dalton Trans**, v. 46, n. 33, p. 10758-10773, Aug, 2017.

- [85] MARÍN-HERNÁNDEZ, A.; GRACIA-MORA, I.; RUIZ-RAMÍREZ, L., and MORENO-SÁNCHEZ, R. Toxic effects of copper-based antineoplastic drugs (Casiopinas) on mitochondrial functions. **Biochem Pharmacol**, v. 65, n. 12, p. 1979-89, Jun, 2003.
- [86] GALINDO-MURILLO, R.; GARCÍA-RAMOS, J. C.; RUIZ-AZUARA, L.; CHEATHAM, T. E., and CORTÉS-GUZMÁN, F. Intercalation processes of copper complexes in DNA. **Nucleic Acids Res**, v. 43, n. 11, p. 5364-76, Jun, 2015.
- [87] BOULSOURANI, Z.; GEROMICHALOS, G. D.; REPANA, K.; YIANNAKI, E.; PSYCHARIS, V.; RAPTOPOULOU, C. P.; HADJIPAVLOU-LITINA, D.; PONTIKI, E., and DENDRINOU-SAMARA, C. Preparation and pharmacochemical evaluation of mixed ligand copper(II) complexes with triethanolamine and thiophenyl-2 saturated carboxylic acids. **Journal of Inorganic Biochemistry**, v. 105, n. 6, p. 839-849, 2011/06/01/, 2011.
- [88] BHUNIA, A.; MISTRI, S.; MANNE, R. K.; SANTRA, M. K., and MANNA, S. C. Synthesis, crystal structure, cytotoxicity study, DNA/protein binding and molecular docking of dinuclear copper(II) complexes. **Inorganica Chimica Acta**, v. 491, n., p. 25-33, 2019/06/01/, 2019.
- [89] BECKFORD, F. A.; THESSING, J.; STOTT, A.; HOLDER, A. A.; POLUEKTOV, O. G.; LI, L., and SEERAM, N. P. Anticancer activity and biophysical reactivity of copper complexes of 2-(benzo[d][1,3]dioxol-5-ylmethylene)-N-alkylhydrazinecarbothioamides. **Inorganic Chemistry Communications**, v. 15, n., p. 225-229, 2012/01/01/, 2012.
- [90] BALAKRISHNA, M. S.; SURESH, D.; RAI, A.; MAGUE, J. T., and PANDA, D. Dinuclear Copper(I) Complexes Containing Cyclodiphosphazane Derivatives and Pyridyl Ligands: Synthesis, Structural Studies, and Antiproliferative Activity toward Human Cervical and Breast Cancer Cells. **Inorganic Chemistry**, v. 49, n. 19, p. 8790-8801, 2010/10/04, 2010.
- [91] ZHANG, Z.; BI, C.; SCHMITT, S. M.; FAN, Y.; DONG, L.; ZUO, J., and DOU, Q. P. 1,10-Phenanthroline promotes copper complexes into tumor cells and induces apoptosis by inhibiting the proteasome activity. **Journal of Biological Inorganic Chemistry**, v. 17, n. 8, p. 1257-1267, December 01, 2012.
- [92] KLABUNDE, T.; EICKEN, C.; SACCHETTINI, J. C., and KREBS, B. Crystal structure of a plant catechol oxidase containing a dicopper center. **Nature Structural Biology**, v. 5, n. 12, p. 1084-1090, 1998/12/01, 1998.
- [93] KOVAL, I. A.; GAMEZ, P.; BELLE, C.; SELMECZI, K., and REEDIJK, J. Synthetic models of the active site of catecholoxidase: mechanistic studies. **Chemical Society Reviews**, v. 35, n. 9, p. 814-840, 2006.
- [94] REY, N. A.; NEVES, A.; BORTOLUZZI, A. J.; HAASE, W., and TOMKOWICZ, Z. Doubly phenoxo-hydroxo-bridged dicopper(II) complexes: individual contributions of the bridges to antiferromagnetic coupling based on two related biomimetic models for catechol oxidases. **Dalton Transactions**, v. 41, n. 24, p. 7196-7200, 2012.
- [95] REY, N. A.; NEVES, A.; SILVA, P. P.; PAULA, F. C. S.; SILVEIRA, J. N.; BOTELHO, F. V.; VIEIRA, L. Q.; PICH, C. T.; TERENCEZI, H., and PEREIRA-MAIA, E. C. A synthetic dinuclear copper(II) hydrolase and its

- potential as antitumoral: Cytotoxicity, cellular uptake, and DNA cleavage. **Journal of Inorganic Biochemistry**, v. 103, n. 10, p. 1323-1330, 10//, 2009.
- [96] REY, N. A.; NEVES, A.; BORTOLUZZI, A. J.; PICH, C. T., and TERENZI, H. Catalytic Promiscuity in Biomimetic Systems: Catecholase-like Activity, Phosphatase-like Activity, and Hydrolytic DNA Cleavage Promoted by a New Dicopper(II) Hydroxo-Bridged Complex. **Inorganic Chemistry**, v. 46, n. 2, p. 348-350, 2007/01/01, 2007.
- [97] REY, N. A.; NEVES, A.; DE ALMEIDA, W. B.; DOS SANTOS, H. F., and COSTA, L. A. S. A promiscuous dicopper(II) system promoting the hydrolysis of bis(2,4-dinitrophenyl)phosphate: Gaining mechanistic insight by means of structural and spectroscopic DFT studies. **International Journal of Quantum Chemistry**, v. 110, n. 7, p. 1432-1442, 2010.
- [98] ESTEVES, L. F.; REY, N. A.; DOS SANTOS, H. F., and COSTA, L. A. S. Theoretical Proposal for the Whole Phosphate Diester Hydrolysis Mechanism Promoted by a Catalytic Promiscuous Dinuclear Copper(II) Complex. **Inorganic Chemistry**, v. 55, n. 6, p. 2806-2818, 2016/03/21, 2016.
- [99] CAI, H.-H.; ZHONG, X.; YANG, P.-H.; WEI, W.; CHEN, J., and CAI, J. Probing site-selective binding of rhodamine B to bovine serum albumin. **Colloids and Surfaces A**, v. 372, n. 1, p. 35-40, 2010/12/03/, 2010.
- [100] KOVAL, I. A.; GAMEZ, P.; BELLE, C.; SELMECZI, K., and REEDIJK, J. Synthetic models of the active site of catechol oxidase: mechanistic studies. **Chemical Society Reviews**, v. 35, n. 9, p. 814-840, 2006.
- [101] REY, N. A.; NEVES, A.; BORTOLUZZI, A. J.; HAASE, W., and TOMKOWICZ, Z. Doubly phenoxo-hydroxo-bridged dicopper(ii) complexes: individual contributions of the bridges to antiferromagnetic coupling based on two related biomimetic models for catechol oxidases. **Dalton Transactions**, v. 41, n. 24, p. 7196-7200, 2012.
- [102] JOVITO, R.; NEVES, A.; BORTOLUZZI, A. J.; LANZMASTER, M.; DRAGO, V., and HAASE, W. A new unsymmetrical dinucleating ligand and its first FeIII ZnII complex: Structure and solid state properties of an unexpected tetranuclear complex containing the [FeIII(μ -OH)₂FeIII] structural motif. **Inorganic Chemistry Communications**, v. 8, n. 3, p. 323-327, 3//, 2005.
- [103] UOZUMI, S.; FURUTACHI, H.; OHBA, M.; ŌKAWA, H.; FENTON, D. E.; SHINDO, K.; MURATA, S., and KITKO, D. J. Dinuclear Nickel(II) Complexes of an Unsymmetric "End-Off" Compartmental Ligand: Conversion of Urea into Cyanate at a Dinuclear Nickel Core. **Inorganic Chemistry**, v. 37, n. 24, p. 6281-6287, 1998/11/01, 1998.
- [104] KARSTEN, P.; NEVES, A.; BORTOLUZZI, A. J.; LANZMASTER, M., and DRAGO, V. Synthesis, Structure, Properties, and Phosphatase-Like Activity of the First Heterodinuclear FeIIIMnII Complex with the Unsymmetric Ligand H₂BPBPMP as a Model for the PAP in Sweet Potato. **Inorganic Chemistry**, v. 41, n. 18, p. 4624-4626, 2002/09/01, 2002.
- [105] GODLEWSKA, S.; JEZIERSKA, J.; BARANOWSKA, K.; AUGUSTIN, E., and DOŁĘGA, A. Copper(II) complexes with substituted imidazole and chlorido ligands: X-ray, UV-Vis, magnetic and EPR studies and chemotherapeutic potential. **Polyhedron**, v. 65, n., p. 288-297, 2013/11/28/, 2013.

- [106] DECKER, H.; SCHWEIKARDT, T., and TUCZEK, F. The First Crystal Structure of Tyrosinase: All Questions Answered? **Angewandte Chemie International Edition**, v. 45, n. 28, p. 4546-4550, 2006.
- [107] STRATER, N.; KLABUNDE, T.; TUCKER, P.; WITZEL, H., and KREBS, B. Crystal structure of a purple acid phosphatase containing a dinuclear Fe(III)-Zn(II) active site. **Science**, v. 268, n. 5216, p. 1489-1492, 1995.
- [108] SIEGBAHN, P. E. M. The catalytic cycle of catechol oxidase. **Journal of Biological Inorganic Chemistry**, v. 9, n. 5, p. 577-590, July 01, 2004.
- [109] KUMAR, P. and NARASIMHAN, B. Hydrazides/hydrazones as antimicrobial and anticancer agents in the new millennium. **Mini-Reviews in Medicinal Chemistry**, v. 13, n. 7, p. 971-87, Jun, 2013.
- [110] DOS SANTOS, M. R. Master. Síntese e caracterização de ligantes binucleares derivados da isoniazida e seus complexos binucleares de cobre(II). p. 106,0912335/CA. 23/02/2011. N.A. Rey, 2011.
- [111] DOS SANTOS, M. R. Doctor. Complexos homo e heterobinucleares de ligantes derivados da isoniazida como potenciais agentes antitumorais. p. 163,1111828/CA. 21/03/2016. N.A. Rey, 2016.
- [112] NEVES, A.; DE BRITO, M. A.; VENCATO, I.; DRAGO, V.; GRIESAR, K., and HAASE, W. FeIII₂FeIII and FeII₂FeIII Complexes as Synthetic Analogues for the Oxidized and Reduced Forms of Purple Acid Phosphatases. **Inorganic Chemistry**, v. 35, n. 8, p. 2360-2368, 1996/01/01, 1996.
- [113] NEVES, A.; VERANI, C. N.; DE BRITO, M. A.; VENCATO, I.; MANGRICH, A.; OLIVA, G.; SOUZA, D. D. H. F., and BATISTA, A. A. Copper(II) complexes with (2-hydroxybenzyl-2-pyridylmethyl)amine-Hbpa: syntheses, characterization and crystal structures of the ligand and [Cu(II)(Hbpa)₂](ClO₄)₂·2H₂O. **Inorganica Chimica Acta**, v. 290, n. 2, p. 207-212, 7/15/, 1999.
- [114] JOVITO, R.; NEVES, A.; BORTOLUZZI, A. J.; LANZMASTER, M.; DRAGO, V., and HAASE, W. A new unsymmetrical dinucleating ligand and its first FeIII₂ZnII complex: Structure and solid state properties of an unexpected tetranuclear Fe₂III₂Zn₂II complex containing the [FeIII(μ-OH)₂FeIII] structural motif. **Inorganic Chemistry Communications**, v. 8, n. 3, p. 323-327, 2005/03/01/, 2005.
- [115] LUO, G.-G.; XIA, J.-X.; FANG, K.; ZHAO, Q.-H.; WU, J.-H., and DAI, J.-C. Discovery of polymorphism-dependent emission for crystalline boron-dipyrromethene dye. **Dalton Transactions**, v. 42, n. 46, p. 16268-16271, 2013.
- [116] ASHOKKUMAR, P.; WEIßHOFF, H.; KRAUS, W., and RURACK, K. Test-Strip-Based Fluorometric Detection of Fluoride in Aqueous Media with a BODIPY-Linked Hydrogen-Bonding Receptor. **Angewandte Chemie International Edition**, v. 53, n. 8, p. 2225-2229, 2014.
- [117] CRYALISPRO. Rigaku Oxford Diffraction. CrysAlisPro. **Rigaku Corporation, Tokyo, Japan.**, v., n., p., 2015.
- [118] SHELDRIK, G. Crystal structure refinement with SHELXL. **Acta Crystallographica Section C**, v. 71, n. 1, p. 3-8, 2015.
- [119] LARSON, A. C. Crystallographic Computing, edited by FR Ahmed, SR Hall & CP Huber. Munksgaard, Copenhagen., n., p. 291-294, 1970.

- [120] BLESSING, R. An empirical correction for absorption anisotropy. **Acta Crystallographica Section A**, v. 51, n. 1, p. 33-38, 1995.
- [121] MACRAE, C. F.; EDINGTON, P. R.; MCCABE, P.; PIDCOCK, E.; SHIELDS, G. P.; TAYLOR, R.; TOWLER, M., and VAN DE STREEK, J. Mercury: visualization and analysis of crystal structures. **Journal of Applied Crystallography**, v. 39, n. 3, p. 453-457, 2006.
- [122] SPEK, A. L. PLATON SQUEEZE: a tool for the calculation of the disordered solvent contribution to the calculated structure factors. **Acta Crystallogr C Struct Chem**, v. 71, n. Pt 1, p. 9-18, Jan, 2015.
- [123] PALATINUS, L. and CHAPUIS, G. SUPERFLIP - a computer program for the solution of crystal structures by charge flipping in arbitrary dimensions. **Journal of Applied Crystallography**, v. 40, n. 4, p. 786-790, 2007.
- [124] DOLOMANOV, O. V.; BOURHIS, L. J.; GILDEA, R. J.; HOWARD, J. A. K., and PUSCHMANN, H. OLEX2: a complete structure solution, refinement and analysis program. **Journal of Applied Crystallography**, v. 42, n. 2, p. 339-341, 2009.
- [125] FARRUGIA, L. WinGX suite for small-molecule single-crystal crystallography. **Journal of Applied Crystallography**, v. 32, n. 4, p. 837-838, 1999.
- [126] <https://www.sisweb.com/mstools/isotope.htm>. Isotope Distribution Calculator and Mass Spec Plotter [cited 2019 April 18th, 2019].
- [127] MOHANRAJ, M.; AYYANNAN, G.; RAJA, G., and JAYABALAKRISHNAN, C. Evaluation of DNA binding, DNA cleavage, protein binding, radical scavenging and in vitro cytotoxic activities of ruthenium(II) complexes containing 2,4-dihydroxy benzyldene ligands. **Materials Science and Engineering: C**, v. 69, n., p. 1297-1306, 2016/12/01/, 2016.
- [128] HAMMOUDA, B. SANS from homogeneous polymer mixtures: A unified overview, in *Polymer Characteristics*. 1993, Springer Berlin Heidelberg: Berlin, Heidelberg. p. 87-133.
- [129] SILVA, E. R.; LISTIK, E.; HAN, S. W.; ALVES, W. A.; SOARES, B. M.; REZA, M.; RUOKOLAINEN, J., and HAMLEY, I. W. Sequence length dependence in arginine/phenylalanine oligopeptides: Implications for self-assembly and cytotoxicity. **Biophysical Chemistry**, v. 233, n., p. 1-12, 2018/02/01/, 2018.
- [130] BRESSLER, I.; KOHLBRECHER, J., and THUNEMANN, A. F. SASfit: a tool for small-angle scattering data analysis using a library of analytical expressions. **Journal of Applied Crystallography**, v. 48, n. 5, p. 1587-1598, 2015.
- [131] IZUMRUDOV, V. A.; ZHIRYAKOVA, M. V., and GOULKO, A. A. Ethidium Bromide as a Promising Probe for Studying DNA Interaction with Cationic Amphiphiles and Stability of the Resulting Complexes. **Langmuir**, v. 18, n. 26, p. 10348-10356, 2002/12/01, 2002.
- [132] CIOTTA, E.; PROSPPOSITO, P., and PIZZOFERRATO, R. Positive curvature in Stern-Volmer plot described by a generalized model for static quenching. **Journal of Luminescence**, v. 206, n., p. 518-522, 2019/02/01/, 2019.
- [133] HELLER, D. P. and GREENSTOCK, C. L. Fluorescence lifetime analysis of DNA intercalated ethidium bromide and quenching by free dye. **Biophysical Chemistry**, v. 50, n. 3, p. 305-312, 1994/06/01/, 1994.

- [134] RICO, M.; BAGLIONI, M.; BONDARENKO, M.; LALUCE, N. C.; ROZADOS, V.; ANDRÉ, N.; CARRÉ, M.; SCHAROVSKY, O. G., and MENACHO MÁRQUEZ, M. Metformin and propranolol combination prevents cancer progression and metastasis in different breast cancer models. **Oncotarget**, v. 8, n. 2, p. 2874-2889, Jan, 2017.
- [135] MOSMANN, T. Rapid colorimetric assay for cellular growth and survival: Application to proliferation and cytotoxicity assays. **Journal of Immunological Methods**, v. 65, n. 1, p. 55-63, 1983/12/16/, 1983.
- [136] REIS, A. C. D. M.; FREITAS, M. C. R.; RESENDE, J. A. L. C.; DINIZ, R., and REY, N. A. Different coordination patterns for two related unsymmetrical compartmental ligands: crystal structures and IR analysis of $[\text{Cu}(\text{C}_2\text{H}_2\text{O}_2\text{N}_3)(\text{OH}_2)(\text{ClO}_4)]\text{ClO}_4 \cdot 2\text{H}_2\text{O}$ and $[\text{Zn}_2(\text{C}_{22}\text{H}_{21}\text{O}_3\text{N}_2)(\text{C}_{22}\text{H}_{20}\text{O}_3\text{N}_2)]\text{ClO}_4$. **Journal of Coordination Chemistry**, v. 67, n. 18, p. 3067-3083, 2014/09/17, 2014.
- [137] ISAAC, J. A.; MANSOUR, A. T.; DAVID, R.; KOCHER, A.; PHILOUZE, C.; DEMESHKO, S.; MEYER, F.; RÉGLIER, M.; SIMAAN, A. J.; CALDARELLI, S.; YEMLOUL, M.; JAMET, H.; THIBON-POURRET, A., and BELLE, C. Tetranuclear and dinuclear phenoxido bridged copper complexes based on unsymmetrical thiosemicarbazone ligands. **Dalton Trans**, v. 47, n. 29, p. 9665-9676, Jul, 2018.
- [138] GEARY, W. J. The use of conductivity measurements in organic solvents for the characterisation of coordination compounds. **Coordination Chemistry Reviews**, v. 7, n. 1, p. 81-122, 1971/10/01/, 1971.
- [139] LANDGE, S. M.; TKATCHOUK, E.; BENÍTEZ, D.; LANFRANCHI, D. A.; ELHABIRI, M.; GODDARD, W. A., and APRAHAMIAN, I. Isomerization Mechanism in Hydrazone-Based Rotary Switches: Lateral Shift, Rotation, or Tautomerization? **Journal of the American Chemical Society**, v. 133, n. 25, p. 9812-9823, 2011/06/29, 2011.
- [140] KUODIS, Z.; RUTAVIČIUS, A.; MATIJOŠKA, A., and EICHERLORKA, O. Synthesis and isomerism of hydrazones of 2-(5-thioxo-4,5-dihydro-1,3,4-thiadiazol-2-ylthio)acetohydrazide. **Central European Journal of Chemistry**, v. 5, n. 4, p. 996-1006, December 01, 2007.
- [141] PALLA, G.; PREDIERI, G.; DOMIANO, P.; VIGNALI, C., and TURNER, W. Conformational behaviour and E/Z isomerization of N-acyl and N-arylohydrazones. **Tetrahedron**, v. 42, n. 13, p. 3649-3654, 1986/01/01/, 1986.
- [142] BALACHANDRAN, V.; JANAKI, A., and NATARAJ, A. Theoretical investigations on molecular structure, vibrational spectra, HOMO, LUMO, NBO analysis and hyperpolarizability calculations of thiophene-2-carbohydrazide. **Spectrochimica Acta Part A: Molecular and Biomolecular Spectroscopy**, v. 118, n., p. 321-330, 2014/01/24/, 2014.
- [143] CARTER, D. C. and HO, J. X. Structure of Serum Albumin, in *Advances in Protein Chemistry*, C.B. Anfinsen, et al., Editors. 1994, Academic Press. p. 153-203.
- [144] STEINHARDT, J.; KRIJN, J., and LEIDY, J. G. Differences between bovine and human serum albumins. Binding isotherms, optical rotatory dispersion, viscosity, hydrogen ion titration, and fluorescence effects. **Biochemistry**, v. 10, n. 22, p. 4005-4015, 1971/10/01, 1971.
- [145] KUMAR, S.; SHARMA, R. P.; VENUGOPALAN, P.; FERRETTI, V.; PERONTSIS, S., and PSOMAS, G. Copper(II) diclofenac complexes:

- Synthesis, structural studies and interaction with albumins and calf-thymus DNA. **Journal of Inorganic Biochemistry**, v. 187, n., p. 97-108, 2018/10/01/, 2018.
- [146] KONGOT, M.; REDDY, D.; SINGH, V.; PATEL, R.; SINGHAL, N. K., and KUMAR, A. Potent drug candidature of an ONS donor tethered copper (II) complex: Anticancer activity, cytotoxicity and spectroscopically approached BSA binding studies. **Spectrochimica Acta Part A**, v. 212, n., p. 330-342, 2019/04/05/, 2019.
- [147] ZHANG, D.-Y.; NIE, Y.; SANG, H.; SUO, J.-J.; LI, Z.-J.; GU, W.; TIAN, J.-L.; LIU, X., and YAN, S.-P. Three structurally related Copper complexes with two isomers: DNA/BSA binding ability, DNA cleavage activity and excellent cytotoxicity. **Inorganica Chimica Acta**, v. 457, n., p. 7-18, 2017/03/01/, 2017.
- [148] ZAREI, L.; ASADI, Z.; DUSEK, M., and EIGNER, V. Homodinuclear Ni (II) and Cu (II) Schiff base complexes derived from O-vanillin with a pyrazole bridge: Preparation, crystal structures, DNA and protein (BSA) binding, DNA cleavage, molecular docking and cytotoxicity study. **Journal of Photochemistry and Photobiology A**, v. 374, n., p. 145-160, 2019/04/01/, 2019.
- [149] HAZRA, M.; DOLAI, T.; PANDEY, A.; DEY, S. K., and PATRA, A. Fluorescent copper(II) complexes: The electron transfer mechanism, interaction with bovine serum albumin (BSA) and antibacterial activity. **Journal of Saudi Chemical Society**, v. 21, n., p. S240-S247, 2017/01/01/, 2017.
- [150] ANJOMSHOA, M.; TORKZADEH-MAHANI, M.; JANCZAK, J.; RIZZOLI, C.; SAHIHI, M.; ATAEI, F., and DEHKHODAEI, M. Synthesis, crystal structure and Hirshfeld surface analysis of copper(II) complexes: DNA- and BSA-binding, molecular modeling, cell imaging and cytotoxicity. **Polyhedron**, v. 119, n., p. 23-38, 2016/11/24/, 2016.
- [151] ANJOMSHOA, M. and TORKZADEH-MAHANI, M. In vitro DNA and BSA-binding, cell imaging and anticancer activity against human carcinoma cell lines of mixed ligand copper(II) complexes. **Spectrochimica Acta Part A**, v. 150, n., p. 390-402, 2015/11/05/, 2015.
- [152] ANNARAJ, B.; BALAKRISHNAN, C., and NEELAKANTAN, M. A. Synthesis, structure information, DNA/BSA binding affinity and in vitro cytotoxic studies of mixed ligand copper(II) complexes containing a phenylalanine derivative and diimine co-ligands. **Journal of Photochemistry and Photobiology B**, v. 160, n., p. 278-291, 2016/07/01/, 2016.
- [153] KOSTELIDOU, A.; KALOGIANNIS, S.; BEGOU, O.-A.; PERDIH, F.; TUREL, I., and PSOMAS, G. Synthesis, structure and biological activity of copper(II) complexes with gatifloxacin. **Polyhedron**, v. 119, n., p. 359-370, 2016/11/24/, 2016.
- [154] KUMAR, M. and MASRAM, D. T. Evaluation of DNA, BSA, and HSA binding propensity of copper(II) complex with N-donor ligand 2,2'-dipyridylamine. **Polyhedron**, v. 157, n., p. 511-520, 2019/01/01/, 2019.
- [155] KUMAR, M.; KUMAR, G.; MOGHA, N. K.; JAIN, R.; HUSSAIN, F., and MASRAM, D. T. Structure, DNA/proteins binding, docking and cytotoxicity studies of copper(II) complexes with the first quinolone drug nalidixic acid and 2,2'-dipyridylamine. **Spectrochimica Acta Part A**:

- Molecular and Biomolecular Spectroscopy**, v. 212, n., p. 94-104, 2019/04/05/, 2019.
- [156] KUMAR, M.; MOGHA, N. K.; KUMAR, G.; HUSSAIN, F., and MASRAM, D. T. Biological evaluation of copper(II) complex with nalidixic acid and 2,2'-bipyridine (bpy). **Inorganica Chimica Acta**, v., n., p., 2019/03/11/, 2019.
- [157] MANNA, S.; ZANGRANDO, E.; PUSCHMANN, H., and MANNA, S. C. Tetranuclear Schiff base copper(II) complexes: Syntheses, crystal structure, DNA/protein binding and catecholase-like activity. **Polyhedron**, v. 162, n., p. 285-292, 2019/04/01/, 2019.
- [158] BHAT, S. S.; KUMBHAR, A. A.; HEPTULLAH, H.; KHAN, A. A.; GOBRE, V. V.; GEJJI, S. P., and PURANIK, V. G. Synthesis, Electronic Structure, DNA and Protein Binding, DNA Cleavage, and Anticancer Activity of Fluorophore-Labeled Copper(II) Complexes. **Inorganic Chemistry**, v. 50, n. 2, p. 545-558, 2011/01/17, 2011.
- [159] JASH, C. and KUMAR, G. S. Binding of alkaloids berberine, palmatine and coralyne to lysozyme: a combined structural and thermodynamic study. **RSC Advances**, v. 4, n. 24, p. 12514-12525, 2014.
- [160] YANG, Y.; GUO, L.; TIAN, Z.; GONG, Y.; ZHENG, H.; ZHANG, S.; XU, Z.; GE, X., and LIU, Z. Novel and Versatile Imine-N-Heterocyclic Carbene Half-Sandwich Iridium(III) Complexes as Lysosome-Targeted Anticancer Agents. **Inorganic Chemistry**, v. 57, n. 17, p. 11087-11098, 2018/09/04, 2018.
- [161] PACHECO, M. E. and BRUZZONE, L. Synchronous fluorescence spectrometry: Conformational investigation or inner filter effect? **Journal of Luminescence**, v. 137, n., p. 138-142, 2013/05/01/, 2013.
- [162] LI, Y.; GUO, Q.; YAN, Y.; CHEN, T.; DU, C., and DU, H. Different effects of Forsythia suspensa metabolites on bovine serum albumin (BSA). **Spectrochimica Acta Part A**, v. 214, n., p. 309-319, 2019/05/05/, 2019.
- [163] CHIPMAN, D. M.; GRISARO, V., and SHARON, N. The binding of oligosaccharides containing N-acetylglucosamine and N-acetylmuramic acid to lysozyme. The specificity of binding subsites. **Journal of Biological Chemistry**, v. 242, n. 19, p. 4388-4394, 1967.
- [164] DOSTANI, M.; KIANFAR, A. H.; MAHMOOD, W. A.; DINARI, M.; FARROKHPOUR, H.; SABZALIAN, M. R.; ABYAR, F., and AZARIAN, M. H. An experimental and theoretical study on the interaction of DNA and BSA with novel Ni(2+), Cu(2+) and VO(2+) complexes derived from vanillin bidentate Schiff base ligand. **Spectrochim Acta A Mol Biomol Spectrosc**, v. 180, n., p. 144-153, Jun 5, 2017.
- [165] FU, H.-L.; ZHENG, K.; ZHANG, M.-J.; LI, Y.-T.; WU, Z.-Y., and YAN, C.-W. Synthesis and structure of new tetracopper(II) complexes with N-benzoate-N'-[3-(diethylamino)propyl]oxamide as a bridging ligand: The influence of hydrophobicity on enhanced DNA/BSA-binding and anticancer activity. **Journal of Photochemistry and Photobiology B**, v. 161, n., p. 80-90, 2016/08/01/, 2016.
- [166] LIU, Y.; CHEN, M.; JIANG, L., and SONG, L. Stereoselective interaction of cinchona alkaloid isomers with bovine serum albumin. **Food Chemistry**, v. 181, n., p. 170-178, 2015/08/15/, 2015.

- [167] LI, Y.; YANG, G., and MEI, Z. Spectroscopic and dynamic light scattering studies of the interaction between pterodonic acid and bovine serum albumin. **Acta Pharmaceutica Sinica B**, v. 2, n. 1, p. 53-59, 2/10/, 2012.
- [168] YU, M.; DING, Z.; JIANG, F.; DING, X.; SUN, J.; CHEN, S., and LV, G. Analysis of binding interaction between pegylated puerarin and bovine serum albumin by spectroscopic methods and dynamic light scattering. **Spectrochimica Acta Part A**, v. 83, n. 1, p. 453-460, 12//, 2011.
- [169] ADEL, A.; NADIA, M.; MOHAMED, O., and ABDELHAFIDH, G. Study of thermally and chemically unfolded conformations of bovine serum albumin by means of dynamic light scattering. **Materials Science and Engineering: C**, v. 28, n. 5-6, p. 594-600, 7/1/, 2008.
- [170] ZOCCHI, G. Proteins unfold in steps. **Proceedings of the National Academy of Sciences**, v. 94, n. 20, p. 10647, 1997.
- [171] GARCÍA-ZUBIRI, I. X.; BURROWS, H. D.; SÉRGIO SEIXAS DE MELO, J.; PINA, J.; MONTESERÍN, M., and TAPIA, M. J. Effects of the Interaction Between β -Carboline-3-carboxylic acid N-Methylamide and Polynucleotides on Singlet Oxygen Quantum Yield and DNA Oxidative Damage. **Photochemistry and Photobiology**, v. 83, n. 6, p. 1455-1464, 2007.
- [172] MANDAL, A.; BHATTACHARYA, P.; DAS, A. K., and BASAK, A. A Garratt-Braverman cyclization route towards the synthesis of phenanthridine derivatives and their DNA-binding studies. **Tetrahedron**, v. 75, n. 13, p. 1975-1987, 2019/03/29/, 2019.
- [173] VARDEVANYAN, P. O.; ANTONYAN, A. P.; PARSADANYAN, M. A.; DAVTYAN, H. G., and KARAPETYAN, A. T. The binding of ethidium bromide with DNA: interaction with single- and double-stranded structures. **Experimental & Molecular Medicine**, v. 35, n. 6, p. 527-33, Dec 31, 2003.
- [174] A. REY, N.; NEVES, A.; B DE ALMEIDA, W.; SANTOS, H., and COSTA, L. A. A Promiscuous Dicopper(II) System Promoting the Hydrolysis of Bis(2,4- dinitrophenyl)phosphate: Gaining Mechanistic Insight by Means of Structural and Spectroscopic DFT Studies. **International Journal of Quantum Chemistry**, v. 110, n., p. 1432-1442, 01/01, 2009.
- [175] MURALI KRISHNA, P.; HUSSAIN REDDY, K.; PANDEY, J. P., and SIDDAVATTAM, D. Synthesis, characterization, DNA binding and nuclease activity of binuclear copper(II) complexes of cuminaldehyde thiosemicarbazones. **Transition Metal Chemistry**, v. 33, n. 5, p. 661-668, August 01, 2008.
- [176] TAN, J.; WANG, B., and ZHU, L. DNA binding and oxidative DNA damage induced by a quercetin copper(II) complex: potential mechanism of its antitumor properties. **Journal of Biological Inorganic Chemistry**, v. 14, n. 5, p. 727-739, June 01, 2009.
- [177] SUNDARAVADIVEL, E. and KANDASWAMY, M. Synthesis, characterization and electrochemical properties of binuclear copper(II) complexes: DNA/protein binding and DNA cleavage studies. **Materials Today: Proceedings**, v. 5, n. 2, Part 3, p. 8707-8717, 2018/01/01/, 2018.
- [178] MINTON, A. P. Recent applications of light scattering measurement in the biological and biopharmaceutical sciences. **Analytical Biochemistry**, v. 501, n., p. 4-22, 5/15/, 2016.

- [179] LATULIPPE, D. R. and ZYDNEY, A. L. Radius of gyration of plasmid DNA isoforms from static light scattering. **Biotechnology and Bioengineering**, v. 107, n. 1, p. 134-142, 2010.
- [180] DIAS, R. S.; INNERLOHINGER, J.; GLATTER, O.; MIGUEL, M. G., and LINDMAN, B. Coil–Globule Transition of DNA Molecules Induced by Cationic Surfactants: A Dynamic Light Scattering Study. **The Journal of Physical Chemistry B**, v. 109, n. 20, p. 10458-10463, 2005/05/01, 2005.
- [181] SUNDARAVADIVEL, E. and KANDASWAMY, M. Synthesis, characterization and electrochemical properties of binuclear copper(II) complexes: DNA/protein binding and DNA cleavage studies. **International Conference On Recent Advances In Material Chemistry, 15-17 February 2017**, v. 5, n. 2, Part 3, p. 8707-8717, 2018.
- [182] MORITA, T.; YUGANDAR, S.; FUSE, S., and NAKAMURA, H. Recent progresses in the synthesis of functionalized isoxazoles. **Tetrahedron Letters**, v. 59, n. 13, p. 1159-1171, 2018/03/28/, 2018.
- [183] SYSAK, A. and OBMIŃSKA-MRUKOWICZ, B. Isoxazole ring as a useful scaffold in a search for new therapeutic agents. **European Journal of Medicinal Chemistry**, v. 137, n., p. 292-309, 2017/09/08/, 2017.
- [184] ZHU, J.; MO, J.; LIN, H.-Z.; CHEN, Y., and SUN, H.-P. The recent progress of isoxazole in medicinal chemistry. **Bioorganic & Medicinal Chemistry**, v. 26, n. 12, p. 3065-3075, 2018/07/23/, 2018.
- [185] HUSSAIN, A.; ALAJMI, M. F.; REHMAN, M. T.; AMIR, S.; HUSAIN, F. M.; ALSALME, A.; SIDDIQUI, M. A.; ALKHEDHAIRY, A. A., and KHAN, R. A. Copper(II) complexes as potential anticancer and Nonsteroidal anti-inflammatory agents: In vitro and in vivo studies. **Scientific Reports**, v. 9, n. 1, p. 5237, 2019/03/27, 2019.
- [186] LEWIS, D. L.; ESTES, E. D., and HODGSON, D. J. The infrared spectra of coordinated perchlorates. **Journal of Crystal and Molecular Structure**, v. 5, n. 1, p. 67-74, January 01, 1975.
- [187] LEITE, S. M. G.; LIMA, L. M. P.; GAMA, S.; MENDES, F.; ORIO, M.; BENTO, I.; PAULO, A.; DELGADO, R., and IRANZO, O. Copper(II) Complexes of Phenanthroline and Histidine Containing Ligands: Synthesis, Characterization and Evaluation of their DNA Cleavage and Cytotoxic Activity. **Inorganic Chemistry**, v. 55, n. 22, p. 11801-11814, 2016/11/21, 2016.
- [188] ANDRADE, G. R.; KUNSMINSKAS, J.; PIZZUTI, L.; ANJOS, A. D.; INGLEZ, S. D.; TIRLONI, B., and SUEGAMA, P. H. Synthesis and X-ray structural characterization of square-pyramidal copper(II) complex with aminoguanidine derivative. **Inorganic Chemistry Communications**, v. 61, n., p. 210-213, 2015/11/01/, 2015.
- [189] KALIA, J. and RAINES, R. T. Hydrolytic stability of hydrazones and oximes. **Angewandte Chemie (International ed. in English)**, v. 47, n. 39, p. 7523-7526, 2008.
- [190] KUMAR, P.; GORAI, S.; KUMAR SANTRA, M.; MONDAL, B., and MANNA, D. DNA binding, nuclease activity and cytotoxicity studies of Cu(II) complexes of tridentate ligands. **Dalton Transactions**, v. 41, n. 25, p. 7573-7581, 2012.
- [191] WOLFE, A.; SHIMER, G. H., JR., and MEEHAN, T. Polycyclic aromatic hydrocarbons physically intercalate into duplex regions of denatured DNA. **Biochemistry**, v. 26, n. 20, p. 6392-6, Oct 6, 1987.

- [192] FEKRI, R.; SALEHI, M.; ASADI, A., and KUBICKI, M. DNA/BSA interaction, bio-activity, molecular docking simulation study and electrochemical properties of hydrazone Schiff base derived Cu(II)/Ni(II) metal complexes: Influence of the nuclearity and metal ions. **Polyhedron**, v. 128, n., p. 175-187, 2017/05/28/, 2017.
- [193] INAMDAR, P. R.; CHAUHAN, R.; ABRAHAM, J., and SHEELA, A. DNA interaction and cytotoxic activity of copper complex based on tridentate hydrazone derived ligand and nitrogen donor heterocycle. **Inorganic Chemistry Communications**, v. 67, n., p. 67-71, 2016/05/01/, 2016.
- [194] DIMITRAKOPOULOU, A.; DENDRINOUSAMARA, C.; PANTAZAKI, A. A.; ALEXIOU, M.; NORDLANDER, E., and KESSISSOGLU, D. P. Synthesis, structure and interactions with DNA of novel tetranuclear, [Mn₄(II/II/II/IV)] mixed valence complexes. **Journal of Inorganic Biochemistry**, v. 102, n. 4, p. 618-628, 2008/04/01/, 2008.
- [195] NUNES, J. H. B.; DE PAIVA, R. E. F.; CUIN, A.; DA COSTA FERREIRA, A. M.; LUSTRI, W. R., and CORBI, P. P. Synthesis, spectroscopic characterization, crystallographic studies and antibacterial assays of new copper(II) complexes with sulfathiazole and nimesulide. **Journal of Molecular Structure**, v. 1112, n., p. 14-20, 2016/05/15/, 2016.
- [196] YADAGIRI, B.; HOLAGUNDA, U. D.; BANTU, R.; NAGARAPU, L.; GUGULOTH, V.; POLEPALLY, S., and JAIN, N. Rational design, synthesis and anti-proliferative evaluation of novel benzosuberone tethered with hydrazide-hydrazones. **Bioorganic & Medicinal Chemistry Letters**, v. 24, n. 21, p. 5041-5044, 2014/11/01/, 2014.
- [197] GEERSING, A.; SÉGAUD, N.; VAN DER WIJST, M. G. P.; ROTS, M. G., and ROELFES, G. Importance of Metal-Ion Exchange for the Biological Activity of Coordination Complexes of the Biomimetic Ligand N4Py. **Inorganic Chemistry**, v. 57, n. 13, p. 7748-7756, 2018/07/02, 2018.
- [198] GAUR, K.; VÁZQUEZ-SALGADO, A. M.; DURAN-CAMACHO, G.; DOMINGUEZ-MARTINEZ, I.; BENJAMÍN-RIVERA, J. A.; FERNÁNDEZ-VEGA, L.; CARMONA SARABIA, L.; CRUZ GARCÍA, A.; PÉREZ-DELIZ, F.; MÉNDEZ ROMÁN, J. A.; VEGA-CARTAGENA, M.; LOZA-ROSAS, S. A.; RODRIGUEZ ACEVEDO, X., and TINOCO, A. D. Iron and Copper Intracellular Chelation as an Anticancer Drug Strategy. **Inorganics**, v. 6, n. 4, p. 126, 2018.
- [199] JIANG, Z.; ZHANG, Y.; YU, Y.; WANG, Z.; ZHANG, X.; DUAN, X., and WANG, S. Study on Intercalations between Double-Stranded DNA and Pyrene by Single-Molecule Force Spectroscopy: Toward the Detection of Mismatch in DNA. **Langmuir**, v. 26, n. 17, p. 13773-13777, 2010/09/07, 2010.
- [200] SERRE, D.; ERBEK, S.; BERTHET, N.; RONOT, X.; MARTELFRACTHET, V., and THOMAS, F. Copper(II) complexes of N3O tripodal ligands appended with pyrene and polyamine groups: Anti-proliferative and nuclease activities. **Journal of Inorganic Biochemistry**, v. 179, n., p. 121-134, 2018/02/01/, 2018.
- [201] CARLISI, D.; DE BLASIO, A.; DRAGO-FERRANTE, R.; DI FIORE, R.; BUTTITTA, G.; MORREALE, M.; SCERRI, C.; VENTO, R., and TESORIERE, G. Parthenolide prevents resistance of MDA-MB231 cells to

- doxorubicin and mitoxantrone: the role of Nrf2. **Cell Death Discovery**, v. 3, n., p. 17078, 12/04/online, 2017.
- [202] MINCH, M. J. An Introduction to Hydrogen Bonding (Jeffrey, George A.). **Journal of Chemical Education**, v. 76, n. 6, p. 759, 1999/06/01, 1999.
- [203] ZIMBRON, J. M.; PASSADOR, K.; GATIN-FRAUDET, B.; BACHELET, C.-M.; PLAŽUK, D.; CHAMOREAU, L.-M.; BOTUHA, C.; THORIMBERT, S., and SALMAIN, M. Synthesis, Photophysical Properties, and Living Cell Imaging of Theranostic Half-Sandwich Iridium–4,4-Difluoro-4-bora-3a,4a-diaza-s-indacene (BODIPY) Dyads. **Organometallics**, v. 36, n. 18, p. 3435-3442, 2017/09/25, 2017.
- [204] BIRKS, J. B. and CHRISTOPHOROU, L. G. Excimer fluorescence spectra of pyrene derivatives. **Spectrochimica Acta**, v. 19, n. 2, p. 401-410, 1963/02/01/, 1963.
- [205] KRYSKOWIAK, E.; DOBEK, K., and MACIEJEWSKI, A. Origin of the strong effect of protic solvents on the emission spectra, quantum yield of fluorescence and fluorescence lifetime of 4-aminophthalimide: Role of hydrogen bonds in deactivation of S1-4-aminophthalimide. **Journal of Photochemistry and Photobiology A: Chemistry**, v. 184, n. 3, p. 250-264, 2006/12/15/, 2006.
- [206] HANSEN, H. K.; RIVEROL, C., and ACREE JR., W. E. Solubilities of anthracene, fluoranthene and pyrene in organic solvents: Comparison of calculated values using UNIFAC and modified UNIFAC (Dortmund) models with experimental data and values using the mobile order theory. **The Canadian Journal of Chemical Engineering**, v. 78, n. 6, p. 1168-1174, 2000.
- [207] YEN, L.; ZENG-RONG, N.; YOU, X.-L.; RICHARD, S.; LANGTON-WEBSTER, B. C., and ALAOUI-JAMALI, M. A. Regulation of cellular response to cisplatin-induced DNA damage and DNA repair in cells overexpressing p185erbB-2 is dependent on the ras signaling pathway. **Oncogene**, v. 14, n. 15, p. 1827-1835, 1997/04/01, 1997.
- [208] BASU, A. and KRISHNAMURTHY, S. Cellular Responses to Cisplatin-Induced DNA Damage. **Journal of Nucleic Acids**, v. 2010, n., p. 16, 2010.
- [209] SLEEP, D. Albumin and its application in drug delivery. **Expert Opinion on Drug Delivery**, v. 12, n. 5, p. 793-812, 2015/05/04, 2015.
- [210] RADA, J. P.; BASTOS, B. S. M.; ANSELMINO, L.; FRANCO, C. H. J.; LANZMASTER, M.; DINIZ, R.; FERNÁNDEZ, C. O.; MENACHO-MÁRQUEZ, M.; PERCEBOM, A. M., and REY, N. A. Binucleating Hydrazonic Ligands and Their μ -Hydroxodicopper(II) Complexes as Promising Structural Motifs for Enhanced Antitumor Activity. **Inorganic Chemistry**, v. 58, n. 13, p. 8800-8819, 2019/07/01, 2019.
- [211] PLAŽUK, D.; ZAKRZEWSKI, J., and SALMAIN, M. Biotin as acylating agent in the Friedel-Crafts reaction. Avidin affinity of biotinyl derivatives of ferrocene, ruthenocene and pyrene and fluorescence properties of 1-biotinylpyrene. **Organic & Biomolecular Chemistry**, v. 9, n. 2, p. 408-17, Jan 21, 2011.
- [212] MATSUSHITA, Y. and MORIGUCHI, I. Binding of pyrene-1-butyric acid to serum albumin: species differences. **Journal of pharmacobio-dynamics**, v. 12, n. 12, p. 762-70, Dec, 1989.
- [213] STIRPE, A.; PANTUSA, M.; RIZZUTI, B.; SPORTELLI, L.; BARTUCCI, R., and GUZZI, R. Early stage aggregation of human serum albumin in the

- presence of metal ions. **International Journal of Biological Macromolecules**, v. 49, n. 3, p. 337-342, 2011/10/01/, 2011.
- [214] LOUDET, A. and BURGESS, K. BODIPY Dyes and Their Derivatives: Syntheses and Spectroscopic Properties. **Chemical Reviews**, v. 107, n. 11, p. 4891-4932, 2007/11/01, 2007.
- [215] HE, H.; LI, D.-W.; YANG, L.-Y.; FU, L.; ZHU, X.-J.; WONG, W.-K.; JIANG, F.-L., and LIU, Y. A novel bifunctional mitochondria-targeted anticancer agent with high selectivity for cancer cells. **Scientific Reports**, v. 5, n., p. 13543, 09/04/online, 2015.
- [216] JANG, Y.; KIM, T.-I.; KIM, H.; CHOI, Y., and KIM, Y. Photoactivatable BODIPY Platform: Light-Triggered Anticancer Drug Release and Fluorescence Monitoring. **ACS Applied Bio Materials**, v. 2, n. 6, p. 2567-2572, 2019/06/17, 2019.
- [217] KUE, C. S.; NG, S. Y.; VOON, S. H.; KAMKAEW, A.; CHUNG, L. Y.; KIEW, L. V., and LEE, H. B. Recent strategies to improve boron dipyrromethene (BODIPY) for photodynamic cancer therapy: an updated review. **Photochemical & Photobiological Sciences**, v. 17, n. 11, p. 1691-1708, 2018.
- [218] ZHU, Z.; ZHOU, X.; WANG, Y.; CHI, L.; RUAN, D.; XUAN, Y.; CONG, W., and JIN, L. Fluorescent staining of glycoproteins in sodium dodecyl sulfate polyacrylamide gels by 4H-[1]-benzopyrano[4,3-b]thiophene-2-carboxylic acid hydrazide. **Analyst**, v. 139, n. 11, p. 2764-2773, 2014.
- [219] BOENS, N.; LEEN, V.; DEHAEN, W.; WANG, L.; ROBEYNS, K.; QIN, W.; TANG, X.; BELJONNE, D.; TONNELÉ, C.; PAREDES, J. M.; RUEDAS-RAMA, M. J.; ORTE, A.; CROVETTO, L.; TALAVERA, E. M., and ALVAREZ-PEZ, J. M. Visible Absorption and Fluorescence Spectroscopy of Conformationally Constrained, Annulated BODIPY Dyes. **The Journal of Physical Chemistry A**, v. 116, n. 39, p. 9621-9631, 2012/10/04, 2012.
- [220] BITTEL, A. M.; DAVIS, A. M.; WANG, L.; NEDERLOF, M. A.; ESCOBEDO, J. O.; STRONGIN, R. M., and GIBBS, S. L. Varied Length Stokes Shift BODIPY-Based Fluorophores for Multicolor Microscopy. **Scientific Reports**, v. 8, n. 1, p. 4590, 2018/03/15, 2018.
- [221] DOLAN, C.; BYRNE, A.; LONG, C.; CZAMARA, K.; KACZOR, A.; BARANSKA, M., and KEYES, T. E. Polypyridyl substituted BODIPY derivatives; water switchable imaging probes that exhibit halogen substituent dependent localisation in live cells. **RSC Advances**, v. 7, n. 69, p. 43743-43754, 2017.
- [222] ZHU, S.; ZHANG, J.; VEGESNA, G.; LUO, F.-T.; GREEN, S. A., and LIU, H. Highly Water-Soluble Neutral BODIPY Dyes with Controllable Fluorescence Quantum Yields. **Organic Letters**, v. 13, n. 3, p. 438-441, 2011/02/04, 2011.
- [223] CANAKCI, D.; KOYUNCU, I.; LOLAK, N.; DURGUN, M.; AKOCAK, S., and SUPURAN, C. T. Synthesis and cytotoxic activities of novel copper and silver complexes of 1,3-diaryltriazene-substituted sulfonamides. **Journal of enzyme inhibition and medicinal chemistry**, v. 34, n. 1, p. 110-116, 2019.
- [224] RODRÍGUEZ, M. R.; DEL PLÁ, J.; BALSÀ, L. M.; LEÓN, I. E.; PIRO, O. E.; ECHEVERRÍA, G. A.; GARCÍA-TOJAL, J.; PIS-DIEZ, R.; PARAJÓN-COSTA, B. S., and GONZÁLEZ-BARÓ, A. C. Cu(ii) and

- Zn(ii) complexes with a poly-functional ligand derived from o-vanillin and thiophene. Crystal structure, physicochemical properties, theoretical studies and cytotoxicity assays against human breast cancer cells. **New Journal of Chemistry**, v. 43, n. 18, p. 7120-7129, 2019.
- [225] NASULEWICZ, A.; MAZUR, A., and OPOLSKI, A. Role of copper in tumour angiogenesis—clinical implications. **Journal of Trace Elements in Medicine and Biology**, v. 18, n. 1, p. 1-8, 2004/09/14/, 2004.
- [226] FINNEY, L.; VOGT, S.; FUKAI, T., and GLESNE, D. Copper and angiogenesis: unravelling a relationship key to cancer progression. **Clinical and Experimental Pharmacology and Physiology**, v. 36, n. 1, p. 88-94, 2009.
- [227] COSTANTINI, P.; JACOTOT, E.; DECAUDIN, D., and KROEMER, G. Mitochondrion as a Novel Target of Anticancer Chemotherapy. **JNCI: Journal of the National Cancer Institute**, v. 92, n. 13, p. 1042-1053, 2000.
- [228] WALLACE, D. C.; FAN, W., and PROCACCIO, V. Mitochondrial Energetics and Therapeutics. **Annual Review of Pathology: Mechanisms of Disease**, v. 5, n. 1, p. 297-348, 2010.
- [229] SKODA, J.; BORANKOVA, K.; JANSSON, P. J.; HUANG, M. L. H.; VESELSKA, R., and RICHARDSON, D. R. Pharmacological targeting of mitochondria in cancer stem cells: An ancient organelle at the crossroad of novel anti-cancer therapies. **Pharmacological Research**, v. 139, n., p. 298-313, 2019/01/01/, 2019.
- [230] WALLACE, D. C. Mitochondria and cancer. **Nature Reviews Cancer**, v. 12, n., p. 685, 09/24/online, 2012.
- [231] GALLUZZI, L.; SENOVILLA, L.; VITALE, I.; MICHELS, J.; MARTINS, I.; KEPP, O.; CASTEDO, M., and KROEMER, G. Molecular mechanisms of cisplatin resistance. **Oncogene**, v. 31, n., p. 1869, 09/05/online, 2011.
- [232] MUKHERJEE, N.; PODDER, S.; MITRA, K.; MAJUMDAR, S.; NANDI, D., and CHAKRAVARTY, A. R. Targeted photodynamic therapy in visible light using BODIPY-appended copper(ii) complexes of a vitamin B6 Schiff base. **Dalton Transactions**, v. 47, n. 3, p. 823-835, 2018.
- [233] MITCHISON, D. A. Role of individual drugs in the chemotherapy of tuberculosis. **International Journal of Tuberculosis and Lung Disease**, v. 4, n. 9, p. 796-806, Sep, 2000.
- [234] SHARGHI, H.; ESKANDARI, M. M., and GHAVAMI, R. A facile conversion of epoxides to halohydrins with elemental halogen using isonicotinic hydrazide (isoniazide) as a new catalyst. **Journal of Molecular Catalysis A**, v. 215, n. 1, p. 55-62, 2004/06/14/, 2004.

12.1

Published paper

Binucleating Hydrazonic Ligands and Their μ -Hydroxodicopper(II) Complexes as Promising Structural Motifs for Enhanced Antitumor Activity

Jesica Paola Rada,[†] Beatriz S. M. Bastos,[†] Luciano Anselmino,[‡] Chris H. J. Franco,[§] Mauricio Lanznaster,^{||} Renata Diniz,[⊥] Claudio O. Fernández,[‡] Mauricio Menacho-Márquez,[‡] Ana Maria Percebom,[†] and Nicolás A. Rey^{*,†}

[†]Pontifical Catholic University of Rio de Janeiro, Rio de Janeiro, 22451-900, Brazil

[‡]Max Planck Laboratory for Structural Biology, Chemistry and Molecular Biophysics of Rosario (MPLbioR, UNR-MPIbpC) and Instituto de Investigaciones para el Descubrimiento de Fármacos de Rosario (IIDEFAR, UNR-CONICET), Universidad Nacional de Rosario, S2002LRK Rosario, Argentina

[§]Federal University of Juiz de Fora, Juiz de Fora, 36036-900, Brazil

^{||}Fluminense Federal University, Niterói, 24020-150, Brazil

[⊥]Federal University of Minas Gerais, Belo Horizonte, 31270-901, Brazil

Supporting Information

ABSTRACT: Very few inorganic antineoplastic drugs have entered the clinic in the last decades, mainly because of toxicity issues. Because copper is an essential trace element of ubiquitous occurrence, decreased side effects could be expected in comparison with the widely used platinum anticancer compounds. In the present work, two novel hydrazonic binucleating ligands and their μ -hydroxo dicopper(II) complexes were prepared and fully characterized. They differ by the nature of the aromatic group present in their aroylhydrazone moieties: while **H₃L1** and its complex, **1**, possess a thiophene ring, **H₃L2** and **2** contain the more polar furan heterocycle. X-ray diffraction indicates that both coordination compounds are very similar in structural terms and generate dimeric arrangements in the solid state. Positive-ion electrospray ionization mass spectrometry analyses confirmed that the main species present in a 10% dimethyl sulfoxide (DMSO)/water solution should be $[\text{Cu}_2(\text{HL})(\text{OH})]^+$ and the DMSO-substituted derivative $[\text{Cu}_2(\text{L})(\text{DMSO})]^+$. Scattering techniques [dynamic light scattering (DLS) and small-angle X-ray scattering] suggest that the complexes and their free ligands interact with bovine serum albumin (BSA) in a reversible manner. The binding constants to BSA were determined for the complexes through fluorescence spectroscopy. Moreover, to gain insight into the mechanism of action of the compounds, calf thymus DNA binding studies by UV–visible and DLS measurements using plasmid pBR322 DNA were also performed. For the complexes, DLS data seem to point to the occurrence of DNA cleavage to Form III (linear). Both ligands and their dicopper(II) complexes display potent antiproliferative activity in a panel of four cancer cell lines, occasionally even in the submicromolar range, with the complexes being more potent than the free ligands. Our data on cellular models correlate quite well with the DNA interaction experiments. The results presented herein show that aroylhydrazone-derived binucleating ligands, as well as their dinuclear μ -hydroxodicopper(II) complexes, may represent a promising structural starting point for the development of a new generation of highly active potential antitumor agents.



INTRODUCTION

Since the fortuitous discovery of the antitumor activity of cisplatin by Rosenberg et al.¹ in the second half of the 1960s, the search for new metal-based anticancer agents has increased dramatically. In spite of this, very few new inorganic antineoplastic drugs have entered the clinic in the last decades, mainly because of toxicity issues. In this context and because copper is an essential trace element of ubiquitous occurrence, decreased side effects could be expected in comparison with the widely used platinum anticancer compounds cisplatin,

carboplatin, and oxaliplatin.² Moreover, because of the fundamental differences between the chemistry of copper complexes and those of platinum, one can also expect diverse mechanisms of action. In a very recent Perspective published by Wehbe and co-workers,³ the potentiality of copper complexes as a novel class of therapeutics for an extensive range of diseases, including cancer, is discussed. The paper

Received: April 24, 2019

Published: June 17, 2019

12.2

Communication and results dissemination

12.2.1

Oral presentation

Potencial antitumoral de um novo ligante e seu complexo binuclear de cobre(II): um desafio às técnicas de espalhamento. **XVI Encontro Regional de Química da SBQ-Rio**. Rio de Janeiro, Brazil. 2017.

Síntese, caracterização e estudo das propriedades biológicas de complexos binucleares de cobre(II) contendo ligantes não-simétricos: uma nova classe de potentes agentes antineoplásicos. **I Jornada de Pós-Graduação e Pesquisa-DQ/PUC-Rio**, Rio de Janeiro, 2017, Brasil.

12.2.2

Posters

A novel hydrazonic ligand and its μ -2-hydroxo dicopper(II) complex: towards new synthetic nucleases with improved antitumor activity” (Poster). **18th International Conference on Biological Inorganic Chemistry**. Florianópolis, Santa Catarina, 2017, Brazil.

Potencial antitumoral de um novo ligante e seu complexo binuclear de cobre(II): um desafio às técnicas de espalhamento. **XVI Encontro Regional de Química da SBQ-Rio**. Rio de Janeiro, 2017, Brasil.

Interaction of the BSA protein as a drug carrier with a copper(II) complex: a study based on Dynamic Light Scattering and Small Angle X-Ray Scattering. **2nd User Workshop on Coherent X-ray Imaging and Small Angle X-ray Scattering**. Campinas, 2017, Brazil.

Efeito de complexos binucleares de cobre, candidatos a fármacos anti-câncer, sobre a estrutura conformacional de macromoléculas biológicas. **I Workshop de Aplicações de Polímeros e Surfactantes em Solução**. Rio de Janeiro, 2017, Brasil.

12.2.3

Other academic events

6th School of Small Angle X-ray Scattering Data Analysis. Campinas, 2017, Brazil.

2° Simpósio PUC-Rio sobre Envelhecimento e Doenças Neurodegenerativas. Rio de Janeiro, 2017, Brasil.

13

Attachment B: Results

13.1

NMR spectra of the ligands and their precursors

13.1.1

NMR spectra of the precursors

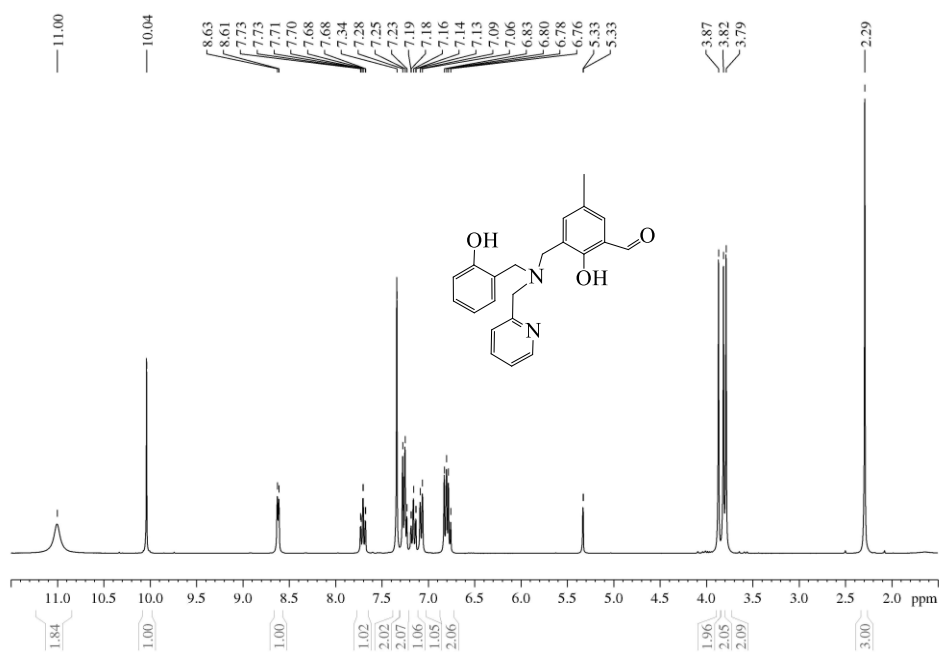


Figure 13.1. ^1H NMR spectrum (400 MHz) of the precursor **HBPAMFF** in $\text{DCM}-d_2$ at room temperature.

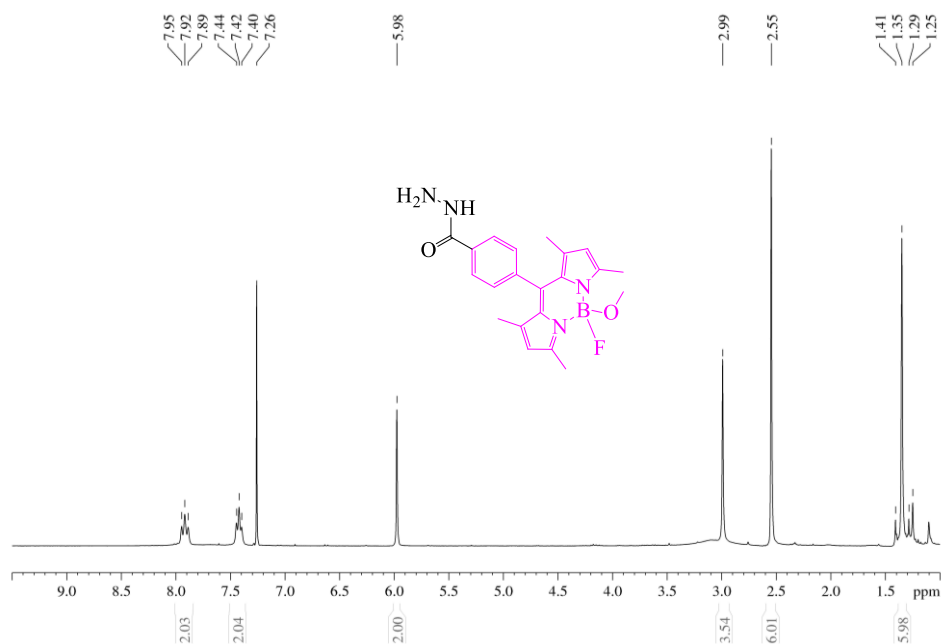


Figure 13.2. ^1H NMR spectrum (400 MHz) of the precursor **FMeO-BODIPY-Hz** in $\text{chloroform-}d$ at room temperature.

13.1.2

NMR spectra of ligand **H₃L1**

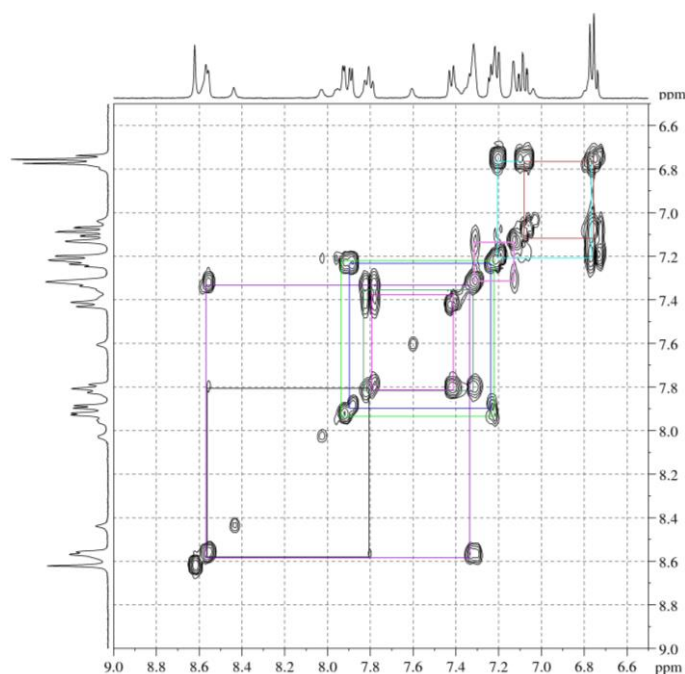


Figure 13.3. Correlation spectroscopy (^1H - ^1H COSY) NMR contour map (400 MHz) of **H₃L1** in $\text{DMSO-}d_6$ at room temperature, in the 6.5–9.0 ppm region. In the other regions, any H–H interaction from different carbons was observed.

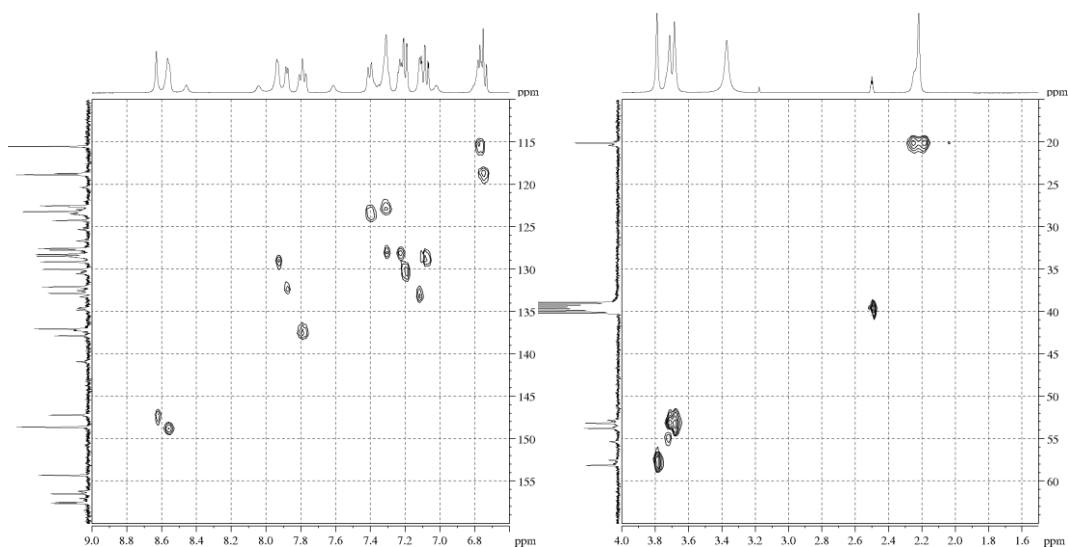


Figure 13.4. Quantum coherence (^1H - ^{13}C HSQC) NMR contour map of **H₃L1** in $\text{DMSO}-d_6$ at room temperature, in 9.0–6.6 ppm (left) and 4.0–1.5 ppm (right) ^1H HSQC region. In the other regions, any C–H interaction was observed.

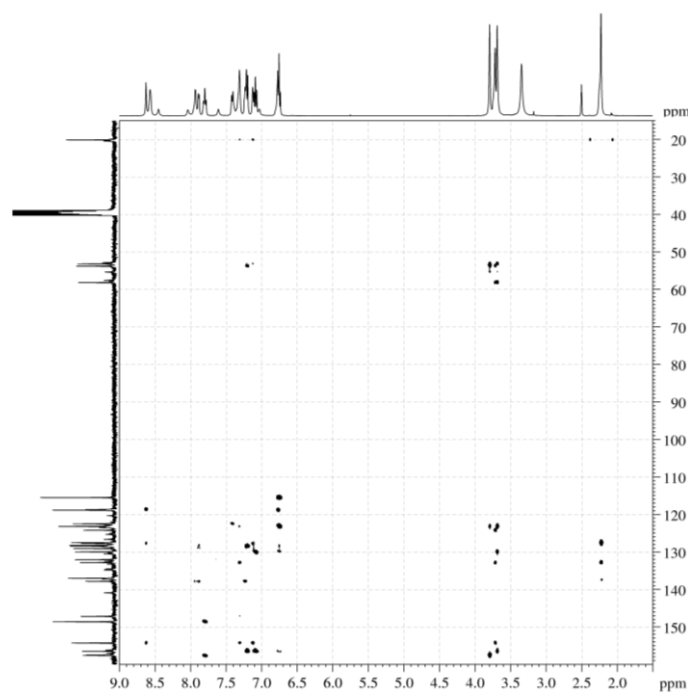


Figure 13.5. Bond correlation (^1H - ^{13}C HMBC) NMR contour map of **H₃L1** in $\text{DMSO}-d_6$ at room temperature, in the 9.0–1.5 ppm ^1H HMBC region. In the other regions, any interaction was observed.

13.1.3

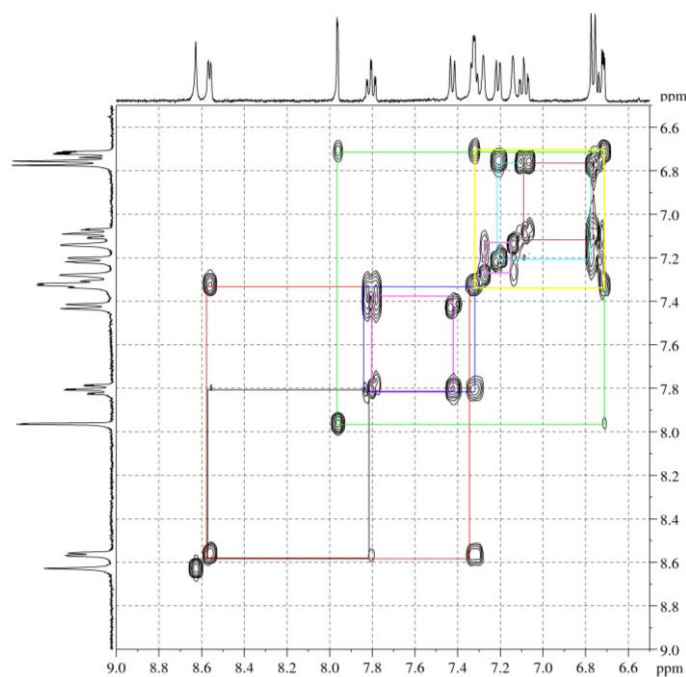
NMR spectra of ligand **H₃L2**

Figure 13.6. Correlation spectroscopy (^1H - ^1H COSY) NMR contour map (400 MHz) of **H₃L2** in $\text{DMSO}-d_6$ at room temperature in the 6.5–9.0 ppm region. In the other regions, any H–H interaction from different carbons was observed.

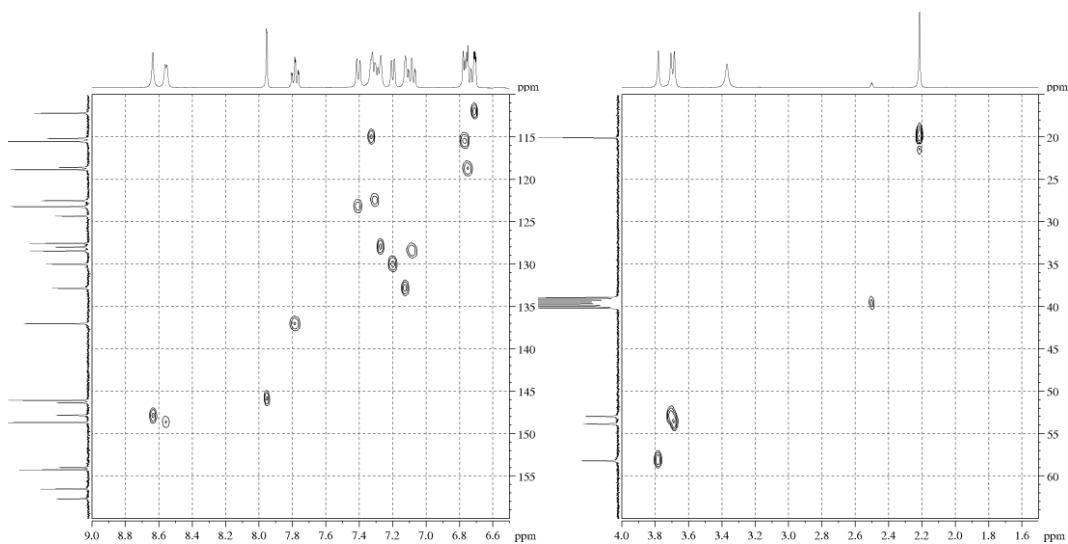


Figure 13.7. Quantum coherence (^1H - ^{13}C HSQC) NMR contour map of **H₃L2** in $\text{DMSO}-d_6$ at room temperature, in 9.0–6.6 ppm (left) and 4.0–1.5 ppm (right) ^1H HSQC region. In the other regions, any C–H interaction was observed.

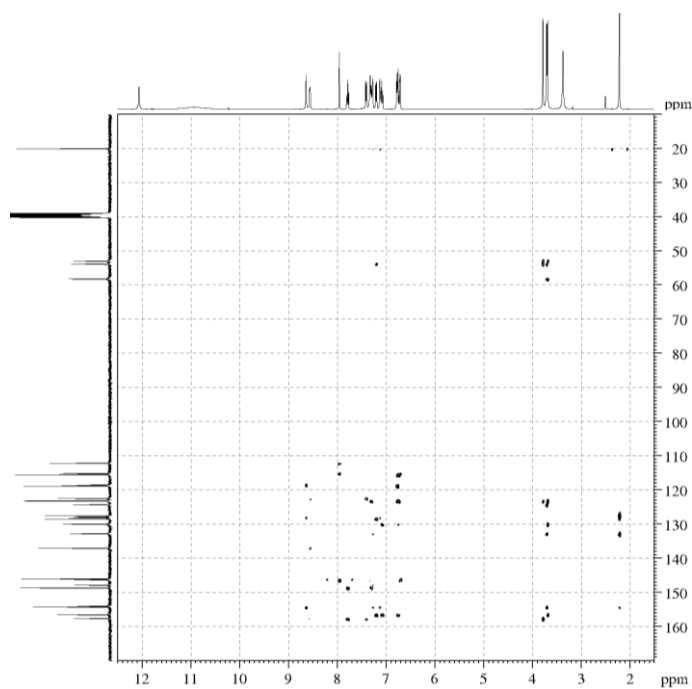


Figure 13.8. Bond correlation (^1H - ^{13}C HMBC) NMR contour map of **H₃L2** in $\text{DMSO}-d_6$ at room temperature.

13.1.4

NMR spectra of ligand **H₃L3**

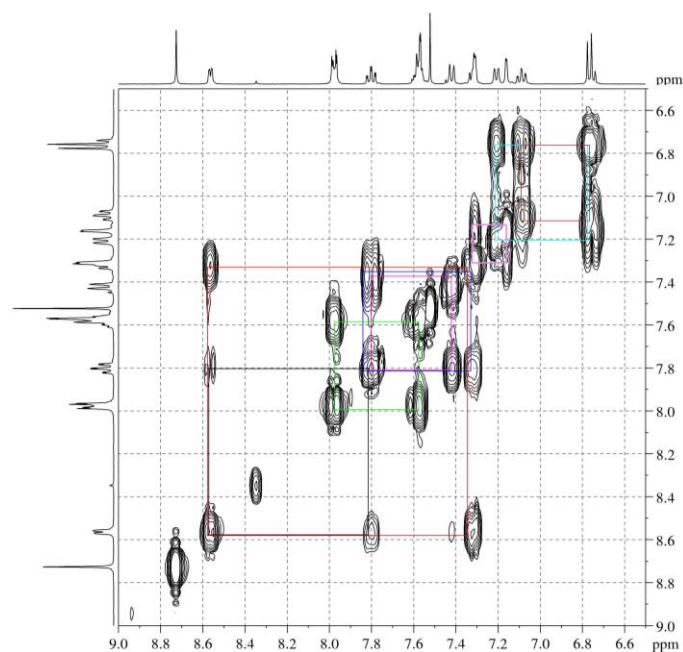


Figure 13.9. Correlation spectroscopy (^1H - ^1H COSY) NMR contour map (400 MHz) of **H₃L3** in $\text{DMSO}-d_6$ at room temperature in the 6.5–9.0 ppm region. In the other regions, any H–H interaction from different carbons was observed.

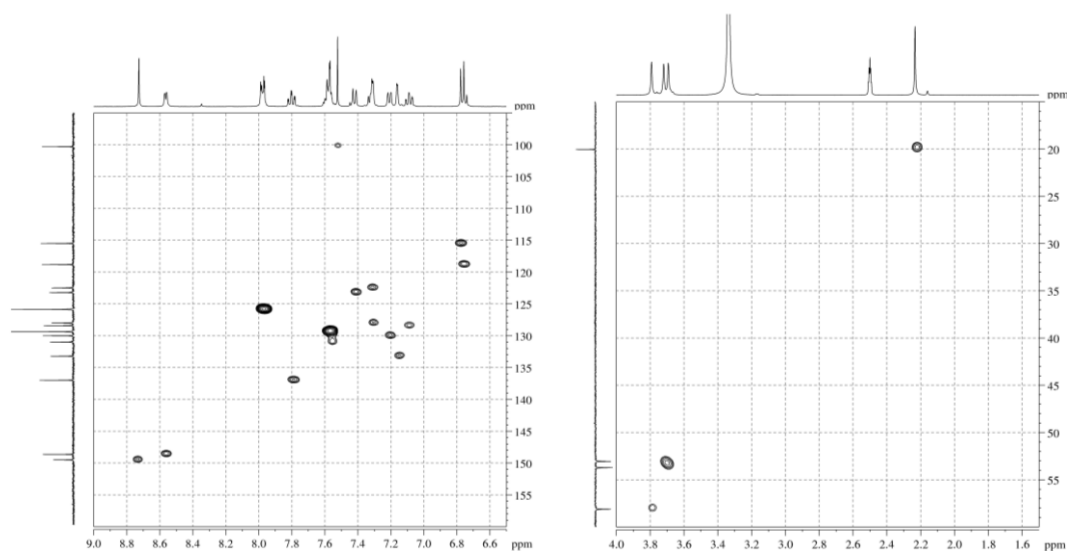


Figure 13.10. Quantum coherence (^1H – ^{13}C HSQC) NMR contour map of **H₃L₃** in $\text{DMSO}-d_6$ at room temperature, in the 9.0–6.6 ppm (left) and 4.0–1.5 ppm (right) ^1H HSQC region. In the other regions, any C–H interaction was observed.

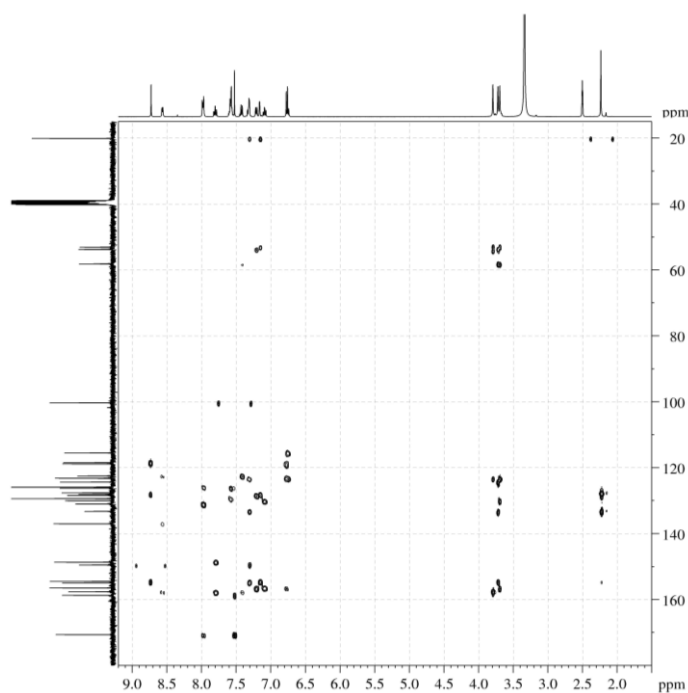


Figure 13.11. Bond correlation (^1H – ^{13}C HMBC) NMR contour map of **H₃L₃** in $\text{DMSO}-d_6$ at room temperature, in the 9.0–1.5 ppm ^1H HMBC region. In the other regions, any interaction was observed.

13.1.5

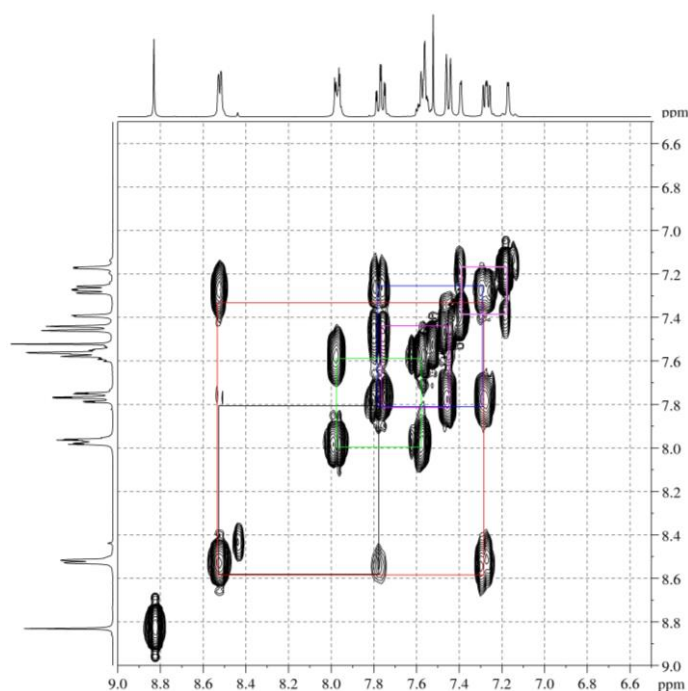
NMR spectra of ligand H₃L4

Figure 13.12. Correlation spectroscopy (^1H - ^1H COSY) NMR contour map (400 MHz) of **H₃L4** in $\text{DMSO}-d_6$ at room temperature in the 6.5–9.0 ppm region. In the other regions, any H–H interaction from different carbons was observed.

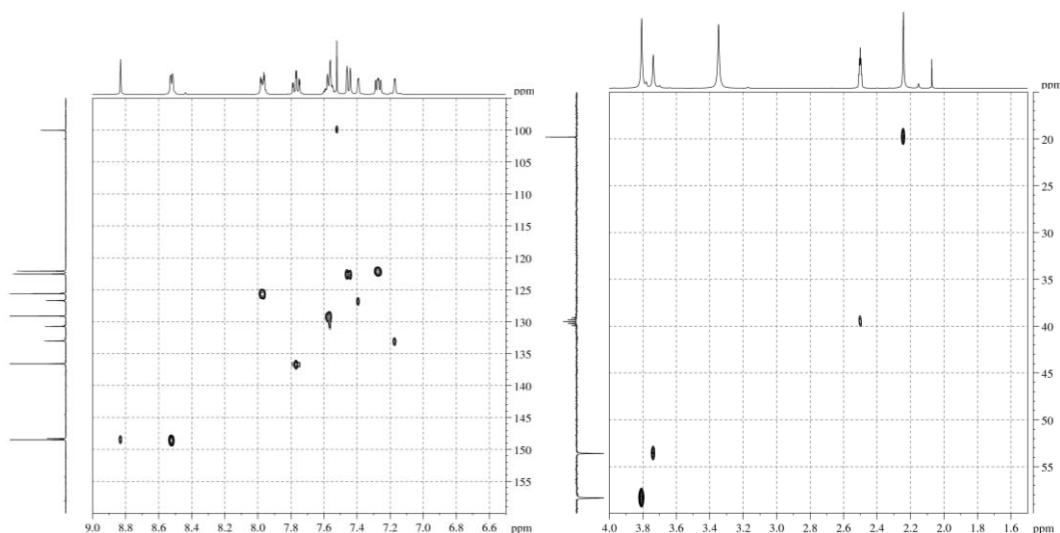


Figure 13.13. Quantum coherence (^1H - ^{13}C HSQC) NMR contour map of **H₃L4** in $\text{DMSO}-d_6$ at room temperature, in the 9.0–6.6 ppm (left) and 4.0–1.5 ppm (right) ^1H HSQC region. In the other regions, any C–H interaction was observed.

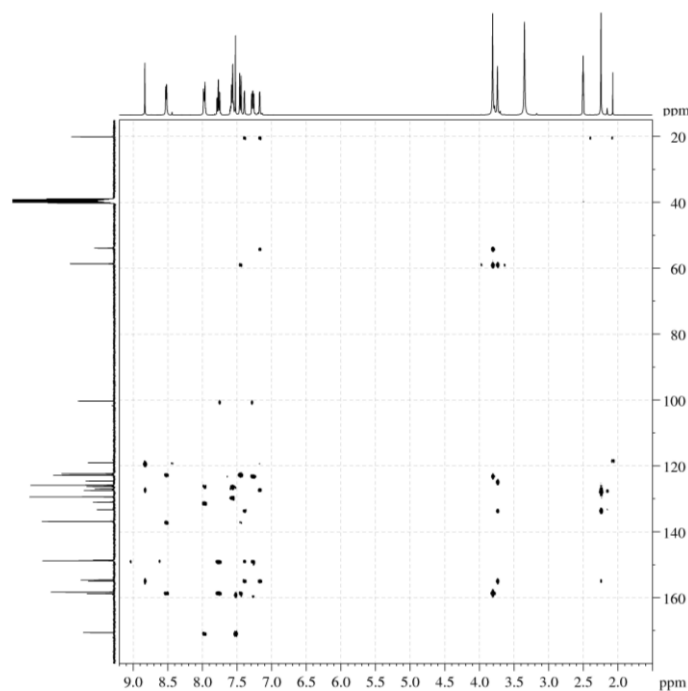


Figure 13.14. Bond correlation (^1H - ^{13}C HMBC) NMR contour map of **H₃L₃** in $\text{DMSO}-d_6$ at room temperature, in the 9.0–1.5 ppm ^1H HMBC region. One additional interaction was observed at 12.4 ppm x 54.7 ppm (^1H - ^{13}C HMBC).

13.1.6

NMR spectra of ligand H₃L₅

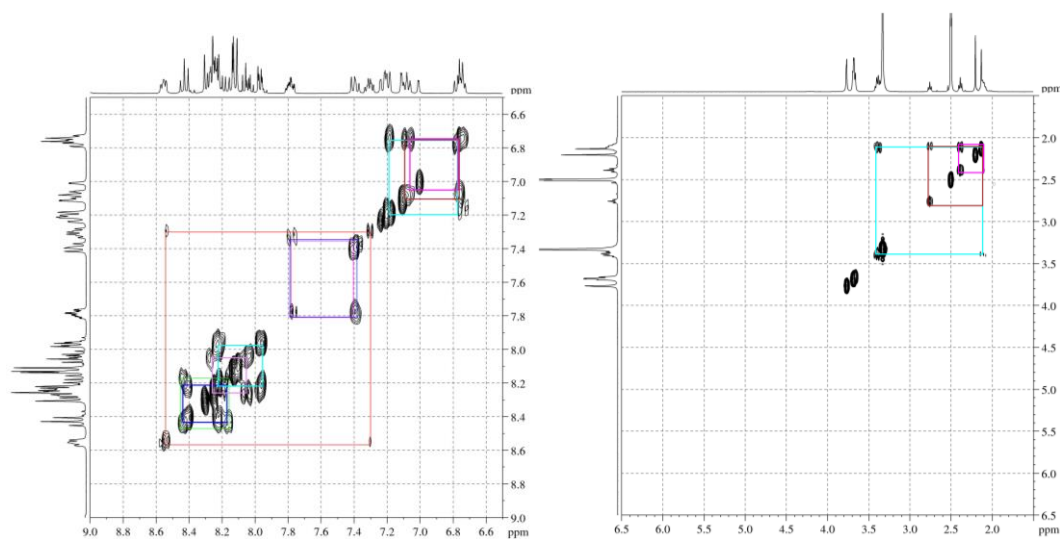


Figure 13.15. Correlation spectroscopy (^1H - ^1H COSY) NMR contour map (400 MHz) of **H₃L₅** in $\text{DMSO}-d_6$ at room temperature in the (left) 9.0–6.5 ppm region and in the (right) 6.5–1.5 ppm region. In the other regions, any H–H interaction from different carbons was observed.

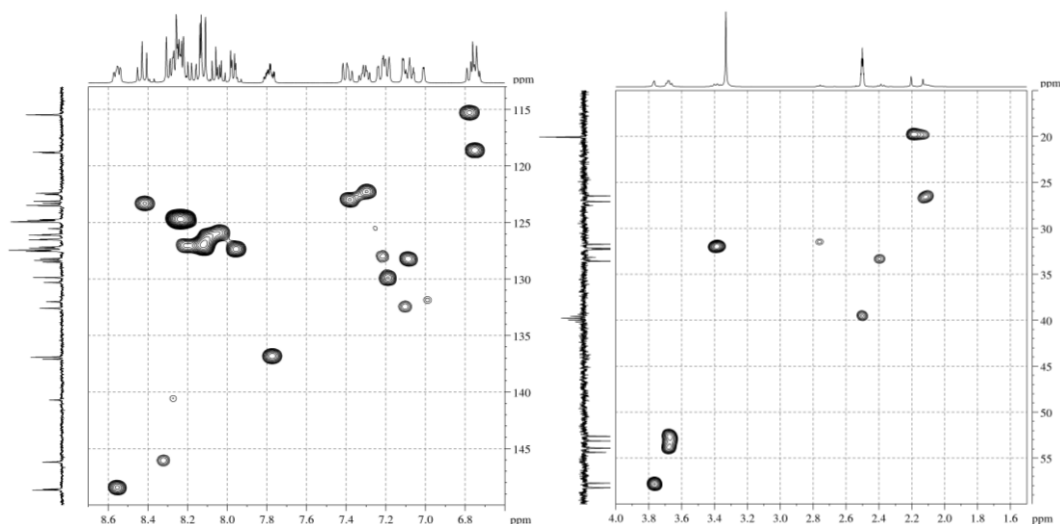


Figure 13.16. Quantum coherence (^1H - ^{13}C HSQC) NMR contour map of **H₃L5** in $\text{DMSO}-d_6$ at room temperature, in the 8.7–6.6 ppm (left) and 4.0–1.5 ppm (right) ^1H HSQC region. In the other regions, any C–H interaction was observed.

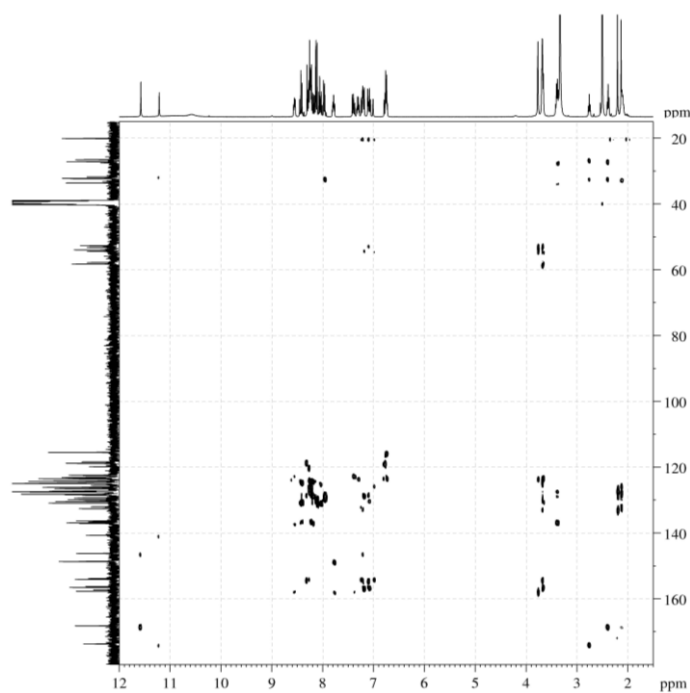


Figure 13.17. Bond correlation (^1H - ^{13}C HMBC) NMR contour map of **H₃L5** in $\text{DMSO}-d_6$ at room temperature, in the 12.0–1.5 ppm ^1H HMBC region.

13.1.7

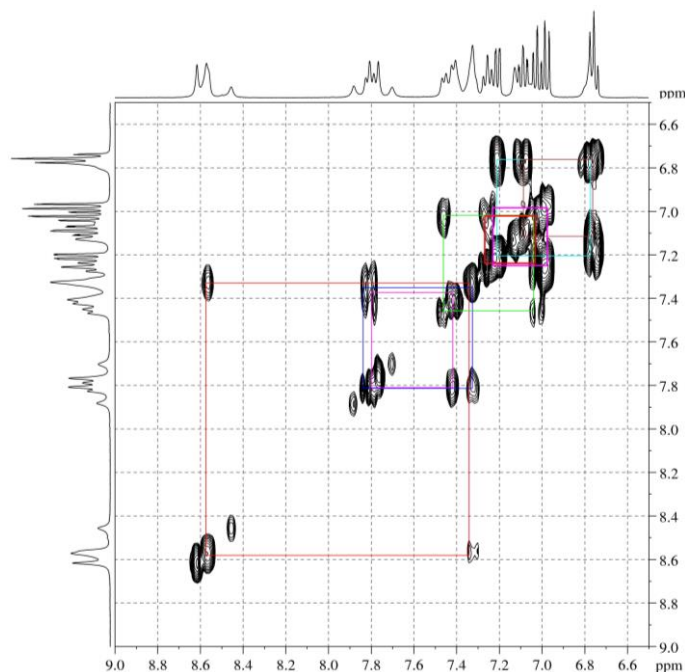
NMR spectra of ligand **H₃L6**

Figure 13.18. Correlation spectroscopy (^1H - ^1H COSY) NMR contour map (400 MHz) of **H₃L6** in $\text{DMSO}-d_6$ at room temperature in the 6.5–9.0 ppm region. In the other regions, any H–H interaction from different carbons was observed.

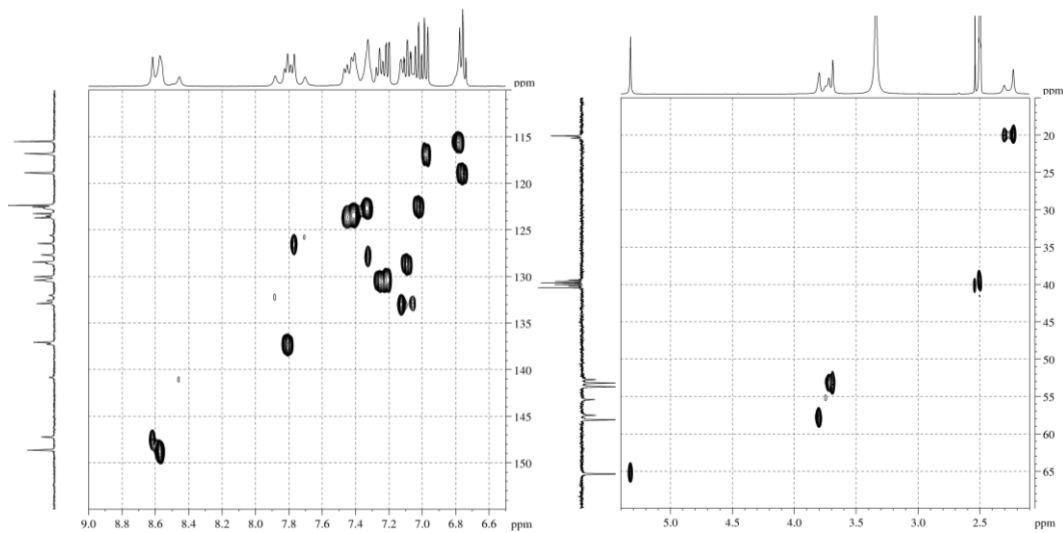


Figure 13.19. Quantum coherence (^1H - ^{13}C HSQC) NMR contour map of **H₃L6** in $\text{DMSO}-d_6$ at room temperature, in the 9.0–6.5 ppm (left) and 5.4–2.1 ppm (right) ^1H HSQC region. In the other regions, any C–H interaction was observed.

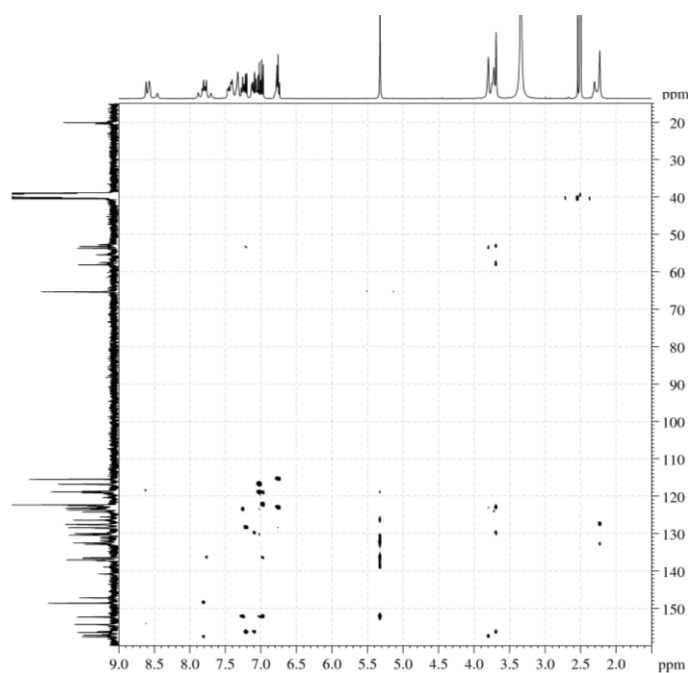


Figure 13.20. Bond correlation (^1H - ^{13}C HMBC) NMR contour map of **H₃L6** in $\text{DMSO}-d_6$ at room temperature, in the 9.0–1.5 ppm ^1H HMBC region. In the other regions, any interaction was observed.

13.1.8

NMR spectra of ligand H₃L7

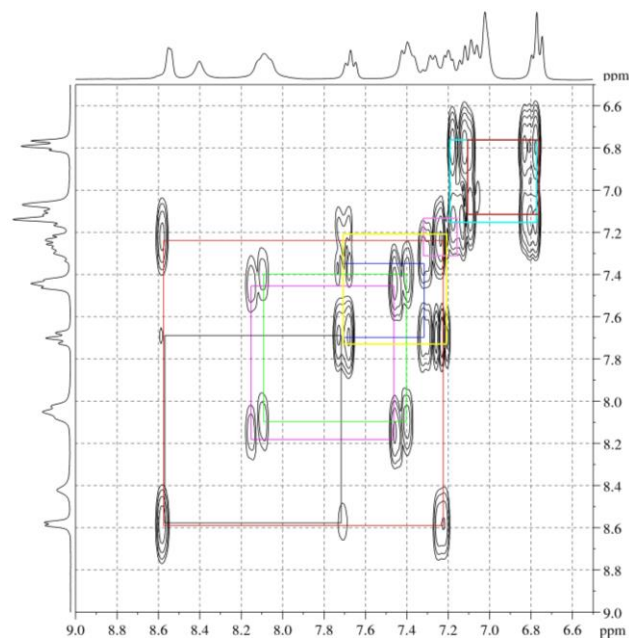


Figure 13.21. Correlation spectroscopy (^1H - ^1H COSY) NMR contour map (400 MHz) of **H₃L7** in $\text{DCM}-d_2$ at room temperature in the 6.5–9.0 ppm region. In the other regions, any H–H interaction from different carbons was observed.

13.1.9

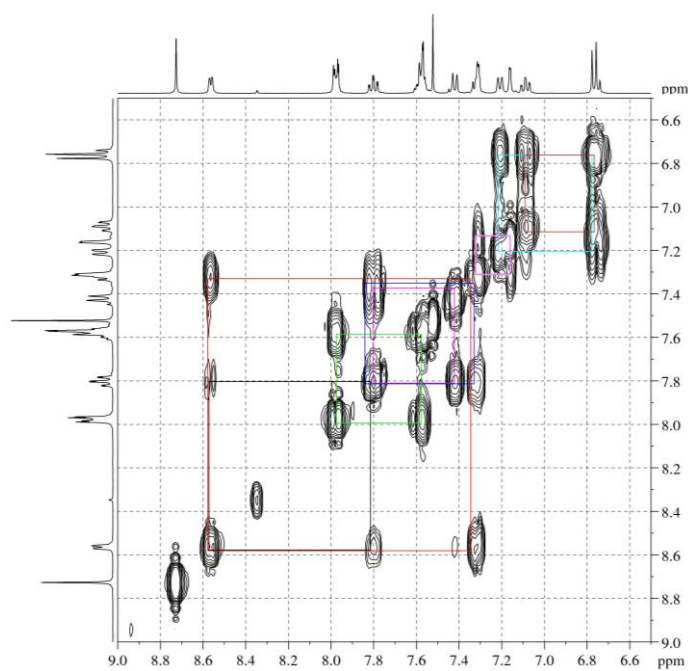
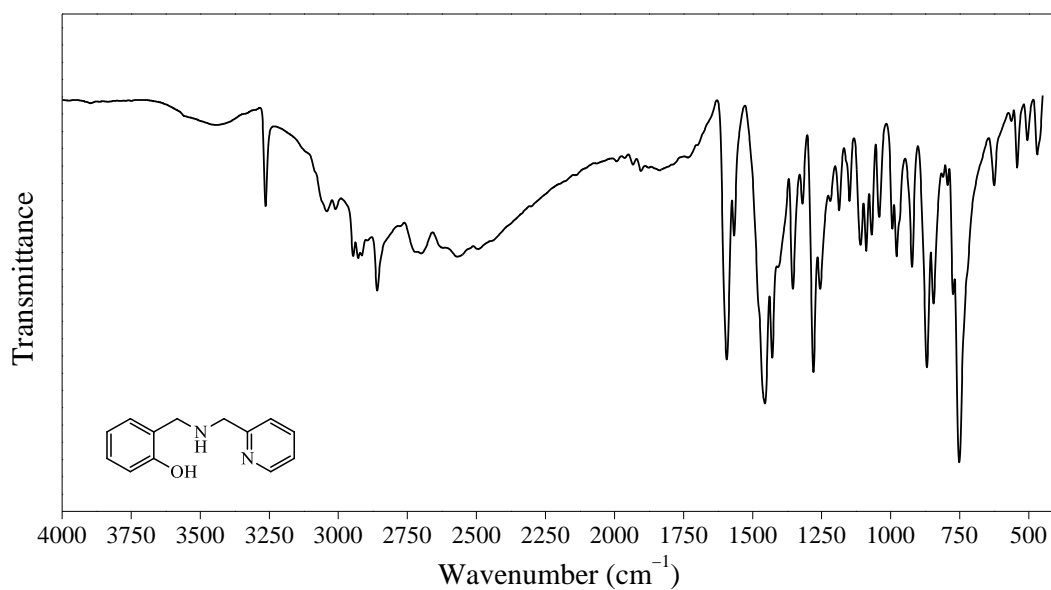
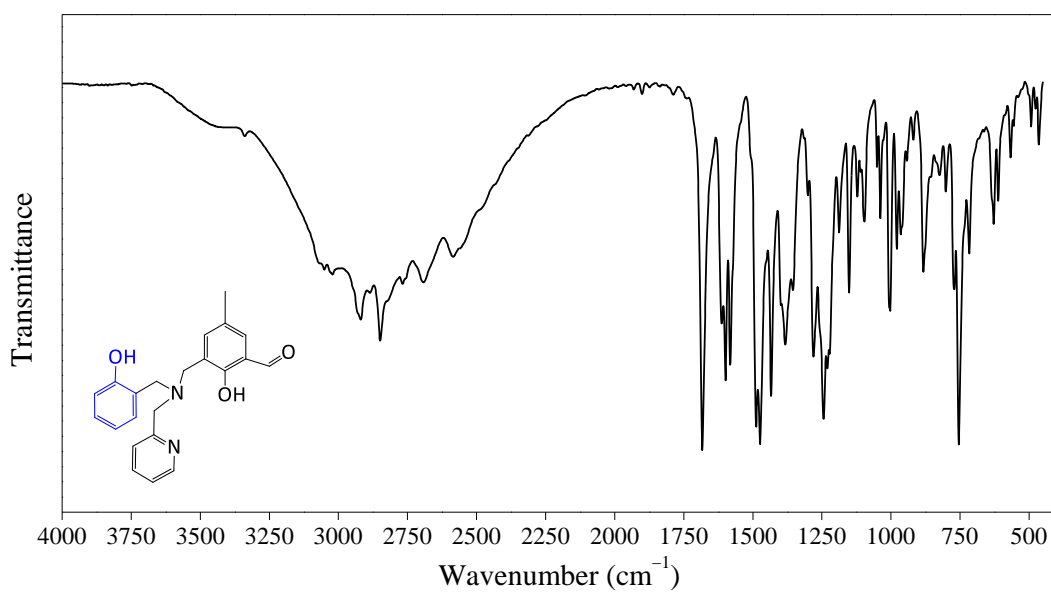
NMR spectra of ligand H₃L8

Figure 13.22. Correlation spectroscopy (^1H - ^1H COSY) NMR contour map (400 MHz) of **H₃L8** in $\text{DMSO}-d_6$ at room temperature in the 6.5–9.0 ppm region. In the other regions, any H–H interaction from different carbons was observed.

13.2

FTIR and Raman spectra

Figure 13.23. FTIR spectra of **HBPA** in KBr pellets.Figure 13.24. FTIR spectra of **HBPAMFF** in KBr pellets.

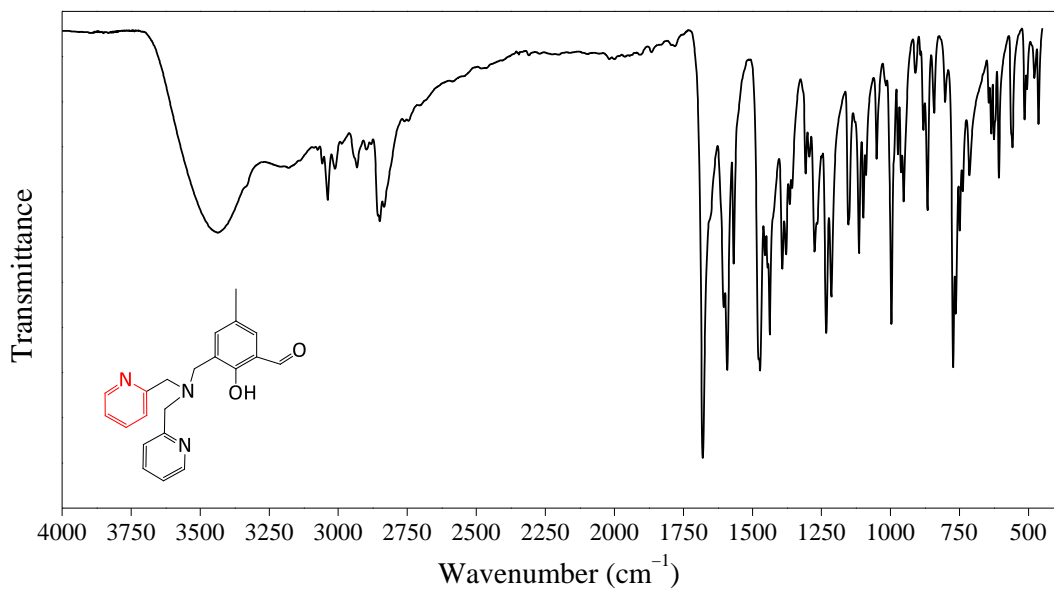


Figure 13.25. FTIR spectra of **BPMAMFF** in KBr pellets.

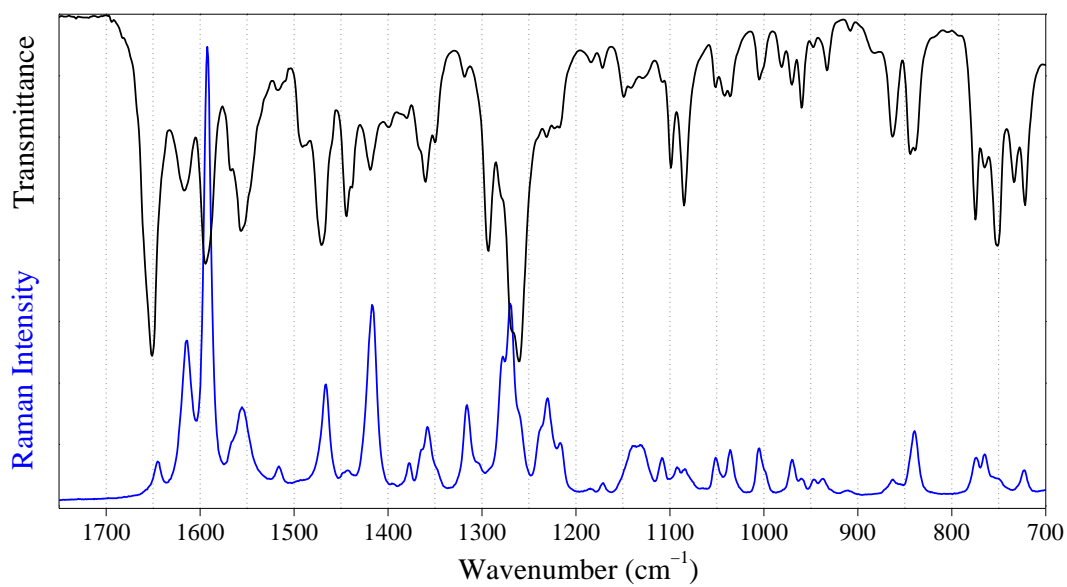


Figure 13.26. FTIR and Raman spectra of **H₃L1** in the region 1700–700 cm⁻¹.

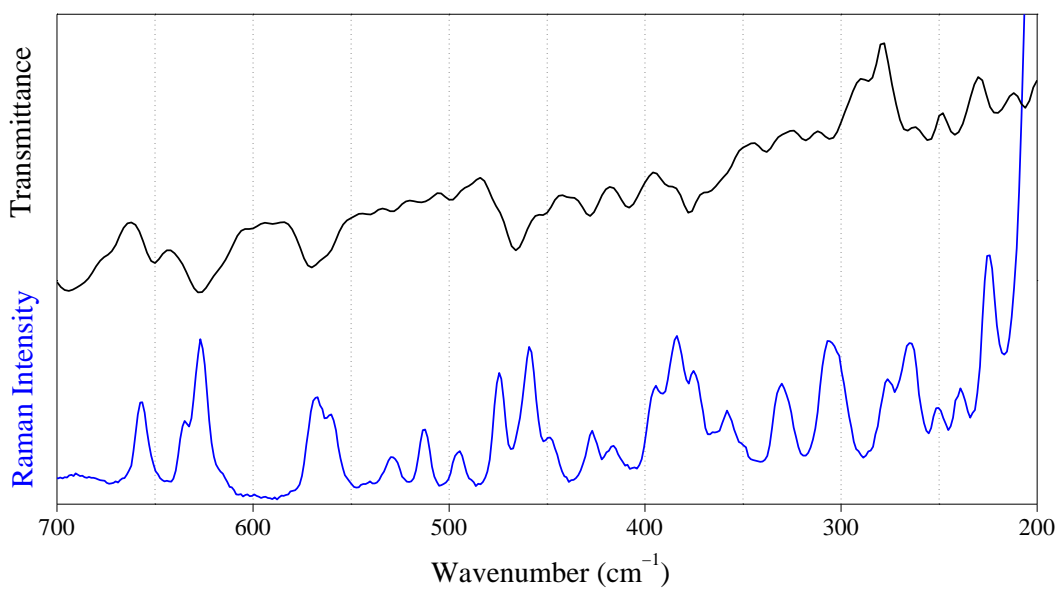


Figure 13.27. FTIR and Raman spectra of **H₃L1** in the region 700–200 cm^{-1} .

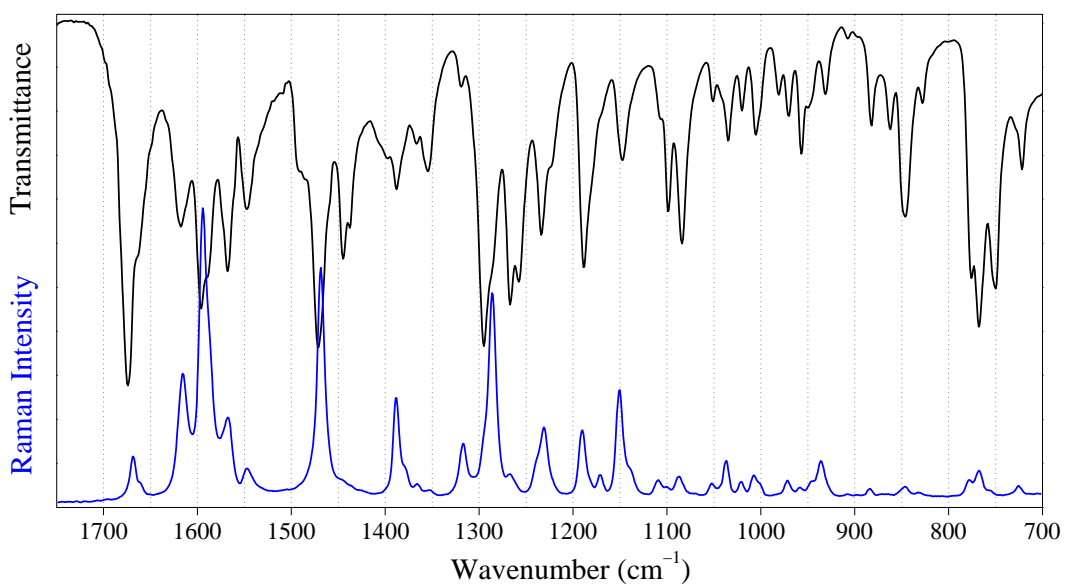


Figure 13.28. FTIR and Raman spectra of **H₃L2** in the region 1700–700 cm^{-1} .

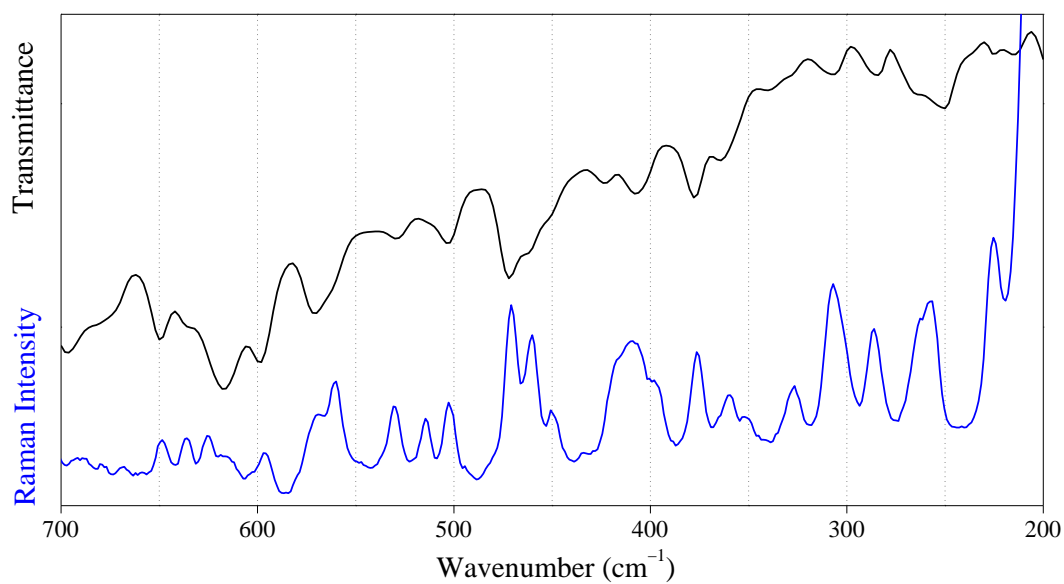


Figure 13.29. FTIR and Raman spectra of **H₃L2** in the region 700–200 cm^{-1} .

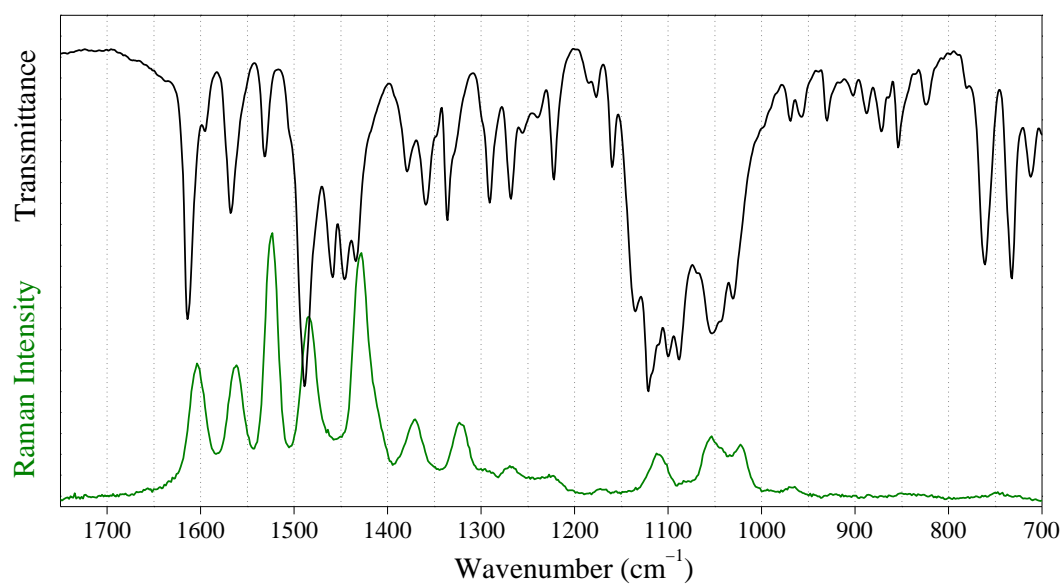


Figure 13.30. FTIR and Raman spectra of complex **1** in the region 1700–700 cm^{-1} .

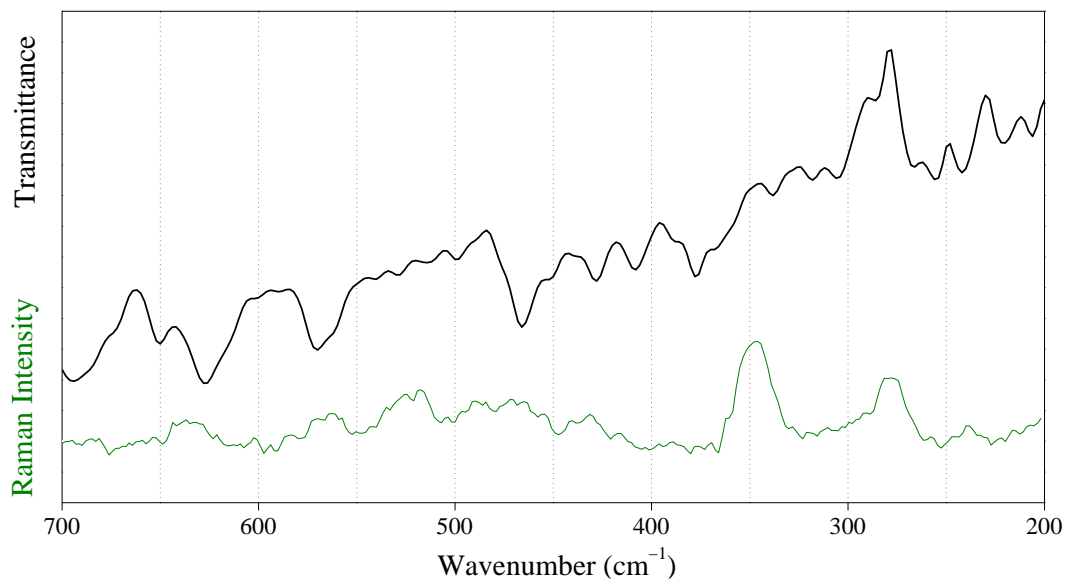


Figure 13.31. FTIR and Raman spectra of complex **1** in the region 700–200 cm^{-1} .

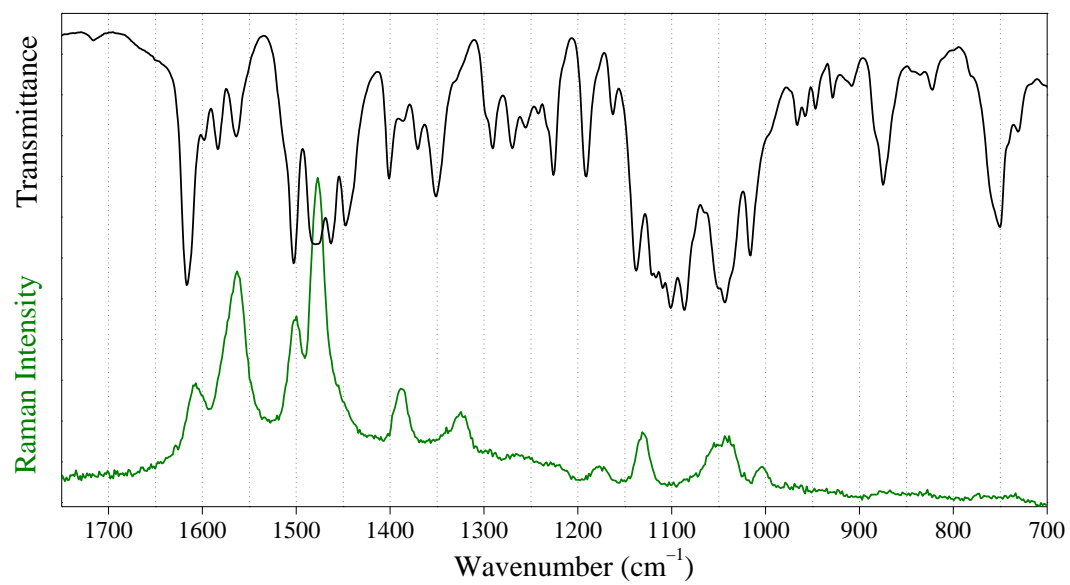


Figure 13.32. FTIR and Raman spectra of complex **2** in the region 1700–700 cm^{-1} .

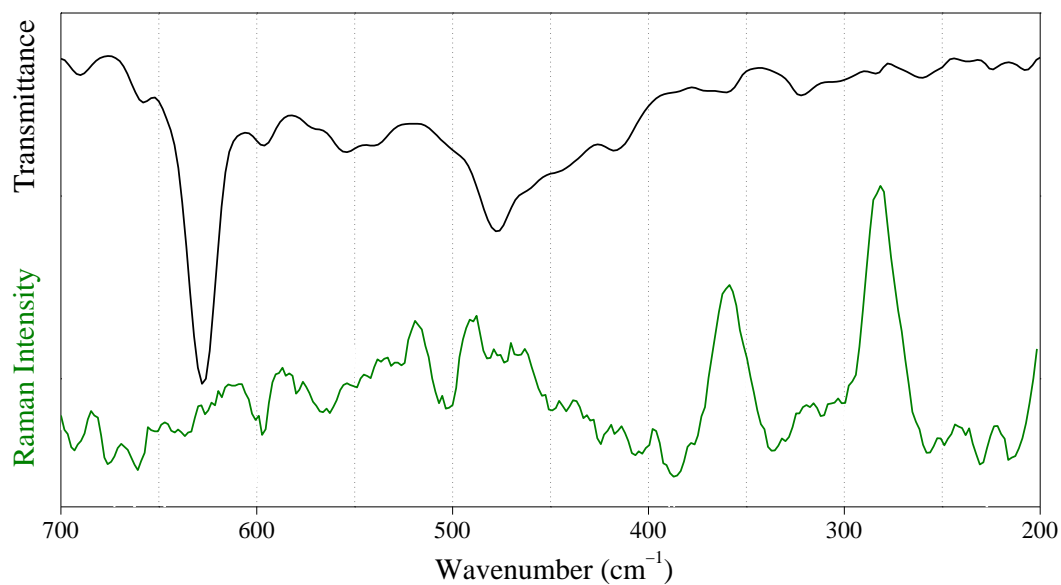


Figure 13.33. FTIR and Raman spectra of complex **2** in the region 700–200 cm^{-1} .

13.3

Fluorescence image of cells by confocal microscopy

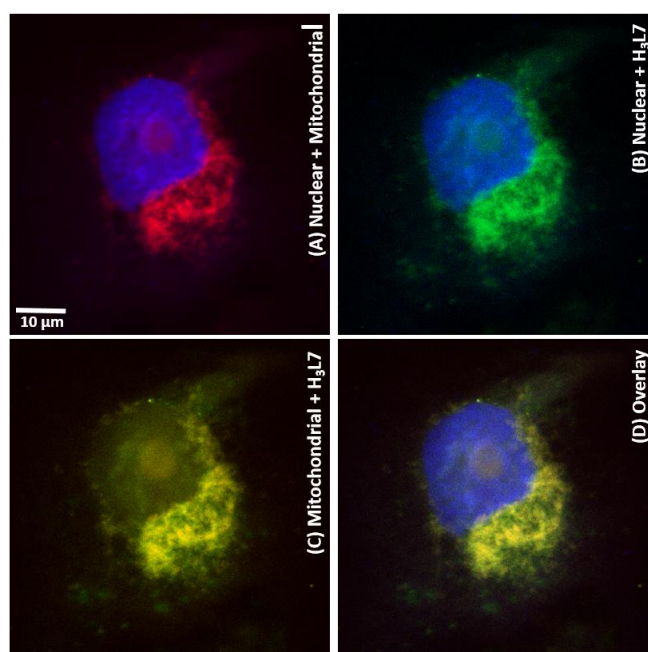


Figure 13.34. Fluorescence images of the cellular uptake and intracellular localization of ligand **H₃L7** in one MDA-MB-231 cell after incubation of 45 min at 37 °C with (A) DAPI (300 nM) and MTDR (200 nM), (B) DAPI and **H₃L7** (1 μM), and (C) MTDR and **H₃L7**. DAPI (A) was excited at 405 nm (emission = 410–450 nm); ligand **H₃L7** (B) at 488 nm (emission = 500–600 nm) and MTDR (C) at 552 nm (emission = 600–700 nm). Scale bar: 20 μM .

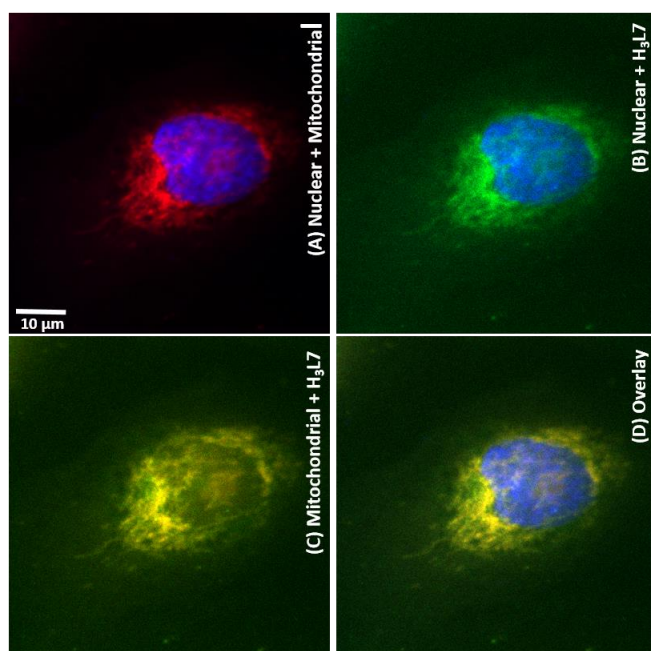


Figure 13.35. Fluorescence images of the cellular uptake and intracellular localization of ligand **H₃L7** in one MDA-MB-231 cell after incubation of 45 min at 37 °C with (A) DAPI (300 nM) and MTDR (200 nM), (B) DAPI and **H₃L7** (1 μM), and (C) MTDR and **H₃L7**. DAPI (A) was excited at 405 nm (emission = 410–450 nm); ligand **H₃L7** (B) at 488 nm (emission = 500–600 nm) and MTDR (C) at 552 nm (emission = 600–700 nm). Scale bar: 10 μM.

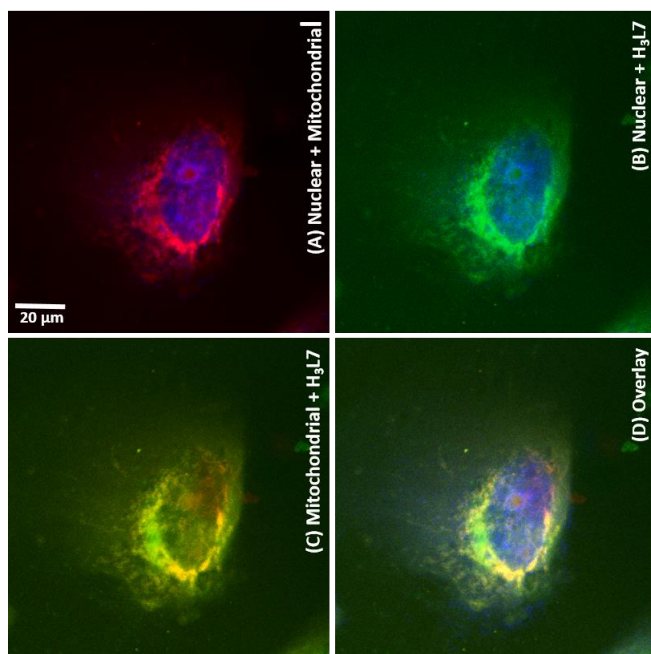


Figure 13.36. Fluorescence images of the cellular uptake and intracellular localization of ligand **H₃L7** in one MDA-MB-231 cell after incubation of 45 min at 37 °C with (A) DAPI (300 nM) and MTDR (200 nM), (B) DAPI and **H₃L7** (1 μM), and (C) MTDR and **H₃L7**. DAPI (A) was excited at 405 nm (emission = 410–450 nm); ligand **H₃L7** (B) at 488 nm (emission = 500–600 nm) and MTDR (C) at 552 nm (emission = 600–700 nm). Scale bar: 20 μM.

13.4

Fluorescence spectra of complexes 9–12

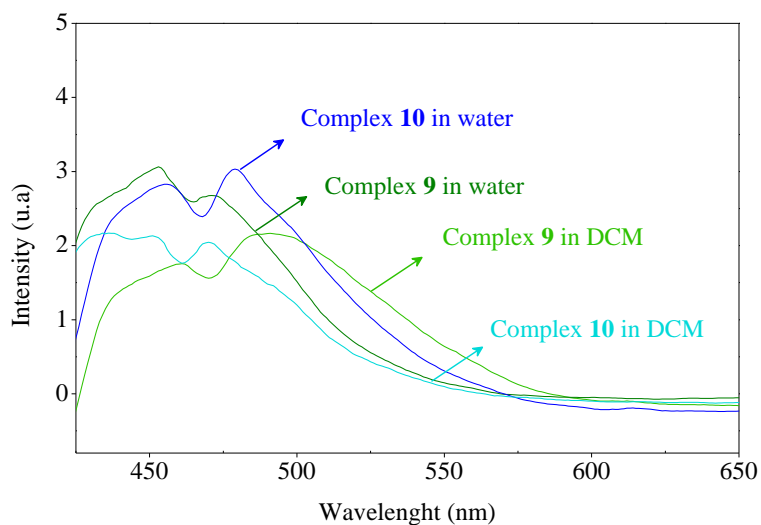


Figure 13.37. Fluorescence emission spectra of complexes **9** ($\lambda_{\text{excitation}} = 406 \text{ nm}$; $7 \mu\text{M}$) and **10** ($\lambda_{\text{excitation}} = 407 \text{ nm}$; $10 \mu\text{M}$) in water and DCM at 298 K.

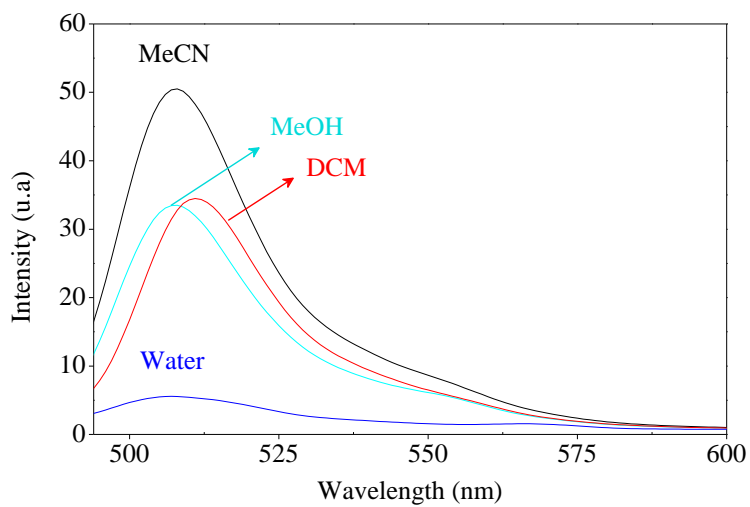


Figure 13.38. Fluorescence emission spectra of complex **11** ($\lambda_{\text{excitation}} = 483 \text{ nm}$; $1 \mu\text{M}$) in water and organic solvents at 298 K.

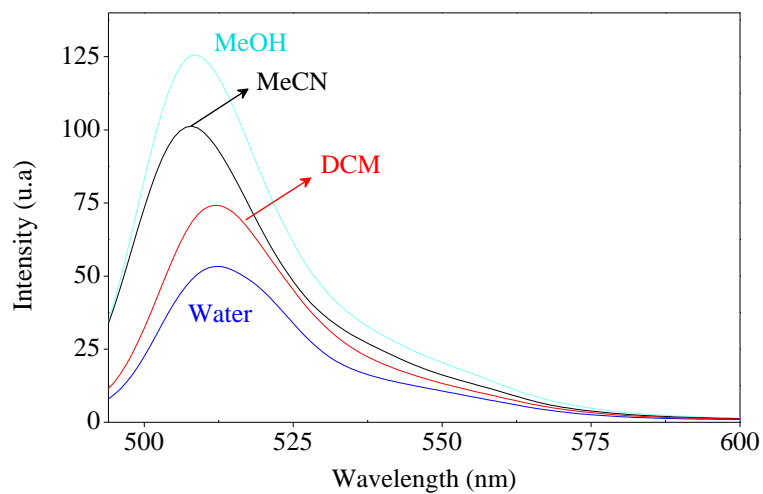


Figure 13.39. Fluorescence emission spectra of complex **12** ($\lambda_{\text{excitation}} = 483 \text{ nm}$; $0.33 \mu\text{M}$) in water and organic solvents at 298 K.

Attachment C: Compounds terminology

Table 13.1. Relation of the ligands terminology between the laboratory notebook, thesis manuscript and redacted papers. Chapter describing each compound is also included.

| Thesis Manuscript | Laboratory notebook | Redacted Paper | Thesis Chapter | Structure |
|-------------------|---------------------|----------------|----------------|-----------|
| H3L1 | L3 | H3L1 | 4 | |
| H3L2 | L2 | H3L2 | 4 | |
| H3L3 | L5 | H3L1 | 5 | |
| H2L4 | L8 | H2L2 | 5 | |
| H3L5 | L4 | H3L1 | 6 | |

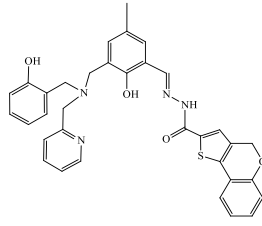
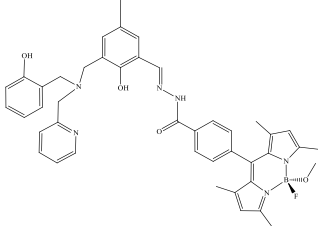
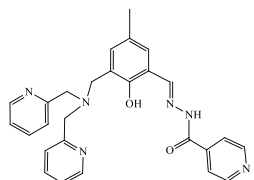
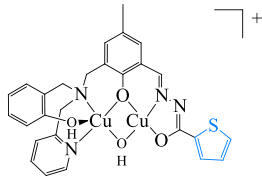
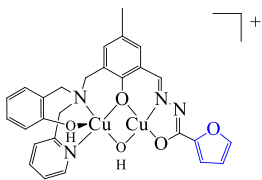
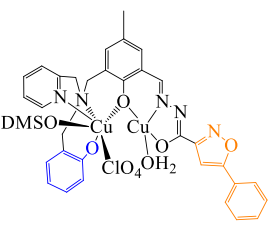
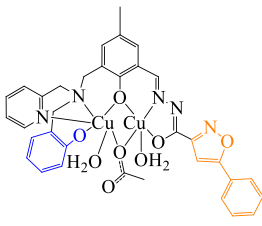
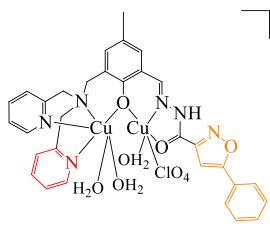
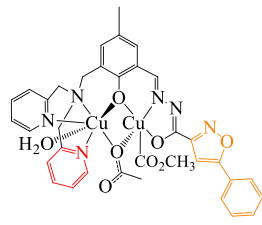
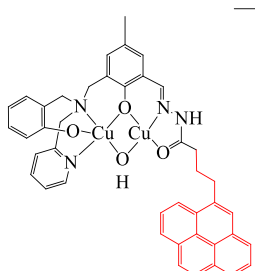
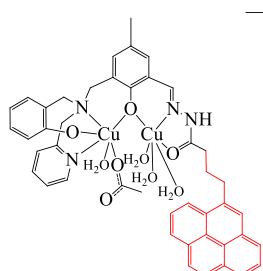
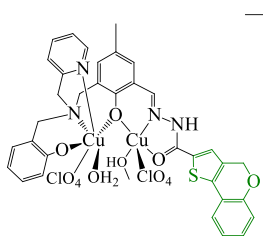
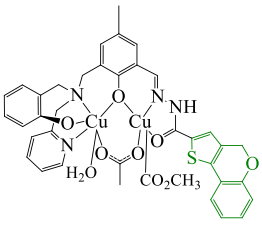
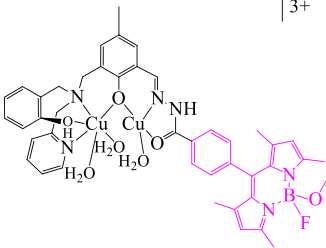
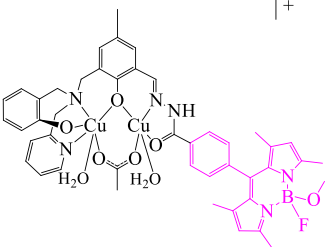
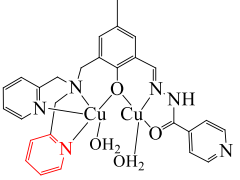
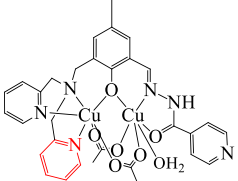
| Thesis Manuscript | Laboratory notebook | Redacted Paper | Thesis Chapter | Structure |
|-------------------|---------------------|----------------|----------------|--|
| H3L6 | L6 | – | 7 |  |
| H3L7 | L9 | – | 7 |  |
| H2L8 | L7 | – | 8 |  |

Table 13.2. Relation of the complexes terminology between the laboratory notebook, thesis manuscript and redacted papers. Chapter describing each compound is also included.

| Thesis Manuscript | Laboratory notebook | Redacted Paper | Thesis Chapter | Structure |
|-------------------|---------------------|----------------|----------------|--|
| Complex 1 | P3/P3OH/C3 | Complex 1 | 4 |  |
| Complex 2 | P2A/P2OH/C2 | Complex 2 | 4 |  |
| Complex 3 | P5A | Complex 1 | 5 |  |

| Thesis Manuscript | Laboratory notebook | Redacted Paper | Thesis Chapter | Structure |
|-------------------|---------------------|----------------|----------------|--|
| Complex 4 | P5B | Complex 2 | 5 |  $\left[\right]^{2+}$ |
| Complex 5 | P8A | Complex 3 | 5 |  $\left[\right]^{2+}$ |
| Complex 6 | P8B | Complex 4 | 5 |  $\left[\right]^{+}$ |
| Complex 7 | P4/P4A/C4 | Complex 1 | 6 |  $\left[\right]^{+}$ |
| Complex 8 | P4B/P4acetato | Complex 2 | 6 |  $\left[\right]^{+}$ |
| Complex 9 | P6A | - | 7 |  $\left[\right]^{+}$ |

| Thesis Manuscript | Laboratory notebook | Redacted Paper | Thesis Chapter | Structure |
|-------------------|---------------------|----------------|----------------|---|
| Complex 10 | P6B | – | 7 |  $\left[\right]^{3+}$ |
| Complex 11 | P9A | – | 7 |  $\left[\right]^{3+}$ |
| Complex 12 | P9B | – | 7 |  $\left[\right]^+$ |
| Complex 13 | P7A | – | 8 |  $\left[\right]^{3+}$ |
| Complex 14 | P7B | – | 8 |  $\left[\right]^{3+}$ |